



ASTES

# Advances in Science, Technology & Engineering Systems Journal



VOLUME 8-ISSUE 3 | MAY-JUN 2023

[www.astesj.com](http://www.astesj.com)

ISSN: 2415-6698

## EDITORIAL BOARD

### Editor-in-Chief

**Prof. Passerini Kazmerski**  
University of Chicago, USA

### Editorial Board Members

**Dr. Jiantao Shi**  
Nanjing Research Institute  
of Electronic Technology,  
China

**Dr. Tariq Kamal**  
University of Nottingham, UK  
Sakarya University, Turkey

**Dr. Hongbo Du**  
Prairie View A&M University, USA

**Dr. Nguyen Tung Linh**  
Electric Power University,  
Vietnam

**Prof. Majida Ali Abed  
Meshari**  
Tikrit University Campus,  
Iraq

**Dr. Mohmaed Abdel Fattah Ashabrawy**  
Prince Sattam bin Abdulaziz University,  
Saudi Arabia

**Mohamed Mohamed  
Abdel-Daim**  
Suez Canal University,  
Egypt

**Dr. Omeje Maxwell**  
Covenant University, Nigeria

**Mr. Muhammad Tanveer Riaz**  
School of Electrical Engineering, Chongqing  
University, P.R. China

**Dr. Heba Afify**  
MTI university, Cairo, Egypt

**Mr. Randhir Kumar**  
National University of  
Technology Raipur, India

**Dr. Serdar Sean Kalaycioglu**  
Toronto Metropolitan University, Canada

**Dr. Daniele Mestriner**  
University of Genoa, Italy

### Regional Editors

**Dr. Hung-Wei Wu**  
Kun Shan University,  
Taiwan

**Dr. Maryam Asghari**  
Shahid Ashrafi Esfahani,  
Iran

**Dr. Shakir Ali**  
Aligarh Muslim University, India

**Dr. Ahmet Kayabasi**  
Karamanoglu Mehmetbey  
University, Turkey

**Dr. Ebubekir Altuntas**  
Gaziosmanpasa University,  
Turkey

**Dr. Sabry Ali Abdallah El-Naggar**  
Tanta University, Egypt

**Mr. Aamir Nawaz**  
Gomal University, Pakistan

**Dr. Gomathi Periasamy**  
Mekelle University, Ethiopia

**Dr. Walid Wafik Mohamed Badawy**  
National Organization for Drug Control  
and Research, Egypt

**Dr. Abhishek Shukla**  
R.D. Engineering College,  
India

**Mr. Abdullah El-Bayoumi**  
Cairo University, Egypt

**Dr. Ayham Hassan Abazid** Jordan  
University of Science and Technology,  
Jordan

**Mr. Manu Mitra**  
University of Bridgeport, USA

**Dr. Qichun Zhang**  
University of Bradford, United Kingdom

## Editorial

In this edition of our journal, we are pleased to present a collection of 31 accepted research papers, each contributing valuable insights to their respective fields. The diverse range of topics covered in these papers reflects the breadth and depth of contemporary research endeavors. From educational strategies to economic modeling, from healthcare applications to technological innovations, these papers showcase the remarkable progress made by scholars and researchers in addressing complex challenges.

The initial paper introduces a computer-based tutoring strategy aimed at addressing school dropout issues in Morocco. Focusing on collaboration between educational administration and teachers at the national level, the proposed strategy utilizes a computerized system based on student learning and evaluation portfolios. This approach aims to provide personalized assistance, considering individual student shortcomings and didactic needs [1].

Employing Markov Regime Switching Analysis, the second paper investigates the dynamic linkages between COVID-19 outbreak situations and the German stock market. The study evaluates the impact of pandemic situations on the market, utilizing log growth rates and GARCH models. Practical econometric methods are presented, demonstrating their applicability in assessing the impact of various epidemics and negative factors on economic activities [2].

The study in the third paper addresses the challenge of limited interactive communication modes in online learning environments. The authors construct and test models to infer student needs based on facial expressions. Utilizing Random Forest models and the Facial Action Coding System, the study suggests methods to enhance real-time understanding of student responses in online learning systems [3].

A measurement system is presented to evaluate radar algorithms for vital signs sensing applications. The system generates reproducible vital sign micro-movement and dynamic clutter scenarios using loudspeakers. The study demonstrates the system's capability to assess the impact of a beamforming algorithm on dynamic clutter, showcasing its potential for medical applications [4].

Addressing the complexity of indoor positioning, the fifth paper provides an agile taxonomy for selecting suitable solutions. The study analyzes a real-world scenario, offering practical recommendations for indoor positioning applications. The research contributes to understanding the diverse requirements and implications of indoor positioning techniques [5].

It introduces a navigation aid device for visually impaired individuals. The device utilizes a depth camera to collect visual information of surrounding objects, representing it through stereophonic sound. The portable and comfortable device demonstrated high accuracy in obstacle detection and navigation, offering a promising solution for visually impaired users [6].

Extending Quantum Machine Learning to weather forecasting, the seventh paper applies classifiers like Quantum Support Vector Machine and Quantum Neural Networks. The study discusses the potential of quantum algorithms in predicting weather conditions and highlights the importance of testing their performance on real-world datasets [7].

Exploring short-term pulse rate variability as a substitute for heart rate variability in evaluating emotional changes during the Trier Social Stress Test, the eighth paper reveals that physiological changes in pulse rate variability may represent psychological changes. The study emphasizes the need for cautious interpretation of physiological alterations as indicators of mental threats [8].

Adopting a human-centered design approach, the ninth paper addresses the lack of situational awareness in power system outages. The study develops interfaces for a microgrid project, emphasizing the need for accessible and timely information for microgrid operators [9].

Introduces HistoChain, a scalable storage scheme for consortium blockchain networks. The system efficiently manages on-chain big data by utilizing both current and historical blockchains, demonstrating its potential for applications requiring secure and immutable data storage [10].

A landmarking technique is proposed to optimize YOLO version 4 for fish recognition in diverse background conditions. The study introduces a method to improve detection accuracy, making it applicable for both underwater and terrestrial fish recognition scenarios [11].

A wireless sensor-based volume estimation technique for sealed boxes, utilizing machine learning algorithms. The proposed system achieves high accuracy in volume estimation without the need for unpacking, offering an efficient solution for monitoring product transportation [12].

It introducing social financial technologies aiming to optimize wages, revenue growth, and contributions to the development fund for enterprise and economic development, the thirteenth paper presents a comprehensive model for improving the efficiency of economic development processes [13].

A phase shifter design with electrically adjustable parameters is introduced, utilizing a single voltage differencing gain amplifier (VDGA) and a floating capacitor. The resistorless design offers practical advantages with a low component count [14].

It conducts a technical, economic, and environmental study of hybrid power systems for grid-connected and standalone applications. The study compares two configurations and emphasizes the suitability and cost-effectiveness of a grid-connected hybrid system for meeting specific power consumption needs [15].

A review of photoluminescence properties of Eu(III) complexes with two different phosphine oxide structures is presented. The study highlights the potential applications of these complexes in micro-LEDs, security, and sensing devices, emphasizing their significance as red phosphors in micro-LED displays [16].

Medical adherence is a global concern, particularly for patients managing multiple medications. Addressing this issue, a proposed automated medicinal-pill dispenser integrates Wi-Fi and cellular IoT, offering a cost-effective solution for home and long-term care settings. The device's web interface allows users to control dosage, potentially improving patient adherence and overall health outcomes [17].

The COVID-19 pandemic has underscored the need for innovative healthcare solutions. In response, a microcontroller-based smart healthcare kit has been developed for measuring vital signs at home. Utilizing multiple sensors, this low-cost system presents a convenient alternative to traditional checkups, especially in regions facing healthcare infrastructure challenges [18].

Renewable energy sources, specifically land-based solar power generation, are gaining significance. A numerical study employing the Strength Reduction Method assesses the safety factor of solar facilities on varying terrains. The research investigates the impact of slope angle and water level changes, providing insights into safety considerations for solar power installations [19].

Bitcoin's exponential growth prompts a study forecasting prices using an LSTM deep-learning approach with On-Chain Data. This research fills a gap by leveraging transaction data from the blockchain network. The application of LSTM provides a novel perspective on predicting Bitcoin prices, considering macroeconomic variables and investor sentiment [20].

In the realm of medical robotics, soft swimming milli-robots designed for magnetic navigation in biomedical environments are explored. The study investigates the influence of magnetic moments, particularly orientation and strength, on swimming behavior and performance. The findings contribute to the design of soft robots for medical applications [21].

Power systems see innovation with the introduction of a three-phase Continuously Variable Series Reactor (CVSR). Modeled using a Gyration-Capacitor approach, the research delves into the performance and operational characteristics of CVSR, considering ferromagnetic core nonlinearities. This deepens our understanding of this device's utilization in power grids [22].

To ensure the quality of electric power systems, another study addresses bad voltage drop buses through minimum static VAR compensation. The research presents a compensating model to increase voltage to the minimum safety limit, showcasing results on the IEEE 9 bus system. The findings contribute to maintaining optimal bus voltages and system stability [23].

Amidst the challenges posed by the COVID-19 pandemic, a design-based research approach supports the development of enriching rural STEM camps. The study outlines barriers, decisions, and best practices in transitioning to virtual STEM enrichment programming. The insights gained from this rapid adaptation can guide other STEM providers facing similar challenges [24].

Decentralized public platforms are explored in the context of the Waterfall platform. This article details the fundamental principles of the economic policy integrated into Waterfall, a DAG-based system architecture. The economic leverages discussed aim to create a favourable environment, ensuring equilibrium and affordable transaction fees across decentralized platforms [25].

In robotics, a simulation of obstacle detection based on optical flow images is presented for mobile robot avoidance control. The study divides optical flow vectors to detect hazardous areas, allowing the robot to avoid obstacles and navigate safely. The proposed simulation enhances the robot's ability to recognize obstacles and ensure effective avoidance [26].

China's internet financial industry evolution is examined, emphasizing fintech's critical role. The study provides an overview of fintech's historical trajectory, recent developments, and potential risks. Using a VAR model, the research identifies key factors influencing China's electronic payment landscape, offering insights into future developments [27].

Addressing the need for robust license plate recognition, a research paper introduces an intelligent model trained on multiple fonts and diverse conditions in Morocco. Leveraging Yolov5 and Detectron2 frameworks, the proposed model achieves high precision in recognizing plates under challenging conditions, contributing to improved public safety [28].

Concluding the compilation, a study focuses on the design, optimization, and experimental study of hub and axial flux BLDC motors for light electric vehicles. The research compares the efficiency of both motors, offering insights into their performance under various parameters. The study's optimization using a genetic algorithm contributes to enhanced motor efficiency. This compilation offers a glimpse into a wide spectrum of technological advancements, providing unique insights in each domain. The research presented here contributes to the ongoing progress and innovation, inspiring further exploration and discussion within the scientific community [29].

## References:

- [1] S. Nai, A. Rifai, A. Sadiq, M. Bakrim, "Detailed Study of a Proposal for a Computer Based Tutoring Strategy," *Advances in Science, Technology and Engineering Systems Journal*, **8**(3), 1–10, 2023, doi:10.25046/aj080301.
- [2] K. Tan, S. Tokinaga, "Markov Regime Switching Analysis for COVID-19 Outbreak Situations and their Dynamic Linkages of German Market," *Advances in Science, Technology and Engineering Systems Journal*, **8**(3), 11–18, 2023, doi:10.25046/aj080302.
- [3] Y. Yan, E.W. Cooper, R. Lee, "Inferring Student Needs Based on Facial Expression in Video Images," *Advances in Science, Technology and Engineering Systems Journal*, **8**(3), 19–28, 2023, doi:10.25046/aj080303.
- [4] C. Domnik, D. Erni, C. Degen, "Measurement System for Evaluation of Radar Algorithms using Replication of Vital Sign Micro Movement and Dynamic Clutter," *Advances in Science, Technology and Engineering Systems Journal*, **8**(3), 29–39, 2023, doi:10.25046/aj080304.
- [5] J.P. Balbela, A.P. Bianzino, "Indoor Positioning: Comparing Different Techniques and Dealing with a user Authentication use Case," *Advances in Science, Technology and Engineering Systems Journal*, **8**(3), 40–47, 2023, doi:10.25046/aj080305.
- [6] H. Kusuma, M. Attamimi, J. Sintara, "Navigation Aid Device for Visually Impaired using Depth Camera," *Advances in Science, Technology and Engineering Systems Journal*, **8**(3), 48–53, 2023, doi:10.25046/aj080306.
- [7] C. Khemapatapan, T. Thepsena, "Forecasting the Weather behind Pa Sak Jolasid Dam using Quantum Machine Learning," *Advances in Science, Technology and Engineering Systems Journal*, **8**(3), 54–62, 2023, doi:10.25046/aj080307.
- [8] A. Sahroni, I. Miladiyah, N. Widiastara, H. Setiawan, "Analysis of Linear and Non-Linear Short-Term Pulse Rate Variability to Evaluate Emotional Changes during the Trier Social Stress Test," *Advances in Science, Technology and Engineering Systems Journal*, **8**(3), 69–79, 2023, doi:10.25046/aj080309.
- [9] M.M. Hossain, T. Ortmeyer, E. Hall, "Human-Centered Design, Development, and Evaluation of an Interface for a Microgrid Controller," *Advances in Science, Technology and Engineering Systems Journal*, **8**(3), 80–88, 2023, doi:10.25046/aj080310.
- [10] M. Felipe, H. Xu, "HistoChain: Improving Consortium Blockchain Scalability using Historical Blockchains," *Advances in Science, Technology and Engineering Systems Journal*, **8**(3), 89–99, 2023, doi:10.25046/aj080311.
- [11] S. Saththamsakul, A. Kuswantori, W. Sriratana, W. Tangsrirat, T. Suesut, "Landmarking Technique for Improving YOLOv4 Fish Recognition in Various Background Conditions," *Advances in Science, Technology and Engineering Systems Journal*, **8**(3), 100–107, 2023, doi:10.25046/aj080312.
- [12] K. Wasayangkool, K. Srisomboon, C. Mahatthanajatuphat, W. Lee, "Accuracy Improvement-Based Wireless Sensor Estimation Technique with Machine Learning Algorithms for Volume Estimation on the Sealed Box," *Advances in Science, Technology and Engineering Systems Journal*, **8**(3), 108–117, 2023, doi:10.25046/aj080313.
- [13] E. Kostyrin, E. Sokolov, "Social Financial Technologies for the Development of Enterprises and the Russian Economy," *Advances in Science, Technology and Engineering Systems Journal*, **8**(3), 118–135, 2023, doi:10.25046/aj080314.
- [14] O. Channumsin, J. Pimpol, T. Pukkalanun, W. Tangsrirat, "Tunable Resistorless Phase Shifter Realization with a Single VDGA," *Advances in Science, Technology and Engineering Systems Journal*, **8**(3), 136–143, 2023, doi:10.25046/aj080315.
- [15] S. Mohamed, H. Cherif, O. Hasnaoui, J. Belhadj, "Design and Comparative Analysis of Hybrid Energy Systems for Grid-Connected and Standalone Applications in Tunisia: Case Study of Audiovisual Chain," *Advances in Science, Technology and Engineering Systems Journal*, **8**(3), 144–153, 2023, doi:10.25046/aj080316.

- [16] H. Iwanaga, "Photoluminescence Properties of Eu(III) Complexes with Two Different Phosphine Oxide Structures and Their Potential uses in Micro-LEDs, Security, and Sensing Devices: A Review," *Advances in Science, Technology and Engineering Systems Journal*, **8**(3), 154–160, 2023, doi:10.25046/aj080317.
- [17] C. Bandara, Y. Kodithuwakku, A. Sandanayake, R.A.R. Wijesinghe, V. Logeeshan, "Design and Implementation of an Automated Medicinal-Pill Dispenser with Wireless and Cellular Connectivity," *Advances in Science, Technology and Engineering Systems Journal*, **8**(3), 161–169, 2023, doi:10.25046/aj080318.
- [18] Y. Kodithuwakku, C. Bandara, A. Sandanayake, R.A.R. Wijesinghe, V. Logeeshan, "Smart Healthcare Kit for Domestic Purposes," *Advances in Science, Technology and Engineering Systems Journal*, **8**(3), 170–177, 2023, doi:10.25046/aj080319.
- [19] S. Lee, M. Park, "A Numerical Study on The Change in Safety Factor (FOS) According to Slope Angle Change for The Establishment of Photovoltaic Facilities Using SRM (Strength Reduction Method)," *Advances in Science, Technology and Engineering Systems Journal*, **8**(3), 178–185, 2023, doi:10.25046/aj080320.
- [20] Y.-J. An, H.-Y. Oh, H.-J. Kim, "Forecasting Bitcoin Prices: An LSTM Deep-Learning Approach Using On-Chain Data," *Advances in Science, Technology and Engineering Systems Journal*, **8**(3), 186–192, 2023, doi:10.25046/aj080321.
- [21] X. Tang, L. Manamanchaiyaporn, "Investigation of Swimming Behavior and Performance of the Soft Milli-Robots Embedded with Different Aspects of Magnetic Moments," *Advances in Science, Technology and Engineering Systems Journal*, **8**(3), 193–201, 2023, doi:10.25046/aj080322.
- [22] M. Hayerikhiyavi, A. Dimitrovski, "Three-phase Continuously Variable Series Reactor – Realistic Modeling and Analysis," *Advances in Science, Technology and Engineering Systems Journal*, **8**(3), 202–211, 2023, doi:10.25046/aj080323.
- [23] H. Zein, A.D. Mulyadi, A. Mudawari, "Minimum Static VAR Compensation Capacity for Bad Voltage Drop Buses in Power Systems," *Advances in Science, Technology and Engineering Systems Journal*, **8**(3), 212–217, 2023, doi:10.25046/aj080324.
- [24] R.Z. Lowe, A. Smith, C. Prout, G. Maresch, C. Bacot, L. Murfee, "How a Design-Based Research Approach Supported the Development and Rapid Adaptation Needed to Provide Enriching Rural STEM Camps During COVID and Beyond," *Advances in Science, Technology and Engineering Systems Journal*, **8**(3), 218–230, 2023, doi:10.25046/aj080325.
- [25] S. Grybniak, Y. Leonchyk, I. Mazurok, O. Nashyvan, A. Vorokhta, "Waterfall: Salto Collazo. High-Level Design of Tokenomics," *Advances in Science, Technology and Engineering Systems Journal*, **8**(3), 231–243, 2023, doi:10.25046/aj080326.
- [26] M.N. Anh, "Simulation of Obstacle Detection Based on Optical Flow Images for Avoidance Control of Mobile Robots," *Advances in Science, Technology and Engineering Systems Journal*, **8**(3), 244–249, 2023, doi:10.25046/aj080327.
- [27] The Influence Analysis of Internet Finance on China's Banking Industry Development, *Advances in Science, Technology and Engineering Systems Journal*, **8**(3), 250–261, 2023, doi:10.25046/aj080328.
- [28] E.M. Ben Laoula, M. Midaoui, M. Youssfi, O. Bouattane, "Improving License Plate Identification in Morocco: Intelligent Region Segmentation Approach, Multi-Font and Multi-Condition Training," *Advances in Science, Technology and Engineering Systems Journal*, **8**(3), 262–271, 2023, doi:10.25046/aj080329.
- [29] O. Tosun, K. Toker, O. Tosun, N.F.O. Serteller, V. Topuz, "The Design, Optimization, and Experimental Study of Hub and Axial Flux BLDC Motor Under Operating Conditions For Light Electric Vehicles," *Advances in Science, Technology and Engineering Systems Journal*, **8**(3), 272–282, 2023, doi:10.25046/aj080330.

**Editor-in-chief**

**Prof. Passerini Kazmersk**

# ADVANCES IN SCIENCE, TECHNOLOGY AND ENGINEERING SYSTEMS JOURNAL

Volume 8 Issue 3

May-June 2023

## CONTENTS

<i>Detailed Study of a Proposal for a Computer Based Tutoring Strategy</i> Soukaina Nai, Amal Rifai, Abdelalim Sadiq, M'hamed Bakrim	01
<i>Markov Regime Switching Analysis for COVID-19 Outbreak Situations and their Dynamic Linkages of German Market</i> Kangrong Tan, Shozo Tokinaga	11
<i>Inferring Student Needs Based on Facial Expression in Video Images</i> Yu Yan, Eric Wallace Cooper, Richard Lee	19
<i>Measurement System for Evaluation of Radar Algorithms using Replication of Vital Sign Micro Movement and Dynamic Clutter</i> Christoph Domnik, Daniel Erni, Christoph Degen	29
<i>Indoor Positioning: Comparing Different Techniques and Dealing with a user Authentication use Case</i> Joaquín Pérez Balbela, Aruna Prem Bianzino	40
<i>Navigation Aid Device for Visually Impaired using Depth Camera</i> Hendra Kusuma, Muhammad Attamimi, Julius Sintara	48
<i>Forecasting the Weather behind Pa Sak Jolasid Dam using Quantum Machine Learning</i> Chaiyaporn Khemapatapan, Thammanoon Thepsena	54
<i>Cache Strategy for Internet based Mobile Adhoc Networks</i> Sugandha Singh	Withdrawn
<i>Analysis of Linear and Non-Linear Short-Term Pulse Rate Variability to Evaluate Emotional Changes during the Trier Social Stress Test</i> Alvin Sahroni, Isnatin Miladiyah, Nur Widiastara, Hendra Setiawan	69
<i>Human-Centered Design, Development, and Evaluation of an Interface for a Microgrid Controller</i> Mohammed Mahfuz Hossain, Thomas Ortmeyer, Everett Hall	80
<i>HistoChain: Improving Consortium Blockchain Scalability using Historical Blockchains</i> Marcos Felipe, Haiping Xu	89
<i>Landmarking Technique for Improving YOLOv4 Fish Recognition in Various Background Conditions</i> Sutham Sathamsakul, Ari Kuswantori, Witsarut Sriratana, Worapong Tangsrirat, Taweepol Suesut	100



<i>Accuracy Improvement-Based Wireless Sensor Estimation Technique with Machine Learning Algorithms for Volume Estimation on the Sealed Box</i>	108
Kitipoth Wasayangkool, Kanabadee Srisomboon, Chatree Mahatthanajatuphat, Wilaiporn Lee	
<i>Social Financial Technologies for the Development of Enterprises and the Russian Economy</i>	118
Evgeniy Kostyrin, Evgeniy Sokolov	
<i>Tunable Resistorless Phase Shifter Realization with a Single VDGA</i>	136
Orapin Channumsin, Jirapun Pimpol, Tattaya Pukkalanun, Worapong Tangsrirat	
<i>Design and Comparative Analysis of Hybrid Energy Systems for Grid-Connected and Standalone Applications in Tunisia: Case Study of Audiovisual Chain</i>	144
Saidi Mohamed, Habib Cherif, Othman Hasnaoui, Jamel Belhadj	
<i>Photoluminescence Properties of Eu(III) Complexes with Two Different Phosphine Oxide Structures and Their Potential uses in Micro-LEDs, Security, and Sensing Devices: A Review</i>	154
Hiroki Iwanaga	
<i>Design and Implementation of an Automated Medicinal-Pill Dispenser with Wireless and Cellular Connectivity</i>	161
Chanuka Bandara, Yehan Kodithuwakku, Ashan Sandanayake, R. A. R. Wijesinghe, Velmanickam Logeeshan	
<i>Smart Healthcare Kit for Domestic Purposes</i>	170
Yehan Kodithuwakku, Chanuka Bandara, Ashan Sandanayake, R.A.R. Wijesinghe, Velmanickam Logeeshan	
<i>A Numerical Study on The Change in Safety Factor (FOS) According to Slope Angle Change for The Establishment of Photovoltaic Facilities Using SRM (Strength Reduction Method)</i>	178
Seungjea Lee, Moonwoo Park	
<i>Forecasting Bitcoin Prices: An LSTM Deep-Learning Approach Using On-Chain Data</i>	186
Yu-Jin An, Ha-Young Oh, Hyun-Jong Kim	
<i>Investigation of Swimming Behavior and Performance of the Soft Milli-Robots Embedded with Different Aspects of Magnetic Moments</i>	193
Xiuzhen Tang, Laliphat Manamanchaiyaporn	
<i>Three-phase Continuously Variable Series Reactor – Realistic Modeling and Analysis</i>	202
Mohammadali Hayerikhiyavi, Aleksandar Dimitrovski	

<i>Minimum Static VAR Compensation Capacity for Bad Voltage Drop Buses in Power Systems</i>	212
Hermagasantos Zein, Ahmad Deni Mulyadi, Achmad Mudawari	
<i>How a Design-Based Research Approach Supported the Development and Rapid Adaptation Needed to Provide Enriching Rural STEM Camps During COVID and Beyond</i>	218
Rebecca Zulli Lowe, Adrienne Smith, Christie Prout, Guenter Maresch, Christopher Bacot, Lura Murfee	
<i>Waterfall: Salto Collazo. High-Level Design of Tokenomics</i>	231
Sergii Grybniak, Yevhen Leonchyk, Igor Mazurok, Oleksandr Nashyvan, Alisa Vorokhta	
<i>Simulation of Obstacle Detection Based on Optical Flow Images for Avoidance Control of Mobile Robots</i>	244
Mai Ngoc Anh	
<i>The Influence Analysis Of Internet Finance On China's Banking Industry Development</i>	250
Yangshichi, Hayoung Oh, HyunJong Kim	
<i>Improving License Plate Identification in Morocco: Intelligent Region Segmentation Approach, Multi-Font and Multi-Condition Training</i>	262
EI Mehdi Ben Laoula, Marouane Midaoui, Mohamed Youssfi, Omar Bouattane	
<i>The Design, Optimization, and Experimental Study of Hub and Axial Flux BLDC Motor Under Operating Conditions For Light Electric Vehicles</i>	272
Ozturk Tosun, Kenan Toker, Ozturk Tosun, Necibe Fusun Oyman Serteller, Vedat Topuz	

## Detailed Study of a Proposal for a Computer Based Tutoring Strategy

Soukaina Nai<sup>\*1</sup>, Amal Rifai<sup>2</sup>, Abdelalim Sadiq<sup>1</sup>, M'hamed Bakrim<sup>3</sup>

<sup>1</sup>Computer research laboratory, Faculty of Sciences, University Ibn Tofail, Kenitra, 14000, Morocco

<sup>2</sup>Team of Research in engineering of Computing Environment for human learning, Regional Center for the Professions of Education and Training, Rabat, 10000, Morocco

<sup>3</sup>Laboratory of Processes for Sustainable Energy and Environment, University Cadi Ayyad, Marrakech, 40000, Morocco

### ARTICLE INFO

Article history:

Received: 15 February, 2023

Accepted: 23 April, 2023

Online: 15 May, 2023

Keywords:

Tutoring

Portfolio

Learning E-portfolio

Assessment E-portfolio

Presentation E-portfolio

### ABSTRACT

*In this article, we propose a new tutoring strategy to combat school dropout in Morocco. This strategy is based on a collaborative approach involving educational administration and teachers at the national level to ensure equity and equal opportunities for all Moroccan students, on the one hand, and the quality of the training, on the other. Its implementation will be ensured through a computerized system based on the student's learning and evaluation portfolios in order to provide individualized assistance, taking into consideration his/her shortcomings and didactic needs. In this work, after defining tutoring and its types, we will present the Moroccan ministerial strategy in terms of tutoring by discussing the relevance of the tutoring systems prevailing in Morocco and the existing platforms accredited by the Ministry of Education. Then, we will study the portfolio concept and its forms, in addition to some criticisms established on this tool in order to identify the components, ensuring the quality of the tutoring to be taken into account in our proposed IT solution. Finally, we will study in detail the design of our system by modeling the evaluation and remediation processes and examining its functional behavior.*

## 1. Introduction

In Morocco, students face serious academic challenges, especially in certain scientific fields. According to statistics published by the Ministry of National Education, quoted by [1], more than 300.000 students dropped out of school in 2019-2020. Indeed, 76.574 students left school at the primary education level, or 2.1%, compared to 95.191 (2.7%) in 2018-2019, whereas at the secondary level, the school abandonment rate has decreased from 8.8% to 7.4% or from 80.560 students to 67.134. These statistics show that the dropout rate for students remains high and has not appreciably declined.

On the other hand, [2] states that there are many different factors that positively or negatively influence retention and success of young students. These factors are interrelated and fall into four categories: environmental or social factors, family factors, personal factors and academic factors (such as quality and/or learning disabilities). When these factors exert a negative influence, they become risk factors that increase the likelihood of more difficulties during their schooling, which can lead to dropping out of school. Whereas [3] announces that school

repetition stems to be an endemic phenomenon with multiple causes. In fact, according to a study conducted on fail, the difficulties in succeeding in class are mainly due and in order of importance to:

- Gaps, students school delays, and a lack of solutions to catch up.
- Inadequate school curricula and assessment systems (difficult, frequent changes).
- Quality and behavior of the teachers (severe, the lack of pedagogy, not conscientious enough).
- Distance from school to home and lack of transportation.
- Financial problems.
- Frequent absences for work or family reasons.

This makes tutoring an important necessity in the fight against school dropout due mainly to learning difficulties. For these reasons, we will propose in this work, a new tutoring strategy to achieve equity and quality at the national level. This strategy focuses on a participative approach between educational administration and teachers via a computerized academic support

\*Corresponding Author: Soukaina Nai, [soukaina.nai@gmail.com](mailto:soukaina.nai@gmail.com)

system based on student portfolios. Thus, a detailed examination of our project will be presented to identify the requirements of our system via a detailed design.

This paper is structured as follows: In the first paragraph, we will discuss the definition of tutoring and its different types, the Moroccan tutoring strategy and the problems envisaged in the proposed platforms. Then, in the second paragraph, we will define the concept of the portfolio, its different types, the advantages of the electronic portfolio (e-portfolio) and the techniques of its design. Next, we will discuss the strengths and weaknesses of the portfolios in order to identify the essential elements to be taken into account in our new solution. In the third paragraph, we will present a general description of our solution, and then we will proceed with a detailed computer study through which we will address the functional behavior of our system by establishing the class, use cases and activity diagrams of the various elements and processes involved. And we will end with a conclusion.

## **2. Tutoring**

### *2.1. Definition of tutoring*

Tutoring is recognized in the academic community by various terminologies, namely : “academic tutoring”, “educational assistance”, “support education”, “tutoring”, “coaching”, “accompaniment”, “collaborative learning”, etc., and defined in different manners.

Indeed, according to the Moroccan Ministry of Education (cited by [4]), it is “a collection of pedagogical and technical tools that can be used both inside and outside of the classroom, usually as part of school-related activities, in order to prevent and avoid any kind of failure that might endanger the student's ability to learn normally”.

As stated in [5], tutoring is a type of “supplemental learning” that involves “assistance given by different speakers outside of class hours and during extracurricular activities”. Its purposes are to:

- Challenges and mitigate insufficiencies in a class of students.
- Compensate for the differential learning levels in the classroom, reduce the dropout and repetition rates, and increase the level of education through cost-effective development and efficiency improvements.
- Support the learner's continuing academic progress in the situation of missed classes due to sickness or poor concentration.

### *2.2. Type of tutoring*

Academic support can be provided internally during school time in the form of instant or deferred tutoring for individuals or groups of students, as well as externally, outside of school time.

“Instant remediation is a set of pedagogical and/or didactic strategies, attitudes, and behaviors that promote the provision of specific help to students suffering from particular difficulties following a [teacher's] assessment” [6] cited by [7]. It is

completely incorporated into the teaching/learning sequence and prevents any kind of stigmatization due to the exclusion of the learner. It instantly responds to needs that emerge during a lesson. It is conducted by the teacher who is familiar with the student and the context in which the difficulty arises and focuses on problems that can be rapidly resolved and do not require specific treatment (occasional blockages, mistakes, barriers to progress...).

While deferred remediation is done separately from the teaching/learning sequence and is conducted either by the teacher of the student needing remediation or by another teacher. It can be planned at a specific time and have a regular duration. According to [8], Its purpose is to meet demands within a specified time frame with a limited group of learners (students with similar challenges, homogenous groups) or to intervene sustainably and simultaneously on obstacles that hinder the learning of multiple operations (heterogeneous groups). It can take on past issues that have existed for a long time or problems that demand a more coherent intervention: scholar delay, return to concepts not previously acquired, total reconstruction of a course sequence.

Deferred remediation can also be offered outside of school hours in the form of fee-based courses provided by teachers other than the student's teachers, in order to be able to upgrade it in a specific subject. In addition, [9] states that due to the lack of teachers and the increase in the school hourly load, the overload of school programs, the increase in the number of students, the form of internal tutoring has been gradually eclipsed to let invade the external tutoring. In fact, private tutoring has undergone significant development in Morocco, as in the rest of the world, and “is deeply rooted in the culture of many countries. [...] In the early of the 21st century, it became established in Eastern Europe and Central Asia and increasingly important in Western Europe, North America, Australasia and Africa. In addition, it has begun to emerge in Latin America” [10].

External tutoring is “paid teaching provided outside school hours in academic areas taught at school. They are provided by suppliers who may be professors or students, either independently or as part of a business framework that pays them or links them to consumers” [11].

### *2.3. Moroccan Ministerial Strategy for Academic Support*

#### *2.3.1. Face-to-face tutoring*

In Morocco, tutoring is still a necessary component of the programs and charters decreed by the Ministry of Education. Indeed, a reform has implemented the recommendations of the National Education and Training Charter (CNEF), stating in Article 27 “every effort will be made to attract learners and guarantee that their education grows continuously, sustainably, and effectively, and that waste, academic failure, or the fictitious or intermittent pursuit of studies are gradually reduced” [12].

Then, the E1.P5 project of the 2009-2012 emergency program placed among its priorities the fight against repetition and dropout, by establishing an individual monitoring system for each student,

providing assistance to those who need it, and setting up refresher courses for them. The same objective has been maintained in the strategic vision (2015-2030) of the Moroccan Higher Council for Education, Training and Scientific Research. In fact, in lever 1 (area 6) of this vision, the focus was on setting up structures able to monitor learners, progressively in the short term, and to envisage intensive academic support for learners in difficulty as a right to be guaranteed and integrated into curricula programs and school time. In the same vision, lever 7 (area 29 (a)) also insisted on “the integration of educational support programs for students with difficulties into the curricula, official programs and school time”.

Whereas, in lever 8 (area 35), in order to ensure the generalization and achievement of equity, it was required to develop new technical requirements for independent schools, adjusted to the types of educational investment, their specific characteristics and geography, including: “the rules for support and strengthening courses and their insertion as an inseparable element of the programs of study and curricula”. This implies that internal tutoring is an integral part of the national education process.

### 2.3.2. Distance tutoring

The Moroccan Ministry of Education has set up several distance learning platforms for tutoring through a system called Massar. It is an integrated educational system, proposed by the Moroccan Ministry of National Education in 2009 as a pilot program in schools to modernize and improve the educational system using technologies of information and communications (ICT).

The Massar system is based on an online platform that manages student, teacher and school data: management of grades, absences and lateness, .... It also aims to improve teaching by hosting learning or training content management platforms. Among these platforms, we can mention the Massar Moutamadris platform, TelmidTice, e-Takwin, ... These platforms set up electronic spaces containing videos, course summaries, courses and exercises, exams, for all subjects and for all levels and school cycles. These resources are accessible and downloadable for free and are created by volunteer teachers, without any prior pedagogical planning to take into consideration the differentiation of typical student profiles.

Students access to these courses is voluntary, depending on their needs, their means (possession of a smartphone or a computer with an internet connection), their desires and their computer skills to explore these platforms and their contents. This implies the lack of serious supervision of tutoring and its individualized implementation for each student. In addition, there is no pedagogical supervision of the students on these platforms to ensure the success of the desired remediation.

In addition, there are other Moroccan websites of content management that are defined as academic support sites and offer students courses and exercises for free or paid download such as SchoolMouv Morocco, Educatix, E-learning Morocco, ...

### 2.4. Issues raised in the tutoring strategies adopted in Morocco:

In [4], the author conducted a research project to diagnose the types of tutoring in Morocco and their educational, and socio-economic impacts on students and their families. This

investigation demonstrated the importance of mentoring for some students, particularly in science courses. But, on the other hand, it identified several problems, as private tutoring is the most widely adopted in Morocco. Among these, this type of tutoring generates an additional burden that hinders the purchasing power of the students' parents, and a considerable loss of energy, money and time. These parents put the responsibility on the Ministry of Education, the teaching system, the overload of the programs, without forgetting the part of the teacher, who gives tutoring lessons despite his overloaded schedule.

A further research paper, produced by the EPI organization [13], was conducted to determine Moroccan students' perception of the different facets of private tutoring in secondary schools, the results achieved, and the students' interest in tutoring websites. For that purpose, a survey was sent to learners, and the result of this study revealed great interest in student tutoring, and that over half of them use online sites for this reason. Nevertheless, about 50% of learners are in favor of free tutoring at school from their teachers.

On the other hand, the same research team, using a sample, evaluated the Moroccan tutoring websites to find out if they provided learners with interactive and social constructivist activities. This research was supported by an assessment matrix developed from already used educational website analysis matrices, each dealing with one or more aspects: technological, ergonomical, pedagogical, etc. Overall, the researchers found that the designers and authors of the sites studied had made great efforts. However, their diagnosis raised many comments, including in particular:

- Usability and ease of navigation are moderate.
- Most sites are quite static.
- There is a quasi-absence of interactivity.
- Some sites present business advertising.
- Teaching strategies are not meaningfully defined.
- The designers simply transfer the content of the textbooks to the net.
- Methodological help is totally absent from all the sites, whereas it would have been more beneficial to help the learner to “work better”.
- There is no return of information to correct the learner's mistakes.

As for the platforms offered by the Ministry of Education via the Massar system, they have raised the following shortcomings:

- Lack of effective implementation of these platforms due to lack of student awareness about their existence, importance and handling;
- The pedagogical support offered is conventional, with similar exercises and lessons for all students, due to the lack of a pedagogical design strategy that takes into consideration the differentiation of student profiles, as well as the lack of an entity specialized in the validation of published pedagogical resources;

- Support remains unofficial, it is optional, it is the student's choice to access the system or not.
- Lack of structuring of learning according to units of the same curriculum, which can make it difficult for learners to progress in their learning.
- Lack of follow-up, which can make it difficult to assess the effectiveness of support and measure learner progress.
- Lack of evaluation of the acquisition of a targeted skill ensuring the quality of the tutoring since these platforms only offer courses and exercises.

Based on the above issues related to tutoring, more effort is needed to:

- Provide academic support in the skills that are part of the official curriculum. This should be free and of high quality to all students nationwide in order to guarantee equity and equal opportunity.
- Establish and supervise tutoring by teachers and educational administration in a participatory approach to put it in an official framework and make it a part of the mission of the Moroccan school.
- To provide individualized tutoring to each student, taking into consideration his/her needs and profile. To do this, we propose to use the student's learning and evaluation portfolios to identify the student's shortcomings and to provide him/her with the precise support appropriate to his/her difficulties.

Before detailing our solution, in the next section, we highlight in the following section, the concept of portfolio, its various types, its advantages and the techniques of its design. We also point out these benefits to be taken into consideration in the design of our proposed system.

### 3. Portfolio

#### 3.1. Definition

The portfolio concept is “derived from the professional and artistic world. In his portfolio, an artist presents a sampling of his works, comments, critical articles that accompanied them. He shows his creative path, shows the traces of his work, of the evolution of his creative thought” [14].

In the educational field, [15] defines a developmental portfolio as a “set of works that records, over a given period of time, the learner's progression in the acquisition of specific professional competencies”. Based on this definition, [16] affirm that “the portfolio serves as a tool for validating prior learning, as well as a means for planning and guiding personal and professional growth. It also allows the individual to become more aware of his or her values, skills, beliefs and professional practice”.

According to the Northwest Evaluation Agency (NWEA), quoted by [17], a portfolio is a collection of a student's work presenting his or her efforts, progress and achievements in one or more areas. This definition is used to define the concept of portfolio in a UNESCO document [18].

In [19], the authors give another definition of the concept, also provided by the NWEA, considering that the portfolio is: “a

finalized and reasoned collection of documents testifying to the quality and progression of a student's work through certain achievements”. This definition adds the notion of selection of documents in the portfolio, which is echoed in the definition given in a report by the Direction of educational resources, of the Quebec Ministry of Education [20], where the working group defines the portfolio as “a selection of students' projects that demonstrate competence by keeping relevant records of their accomplishments”. We can also read below that « the portfolio reports on the student's personal progress”. [21] states that in general, a portfolio can contain:

- Written documents (texts, graphs, printouts, copies of evaluations, etc.),
- Photographs (taken during an open house, the completion of a project, an organized trip, etc.),
- Multimedia elements in the form of CD-ROM (video recording of a student presentation), etc.

#### 3.2. Types of portfolios

In [15], the writer distinguishes three types of professional development portfolios, namely:

1. Portfolio “Just for me”: this type of portfolio is based on a personalized and individualized approach. “It is the learning portfolio that the student controls, manages and opens to whomever he/she wants.” [15]. It is designed by the learner by indexing and storing various documents and reflections to learn and evaluate their learning in order to self-regulate and facilitate metacognition. However, “it does not offer a satisfactory space for telecollaboration, regulation and evaluation.” [15].
2. Portfolio all-in-one based on the “Big Brother's gas factory”: This is the institutional portfolio, designed to perform a summative evaluation, to certify, to establish a grade, to assess learning. This type of portfolio will also be very useful to future employers.
3. The three distinct portfolios approach: Learning, Presentation and Evaluation Portfolios. This approach favors a reflective approach. The learning portfolio “is a collection of works of all kinds, completed or not, accompanied by the student's reflections on their achievements” [20]. In [22], the researcher states that the portfolio can be used for a variety of purposes, such as focusing on student progress or for diagnostic purposes. In the first case, we choose works showing the student's progress over a given period of time, which allows us to motivate the student and illustrate his or her progress, mainly for the parents. In the second case, work is chosen that illustrates the student's weaknesses and strengths, or notes on work methods and preferences.

In a learning portfolio, the student must comment on his methods and the means used to achieve his work. They can record their most significant work, comment on it and reorganize the content. All these transactions permit the student to engage with the teacher and other learners on the same subject [20]. The reorganization of the content also makes the student conscious of what has been learned [20]. According to [22], This type of

portfolio helps teachers who adopt it in the classroom to change the way they view students and assess student work by taking more variables into account than before.

The presentation portfolio: “This type of portfolio is the most similar to the artists' portfolio” [22]. It allows to “present the best productions of the student or those he prefers” [20]. “These productions are most often selected by the student who has to justify his preferences by annotating the documents” [23]. “It is intended to be presented to others: peers, teachers, friends, but also parents, and even to a wider public during an exhibition” [20]. By creating this portfolio, the student summarizes what he/she thinks at a given moment about his/her productions, his/her progress or his/her learning.

The evaluation portfolio: according to [20], this type of portfolio makes it possible to evaluate a student's skills throughout and at the end of a school term. It is similar to a summative evaluation process. It is used for self-assessment, evaluation, and certification. In this type of portfolio, the teacher selects and inserts several samples of the student's accomplishments so that a judgment can be made about the level of competency achieved. The student places in the portfolio the productions that he or she deems appropriate to demonstrate the development of the competency.

The three portfolios of learning, assessment, and presentation are interconnected, interoperable (including a password and a data protection system), and portable (can be deleted, redone, saved).

For all three files, the student participates in the evaluation (self-evaluation and student-teacher co-evaluation).

### *3.3. Benefits of the electronic portfolio*

According to [17], the electronic portfolio (e-portfolio) appeared in the early 1990s. It has some benefits over the paper portfolio. In [19], the editors identified some of these benefits namely:

- It is easier to revise and modify than its printed counterpart.
- It can be put online, fully or partially, and thus be rendered public, making it more portable, better distributed and more secure.
- It can also provide the institution with information on the progress and results of a course.

In [14], the essayist defines several advantages of the digital portfolio by considering that the portfolio is:

- A reflective space, it “seeks to respond to a fundamental problem for the teacher in charge of accompanying and training trainees”. Indeed, it allows him to appropriate the work, discussions, productions, etc., carried out by himself or by the trainees during the didactic sessions to rethink the class. It also allows him to build writing and working habits and “learn to record pre-course expectations, critical incidents that have occurred, specific student behaviors, comments from colleagues, interesting materials, ideas for new projects, etc.”
- It keeps track and makes it possible to come back to it, it allows reformulation, [...], filing but also deletion [...]. Its purpose is to record the training over time and to keep track of it [...] to give trainees time to acquire knowledge, methods

and intellectual attitudes, and to become familiar with the space in which and through which they learn. This contributes to the development of skills and identity.

- It favors the weaving of knowledge between them and with the knowledge of action, professional, intellectual, emotional experience, this helps the teacher to progressively elaborate complex conceptual frameworks, from which he/she can think, decide on the pedagogical action to be taken.
- “The social structure of knowledge, a construction that accompanies the progressive development of professional identity”, in the first instance, with his peers.
- A possible space to dialogue with the trainers.
- An instrument among others of evaluation, by referring in this process, within the framework of certification commissions, to the discourses established by the trainees on their work, on their practices, on their attitudes in the establishment.

### *3.4. Conception of an electronic portfolio*

In [21], the writer states that the structuring of a portfolio depends on the goals pursued by its designer. Then, he emphasized that the best organization of a portfolio amounts to thinking and answering several questions about the type of portfolio to be created, the content that should be saved in this portfolio, the category of work to be presented in the portfolio, the person responsible for the choice of the productions presented in the portfolio, the way of ordering the productions,..., the criteria for selecting the productions.

Technically, “it may be necessary to set up an IT environment to manage student e-portfolios” [23]. The report [20] identifies the essential components of a digital portfolio:

- Student management software (creating student groups, assigning passwords, privileges and disk space to each student).
- A document management function (identification, filing, copying, deletion, etc.).
- A function for recording and managing student, teacher and parent comments and annotations on student work.
- A function for displaying the student's work and for limited and secure consultation of the comments attached to this work.
- A secure area management function.

### *3.5. Discussion*

The interest of such a portfolio is, in particular, to make it possible to see the evolution of a student's learning over the long term. In [23], the writer summarizes the gaps in the learner's portfolio in an assessment context in the following points:

- The learner's portfolio includes the work completed and selected by the student, not those specified by the teacher. “Successful completion of a specific task does not infer generalized competence” [22]. Therefore, it is important to use the student's portfolio within an official framework that is inseparable from the school program, and the validation of the student's competencies and the selection of his or her representative productions must be carried out according to a

standardized evaluation and assessment program validated by the educational administration and the teachers.

- Saving learner information in the electronic portfolio is not durable enough because it is not possible to “leave visible elements that the learner may wish to remove” [19]. Therefore, the selection of student productions to be presented to the public must be well thought out and carried out within an official framework of validation of academic skills.
- Finally, in [19] the editors wonder if the move to standardize the portfolio in order to simplify its evaluation, or the use of the electronic portfolio by users who are not very familiar with the technology, will lead to the loss of creativity associated with the portfolio. Therefore, we propose that the use of the portfolio must fulfill a consequent need to ensure the educational and personal development of the student. Therefore, it must be based on a study that takes into consideration all the elements related to the management and monitoring of the student's learning through a semantic computer system with ergonomic and easy-to-use interfaces.

In the following paragraph, we will present our tutoring solution basing on the points from above discussion and those highlighted in paragraph 1.4.

#### 4. Description of the proposed tutoring system

##### 4.1. Overview of the Proposed Academic Support Strategy

According to [15], the portfolio professional development has two functions, the first one is to enhance the quality of education, to promote support and monitoring of learning, while the second one is to promote the learner's authentic self-assessment, which leads to better knowledge and self-esteem. In [14], the essayist indicates that “[...] The portfolio [...] is reflexive because it puts people on hold. It allows for deferred feedback, and thus the distancing of decisions taken in the heat of the intervention, but also of school situations and contexts, the actors, and the worked objects”.

Our new strategy is based on a nationally standardized participatory approach of school support between educational administration and teachers, according to [24], based on the institutionalization of the use of the student's portfolio in support and monitoring of their learning.

This process will be accomplished by setting up an ergonomic computer platform. This platform must be based on a semantic system that provides students with assessment activities of their skills acquired at the end of one or more school units and remediation activities in case they do not succeed in validating the school skills targeted by the assessment. The purpose of these remediation activities is to help students acquire their school skills. Competency assessment time slots are to be determined regionally by regional education and training academies.

The preparation of the evaluations must be ensured by the teachers and the inspectors of the subject.

The latters, based on the competence to be validated and the targeted cognitive level, must propose suitable differentiated pedagogical activities in the form of problem situations or open questions that must be corrected by subject teachers, or closed questions (multiple choice questions, multiple choice questions,

short answer questions, fill-in-the-blank questions, ...) generated by numerical exercises that can be corrected automatically. The result of the assessment and the student's production should be recorded in their assessment e-portfolio.

When a student is unable to pass an assessment, the failure score must be reported in the student's assessment portfolio. Then, in order to ensure that the student follows up on the same failed skill, the system should send a message to the student's account notifying him/her of the completion of the differentiated remediation activities, indicating the time allotted for this process and stating that the student will be receiving the remediation.

The remediation process must be carried out by the student's teacher at the local level. The remediation activities completed by the student should be recorded in the student's learning portfolio and commented on by the student's teacher.

Once the remediation activities have been completed according to the time frame given by the system, the student must be re-evaluated to determine his or her degree of mastery of non-validated skills. The class diagram in Figure 1 sketches the academic support process under the proposed system.

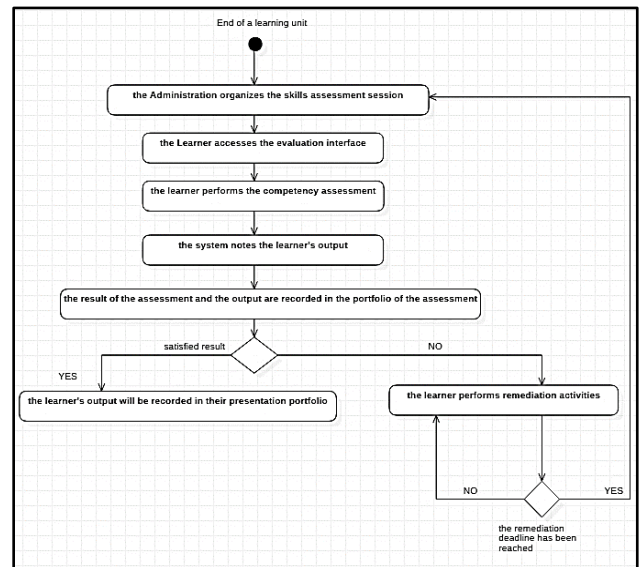


Figure 1: Activity diagram

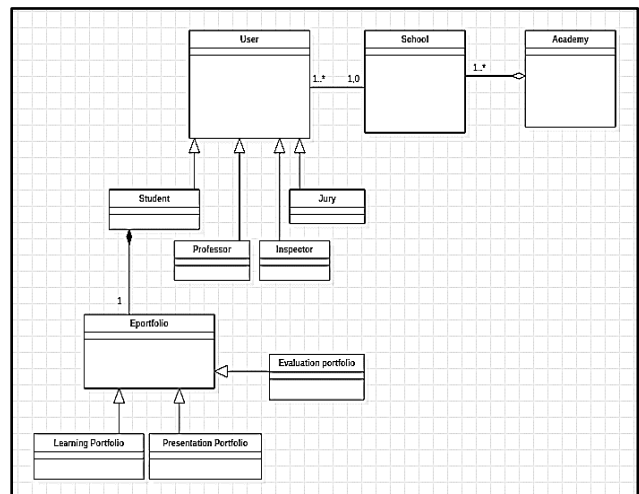


Figure 2: Class diagram of roles



4.2. System roles.

The main agents who act with the system are : students, teachers, inspectors and the jury whose role is to approve the assessment and remediation activities. There are two juries, a regional one nominated by the academy and a national one that approves the propositions of the academies' regional juries in such a way as to unify the tutoring policy at the national level. The class diagram in Figure 2 models the actors that interact with the proposed tutoring system.

4.3. Model the assessment and remediation processes

The system of tutoring is principally composed of a skills assessment interface, a learning interface and student portfolios. These two first areas are connected together. The assessment space contains the assessment activities corresponding to a learning unit within a curriculum. They are elaborated by professors and inspectors and approved successively by a regional jury and a specialized jury at the national level. The student must have an account in order to access this interface and complete the assessment activities corresponding to a learning unit after its completion or at the end of the remediation period. The activities completed as well as the marks and feedback will be recorded in the student's assessment portfolio in order to evaluate the level of their acquisition of the school skills targeted by the assessment process.

If the assessment result is satisfying, then the school's competency will be declared validated in the student's presentation e-portfolio while recording their production of the assessment therein. The class diagram in Figure 3 is used to model the evaluation process.

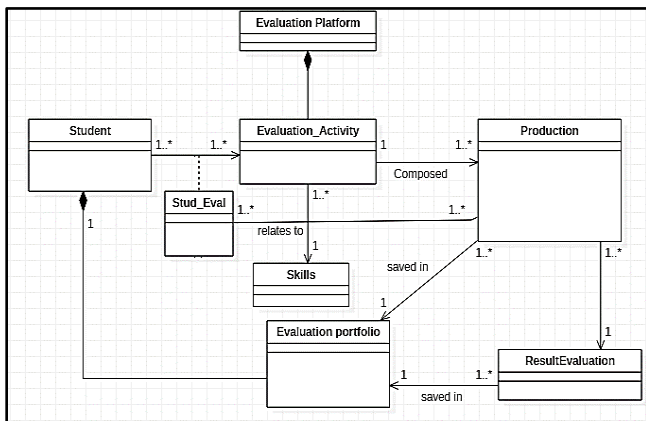


Figure 3: Class diagram of the evaluation process

If the outcome of the skills assessment is not satisfactory, the student will be required to complete the remediation activities that the system will suggest to overcome his difficulties, and then he will assess himself again on the same skill that he failed. The class diagram in Figure 4 illustrates the modeling of the remediation process.

4.4. Functional behavior of the proposed system

To improve understanding the system functioning and the interactions with users, we detail in this section the scenarios of the main use cases.

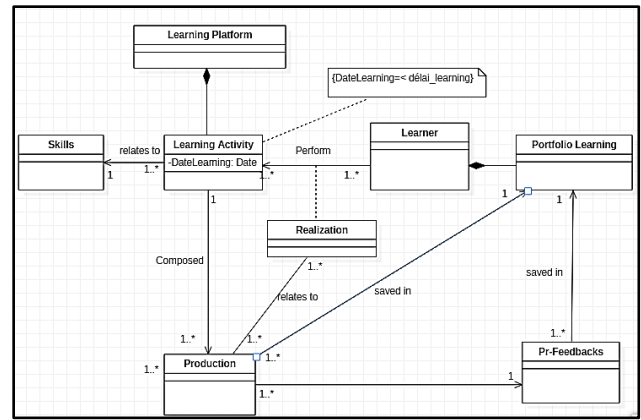


Figure 4: Class diagram of the remediation process

4.4.1. Administrator's use case diagram

The administrator plays a central role in the platform and is responsible for creating student and teacher accounts, managing the user list, updating the database, administering all documents and responding to reported complaints. The administrator must authenticate himself in order to access his administration interface. The use case diagram in Figure 5 illustrates the different tasks assigned to the administrator.

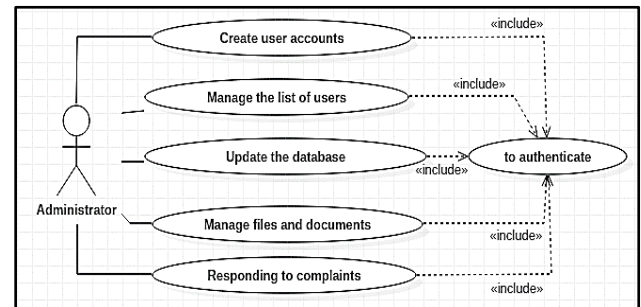


Figure 5: Administrator's use case diagram

This diagram describes the set of functionalities provided to the administrator (main actor) to ensure the management process of the proposed system (goal). The actor must log on to the system as an administrator (Precondition) in order to perform all the functionalities offered by the system.

The administrator links to the use cases via 2 types of relationships: association; meaning that the administrator can trigger a feature, and inclusion which indicates that the actor can only perform the use case features after a correct authentication to his account.

4.4.2. Student's use case diagram

The main objective of the proposed system is to support students in their learning. To do this, the student can interact with the system to:

- Complete his registration to the tutoring platform,
- Change his passwords,
- Authenticate himself,
- Manage his e-portfolio profile (update his personal and professional information),

- View other presentation portfolios,
- Access to the assessment & remediation/learning interface, open the proposed assessment, process it and submit the answer,
- Consult his scores, incorrectly answered questions and correct answers to incorrect questions,
- View the list of remediation activities offered to overcome deficiencies,
- Complete the remediation activity and save it in his learning portfolios,
- View the answer key for remediation activity and the teacher's feedback,
- Claim a problem, communicate with colleagues and the teacher (Forum area),
- Download documents from the platform and import documents into the platform and manage his e-portfolios (comment on productions).

The diagram describes all the functionalities provided to the student (main actor) for better use of the system. The student must log in to the system with his own account (Precondition) in order to benefit from all the functionalities offered by this system. The student links to the use cases also via 2 types of relationships: association and inclusion.

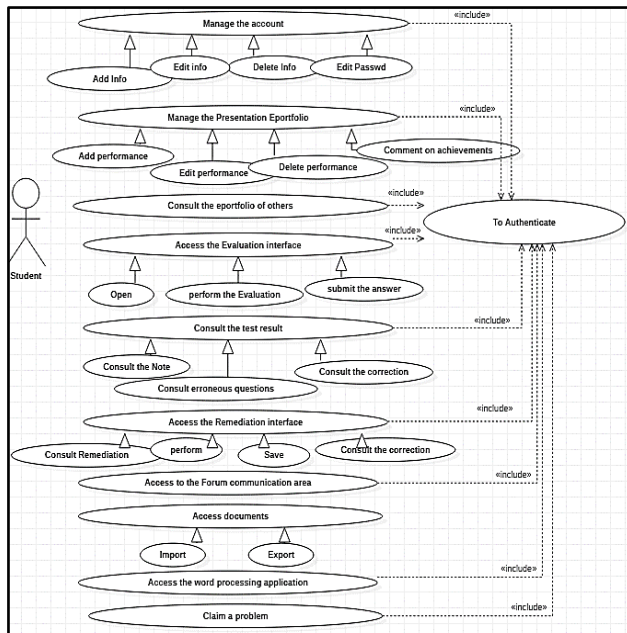


Figure 6: Student's use case diagram

#### 4.4.3. Teacher/Inspector's use case diagram

The proposed solution can be operational only with the appreciated participation of our teachers. Indeed, they have access to the platform to:

- Complete their registration to the tutoring platform. (School levels at which the teacher provides courses, regions, institutions, ...),

- Modify their passwords,
- Authenticate themselves,
- Manage the e-portfolio profile (update personal and professional information),
- View student portfolios,
- Enter comments, feedbacks, instructions and grades to students,
- View teacher and inspector profiles,
- Import and export documents to and from the platform,
- Communicate with colleagues (Forum space: communication space between teachers and inspectors of the same specialty),
- Prepare evaluation quizzes in a questionnaire interface in the platform,
- Prepare remediation activities,
- Collaborate with teachers and inspectors to prepare evaluation and remediation activities using online collaboration tools,
- Send developed activities to the pedagogical jury for validation,
- Communicate with students to discuss a lesson or activity,
- Apply to be a member of the regional or national jury,
- Claim a problem,
- The Inspector can also Consult the success rate of students.

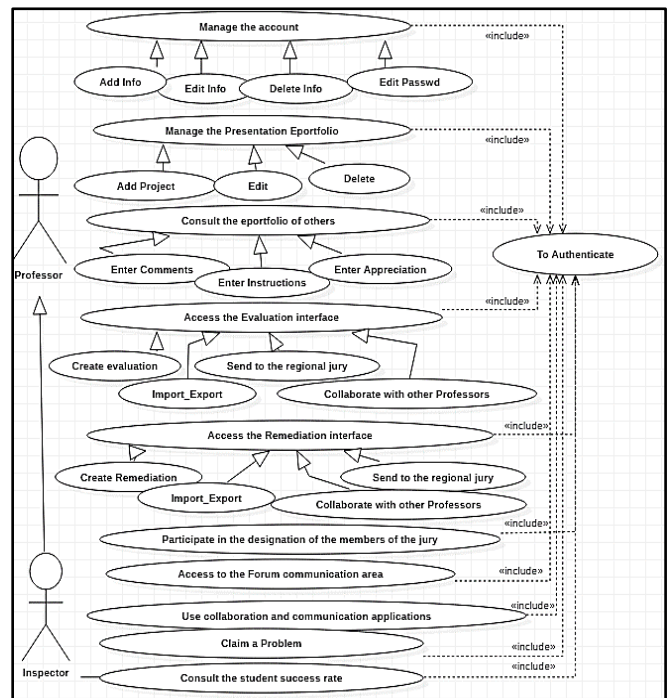


Figure 7: Teacher/Inspector's use case diagram

The diagram describes all the functionalities provided to the teacher and the inspector (main actors) for better use of the system. Both actors must log in to the system with their own accounts (Precondition) in order to benefit from all the functionalities offered. The system gives the inspector the right to

perform the same functions offered to the teacher: inheritance relationship, and to consult the success rate of the students.

#### 4.4.4. Regional jury's use case diagram

The regional juries can also access this platform to:

- Authenticate themselves.
- Comment on assessment/remediation activities,
- Update assessment activities,
- Update Remediation activities
- Validate assessment activities,
- Validate remediation activities,
- Submit the assessment and remediation activities to the national jury for validation,
- Publish the assessment and remediation activities validated by the national jury,
- Set dates for assessments,
- Communicate with teachers and inspectors.

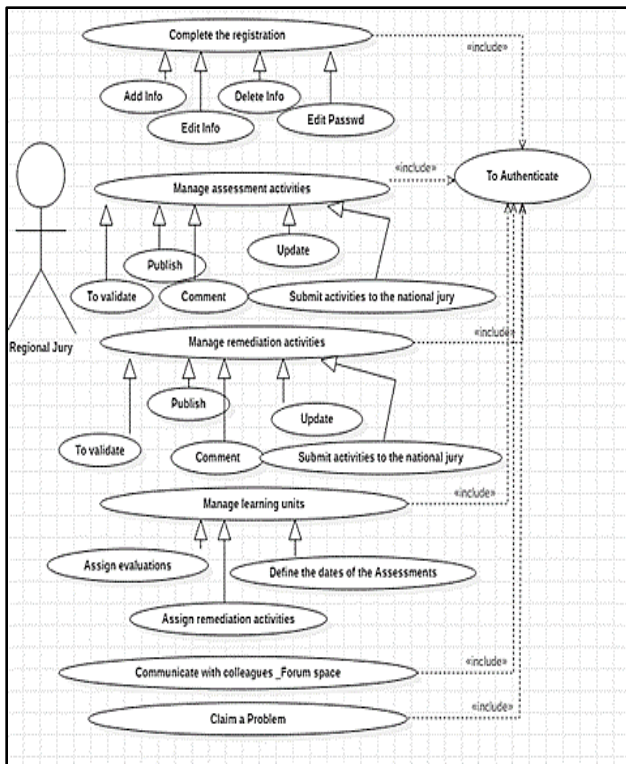


Figure 8: Regional jury's use case diagram

#### 4.4.5. Diagram of evaluation sequences

The evaluation process takes place according to the following scenario:

- The system sends messages to students to inform them of assessment date, the message contains a link to access the assessment activities.

- The students achieve the assessment activities and record their work,
- The system corrects the assessments made by the students,
- The system transmits the assessment activities achieved by students and the result to his assessment e-portfolio,
- The system transmits the good student achievement (all the productions with confirmation of the acquisition of competence) in his presentation portfolio.

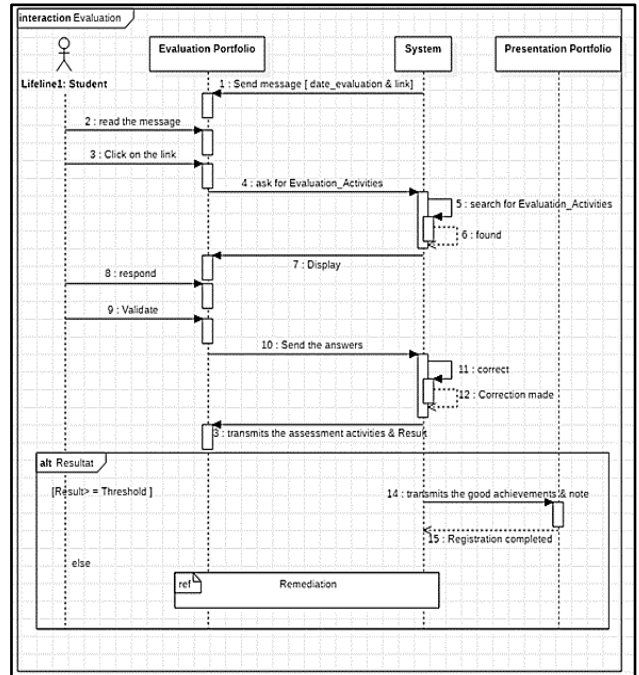


Figure 9: Diagram of evaluation sequences

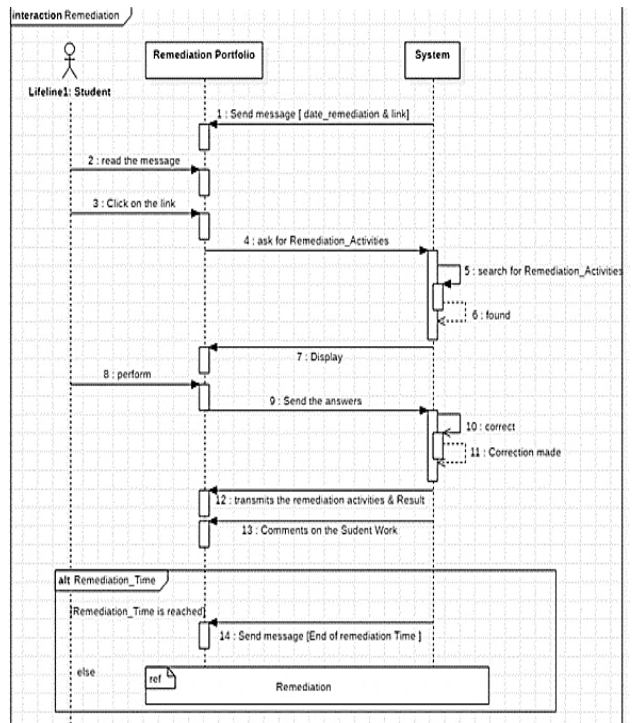


Figure 10 : Diagram of remediation sequences

#### 4.4.6. Diagram of remediation sequences

The remediation process takes place according to the following scenario:

- The system sends messages to students to notify them of remediation date, the message contains a link to access the remediation activities,
- The students achieve the remediation activities and record their work,
- The system transmits the remediation activities achieved by students and the result to his learning e-portfolio,
- The system/ teacher corrects the student work, comments on it and discuss with student.
- When the remediation time is reached, the system sends a notification to the student.

#### 5. Conclusion

In this article, we have proposed a computerized tutoring system based on a participatory approach involving educational administration and teachers to ensure equity and quality in education at the national level.

After introducing the concept of tutoring, defining its types and raising the problems of tutoring strategies in Morocco, we discussed the portfolio concept, its different kinds, the advantages of the electronic portfolio and the criticisms made about this tool.

Next, we presented a detailed study of our computerized tutoring system designed using student portfolios. In this study, we specified the adopted tutoring strategy, modeled the learning and assessment processes addressed in this system, and detailed its functional behavior.

#### References

[1] K. Rachdi, "Enseignement : 300.000 élèves ont quitté les bancs de l'école en 2020," Kiosque 360, 2021.

[2] M. Intérieur, "Promouvoir la réussite scolaire et l'épanouissement des enfants et des jeunes," Ministère De L'intérieur, 2021.

[3] M. Education, "Morocco Programme Urgence," Ministère De l'Education Nationale, 2008, Planipolis.Liep.Unesco.Org/Sites/Default/Files/Ressources/Morocco\_Programme\_Urgence\_Najah\_Rapport\_Detaille\_Version\_Projet.Pdf.

[4] A. Zbadi, "La problématique du soutien scolaire au maroc. diagnostic et perspectives," Haut Commissariat Au Plan, Centre National De Documentation, 2018.

[5] W. Wikipedia, "Soutien scolaire," Wikipedia, 2020, fr.wikipedia.org/wiki/Soutien\_scolaire.

[6] A. Hirsoux, "Aider les élèves en difficulté d'apprentissage par la remédiation immédiate : expérimentation de deux outils pédagogiques dans l'enseignement fondamental," Mémoire de licence en sciences de l'éducation Université de Mons, 2006.

[7] A. Dehon, A. Derobertmasure, "La Remédiation Immédiate," Université de Mons, 2009.

[8] M. Saibi, T. Ouaguenoun, "La remediation au cycle primaire," 2016, www.facebook.com/TimizartOuaguenoun/posts/la-remediation-au-cycle-primairei-défini-tion-de-la-remédiation1-la-remédiation-p/199630273741523/

[9] A. Zbadi, "La Problématique Du Soutien Scolaire Au Maroc. Diagnostic Et Perspectives," Semion Med, Haut Commissariat Au Plan, Centre National De Documentation, 107–129, 2018.

[10] M. Bray, "L'ombre Du Système Educatif : Quel Soutien Scolaire Privé, Quelles Politiques Publiques ?," Institut International De Planification De L'éducation (UNESCO, France), 110–111, 2011.

[11] D. Glasman, B. Leslie, "Le Travail Des Elèves Pour L'école En Dehors De

L'école," Haut conseil de l'évaluation de l'école France, 52–53, 2004.

[12] Conseil supérieur de l'éducation et de la formation , "Charte nationale d'éducation et de formation, Maroc, Rabat," 1999, www.takween.com/charte-part2.html.

[13] A. Rhazal, N.E. Elidrissi, A. Elhajjami, "Les Elèves Marocains Et Le Soutien Scolaire : Recours Au Soutien Privé Et Usage D'internet," EpiNet, 2014.

[14] D. Bucheton, "Du Portfolio Au Dossier Professionnel : Eléments De Réflexion," Montpellier, IUFM de Montpellier Equipe LIRDEF ALFA, 2003, http://probo.free.fr/textes\_amis/portfolio\_bucheton.pdf.

[15] R. Bibeau, "L'usine a gaz ou le eportfolio de Big Brother," Formation et Profession , 33–36, 2006.

[16] A. Vallerand, S. Martineau, "Recension Des Ecrits Sur Le Portfolio Et Le E-Portfolio, En Tant Qu'outils Pouvant Favoriser L'insertion Professionnelle En Enseignement," Québec: Laboratoire D'analyse De L'insertion Professionnelle En Enseignement, Université du Québec à Trois-Rivières, 2007.

[17] H. Barrett, "Electronic Portfolios," Abc Clio, 2001, transition.alaska.edu/www/portfolios.ht.

[18] United Nations Educational Scientific and Cultural Organization, "Information and Communication Technologies in Teacher Education. A planning guide," unesdoc.unesco.org/images/0012/001295/129533e.pdf.

[19] G. Baron, E. Bruillard, "Les Technologies De L'information Et De La Communication En Education Aux USA : Eléments D'analyse Sur La Diffusion D'innovations Technologiques," Revue Française de Pédagogie, 37–49, 2003.

[20] M. Quebec, "Portfolio Sur Support Numérique: Ministère De L'éducation Du Québec, Direction Des Ressources Didactiques," Ministère de l'Education du Québec , 2002 , www.education.gouv.qc.ca/fileadmin/site\_web/documents/dpse/ress\_didactiques/portfolio.pdf.

[21] N. Duroisin, "L'approche Orientante, Le Portfolio, Conception Et Modèle D'utilisation, En Route Vers La Réussite Scolaire Et Professionnelle Des Elèves," Hainaut: UMONS, 2011.

[22] J. Pierrette, "Le Portolio Scolaire : Une Autre Façon D'évaluer Les Apprentissages," Vie pédagogique, 31–33, 1997.

[23] C.E. Bavay, "Le Portfolio En Education : Concept Et Usages," Journal International des Sciences de l'Information et de la Communication, 9–11, 2004. isdm.univ-tln.fr/PDF/isdm18/27-eyssautier.pdf.

[24] S. Nai, A. Rifai, A. Sadiq, "Proposal For a Computer-based Tutoring Strategy," IEEE INISTA Kocaeli, Turkey, 2021, doi: 10.1109/INISTA52262.2021.9548452.

# Markov Regime Switching Analysis for COVID-19 Outbreak Situations and their Dynamic Linkages of German Market

Kangrong Tan<sup>\*1</sup>, Shozo Tokinaga<sup>2</sup>

<sup>1</sup>Faculty of Economics, Kurume University, Fukuoka, 839-8502, Japan

<sup>2</sup>Department of Economics, Kyushu University, Fukuoka, 819-0395, Japan

## ARTICLE INFO

### Article history:

Received: 22 February, 2023

Accepted: 25 April, 2023

Online: 15 May, 2023

### Keywords:

COVID-19 outbreak

German stock index(DAX)

Markov Regime Switching Analysis (MRSA)

GARCH(Generalised Autoregressive heteroscedasticity)

Stock returns

Growth rates of the disease

Volatility

## ABSTRACT

This paper deals with the analysis of the dynamic linkage, co-movement between COVID-19 outbreak situations and German stock market. Firstly, Markov Regime Switching Analysis(MRSA) is proposed and employed to investigate the situations in the pandemic, as to catch the dynamics of how the daily number of the newly-infected changes, and also to assess the impact of the pandemic situations on German Market. Secondly, we compute the log growth rates of the weekly new cases and the log-returns of weekly DAX index, then fit the GARCH models to both of them to acquire their volatilities. We then employ the MRSA model once more to expose the dynamic linkages and co-movement between these two volatilities series. Through our empirical analyses, we find that GARCH models can capture the dynamics of stock returns and the growth rates. On the other hand, the MRSA models work well to identify the dynamics between different regimes with different states in dealing with the volatilities obtained from the estimated GARCH models. Our proposed econometric methods are highly practical, it indicates the possibility of replicating the results obtained in this study to assess the impact of other epidemics and negative factors on economic activities. Knowing what may happen during a pandemic, more effective measures and actions can be taken to protect people while dealing with another pandemic in the future.

## 1 Introduction

This paper is an extension of work originally presented in CICS2021 [1]. After the presentation at the conference CICS2021, we have done more researches on this issue and more interesting empirical results are obtained and updated in this extension version.

In the past decades, many approaches have been developed to tackle a time-varying time series. The main idea is how to separate the whole data set(interval) into several subsets(subintervals) with different statistical characteristics.

One of the methodologies is to detect change point or structural change in data [2]–[9]. One is to track the time-varying series using a Particle Filter [10], [11]. But, in this study, we propose to apply the Markov Regime Switching Analysis (MRSA) models to the time-varying data. The reason is that a time-varying series can be efficiently and appropriately split into several subintervals with different statistical characteristics(or different state-specific regimes) by using the MRSA models. Namely, the dynamics of these subintervals can be well captured by MRSA [12]–[21].

And in many cases the regime changes are corresponding to the

change points. Regimes indicate the situations of the infected cases, or the specific-state subintervals(market states).

Another methodology we employ in this study is GARCH(Generalised Autoregressive heteroscedasticity) model [22], [23]. Since GARCH model can help us get different and consecutive subintervals based on the conditional heteroscedasticity and has been utilized ranging from finance to psychology [24]–[27]. We fit the stock returns of DAX Index and the growth rates of COVID-19 to GARCH models to get their volatilities. And then apply MRSA to the volatilities, to investigate and assess the impact of the pandemic on the German stock market [1], [12]–[21].

Focusing upon the changes of DAX Index is that Germany is the industry leader country in the Europe Union(EU), it is important to know what impact had on the German stock market during the COVID-19 pandemic. Knowing what may happen during a pandemic, we can predict and do more better while dealing with another pandemic in the future.

The remainder of this paper is organized as follows. Section 2 shows an overview of our proposed Markov Regime Switching

\*Corresponding Author: Kangrong Tan, Faculty of Economics, Kurume University, Japan. Tel: 0942-43-4411 & Email: camox.wein.london@gmail.com

Analysis(MRSA). Section 3 explains the data sets we use in this study. Section 4 summarizes the outbreak situations in Germany. Section 5 presents our empirical results in situation analysis of the disease outbreak, and its impact on the market, by using the MRSA models. Section 6 displays the MRSA results by using the volatilities obtained by the GARCH model fittings. Section 7 gives concluding remarks.

## 2 An Overview of Markov Regime Switching Analysis

We here just give an overview of Markov Regime Switching Analysis before we present the results of our empirical analyses below [12]–[21].

Usually MRSA is utilized to depict the dynamics of a time series by using regime states. Regime states describe the different segments of a time series in different states. The common example of regime states is of two different states, denoted as  $s_t$ , either  $s_t = 0$  or  $s_t = 1$ , presenting two different regimes.

A common MRSA model is to do regression assuming different regime states existing in the data. The advantage of this method is that one can expose the varieties around the means. Such as,

$$y_t = \mu_{s_t} + \epsilon_t \quad (1)$$

where  $s_t = 0$  or 1 means that data  $y_t$  have two different mean levels in different segments, where  $\epsilon_t$  follows a Gaussian process with mean zero and variance  $\sigma^2$ . State zero ( $s_t=0$ ) corresponds to Regime 1, and vice vice.

Another usage of MRSA is to build an Markov regime switching autoregressive Model. A generalised presentation of the model can be described as follows, assuming the AR model with order  $p$ , namely,

$$y_t = c_{s_t} + \alpha_{s_t} x_t + \beta_{1s_t} y_{t-1} + \dots + \beta_{ps_t} y_{t-p} + \epsilon_{s_t} \quad (2)$$

where  $x_t$  is called as exogenous variable. The transition probabilities are usually defined as a first order Markov chain. Thus, a transition probability matrix  $P$  with  $n$  states can be represented as follows.

$$P = (p_{ji}) = \begin{pmatrix} p_{11} & p_{12} & \dots & p_{1n} \\ p_{21} & p_{22} & \dots & p_{2n} \\ \vdots & \vdots & \ddots & \vdots \\ p_{n1} & p_{n2} & \dots & p_{nn} \end{pmatrix} \quad (3)$$

where  $i, j = 1, 2, \dots, n$ , with  $\sum_{j=1}^n p_{ji} = 1$ , and  $p_{ji}$  is the probability of transitioning from regime  $i$  to regime  $j$ .

While, a simplified case of (2) is that a Markov regime switching autoregressive model without an exogenous variable.

The following model shows the time-varying data  $y_t$  follows two different AR(1) equations with different parameters, for example.

$$y_t = \begin{cases} \beta_0 + \beta y_{t-1} + \epsilon_t, & (s_t = 0) \\ (\beta_0 + \beta_1) + \beta y_{t-1} + \epsilon_t, & (s_t = 1) \end{cases} \quad (4)$$

What (1)-(4) mean is that the time-varying observations fluctuate when state or regime shifts from one to another.

The estimation of parameters of regime-switching models is implemented by maximizing the likelihood function.

## 3 Data Description

In this study, we use the following two data sets.

1) DAX(daily), which is known as the GER40 as well, comprised of 40 German companies traded on the Frankfurt Exchange. We obtained the data from Yahoo(<https://de.finance.yahoo.com>). The period of the data set is ranged from Jan, 2020 to Jul, 2021.

2) The newly infected cases of COVID-19(daily). We obtained the data from WHO's Website, in the same period.

These two data sets are open to the public on above-mentioned websites, and can be downloaded freely, at any time.

## 4 Situations of COVID-19 Outbreak

Germany is the industry leader in the Europe Union(EU), and it is important to investigate how the German stock market was impacted from the pandemic. We thus focus upon the situations in Germany.

In Germany, the ups and downs of the newly confirmed number(daily) are shown in Figure 1, duration from January 22, 2020 to July 30, 2021.

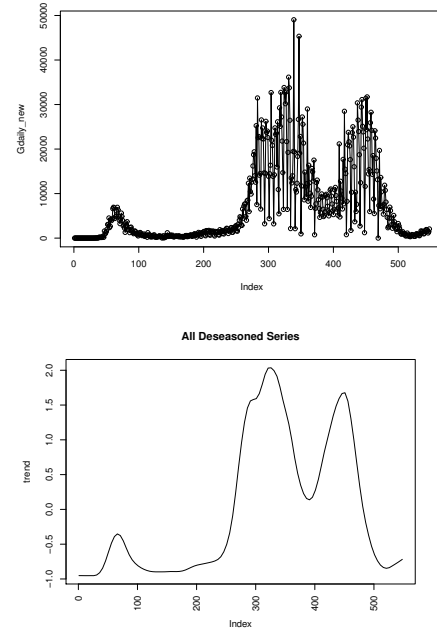


Figure 1: Daily newly confirmed number(left) and its trend(right)

It shows the newly confirmed number(daily) fluctuated with the lapse of time. The left small peak appeared when fewer cases were confirmed. However, gradually the newly confirmed number rose from zero level up to a big peak, and then decayed to its half level around. Sooner, the third peak appeared when the newly confirmed number surged once more. One may be interested in identifying change points, we had successfully identified the change points in this time series based upon a Bayesian approach[8], [9].

With the spread of infection of COVID-19 in Europe, lockdown policy had been employed in many countries, since the newly confirmed cases were growing up and up. The government enforced lockdown in Nov, 2020, and it had not been lifted until Jun, 2021, about 8 months long.

Besides, mask-wearing, social distancing, staying home and other public health measures had been also implemented, these measures had shown their effects on reducing newly infected cases.

## 5 Empirical Research

We then carry out some empirical analyses by using the above-mentioned two data sets.

### 5.1 Markov Switching Regression Analysis

Firstly, the Markov regime switching regression model is applied to the data. Table 1 shows the estimated results.

Table 1: Estimated results

Intercept	Regime 1	Regime 2
Estimate	12889	844.336
Std. Error	557	43
t value	23	19
$Pr(>  t )$	2.2e-16***	2.2e-16***
AIC	10178.62	
Likelihood	-5087.31	

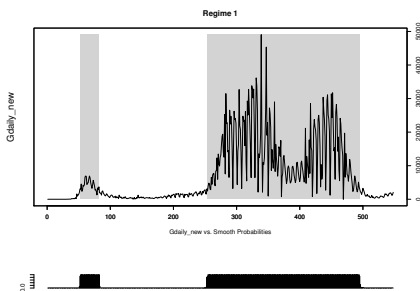


Figure 2: Regime 1 is represented in gray

Figure 2 shows the estimated areas of Regime 1 in gray. Seen from the figure, the peaks of daily infected number are identified as Regime 1 in gray, and vice vice.

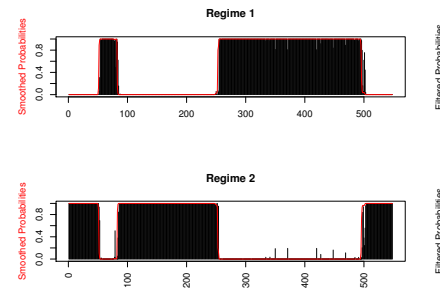


Figure 3: Plots of estimated probabilities of Regime 1 and 2

Figure 3 displays the estimated transition probabilities of Regime 1 and 2.

The corresponding transition probabilities are estimated and shown in Table 2. While, the corresponding confidence intervals(Level= 0.95) for the Intercepts estimated above are shown in Table 3.

Table 2: Estimated transition probabilities

	Regime 1	Regime 2
Regime 1	0.9926	0.0074
Regime 2	0.0074	0.9926

Table 3: Confidence intervals for the estimated intercepts

Intercept	Regime 1	Regime 2
Estimation	12889.56	844.34
Lower	11796.06	760.02
Upper	13983.05	928.65

Thus, the ability and the practicality of MRSa to precisely identify the different subintervals with their-own specific states have been confirmed distinctly.

### 5.2 Daily Growth Rate of the Disease

In this section, we discuss how the daily growth rates of the disease evolved. The daily growth rate is defined as follows.

$$dailygrowthrate_t = \log(dailynewcases)_t - \log(dailynewcases)_{t-1} \quad (5)$$

The plot of the calculated daily growth rates is shown in Figure 4.

It is shown that the daily infected cases were increasing(the first surge of the growth rates) in the early stages, and those infected people mostly got proper treatment in hospitals and discharged from the hospitals later.

We also can confirm the second surge of the growth rates around the Xmas holidays. And the growth rates got lower around the 500th day. We then apply the Markov regime switching regression model to the daily growth rates.

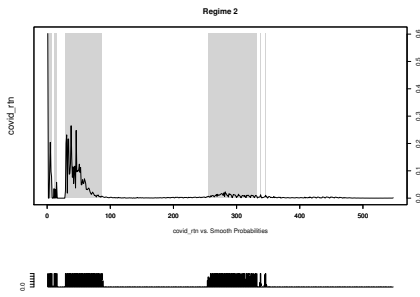


Figure 4: Regime 2 in gray indicates the areas of increasing growth rates

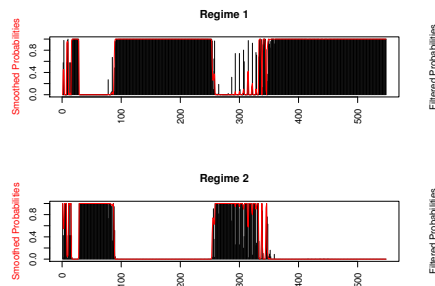


Figure 5: The Smoothed transition probabilities

Figure 4 and 5 display the two switching regimes and their corresponding smoothed transition probabilities, respectively.

The estimated results are summarized in the following Table 4 and 5. Table 4 shows the estimated intercept and its standard error, t value, and  $Pr(> |t|)$ , and Table 5 gives the estimated transition probabilities, respectively.

Table 4: Estimated intercept and the corresponding statistics

Intercept	Regime 1	Regime 2
Estimate	0.0016	0.0395
Std. Error	0.0001	0.0058
t value	16	6.8103
$Pr(>  t )$	2.2e-16 ***	9.7e-12 ***
AIC	-4408.92	
Likelihood	2206.46	

Table 5: Estimated transition probabilities

Transition probabilities	Regime 1	Regime 2
Regime 1	0.9807	0.0444
Regime 2	0.0193	0.9556

### 5.3 Applications of Markov Switching Autoregression Model

Here we apply the above-mentioned Markov switching autoregressive model of order  $p$  to our two data sets. In the following appli-

cations, we transform these two daily data sets into weekly ones, namely,  $DAX_{weekly}$ , and  $Newcases_{weekly}$ .

#### Application 1: Autoregressive model of order 1

That is to say, we fit the variables as follows.

$$DAX_{weekly} \sim Newcases_{weekly} + DAX_{weekly}(t - 1). \quad (6)$$

As a result of this model setting, the following facts are revealed and summarized in Table 6 and 7.

Looking at these tables, it is clear that most of the estimated parameters are statistically significant, except the intercept in Regime 1, and the coefficient of  $Newcases_{weekly}$  in Regime 2.

The multiple R-squared is estimated as 0.8053, and 0.986 in Regime 1 and 2, respectively.

Meanwhile, the state transition probabilities are summarized in Table 8.

The confidence intervals(CI)(Level= 0.95) for the estimated parameters, namely, intercept, the coefficients of  $Newcases_{weekly}$  and  $DAX_{weekly}(t - 1)$  are displayed in Table 9 and 10.

Table 6: Estimated results of Regime 1

Regime 1	Intercept	$Newcases_{weekly}$	$DAX_{weekly}(t - 1)$
Estimate	1325.08	0.3516	0.8482
Std. Error	1376.41	0.1887	0.1116
t value	0.963	1.8633	7.6004
$Pr(>  t )$	0.3357	0.06242 .	2.95e-14***
AIC	1101.393		
Likelihood	-544.6966		

Table 7: Estimated results of Regime 2

Regime 2	Intercept	$Newcases_{weekly}$	$DAX_{weekly}(t - 1)$
Estimate	521.332	-0.007	0.9700
Std. Error	221.256	0.016	0.0167
t value	2.356	-0.409	58.0838
$Pr(>  t )$	0.01846*	0.683	2e-16***

Table 8: Estimated state transition probabilities

	Regime 1	Regime 2
Regime 1	0.6348	0.0852
Regime 2	0.3652	0.9148

Table 9: Confidence intervals for the parameters in Regime 1

	Intercept	$Newcases_{weekly}$	$DAX_{weekly}(t - 1)$
Estimation	1325.0807	0.3516	0.8482
Lower	-1367.0203	-0.0182	0.6298
Upper	4017.1817	0.7214	1.0665



Table 10: Confidence intervals for the parameters in Regime 2

	Intercept	Newcases <sub>weekly</sub>	DAX <sub>weekly</sub> (t - 1)
Estimation	521.3317	-0.0067	0.97
Lower	87.5582	-0.0386	0.937
Upper	955.1051	0.0252	1.0027

These two shifting regimes and their corresponding transition probabilities are displayed in Figure 6 and 7, respectively. Seen from the Figure 6, Regime1(in gray) captures the steep descent of DAX.

As can be seen from the results above, it is clear that, the Markov regime switching autoregressive model of order one captures the sudden ups and downs of the observations. It means that, in the early stages, volatile movements in the market are observed due to the growth of daily new cases, but, after the fortieth day, the change of the stock index slowed down, as if the market had acclimatized to the disease.

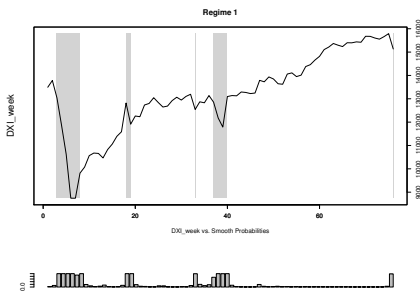


Figure 6: Regime 1(in gray) captures the steep descent of DAX

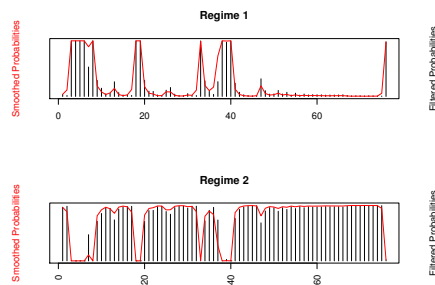


Figure 7: Smoothed transition probabilities

**Application 2: Autoregressive model of order 2**

We here fit the variables of our data sets by using Markov regime switching autoregressive model of order 2. Namely,

$$DAX_{weekly} \sim Newcases_{weekly} + DAX_{weekly}(t-1) + DAX_{weekly}(t-2).$$

The numerical results are summarized in Table 11 and Table 12. Seen from these tables, it is clear that most of the estimated statistics are better than the results of AR(1) model obtained above, even the multiple R-Squared is better in each Regime.

Table 11: Corresponding statistics of Regime 1

	Intercept	Newcases <sub>weekly</sub>	DAX <sub>weekly</sub> <sup>(t-1)</sup>	DAX <sub>weekly</sub> <sup>(t-2)</sup>
Estimate	2642.633	0.367	1.337	-0.584
Std. Error	1365.812	0.170	0.227	0.262
t value	1.935	2.152	5.892	-2.231
Pr(>  t )	0.0530	0.0314*	3.8e-9***	0.0257*
R-squared	0.857			
AIC	1083.065			
Likelihood	-533.5325			

Table 12: Corresponding statistics of Regime 2

	Intercept	Newcases <sub>weekly</sub>	DAX <sub>weekly</sub> <sup>(t-1)</sup>	DAX <sub>weekly</sub> <sup>(t-2)</sup>
Estimate	586.227	0.0006	0.867	0.098
Std. Error	217.604	0.016	0.078	0.075
t value	2.694	0.038	11.134	1.302
Pr(>  t )	0.0071**	0.9699	2e-16***	0.193
R-squared	0.9871			

The estimated state transition probabilities are listed in Table 13.

Table 13: Estimated state transition probabilities

	Regime 1	Regime 2
Regime 1	0.7071	0.0904
Regime 2	0.2929	0.9096

Furthermore, looking at Table 11, we see that the weekly new cases do have impact on the market, meanwhile DAX<sub>weekly</sub>(t-1), DAX<sub>weekly</sub>(t-2) show statistically significant in this AR(2) model setting. It also can be confirmed that Figure 8 captures the stock market plunges precisely. In other words, it reveals that Markov Switching Autoregressive Analysis can identify change points precisely as well as other tools, the change point identification based upon a Bayesian approach, for example.

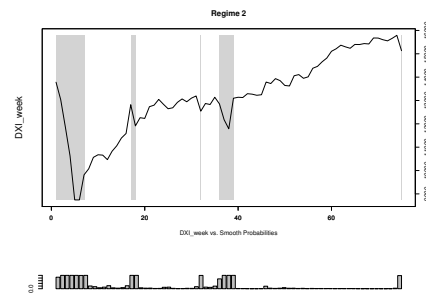


Figure 8: Regime 2(in gray) captures the market plunges

**6 Fitting the Datasets Using GARCH Models**

In this section, we first fit our two datasets using GARCH models, since GARCH model is considered to be a useful mean for capturing

the dynamics in data.

The dynamics or the momentum can be described by the volatilities series obtained from GARCH model. Second, we apply MRSA to the volatilities to see whether there exists some sort of co-movement between the weekly growth rates of the disease and the weekly returns of stock index.

Details of GARCH model are omitted here, one may get more information from other references, such as, [22], [23]. Hereafter, we just display our empirical results.

Our model fittings reveal that GARCH(1,1) and GARCH(1,0) are the best choices for the weekly returns of DAX and the weekly growth rates of the disease.

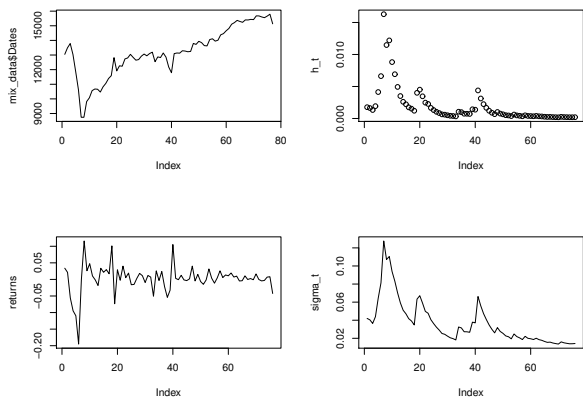


Figure 9: Plots of the results of GARCH(1,1) for returns

Table 14: Summarized results for GARCH(1,1)

	omega	alpha1	beta1	skew
Estimation	4.4675e-05	0.30499	0.70171	0.84704
Std err	3.785e-05	0.1497	0.1032	0.1021
t Value	1.180	2.037	6.798	8.299
Pr(>  t )	0.2379	0.0416*	1.1e-11***	2e-16***
AIC				-4.0190
BIC				-3.8964
HQIC				-3.9700
Likelihood				-156.72

The plots of weekly stock returns and the weekly number of the newly infected are shown in Figure 9 (leftup) and Figure 10 (leftup) below. It seems that the DAX Index didn't react sensitively, in corresponding to the changes of the weekly new cases. However, we get completely different results if we fit the weekly stock returns and growth rates using GARCH models, and then apply the Markov regime switching autoregressive model to volatilities obtained from the GARCH model fittings.

### 6.1 Fitting Results of DAX Index

By setting different  $p, q$  values in GARCH(p,q), we find that GARCH(1,1) fits the weekly DAX returns most appropriately, where  $returns_{weekly} = \log(r_t) - \log r_{t-1}$ , where  $r_t$  is the price at week  $t$ . It

indicates the weekly returns follow a skewed normal distribution based upon the numerical results.

The fitting results are shown in Table 14. Looking at the table, we see it is a good fit.

The original time series of weekly DAX Index, its returns,  $h_t$ , and  $\sigma_t$  values obtained from the GARCH(1,1) model, are shown in Figure 9, respectively.

It can be confirmed in both Table 14 and Figure 9, that the dynamics of the weekly stock returns is well-captured by GARCH(1,1) model.

### 6.2 Fitting Results of Weekly Confirmed Number

Similarly to the DAX index above, we calculate the corresponding weekly growth rates of the disease, namely,  $growthrate_{weekly} = \log n_t - \log n_{t-1}$ , where  $n_t$  is the number at week  $t$ . We then fit the weekly data set using GARCH(p,q) model. By setting different  $p, q$  values in the model, we find that GARCH(1,0) fits the weekly growth rates most appropriately.

The fitting results are shown in Table 15. Looking at the table, we see a skewed normal distribution is detected, because of the data's statistical properties. It indicates that the dynamics of the statistical properties of the data is well captured by a skewed normal distribution. And what is more important is that all the corresponding statistics are statistically significant, a good fit as well.

Table 15: Summarized results for GARCH(1,0)

	omega	alpha1	skewness
Estimate	0.2337	0.2936	1.0158
Std. Error	0.0465	0.1534	0.1322
t value	5.025	1.914	7.685
Pr(>  t )	5.03e-07***	0.0557.	1.53e-14***

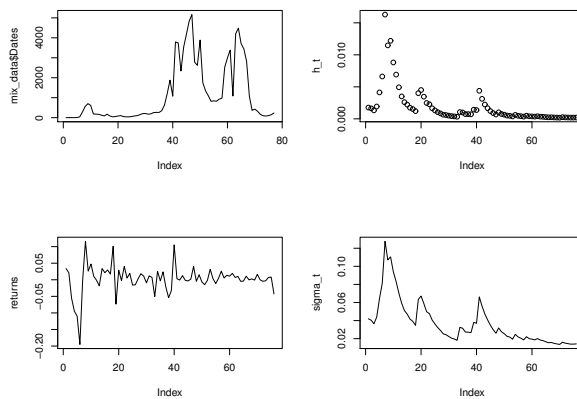


Figure 10: Plots of the results of GARCH(1,0) for growth rates

Similarly, the original time series of weekly number of new cases, weekly growth rates,  $h_t$ , and  $\sigma_t$  values obtained from the GARCH(1,0) model, are shown in Figure 10, respectively.

It can be confirmed in both Table 15 and Figure 10, that the dynamics of the weekly growth rates is well captured by GARCH(1,0) model.

### 6.3 MRSA for Volatilities Obtained from GARCH Models

In order to investigate the linkage and co-movement between the stock returns and the growth rates of the disease, we carry out MRSA based upon (2) using these two volatilities series ( $\sigma_t^{return}, \sigma_t^{growthrate}$ ), which are obtained from the GARCH(1,1) and the GARCH(1,0) models for the weekly returns and growth rates, respectively.

The estimated results are summarized in Table 16 and 17. And the linkage and co-movement are shown in Figure 11 and 12.

Seen from Table 16, the growth rate of the disease, which is regarded as an exogenous variable in the model setting, makes a severe impact on the stock change no matter which regime it stays.

Table 16: Estimated parameters for MRSA

Regime 1	Estimation	Std. Error	t value	Pr(>  t )
(Intercept)	0.0007	0.0009	0.7778	0.4367
$\sigma_t^{growthrate}$	0.0031	0.0016	1.9375	0.0527 .
$\sigma_{t-1}^{return}$	0.8264	0.0059	140.068	2e-16***
R-squared	0.9972			
Regime 2	Estimation	Std. Error	t value	Pr(>  t )
(Intercept)	-0.0151	0.0070	-2.1571	0.031*
$\sigma_t^{growthrate}$	0.0424	0.0107	3.9626	7.4e-05***
$\sigma_{t-1}^{return}$	0.9644	0.1090	8.8477	2.2e-16***
R-squared	0.8972			

The estimated state transition probabilities are shown in Table 17.

Table 17: Transition probabilities

	Regime 1	Regime 2
Regime 1	0.8075	0.5387
Regime 2	0.1925	0.4613

The smoothed state transition probabilities are shown in Figure 11, Regime 1(up), and Regime 2(down).

And Regime 1 is displayed in Figure 12. It can be seen that the decayed  $\sigma_{t,s}$  of DAX Index are captured in gray(Regime 1). These decayed parts (intervals) are corresponding to the change points as well.

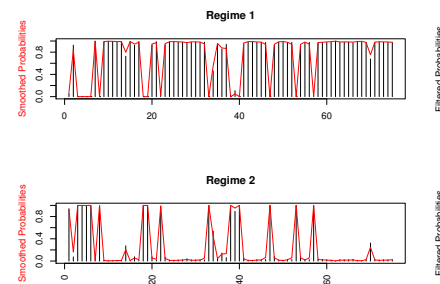


Figure 11: Smoothed state transition probabilities of regimes

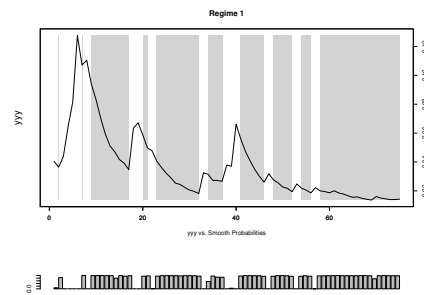


Figure 12: Regime 1 shows the decayed parts of DAX(YY=σ<sub>t</sub>)

Through our numerical analyses, it is confirmed that our proposed the Markov Regime Switching Analysis models are effective in investigating the dynamics, linkage and co-movement between the stock returns and the growth rates of the disease, namely, the statistical characteristics of the data are captured more precisely by using the volatilities obtained from GARCH models.

## 7 Concluding Remarks

In this paper, we have proposed and employed econometric apparatus and tools, the Markov Regime Switching Analysis method and other methods to investigate the situations of the outbreak of COVID-19 and its impact on German stock market.

It has been confirmed that the dynamics, linkage and co-movement between stock returns and growth rates of the disease are well captured by our proposed MRSA models through our numerical analyses.

Moreover, it has been confirmed that it is effective in precisely capturing the linkages between the stock returns and the growth rates of the disease by using volatilities obtained from GRACH models.

Our proposed methods are highly practical, it indicates the possibility of replicating the results obtained in this study to assess the impact of other epidemics and negative factors on economic activities, and provide researchers and policy-makers with a clue of how a pandemic evolved and what impact on the economies. It may lead to better measures and actions while dealing with another pandemic in the future.

## Acknowledgment

The authors are grateful to the reviewers' valuable comments that improved the manuscript. This study was partly supported by the Japan Society for the Promotion of Science(JSPS) KAKENHI Grant Number(c)18K04626. The authors would like to thank the organization.

## References

- [1] K.R. Tan, S. Tokinaga, "Markov Regime Switching Analysis for the Pandemic and the Dynamics of German Market," Proceedings of International Conference on Computational Science and Computational Intelligence(CSCI), IEEE Xplore, 2021.
- [2] D.W.K. Andrews, "Tests for parameter instability and structural change with unknown change points," *Econometrica*, **61**, 821-856, 1993.
- [3] J. Chen, A.K. Gupta, "Change point analysis of a Gaussian model," *Statistical Papers*, **40**, 323-333, 1999.
- [4] F. Desobry, M. Davy, C. Doncarli, "An online kernel change detection algorithm," *IEEE Trans. Signal Process*, **53**(8), 2961-2974, 2005.
- [5] G. Koop, S.M. Potter, "Estimation and forecasting in models with multiple breaks," *Review of Economic Studies*, **74**(3), 763-789, 2007.
- [6] R. Malladi, G.P. Kalamangalam, B. Aazhang, "Online Bayesian Change Point Detection Algorithms for Segmentation of Epileptic Activity," *Asilomar Conference on Signals, Systems and Computers*, 1833-1837, 2013.
- [7] J. Knoblauch, T. Damoulas, "Spatio-temporal Bayesian On-line Change-point Detection with Model Selection," Proceedings of the 35th International Conference on Machine Learning(ICML-18), 2718-2727, 2018.
- [8] K.R. Tan, "Detecting structural changes in stochastic differential equation system based upon a Bayesian approach," *Journal of Economic and Social Research*, **58**(1-2), 51-67, 2018.
- [9] K.R. Tan, "Identifying the pandemic change points of COVID-19 outbreak: case studies in Germany, Italy and Austria," *Journal of Economic and Social Research*, **61**(2-3), 19-33, 2021.
- [10] S. Tokinaga, S. Matsuno, "Estimation of Transition of Credit Rating by Using Particle Filters Based on State Equations Approximated by the Genetic Programming," *IEICE Proceeding Series*, **45**, 397-400, 2011.
- [11] F. Caron, A. Doucet, R. Gottardo, "On-line changepoint detection and parameter estimation with application to genomic data," *Stat Comput*, **22**, 579-595, 2012.
- [12] J.D. Hamilton, "Rational-expectations econometric analysis of changes in regimes: an investigation of the term structure of interest rates," *Journal of Economic Dynamics and Control*, **12**, 385-423, 1998.
- [13] J.D. Hamilton, "A new approach to the economic analysis of nonstationary time series and the business cycle," *Econometrica*, **57**, 357-384, 1989.
- [14] J.D. Hamilton, *Time series analysis*, Princeton University Press, 1994.
- [15] S. Goutte, B. Zou, "Foreign exchange rates under Markov regime switching model," *Center for Research in Economic Analysis Discussion Paper*, **16**, 1-29, 2011.
- [16] A. Ramponi, "VaR-optimal risk management in regime-switching jump-diffusion models," *Journal of Mathematical Finance*, **3**(1), 103-109, 2013. DOI: 10.4236/jmf.2013.31009
- [17] S. Choi, M. Marozzi, "A regime switching model for the term structure of credit risk spreads," *Journal of Mathematical Finance*, **5**, 49-57, 2015. DOI: 10.4236/jmf.2015.51005
- [18] H. Boubaker, N. Sghaier, "Markov-switching time-varying copula modeling of dependence structure between oil and GCC stock markets," *Open Journal of Statistics*, **6**, 565-589, 2016. DOI: 10.4236/ojs.2016.64048
- [19] S. Gyamerah, P. Ngare, "Regime-switching model on hourly electricity spot price dynamics," *Journal of Mathematical Finance*, **8**, 102-110, 2018. DOI: 10.4236/jmf.2018.81008
- [20] G. Stefano, O. Aydin, S. Abhijit, J. Mazin, "Pricing of time-varying illiquidity within the Eurozone: evidence using a Markov switching liquidity-adjusted capital asset pricing model," *International Review of Financial Analysis*, **64**, 145-158, 2019. DOI: 10.1016/j.irfa.2019.05.002
- [21] Z. Qu, Z. Fan, "Likelihood ratio-based tests for Markov regime switching," *Review of Economic Studies*, **88**(2), 937-968, 2021. DOI: 10.1093/restud/rdaa035
- [22] R. Engle, "Autoregressive conditional heteroscedasticity with estimates of the variance of United Kingdom inflation," *Econometrica*, **50**, 987-1007, 1982.
- [23] T. Bollerslev, "Generalized autoregressive conditional heteroskedasticity," *Econometrics*, **31**, 307-327, 1986.
- [24] P. Yu, T. Liu, Q. Ding, "Volatility analysis of web news and public attitude by GARCH model," *Psychology*, **3**, 610-612, 2012. DOI: 10.4236/psych.2012.38092
- [25] C. Dritsaki, "An empirical evaluation in GARCH volatility modeling: evidence from the Stockholm stock exchange," *Journal of Mathematical Finance*, **7**, 366-390, 2017. DOI: 10.4236/jmf.2017.72020
- [26] W. Zhang, P. Yang, "Research on dynamic relationship between exchange rate and stock price based on GARCH-in-mean model," *Journal of Service Science and Management*, **11**, 691-702, 2018. DOI: 10.4236/jssm.2018.116046
- [27] A. Ngunyi, S. Mundia, C. Omari, "Modelling volatility dynamics of cryptocurrencies using GARCH models," *Journal of Mathematical Finance*, **9**, 591-615, 2019.

# Inferring Student Needs Based on Facial Expression in Video Images

Yu Yan\*, Eric Wallace Cooper, Richard Lee

Information Systems Science and Engineering, College of Information Science and Engineering, Ritsumeikan University, Kusatsu, 525-8577, Japan

---

## ARTICLE INFO

Article history:

Received: 28 February, 2023

Accepted: 26 April, 2023

Online: 15 May, 2023

---

Keywords:

Student needs

Online education

Facial Action Units

Exploratory Factor Analysis

Random Forests

---

---

## ABSTRACT

Limited interactive communication modes between students and teachers in online environments may lead to teachers misinterpreting or overlooking student needs during online teaching. Students learning online may also hesitate to make their needs known even when latent desires in teaching flow, pacing, and review, may be beneficial to the quality of the learning experience. The objective of the study is to construct and test models to infer student needs based on the facial expressions of students while they are learning online. Several Random Forest models were constructed to infer the reported conditions and tested using facial expression data extracted from the videos as action units in Facial Action Coding System (FACS). Exploratory Factor Analysis (EFA) was adopted to extract and combine the highly-related facial action units for building the training and testing data. The testing of the inference model yielded a result of 0.028 on the mean average error (MAE). This result suggests these methods would contribute to the development of improved online learning systems that assist teachers in understanding in real-time how students are responding to a lecture or other classroom experience.

---

## 1 Introduction

With the sudden expansion of online teaching from 2020, due in large part to measures intended to prevent opportunities for transmission of the SARS-Cov-2 virus, teachers and students were suddenly confronted by many of the difficulties associated with online learning environments. Among those difficulties is significantly fewer points at which a student can indicate feedback to a teacher, or a teacher can take a quick reading of the room to investigate facial expressions, sounds, body movements, and the like. The objective of this research is to investigate the feasibility of using video of students to monitor their facial movements in order to infer needs the students may wish to communicate to the teacher without unnecessarily interrupting the flow of the class. Here, student needs refers to implicit or latent requests about class flow and pace, such as increased or decrease in teaching speed, review of material introduced in this lecture, requests for breaks, and the like. The concept, as envisioned here, uses only local video monitoring and therefore can avoid privacy issues, as well as video and audio resolution difficulties, involved when classrooms rely on direct video of student faces during learning. The present study extends a study originally presented in the 10th International Conference on Information and Education Technology (ICIET 2022) by describing an investigation of new methods of inferring student needs in an online teaching

scenario and the results of testing these methods on the experiment data presented in the previous work [1]

During the 2020 and 2021 academic years, schools of all types but especially institutions of higher learning, greatly expanded the use of online platforms to deliver lectures and other teaching activities. Platforms such as Zoom [2], Skype [3], and Google Hangouts [4] were quickly adopted to allow student and faculty participation from home in order to minimize contact and quell the spread of the Covid-19 pandemic. Teachers who were mostly accustomed to lecturing, and students who had for the most part attended class, in a conventional classroom, quickly discovered that many common, established objectives of communication between student and teacher [5] may become far more difficult when learning online [6], [7]. For example, in a conventional classroom, teachers may more easily gauge student needs, such as, by periodically checking their facial expressions. In addition to monitor resolution and video quality questions, the direct use of video has also been a privacy concern for students studying in their own abodes or in shared spaces [8].

This study provides a model for automatically inferring student needs based on their facial expressions during online lectures. The Facial Action Coding System (FACS) [9] provides a methodology to identify human facial emotions by collecting a group of facial Action Units (AUs), which are collections of facial muscle movements. In this study, FACS is used to identify a student need from facial

---

\*Corresponding Author: Yu Yan, Ritsumeikan University, 1-chome-1-1, Nojihigashi, Kusatsu, Shiga, Japan, [yuyan@fc.ritsumei.ac.jp](mailto:yuyan@fc.ritsumei.ac.jp)

muscle movement at a certain moment. The inputs of the model are the intensity levels of AUs. Exploratory Factor Analysis (EFA) [10] is performed to reduce the number of inputs and determine the most effective combinations of AUs. Finally, Random Forests (RF) [11], a popular machine learning method for classification models were adopted to implement the inference models.

This article differs from the previously published conference paper titled “Inference of Student Needs in an Online Learning Environment Based on Facial Expression” in the following aspects. The introduction was significantly changed and expanded to discuss the relevance of this system for online learning support. The inference model was implemented with ten RF models to infer each student need rather than using one neural network model to infer ten student needs at once as in the conference paper, showing significantly improved accuracy. The experiment settings were significantly expanded, adding detail to the experimental methods, as well as deeper analysis and discussion of the experimental results. This paper further confirms the feasibility previously presented methods with added accuracy reported and further details for implementation in future online learning systems.

## 2 Related Work

Previous studies have investigated methods of automatically assessing student emotions during classroom activities. For example, in [12], the authors describe a method to provide teachers with emotional signals from their students based on measurements of electrodermal activity. Such methods, while offering immediate and relevant signals, also require shipping and local set up of equipment that is not typically part of the student’s hardware and software. This paper, on the other hand, describes methods that use hardware and software typically part of most student online equipment available in laptops (as in the present work) or other devices commonly used to participate in online learning.

Some approaches use the camera for eye tracking in an effort to use gaze detection signals, as such signals are thought to be relevant to both emotional responses and learning activities. For example, the authors in [13] propose a system that collects data on eye movements, such as blinking or the duration of a gaze in a single location, to determine how well a student is progressing in the visual contents during a lesson. Signals reporting on student concentration during a lesson, while certainly providing what could be processed into useful information for instructors, do not on their own give the teacher some understanding of how to respond in a positive manner. In other words, simply telling the teacher that students may not be concentrating does not necessarily assist the teacher in responding to that situation. Facial expressions allow acquisition of more specific states of emotional reaction than concentration alone.

Several systems have been developed to track student facial landmarks, head positions, facial actions, and eye movements in order to infer a student’s emotional state. For example, the systems described in [14] and [15] propose models to measure student engagement during video engagement based on facial expression data. The system described in [14] uses the Microsoft Kinect camera to acquire input data for a model to infer labels attached by a separate set of video observers. The work in [15] uses OpenPose [16] in a

similar manner to that in [13]. In such systems, video observers may not be able to pick up relevant but subtle cues in student expressions. Additionally, as noted above, tracking student emotions or concentration during learning does not necessarily yield information directly applicable to assisting teachers grasp student needs.

Therefore, the contributions of this study can be listed as follows:

- To propose a new approach to the improvement of online learning environments by providing teachers specific information about student status in terms of specific needs.
- To propose a novel model of inferring student needs based on their facial expressions and, according to the model proposed, an online education platform using commonly available device tools and processing power.
- To find and identify associations between specific needs and facial emotions.

## 3 Proposed Inference Model

A student needs inference model was proposed. Figure. 1 shows each component of the model. The following shows a detailed explanation:

- *Facial expression video recordings*: A front-facing camera continuously records facial expressions while students attend real-time online lectures or watch video lectures. The tracking system simultaneously transfers the facial expression recordings to the FACS server.

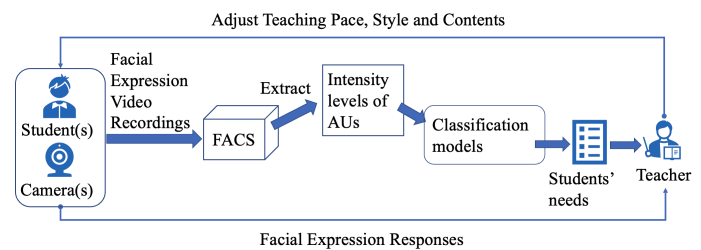


Figure 1: Model architecture for a student needs tracking system

- *Facial Action Coding System (FACS)*: FACS detects human facial emotions like surprise or fear using forty-six facial Action Units (AUs), each of which represents a collection of human facial movements. For example, levator palpebrae superioris, superior tarsal muscle facial muscle movements align to AU05’s definition of “Upper lid raiser”. Student needs depend only partly on their emotions. Therefore, the FACS method is used in this model to pre-process the video recordings. The input data of the classification models is composed of the intensity levels of the AUs from the pre-processing results. Here, an intensity level of each facial AU represents the confidence level of that facial AU.
- *Classification models*: In order to infer a list of student needs at a given moment, pre-trained supervised classification models are also necessary. These models are based on the intensity levels of the AUs.

- *Average of each need across all students:* In the end, the tracking system reports the average value of each need in the list, across all students, at a given moment. Ideally, the teacher will adjust the teaching pace, style and contents based on the reports from the tracking system.

This model can be used to build a student need tracking system for either real-time or on-demand online education. In the latter case, a teacher can adjust the teaching style and contents according to the overall output of the system.

## 4 Experiment Settings

This experiment simulates a situation in which students observe a college-level class given in an online video format with web cameras facing the students during the learning. Students were asked to watch educational videos that ranged from 8 to 9 minutes in length. Figure 2 shows the experiment flow for one viewing session. The experiment system automatically pauses the video every two minutes and requests that the student complete a survey on their current needs. After completing the survey the participant presses the “Play video” button in order to resume watching the video lesson. Other controls for the flow of the video were disabled in order to resemble real-time streaming participation. The web camera facing the student recorded facial expressions while the participants were watching the videos.

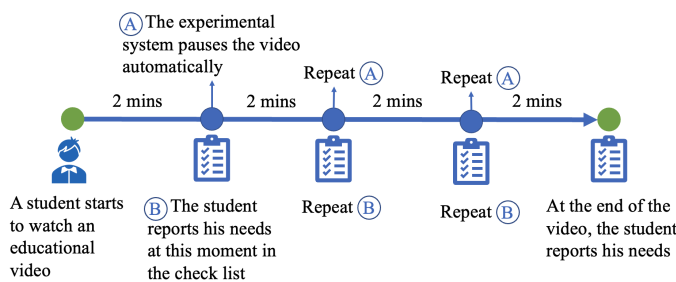


Figure 2: Human interaction experiment flowchart

The videos used in the experiment were three college-level educational videos, two selected from the Massachusetts Institute of Technology (MIT) OpenCourse [17] lectures on propositional logic and computing mathematics, and one of a recorded lecture given as a part of a C Language programming lecture at Ritsumeikan University, Japan, in which the topic is function declarations. This course is intended for students with no C programming experience and therefore precedes at a slower pace than the MIT courses selected. Due to privacy and consent considerations, the faces of students and teachers, as well as the voices of the students were omitted from this video. The three videos used in the experiments are each about fundamental computer science topics typically given to computer science students an intermediate level of difficulty in the curriculum. All three of the videos lectures employed a typical teaching format for such college courses, for example using slides to introduce and detail each main topic.

Seven students participated in the experiment. All of the students were in their 4th year of an undergraduate information systems

engineering curriculum.

### 4.1 Creation of a Student Needs Survey

Based on previous studies and investigations of student needs, in [18] and [6], with consideration for their findings on needs that would be of practical use during teaching, the survey asked students about ten specific needs or requests for the teacher. Table 1 shows the list of student needs surveyed after each video session. These student needs were also intended to be helpful for learning and may be classified by their general teaching objectives:

- Needs that allow the teacher to adjust teaching pace in order to allow enough time for teachers and students to progress in their learning activities, which includes the needs numbered 01, 02, 03, 05, 06, 07, 08 and 10.
- Needs that inform the teacher on teaching style in order to increase engagement and understanding during the lecture and subsequent activities, which includes the need numbered 09.
- Needs that give the teacher feedback on adjust teaching contents so that the teaching materials may be more effectively paired with subsequent lectures, as in the need numbered 04.

Table 1: List of student needs investigated

Student Needs No.	Student Needs Descriptions
01	Please teach faster
02	Please teach slower
03	Please wait a moment
04	Please skip this part
05	Please go back to the last part
06	Please explain more
07	Please let me ask a question
08	Please let me take a break
09	Please make the class more interesting
10	I don't need anything; please continue

### 4.2 Facial Action Unit Extraction using OpenFace Technology

The FACS toolkit, OpenFace [19] was used to extract AU intensity levels (or AU values) in each recorded facial expression video. Seventeen AU features have been extracted as shown in Table 2. Although OpenFace can not extract all forty-six AUs as mentioned in Section 3, the seventeen AU features extracted were enough for the purpose of this study.

Additionally, an AU correlation matrix, which is given in Table 3, was also calculated to show the linear correlations among the AU features using all of the recorded videos. The AU correlation matrix calculation method is by Equation 1, which is based on the Pearson correlation matrix [20].

$$r = \frac{Cov(x,y)}{\sigma_x \sigma_y} \quad (1)$$

where,  $r$  is the correlation coefficient between two AU features:  $x$  and  $y$ , which are two sets of AU values.

The AU correlation matrix shows there are many features with correlation coefficients greater than 0.30 and some of the correlation coefficients are relatively high, such as the correlation coefficient (0.78) between AU01 and AU02. Therefore, factor analysis models may be implemented to identify interrelationships among the AU features. In this study, an Exploratory Factor Analysis (EFA) model was adopted to find the factor analysis clusters, which were also used to construct the sample data for training and testing the classification models.

Table 2: Action Unit feature list extracted by OpenFace

Action Unit No.	Action Unit Descriptions
AU01	Inner Brow Raiser
AU02	Outer Brow Raiser
AU04	Brow Lowerer
AU05	Upper Lid Raiser
AU06	Cheek Raiser
AU07	Lid Tightner
AU09	Nose Wrinkler
AU10	Upper Lid Raiser
AU12	Lid Corner
AU14	Dimpler
AU15	Lip Corner Depressor
AU17	Chin Raiser
AU20	Lip Stretcher
AU23	Lip Tightener
AU25	Lips Part
AU26	Jaw Drop
AU45	Blink

### 4.3 Construction of Sample Data using Exploratory Factor Analysis (EFA)

In order to implement EFA, three major steps were conducted:

1. *Assessment of the factorability of the AU features:* Both the Kaiser-Meyer-Olkin (KMO) test [21] (given by Equation 2) and Bartlett's Test of Sphericity (BTS) [21] (given by Equation 3) were performed on the AU correlation matrix.

$$KMO_j = \frac{\sum_{i \neq j} R_{ij}^2}{\sum_{i \neq j} R_{ij}^2 + \sum_{i \neq j} U_{ij}^2} \quad (2)$$

where,  $KMO_j$  is the KMO value for the given AU dataset;  $R$  is the AU correlation matrix shown in Table 3;  $i$  and  $j$  indicate the indices of the AU correlation matrix; and  $U$  is the partial covariance matrix.

$$\chi^2 = -\left(n - 1 - \frac{2p + 5}{6}\right) \times \ln|R| \quad (3)$$

where,  $p$  is the number of variables;  $n$  is the total sample size in the given AU dataset; and  $R$  is the AU correlation matrix shown in Table 3.

The KMO statistic was equal to  $0.63 > 0.60$ , which indicates that the collected AU features are adequate and it is appropriate to use EFA for the data. The BTS was highly significant

with a test statistic of 146,276.26 and an associated degree of significance,  $p < 0.0001$ , which shows that the AU correlation matrix has significant correlations among at least some of the features. Hence, the hypothesis that the AU correlation matrix is an identity matrix is rejected, also indicating that an EFA model is worthwhile for the AU features.

2. *Factor extraction:* In this study, Kaiser's (Eigenvalue) Criterion [22] and the Scree Test [23] were used to determine the number of the initial unrotated factors to be extracted. The eigenvalues associated with each component represent the total amount of variance that can be explained by this component. They were plotted based on the Scree Test. Six remarkable factors having an eigenvalue greater than one were retained. In the end, the Varimax rotation method [24] was adopted to implement the factor extractions.
3. *Sample data construction:* Six remarkable factors were used to describe the sample data for classification models in six dimensions. Each factor score for each dimension was calculated from the factor loadings extracted from EFA. The calculation is a weighted average as shown in Equation 4.

$$Score(f) = \frac{\sum_{i=1}^n AU_i l_i}{\sum_{i=1}^n l_a} \quad (4)$$

where,  $f$  is the  $f$ th factor;  $n$  is the number of AU features involved;  $AU_i$  is the  $i$ th AU value in each sample;  $l_i$  is the corresponding factor loading for the  $i$ th AU feature.

### 4.4 Classification Models

Random Forests (RF) were adopted to build the student needs inference model. Figure 3 shows the architecture of the inference model. The inputs of the inference model were the floating factor scores, and the outputs were the ten student needs listed in Table 1. The factor loadings for each corresponding AU feature and the AU values for the final 300 frames in each video clip were used to generate the factor scores. Ten RF models were trained to target each of the ten student needs for classifying whether this sample data corresponds to the need or not, indicated with an integer value "zero" (not corresponding) or "one" (is corresponding). In the end, the outputs from the ten models were combined as the output of the inference model.

### 4.5 Construction of the Experiment

A web application was built on the frontend to show and control the flow of the educational videos and survey to students. The survey results were stored in a local web server. A web 720p front-facing camera was also used to record the facial expression videos.



Table 3: Linear correlation matrix for AU features: correlation coefficients above 0.30 are highlighted; columns and rows are corresponding to AU No. shown in Table 2

	01	02	04	05	06	07	09	10	12	14	15	17	20	23	25	26	45
01	1																
02	0.78	1															
04	0.16	0.13	1														
05	0.01	0.12	-0.10	1													
06	0.15	0.08	0.55	-0.11	1												
07	0.19	0.08	0.73	-0.13	0.70	1											
09	-0.09	0.00	0.00	0.06	-0.05	0.02	1										
10	0.24	0.20	0.16	0.02	0.45	0.24	0.01	1									
12	0.08	0.11	0.08	0.01	0.57	0.17	-0.04	0.68	1								
14	-0.08	0.02	0.17	-0.13	0.33	0.15	-0.04	0.31	0.37	1							
15	0.01	-0.01	-0.07	0.05	0.02	-0.07	0.02	0.12	0.03	-0.05	1						
17	-0.07	-0.04	-0.08	0.08	-0.01	0.00	0.05	0.15	0.06	0.03	0.36	1					
20	0.33	0.35	0.07	0.11	0.15	0.06	0.08	0.30	0.21	0.07	0.43	0.30	1				
23	-0.10	0.03	-0.13	0.36	-0.07	-0.08	0.07	-0.04	-0.01	0.07	0.01	0.42	0.11	1			
25	0.32	0.27	-0.03	0.11	0.04	-0.07	0.00	0.18	0.14	-0.04	0.07	-0.08	0.13	-0.02	1		
26	-0.01	0.12	-0.04	0.04	0.08	-0.02	-0.02	0.15	0.25	0.17	0.00	0.22	0.08	0.21	0.03	1	
45	0.31	0.21	0.01	-0.07	-0.01	0.02	0.08	0.01	0.03	-0.08	0.02	-0.04	0.04	-0.04	0.16	-0.06	1

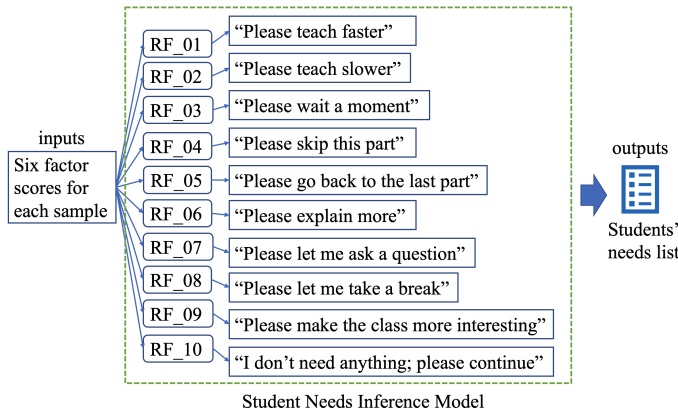


Figure 3: Student needs inference model architecture

Table 4: An example of labeled partial clips: the student need numbers are corresponding to those in Table 1

Student Needs No.	Clip No.			
	A2-1	A2-2	B2-1	C2-4
01	1	1	0	1
02	1	0	0	0
03	0	1	0	0
04	0	0	0	0
05	0	0	0	1
06	0	0	1	0
07	0	0	0	0
08	0	0	0	0
09	0	0	0	0
10	0	0	0	0

## 5 Experimental Results and Discussion

The experiment data includes a total of 84 segments of participant facial expression data, each recorded at the end of a two-minute viewing session. Two of the seven participants completed all three educational videos. Four participants watched two of the video lectures. One subject watched one video lecture. Each educational video includes four clips; for each clip, one survey result was produced. OpenFace recorded all AU intensity levels (ranging from 0.0 to 5.0) for each video frame of the participants face for an average of 3485 frames for each two-minute session. As mentioned in Section 4, the final 300 frames of each clip (ten seconds) prior to each survey response were used as the input data for training and testing the classification models. Therefore, the 84 data sets of 300 video frames each resulted in a total of 25,200 sets of AU intensity levels as input data in the models. The labels for the supervised classification models tested were each student need selected immediately after the given video clip. Table 4 shows an example of labeled clips; “A2-1” and “B2-1” represent two clips from two participants, where a “one” indicates that particular student need was selected in the survey and a “zero” indicates it was not selected.

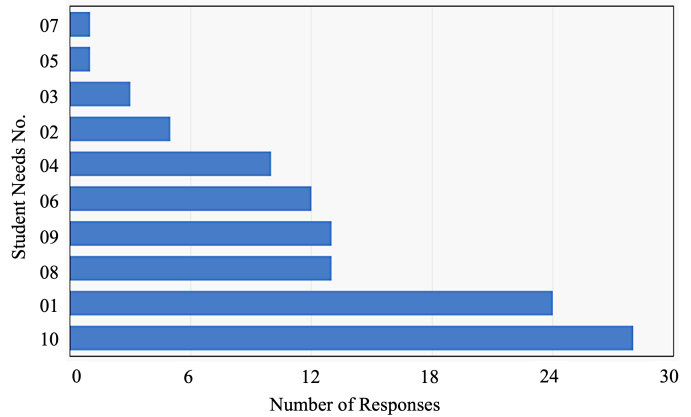


Figure 4: Distribution of student needs responses: the vertical labels are student needs numbers corresponding to those in Table 1.

### 5.1 Student Needs Survey Results

Figure 4 shows the frequency for each response in the student needs survey data for all 84 sessions. The most frequently selected need was No. 10 (“I don’t need anything; please continue”) at 35% of the total responses. The second most frequently selected was

No. 01 (“Please teach faster”) at 29%. These results indicate that the level of difficulty in these lessons may have been slightly low but not to the degree that it would interfere with the collection of data about the other surveyed needs. The overall distribution of the frequencies lends support to the validity of the inclusion of these particular needs in the survey, with each one selected by at least one participant and no need selected more than half of the time.

Table 5: Eigenvalues (EV) and total variance explained:

Component	Initial Eigenvalues		
	Total	% of Variance	Cumulative %
01	3.289	19.347	19.347
02	2.254	13.257	32.604
03	2.027	11.925	44.529
04	1.416	8.331	52.860
05	1.217	7.478	60.337
06	1.042	6.130	66.467
07	0.997	5.863	72.331
08	0.844	4.965	77.296
09	0.769	4.525	81.821
10	0.712	4.186	86.007
11	0.623	3.667	89.674
12	0.454	2.669	92.342
13	0.407	2.394	94.736
14	0.319	1.876	96.612
15	0.270	1.588	98.200
16	0.158	0.930	99.130
17	0.148	0.870	100.000

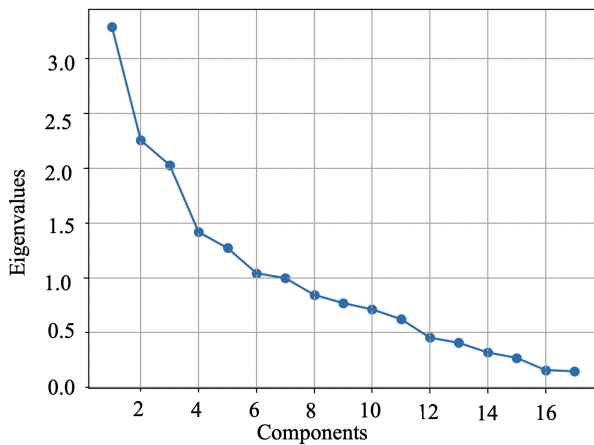


Figure 5: Scree Plot

### 5.2 Exploratory Factor Analysis Results

Based on the presumption that isolated facial actions taken out of context would be difficult for observers to interpret, EFA was used to determine effective combinations of the AU sets, as mentioned in Section 4. Table 5 shows the eigenvalues and total variance explained. Figure 5 shows the results of a Scree test, plotting the seventeen components on the x-axis and the respective eigenvalues for each number of components on the y-axis. Following the

general rule of including the distinct linear components of the AU features with eigenvalues of greater than one, six of the seventeen components are included after extraction and rotation. The validity of this decision is further supported by the fact that the proportion of the total variance explained by the factors retained(66.5%) is greater than 50% [25]. Therefore, six factors were used for the subsequent EFA.

The present study performed EFA based on the Varimax rotation method. Table 6 shows factor loadings after EFA extraction, the mean and standard deviation of each corresponding AU features of all 25,200 frames. Here, the range of the intensity level of an AU is from 0.0 to 5.0 and is measured by OpenFace. AU features with loading values **less than** 0.40 are in grey, which indicates that they are not able to represent the corresponding factor.

Table 6: Factor loadings for each AU types

Action Units	Mean	SD	Factor Loadings
Factor 1: Scowling			
Brow Lowerer	1.002	1.045	0.765
Cheek Raiser	0.331	0.518	0.668
Lid Tightner	0.871	1.081	0.943
Factor 2: Squinting			
Upper Lid Raiser	0.451	0.501	0.687
Lid Corner	0.496	0.646	0.945
Dimpler	0.907	0.675	0.432
Factor 3: Blinking			
Inner Brow Raiser	0.299	0.682	0.957
Outer Brow Raiser	0.133	0.338	0.809
Lips Part	0.270	0.351	0.356
Blink	0.264	0.442	0.304
Factor 4: Frowning			
Nose Wrinkler	0.056	0.164	0.074
Lip Corner Depressor	0.137	0.293	0.796
Lip Stretcher	0.151	0.315	0.529
Factor 5: Raising			
Upper Lid Raiser	0.088	0.252	0.978
Factor 6: Pursing			
Chin Raiser	0.370	0.457	0.575
Lip Tightener	0.121	0.272	0.668
Jaw Drop	0.320	0.391	0.351

In addition, the top three highest mean values are highlighted. The AUs with the three highest mean intensity levels are “Brow Lowerer”, “Dimpler” and “Lid Tightener”, indicating that the brow, lid and dimple are the most significant signals. Each extracted factor was also given a name. These names do not necessarily reflect the emotions that might typically be expressed with these face actions. They are only intended as convenient labels for the discussion and analysis.

The factor analysis results appear to include principles of physical vicinity. For example, Factor 3 (Blinking) is associated with “Inner Brow Raiser” and “Outer Brow Raiser”. When a person elevates their inner brow, he is very likely to raise the outer brow as well. The sample data used for the inference was, therefore, the combinations between factor loadings and the actual AU values of

each frame in each facial expression video. Here, only AU features with loading values that are not in grey in Table 6 were used.

### 5.3 Classification Model Evaluations

The training and testing data for all of the classification models were based on frames rather than clips. They were randomly split in a training-to-testing ratio of eight to two from the 25,200 frames. During training, for all of the models, 5-fold Cross-Validation [26] was done to reduce overfitting.

Random Forest is a popular machine learning procedure which can be used to develop prediction models. In the random forest settings, many classification and regression trees are constructed using randomly selected training datasets and random subsets of predictor variables for modeling outcomes. Results from each tree are aggregated to give a prediction for each observation [27]. In this study, “sklearn.ensemble.RandomForestClassifier” was used, which is a class of the “sklearn” machine learning package to train and test the RF models. In addition, considering the training time and overall accuracy, the basic parameter settings of all of the RF models are {number of estimators: 100 (default); max depth: 40}.

Figure 6 shows the confusion matrices for each trained RF model for each student need using the test data. As shown in Figure 6, in terms of all RF model evaluation results, the performance on true negatives was higher than that of the true positives due in part to an imbalance of the training data where there were far fewer positives than negatives in each category. For example, the lowest ratio of positives to negatives was approximately 0.01, and the highest ratio was less than 0.50. The highest two true positives were 89.3% and 86.0% on the student needs “I don’t need anything, please continue” and “Please teach faster”, indicating the model has better prediction abilities when the amount of training data is higher. However, while the amount of the training data may affect the model performance, it is not the only factor that affects the performance. For example, when comparing the performance on the student needs “Please wait a moment” and “Please go back to the last part”. The first need has a lower true positive rate than the second one, even though the amount of training data of the second need is twice the first one. In addition, the performance on false positive is worse than the false negative for all of the models, due in part to the issue of imbalance.

Figure 7 and Figure 8 show the validation curve and learning curve for each trained RF model for each student need using the test data. The left figure in each subfigure shows the validation curve, indicating the appropriate max depth for each RF model. The right figure shows the learning curve, summarizing the whole learning process during the 5-folder cross validation. The shading around the lines represents a 95% Confidence Interval (CI) [28] (given by the Equation 5) of each data point. From the validation curves, the maximum depth for nearly all of the RF models was between 20 and 30, indicating that a max depth in between 20 and 30 is appropriate and the most efficient for this task. The learning curves show increased accuracy with an increase in the number of cross-validations for most of the RF models.

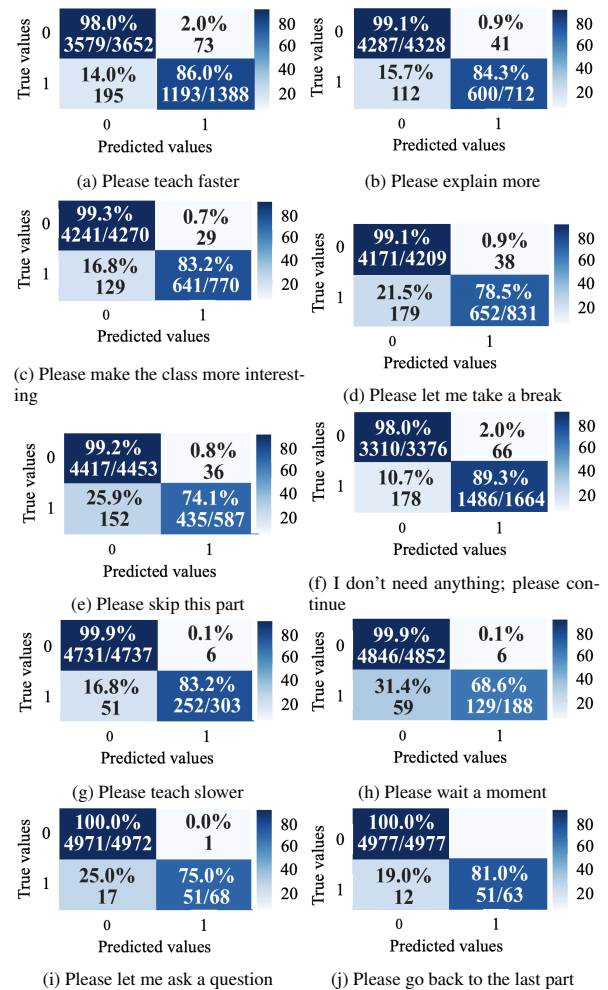
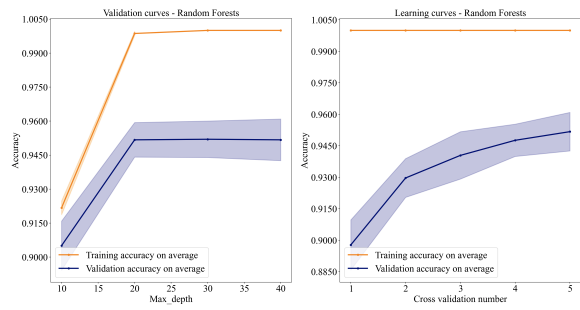


Figure 6: Confusion matrices for each trained RF model using the test dataset

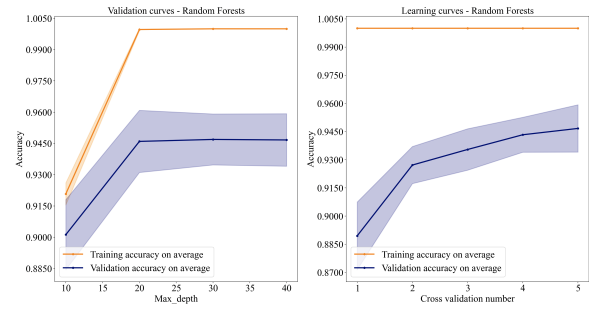
$$CI = \bar{X} \pm Z \times \frac{\sigma}{\sqrt{n}} \tag{5}$$

where,  $X$  is the mean of the training or validation scores;  $Z$  is the z-statistic for the confidence level (for 95%,  $Z = 1.96$  approximately);  $n$  is the sample size.

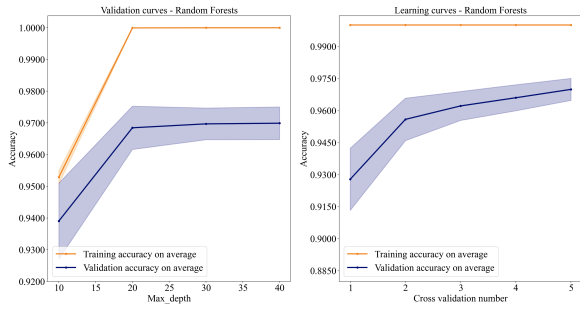
Finally, all of the RF model outputs were combined into one student needs list, including all ten possible needs. Table 7 shows the over-all evaluation of the inference model. Student need numbers: 08 (“Please let me take a break”), 09 (“Please make the class more interesting”) and 10 (“I don’t need anything; please continue”) received relatively lower average errors than other needs. This may be because those needs are more related to emotions. Student need numbers: 06 (“Please explain more”) and 01 (“Please teach faster”) received higher mean average errors. This may be because of individual differences. For example, some people hide their emotions when they are thinking. The over-all MAE was 0.0283, which indicates the inference model could correctly infer more than nine students needs out of ten for each test video frame.



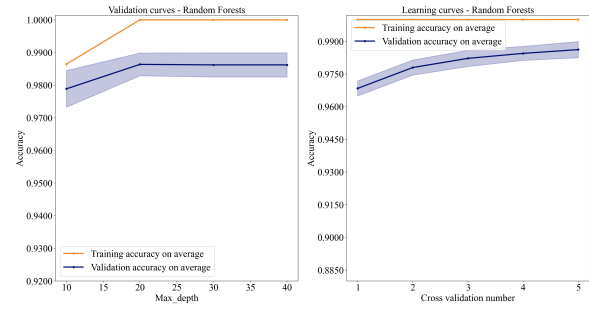
(a) Please teach faster



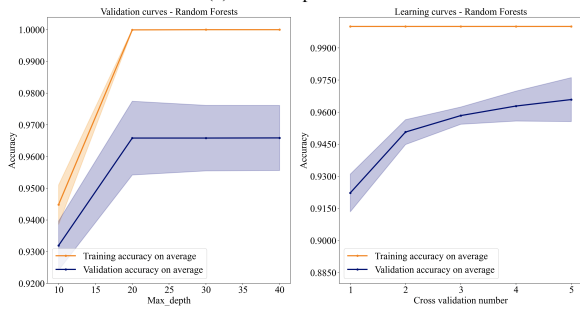
(a) I don't need anything; please continue



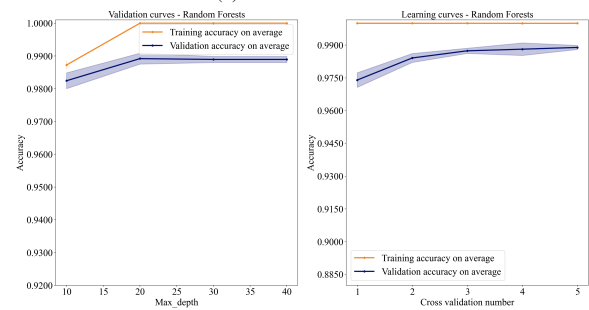
(b) Please explain more



(b) Please teach slower



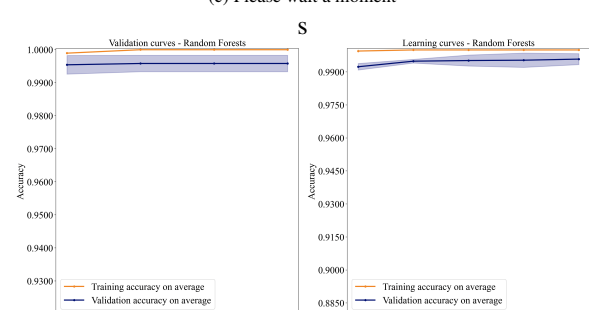
(c) Please make the class more interesting



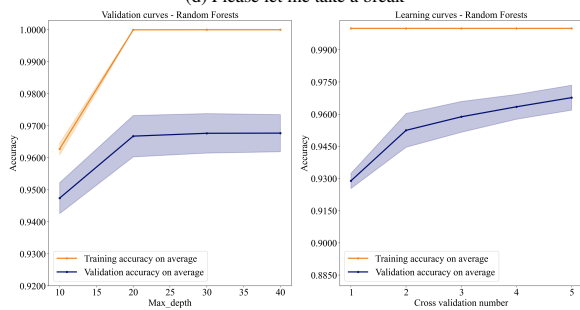
(c) Please wait a moment



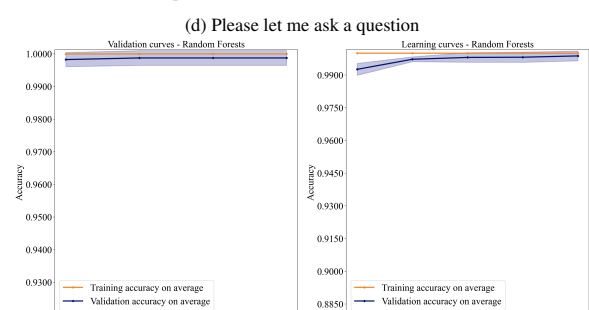
(d) Please let me take a break



(d) Please let me ask a question



(e) Please skip this part



(e) Please go back to the last part

Figure 7: The validation curves (left) and learning curves (right) of RF models (RF01 to RF05)

Figure 8: The validation curves (left) and learning curves (right) of each RF models (RF06 to RF10)

Table 7: Mean average error (MAE) of the inference model for predicting each student need: the student need numbers are corresponding to the ones in Table 1

Student Needs No.	MAE for Each Need ( $1 \times 10^{-2}$ )
01	5.595
02	2.778
03	3.472
04	4.345
05	3.671
06	5.238
07	1.488
08	1.032
09	0.456
10	0.198
MAE of all sample data ( $1 \times 10^{-2}$ ): 2.827	

## 6 Conclusion

This study demonstrates the feasibility of inferring student needs from real-time video data in online learning situations based on models trained on video and survey data collected from students learning from video learning materials. The video data was extracted as facial points which were further encoded using facial expression modeling methods, all of which can be collected in real-time during online teaching with the permission of the student. The survey was collected at the end of each two-minute video segment to label the needs of the student in terms of what the student would prefer in terms of change (or no change) in the teaching. This survey and the system itself is intended to allow students to give meaningful feedback that teachers may use to assist in decisions about class flow and student interaction, including teaching speed, class breaks, review of new material, etc. Facial actions were further classified using factor analysis to result in a final set of input parameters for the inference based on what may be described as facial expressions.

Of several models tested to infer the student needs from the facial expression data, the Random Forest models performed best. The results show each Random Forest is trained to classify a single need performs very well, especially excelling at excluding individual cases of need at which the model consistently performs with greater than 98% accuracy. When indicating a need, the model accurately classifies at a greater than 80% accuracy, a rate that could be extremely useful for teachers who, in online scenarios, typically cannot closely monitor each face or stop the flow of a lecture to inquire about feedback. More importantly, this accuracy in a class of even a small group could amalgamate several students inferred needs to give teachers a more accurate reading of the general mood about the class without needing any video transmission, or allowing complete anonymity.

The proposed inference model can also be tested in real learning situation given a flexible method of interaction and, as similar data is collected on the models' accuracy in various situations, and the system accuracy improved, the interface may be adjusted to give teachers more confidence in relying on such systems to assist them in deciding who to respond to lecture flow and, eventually, to in responding to individual students. At the same time, as teachers become more comfortable with using such systems to determine the

timing of specific feedback, they will also become more aware of the influence of their pacing and feedback on teaching in general.

**Acknowledgment** This study was done using funds from Japan KAKENHI grant No. 21K17865.

## References

- [1] Y. Yan, J. C. Lee, E. W. Cooper, "Inference of student needs in an online learning environment based on facial expression," in the 10th International Conference on Information and Education Technology (ICIET), 113-117, 2022, doi: 10.1109/ICIET55102.2022.9779022.
- [2] B. B. Wiyono, H. Indreswari, A. P. Putra, "The utilization of 'Google Meet' and 'Zoom Meetings' to support the lecturing process during the pandemic of COVID-19;" in the International Conference on Computing, Electronics & Communications Engineering (iCCECE), 25-29, 2022, doi: 10.1109/iCCECE52344.2021.9534847.
- [3] A. Karabulut, A. Correia, "Skype, Elluminate, Adobe Connect, Ivisit: a comparison of web-based video conferencing systems for learning and teaching," in the Society for information technology & teacher education international conference, 484-484, 2008.
- [4] H. Pratama, M. N. A. Azman, G. K. Kassymova, S. S. Duisenbayeva, "The trend in using online meeting applications for learning during the period of pandemic COVID-19: A literature review," *Journal of Innovation in Educational and Cultural Research*, **1**(2), 58-68, 2020, doi:10.46843/jiecr.v1i2.15.
- [5] E. A. Skinner, M. J. Belmont, "Motivation in the classroom: reciprocal effects of teacher behavior and student engagement across the school year," *Journal of Education Psychology*, **85**(4), 571-581, 1993, doi:10.1037/0022-0663.85.4.571.
- [6] Y. Nailufar, S. Safruddin, M. I. Zain, "Analysis of teacher difficulties in online learning on mathematics subjects," *Prisma Sains: Jurnal Pengkajian Ilmu dan Pembelajaran Matematika dan IPA IKIP Mataram*, **9**(2), 280-288, 2021, doi:10.33394/j-ps.v9i2.4376.
- [7] X. Lu, M. Wang, J. Fang, H. Liao, "Investigation on the difficulties and challenges of teachers online teaching in primary and middle schools of guangxi middle school," in the International Conference on Computer Vision, Image and Deep Learning (CVIDL), 542-545, 2020, doi:10.1109/CVIDL51233.2020.00-31.
- [8] M. H. Rajab, M. Soheib, "Privacy concerns over the use of webcams in online medical education during the COVID-19 pandemic," *Cureus*, **13**(2), 2021, doi:10.7759/cureus.13536.
- [9] P. Ekman, W. V. Friesen, "Facial Action Coding System (FACS)," *Environmental Psychology & Nonverbal Behavior*, 1978, doi:10.1037/t27734-000.
- [10] A. G. Yong, S. Pearce, "A beginner's guide to factor analysis: focusing on exploratory factor analysis," *Tutorials in quantitative methods for psychology*, **9**(2), 79-94, 2013.
- [11] G. Biau, E. Scornet, "A random forest guided tour," *Test*, **25**, 197-227, 2016, doi: 10.1007/s11749-016-0481-7.
- [12] P. W. Kim, "Real-time bio-signal-processing of students based on an intelligent algorithm for internet of things to assess engagement levels in a classroom;" *Future Generation Computer Systems*, **86**, 716- 722, 2018, doi: 10.1016/j.future.2018.04.093.
- [13] M. Porta, S. Ricotti, C. J. Perez, "Emotional e-learning through eye tracking;" in IEEE Global Engineering Education Conference (EDUCON), 1-6, 2012, doi:10.1109/EDUCON.2012.6201145.
- [14] B. M. Booth, A. M. Ali, S. S. Narayanan, I. Bennett, A. A. Farag, "Toward active and unobtrusive engagement assessment of distance learners;" in the Seventh International Conference on Affective Computing and Intelligent Interaction (ACII), 470-476, 2017.

- [15] X. Zheng, S. Hasegawa, M.-T. Tran, K. Ota, T. Unoki, "Estimation of learners' engagement using face and body features by transfer learning," in the International Conference on Human-Computer Interaction, 541-552, 2021, doi:10.1109/ACII.2017.8273641.
- [16] Z. Cao, G. Hidalgo, T. Simon, S.-E. Wei, Y. Sheikh, "Openpose: realtime multi-person 2d pose estimation using part affinity fields," *IEEE Transactions on Pattern Analysis and Machine Intelligence*, **43**(1), 172-186, 2021, doi:10.1109/TPAMI.2019.2929257.
- [17] D. Cecilia, S. Carson, K. James, J. Lazarus, "MIT OpenCourseWare: unlocking knowledge, empowering minds," *Science*, **329**(5991), 525-526, 2010, doi:10.1126/science.11826962.
- [18] D. Patel, D. Ghosh, S. Zhao, "Teach me fast: how to optimize online lecture video speeding for learning in less time?," in the Sixth International Symposium of Chinese (CHI), 160-163, 2018, doi: 10.1145/3202667.3202696.
- [19] T. Baltrusaitis, A. Zadeh, Y. C. Lim, L. P. Morency, "Openface2.0: facial behavior analysis toolkit," in the 13th International Conference on automatic face & gesture recognition (FG 2018), 59-66, 2018, doi:10.1109/FG.2018.00019.
- [20] J. Benesty, J. Chen, Y. Huang, I. Cohen, "Pearson correlation coefficient," *Noise Reduction in Speech Processing*, **2**, 2009, doi:10.1007/978-3-642-00296-0\_5.
- [21] C. D. Dziuban, E. C. Shirkey, "When is a correlation matrix appropriate for factor analysis? some decision rules," *Psychological Bulletin*, **81**(6), 358-361, 1974, doi:10.1037/h0036316.
- [22] K. A. Yeomans, P. A. Golder, "The Guttman-Kaiser Criterion as a predictor of the number of common factors," *Journal of the Royal Statistical Society. Series D (The Statistician)*, **31**(3), 221-229, 1982, doi:10.2307/2987988.
- [23] B. Raymond, Cattell, "The Scree Test For The Number Of Factors," *Multivariate Behavioral Research*, **1**(2), 245-276, 1966, doi:10.1207/s15327906mbr0102\_10.
- [24] E. E. Cureton, S. A. Mulaik, "The weighted varimax rotation and the promax rotation," *Psychometrika*, **40**, 183-195, 1975, doi:10.1007/BF02291565.
- [25] N. Shrestha, "Factor analysis as a tool for survey analysis," *American Journal of Applied Mathematics and Statistics*, **9**(1), 4-11, 2021, doi:10.12691/ajams-9-1-2.
- [26] T. Fushiki, "Estimation of prediction error by using K-fold cross-validation," *Statistics and Computing*, **21**, 137-146, 2011, doi:10.1007/s11222-009-9153-8.
- [27] J. L. Speiser, M. E. Miller, J. Tooze, E. Ip, "A comparison of random forest variable selection methods for classification prediction modeling," *Expert Systems with Applications*, **134**(15), 93-101, 2019, doi: 10.1016/j.eswa.2019.05.028.
- [28] H. W. David, L. Stanley, "Confidence Interval Estimation of Interaction", *Epidemiology*, **3**(5), 452-456, 1992.

# Measurement System for Evaluation of Radar Algorithms using Replication of Vital Sign Micro Movement and Dynamic Clutter

Christoph Domnik<sup>\*,1,2</sup>, Daniel Erni<sup>2</sup>, Christoph Degen<sup>1</sup>

<sup>1</sup>Faculty of Electrical Engineering and Computer Science, Hochschule Niederrhein - University of Applied Sciences, D-47805 Krefeld, Germany

<sup>2</sup>General and Theoretical Electrical Engineering (ATE), Faculty of Engineering, University of Duisburg-Essen, and CENIDE – Center for Nanointegration Duisburg- Essen, D-47048 Duisburg, Germany

## ARTICLE INFO

Article history:

Received: 27 February, 2023

Accepted: 24 April, 2023

Online: 15 May, 2023

Keywords:

FMCW Radar

Vital sign detection

Dynamic clutter

Digital beamforming

Radar measurement system

## ABSTRACT

*In this paper we present a measurement system that is able to evaluate radar algorithms for vital signs sensing applications. For such medical applications, it is crucial to develop robust and reliable algorithms that are tested in a laboratory environment. The presented measurement system generates reproducible vital sign micro movement and dynamic clutter using loudspeakers to replicate realistic scenarios with two moving objects. It is described how realistic vital sign movement patterns are prepared using signal synthesis or recorded measurements, e.g. from a published dataset. The capability of the system to evaluate radar algorithms is demonstrated by investigating the impact of a beamforming algorithm on dynamic clutter. During the measurements presented in this paper, one loudspeaker replicates different vital sign movement patterns and the other loudspeaker creates dynamic clutter. It is shown that a digital beamforming improves the dynamic clutter rejection and leads to a better quality of the radar phase signal.*

## 1 Introduction

This paper is an extension of work originally presented in the 44th Annual International Conference of the IEEE Engineering in Medicine and Biology Society (EMBC) [1]. The concept of both publications is to create repeatable and realistic scenarios for testing, comparing and optimizing different post processing algorithms for radar technology used in vital sign sensing scenarios. Those algorithms should be tested in corresponding laboratory environment before used in clinical studies or real world applications.

Research in radar technology for medical applications recently gains increased attention. The ability of radar sensors to measure movement and micro movement like vibration [2] or movement from vital signs [3] [4] [5] leads to many applications. Doppler cardiograms, for example, can be used for measurements that make significant conditions of the heart visible comparable to the electrocardiogram [6]. Another discussed application is respiration movement measurement for motion-adaptive cancer radiotherapy [7].

Medical scenarios have special requirements for the technology used. It is very important to have a robust and reliable system. The system has to be easy in use for medical professionals without creat-

ing a huge amount of additional work. This means, the system must be tolerant against inaccurate positioning, random body movement of the target person [8] [9], radar self-motion [10] and clutter. A challenge for many medical scenarios is the clutter of other moving or stationary objects in proximity to the person, whose vital signs are to be measured. FMCW radars can help to distinguish objects at different distances. A limitation of the field of view by using a dielectric lens or smart antennas with beamforming capabilities could reduce this problem further. However, the dielectric lens would require a very accurate positioning of the radar, and problems in measuring the target due to unconscious movements occurred. This can be improved in terms of achieving a more robust condition with digital beamforming in post processing. By applying digital beamforming in post processing, a wide angle range is recorded first and, then, the target angle can be found and tracked afterwards. In this paper, we will address the mentioned effect by introducing a measurement system for evaluating radar post processing algorithms, e.g. beamforming algorithms.

In contrast to the setup presented in our previous paper [1], the setup that will be introduced in the following will use a second loudspeaker to replicate clutter from a second moving object. The

\*Corresponding Author: Christoph Domnik, [christoph.domnik@hs-niederrhein.de](mailto:christoph.domnik@hs-niederrhein.de)

previous paper [1] introduced a setup to generate reproducible movement patterns analog to chest wall micro movement from vital signs. That setup consisted of a single loudspeaker actuated by a function generator. It was shown that the diaphragm deflection measured by radars is linear to the voltage applied to the loudspeaker. Although this means that accurate measurements of the replicated micro movement are possible with the presented setup in [1], the replication of more realistic vital sign micro movement is problematic with that setup, which was addressed by the reviewers and numerous readers at the conference. To meet this request in this present paper, we will describe a new hardware setup using more flexible signal generation.

A loudspeaker for the replication of vital signs is also used in [11]. Another approach for generating movement of vital signs is introduced in [12] and [13]. There, a mechanical chest model for testing a wearable device is used to measure the chest circumference change. The simulation of the chest circumference change is not necessary for testing radar sensors and algorithms because the radar would only measure the movements effective to its range. A simulation approach based on a mathematical model that simulates the chest wall movement is presented in [14]. The chest wall motion simulation is useful to develop new algorithms for medical diagnosis while we focus more on the algorithms of the radar signal processing.

In the following chapters, at first, we will describe the radar signal processing used in this paper. Afterwards, the hardware of the measurement setup will be presented as well as the generation of realistic movement signals. Then, the impact of dynamic clutter will be investigated and a digital beamforming algorithm is tested concerning its rejection of the dynamic clutter. Finally, realistic heartbeat movement from the clinical recorded dataset from Schellenberger [15] will be used.

## 2 Radar and Signal Processing

A moving target creates a Doppler shift, which can be measured by continuous wave radars [16] as well as by FMCW radars [17]. Using FMCW radar sensors, multiple frequency ramps have to be captured consecutively. After range FFT and target finder algorithm mentioned in section 2.2, the range difference  $\Delta R$  results in a phase difference  $\Delta\Phi$ . The phase difference  $\Delta\Phi$  can be described as

$$\Delta\Phi = \frac{4\pi}{\lambda} \cdot \Delta R \quad (1)$$

using the wavelength  $\lambda$  [18]. The equation is unambiguous if  $-\pi < \Delta\Phi < \pi$ . Hence, larger macro movement of an object and a low sample rate of the phase signal can cause problems in measurements. It is also notably that only movement radial to the radar is measured.

### 2.1 Radar Hardware and Settings

During all measurements, the Radarbook2<sup>1</sup> from INRAS with the 77 GHz RF77II-IFX-TX2RX16.D01 frontend is used. Figure 1 shows a picture of the radar frontend.

<sup>1</sup><https://inras.at/en/radarbook2/>

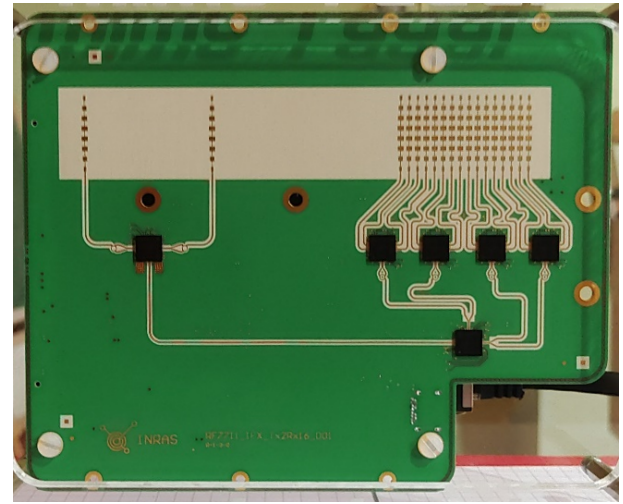


Figure 1: Picture of 77 GHz frontend of Radarbook2.

The Radarbook2 with 77 GHz frontend is configured according to the parameters depicted in Table 1. No further signal processing is done internally by the radar FPGA during the measurements conducted for this article. The raw ADC samples are transferred to the post processing device via LAN interface.

Table 1: Radar parameters and our default settings of Radarbook2 77 GHz. These default values are used, if not otherwise specified.

Radar antenna characteristic 3 dB beamwidth	Horizontal (RX, TX)	76.5°
	Vertical (RX, TX)	12.8°
	No. of used TX channels	1
	No. of used RX channels	16
Radar settings	Mode of operation	FMCW
	EIRP	3.2 dBm
	ADC sample rate $f_s$	5 MHz
	Frame time $T_F$	5 ms
	Samples per chirp N	1024
	Chirps per frame	1
Chirp configuration	Start frequency $f_{start}$	76 GHz
	Stop frequency $f_{stop}$	78 GHz
	Bandwidth B	2 GHz
	Ramp up time $T_C = \frac{N}{f_s}$	204.8 $\mu$ s
	Slope $S = \frac{B}{T_C}$	9.7656 $\frac{\text{MHz}}{\mu\text{s}}$

### 2.2 Signal Processing

The key point of the presented measurement system is the evaluation of radar algorithms. This means that the software framework can be adapted to different algorithms used in different scenarios. In this work we use a post processing of the raw FMCW radar data as displayed in Figure 2.



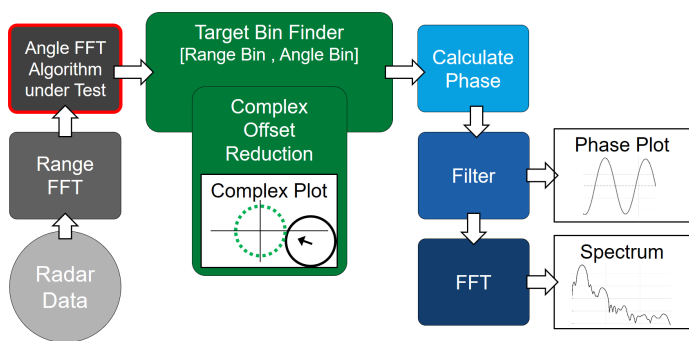


Figure 2: Block diagram of radar signal processing with angle FFT algorithm under test.

The first step in the signal post processing is a range FFT of the radar ADC data. The spectral lines of the range FFT stand for different distances. The range resolution or real bin width  $Bin_W$  can be calculated with

$$\text{Range Resolution} = Bin_W = \frac{c_0}{2 \cdot B} \approx 7.5 \text{ cm} \quad (2)$$

using the parameters presented in Table 1. Two different objects can only be distinguished if their distance to the radar has at least one bin width difference, otherwise they are measured as a single object. The distance  $R$  between radar and target object can be calculated with

$$R = Bin \cdot Bin_W \quad (3)$$

using  $Bin_W$  and the index of the spectral line where the target object can be found called  $Bin$ .

In this paper we use zero padding to increase the number of spectral lines with a factor of four. So, the bin with zero padding  $Bin_{ZP}$  result in  $Bin \cdot 4$  and the reading accuracy of the distance will be higher but the range resolution does not change.

The next step, which is highlighted with a red outline in the block diagram in Figure 2, is an optional digital beamforming algorithm. As mentioned in the introduction, digital beamforming is of special interest in this work and will be used to demonstrate the benefits of this measurement system. The used radar has 16 receiving channels, which allows to calculate a digital beamforming post processing algorithm. Further explanation of digital beamforming algorithm and clutter rejection with and without digital beamforming can be found in chapter 5.4.

Necessary in any case is a target bin finder. The easiest way is to find the bin with the maximal magnitude. However, in measurements with static clutter this could lead to a wrong range bin and angle bin. Moreover, the phase signal of the target can be distorted by static clutter. We use the complex offset reduction algorithm (COR) for elimination of static clutter as signal processing step shown in Figure 2.

After the range and angle FFT, the complex signals of a moving target without clutter will be on a circle in the complex plot. The center of the circle is in the point of origin. When the magnitude of the target is changing over time, the complex plot can show a helix but the center has to be in the point of origin. When the center of the complex signal is not in the point of origin, this is because of a

second, not moving object in proximity to the target object, where the overall effect is attributed to static clutter. More about static clutter can be found in [17]. Our COR algorithm finds the complex offset and subtracts it from the complex signal. This will be done in an area around the previously found range bin and angle bin.

After COR, the target bin finder determines the correct maximal magnitude again and, then, outputs the target data at correct range and angle bin to the phase calculation. The phase signal is calculated using the arctangent function and a phase unwrapping. After the phase calculation, other signal processing algorithms can be used for performance tests, e.g. in medical applications. An example for a performance test of beamforming algorithms is presented in chapter 5 by calculating the clutter rejection with and without digital beamforming.

### 2.3 Measurement of Human Heartbeat and Respiration

Using the previously described radar sensor and signal post processing, we have done measurements with a sitting person. The person was sitting still on a chair with a distance of 60 cm to the radar. The respiration and heartbeat curves are shown in Figure 3. The respiration measurement was recorded under resting conditions, and the heartbeat measurement was recorded during an apnea after exhalation scenario.

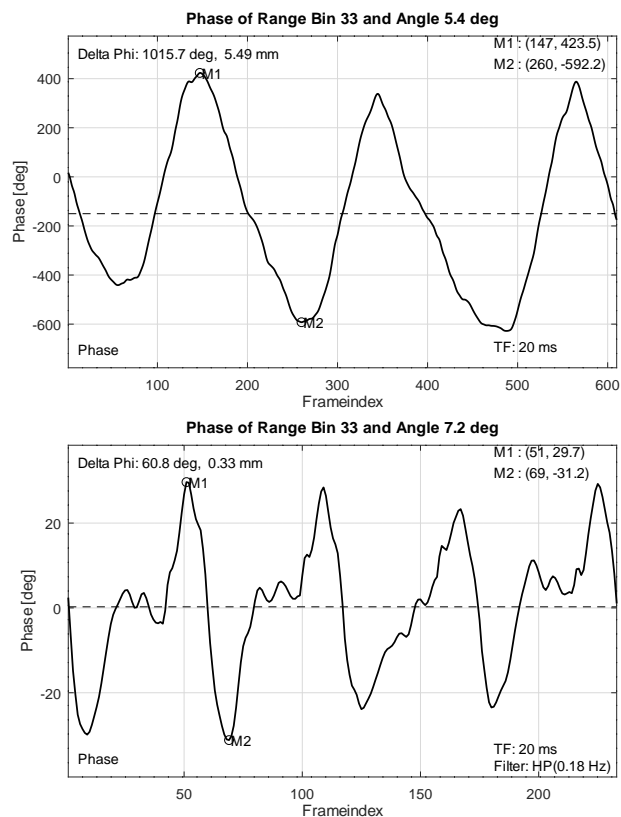


Figure 3: Radar measurements of human respiration (top) and heartbeat (bottom).

The movement amplitude of the respiration measurement is 5.49 mm with a breathing rate of approximately 15 breaths per minute. For the heartbeat measurement, the movement amplitude

is 0.33 mm with a heart rate of approximately 52 beats per minute. The maximal movement that can be expected from the heartbeat is 0.6 mm in average according to different studies mentioned in [19].

### 3 Hardware Setup

In this chapter, the hardware of the introduced measurement system is described. It is the foundation for the investigations of this work. In our previous work we evaluated a loudspeaker setup and different radar sensors in regard to the ability of replicating and recording micro movement from vital signs. The results showed that “the setup is particularly suitable for the generation of micro movement analog to CWmM<sup>2</sup> of vital signs. The diaphragm deflection is linear to the applied voltage [...]” as outlined in [1]. This result is displayed again in Figure 4. The following sections describe the differences of the hardware used for the present paper.

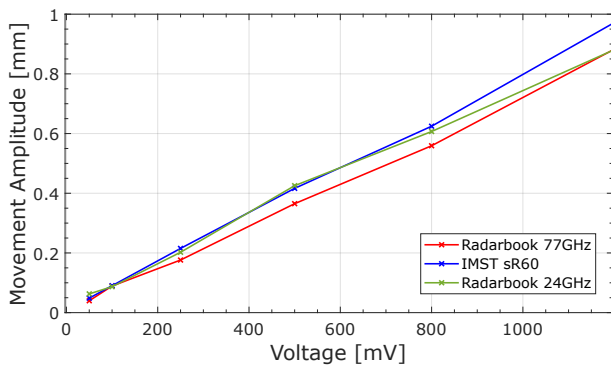


Figure 4: Measured micro movement using three radars at different voltage amplitudes on the loudspeaker. Figure from [1].

#### 3.1 Loudspeaker

As mentioned in the introduction, the evaluation of beamforming algorithms is an important feature of the presented measurement system. In order to realize this, it is necessary to have two loudspeakers that can be positioned independently. In preparations of the measurements, we built two identically constructed casings for the low-frequency loudspeakers W 300 - 8 Ohm from Visaton<sup>3</sup>. The specifications of the loudspeaker include a maximal stroke of  $\pm 14$  mm and a DC impedance of  $6.6 \Omega$ . The outcome is depicted in Figure 5.

We applied copper foil to both loudspeaker diaphragms. The diameter of the copper foil is 22.3 cm, which is much larger than it was in the previous setup. A new feature, however, is the static foil ring around the diaphragm. The foil ring is used to shadow the inside of the loudspeaker that is not covered with the copper foil on the diaphragm. The static clutter that is resulting from the foil ring can be eliminated using the complex offset reduction mentioned in 2.2.

<sup>2</sup>CWmM abbr. of chest wall micro movement

<sup>3</sup><https://www.visaton.de/de/produkte/chassis/tieftoener/w-300-8-ohm>

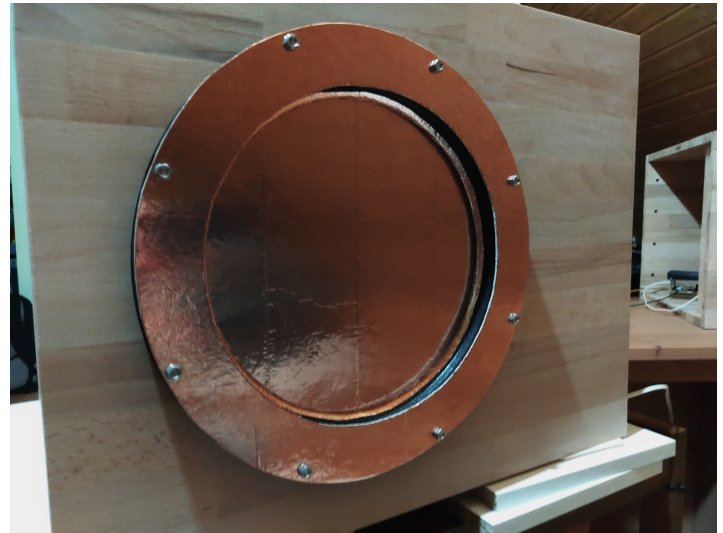


Figure 5: One of the new loudspeakers with copper foil on diaphragm and foil ring.

#### 3.2 Amplifier

The loudspeakers need a suitable signal to generate a movement. In [1] a function generator is used to drive the loudspeakers, but this approach is very limited as mentioned before. A flexible strategy is necessary to reproduce real chest wall micro movement from vital signs. The best results were achieved using a sound card and an amplifier built for this measurement system. The amplifier is based on the TDA 2050 audio amplifier. All circuits that usually block low frequencies are excluded in the amplifier circuit. In Figure 6 you can see an amplifier.

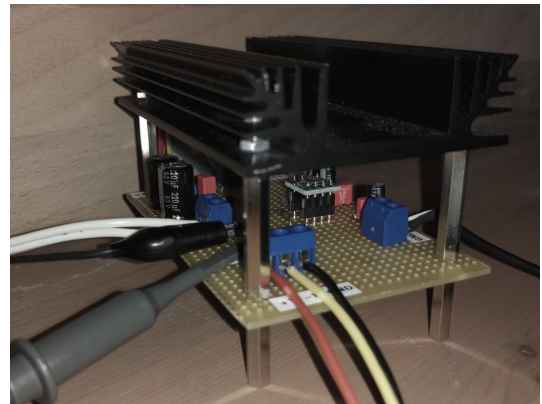


Figure 6: One of the new amplifiers.

The circuit also contains a low pass filter to prevent aliasing during the recording by the radar. The cut off frequency is currently adjusted to 10 Hz. Furthermore, an attenuation is integrated for achieving very small movements with the full bandwidth of the sound card. Different attenuation factors can be used to optimize the system for different micro movements like heart beat and respiration. The movement achieved with the current configuration is up to 10 mm using the full sound card’s dynamic range.

## 4 Signal Preparation for the Measurement System

The hardware described in the previous chapter needs audio signals to generate micro movement. In this chapter, we will explain how audio signals for our measurement system are generated. In our previous work, we took a simpler approach to generate movement with a loudspeaker. It is further described in [1]. There, we applied a waveform generator to generate the signal that moves the loudspeaker. The signal applied in the previous setup was a sine signal for replicating respiration movement and an asymmetric sine signal for replicating heartbeat movement. Unfortunately, this approach is limited in terms of replication of realistic vital sign micro movement or of special conditions of the pulmonary or cardiovascular system like diseases. Therefore, the generation of realistic signals was a key point in the development of the new measurement system.

Because the signals are all played back by a sound card, they have to be saved as regular audio files. For the measurements for this article, the audio files are saved in the uncompressed waveform audio file format (.wav). The signals are saved with a sampling frequency of 44100 Hz and a resolution of at least 16 bits per sample.

### 4.1 Signal Synthesis

One strategy to generate movement signals is to synthesize them. It is possible to create a signal based on signature points and interpolation. Another approach is to use Fourier-synthesis for periodical signals.

For the signal synthesis we started with the generation of sine signals as fundamental oscillations. Those fundamental sine signals were used as signals during testing and calibration of the hardware setup. Additionally, in some measurements it is advantageous to use sine signals to show an investigated effect more clearly. This is why a sine signal is used for each loudspeaker during the investigation of dynamic clutter and beamforming algorithms that will be described in chapter 5.

By using Fourier-synthesis, periodical signals with higher complexity are created in the following:

$$f(t) = \frac{a_0}{2} + \sum_{k=1}^N a_k \cdot \cos(k \cdot \omega \cdot t) + \sum_{k=1}^N b_k \cdot \sin(k \cdot \omega \cdot t) \quad (4)$$

Figure 7 shows a synthesized heartbeat signal using 0.88 Hz as fundamental oscillation and eight harmonics. The Fourier coefficients are  $a_0=0$ ,  $a_k=0$  and  $b_k=[1.00, 0.97, 0.35, 0.06, 0.03, 0.03, 0.11, 0.06, 0.05]$  for  $k = 1, 2, \dots, 9$ . The coefficients  $b_k$  are optimized to synthesize a heartbeat movement signal based on the frequency components of the heartbeat movement measurement presented in chapter 2.3. It has much more resemblance to a real heartbeat micro movement than the asymmetric sine signal used with the previous setup in [1].

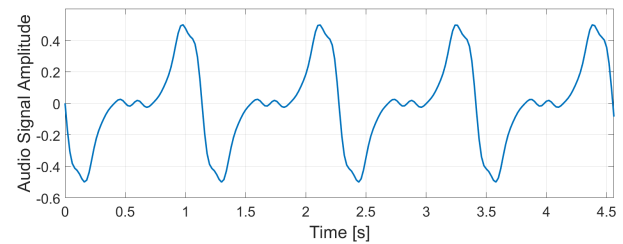


Figure 7: Pattern of heartbeat micro movement created with signal synthesis.

### 4.2 Vital Sign Micro Movement Patterns

For replication of real respiration and heartbeat movement, it is utterly important to use recordings of previous measurements as data source. Those recordings contain movement patterns of diseases and relevant conditions of the pulmonary or cardiovascular system, which are indispensable in the development of medical analysis and radar algorithms. Each measurement containing a movement pattern of the chest wall could be used independently of the technology that recorded those movement patterns. This gives us the opportunity to use published libraries of micro movement from vital signs. In our work we used the clinical recorded dataset published from Schellenberger in [15]. Figure 8 shows a heartbeat signal extracted from the dataset. The extracted part of the signal shows the heartbeat during apnea after exhalation from the measurement GDN0009\_3\_Apnea from the clinical recorded dataset.

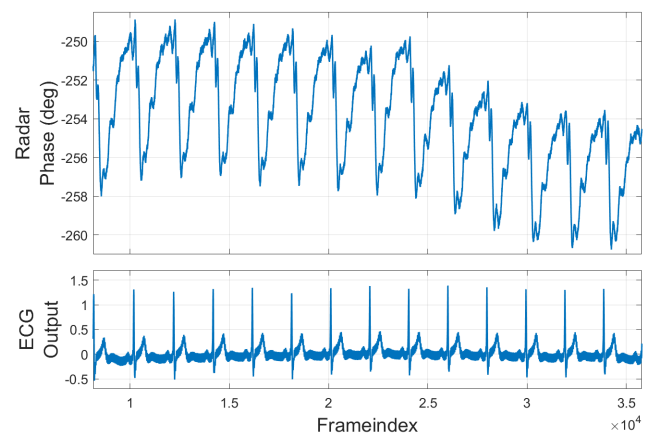


Figure 8: Heartbeat movement GDN0009\_3\_Apnea data from Schellenberger [15]. Top curve: Radar phase calculated from CW radar IQ values of the dataset. Bottom curve: Reference ECG measurement of the dataset.

The measurements were done using a 24 GHz continuous wave radar. Also signals of synchronized reference sensors like three channel ECG and Continuous Noninvasive Arterial Pressure (CNAP) were recorded during each of their measurements. For more information on how the dataset is recorded please refer to [20] and [21]. The following paragraphs explain how to prepare previously recorded data containing chest wall micro movement to use them as signals for our radar measurement system.

The first step is to cut one part from the recorded measurement with the targeted length and content. If the signal contains decisive changes like the shift from respiration to heartbeat in an apnea after

exhalation scenario, it would contain a DC offset during the heartbeat movement. This DC component will not be included in the played signal. The part of the heartbeat signal in Figure 8 starts with a QRS complex followed by the systole part of the cardiac cycle. The systole containing the contraction of the heart is visible as a falling edge in the radar phase signal of the dataset.

The next step is the scaling of the signal amplitude. For data recorded with radar sensors, the movement amplitude can be calculated using (1). Then the signal has to be scaled to the corresponding audio signal amplitude to generate the calculated movement amplitude. For special investigation or medical scenarios, movement amplitude can be increased or decreased during this preparation step. The movement amplitude of the dataset signal shown in Figure 10 as green curve was increased from 0.15 mm to approximately 0.5 mm.

After scaling the signal, it is necessary to adjust the sampling rate to 44100 Hz. As mentioned in chapter 2 we are recording our measurements with a sampling frequency of 200 Hz, and the measurements from the clinical recorded dataset published in [15] are recorded with a sampling frequency of 2 kHz. That is, oversampling to 44100 Hz is the next preparation step with additional low pass filtering to reduce oversampling artifacts. This filter also prevents aliasing during recording with the radar. Because of the typically configured frame time of 5 ms the highest frequency in the movement signal must be lower than 100 Hz. The signal is now ready to be used in the measurement system to generate realistic vital sign micro movement.

A performance test of our measurement system with play back of the prepared signal and recording with the radar was realized. Figure 9 shows the complex data of the radar recording with complex offset reduction.

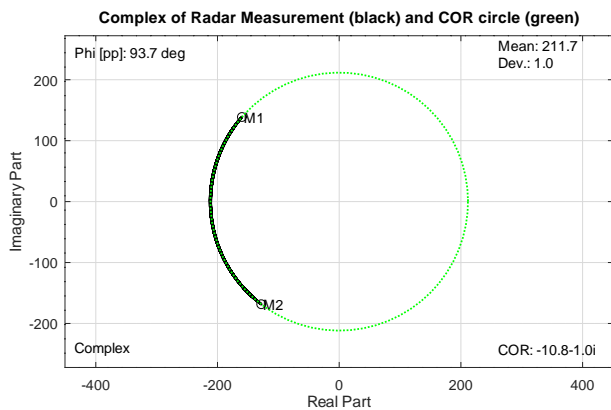


Figure 9: Complex signal of radar measurement (black) of realistic vital sign micro movement using the measurement system and COR circle (green).

Figure 10 shows the prepared signal and the recorded radar phase curve. When comparing both curves you can see, that the measured radar phase fits the prepared signal very good. Only the short peaks are decreased. These small differences between both curves are related to the low pass filter inside the amplifier that controls the loudspeaker mentioned in chapter 3.2. To allow higher frequency components, we have to increase the low pass cutoff frequency.

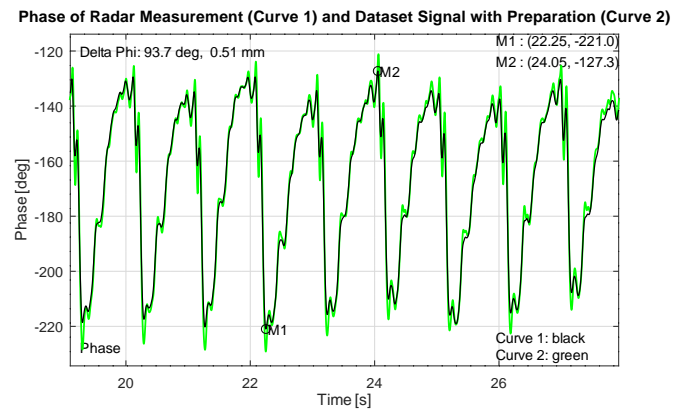


Figure 10: Schellenberger dataset signal after preparation (green) and the related phase curve of the radar measurement using our measurement system (black).

## 5 Investigation of Dynamic Clutter

All objects in the field of view of the radar sensor have an impact on the measured data. In real measurement scenarios, multiple objects are in the field of view and not all of them are static. Figure 11 displays the complex target signal and phase signal of a measurement with a second moving object close to the target object. A complex offset reduction as mentioned in chapter 2.2 is not able to reduce the clutter that is changing dynamically over time. This is called dynamic clutter. To investigate the effect of dynamic clutter, we created the following scenario with the hardware described in 3.

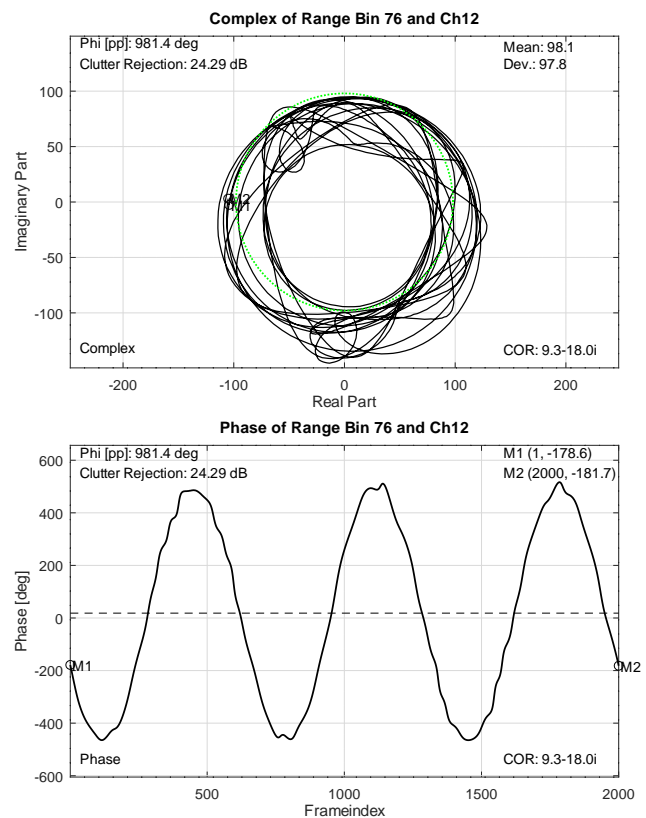


Figure 11: Complex and phase plot from dynamic clutter measurement in range bin<sub>ZP</sub> 76 without beamforming using the measurement scenario explained below.

## 5.1 Measurement Setup

To investigate the impact of dynamic clutter, we used two loudspeakers close to each other in our evaluation setup. They are positioned in different distances and different angles in front of the radar. Figure 12 shows a picture of the used measurement setup. The right loudspeaker is the target object, whose movement we want to measure, and is called *target loudspeaker* in the following chapters. It is placed at 150 cm at an angle of  $-9^\circ$  relative to the radar position. Angles left to the radar are defined as negative angles. The left loudspeaker is the additional moving object next to the target. It is used to generate the clutter movement and is called *clutter loudspeaker* in the following chapters. The clutter loudspeaker is placed at 130 cm at an angle of  $-36^\circ$ .

The measurement setup is chosen to simulate realistic scenarios. The two loudspeakers stand in alike position and distance to each other mimicking a patient lying on a hospital bed and a healthcare professional standing next to the patient during a diagnostic measurement using a radar from above. In this scenario the patient is represented by the target loudspeaker, and the healthcare professional is represented by the clutter loudspeaker. For easier measurement using the loudspeaker setup, the arrangement is shifted to the horizontal plane with the radar standing in front of the loudspeakers instead of being mounted on the ceiling.



Figure 12: Picture of the measurement setup to investigate dynamic clutter with two loudspeakers.

## 5.2 Movement Signal

Each loudspeaker needs to play a suitable signal so that it is possible to investigate the impact of dynamic clutter. In this paper we present a measurement, in which each loudspeaker plays a sine signal. This ensures that the effect of dynamic clutter is not overlaid with other effects using more complex signals. The oscillation frequencies of the sine signals are chosen to fit usual respiration frequencies. With 0.3 Hz frequency and a movement peak-to-peak amplitude of 5.2 mm the target loudspeaker represents a typical respiration movement for resting humans, while the 0.5 Hz sine with a movement peak-to-peak amplitude of 4.7 mm on the clutter loudspeaker represents a faster respiration.

For the investigation of the dynamic clutter, it is important to compare the signal with dynamic clutter to a reference signal without clutter. Therefore, the clutter movement is not active the whole measurement time. Figure 13 shows the structure of the used audio signal. The full measurement time is 30 s. The signal is designed to have three equal parts. At first, both signals are active and the signal with dynamic clutter can be examined. This part has to be the first part in the signal because the hardware setup including the amplifier with the low pass filter and the loudspeakers need some seconds before the measurement to settle to a stable state for those low frequencies. It is important to consider this settling time while generating the audio signal, but it will not be measured by the radar. In Figure 13 this settling time is not displayed. The middle part of the signal is used to turn off the signal of the clutter loudspeaker. After turning the clutter signal off, the hardware setup also needs a settling time, but it is shorter than the settling time after turning a signal on. The last part, named part C in Figure 13, of the measured signal is used as a reference. Only the 0.3 Hz sine signal on the target loudspeaker is active.

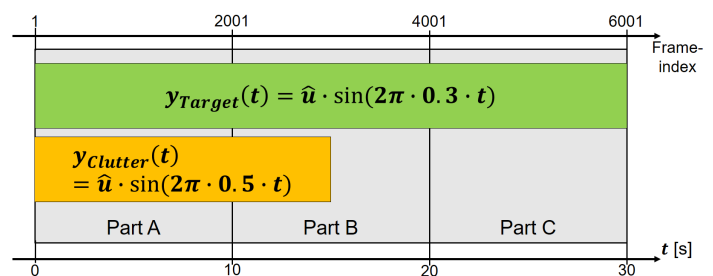


Figure 13: Audio signal during the dynamic clutter measurement.

Each part of the signal is 10 s long and, therefore, three oscillations of the 0.3 Hz target signal and five oscillations of the 0.5 Hz clutter signal fit exactly in each part. This is very important for the subsequent processing of the radar measurement. There, the signal of “Part A” in Figure 13 is compared with the reference signal in “Part C”. This is only possible if both signals are in synchronized state. A synchronized state means that the signals are in the exact same state at the beginning of each part. Also the sampling of the radar phase signal has to fit to the synchronization, otherwise a systematic error would occur during the calculations described in the next section. With the radar frame time mentioned in Table 1 of 5 ms, the synchronization points of the audio signal occur at the radar frame indices 1, 2001 and 4001.

### 5.3 Dynamic Clutter Rejection

The measurements for this investigation are realized with the Radarbook2 using the post processing presented in chapter 2.2. In the dynamic clutter rejection measurements, the COR algorithm is used slightly different than usual to achieve a better performance. For every bin, the COR algorithm finds the complex offset only using the signal “Part C” and uses this complex offset for all three signal parts. The result is that in “Part A” no static clutter is remaining, and the dynamic clutter can be investigated now. The quantification of the impact of dynamic clutter needs an extra step of processing. In (5) the dynamic clutter is defined as additive noise on the reference signal.

$$\Phi_{Clutter} = \Phi - \Phi_{Ref} \quad (5)$$

Equation (5) includes  $\Phi$  as the signal with dynamic clutter,  $\Phi_{Ref}$  as reference signal without clutter and  $\Phi_{Clutter}$  as the dynamic clutter we want to investigate. Therefore, the dynamic clutter can be calculated as the difference between the measured signals of the different synchronized parts.  $\Phi$  and  $\Phi_{Ref}$  are measured radar phase signals that contain the information about the loudspeaker movement as described in (1). After calculating  $\Phi_{Clutter}$ , the dynamic clutter rejection  $R_C$  in dB can be defined as in (6) using the peak to peak value of the reference signal  $\Phi_{PP,Ref}$  and the peak to peak value of the clutter curve  $\Phi_{PP,Clutter}$ .

$$R_C = 20 \cdot \log_{10} \left( \frac{\Phi_{PP,Ref}}{\Phi_{PP,Clutter}} \right) \quad (6)$$

In the measurement scenario described in section 5.1, there are two loudspeakers at the distances 130 cm and 150 cm. With the range resolution of the radar mentioned in 2.2, these targets could be measured in range Bin 17 and 20. Therefore, the targets will be measured at  $Bin_{ZP}$  68 and 80 with using zero padding. Nevertheless, it is important to keep in mind that the real range resolution of the radar is lower than the  $Bin_{ZP}$  suggests.

The chosen scenario allows to specifically investigate the range bins in between the two moving loudspeakers to indicate the robustness of the evaluated algorithms. The following Table 2 shows the results of the dynamic clutter investigation measurement.

Table 2: Dynamic clutter rejection in different range bins without beamforming.

Bin <sub>ZP</sub>	$\Phi_{PP,Clutter}$ [°]	Clutter Rejection [dB]
80	13	37.36
79	14.4	36.49
78	17.1	34.98
77	24.7	31.76
76	58.5	24.29
75	547.1	4.87

All range bins in which the dynamic clutter rejection in dB is higher than zero are evaluated. The according peak to peak value of the reference signals in all bins is about 958°. For the calculation of the dynamic clutter rejection, the exact value of each range bin was certainly used. The peak to peak value is equivalent to a movement of 5.18 mm of the target loudspeaker diaphragm. This is a typical movement range of the chest wall generated by the respiration, but

it is important to note that the dynamic clutter rejection will be lower for signals with lower movement amplitude like the heartbeat movement.

In the range bin corresponding to the target loudspeaker, the dynamic clutter rejection is 37.36 dB, and it drops to 24.29 dB in range bin 76. This means that with a target detection one real range bin too low, the signal quality of the target movement measurement in this detected range bin is greatly reduced. The graphs in Figure 11 clearly visualize the changes due to the dynamic clutter. The problem with visible differences in the signal becomes apparent when considering the visual analysis by healthcare professionals.

### 5.4 Impact of Beamforming on Dynamic Clutter

In this paper we not only want to investigate the dynamic clutter but also how a digital beamforming can reduce the dynamic clutter for a scenario with multiple radar targets. With the presented measurement system, it is possible to test the performance of different beamforming algorithms concerning their capability to reduce dynamic clutter. In the scope of this article, we will demonstrate this by discussing a beamforming algorithm and its effect on the dynamic clutter.

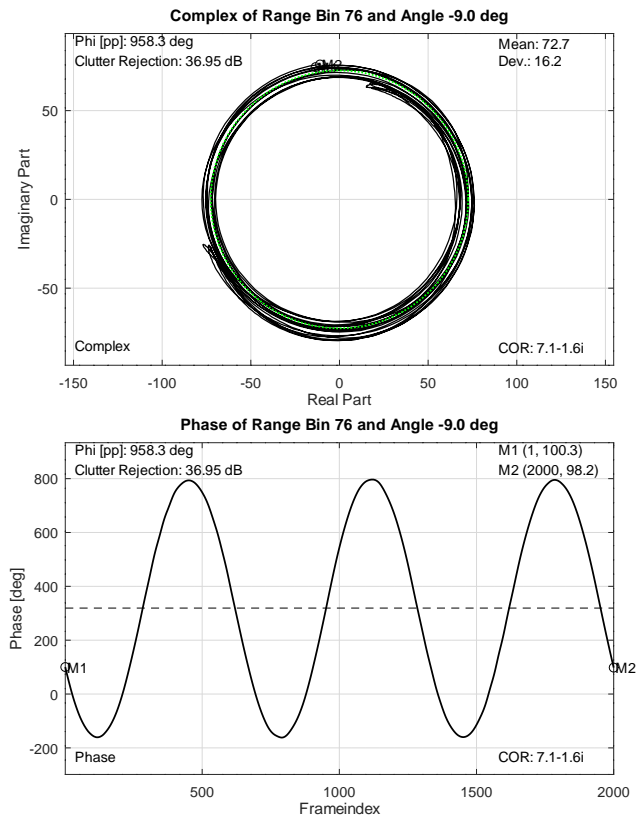


Figure 14: Complex and phase plot from dynamic clutter measurement in range bin<sub>ZP</sub> 76 with beamforming.

In [22], three different beamforming algorithms are compared, Bartlett, Capon and MUSIC algorithm. Those algorithms are candidates for future studies using our presented measurement system. By now, we implemented a second Fourier transform on all radar RX channels as mentioned in chapter 2.2. As already used in the

range FFT, a zero padding with factor four is used in the angle FFT. Like mentioned before, this does not change the angle resolution of the radar, but adds more points to the spectral curve.

After the angle FFT, the same processing was done on the data as in section 5.3. The angle of the target loudspeaker for all presented results is found by the target bin finder described in chapter 2.2. The results of the processed data are presented in Table 3. Figure 14 shows the radar phase and complex curves with dynamic clutter in range bin 76. In comparison to the curves in Figure 11 this is a great improvement.

Table 3: Dynamic clutter rejection of different range bins with beamforming.

Bin <sub>ZP</sub>	$\Phi_{PP,Clutter}$ [°]	Clutter Rejection [dB]
80	10.4	39.26
79	10.6	39.15
78	10.9	38.90
77	11.3	38.60
76	13.6	36.95
75	33.2	29.19

Figure 15 condenses all values from the Tables 2 and 3 into two curves. There you can see that the usage of beamforming greatly increases the signal quality in the observed range bins. Even when analyzing the data in range bin 80, where we expect the target signal to be, a slight improvement thanks to digital beamforming is measurable. Further, dealing with movements with smaller micro movement (like the one from the heartbeat), this could be even more important. As mentioned before, the visual representation of the phase signal related to the chest wall micro movement could be important to healthcare professionals in future diagnosis. A comparison of the curves in Figure 11 and 14 distinctly visualizes that the dynamic clutter rejection is more effective when using beamforming. Especially in real scenarios it is important to achieve a high robustness because the perfect adjustment cannot be expected at all times.

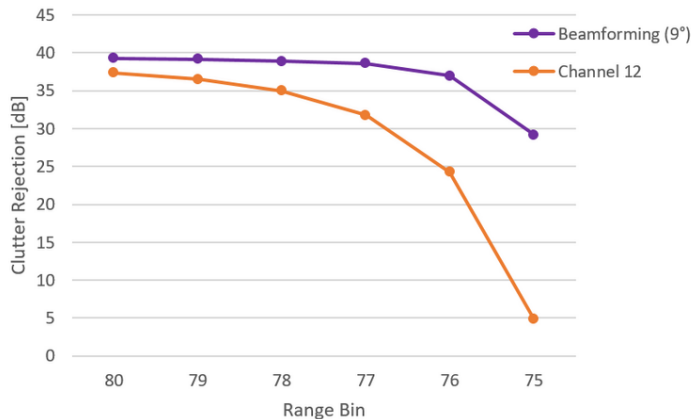


Figure 15: Dynamic clutter rejection with and without beamforming in different range bins.

## 6 Replication and Recording of realistic Micro Movement

In this chapter, measurements of realistic heartbeat movements are presented. The objective is to survey the effect of dynamic clutter on realistic micro movement with smaller movement amplitude. As already mentioned in 4.2, we used an apnea after exhalation scenario from the GDN0009\_3\_Apnea measurement of the clinical recorded dataset of Schellenberger [15]. Also, the chapter 4.2 explains the preparation of the dataset data for measurements.

For the measurement presented in this chapter, the prepared heartbeat motion signal is replayed on the target loudspeaker. In addition, a clutter movement is generated by the clutter loudspeaker at the same time. The used clutter signal is a sine with 0.4 Hz frequency and 4.7 mm movement peak-to-peak amplitude.

The recorded radar phase signal is shown in Figure 16. The investigated range bin is 76, which is one real  $Bin_W$  apart from the target bin. This constellation was already used in chapter 5. On the recorded data, the signal processing from 2.2 is used without a digital beamforming.

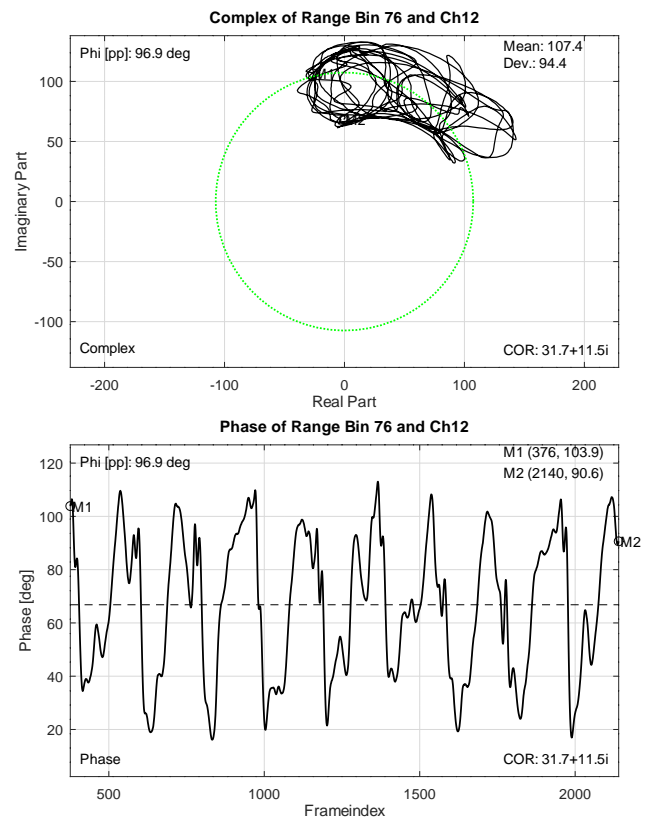


Figure 16: Complex and phase plot of radar measurement using heartbeat movement from dataset without digital beamforming.

In the performance test without any dynamic clutter presented in Figure 10 the heartbeat curve is clearly visible. However, during the measurement with dynamic clutter, the signal is strongly disturbed and the heartbeat movement is hardly visible. To improve the signal quality, the measured data were then processed again, this time with an additional angle FFT as digital beamforming. The results of the

second signal processing using digital beamforming is presented in Figure 17. There, the quality of the curve is significantly higher.

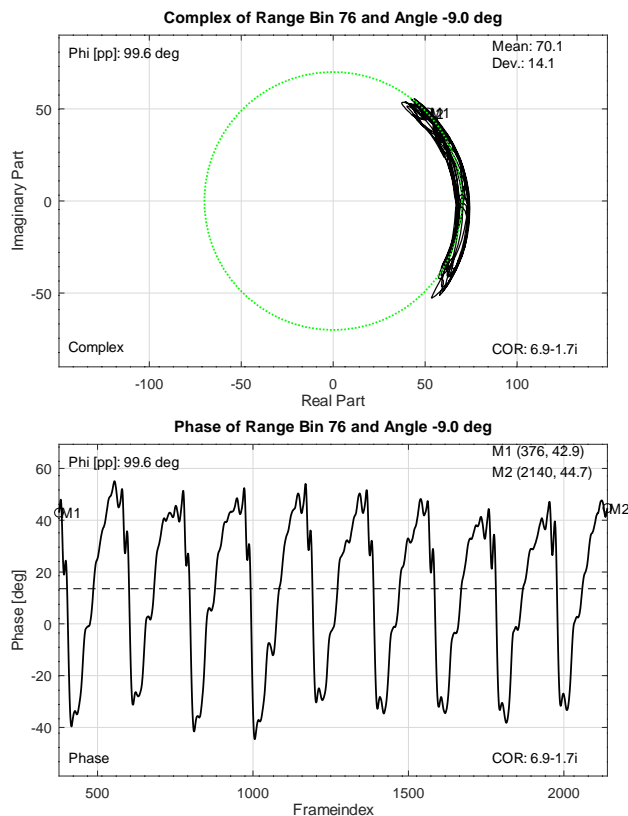


Figure 17: Complex and phase plot of radar measurement using heartbeat movement from dataset with digital beamforming.

The measurements in this chapter confirm once again the relevance of digital beamforming for vital sign sensing scenarios. They are an important supplement to the results of the previous chapter, in which the influence of dynamic clutter was quantitatively evaluated using the clutter rejection. Both measurement methods are steps in the evaluation of different beamforming algorithms.

## 7 Conclusion

In this paper we presented a measurement system that can be used for evaluating radar algorithms by replication of vital sign micro movement and dynamic clutter. It is an extension of work originally presented in the 44th Annual International Conference of the IEEE Engineering in Medicine and Biology Society (EMBC) [1]. In contrast to the previous work, the measurement setup was completely re-designed to be able to replicate realistic micro movement from vital signs and to enable scenarios with two moving objects. Movement data used for the replication was synthesized or taken from recorded movement data. The heartbeat movement from the clinically recorded dataset [15] was successfully reproduced and recorded by the measurement setup.

The ability to evaluate radar algorithms was demonstrated by the investigation of dynamic clutter. It was shown that an angle FFT algorithm increases the dynamic clutter rejection and signal quality

in a scenario with dynamic clutter. This increase in signal quality is also clearly visible in the phase signal related to the chest wall micro movement, which can be important to healthcare professionals in future diagnosis.

In future studies, different beamforming algorithms like Capon and MUSIC can be compared using the presented measurement system. It is suitable to evaluate signal processing algorithms for radar applications by replicating real micro movement scenarios. This is crucial in optimizing robust and reliable systems for medical applications. In addition, it is also possible to test radar algorithms implemented in a signal processor inside of the radar sensor at realtime using the measurement system.

## References

- [1] C. Domnik, M. Meuleners, C. Degen, "Radar Evaluation Setup for the Replication of Chest Wall Movement from Vital Signs," in 2022 44th Annual International Conference of the IEEE Engineering in Medicine and Biology Society (EMBC), IEEE, 2022, doi:10.1109/embc48229.2022.9871203.
- [2] V. Chen, F. Li, S.-S. Ho, H. Wechsler, "Micro-doppler effect in radar: phenomenon, model, and simulation study," *IEEE Transactions on Aerospace and Electronic Systems*, **42**(1), 2–21, 2006, doi:10.1109/taes.2006.1603402.
- [3] Y. Zhang, F. Qi, H. Lv, F. Liang, J. Wang, "Bioradar Technology: Recent Research and Advancements," *IEEE Microwave Magazine*, **20**(8), 58–73, 2019, doi:10.1109/mmm.2019.2915491.
- [4] J. C. Lin, "Microwave sensing of physiological movement and volume change: A review," *Bioelectromagnetics*, **13**(6), 557–565, 1992, doi:10.1002/bem.2250130610.
- [5] C. Feng, X. Jiang, M.-G. Jeong, H. Hong, C.-H. Fu, X. Yang, E. Wang, X. Zhu, X. Liu, "Multitarget Vital Signs Measurement With Chest Motion Imaging Based on MIMO Radar," *IEEE Transactions on Microwave Theory and Techniques*, **69**(11), 4735–4747, 2021, doi:10.1109/tmtt.2021.3076239.
- [6] S. Dong, Y. Zhang, C. Ma, C. Zhu, Z. Gu, Q. Lv, B. Zhang, C. Li, L. Ran, "Doppler Cardiogram: A Remote Detection of Human Heart Activities," *IEEE Transactions on Microwave Theory and Techniques*, **68**(3), 1132–1141, 2020, doi:10.1109/tmtt.2019.2948844.
- [7] C. Gu, R. Li, H. Zhang, A. Y. C. Fung, C. Torres, S. B. Jiang, C. Li, "Accurate Respiration Measurement Using DC-Coupled Continuous-Wave Radar Sensor for Motion-Adaptive Cancer Radiotherapy," *IEEE Transactions on Biomedical Engineering*, **59**(11), 3117–3123, 2012, doi:10.1109/tbme.2012.2206591.
- [8] M.-C. Tang, F.-K. Wang, T.-S. Horng, "A single radar-based vital sign monitoring system with resistance to large body motion," in 2017 IEEE MTT-S International Microwave Symposium (IMS), IEEE, 2017, doi:10.1109/mwsym.2017.8058758.
- [9] J.-M. Munoz-Ferreras, Z. Peng, R. Gomez-Garcia, C. Li, "Random body movement mitigation for FMCW-radar-based vital-sign monitoring," in 2016 IEEE Topical Conference on Biomedical Wireless Technologies, Networks, and Sensing Systems (BioWireless), IEEE, 2016, doi:10.1109/biowireless.2016.7445551.
- [10] E. Cardillo, C. Li, A. Caddemi, "Vital Sign Detection and Radar Self-Motion Cancellation Through Clutter Identification," *IEEE Transactions on Microwave Theory and Techniques*, **69**(3), 1932–1942, 2021, doi:10.1109/tmtt.2021.3049514.
- [11] A. Marnach, D. Schmiech, A. R. Diewald, "Verification of Algorithm for an I/Q-Radar System for Breathing Detection in an Incubator," in 2019 International Conference on Electromagnetics in Advanced Applications (ICEAA), IEEE, 2019, doi:10.1109/iceaa.2019.8879336.
- [12] B. Padasdao, E. Shahhaidar, C. Stickley, O. Boric-Lubecke, "Electromagnetic Biosensing of Respiratory Rate," *IEEE Sensors Journal*, **13**(11), 4204–4211, 2013, doi:10.1109/jsen.2013.2266253.



- [13] B. Padasdao, E. Shahhaidar, O. Boric-Lubecke, "Measuring chest circumference change during respiration with an electromagnetic biosensor," in 2013 35th Annual International Conference of the IEEE Engineering in Medicine and Biology Society (EMBC), IEEE, 2013, doi:10.1109/embc.2013.6609906.
- [14] A. Singh, S. U. Rehman, S. Yongchareon, P. H. J. Chong, "Modelling of Chest Wall Motion for Cardiorespiratory Activity for Radar-Based NCVS Systems," *Sensors*, **20**(18), 5094, 2020, doi:10.3390/s20185094.
- [15] S. Schellenberger, K. Shi, T. Steigleder, A. Malessa, F. Michler, L. Hameyer, N. Neumann, F. Lurz, R. Weigel, C. Ostgathe, A. Koelpin, "A dataset of clinically recorded radar vital signs with synchronised reference sensor signals," 2020, doi:10.6084/M9.FIGSHARE.12186516.V2.
- [16] A. Singh, B.-K. Park, O. Boric-Lubecke, I. Mostafanezhad, V. M. Lubecke, "Physiological Doppler Radar Overview," in *Doppler Radar Physiological Sensing*, 69–94, John Wiley & Sons, Inc, 2016, doi:10.1002/9781119078418.ch4.
- [17] J. Liu, Y. Li, C. Li, C. Gu, J.-F. Mao, "Accurate Measurement of Human Vital Signs With Linear FMCW Radars Under Proximity Stationary Clutters," *IEEE Transactions on Biomedical Circuits and Systems*, **15**(6), 1393–1404, 2021, doi:10.1109/tbcas.2021.3123830.
- [18] Y. Wang, A. Ren, M. Zhou, W. Wang, X. Yang, "A Novel Detection and Recognition Method for Continuous Hand Gesture Using FMCW Radar," *IEEE Access*, **8**, 167264–167275, 2020, doi:10.1109/access.2020.3023187.
- [19] A. D. Droitcour, O. Boric-Lubecke, "Physiological Motion and Measurement," in *Doppler Radar Physiological Sensing*, 39–68, John Wiley & Sons, Inc, 2016, doi:10.1002/9781119078418.ch3.
- [20] S. Schellenberger, K. Shi, T. Steigleder, A. Malessa, F. Michler, L. Hameyer, N. Neumann, F. Lurz, R. Weigel, C. Ostgathe, A. Koelpin, "A dataset of clinically recorded radar vital signs with synchronised reference sensor signals," *Scientific Data*, **7**(1), 2020, doi:10.1038/s41597-020-00629-5.
- [21] K. Shi, S. Schellenberger, C. Will, T. Steigleder, F. Michler, J. Fuchs, R. Weigel, C. Ostgathe, A. Koelpin, "A dataset of radar-recorded heart sounds and vital signs including synchronised reference sensor signals," *Scientific Data*, **7**(1), 2020, doi:10.1038/s41597-020-0390-1.
- [22] C. Degen, "On single snapshot direction-of-arrival estimation," in 2017 IEEE International Conference on Wireless for Space and Extreme Environments (WiSEE), IEEE, 2017, doi:10.1109/wisee.2017.8124899.

# Indoor Positioning: Comparing Different Techniques and Dealing with a user Authentication use Case

Joaquín Pérez Balbela<sup>\*1</sup>, Aruna Prem Bianzino<sup>2</sup>

<sup>1</sup>Universidad Internacional de La Rioja - UNIR, Uruguay

<sup>2</sup>Fundación Tecnológica Advantx - FUNDITEC, Madrid, Spain

## ARTICLE INFO

Article history:

Received: 28 February, 2023

Accepted: 26 April, 2023

Online: 15 May, 2023

Keywords:

Indoor Positioning

Taxonomy

Technique Comparison

Real Scenario

## ABSTRACT

Indoor positioning is a complex issue with many, heterogeneous application cases, each one presenting different requirements and environments. In such a complex ecosystem, an agile<sup>1</sup> taxonomy is needed to be able to select a proper solution for a given scenario, as well as practical recommendations for the most used solutions. Besides providing these tools, we analyze a real-world scenario and its requirements, selecting a practical solution and evaluating it together with its implications and consequences, providing a reference guideline for practical applications of indoor positioning.

## 1 Introduction

The location of objects and people in spaces where satellite technologies fail, or lack precision (e.g., inside complex buildings and underground locations) is a complex issue, while it represents a needed feature with many application cases, including access control, offering of personalized services, navigation in complex structures, crowd control, etc. User location may also be used as an authentication element in the case of critical infrastructure control, such as power plants.

Due to the strong need and the heterogeneity of the use cases, many different solutions have been proposed and developed. Each different context (e.g., commercial building, military facility, critical infrastructure, etc.) presents different scenarios (e.g., available network and infrastructure, barriers, variability and people presence, etc.) and different needs (e.g., cost limits, precision needs, security, privacy, etc.). Similarly, different solutions present different requirements, technologies, costs, and precision. Due to the complexity of the resulting ecosystem, it is important to properly understand the needs of the scenario and the implications of the available solutions. In this paper, we will contrast different techniques for indoor positioning, focusing on different key aspects with the aim of producing guidelines for the technology selection in common scenarios. Finally, we will evaluate different solutions in a real environment

and will consider a practical case of location as an authentication element in the context of critical infrastructure management and monitoring in energy production and usage.

The rest of this paper is organized as follows: in Section II we introduce a taxonomy for Indoor positioning solutions, analyzing the different relevant aspects, their solution space, and practical implications. In Section III we analyze different available techniques for indoor positioning, placing them in the proposed taxonomy, analyzing their practical implication, and providing recommendations for the scenarios and environments in which its deployment could be more suitable. In Section IV we present some real-world examples of commercial applications integrating Indoor Positioning, together with the corresponding main characteristics, limitations, and requirements. This analysis includes examples covering applications in the Sport, Logistics, and Food industries. In Section V we evaluate a real-world use case, i.e., the use of indoor location as an authentication factor in critical infrastructure (i.e., energy production management and monitoring), detailing its requirements, selecting a practical solution and testing it in a real, relevant environment, and analyzing its use accounting for the relevant evaluation criteria, i.e., precision, security, confidentiality, integrity, and availability. Finally, in Section V we draw the conclusion of our research work and describe possible future extensions.

\*Corresponding Author: Joaquín Pérez Balbela, Email: [joaquinperezbalbela@gmail.com](mailto:joaquinperezbalbela@gmail.com)

## 2 Solution Taxonomy

Different attempts are available in the literature presenting a classification of positioning techniques. Among the most recent ones, we would like to highlight [1] and [2]. Still, these works perform a much wider analysis and include dimensions that may not be relevant to the scenario analysis and technology selection, such as the purpose (i.e., healthcare, retail, etc.), resulting in a less agile overview and lacking practical recommendations for real-world scenarios. This is why we present here a minimal, yet relevant taxonomy, allowing to order the most used and relevant solutions for indoor positioning.

As introduced, many different techniques are available for indoor positioning, targeting different scenarios and contexts, using different technologies and different base solutions. In this section, we will describe the resulting solution space and define how we limited our scope.

First of all, in the remaining of this paper, we will refer to the object or person to be located as the “target device” (TD), as we will consider solutions where the location is calculated for a device, co-located with the target object or person.

For what concerns the taxonomy dimensions, in the first place, the scope of the techniques may range from (i) knowing the location of a TD in space from an external system (i.e., **location**), (ii) allowing a TD to know their location in space (i.e., **positioning**), (iii) following the location of a TD over time (i.e., **tracking**), (iv) to computing an (optimal) path from the current location of a TD to a specified destination (i.e., **navigation**). This dimension actually depends on the problem to be solved and most solutions may be used for any scope. Eventual differentiation points in this dimension may be represented by the frequency at which the location is estimated, e.g., if a solution estimated the TD’s location once every minute, it will result in a poor user experience if used in a navigation context.

Secondly, different information may be used as input for the solution, including input from different sensors of the TD and/or from the environment. The solution may use one or more of the following:

- **Device motion**, including acceleration and changes in the acceleration, tilting angle and its change rate, proximity to specific or generic nearby objects, etc.
- **Environment sensing**, including light intensity, environmental noise, magnetic field, atmospheric pressure, temperature, environment recognition through the camera, etc.
- **Audio** production and/or sensing of specifically generated signals.
- Communication with an **existing network infrastructure**, including Bluetooth beacons, cellular towers, satellite signals, WiFi, etc.
- Detection of specific **tags**, including visual tags, RFID tags, etc.

Different information may derive from different sensors, whose availability should be checked with the target device set, which may result in different power consumption and costs, may require

different infrastructure (e.g., a specific wireless network in the target area), may result in different precision and availability depending on the target scenario, and, finally, may impact in different ways the user’s privacy.

Finally, how this information is used is another big differentiation point among different solutions for indoor positioning. In particular, the input information may be analyzed:

- as a **single value** (e.g., an intensity measure to calculate the distance from a reference point),
- as a **value variation** (e.g., acceleration to estimate a path of the TD into an area), or
- against **reference values** (e.g., pre-mapping of values in the target area and contrasting the measured value against the map).

Solutions belonging to different categories result in different compatibility (e.g., need for specific sensors in the TD, or specific infrastructure in the area), different costs (sensors, infrastructure), and energy consumption and workload for the TD (different sensors, infrastructure, sampling frequency, tracking/navigation, vs. location/positioning), different needs for information exchange between the infrastructure and the TD, resulting in different privacy level for the device user, and, certainly, different precision levels. As such, the selection of the solution to be used in a specific context should be carefully evaluated, taking into account all the relevant aspects.

## 3 Main Techniques Considered

In this work, we considered techniques not needing an existing infrastructure (i.e., Magnetic Map), or based on the communication with an existing network infrastructure and using standard sensors on the TD, specifically considering WiFi and Bluetooth as network infrastructures, due to their high availability and compatibility with existing mobile devices. In particular, we detected four main solution classes for solutions leveraging on existing WiFi infrastructure, on the basis of the used information: Radio Signal Strength (RSS), Angle of Arrival (AoA), Time of Arrival (ToA), and Fingerprinting. For each considered solution type, recommendations on real-world scenarios in which they may be used are included. A summary of the analyzed solutions is reported in Table I.

The different techniques described can be combined with each other to obtain hybrid solutions (e.g., [3] combining RSS and Fingerprinting, [4], combining Bluetooth Beacons and Fingerprinting, or [5], combining RSS and AoA). This generally results in a higher accuracy compared to the use of solutions using a single technique [6], and/or higher system availability, as if one of the combined solutions alone would not be available in certain areas/settings, the others may be. On the other hand, solution hybridization generally results in higher costs as more infrastructure and/or sensors are needed, as well as more computational power. Still, each individual solution results in a baseline for the combination, considering costs and performance.

### 3.1 Radio Signal Strength (RSS)

The solutions belonging to this classification use the signal strength of the WiFi network as measuring input. This may either be directly measured or as a Signal-to-noise ratio. This allows for estimating the distance from the WiFi transmitter, whose location is known. Using at least 3 different transmitters, a triangulation is possible and the location may be estimated, like in [7], [8], or [9]. The human body itself alters the received signal strength, as such, the body position with respect to the device should be taken into account.

In general, this class of solutions presents a significant variation in the measured distance between the TD and the signal emission points, due to the TD motion pattern, user positioning with respect to the device, and the presence of eventual obstacles (e.g., metal elements in the building structure). On the other hand, this class of solutions is based on commonly available infrastructure, HW available on any device, and uses standard functions. This class of solutions is recommended for usage in areas clear from obstacles and with a line of sight to the access points.

### 3.2 Angle of Arrival (AoA)

The solutions belonging to this class use the angle at which the WiFi signal is received as input. In this case, a multidirectional antenna emits broadcast signals with a given frequency, while directional antennas emit specific signals at different given frequencies. The time interval between the reception of the multidirectional and the directional signals allows for calculating the distance between the TD and the emitting antenna. This method, originally used to locate flying devices, has been adapted to indoor positioning, providing higher precision [10], [11], [12].

Similarly to what happens in the RSS case, the presence of obstacles between the TD and the emitting antenna may distort the power and direction of the signal. In general, this class of solutions presents higher precision when the TD is far from the base station, especially in spaces with few or no obstacles (e.g., hangars, open spaces, etc.). This class of solutions is recommended for usage in areas clear from obstacles and with a high distance between the TD and the access points.

### 3.3 Time of Arrival (ToA)

The solutions belonging to this class use the time difference between the signal emission from the base station and its reception at the TD. This input is then used to estimate the distance between the two elements. Also in this class of solution, the location may be estimated using a triangulation (i.e., at least 3 different transmitters) [13], [14]. In this case, the estimation is affected by the signal attenuation introduced by obstacles, which is reduced using higher frequency signals (e.g., UltraWideband - UWB), resulting in higher precision. Still, the precision of this class of solutions is drastically reduced by obstacles between the transmitter and the TD, even using UWB signals [15]. Another solutions that is ToA-based is LiDAR (Light Detection and Ranging) which is used to measure distance using light or laser beams.

Overall, this class of solutions accounts for higher precision, but requires specific hardware (e.g., UWB transmitters and receivers) and higher area coverage, resulting in higher costs. For the usage of

this class of solutions in areas with a high number of obstacles, a higher number of transmitters should be used.

### 3.4 Fingerprinting

The solutions belonging to this class require a preliminary mapping of the signal fingerprint in the target area (e.g., [16] where the WiFi signals are mapped, or [17] where mapping of WiFi as well as of other signals are considered, or [18], where AoA samplings are mapped). The solution then measures the current signals in the TD and maps them to the most similar fingerprint to estimate the TD location.

On the one hand, this class of solutions does not require special hardware, but it is instead based on the present infrastructure (e.g., WiFi network) and on sensors commonly present on mobile devices (e.g., WiFi antenna), using measurements already commonly performed by mobile devices (e.g., WiFi signal strength). On the other hand, any change in the area setting (e.g., replacing/moving an access point, introduction/elimination repositioning of an interfering element, etc.) requires a new mapping. Fingerprinting introduces ambiguity points, where the fingerprint may be similar and therefore it may not be possible to estimate an accurate location in all cases [6]. Finally, the precision of this class of solutions depends on the number of wireless networks present in the area: the higher, the better. This class of solutions is recommended for usage in areas whose configuration and status are stable in time.

### 3.5 Bluetooth Beacons

Other kinds of wireless networks may be used to communicate with the TD and estimate its location. Solutions belonging to this class use Bluetooth beacons, with a known location, transmitting any payload to know which devices are present in their coverage area. Intersecting the areas to which a device belongs, it is possible to estimate its location. RSS solutions based on Bluetooth are also possible but result in higher energy consumption and lower precision [19], [20], [21].

The energy consumption of this kind of solution is really low, especially if Bluetooth low energy (BLE) or similar standards are used. At the same time, the payload transmitted by the beacons may be used to transmit useful information (push notifications, localized advertisement or service description, etc.), even if, it should be said, the infrastructure does not provide further services as the internet connectivity provided by the WiFi infrastructure of the solution classes analyzed up to now. On the other hand, specific hardware is required (Bluetooth beacons), in a number (and cost) proportional to the required precision and area to be covered. For the usage of this class of solutions in areas with a high number of obstacles, a higher number of beacons should be used.

### 3.6 Magnetic Map

Similarly to the solutions explored in section III-D, a mapping of the magnetic field present in the different points of the target area may be performed [22], [23], [24]. This kind of solution requires specialized hardware (i.e., at least 3 magnetic field sensors, specifically aligned and placed on the TD). On the other hand, this type of

solution results in higher precision than other methods, although it faces the same drawback as other fingerprinting methods: changes in the environment require the area to be mapped again since its magnetic map may have changed. We have not found evidence of this method being widely implemented, mainly due to its specific hardware requirements.

### 3.7 Summary

A summary of the analyzed solutions is reported in Table I, together with their classification on the basis of the proposed taxonomy. All these solutions may be used for any *scope*, depending on the application processing the info they return. As we can see, different solutions result in different tradeoffs, especially regarding costs and precision (“Avg. Error” in Table I). Note that, for each technique, a specific implementation and environment should be taken into account to determine its precision. For each technique, in Table I, the reference implementation is reported in the first column. This should be carefully evaluated, together with the other relevant parameters (i.e., confidentiality, availability, security, integrity), when selecting a practical solution for a specific application scenario. An example of this process will be provided in Section V.

Table I: Solution summary

Name	Info	Usage	Cost	Avg. Error
RSS [7]	Existing Net.	Single value	Low	2.9-16.3m
AoA [10]	Existing Net.	Single value	Low	2.1m
ToA [15]	Existing Net.	Single value	High	2m
Fingerp. [16]	Existing Net.	Ref. values	Mid	0.6-1.3m
Beacons [19]	Existing Net.	Single value	Mid	9.7m
Magn. Map [22]	Environment	Ref. values	High	0.1m-0.16m

## 4 Using Indoor Positioning: Real World Examples

In this section, we provide some examples of Indoor Positioning as used in real-world commercial applications, together with the corresponding main system characteristics, limitations, and requirements. We will analyze a few examples through Sport, Logistics, and Food industries.

### 4.1 Using Indoor Positioning in Sports

Some sports have benefited from using indoor positioning techniques, notable examples include tennis, football, and handball.

In tennis, precise ball tracking is required to determine whether it is in or out, and many commercial systems are based on optical cameras that track the ball’s position and gather the necessary information for the Hawk-Eye to process. The optical Hawk-Eye system has an estimated error range of 3.6mm at impact [25].

Validations of UWB technology have been executed to compare the accuracy of the optical Hawk-Eye system versus the UWB-based one. In this study, an optical system was paired with a UWB-based Local Positioning System (LPS), and a tennis match was tracked using both systems. Depending on the considered parameters, the

mean error range between both systems was in the range of 13.1 to 17.8cm [26]. However, taking the cost of deploying a Hawk-Eye system into consideration, it becomes a competitive alternative. The cost of a professional Hawk-Eye system using 10 high-speed cameras starts at between 60000 to 70000 US dollars per Tennis court [27], while other UWB-based systems’ cost can start at approximately half of this value [28].

The last FIFA World Cup 2022 in Qatar used a UWB-based live ball tracking system developed by Kinexon. The official ball contained an internal sensor weighing 7 grams transmitting in the 500Hz band which, according to Kinexon, tracked the ball’s movement 100 times per second with centimeter accuracy when paired with their real-time locating system (RTLS). Additional metrics can be derived from this data such as ball possession and speed, among others [29].

A study was conducted to assess Kinexon’s solution and compare its error rate to other systems. In this study, the system was used to track both players and the ball, and it was measured in a specially designed circuit on the Fraunhofer L.I.N.K test circuit and in a football game, to gather knowledge regarding how the system would react in different situations. The image of the circuit is included below, and it includes linear sprints, curved sprints, agility tests, and direction changes, among other tests [30].

This system can also be used in handball, although its accuracy is approximately 18,9% lower compared to football due to different sport kinematics [30]. Standard deployment of this system may cost between 20000 to 30000 US dollars per field [28].

As a brief summary, although UWB-based LPS may have a larger error rate compared to visual or infrared systems which are considered the *gold standard* when taking cost into account, those solutions become an interesting choice.

### 4.2 Using Indoor Positioning in the storage and distribution industry

An important part of shipping orders is the picking phase, in which the desired items are located in the various warehouses and included in the customer’s order. Depending on the number of items to be picked, this phase may be a time-consuming one, and, as warehouses grow in size, finding the necessary items to complete orders may be a challenging task.

Indoor positioning solutions can be used to guide the worker or smart robot as it navigates the store searching for items (using an optimized route) or to generate real-time product location maps, for example.

Amazon is one of the biggest worldwide retailers and has a large number of warehouses around the world. Those warehouses are run using a technique called “chaotic storage”, in which the items are placed in random locations trying to use the spare space as efficiently as possible, using no predefined zones or locations for those items. This translates into items being tracked solely by software, without relying on the worker or any other method. In Amazon’s case, this storage method generates a large amount of raw data that can be used to improve internal processes, such as tracking stock or sending items first with a closer expiration date [31].

### 4.3 Using Indoor Positioning in the food industry

Restaurants have benefited from using indoor positioning systems to enhance their efficiency, reduce wait times and offer a better customer experience. As an example, fast food restaurants use these LPS to track food delivery after the order is placed through kiosks. A marker is assigned to the order and allows the restaurant's personnel to determine where the customer is seated in order to deliver the order.

For example, one such platform is the LPS deployed at select McDonald's locations, which is based on Bluetooth Low Energy (BLE) technology developed by Acrelec and Radius Technology Inc. These devices are located on plastic table markers, powered by a button cell Lithium battery and their size is approximately two regular coins.

According to the manufacturer, the device's main microprocessor is an ARM-based Cortex M4 SOC (Nordic Semiconductor nRF52832) and includes different sensors such as an accelerometer and fall detection. This SOC states it supports different protocols such as Apple's iBeacon, AltBeacon, and Google's Eddystone, allowing for device interoperability, and has a maximum transmission distance of 100 meters [32]. This SOC is also very popular among enthusiasts, mainly due to its features, cost, and compatibility with Arduino development boards, even though it does not include integrated Wi-Fi functionality.

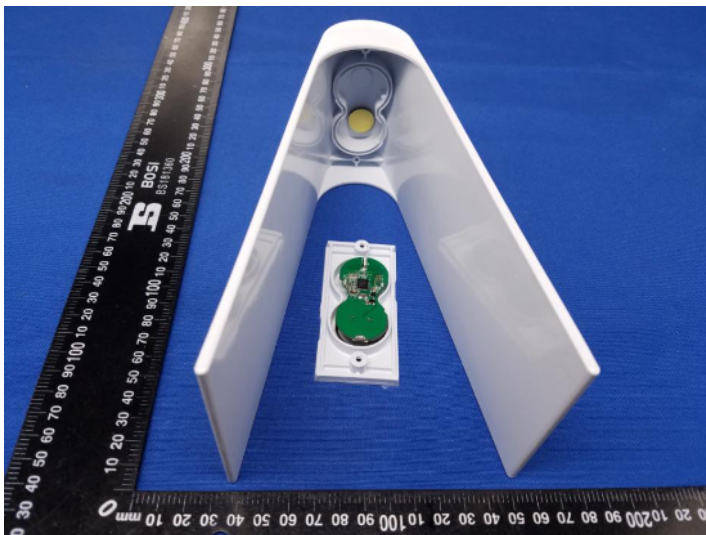


Figure 1: View of the plastic table marker and the internal BLE beacon [32].

Acrelec's platform allows floor maps to be included in their platform, showing the location of the marker on the restaurant's floor plan to help the staff locate the customer in a timely manner.

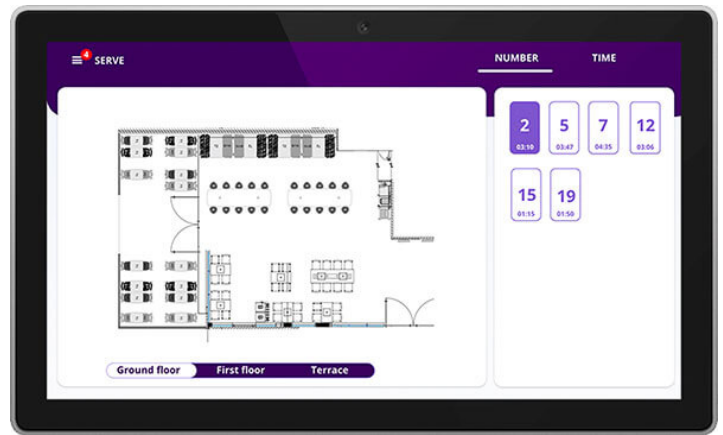


Figure 2: View of Acrelec's Table Service platform [33].

## 5 The User Authentication Case

More and more users consume resources and services from mobile devices. Authenticating these users is of paramount importance to regulate the access to services, resources, and sensitive data, and to limit it to only authorized users. User authentication is the process of establishing with reasonable accuracy whether users are who they claim to be. The process is usually based on some credentials, whose ownership and verification guarantee to check the user identity, and that may fall into one of the following categories: (i) something that the user knows (e.g., a secret keyword), (ii) something that the user owns (e.g., a physical object like a smart card), (iii) something that the user is (e.g., any measurable physical feature, univocally identifying the user, like fingerprints or iris identification, for instance), (iv) something that the user does (e.g., motion patterns, signature, etc.), or (v) somewhere that the user is (e.g., being in a specific location). This information (identifier), may be combined including information belonging to different categories, to improve security (i.e., Multi-factor authentication, like when a user is asked for a password - something that the user knows - and to enter a code received at their mobile phone - something that the user owns). In particular, in the case of power-plant control and monitoring, as in the Robinson Project, due to the sensitivity of the context and to the possible consequences of identity theft, we proposed an identification mechanism including positioning among the used identification elements: the user must be physically present where they are accessing the service (Power plant monitoring and control), in order for them to be allowed to access the service itself. As physical access is subject to other external security measures, this solution guarantees a very strong identification.

### 5.1 Target Requirements

In order to select a specific solution for the considered context, we must keep into account the different analyzed parameters. In the considered scenario, location is the only relevant scope of the solution, while the other leading factors are the technology availability and compatibility, the solution availability, precision (Maximum error lower than the distance between the control panel and the access to the closest room, 2.5m in the example taken into account). A differ-

ent threshold or a confidentiality interval may be set depending on the environment), and data security and privacy (extremely relevant in an authentication context). On the other hand, the environment is not subject to frequent changes or variable interference (e.g., crowd presence). As such, the natural choice is to use a Fingerprinting solution based on WiFi.



Figure 3: Devices used for the solution evaluation: (a) Mikrotik access point, (b) laptop, (c) Galaxy S8 (TD), and (d) Galaxy S21.

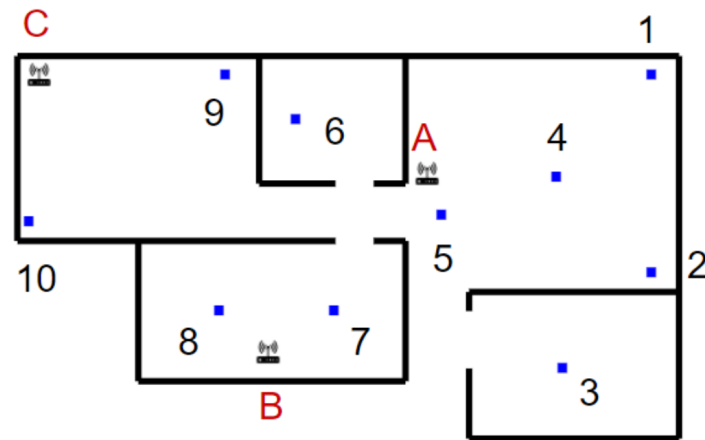


Figure 4: Evaluation environment, including equipment placement (A, B, and C) and measurement points (1 to 10).

### 5.2 Evaluation Scenario

We used a real environment and deployed the Anyplace tool [34] to evaluate the selected solution. Anyplace relies on fingerprinting, as well as RSS, and combines several methods to obtain a lower error margin. Networking equipment was installed in this environment, using a Mikrotik hap AC<sup>2</sup> access point broadcasting on both 2.4 and 5GHz bands, a laptop equipped with a Killer AC1550i WiFi card, and a Galaxy S21 mobile phone acting as a hotspot, both broadcasting on the 2.4GHz band. A Galaxy S8 mobile phone acted as TD. The used devices are depicted in Figure 1. The software solution used in this scenario was Anyplace, running on the University of Cyprus’ public servers. A single-floor, multi-room space divided with masonry walls was used as an evaluation environment. The equipment was placed as shown in Figure 2 to cover an area of about 52m<sup>2</sup>.

Measurements were taken on the points highlighted in Figure 2. At each point, we took four consecutive readings and averaged the result to smoothen possible interference or disruption, measuring the error as the linear distance between the detected and real

location. This measurement-taking procedure was repeated on three occasions: with a single access point (i.e., the Mikrotik access point - A), with two access points (i.e., including also the laptop - B), and with three access points (i.e., including also the Galaxy S21 hotspot - C).

### 5.3 Results

As introduced above, in order to evaluate the solution, we take into account different aspects: the solution precision in estimating the TD location, and the solution security, confidentiality, integrity, and availability.

Evaluating the solution **precision**, the measurement error for the different configurations is reported in Table II for the different measurement points, on average, and as an improvement with respect to the base configuration with a single access point (i.e., “Difference” in Table II).

Table 2: Measurements results: error in the location estimation for the different measurement points, in meters. The difference percentage is calculated from reference measurement (1 AP).

Point	1 AP	2 APs	3 APs
1	0.91	0.83	0.81
2	0.85	0.79	0.78
3	1.09	0.93	0.90
4	0.68	0.64	0.63
5	0.48	0.47	0.44
6	1.15	1.11	1.11
7	1.03	0.83	0.74
8	1.29	0.74	0.69
9	2.88	2.45	2.38
10	3.28	3.4	2.11
Average	1.36	1.22	1.06
Difference	Reference	10.63%	22.36%

As expected, as the number of reachable access points increases, the location estimation becomes more accurate, since the TD can use more anchors to perform distance calculations. As such, by increasing the number of available access points, the precision may be tuned to meet the system requirements and to reduce the probability of false room location to an amount irrelevant even for critical scenarios such as energy-production management and monitoring.

In order to evaluate the measurement error against the set threshold, a similar measurement campaign should be carried out in the target scenario (i.e., the power plant control room), which was not accessible to the authors, but this analysis may be considered a guideline for the one targeting a specific deployment.

Regarding **confidentiality**, Anyplace uses fully-encrypted communications using Transport Layer Security (TLS) between its API, internal components, and clients. Furthermore, devices are identified by their system certificates. This provides an additional layer of protection and makes Man-In-The-Middle (MITM) attacks more difficult, mitigating the risk of modifying the encrypted traffic. Finally, the building may be configured as private, protecting its information through a random string identifier (Universal Unique Identifier - UUID).

Considering the **availability** of this solution, a mirror service may be added to provide redundancy and/or to scale the solution. In this evaluation, Anyplace public productive environment was used, but it can also be downloaded and deployed in a local environment to add eventual mirror services and offer this way a configurable level of availability, and/or load balancing. Additionally, its components can be deployed in containers, which can provide means for automatic autoscaling in cloud environments.

Analyzing the solution's **security**, it supports the integration of a Web Application Firewall (WAF). The WAF is not integrated into the public instancing of Anyplace, but it may be integrated into the case of a local deployment. The WAF integration allows checking the network traffic directed toward the application (i.e., identifying potential attacks), and acting on it if needed. Still, Anyplace does not allow to set an expiration time for active sessions, neither in the case of inactivity, opening the possibility for a malicious third party to use an open session from an unattended device, contrary to the recommendations from the Open Web Application Security Project (OWASP) [35]. As the location is not the only authentication factor in the target solution, this flaw is considered minor.

Finally, we will analyze the solution **integrity**, i.e., the data exchanged among the different solution components is guaranteed to not be altered during transmission. The communication among system components is encrypted using the HTTPS protocol using TLS, and they require a valid certificate, signed by a Certification Authority (CA), protecting data transmission from MITM attacks and other transmission alterations. Finally, on every single node, redundancy may be set allowing for a configurable fault tolerance threshold.

## 6 Conclusions

In this paper, we analyzed the general problem of indoor positioning, reviewing the different characteristics offered by the different available solutions. We proposed a simple, yet agile and effective taxonomy to sort the solution space, a needed task when selecting the optimal solution for a specific use case. Then we analyzed different available solutions, offering practical recommendations for the scenarios in which they may be used, as well as the requirements they may or may not meet. This represents an addition to previous analysis for similar solution sets. As a following step, we present different real-world applications integrating indoor positioning. We analyze their main characteristics, requirements, and limitations. Finally, we evaluated a real scenario, i.e., location as an authentication factor for a management and monitoring system for energy production. For the analyzed scenario, we select and evaluate a solution in a real test environment. The selected solution was able to meet the precision, security, confidentiality, integrity, and availability requirements of the target system.

As a future work, it would be interesting to evaluate different real case scenarios, possibly involving different application domains. For each scenario, the corresponding system requirements must be evaluated, and a set of guidelines for solutions to be selected would be generated as output, together with guidelines for the configuration to be used. Furthermore, we would compare the performance of indoor positioning solutions across different types of environ-

ments, in order to be able to provide more specific guidelines for the technology selection and configuration.

## Acknowledgment

This work was funded by EU Horizon 2020 research and innovation programme, Robinson Project, grant agreement N° 957752.

## References

- [1] F. Zafari, G. Athanasios, K. L. Kin, "A survey of indoor localization systems and technologies," *IEEE Communications Surveys & Tutorials*, **21**, 2568–2599, 2019, doi:10.1109/comst.2019.2911558.
- [2] K. Nguyen, Z. Luo, G. Li, C. Watkins, "A review of smartphones-based indoor positioning: Challenges and applications," *IET Cyber-Systems and Robotics*, **3**, 1–30, 2021, doi:10.1049/csy2.12004.
- [3] S. Li, R. Rashidzadeh, "Hybrid indoor location positioning system," *IET Wireless Sensor Systems*, **9**, 257–264, 2019.
- [4] V. Nair, C. Tsangouri, B. Xiao, G. Olmschenk, W. Seiple, Z. Zhu, "A hybrid indoor positioning system for blind and visually impaired using Bluetooth and Google tango," *Journal on technology and persons with disabilities*, **6**, 2018, doi:10.1049/iet-wss.2018.5237.
- [5] A. Catovic, S. Zafer, "The Cramer-Rao bounds of hybrid TOA/RSS and TDOA/RSS location estimation schemes," *IEEE Communications Letters*, **8**, 626–628, 2004, doi:10.1109/lcomm.2004.835319.
- [6] A. Yassin, Y. Nasser, M. Awad, A. Al-Dubai, R. Liu, C. Yuen, R. Raulefs, E. Aboutanios, "Recent Advances in Indoor Localization: A Survey on Theoretical Approaches and Applications," *IEEE Communications Surveys & Tutorials*, **19**, 1327–1346, 2017, doi:10.1109/comst.2016.2632427.
- [7] P. Bahl, V. Padmanabhan, "RADAR: An In-Building RF-based User Location and Tracking System," in *Proceedings IEEE Infocom 2000 Conference on Computer Communications. Nineteenth Annual Joint Conference of the IEEE Computer and Communication Societies*, 775–784, 2000, doi:10.1109/infcom.2000.832252.
- [8] W. Chen, K. Kao, Y. Chang, C. Chang, "An RSSI-based distributed real-time indoor positioning framework," in *2018 IEEE International Conference on Applied System Invention (ICASI)*, 1288–1291, 2018, doi:10.1109/icas.2018.8394528.
- [9] J. Yang, C. Yingying, "Indoor localization using improved rss-based lateration methods," in *GLOBECOM 2009-2009 IEEE Global Telecommunications Conference*, 1–6, 2009, doi:10.1109/glocom.2009.5425237.
- [10] D. Niculescu, B. Nath, "VOR Base Stations for Indoor 802.11 Positioning," in *MobiCom '04: Proceedings of the 10th annual international conference on Mobile computing and networking*, 58–69, 2004, doi:10.1145/1023720.1023727.
- [11] M. Kotaru, K. Joshi, D. Bharadia, S. Katti, "Spotfi: Decimeter level localization using wifi," in *Proceedings of the 2015 ACM Conference on Special Interest Group on Data Communication*, 269–282, 2015, doi:10.1145/2785956.2787487.
- [12] C. Lim, P. N. Boon, D. Duan, "Robust methods for AOA geo-location in a real-time indoor WiFi system," *Journal of Location Based Services*, **2**, 112–121, 2008, doi:10.1080/17489720802415189.
- [13] A. Fedotov, V. Badenko, V. Kuptsov, S. Ivanov, I. Struchkov, "Location measurement of an object using radio networks for Industry 4.0 applications," in *E3S Web of Conferences*, EDP Sciences, 2021, doi:10.1051/e3sconf/202126405060.
- [14] J. Shen, A. F. Molisch, J. Salmi, "Accurate passive location estimation using TOA measurements," *IEEE Transactions on Wireless Communications*, **11**, 2182–2192, 2012, doi:10.1109/twc.2012.040412.110697.



- [15] G. Hu, P. Feldhaus, Y. Feng, S. Wang, J. Zheng, H. Duan, J. Gu, "Accuracy Improvement of Indoor Real-Time Location Tracking Algorithm for Smart Supermarket Based on Ultra-Wideband," *International Journal of Pattern Recognition*, **33**, 1–27, 2019, doi:10.1142/s0218001420580045.
- [16] M. Youssef, A. Agrawala, "The Horus WLAN location determination system," in *Proceedings of the 3rd International Conference on Mobile Systems, Applications, and Services - MobiSys*, 205–218, 2005, doi:10.1145/1067170.1067193.
- [17] X. Zhu, W. Qu, T. Qiu, L. Zhao, M. Atiquzzaman, D. Wu, "Indoor intelligent fingerprint-based localization: Principles, approaches and challenges," *IEEE Communications Surveys & Tutorials*, **22**, 2634–2657, 2020, doi:10.1109/comst.2020.3014304.
- [18] L. Chen, I. Ahriz, D. L. Ruyet, "AoA-aware probabilistic indoor location fingerprinting using channel state information," *IEEE Internet of Things Journal*, **107**, 10868–10883, 2020, doi:10.1109/jiot.2020.2990314.
- [19] F. Zafari, I. Papapanagiotou, K. Christidis, "Micro-location for Internet of Things equipped Smart Buildings," *IEEE Internet of Things Journal*, **3**, 96–112, 2016, doi:10.1109/jiot.2015.2442956.
- [20] L. Bai, F. Ciravegna, R. Bond, M. Mulvenna, "A low cost indoor positioning system using bluetooth low energy," *IEEE Access*, **8**, 136858–136871, 2020, doi:10.1109/access.2020.3012342.
- [21] S. S. Chawathe, "Beacon placement for indoor localization using bluetooth," in *2008 11th International IEEE Conference on Intelligent Transportation Systems*, 980–985, 2008, doi:10.1109/itsc.2008.4732690.
- [22] H. Kim, W. Seo, K. Baek, "Indoor Positioning System Using Magnetic Field Map Navigation and an Encoder System," *Sensors*, **17**, 2017, doi:10.3390/s17030651.
- [23] D. Almeida, E. Pedrosa, F. Curado, "Magnetic mapping for robot navigation in indoor environments," in *2021 International Conference on Indoor Positioning and Indoor Navigation (IPIN)*, 1–8, 2021, doi:10.1109/ipin51156.2021.9662528.
- [24] M. Frassl, M. Angermann, M. Lichtenstern, P. Robertson, B. J. Julian, M. Doniec, "Magnetic maps of indoor environments for precise localization of legged and non-legged locomotion," in *2013 IEEE/RSJ International Conference on Intelligent Robots and Systems*, 913–920, 2013, doi:10.1109/iros.2013.6696459.
- [25] F. Rioult, S. Mecheri, B. Mantel, F. Kauffmann, N. Benguigui, "What Can Hawk-Eye Data Reveal about Serve Performance in Tennis?" in *MLSA15 - Machine Learning and Data Mining for Sports Analytics workshop (ECML / PKDD 2015)*, Porto, Portugal, 36–45, 2015.
- [26] A. Umek, A. Kos, "Validation of UWB positioning systems for player tracking in tennis," *Personal and Ubiquitous Computing*, **26**, 1023–1033, 2022, doi:10.1007/s00779-020-01486-0.
- [27] K. Wong, "Low-cost Tennis Line Call System with Four Webcams," Department of Applied Physics, Stanford University, 2016.
- [28] Compare Sport Tech, "Compare LPS," <https://www.comparesportstech.com/compare-lps-tracking-systems>, retrieved on February 14th, 2023.
- [29] KINEXON, "Everything You Need To Know About Ball Tracking," <https://kinexon.com/blog/everything-you-need-to-know-about-ball-tracking/>, retrieved on February 14th, 2023.
- [30] P. Blauburger, R. Marzilger, M. Lames, "Validation of Player and Ball Tracking with a Local Positioning System," *Sensors*, **21**, 2021, doi:10.3390/s21041465.
- [31] A. Delfanti, *The Warehouse*, Pluto Press, 2021, doi:10.2307/j.ctv2114fnm.
- [32] Federal Communications Commission, "OET Authorization Search Results," <https://gov.fccid.io/2ABYU-RBT003>, retrieved on February 14th, 2023.
- [33] ACRELEC, "Table service," <https://acrelec.com/table-service/>, retrieved on February 14th, 2023.
- [34] K. Georgiou, T. Constambeys, C. Laoudias, L. Petrou, G. Chatzimilioudis, D. Zeinalipour-Yazti, "Anyplace: A Crowdsourced Indoor Information Service," in *Proceedings of the 16th IEEE International Conference on Mobile Data Management (MDM '15)*, 291–294, 2015, doi:10.1109/mdm.2015.80.
- [35] OWASP, "Session Management - OWASP Cheat Sheet Series," [https://cheatsheetseries.owasp.org/cheatsheets/Session\\_Management\\_Cheat\\_Sheet.html](https://cheatsheetseries.owasp.org/cheatsheets/Session_Management_Cheat_Sheet.html), retrieved on February 14th, 2023.

## Navigation Aid Device for Visually Impaired using Depth Camera

Hendra Kusuma\*, Muhammad Attamimi, Julius Sintara

Department of Electrical Engineering, Institut Teknologi Sepuluh Nopember, Surabaya, 60111, Indonesia

---

### ARTICLE INFO

Article history:

Received: 07 February, 2023

Accepted: 26 April, 2023

Online: 15 May, 2023

---

Keywords:

Assitive technology

Disability Inclusion

Depth camera

Navigation aid

Stereo audio

Visual impairment

---

---

### ABSTRACT

People with visual impairment face daily struggle of navigating through unfamiliar places. This problem mainly caused by their lack of spatial awareness, i.e., the ability to estimate the distance between themselves and their surroundings. In order for visually impaired people to navigate independently, an effective navigation aid is required. The proposed navigation aid device utilizes depth camera to collect visual information of surrounding objects. Then, it represents the obtained visual data into stereophonic sound to notify the user directly through an audio device. The aid device is designed to be portable, comfortable, and easy to use. It can further be developed and upgraded to suit the needs of visually impaired users. Designed to be wearable, this proposed device was tested and received excellent score in portability, comfortability, and ease of use. The subjects were able to detect the position of obstacles in front of them with 92.47% accuracy, and could also estimate the distance of the object with Mean Absolute Error of 0.8. Examination on their navigation ability indicated that the subjects could stop before collision with an object and maneuvers through the gap between two parallel obstacles.

---

### 1. Introduction

There are approximately 285 millions visually impaired people in the world with 13.68% of them are totally blind and the rest suffer from low vision [1]. In their daily life, people with visual impairment face many difficulties, especially in navigation due to their inability to observe surrounding environment. The sense of sight is the most fundamental sense to navigate, to perceive the environment, and to identify as well as estimate distance of surrounding objects [2]. Of course, these cannot be achieved by visually impaired so that they have to use other senses to produce spatial perception.

In Indonesia, the infrastructure and public facilities for people with disability are limited. Compared to the others, facilities for visually impaired people are still insufficient. For example, considerable amount of public areas in Indonesia are not equipped with tactile paving [3]. Similarly, for public transportation such as bus and train, assistance for blind people is lacking so that it is very difficult for them to travel independently without the help of others.

In consideration of rapid development in technology, we should be able to help people with visual impairment in overcoming those limitations. With the aid of technology like

camera, the visual ability could be conveyed though other senses. Some technologies have been implemented to help people with visual impairments, such as Blind People Guidance System using Stereo Camera [4], as well as facial expression recognition technology using deep learning [5]. However, there are still many other opportunities for application of technology to help people with visual impairments, such as navigate aid device for them to navigate independently .

Of those needs, a wearable navigation aid for visually impaired is necessary. This assistive device needs to be portable, comfortable, and also easy to use. It is also important for this device to have capability for further development, so that the users do not need to change or use more than this navigation aid. In this research, a depth camera is implemented as a sensor to collect visual information of surrounding environment in form of color and depth image. Hereafter, the visual information will be processed and represented though a sound to visually impaired. Visual representation in audio is carried out by various frequencies and amplitudes combination of stereophonic sound to reproduce a spatial perception.

The formatter will need to create these components, incorporating the applicable criteria that follow.

---

\*Corresponding Author: Hendra Kusuma, [hendraks@ee.its.ac.id](mailto:hendraks@ee.its.ac.id)

## 2. Research Method

In general, the method of this device could be divided into three: data collection, processing, and audio output. First, data is taken using a depth camera, which in this research uses Intel Realsense D435i [6]. This device is chosen because of the active stereo IR technology for depth imaging, equipped with a built-in IMU sensor. Its relatively small shape and low power consumption make this tool suitable for use as a wearable device. The depth camera will capture the user's surroundings for processing. For data processing, NVIDIA Jetson Nano [7] is used as the embedded computing unit. Its compact form, low power, and computability make this device also suitable as a wearable device. After processing, the sound information consisting a combination of tones with certain frequency and pattern, which represents the position and the distance estimation of the obstacle, is output through the stereo headphone or earphone directly to the user.

The block diagram of this navigation aid system is shown in Figure 1.

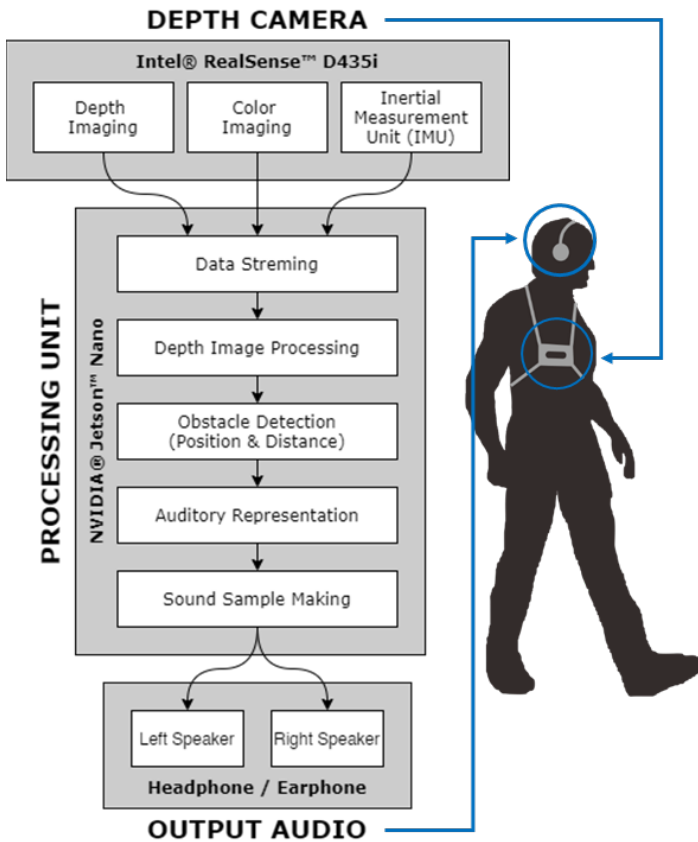


Figure 1: Block Diagram of Navigation Aid Device

### 2.1. Hardware Design

One of the important points of a wearable device is its design. The hardware design aims to make the device portable, comfortable, and easy to use. First is portability, where all the components used are small in size and light in weight. The power supply used is a battery, so all components must be able to work on a battery, which is why low power consumption is considered. For comfortability, it is necessary for a wearable support to put all the components used in one unit. Therefore, the users do not need

to hold anything by hand and the device is integrated into their outfit. Last is ease of use, so that users can use this device independently every day, without the need for help from others or any complicated installation.

The following Figure 2 is the hardware design scheme with all of the components. Thereafter, an illustration of the wearing of this device is shown in Figure 3.

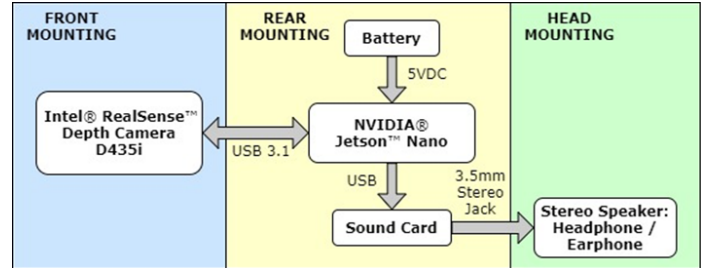


Figure 2: Hardware design scheme

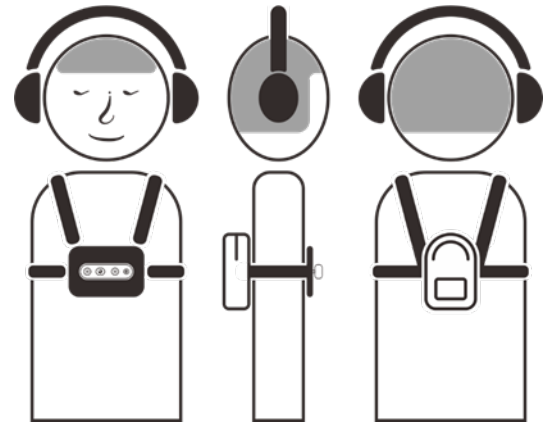


Figure 3: Wearable device installation design

The device is powered by a Lithium-Polymer battery 3 cells with 5200mAH capacity. Two devices that consume most of the power are NVIDIA Jetson Nano and Intel RealSense. NVIDIA Jetson Nano has 7-watt average power, while Intel RealSense consumes 3.5-watt power. The total power consumption is 10.5-watt. With the battery, our device could last about 6 hours of the use.

### 2.2. Software Design

In software design, there are several processes before an image can be represented in audio. First is data retrieval from RealSense™. Information such as depth images, color images, and IMU data can be retrieved from RealSense™ using the SDK provided by Intel® which was developed in open source [8]. The Intel® RealSense™ SDK 2.0, or librealsense, is equipped with a cross-platform library that can be used for various RealSense™ depth camera products. In this study, the Python wrapper from librealsense was used in the Python 3.0 programming environment.

In streaming mode, a callback function will be called every time a new data is available from the sensors. The callback function is run in different thread from the main loop and will store the data from the sensors to variables that could be accessed from

the main loop. Therefore, the information could be obtained simultaneously and the main process could be run at the same time.

Next is depth image processing. Intel® RealSense™ products are equipped with an API that is easy to use for various purposes, either with a GUI or in the form of a library, to retrieve data, both depth and color images, in standard units (millimetres for depth images and 8-bit RGB bits for color images). However, the results obtained cannot be used directly. Image processing is required so that the image can be used for the next step. There are several problems in depth images, including depth images and color images that have different viewpoints, unreadable depth values, and how to take values that represent an area of a certain size in the depth image. Depth image processing plays an important role so that the image can be further processed to extract the information. Figure 4 shows the results before and after depth image processing, and also the area that is being used for obstacle detection.

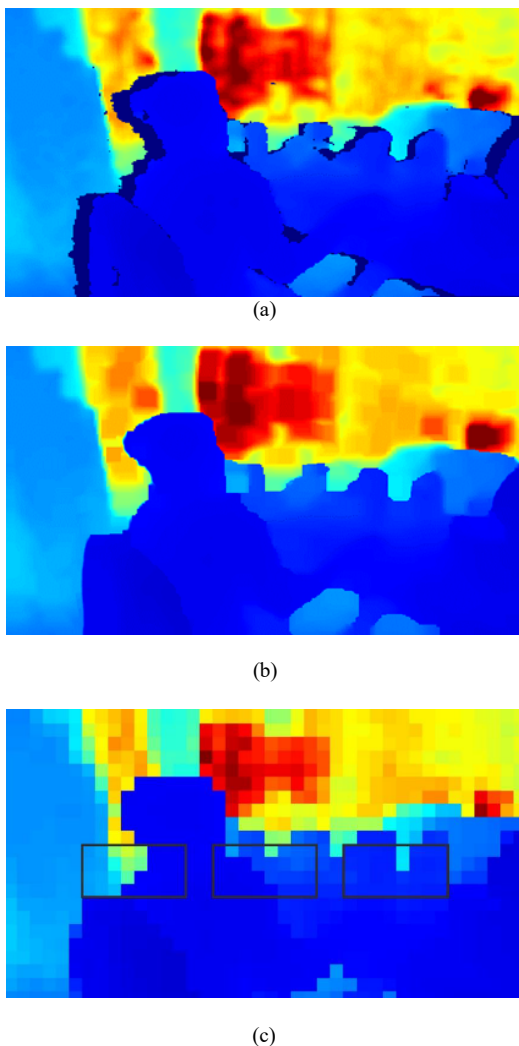


Figure 4. Depth image processing, (a) before processing, (b) after processing, (c) the area used for obstacle detection

The next step is detection of obstacles and their position. From the processed image, it will then be processed to detect existing obstacles. In this study, the position of the obstacle was limited into three parts: front left, front middle, and front right. Each position represents an area with a number of pixels in the depth image. The following Figure 5 is an illustration of the division of the depth

image position with  $\alpha$ ,  $\beta$ , and  $\gamma$  angle for front left, front middle, and front right respectively. For vertical field of view, we used  $\pm 20^\circ$

For the depth distance in this study, the minimum depth distance is 40 cm, and the maximum depth distance is 160 cm. The meaning of the minimum depth distance is that if the object is closer than the minimum depth distance, the object will be considered very close to the minimum depth measurement of the camera. The meaning of the maximum depth distance is that if the object is farther than the maximum depth distance, then the object will be ignored or considered as no object. This value can be changed and adjusted according to the needs and convenience of each user, but in this study the determined value is used. Distance is also determined based on the accuracy of the depth in this system. In this study, a system depth accuracy of 40 cm was determined, which means that the depth information in the 40 cm range would be considered the same. Thus, there will be 5 categories. First, the undetectable depth beyond the maximum depth limit (160 cm). Second, namely the depth between the maximum limit to the depth accuracy in this case between 120 cm to 160 cm. The third is between 80 cm to 120 cm. The fourth is between 40 cm and 80 cm. The last is a depth that is smaller than the minimum depth limit (40 cm). At this stage the data obtained is in the form of three depth information (front left, front center, and right front) which have been classified into their respective categories (in this case categories 1 to 5).

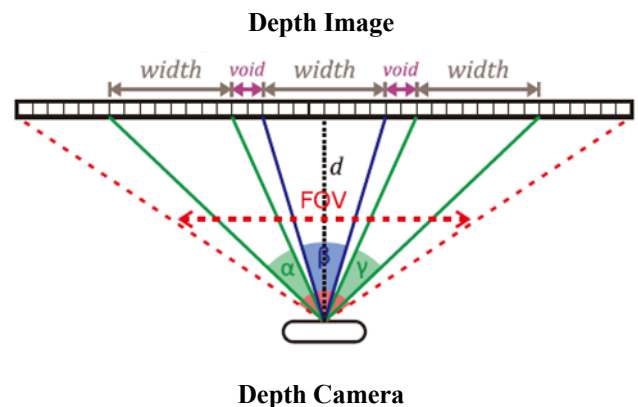


Figure 5: Position division in the depth image

After obtaining depth information to be conveyed in the form of position and depth or distance, it is necessary to represent the information in audio.

The most important thing about this step is to choose the right parameters to represent the depth information that is available. In this experiment, through try and error, the following parameter settings were obtained:

1. For stereo audio, use the volume settings for the right channel and the left channel. When the object is on the front left, the audio will give full volume to the left channel. When the object is in front of the center, the audio will give half volume to the right channel and the left channel. Likewise, when the object is in front of the right, the audio will give full volume to the right channel.
2. For frequency selection, after going through the try and error process, three types of frequencies are used, namely the tones C5, D5, and E5. The respective frequencies are 523.25 Hz,

587.33 Hz, and 659.26 Hz to represent the positions of the front left, front center, and front right, respectively. It is observed that the use of do re mi tones is easier for users to understand and remember.

3. For duration, beeps pattern is used to provide the user with a perception of distance. The farther the object, the slower the beep, as well as the closer the object, the beep will be faster and the pause between beeps will also be faster. Since 5 categories have been determined, and for the first category there are no objects, there are 4 beeps sound patterns, each of which represents the depth distance category. In writing this report, to make it easier to describe the depth category, a simple name is used, namely "no object" for the category of depth further than the maximum limit, then respectively "far", "medium", "close", and finally "very close" for categories where the object is closer than the minimum limit.

Sound information is conveyed through the stereo headphone through periodic cycle. The speed of one cycle will be adjusted according to the user's capability. In one cycle, amplitude of the right audio will be decreased from maximum amplitude, while the left audio will be increased toward maximum amplitude. Three different tones will sound according to the Figure 5 with smooth transition. Therefore, the user could experience surround audio to visualize the spatial information.

### 3. Results And Discussion

#### 3.1. Installation Test: Portability, Comfortability, and Ease of Use

As a wearable device, the first test is regarding the wear of the device Prototype design of the navigation aid for the visually impaired that has been assembled is installed to the subjects with visual impairment to test the design results. The results of installing a navigation aid on visually impaired subjects are as shown in Figure 6.



(a)



(b)

Figure 6: Installation of navigation aid device on visually impaired subjects, (a) back view, (b) front view

From this installation, we tested the portability, comfort and ease of use of the device in visually impaired subjects. After use for a while, visually impaired subjects were asked to provide an assessment of the value of portability, comfortability, and ease of use with several questions that had a correspondence with the three aspects being measured.

The answers to the questions are classified into positive answers, negative answers, or neutral answers. Answers which are positive answers include comfortable when used, not burdensome, easy to use daily, no difficulty in wearing the device, not limiting movement, not disturbing, etc. For answers that are negative answers include uncomfortable when used, burdensome, difficult to use, cannot be used daily, difficult wear in and / or remove the device, the device limits movement, annoying use of headphones / earphones. Answers that are neutral answers are answers that do not include positive or negative answers including answers with certain reasons or conditions such as a comfortable tool to use but within a certain period, the use of the tool does not limit movement if it is used at certain times, etc.

From the use experiments carried out on two blind subjects, the results are shown in table 1.

Table 1: Result of Qualitative Test On The Device Usage

Question Number	Measured Aspect	Subject 1	Subject 2
I	Comfortability	Positive	Positive
II	Portability	Positive	Positive
III	Portability & Comfortability	Positive	Positive
IV	Ease of use	Positive	Neutral
V	Ease of use	Positive	Neutral
VI	Comfortability	Positive	Positive
VII	Comfortability	Positive	Positive

In addition to qualitative questions, subjects were also asked to provide quantitative assessments for the value of portability, comfortability, and ease of use. Subjects were asked to give an assessment in the form of a number between one and ten (1-10)

with a value of 1 being the lowest and 10 being the highest. The results of the quantitative assessment of two blind subjects are obtained in Table 2.

Table 2 : Result of Quantitative Test On The Device Usage

Measured Aspect	Subject 1	Subject 2
Portability	10	10
Comfortability	10	9
Ease of use	9	9

From the results of the hardware installation testing carried out, the portability, comfortability, and ease of use values were quite good by both subjects. Furthermore, for quantitative assessments with an assessment range of one to ten (1-10) with a value of 1 being the lowest and a value of 10 being the highest, an average value of 10 was obtained for portability, 9.5 for comfortability, and 9 for ease of use.

### 3.2. Functionality Test: Obstacle Position Detection

The overall system in the form of a navigation aid for the visually impaired is tested on a visually impaired subjects for the functionality of the device.

First, according to the system design, obstacle detection is grouped into three areas, namely obstacles in front of the left, obstacles in front of the middle, and obstacles in front of the right. From these three areas, each obstacle was tested in each area individually and also in combination to find out whether the blind subject could tell whether there were obstacles in that area.

The test was carried out with a combination of laying obstacles according to Table 3. From the tests carried out by two blind subjects, the results obtained in Table 4.

Table 3 : Obstacle Position For Testing

Obstacle Position		
Front Left	Front Middle	Front Right
None	None	None
Exist	None	None
None	Exist	None
None	None	Exist
Exist	Exist	None
Exist	None	Exist
None	Exist	Exist
Exist	Exist	Exist

Table 4. Result of functionality test on the device usage

Test Subjects	Subject 1	Subject 2
True Positive (TP)	12	9
True Negative (TN)	10	10
False Positive (FP)	2	4
False Negative (FN)	0	3
Accuracy	0.92	0.73
Precision	0.86	0.69
Recall	1	0.75
F1 Score	0.9247	0.7188

The results of this test is maximum accuracy of 92.47%. From the accuracy value obtained, this device can function properly to detect the presence or absence and position of obstacles.

For precision, the maximum value is 86%, and the maximum recall is 100%. From these two values, the F1 score was 92%.

### 3.3. Functionality Test: Obstacle Distance Estimation

Furthermore, a test is conducted to determine the distance estimation between the subject and the existing obstacles. In accordance with the system design, because the minimum and maximum depth values chosen are 0.4 meters and 1.6 meters with depth accuracy in the system design of 0.4 meters, so the depth is divided into 5 bucketized categories, namely distances above 1.6 meters detected as not obstacles, distances between 1.6 meters and 1.2 meters, the distance between 1.2 meters and 0.8 meters, the distance between 0.8 meters and 0.4 meters, and also the distance that is closer than 0.4 meters.

From the tests carried out on two blind subjects, the results are in Table 5.

From the tests that have been done, the best MAE value or mean absolute error is 0.8 (for bucketized categories). The obtained value is decent for the error rate in distance estimation. A small MAE value indicates that distance estimation errors occur for adjacent category.

Table 5 : Result of Obstacle Distance Estimation Test

	Subject	Subject 1	Subject 2
Mean Absolute Error (MAE)	< 0.4 meter	1	1
	0.4 – 0.8 meter	1	2
	0.8 – 1.2 meter	1	3
	1.2 – 1.6 meter	1	1
	> 1.6 meter	0	0
	Average	0.8	1.6

### 3.4. Functionality Test: Simple Paths

The final test is the application of tools to blind subjects in walking on a predetermined route, to simulate some of the conditions that occur in daily navigation. In this test, there are two routes as illustrated in Figure 7.

In this test, there are two aspects tested. The first is whether visually impaired subjects can avoid collisions with the wall by stopping right before the wall without any other assistive devices. The second is whether the blind subject can spot and manoeuvre through the gap between two parallel obstacles.

From the conducted test, visually impaired subjects can stop before a collision occurs with the obstacle in front of them, in this case is a wall. Visually impaired subject can also manoeuvre through the gap between two parallel obstacles, in this case is a opened gate.

## 4. Conclusion

A navigation device is needed by visually impaired people to navigate in their daily life. Therefore, this navigation aid device is design to be portable, comfortable, and ease to use; as evidenced by questionnaire given to blind subjects after wearing this device.

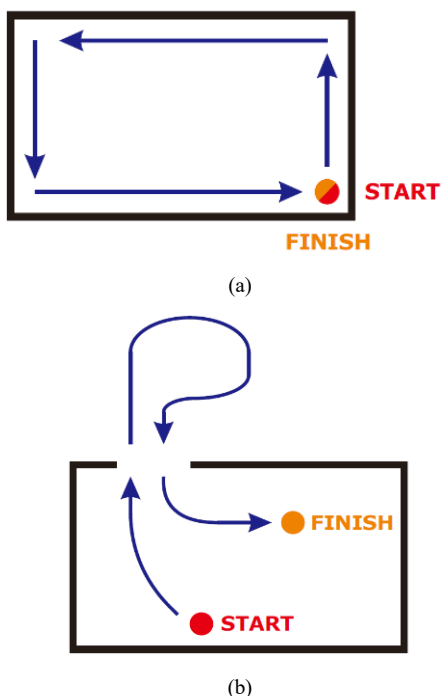


Figure 7: Simple paths for navigation aid device testing, (a) first route, (b) second route

The sensor used is Intel® Realsense D435i, which could capture color and depth images sufficiently, and is equipped with IMU. For this research, the information used is only the depth image, but could be developed further using various techniques to maximize the use of the information. The CPU used is Jetson™ Nano with very limited computational capabilities. For additional features and more complex object detection, a CPU that is more powerful with high computational capabilities is required, but still portable in size and could be powered by a battery.

The navigation aid functionality test shows the accuracy of the obstacle detection within three position division is 92.47% and the MAE error (mean absolute error) of the distance estimation to the obstacle is 0.8 for the obstacle distance setting that is less than 1.6 meters from the user. Furthermore, without the help of other tools such as cane, the users can stop before a collision with an obstacle in front, and walk through the gap between two parallel obstacles, according to testing on the simple paths.

This device testing is still limited to a few subjects. Henceforth, for future works, this device can be tested on more subjects with various ages, levels of visual impairment, and backgrounds. Additionally, different method of amplitude and frequency transition can also be explored to observe the effectivity of the device usage to the users.

### Conflict of Interest

The authors declare no conflict of interest.

### Acknowledgment

The authors gratefully acknowledge financial support from the Institut Teknologi Sepuluh Nopember for this work, under project scheme of the Publication Writing and IPR Incentive Program (PPHKI).

### References

- [1] D. Pascolini, S. P. Mariotti, "Global estimates of visual impairment : 2010," *Br. J. Ophthalmol*, **96**(5), 614-618, 2012.
- [2] "Daily Life Problems Faced by Blind People." [Online]. Available: <https://wecapable.com/problems-faced-by-blind-people/>. [Accessed: Oct. 30, 2019].
- [3] E. Khoirunisa, D. Aries Himawanto, "The comparison of guide texture tiles for blind people in public areas between Surakarta and Nagoya city," *Jurnal Kajian Wilayah*, **9**(1), 34, 2018.
- [4] I. P. Adi, H. Kusuma, M. Attamimi, "Blind People Guidance System using Stereo Camera," in 2019 International Seminar on Intelligent Technology and Its Applications (ISITIA), Surabaya, Indonesia, 298-303, 2019, doi: 10.1109/ISITIA.2019.8937173.
- [5] H. Kusuma, M. Attamimi, H. Fahrudin, "Deep learning based facial expressions recognition system for assisting visually impaired persons," *Bulletin of Electrical Engineering and Informatics*, **9**(3), 1208-1219, 2020.
- [6] Intel, "Intel® RealSense™ Camera D400 series Product Family Datasheet Rev. 01/2019," 2019.
- [7] NVIDIA, "DATA SHEET NVIDIA Jetson Nano System-on-Module Maxwell GPU + ARM Cortex-A57 + 4GB LPDDR4 + 16GB eMMC," 2020.
- [8] Intel, "IntelRealSense/librealsense: Intel® RealSense™ SDK." [Online]. Available: <https://github.com/IntelRealSense/librealsense>. [Accessed: Jun. 3, 2020].

## Forecasting the Weather behind Pa Sak Jolasid Dam using Quantum Machine Learning

Chaiyaporn Khemapatapan\*, Thammanoon Thepsena

Computer Engineering Program, College of Innovative Technology and Engineering Dhurakij Pundit University Bangkok, Thailand

### ARTICLE INFO

Article history:

Received: 27 February, 2023

Accepted: 30 April, 2023

Online: 15 May, 2023

Keywords:

Machine Learning

Quantum Machine Learning

Quantum Circuit

Variational Quantum Classifier

Pa Sak Jolasid Dam

### ABSTRACT

*This paper extends the idea of creating a Quantum Machine Learning classifier and applying it to real weather data from the weather station behind the Pa Sak Jonlasit Dam. A systematic study of classical features and optimizers with different iterations of parametrized circuits is presented. The study of the weather behind the dam is based on weather data from 2016 to 2022 as a training dataset. Classification is one problem that can be effectively solved with quantum gates. There are several types of classifiers in the quantum domain, such as Quantum Support Vector Machine (QSVM) with kernel approximation, Quantum Neural Networks (QNN), and Variational Quantum Classification (VQC). According to the experiments conducted using Qiskit, an open-source software development kit developed by IBM, Quantum Support Vector Machine (QSVM), Quantum Neural Network (QNN), and Variable Quantum Classification (VQC) achieved accuracy 85.3%, 52.1%, and 70.1% respectively. Testing their performance on a test dataset would be interesting, even in these small examples.*

## 1. Introduction

Programming computers to learn from data is the subfield of artificial intelligence (AI) known as machine learning (ML). In machine learning, support vector machines (SVM) are among the most frequently used classical supervised classification models [1]. The decision boundary and the hyperplane of the data points are divided into two classes by a pair of parallel hyperplanes that are discovered by SVM [2, 3]. However, there is also machine learning at the particle level called quantum computing. Quantum computing is computation using quantum mechanical phenomena such as superposition and entanglement. The difference is from the computer we use today, which is an electronic base on binary state based on transistors. Whereas simple digital computing requires data to be encoded into a binary number where each bit is in a certain state 0 or 1, quantum computing uses quantum bits (qubit). This can be a superposition of state, both 0 and 1 simultaneously. In quantum computing, a new algorithm is required for that problem, i.e., a normal algorithm used in a classical computer cannot be copied and run on a quantum computer at all. The Quantum Computer Algorithm for popular algorithms such as Prime factorization of integers Shor's algorithm is a quantum algorithm that can attack the algorithm RSA and encryption process of 90% of computer systems worldwide in a short period. Quantum computers can also operate on qubits using quantum

gates and measurements that change the observed state. Quantum gates and problems encode input variables into quantum states. To facilitate further modeling of the quantum state, quantum algorithms often exhibit probabilities in which they provide guidance for valid only for known probabilities. Quantum machine learning (QML) is an emerging interdisciplinary research field that combines quantum physics and machine learning, using it to help optimize and speed up data processing on the quantum state. In addition to the widespread popularity of QML, there is also the variational quantum classifier (VQC) for solving classification problems. At present, IBM has developed a quantum computer open to researchers or anyone interested in using it called IBM Q Experience, with a set of instructions developed in Python called Qiskit, which has a simulated quantum computer and real 5- and 15-qubit quantum computers to develop and test circuits. In this article, we present an experiment, which is a continuation of previous experiments [4, 5], that studied the forecast of water release from the dam and the weather forecast behind Pa Sak Jolasid Dam, respectively. Both experiments used a classical machine learning process that measures all model results as model accuracy. The model results are satisfactory."

In this paper, an experiment was performed using a Quantum Machine Learning classifier and applying it to real data, which brought information from the weather station located behind the Pa Sak Jonlasit Dam. The Pa Sak Jolasid Dam is an earth dam with a clay core, 4,860 meters long, and 31.50 meters high. The

\*Corresponding Author: Chaiyaporn Khemapatapan, [chaiyaporn@dpu.ac.th](mailto:chaiyaporn@dpu.ac.th)



maximum storage water level is +43.00 MSL, and the water storage capacity is 960 million cubic meters. The total operational budget is 19,230.7900 million baht, and the satellite coordinates are n14.964687, e101.022677 (see Fig.1). The red dot on the map represents the location of the weather station. Studying weather conditions, especially forecasting rainy days, can benefit water inflow management from quantum machine learning classifier techniques applied to actual weather data from Table 1. The total number of data is 1743 samples, divided into 1220 samples of training data and 523 samples of testing data. The number of features has 4 samples or 4 input qubits, and the label has 2 classes. Table 2 shows a sampling of the values of the features, which are average wind, average temperature, average pressure, average humidity, and label values.

A systematic study of the classical feature and optimizer with the different iterations of the parametrized circuits is presented. The study of the weather behind the dam is based on weather data from 2016 to 2022 as a training dataset. Classification is one problem that can be effectively solved with quantum gates. There are several types of classifiers in the quantum domain, such as Quantum Support Vector Machine (QSVM) with kernel approximation, Quantum Neural Networks (QNN), and Variable Quantum Classification (VQC). According to the experiment, Quantum Support Vector Machine (QSVM), Quantum Neural Network (QNN), and Variable Quantum Classification (VQC) achieved 90% accuracy. All of these algorithms were performed using Qiskit, an open-source software development kit (SDK) developed by IBM.

The classification is one problem that can be effectively solved with quantum gates. There are several types of classifiers in the quantum domain such as Quantum Support Vector Machine (QSVM) with kernel approximation [6-8], Quantum Neural Networks (QNN) [9, 10], and Variable Quantum Classification (VQC) [11-14]. The experimental results proved that we can use QML to solve real-world problems that are classically trained and tested before encoding the feature map, evaluating the model, and optimizing it from the algorithm above.

In this article, we will discuss the origin of the theory of quantum applied in section 2, followed by the steps and methods in section 3. Section 4 discusses the experimental results and explains the reasoning. Finally, section 5 provides a summary of the experiments and recommendations.

Regarding the experiment, we applied Quantum Machine Learning classifiers to real data from the weather station located behind the Pa Sak Jolasid Dam. This earth dam has a clay core, and it is 4,860 meters long and 31.50 meters high, with a maximum storage water level of +43.00 MSL, and a water storage capacity of 960 million cubic meters. The total operational budget is 19,230.7900 million baht, with satellite coordinates: n14.964687, e101.022677 (see Fig.1). The red dot on the map represents the location of the weather station, which studies weather conditions, especially forecasting rainy days, and can benefit water inflow management from quantum machine learning classifier techniques applied to actual weather data from Table 1.

The total number of data is 1743 samples, divided into 1220 samples of training data and 523 samples of testing data. The number of features has 4 samples or 4 input Qubits, and the label

has 2 classes. Table 2 shows a sampling of the values of the features, which are average wind, average temperature, average pressure, average humidity, and label values. We present a systematic study of the classical feature and optimizer with the different iterations of the parametrized circuits.

In conclusion, the experimental results demonstrate that QML can be used to solve real-world problems, which are classically trained and tested before encoding the feature map, evaluating the model, and optimizing it from the algorithm above. Therefore, the potential applications of quantum machine learning classifiers are promising, and more research in this area should be encouraged

## 2. Related work

Since we have the weather dataset for the dam, we can make predictions based on the training data. This is a binary classification problem with an input vector  $x$  and binary output  $y$  in  $\{0, 1\}$ . The goal is to build a quantum circuit that produces a quantum state based on the following study.

### 2.1. Quantum Computing

What exactly is a quantum computer then? In a nutshell, it could be described as a physical implementation of  $n$  qubits with precise state evolution control. A quantum algorithm, according to this definition of quantum computers, is a controlled manipulation of a quantum system followed by a measurement to obtain information from the system. This basically means that a quantum computer can be thought of as a special kind of sampling device. However, because it is a quantum state, the configurations of the experiments are very important. Any quantum evolution can be approximated by a series of elementary manipulations, known as quantum gates, according to a theorem in quantum information [15]. Quantum circuits of these quantum gates are the basis for many quantum algorithms. The idea of a qubit came from upgrading classical bits [16, 17], which are 0 or 1, to a quantum state.

$$0 \rightarrow |0\rangle = \begin{pmatrix} 1 \\ 0 \end{pmatrix}, 1 \rightarrow |1\rangle = \begin{pmatrix} 0 \\ 1 \end{pmatrix}$$

However, what are qubits? Because it is a two-level system defined on  $\mathbb{C}^2$ , a qubit is frequently referred to as the simplest possible quantum system. This state can be formulated as

$$|\psi\rangle = \alpha|0\rangle + \beta|1\rangle \quad (1)$$

with  $\mathbb{C}(\alpha, \beta)$  and  $|\alpha|^2 + |\beta|^2 = 1$ , where  $|0\rangle$  and  $|1\rangle$  are hardware-defined orthonormal states known as computational basis states. The qubit is significant because it is in a superposition—that is, it is a either  $|0\rangle$  or  $|1\rangle$  at the same time—which means that, in contrast to classical bits, it possesses a mixture of both. Using tensor products, we can generalize this to include  $n$  unentangled qubits.

$$|\psi\rangle \equiv |q_1\rangle \otimes |q_2\rangle \otimes \dots \otimes |q_n\rangle \quad (2)$$



Figure 1: Pa Sak Jolasid Dam, Coordinates: n14.964687, e101.022677.

Table 1. Dataset Attributions

Datasets	Number of Class	Number of Features	Train Size	Test Size	Total Size
Weather behind Dam	2	4	1220	523	1743

Table 2. Partial Dataset

Date	Avg. Wind	Avg. Temp	Avg. Pressure	Avg. Humid	Rainfall
2016/10/14	2.3	28	999.4	46	Yes
2017/01/04	6.6	26	1003.7	64	No
2018/03/07	3.3	25.9	1002.8	27	Yes
2019/08/01	3.9	25.4	998.4	86	Yes
2020/10/11	3.4	27.8	999.3	73	Yes
2021/02/22	2.1	26.9	1003.2	48	No
2022/05/12	2.7	28	1000.5	82	Yes

where  $|q_i\rangle$  stands for qubits. However, the state  $|\psi\rangle$  would no longer be separable if the qubits were entangled, and every qubit would either be  $|0\rangle$  or  $|1\rangle$ , resulting in

$$|\psi\rangle = \alpha_1|0 \dots 00\rangle + \alpha_2|0 \dots 01\rangle + \dots + \alpha_{2^n-1}|1 \dots 11\rangle \quad (3)$$

with  $\alpha_i \in \mathbb{C}$ , and  $\sum_{i=0}^{2^n-1} |\alpha_i|^2 = 1$ . Wherever we use the abbreviated notation  $|a\rangle \otimes |b\rangle := |ab\rangle$ . To make the notation more elegant, we see that the basis states can be written as follows:  $|000\rangle \leftrightarrow |0\rangle, \dots, |111\rangle \leftrightarrow |7\rangle$  giving us the straightforward equation. This allows us to translate the notation from binary numbers to integers.

$$|\psi\rangle = \sum_{i=0}^{2^n-1} \alpha_i |i\rangle \quad (4)$$

As a result,  $\{|0\rangle \dots, |i\rangle\}$  and  $n$  serve as the computational foundation for  $n$  qubits. Since there are  $2^n$  distinct strings, one requires  $2^n$  amplitudes  $\alpha_i$  to describe the state of  $n$  qubits, as we can see. In other words, quantum information is "larger" than classical information because the information stored in a quantum state with  $n$  qubits is exponential in  $n$ , whereas classical information is linear in  $n$ . which suggests quantum advancements thus far.

### 2.2. Quantum Circuit

We must begin by examining quantum gates in order to construct a quantum algorithm or quantum circuit [18, 19, 20], as mentioned earlier. Unitary transformations are the means by which quantum gates, or rather quantum logic gates, are produced. A straightforward transformation can serve as a quick reminder of what this means.

$$|\phi\rangle = U|\psi\rangle$$

where  $|\phi\rangle$  and  $|\psi\rangle$  are two vector spaces in which  $U$  is a unitary operator. By "unitary," mean that the hermitian conjugate of the operator is the inverse,  $U^\dagger = U^{-1}$ , and that the operator is linear. This is important because we can use it to, for example, display

$$\langle \phi | \phi \rangle = \langle \psi | U^\dagger U | \psi \rangle = \langle \psi | \psi \rangle = 1$$

where, if  $|\psi\rangle$  is normalized, then by construction it is  $|\phi\rangle$ .

#### 2.2.1 A single Qubit

If we return to the subject of quantum gates, equation (1), the state would either be in the state  $|0\rangle$ , which has a probability of  $|\alpha|^2$  or in the state  $|1\rangle$ , which has a probability of  $|\beta|^2$ . Formally,  $2 \times 2$  unitary transformations are used to describe single-qubit gates. We can begin by considering the X gate, which functions as the quantum equivalent of the classical NOT gate.

$$|0\rangle \mapsto |1\rangle$$

and the reverse This matrix is easily identifiable as one of the Pauli matrices, which are unitary by definition. As a result, we know that we can have at least X, Y, and Z gates with the unitary operators Pauli matrices.

$$\sigma_x = \begin{pmatrix} 0 & 1 \\ 1 & 0 \end{pmatrix}, \quad \sigma_y = \begin{pmatrix} 0 & -i \\ i & 0 \end{pmatrix}, \quad \sigma_z = \begin{pmatrix} 1 & 0 \\ 0 & -1 \end{pmatrix} \quad (5)$$

The Pauli rotations are yet another useful set of gates. which are expressed as Pauli gates that are exponential

$$R_j(\theta) = e^{-i\frac{\theta}{2}\sigma_j} \quad (6)$$

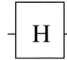
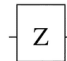
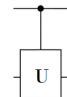
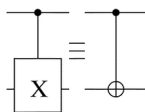
where  $j$  is  $(x, y, z)$ . Since the global phase ( $e^{i\gamma}$ ), the azimuthal ( $\theta$ ) and polar ( $\phi$ ) angles can be written into any quantum state,

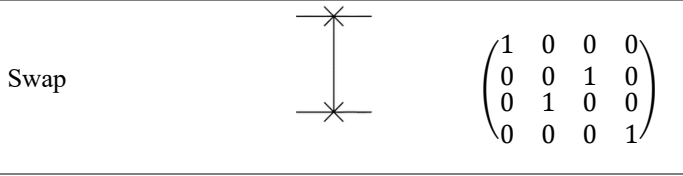
$$\begin{aligned} |\psi\rangle &= \alpha|0\rangle + \beta|1\rangle \\ &= e^{i\gamma} (\cos \frac{\theta}{2} |0\rangle + e^{i\phi} \sin \frac{\theta}{2} |1\rangle) \end{aligned} \quad (7)$$

#### 2.2.2 Multi Qubit

The controlled  $U$  gate is introduced because that work on multiple qubits simultaneously. where  $U$  can be any unitary gate with one qubit. For instance, the CNOT gate is obtained by setting  $U = x$ , and the NOT (X) operation is carried out when the first qubit is in state  $|1\rangle$ ; otherwise, nothing changes in the first qubit. A variety of quantum gates, their circuit, and how they are represented in a matrix show table 3. In a controlled gate, the  $U$  is a general unitary operator. We refer to  $j$  as  $(x, y, z)$  and  $\sigma_j$  denotes the appropriate Pauli matrix Eq. (5)

Table 3. Summary of all the gates in circuit and matrix representation.

Gate	Circuit representation	Matrix representation
H, Hadamard		$\frac{1}{\sqrt{2}} \begin{pmatrix} 1 & 1 \\ 1 & -1 \end{pmatrix}$
Z, Phase Flip		$\begin{pmatrix} 1 & 0 \\ 0 & -1 \end{pmatrix}$
U, Unitary		$\begin{pmatrix} 1 & 0 \\ 0 & U \end{pmatrix}$
Controlled Not Controlled X CNot		$\begin{pmatrix} 1 & 0 & 0 & 0 \\ 0 & 1 & 0 & 0 \\ 0 & 0 & 0 & 1 \\ 0 & 0 & 1 & 0 \end{pmatrix}$



### 2.3. Validation and Measurement

The measurement process is the final step in the theory for quantum computers regarding the quantum circuits that make up a quantum evolution [20]. From quantum mechanics, projectors of the Eigen spaces provide the probability of measuring a state. The probability of measuring  $i = \{0, 1\}$  is

$$p(i) = Tr(P_i|\psi\rangle\langle\psi|) = \langle\psi|P_i|\psi\rangle = |\alpha_i|^2 \quad (9)$$

The qubit's state changes to

$$|\psi\rangle \rightarrow \frac{P_i|\psi\rangle}{\sqrt{\langle\psi|P_i|\psi\rangle}} = |i\rangle$$

The qubits that are able to write the observables as a spectral decomposition of the computational basis are used to estimate the expectation value.

$$\hat{O} = \sum_{i=1} \lambda_i |i\rangle\langle i|$$

where  $P_i$  is present. Using a Z gate, the observable yields an eigenvalue of +1 for state  $|0\rangle$  and -1 for state  $|1\rangle$  so that we can computationally determine which state it is in (9).

$$\langle\psi|\hat{O}|\psi\rangle = \sum_i \lambda_i |\alpha_i|^2 \quad (10)$$

Since all that is required to determine the eigenvalues,  $\lambda_i$  is an estimation of the state's amplitudes. Since statistics can be used to measure states' amplitudes directly. They introduce a random Bernoulli variable called  $y_{ij}$ , where  $P(y_{ij} = 0) = 1 - |\alpha_i|^2$  and  $P(y_{ij} = 1) = |\alpha_i|^2$  [21]. If repeatedly prepare the state  $|\psi\rangle$  and measure it in the computational basis and collect  $S$  samples ( $y_{i1}, \dots, y_{iS}$ ), additionally, be aware that  $|\alpha_i|^2$  the frequents estimator  $\hat{p}_i$  can estimate  $|\alpha_i|^2$  by

$$|\alpha_i|^2 \approx \hat{p}_i = \frac{1}{S} \sum_{j=1}^S y_{ij}$$

where  $\hat{p}_i$ 's standard deviation can be found

$$\sigma(\hat{p}_i) = \sqrt{\frac{\hat{p}_i(1 - \hat{p}_i)}{S}}$$

where  $\mathcal{O}(S^{-1/2})$  represents the error. Can now approximate (10) to

$$\langle\psi|\hat{O}|\psi\rangle \approx \sum_i \lambda_i \hat{p}_i \pm \sqrt{\frac{\hat{p}_i(1 - \hat{p}_i)}{S}} \quad (11)$$

### 2.4. Quantum Support Vector Machine (QSVM)

To efficiently compute kernel inputs, the quantum support vector machine QSVM and the quantum kernel estimator (QSVM-Kernel) [20, 22] make use of the quantum state space as a feature space. By applying a quantum circuit  $\Gamma_{\phi(\vec{x})}$  to the initial state  $|0^{\otimes n}\rangle$ , this algorithm nonlinearly maps the classical data  $x$  to the quantum state of  $n$  qubits:

$$|\phi(\vec{x})\rangle = \Gamma_{\phi(\vec{x})}|0^{\otimes n}\rangle \quad (12)$$

The  $2^n$ -dimensional feature space created by the quantum circuit  $\Gamma_{\phi(\vec{x})}$  (where  $n$  is the number of qubits) is challenging to classically estimate. There are two consecutive layers in this circuit.

$$\Gamma_{\phi(\vec{x})} = U_{\phi(\vec{x})}H^{\otimes n}U_{\phi(\vec{x})}H^{\otimes n} \quad (13)$$

where  $U_{\phi(\vec{x})}$  is a unitary operator that encodes the traditional input data, and  $H$  is a Hadamard gate Fig. 2.

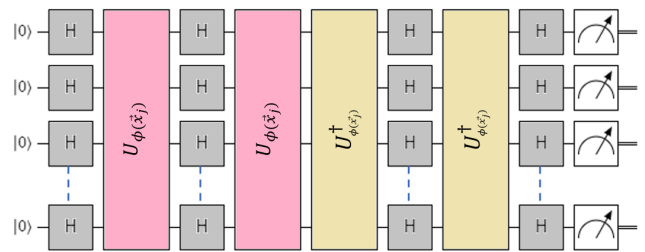


Figure 2: The Circuit of QSVM

During the training phase, the kernel entries are evaluated for the training data and used to locate a separation hyperplane. After that, during the test phase, the new data  $x$  and the training data, which are used to classify the new data  $x$  according to the separation hyperplane, are used to evaluate the kernel inputs. Quantum computers evaluate the kernel inputs, while classical computers, like those used in a traditional SVM, are used for data classification and separation hyperplane optimization.

### 2.5. Variational Quantum Circuit

A variational circuit with four features is proposed in [22] to classify the dataset Fig. 3. The variational circuit performs the following operations. The  $|0\rangle$  state is used to initialize the circuit's four qubits. The qubits are then placed in a superposition of  $|0\rangle$  and  $|1\rangle$  by applying the Hadamard gate one at a time. Then, a unitary square matrix designed for state preparation is used to perform a unitary operation on each qubit. The classical data (bits) are encoded into qubits in this method.

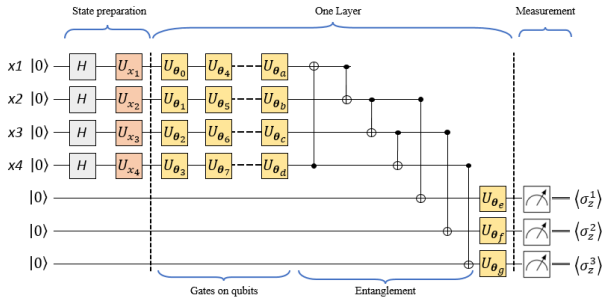


Figure 3. Variational Quantum Circuit

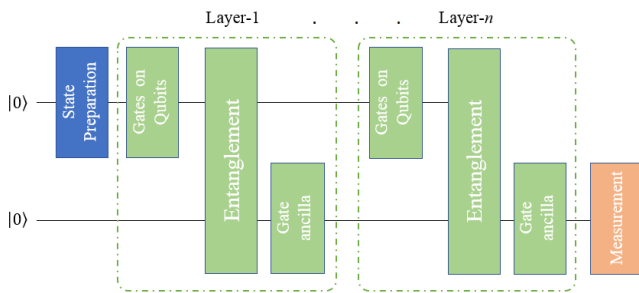


Figure 4. The Variational Quantum Circuit Architecture

Using multiple layers of interleaved rotational gates in data and auxiliary qubits, the variational circuit is designed following state preparation. Optimization is used to adjust the parameters. Fig. 4. shows the seven-layer initial implementation of the circuit as well as the architecture of the variational circuit model. The class label is obtained by processing the resulting qubits and measuring the auxiliary qubits.

2.6. Quantum Amplitude Estimation (QAE)

In [20, 23], a hybrid quantum autoencoder (HQA) variant of the Quantum Amplitude Estimation (QAE) algorithm was proposed [24, 25]. Quantum neural networks (QNNs) based on parameterized quantum circuits (PQC) were utilized in this model, which incorporates both classical and quantum machine learning. The model's overall structure consists of an encoder and a subset of real vector space  $V$  of dimension  $v = dim(V)$ , that transports a quantum state from Hilbert space  $H^{\otimes n}$ , as well as a decoder that does the opposite of that. The encoder and decoder's functional forms are specified, but the models themselves are not specified. As depicted in Fig. 5, the  $\mathcal{E}$  encoder is a vector  $\alpha$  controlled quantum circuit. The circuit applies the unitary  $U_1(\alpha)$  after

receiving some  $|\psi_{in}\rangle$  states. On the system that combines the input state ( $v-n$ ) with auxiliary qubits.

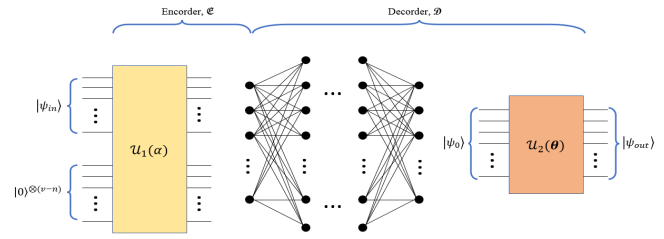


Figure 5. The Quantum Amplitude Estimation Architecture

3. Methodology

The weather dataset from the Thai Meteorological Department was used as the comparative dataset in the research. The dataset consists of 1773 data sets collected from 2016 to 2022, with 1220 of them being designated for training and 523 for testing. The data is divided into 4 variables for the features and 2 classes for the labels, as shown in Tables 2 and 3. However, there is a fairly standard approach to preprocessing. These strategies are not generally reasonable for planning adequate information for quantum classifiers while working with genuine informational collections. It has proposed a preprocessing strategy in this study, as depicted in Fig. 6, which encrypts the data before the QML algorithm uses it. Two QML classifiers are used in this article:

- A quantum support vector machine
- Build a quantum neural network (also known as Variational Classifier)

Both of the QML classifiers utilized preparation of feature maps, implementation of variational circuits, and measurement. The study analyzed the optimizer's feature map, the depth of the variational circuit [26], and the depth of the feature map to understand why these models perform optimally, and attempted to determine if the new information can be effectively condensed.

We have using the Qiskit framework for quantum computing. A typical quantum machine learning model consists of two parts, as shown in Fig. 6, A classical part for pre- and post-processing data and a quantum part for leveraging the power of quantum mechanics to simplify certain calculations.

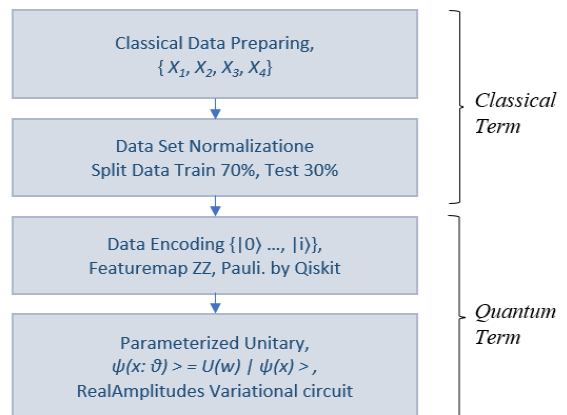


Figure 6: Experimental procedures

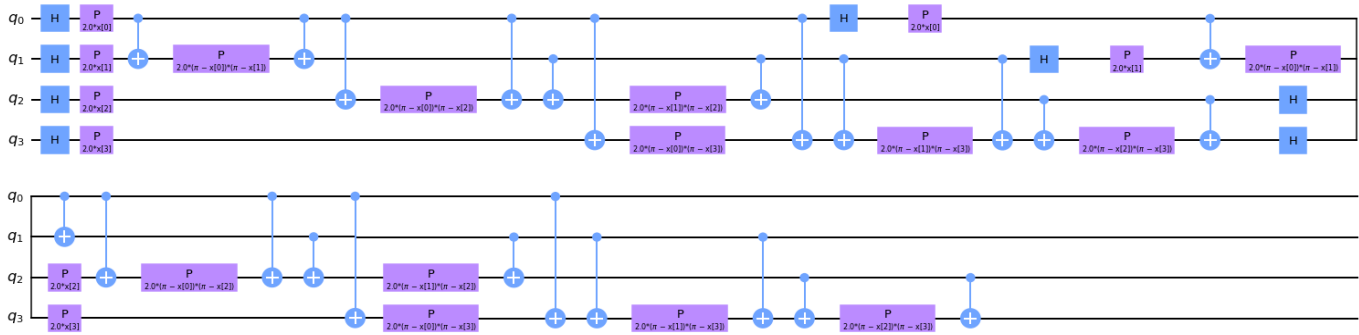


Figure 7: QSVM Featuremaps depths (2).

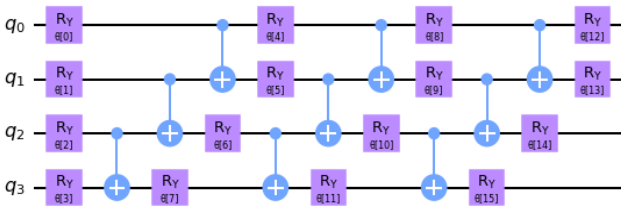


Figure 8: QSVM RealAmplitudes Variational circuit depths (3).



Figure 9: QNN Featuremaps and RealAmplitudes Variational

This study's experimental design is depicted in Fig. 7. The challenge of training very complex machine learning models on large data sets is one reason for utilizing quantum machine learning.

### 3.1. Data preparing and normalization

We shuffle the data to ensure randomness, remove less relevant features, and normalize the information between the ranges of 0 and  $2\pi$ , and 0 and 1 to properly use the Hilbert space. The data is divided into a training set for model building and a testset for model testing, with the testset size being kept at 30% of the total dataset. This is a common practice in traditional machine learning such as neural networks and support vector machines.

### 3.2. Data encoding

Data encoding or state preparation in quantum feature mapping is similar to a classical feature map in that it helps translate data into a different space. In the case of quantum feature mapping, the data is translated into quantum states to be input into an algorithm. The result is a quantum circuit where the parameters depend on the input data, which in our case is the classical weather behind the dam.

It's worth noting that variational quantum circuits are unique in that their parameters can be optimized using classical methods. We utilized two types of feature maps pre-coded in the Qiskit circuit library, namely the ZZFeaturemap and PauliFeaturemap. To evaluate the performance of different models [27, 28], we varied the depths of these feature maps.

### 3.3. Variational quantum circuit

The model circuit is constructed using gates that evolve the input state. It is based on unitary operations and depends on

external parameters that can be adjusted. Given a prepared state,  $|\psi_i\rangle$ , the model circuit  $U(w)$  maps  $|\psi_i\rangle$  it to another vector,

$$|\psi_i\rangle = U(w) |\psi_i\rangle.$$

$U(w)$  is comprised of a series of unitary gates.

## 4. Results & Discussion

In this research, we make use of the ZZFeaturemap and PauliFeaturemap precoded featuremaps from the Qiskit circuit library. To test the effectiveness of the various models, we changed the featuremaps depths (2). We incorporate more entanglement into the model and repeat the encoding circuit by increasing the depth of a feature map. After we used our feature map, a classifier may locate a hyperplane to divide the input data, and a quantum computer can evaluate the data in this feature space as Fig.7. Then we utilized the RealAmplitudes variational circuit from Qiskit. By increasing the depth of the variational circuit, more trainable parameters are introduced into the model that show in Fig. 8. The variational Featuremaps and RealAmplitudes reduced form was applied to write the QNN in Fig. 9. In order to determine the experimental target value in each cycle, the objective function value per iteration of the test was shown in Fig. 10, i.e. QSVM gave less objective value than QNN and VQC in Fig. 11 and Fig. 12, respectively.

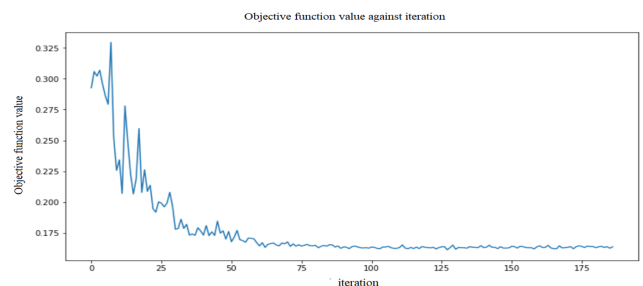


Figure 10: QSVM objective function value per iteration.

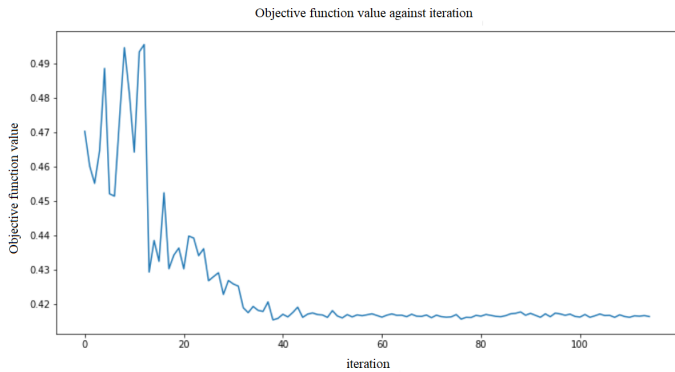


Figure 11: QNN objective function value per iteration.

Table 4 presents the performance of our models: QSVM, QNN, and VQC. The QSVM obtained an accuracy of 85.3%, while the quantum models QNN and VQC recorded 52.1% and 70.1% accuracy, respectively. The ZZFeaturemap encoding with RealAmplitudes technique was implemented on the model using the weather dataset, with a depth of 3 layers and 300 epochs. The validation accuracy achieved is depicted in Figure 8. Despite the use of three separate attention processes in conjunction with the VQC model, the results of this investigation were satisfactory.

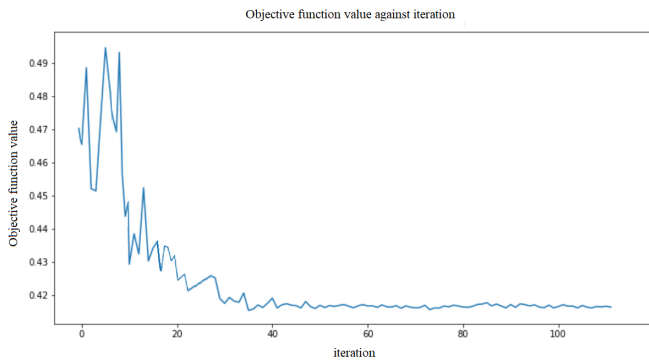


Figure 12: VQC objective function value per iteration.

Table 4. Classifier test score

Classifier	Score
QSVM	0.853
QNN	0.521
VQC	0.701

## 5. Conclusion

In this article, we implemented three quantum models using RealAmplitudes techniques. We used ZZFeaturemap encoding as an evaluation optimization, but we acknowledge that this should not be the only optimization used to improve a quantum framework. Furthermore, state preparation is just one aspect of QML algorithms to benefit from when implemented into quantum machine learning. We suggested a pre-processing approach to improve the quantum state preparation for VQC. Our results showed achieved efficiencies of 85.3%, 52.1%, and 70.1%. According to our findings, the QSVM optimizer had the best performance, followed by VQC and QNN. We used ZZFeatureMap with a depth of two and the RealAmplitudes variational form with a depth of three. Moving forward, we plan to

explore the use of different data encoding techniques such as RealAmplitudes, amplitude encoding, angle encoding, or other encoding methods to enhance the QML models and increase the number of features to improve performance relative to the established models and cutting-edge techniques. The study was based on a relatively small data set. Therefore, it may influence the assessment of model effectiveness and not discuss data pre-processing techniques because we are primarily interested in the efficiency of quantum models.

## Abbreviation

QML	Quantum Machine Learning
QSVM	Quantum Support Vector Machine
QNN	Quantum Neural Networks
VQC	Variational Quantum Classifier
SDK	Software Development Kit
HQA	Hybrid Quantum Autoencoder
QAE	Quantum Amplitude Estimation
PQC	Parameterized Quantum Circuits

## Conflicts of Interest

The authors declare that there are no conflicts of interest.

## Acknowledgements

The authors would like to acknowledge the support from the Computer Engineering Program, College of Innovative Technology and Engineering Dhurakij Pundit University Bangkok, and the support for the information data from the Meteorological Department Thailand.

## References

- [1] J.C. Christopher, Tutorial on Support Vector Machines for Pattern Recognition Data Mining and Knowledge Discovery 2, 121–167 1998.
- [2] C. Khemapatapan, "Service Oriented Classifying of SMS Message", 2011 Eighth International Joint Conference on Computer Science and Software Engineering (JCSSE), May 2011, Thailand, 101-106.
- [3] C. Khemapatapan, "2-Stage Soft Defending Scheme Against DDOS Attack Over SDN Based On NB and SVM", Proceeding of 8th International Conference from Scientific Computing to Computational Engineering, Jul 4-7, 2018, Athens Greece, 1-8, 2018.
- [4] T. Thepsena, "Reservoir Release Forecasting by Artificial Neural Network at Pa Sak Jolasid Dam" International STEM Education Conference (iSTEM-Ed 2022), July 6-8, 2022
- [5] T. Thepsena et al., "Rainfall Prediction over Pasak Jolasid Dam By Machine Learning Techniques " National Conference on Wellness Management: Tourism, Technology, and Community (H.E.A.T Congress 2022), August 18-20, 2022
- [6] C. Khemapatapan, "A Classifiers Experimentation with Quantum Machine Larning" The 2023 International Electrical Engineering Congress (iEECON2023) 2023,
- [7] V. Heyraud, Z. Li, Z. Denis, A. Le Boité, and Cristiano Ciuti, "Noisy quantum kernel machines.", Phys. Rev. A 106, 052421 – Published 18 November 2022. DOI 10.1103/PhysRevA.106.052421
- [8] S. Omar et al.; "Quantum kernels for electronic health records classification.", APS March Meeting 2022, abstract id.S37.006
- [9] W. Li, Z. Lu and D. Deng, "Quantum neural network classifiers: A tutorial, SciPost Phys. Lect.Notes 61 (2022).
- [10] S. Laokondee, P. Chongstittvatana, Quantum Neural Network model for Token allocation for Course Bidding, Computer Science, Physics 2021(ICSEC).

- [11] Elham Torabian, Roman V. Krems, "Optimal quantum kernels for small data classification.", Quantum Physics[Submitted on 25 Mar 2022] 14
- [12] S. Aaronson and A. Ambainis, "Forrelation: A problem that optimally separates quantum from classical computing.", SIAMJ. Comput. **47**, 982 (2018).
- [13] L.Zhou, S.T.Wang, S.Choi, H. Pichler and M.D. Lukin, "Quantum Approximate Optimization Algorithm: Performance, Mechanism, and Implementation on near term device," Physical Review X, vol.10, June 2020.
- [14] E. Farhi, S. Gutmann and J. Goldstone, "A quantum approximate optimization algorithm," Nov 2014
- [15] S. Nath Pushpak, S. Jain, "An Introduction to Quantum Machine Learning Techniques", 2021 9<sup>th</sup> International conference on Reliability, Infocom Technologies and Optimization, Amity University, Noida, India, 2021
- [16] Valentin Heyraud, Zejian Li, Zakari Denis, Alexandre Le Boité, and Cristiano Ciuti, "Noisy quantum kernel machines.", Phys. Rev. A **106**, 052421 – Published 18 November 2022, DOI: 10.1103/PhysRevA.106.052421
- [17] Shehab, Omar ; Krunic, Zoran ; Floether, Frederik ; Seegan, George ; Earnest-Noble, Nate, "Quantum kernels for electronic health records classification.", APS March Meeting 2022, abstract id.S37.006 DOI:10.1109/TQE.2022.3176806
- [18] W. Li, Z. Lu and D. Deng, "Quantum neural network classifiers: A tutorial", SciPost Phys. Lect. Notes **61** 2022, DOI: 10.21468/SciPostPhysLectNote.61
- [19] S. Aaronson and A. Ambainis, "Forrelation: A problem that optimally separates quantum from classical computing.", SIAMJ. Comput. **47**, 982 (2018), DOI:10.1137/15M1050902
- [20] L.Zhou, S.T.Wang, S.Choi, H. Pichler and M.D. Lukin, "Quantum Approximate Optimization Algorithm: Performance, Mechanism, and Implementation on near term device," Physical Review X, vol.10, June 2020, DOI:10.1103/PhysRevX.10.021067
- [21] E. Farhi, S. Gutmann and J. Goldstone, "A quantum approximate optimization algorithm," Nov 2014, DOI:10.48550/arXiv.1411.4028
- [22] Maria Schuld and Nathan Killoran "Quantum Machine Learning in Feature Hilbert Spaces.", Phys. Rev. Lett. **122**, 040504 – Published 1 February 2019, DOI:10.1103/PhysRevLett.122.040504
- [23] Vojtech Havlíček, Antonio D. Córcoles, Kristan Temme, Aram W. Harrow, Abhinav Kandala, Jerry M. Chow & Jay M. Gambetta, "Supervised learning with quantum-enhanced feature spaces.", Nature **567**, 209–212, 2019, DOI:10.1038/s41586-019-0980-2
- [24] M. L. LaBorde, A. C. Rogers, J. P. Dowling, Finding broken gates in quantum circuits: exploiting hybrid machine learning, Quantum Information Processing **19** 8, aug 2020, DOI:10.1007/s11128-020-02729-y
- [25] S. L. Wu, S. Sun, W. Guan, C. Zhou, J. Chan, C. L. Cheng, T. Pham, Y. Qian, A. Z. Wang, R. Zhang, et al. "Application of quantum machine learning using the quantum kernel algorithm on high energy physics analysis at the LHC 2021, DOI: 10.1103/PhysRevResearch.3.033221
- [26] A. Chalumuri, R. Kune, B. S. Manoj, A hybrid classical-quantum approach for multi-class classification, Quantum Information Processing **20**, 3 mar 2021, DOI:10.1007/s11128-021-03029-9
- [27] G. Brassard, P. Hoyer, M. Mosca, A. Tapp, Quantum amplitude amplification and estimation, Quantum Computation and Information 2002, P.53–74, DOI: 10.1090/conm/305/05215
- [28] M. Danyai, Daniel S., Begonya G. " Variational Quantum Classifier for Binary Classification: Real vs Synthetic Dataset." IEEE Access. DOI: 10.1109/Access.2021.3139323



## Analysis of Linear and Non-Linear Short-Term Pulse Rate Variability to Evaluate Emotional Changes during the Trier Social Stress Test

Alvin Sahroni<sup>\*1</sup>, Isnatin Miladiyah<sup>2</sup>, Nur Widiastara<sup>3</sup>, Hendra Setiawan<sup>1</sup>

<sup>1</sup>Electrical Engineering Department, Universitas Islam Indonesia, Yogyakarta, 55584, Indonesia

<sup>2</sup>Pharmacology Department, Universitas Islam Indonesia, Yogyakarta, 55584, Indonesia

<sup>3</sup>Psychology Department, Universitas Islam Indonesia, Yogyakarta, 55584, Indonesia

### ARTICLE INFO

#### Article history:

Received: 31 December, 2022

Accepted: 05 May, 2023

Online: 15 May, 2023

#### Keywords:

Mental Stress

Emotion

Pulse Rate Variability

Short-term

TSSST

### ABSTRACT

*In conjunction with psychological stress, physiological indicators such as heart rate (HR) and heart rate variability (HRV) are frequently employed. This study uses a substitute for heart rate variability (HRV) known as short-term pulse rate variability (PRV) to evaluate emotional changes. We examined sixteen college students using a low-cost photoplethysmograph and obtained a short-term PRV reading from one of their index fingers. Each PRV's parameters during resting condition were established using a particular Trier Social Stress Test (TSST) and divided into four phases (R1: baseline rest, R2: anticipatory stress, R3: stressful event, and R4: recovery period). The Positive Affect and Negative Affect Schedule (PANAS) questionnaire was used to assess the participants' moods during the experiment. The psychological assessment based on PANAS shows that negative affect tends to increase along the TSST procedure, especially from the baseline rest (R1) to the stressful event (R3), even though it is not statistically significant ( $p > 0.05$ ). The physiological assessment using PRV revealed that between R1 and R3, the short-term SDRR, pNN50, RMSSD, LF, HF, total power, SD1, and elliptical area of PRV tended to rise considerably ( $p < 0.01$ ). The properties of PRV show that the heart rate fluctuation also represents psychological changes. We concluded that applying the TSST procedure to induce stress modulates the features of PRV, particularly the time and frequency domain variability properties. Observed patterns following stressful events (interview sessions) indicated an increase in PRV values, mainly the RMSSD, HF, SD1, and elliptical area ( $p < 0.001$ ). Caution should be applied while perceiving physiological alterations as an immediate sign of mental threats. Nonetheless, these alterations are likely caused by the association between stress and negative emotions.*

## 1. Introduction

Individuals may encounter a variety of stressful situations in their daily lives, and if not managed correctly, these events can have adverse effects [1]. Negative emotions, such as anxiety, fear, and anger, are the primary reasons for certain psychological states and the negative reactions resulting from stress [2]. Negative emotions can also shorten attention spans and reduce concentration [3]. Mental stress is spreading rapidly in modern society, permeating practically all aspects of daily life [4]. Therefore, stress is receiving much attention in contemporary society, as most people in developed countries regularly endure physical or

psychological symptoms caused by stress [5]. Additional symptoms include persistent illness, fatigue, and headaches [6].

Furthermore, stress is already recognized as a mutually beneficial connection between individuals and their surroundings, that strains or exceeds an individual's ability to cope. Harmful, frightening, or unpleasant circumstances frequently cause stress, leading to anger, embarrassment, and anxiety, showing a connection between stress and emotion [7]. According to researchers, the link between stress and negative emotions is inexorably linked. For instance, some research suggests that depression is a stress reaction [8, 9]. Similarly, stress can foster the onset of disease by compromising the immune system as it worsens [10]. Consequently, it is essential to address the source of

\*Corresponding Author: Alvin Sahroni, [alvinsahroni@uii.ac.id](mailto:alvinsahroni@uii.ac.id)

tension. Additionally, developing a system that can readily and accurately evaluate and detect mental stress and other negative emotions is crucial.

Modern methods have been developed for scientifically evaluating psychological changes. The most popular methods for evaluating psychological traits involve completing surveys, scheduling consultations with psychologists, or evaluating online encounters during the pandemic. However, these procedures are time-consuming, expensive, and not always practical for everyone. Inconsistency in filling out the response sheets and failing to understand the instructions render questionnaires worthless as objective assessments [11-13].

Psychophysiological studies have been conducted to objectively improve the psychological assessment to observe how psychological changes can affect the physiological aspects. Thus, experimental studies were conducted to evaluate physiological responses after inducing stress or other emotions and moods. Most studies use a mental arithmetic test or another task demanding participants to accomplish it while measuring their body's response. The Trier Social Stress Test (TSST) was established and developed more than two decades ago, and researchers have discovered that it has become one of the most prevalent methods for inducing stress under controlled conditions [14].

Another way to assess mental wellness accurately is by utilizing biochemical and hormone details. Objectively evaluating salivary cortisol levels is one of the best ways to measure psychological conditions associated with human physiology. It is predicated on a specific feeling or thought, such as stress, which releases cortisol and adrenaline stress hormones by activating the sympathetic nervous system and the hypothalamic-pituitary-adrenal (HPA) axis [15]. Cortisol is unreliable for quickly estimating mental stress because of the handling period and the possibility of inaccuracy during repeated measurements [16, 17].

Previous electrophysiological studies suggest that electric biosignals, such as trapezius muscle activity, electroencephalogram (EEG), and electrocardiogram (ECG) data, as well as an assortment of these methods, can be used to detect mental tension and a range of emotions [18]. Biosignals are seen as a practical, unbiased way to evaluate psychological changes because there are few psychological tests, and salivary cortisol preparation is technically challenging. Another issue is the wearable feature of evaluating psychological characteristics while engaging in ordinary tasks.

Notably, most of the previously described research used HRV parameters from standard ECG equipment as the objective assessment to extract the heart's bio-signal information to quantify emotions or mental stress [18]. Regardless, the pulse rate variability (PRV) using photoplethysmography as an instrument for examination still has several limitations, particularly given its low-cost development. The fact that PRV cannot entirely substitute HRV in some circumstances is one of the main arguments against using it in place of an ECG [19, 20]. A wearable device for daily use may not be appropriate for ECG's HRV since it requires numerous electrodes to be hooked to the body, which may be discomfiting for certain people. The latest research that utilized PPG to encounter the uncomfortable issue also showed that remote

PPG (rPPG) could detect mental health conditions with 96% accuracy using the heart rate parameter during cognitive stress tasks [21]. This report shows that our proposed study is not the first time PPG has been used as a physiological tool to detect stress, and the development cost is also considered low. Therefore, more research is needed in this area to discover if PRV can be utilized to evaluate emotions or other psychological states throughout different settings.

The majority of studies on the TSST procedure still rely on through traditional heart rate measurement devices to quantify the physiological properties. However, the study that measured the pulse transit time (PTT) using the fingertip photoplethysmograph (PPG) and the electrocardiogram (ECG) during TSST sessions uncovered extensive information concerning the cardiovascular system that enabled observation of physiological changes after stress induction [22]. The most recent PPG result have a comparable capacity to identify mental stress as well as emotions, producing results with an accuracy of over 80%. Instead of using the Trier Social Stress Test (TSST) to exploit the susceptibility to the stress response, the majority of studies employed Mental Arithmetic Tests (MAT) and Stroop Tests to induce negative emotions [23].

This study aims to determine if stress inducement can affect negative emotions, as well as which interview events have the greatest impact on an individual's mental state. To better quantify and objectively evaluate this relationship between physiological characteristics and emotions as a sign of mental stress, a more thorough understanding is necessary. Therefore, we recommend employing the Trier Social Stress Test (TSST) to induce psychological stress, assess the subsequent affective changes, and extend the biosignal analysis to measure mental stress. This study may demonstrate the importance of identifying emotional traits in addition to mental stress, which could contribute to incorrect diagnoses of various stress symptoms. In contrast to our previous findings, which only analyzed specific PRV parameters (time domain and linear analysis), we expand the study by applying the common objectives of PRV's linear and non-linear, as well as the frequency domain analysis. The motivation is to discover additional parameters that can identify and better understand psychological changes.

Our previous study reported that a portable photoplethysmograph sensor could measure emotional changes after stress induction [24]. A low-cost device can objectively present emotional or mental changes based on physiological changes. As a result of our analysis of the pulse rate variability (PRV) time series, data revealed that RMSSD was the most crucial metric for capturing negative feelings and moods following the generated stress process. RMSSD was substantially higher after the main task or during the stressful event (R3) compared to before the interview or baseline rest (R1) ( $p < 0.01$ ) [24]. We believe that additional linear and non-linear analysis could further explain the understanding of electrophysiological properties during stress or adverse effects from a psychological aspect in terms of the autonomic nervous system, even though our previous report already found a critical finding demonstrating physiological changes during mental state discrepancy.

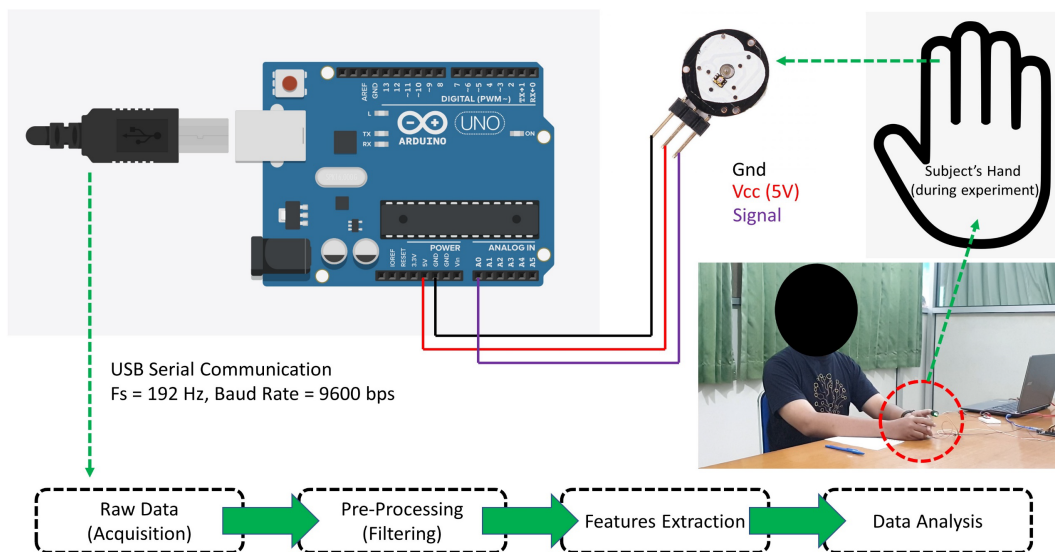
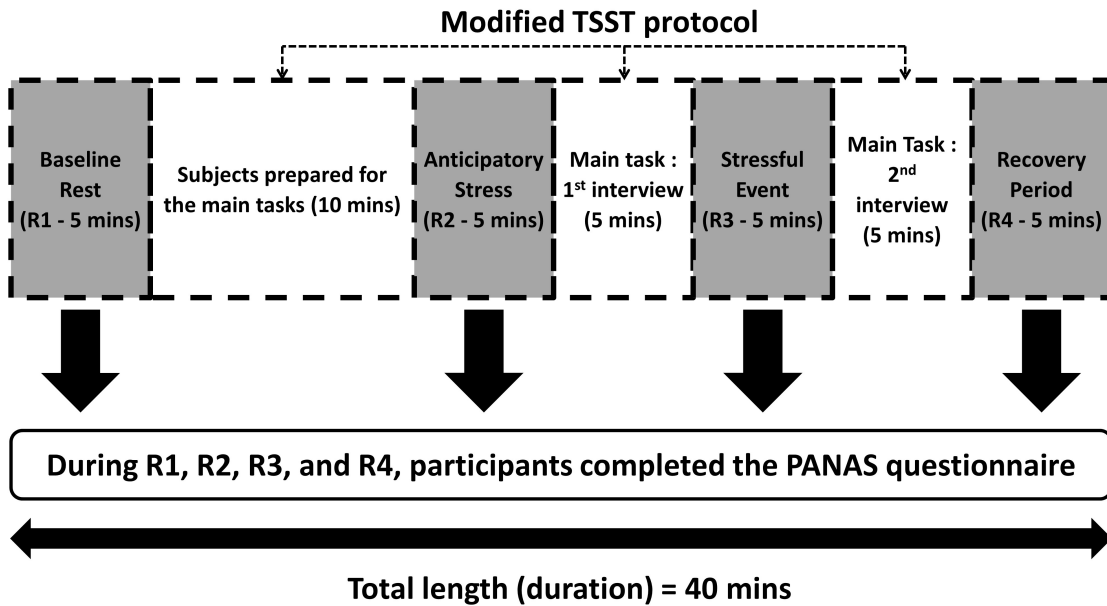


Figure 1: Trier Social Stress Test (TSST) experimental design and apparatus for evaluating psychological factors based on the Positive Affect Negative Affect Scale (PANAS) questionnaire and physiological properties [24]

## 2. Methods and Materials

### 2.1. Research Ethics

Prior to the conducting the investigations, the research topic and methodology were disclosed to the participants, and their informed consent was obtained. In pursuance of the principles of the Declaration of Helsinki, the Ethics Committee of the Faculty of Medicine at Universitas Islam Indonesia Yogyakarta approved this study (approval number 80/Ka.Kom.Et/70/KE/II/2019). The information of every subject's was kept secure and confidential.

### 2.2. Participants and Procedures

This investigation included sixteen healthy male and female students between the ages of 19 and 21 who were participated in

this study. The participants were undergraduate or graduate students majoring in social, medical, or engineering fields. Each participant signed an informed consent form. The participants declared in the informed consent document that they were in healthy condition, had not taken any regular medications before the studies, had slept well, had abstained from smoking, had normal weight based on Body Mass Index (BMI), and had no record of cardiovascular or other severe disorders in their families. Prior to involvement, the study was unknown to the participants, and the requirements of the entire procedure were confirmed by the research team during a short interview before signing the consent.

### 2.3. Experimental Design

The Trier Social Stress Test (TSST) Protocol created by Kirschbaum served as the foundation for the experimental design. We adjusted the protocol to consider regional preferences. The TSST standard protocol includes inducing psychological stress and monitoring the body's reaction [25]. The meta-analysis suggested that TSST is a considerably valuable and relevant standardized protocol for examinations of stress hormone reactivity [26, 27]. The modification related to the language and scope focused on providing opportunities with specific needs and how to ensure the interviewer includes them in the list. The task subjects had to complete was applying for a special opportunity through interviews, and the interview conducted in the local language was required. The purpose of using the modified procedure is based on the significant limitation of TSST, which is considered to have a higher degree of habituation of the HPA axis response with repeated exposures [28, 29]. Thus, modification of TSST procedure is needed. The experiment was divided into seven distinct phases and took around 40 minutes.

Figure 1 depicts the entire experiment in detail. To evaluate the physiological condition, we retrieved the pulse rate signal during the rest condition to avoid any disruptions. We categorized the rest condition into four states: baseline rest (R1), anticipatory stress (R2), stressful event (R3), and recovery period (R4) [30, 31]. Baseline rest (R1) was an initial condition to record the participant's current state before enrolling in the experiment. The anticipatory stress (R2) was a rest condition after each participant prepared for the interviews. The stressful event rest (R3) was a rest situation where the main task was held. Each participant met an interviewer and had a conversation. In the end, the recovery period (R4) was a rest state after completing all phases, and the debrief session was also held during that period. The stressful periods in segments R3 and R4 are crucial components of this procedure, where the duration of these stressful events is around ten minutes during the interviews to elicit psychological stress. Throughout the experiment, biosignals from the individuals were captured. To enhance the stress effect, we hired a professional interviewer who often did the main tasks as the interviewer.

### 2.4. Data Acquisition

From the commencement of the experiment during baseline rest (R1) to the conclusion of the primary task (R4), approximately 40 minutes of biosignals were collected. We utilized data from four different areas (R1, R2, R3, and R4), as shown in Figure 1. Figure 1 also demonstrates that a photoplethysmography (PPG) sensor was used to record biosignals and estimate short-term pulse rate variability (PRV) properties. During the investigation, the PPG sensor was attached to the index fingers of those who participated. We connected the sensor to an Arduino device, which captured the analog data (via the ADC interface), converted it to digital format, and then transmitted it to a computer at a sampling rate of 192 Hz and a transmission baud rate of 9600 bps. After obtaining the raw data, we extracted the features for subsequent analysis through pre-processing (filtering).

### 2.5. Data Processing and Feature Extraction

We ensure that there is no powerline interference by applying pre- and post-processing to the PRV signals of the participants. We utilized a digital band-pass filter to accommodate the 50–60 Hz frequency of the powerline. In addition, we used a low-pass filter with a cut-off frequency of 20 Hz to eliminate noise from the PPG's pulse rate data. Each parameter can be found in Table 1. We extracted the short-term PRV parameters (5 minutes) consisting of the mean peak-to-peak (R-R) interval (MeanRR), heart-rate change deviations (SDRR/Standard Deviation of RR), NN50, pNN50, square root of the mean squared difference between adjacent R-R intervals (RMSSD), mean heart rate (MeanHR), and standard deviation of heart rate (STDHR). The analysis of these parameters is known as linear time-domain analysis. In addition, we demonstrated linear frequency-domain analysis, which included very low frequency (VLF), low frequency (LF), high frequency (HF), and total power (TotPower). We also derived the LF normalization units (LFnu), HF normalization units (HFnu), and the ratio of LF and HF (LFHF). Pulse rate variability analysis also serves the purpose of non-linear analysis. We utilized the Poincaré analysis by extracting the SD1 and SD2 parameters and then calculating the SD1 and SD2 ratio (SDrat) and elliptical area.

### 2.6. Psychological Assessments

We created the PANAS scale, which has positive and negative subscales, to evaluate the effects of psychological stress that has been intentionally caused [32]. We assessed respondents' positive (interested, happy, tough, enthusiastic, proud, alert, inspired, diligent, considerate, active) and negative emotions (stressful, disappointed, guilty, fear, unfriendly, angry, embarrassed, nervous, anxious, worry) after the task using the TSST procedure during baseline rest (R1), anticipatory stress (R2), stressful events (R3), and recovery period (R4), which attempts to assess emotional changes in the negative direction or stress. The PANAS-based questionnaire asked sixteen participants to score their emotional state using twenty words covering positive and negative emotions during the TSST experiences. The twenty words were divided into ten descriptors expressing positive and negative sentiments and emotions in each subscale. The following are the five categories used to grade the questions based on the Likert scale: very irrelevant (1), irrelevant (2), neutral (3), relevant (4), and highly relevant (5). The most significant adverse effect suggests representing great psychological tension, and we calculated the questionnaire scores for positive and negative effects to quantify mental stress. The total score for each positive or negative feeling assessment can range from 10 to 50. Lower scoring means the corresponding emotion is less significant.

### 2.7. Data Analysis

We used the mean and standard error (SE) to present comprehensive data on the PANAS scale questionnaire's score to analyze psychological effects and PRV's parameters data to evaluate physiological traits. We employed the non-parametric Kruskal-Wallis test to identify the significant changes between states because the data would likely be less regularly distributed.

Table 1: The list of equations for the linear and non-linear analysis of pulse rate variability measurement

<p><b>Linear Methods</b></p>	
$MeanRR = \frac{1}{n} \sum_{i=1}^n RR_i$	(1)
$SDRR = \sqrt{\frac{\sum_{i=1}^n RR_i - MeanRR}{n}}$	(2)
$NN50 = count( RR_{i+1} - RR_i )_{>50ms}$	(3)
$NN50 = count( RR_{i+1} - RR_i )_{>50ms}$	(4)
$pNN50 = \frac{count( RR_{i+1} - RR_i )_{>50ms} \times 100\%}{n - 1}$	(5)
$RMSSD = \sqrt{\frac{\sum_{i=1}^N (RR_{i+1} - RR_i)}{N}}$	(6)
$MeanHR = \frac{\sum_{i=1}^N (60000/RR_i)}{n}$	(7)
$STDHR = \sqrt{\frac{\sum_{i=1}^n \left(\frac{60000}{RR_i}\right) - MeanHR}{n - 1}}$	(8)
$PF = \sum_{k=1}^{K_f} f_k$	(9)
<p>VLF &lt; 0.04 Hz          LF = 0.04 – 0.15 Hz, LFnu = LF/(LF + HF)          HF = 0.15 – 0.40 Hz, HFnu = HF/(LF + HF)</p>	(9)
$LFHF = LF/HF$	(10)
<p><b>Non-Linear Methods</b></p>	
$SD1 = \sqrt{var(x_1)}, SD2 = \sqrt{var(x_2)}$ <p>where, <math>x_1 = \frac{RR_1 - RR_{i+1}}{\sqrt{2}}, x_2 = \frac{RR_1 + RR_{i+1}}{\sqrt{2}}</math></p>	(11)
$EllipArea = \pi \times SD1 \times SD2$	

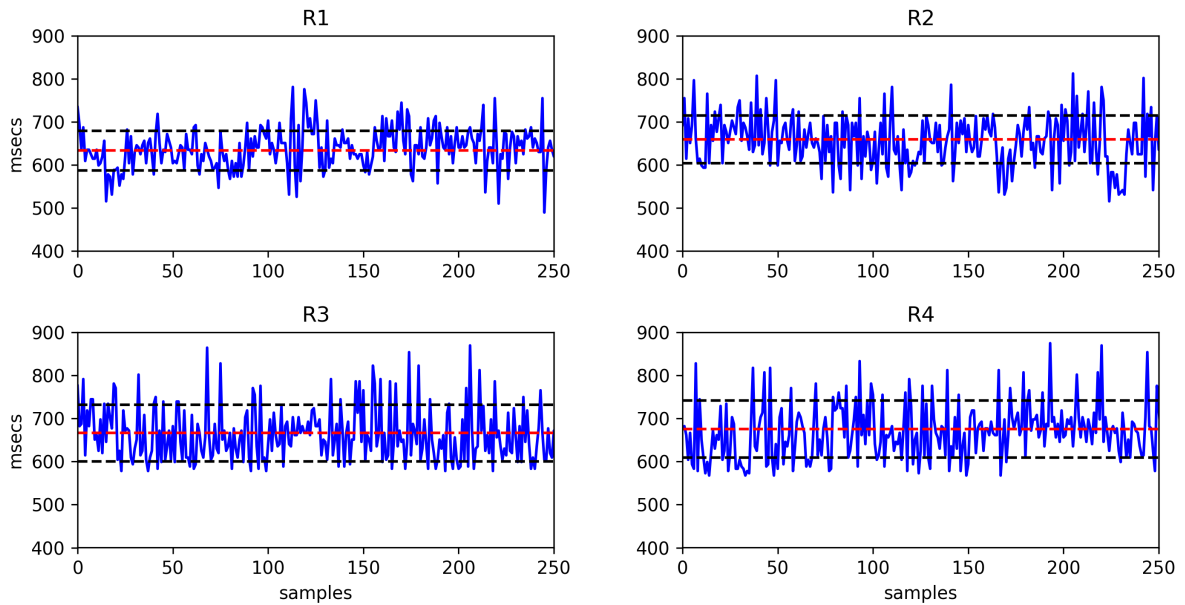


Figure 2: The raw data of peak-to-peak interval (RR) time series data from R1, R2, R3, and R4 on a subject (red dot line : average, black dot line : standard deviation)

statistical test, including the multiple comparisons (posthoc) and correlation test. Python libraries were used to process entire data sets.

### 3. Results

#### 3.1. Pulse Rate Variability Properties

Firstly, we examined the raw peak-to-peak interval time series to determine how the rest segments during baseline rest (R1), anticipatory stress (R2), stressful event (R3), and recovery period (R4) differed from one another before extracting and analyzing the features from the pulse-rate time series data. The PRV time series for each segment (R1, R2, R3, and R4) from a single subject are displayed in Figure 2. We can see in Figure 2 that there are no significant differences between segments in the peak-to-peak average of PRV values (MeanRR). The MeanRR increases from 633 msec in R1 to 660 msec in R2. During R3 and R4, the MeanRR continued to rise, reaching 666 and 676 msec, respectively. These findings show that the heart beats consistently more slowly after the primary task.

We also found that the gap between intervals expanded from baseline rest (R1) to recovery period (R4) as we observed the standard deviation from the RR array list. The standard deviation for R1 is 46 msec before the primary assignment (interview session), and R2's is 56 msec. R3 and R4 were slightly stable at 66 msec after the preparation phase (R2). According to the data, the heart rate varies more during the stressful events (R3 and R4) than during the preparation portions of baseline rest and anticipatory stress sessions (R1 and R2).

#### 3.2. Psychological Assessment during Stress Induction

Figure 3 illustrates that the positive affect (PA) scores remained constant throughout all rest conditions, with an average score of around 28.59 within the range of 28 to 31 (R1, R2, R3, and R4).

These findings indicate that participants were able to continuously regulate their emotions under various experimental conditions. However, individuals' negative effect scores varied amongst the

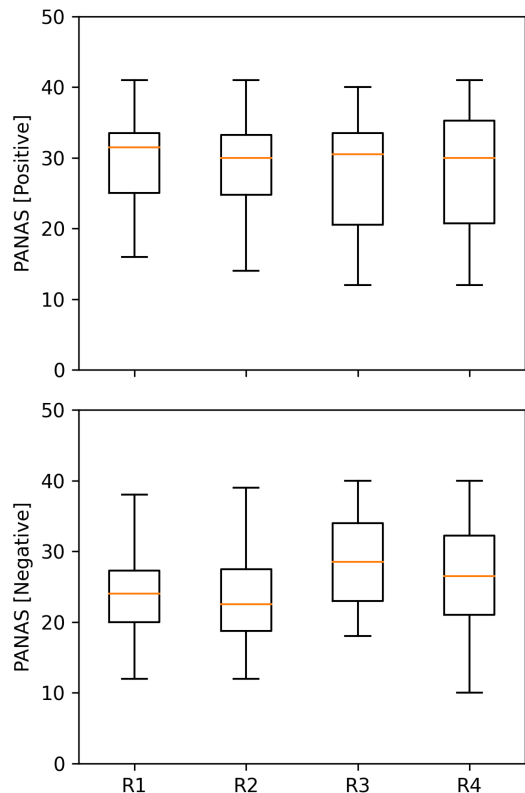


Figure 3: The psychological assessment using the Positive Affect Negative Affect Scale (PANAS) to evaluate the emotional changes PANAS [positive]: positive emotions; PANAS [negative]: negative emotions

Table 2: Summary of feature extraction (linear and non-linear methods) for physiological and psychological metrics

Parameters	R1		R2		R3		R4	
	Mean	SE	Mean	SE	Mean	SE	Mean	SE
<b>Linear</b>								
MeanRR (msec)	700.86	26.53	708.48	20.32	748.88	20.17	761.67	20.83
SDRR (msec)	56.58	4.35	64.63	3.84	83.20	5.35	82.16	5.47
NN50	108.44	13.89	90.06	12.00	102.00	12.38	126.25	16.28
pNN50 (%)	32.38	4.58	39.18	4.73	55.16	3.86	49.91	3.59
RMSSD (msec)	58.72	6.23	71.68	7.28	109.05	5.75	97.18	6.52
MeanHR (bpm)	88.05	3.31	86.47	2.52	82.02	2.27	80.68	2.35
STDHR (bpm)	7.03	0.53	7.62	0.41	8.85	0.50	8.59	0.54
LF (msec <sup>2</sup> /Hz)	628.28	107.10	756.24	82.61	1388.12	259.77	1248.16	195.92
HF (msec <sup>2</sup> /Hz)	596.00	121.83	974.85	182.58	1974.66	281.30	1848.86	328.69
LFHFrat	1.26	0.16	1.37	0.41	0.77	0.09	0.84	0.11
LFnu	52.78	2.86	49.16	3.94	41.08	3.33	42.66	3.31
HFnu	47.22	2.86	50.84	3.94	58.92	3.33	57.34	3.31
TotPow (msec <sup>2</sup> /Hz)	1685.15	273.24	2293.90	234.91	3974.85	719.27	4016.15	566.44
VLF (msec <sup>2</sup> /Hz)	460.86	100.28	562.82	93.40	612.08	245.85	919.13	181.71
<b>Non-Linear</b>								
SD1 (msec)	41.52	4.40	50.68	5.15	77.11	4.07	68.71	4.61
SD2 (msec)	67.06	5.37	74.01	4.51	87.83	6.84	92.05	7.12
SDrat	1.86	0.21	1.91	0.39	1.14	0.05	1.38	0.09
EllipArea (msec <sup>2</sup> )	9293.42	1412.48	12173.47	1761.88	22353.27	3278.50	20738.29	2508.50
<b>Psychological Assessment – Positive Affect Negative Affect Scale (PANAS)</b>								
Positive Affect (PA)	29.25	1.88	28.38	2.06	28.00	2.24	28.75	2.32
Negative Affect (NA)	24.44	1.56	23.19	1.76	28.56	1.70	26.75	2.00

MeanRR: Mean of RR/NN (peak-to-peak) intervals, SDRR: Standard Deviation of RR/NN (peak-to-peak) Intervals, NN50: number of peak-to-peak intervals > 50 msec; pNN50: NN50 over total numbers of peak-to-peak; RMSSD: root mean square of successive differences, MeanHR: Mean of Heart Rate, STDHR: Standard Deviation of Heart Rate, LF: low-frequency, HF: high-frequency, LFHF: ratio of LF over HF; LFnu: low-frequency normalized unit; HFnu: high-frequency normalized unit; TotPow: total power, VLF: very-low-frequency, SD1: standard deviation perpendicular to the line of identity; SD2: standard deviation along the line of identity; SDrat: ratio of SD1 over SD2. EllipArea: elliptical area.

various rest scenarios after stress induction. Although the significance test p-value was higher than 0.05, the scores increased from 23 at the start of the trial to 29 at its completion. There was a difference in the negative effect score between the baseline rest (R1) and stressful event when the assessments were made after the interviews (R3) ( $p = 0.72$ ) and recovery period after the interviews (R4) ( $p = 1$ ). However, no observable differences were found between the stressful period and after interviews (R3, R4), as well as the initial baseline rest (R1) and anticipatory stress period (R2).

These results revealed that the PANAS assessment could reliably identify the increase in negative emotions adhering to stress exposure. The effects of this subjective assessment should be contrasted to physiological data.

### 3.3. Physiological Assessment during Stress Induction

We performed a short-term PRV analysis for each resting condition (R1, R2, R3, and R4) for 5 minutes. The linear method consists of the time and frequency domain analysis, while the non-

linear analysis is based on Poincaré representing the geometrical analysis. We presented the linear and non-linear analysis features in Table 1 and provided the overall parameter summary in Table 2.

We compared the time domain characteristics that we retrieved, such as MeanRR, SDRR, RMSSD, NN50, pNN50, MeanHR, and STDHR, between the baseline rest (R1) and anticipatory stress (R2) to the main task as the stressful event (R3) and recovery period (R4), where the parameters frequently increased. When compared to R1 and R2, where the values were lower, the average of MeanRR during R3 and R4 is higher than 700 msec. As a result, following the interviews, the heart rate decreased to less than 85 beats per minute. The variations in pulse rate variability for SDRR, RMSSD, and STDHR also increased.

We discovered that R3 and R4 had more significant overall frequency components than R1 and R2. In contrast to the low-frequency component, the high-frequency component is more

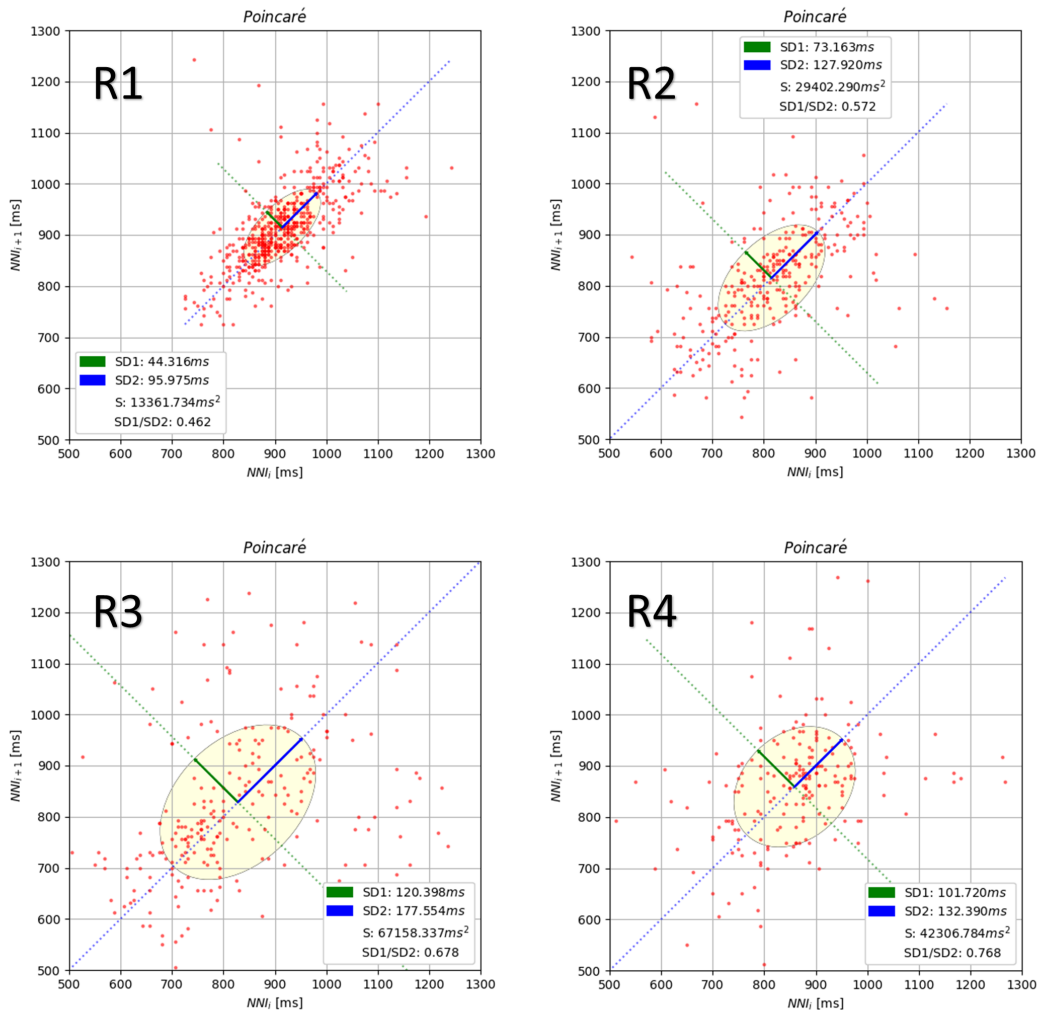


Figure 4: The Poincaré properties (SD1, SD2, and elliptical area) during R1, R2, R3, and R4

interesting. As a result of the interviews, the LF to HF ratio is lower, indicating that during the assignment, sympathetic activity predominated over parasympathetic activity.

Since the parameters, especially SDRR and RMSSD, had comparable characteristics, we discovered that the characteristics of SD1, SD2, and elliptical area are equivalent to the deviation of time series parameters. Figure 4 illustrates Poincaré properties on a topic during R1, R2, R3, and R4. As we can see, following the preparation stages, the distribution of the RR time series is dispersed. The SD1 parameter follows the R2 by more than 100 msec and is followed by a larger elliptical area by more than 30000 msec<sup>2</sup>.

To assess the significance of the link between the various resting states (R1, R2, R3, and R4), we evaluated all parameters using both the linear and non-linear methods. Figure 5 demonstrates that the differences between resting state segments are mostly found at the baseline rest (R1) and stressful event (R3), the baseline rest (R1) and recovery period (R4), and the anticipatory stress (R2) and stressful event (R3). From the baseline

rest (R1) to the stressful event (R3), the features that distinguish R1-R3 significantly with p-values less than 0.01 are SDRR ( $p = 0.0016$ ), pNN50 ( $p = 0.0021$ ), RMSSD ( $p < 0.0001$ ), LF ( $p = 0.0097$ ), HF ( $p = 0.0002$ ), total power ( $p = 0.0029$ ), SD1 ( $p < 0.0001$ ), SD2 ( $p = 0.0420$ ), SD ratio ( $p = 0.0046$ ), and elliptical area ( $p = 0.0005$ ).

According to the baseline rest (R1) and recovery period (R4) segments, the features that discriminate the two segments (R1-R4) are SDRR ( $p = 0.0023$ ), RMSSD ( $p = 0.0026$ ), LF ( $p = 0.0097$ ), HF ( $p = 0.0014$ ), total power ( $p = 0.0015$ ), SD1 ( $p = 0.0026$ ), SD2 ( $p = 0.0077$ ), and elliptical area ( $p = 0.0019$ ).

Other of the PRV's features that can be utilized to separate between the anticipatory stress segment (R2) and stressful event (R3) are RMSSD ( $p = 0.0061$ ), SD1 ( $p = 0.00611$ ), HF ( $p = 0.0471$ ), and elliptical area ( $p = 0.0166$ ). The elliptical area can also differentiate the anticipatory stress (R2) and recovery period (R4) with a p-value of 0.0471.



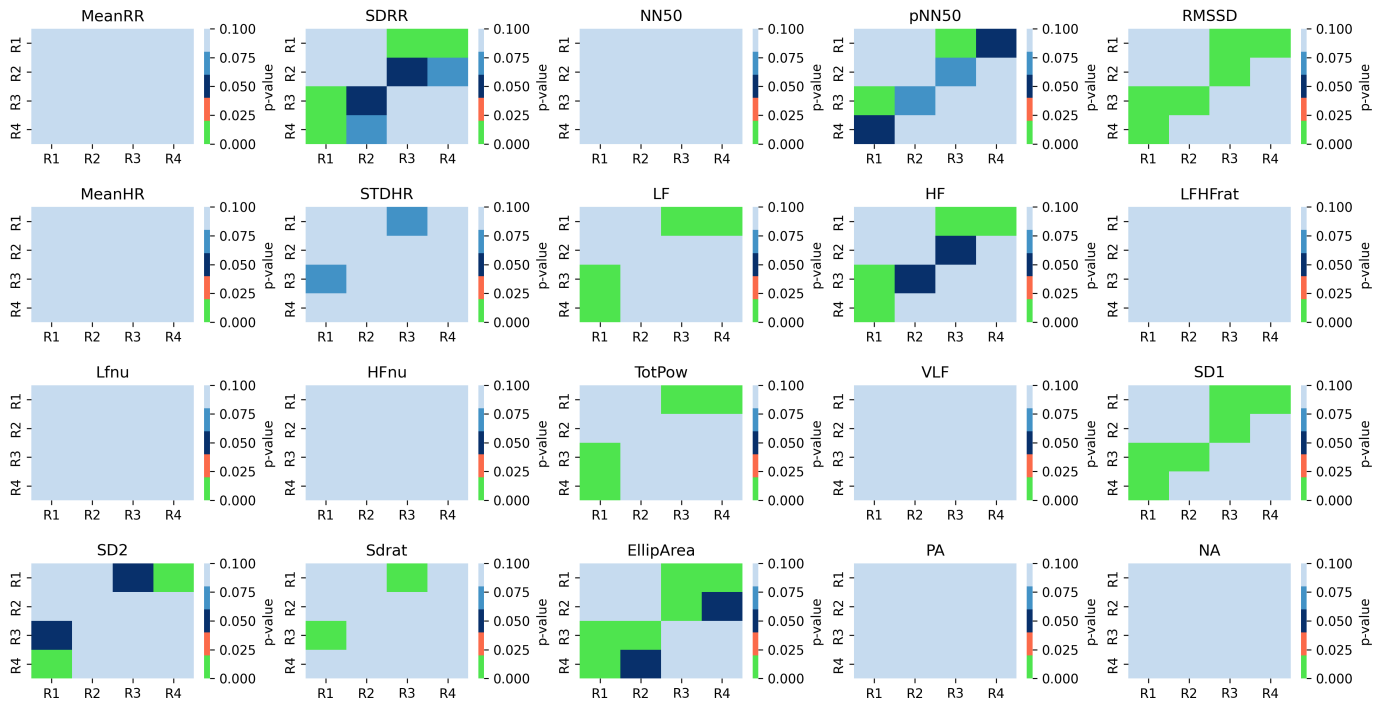


Figure 5: Multiple-comparison statistical test to evaluate the physiological and psychological evaluation under conditions R1, R2, R4, and R4. The color of the heatmap represents the p-value for each pair of comparisons

In general, with various PRV parameters that can distinguish two segments (R1-R3, R1-R4, R2-R3, and R2-R4), the most sensitive physiological parameters are RMSSD, HF, SD1, and elliptical area ( $p < 0.001$ ). Finally, we found that the statistical results point out that the baseline rest (R1) and stressful event (R3) are considered to be able to elicit psychological changes, followed by the baseline rest (R1) and stressful periods (R4).

### 3.4. Correlation between the physiological and psychological measurement

We performed a correlation analysis to determine the relationship between the negative emotions measured by the PANAS scale and the overall linear and non-linear PRV properties. Since the negative effects of the PANAS questionnaire raise differences between segments, PRV features tend to follow the changes in subjective evaluation in the opposite direction. We established a correlation analysis using all segments and on each segment of R1, R2, R3, and R4. We combined the PRV features values from the overall segment and correlated them to the negative effects of PANAS. We found no correlation between the PRV features and negative scores. We also employed the correlation analysis on each segment and found that only the recovery period (R4) presents a good negative correlation on low-frequency component (LF) (correlation = -0.6;  $p = 0.0142$ ) and total power (correlation = -0.5;  $p = 0.0412$ ). We concluded that an increasing negative affect score represents a lower power of frequency components on physiological measurement during a specific segment (recovery period/R4).

## 4. Discussion

Our proposed study employs heart rate variability (HRV) to measure physiological changes induced by purposefully inducing mental stress. We used a low-cost portable photoplethysmograph (PPG) sensor to retrieve the pulse rate and extract the pulse rate variability (PRV) properties as the surrogate for HRV, which necessitates a heart rate sensor on the chest. To see how the physiological traits relate to the psychological changes, we fully exploited the features of PRV using linear and non-linear analysis. Instead of having participants perform commonly used particular tasks, we developed a modified Trier Social Stress Test (TSST) protocol to create a naturally stressful situation. To further our understanding, we compared the findings with those from earlier studies and confirmed several results.

Pulse rate variability (PRV) is considered a tool to surrogate heart rate variability (HRV) [33, 34]. HRV changes are already known as part of the autonomic nervous system modulation changes [35]. A psychological stimulus triggers an autonomic response in panic disorder, including flushing, tachycardia, palpitations, hypertension, and gastrointestinal symptoms. The autonomic response may occasionally disappear by repeatedly exposing ourselves to the stimuli in comforting conditions. Salivation, stomach motility, and acid secretion can all be induced by food-related thoughts. When stress activates the sympathetic nervous system, norepinephrine is mainly released at the synaptic junction with the enteric nervous system, which decreases GI motility [36]. Therefore, using PRV's parameters is considered a meaningful way to represent stress and how physiological changes affect the autonomic nervous system.

The RMSSD, SD1, and elliptical area of the PRV were the parameters that were most sensitive to differentiate between before (baseline rest (R1) and anticipatory stress (R2)) and after inducing stress (stressful event (R3) and recovery period (R4)) ( $p < 0.01$ ), followed by SDRR, pNN50, LF, HF, and total power ( $p < 0.05$ ). We discovered that the negative emotions that occurred corresponded to these parameters. The peak-to-peak interval was primarily observed to decrease in stressful circumstances in prior studies [37]. Another study demonstrated that the heart rate of HRV rose in response to feelings of relaxation and fear, but no other measures showed any discernible variations [38]. In our opinion, stress or other negative circumstances are more closely related to changes in HRV than changes in heart rate. Therefore, a declining heart rate (lower peak-to-peak interval) might not indicate psychological adjustments. Otherwise, it could be a good idea to investigate the variance of the peak-to-peak interval in the future.

According to the feature extraction, the PRV variants SDRR, RMSSD, and SD1 better differentiate between psychological states before and after stressful events (R3). The high-frequency component (HF), which reflects sympathetic activity, best represents the SDRR, RMSSD, and SD1 [39]. Before the interview session, as the stressful events, the baseline rest (R1) and anticipatory stress (R2) demonstrate that mental tension and negative feelings were present and extended before the main stress events (R3) and recovery period (R4). Our data demonstrate that the changes of PRV had lower values before the stressful period during the main task (R1, R2) than after the interview (R3, R4). It implies that the primary task (assessing anxious sensations) is completed first, followed by mental tension and negative emotions verified through a questionnaire. As a result, the physiological aspect becomes more crucial to analyze as an objective measurement and takes precedence over the subjective assessment.

The PANAS scale can only measure psychological shifts in positive and negative directions while recognizing positive and negative feelings through a numerical score. Although emotion and stress can be associated, it is essential to consider whether the results of this study represent changes in emotion or stress itself because they showed the same negative sentiments as prior reports when stress was induced [3]. Additionally, the study we suggest offers fresh perspectives on assessing each component of happy and negative emotions to provide a helpful study of mental stress needed to create an objective physiological measuring system. The findings of this study imply that although stress and particular unpleasant emotions are connected and share similar physiological characteristics, alterations in physiological signals during stress induction cannot be utilized alone to quantify stress directly. However, stress symptoms, such as alterations in negative emotions, are the primary driver of physical changes and should be investigated to identify the emotions that lead to mental stress.

Based on our results of proposed study, we can confirm that that the stressors are affecting the changes in HRV properties, even though we are using PRV as a surrogate [21,40]. The variability of PRV's properties represents the changes in both linear and non-linear parameters corresponding to psychological changes. However, we observed that the stressful event (R3) tends to increase the PRV's parameters (RMSSD, pNN50, and elliptical area), whereas previous studies reported that the properties tend to

decrease [18]. During the stress-induced procedure using the TSST protocol, the cardiovascular characteristics change before the stressful event (R1/R2), where they have lower feature properties. The features rise after the anticipatory stress (R3/R4), which means that our study does not contradict the previous findings because the lower HRV properties were found before the stressful events and started to increase during the recovery period after inducing the TSST procedure. To strengthen the findings, we need further studies to establish a more extended observation period where we utilize the daily stress recording and assessment.

## 5. Conclusion

During stress induction, the modified TSST protocol reliably induced negative emotions in subjects, as demonstrated by this study. The majority of short-term PRVs for SDRR, pNN50, RMSSD, LF, HF, total power, SD1, and elliptical area exhibited increased activity in correlation with negative emotion levels ( $p < 0.01$ ). This study implies that negative emotions, believed to be a symptom of mental stress, increased immediately from the baseline condition following the first interview session (after inducing stress). In addition, significant differences were observed only between the onset of the resting state or baseline rest (R1) and after the interview as stressful events (R3). As adverse effects increase, the parameters demonstrate an increase in sympathetic activity based on their overall characteristics. In addition, the undesirable physiological properties observed were identical to the mental stress-related alterations reported in previous studies. Future research should examine the detection of mental tension from the viewpoint of adverse emotions.

## Conflict of Interest

The authors declare no conflict of interest.

## Acknowledgment

The Directorate of Research and Community Service, Universitas Islam Indonesia, Yogyakarta, as an Excellence Interdisciplinary Research Program with grant number 014-Dir-DPPM-70-PUPT-PIII-XII-2018, financially funded this work. We also want to express our highest gratitude to the participants who have willingly joined this study.

## References

- [1] J. Du, J. Huang, Y. An, and W. Xu, "The Relationship between stress and negative emotion: The Mediating role of rumination," *Clinical Research and Trials*, **4**(1), 2018, doi: 10.15761/crt.1000208.
- [2] J. Lee and S.K. Yoo, "Recognition of Negative Emotion Using Long Short-Term Memory with Bio-Signal Feature Compression," *Sensors*, **20**(2), 573, 2020. doi: 10.3390/s20020573.
- [3] C. Degroote, A. Schwaninger, N. Heimgartner, P. Hedinger, U. Ehlert, and P. H. Wirtz, "Acute stress improves concentration performance: Opposite effects of anxiety and cortisol," *Experimental Psychology*, **67**(2), 88-98, 2020. doi: 10.1027/1618-3169/a000481.
- [4] H. Selye H, *The stress of life*. McGraw-Hill, New York, 1956.
- [5] American Psychological Association, "Stress in America: The State of Our Nation," *Stress in America TM Survey*, 2017.
- [6] S. Singh, and A. Vats, "Impact of physiological and psychological stress on students," *Headache*, **9**(4), 111-113, 2020.
- [7] R. S. Lazarus, *Psychological Stress and the Coping Process*. McGraw-Hill, 1966.

- [8] J. K. Kiecolt-Glaser, L. McGuire, T. F. Robles, and R. Glaser, "Emotions, Morbidity, and Mortality: New Perspectives from Psychoneuroimmunology," *Annual Review of Psychology*, **53**(1), 83–107, 2002, doi: 10.1146/annurev.psych.53.100901.135217.
- [9] E. M. Sternberg, "The Stress Response and the Regulation of Inflammatory Disease," *Annals of Internal Medicine*, **117**(10), 854, 1992, doi: 10.7326/0003-4819-117-10-854.
- [10] A. Seiler, C. P. Fagundes, and L. M. Christian, "The impact of everyday stressors on the immune system and health," In *Stress Challenges and Immunity in Space*, Springer, Cham, 71-92, 2020.
- [11] S. Gamonal-Limcaoco, E. Montero-Mateos, M. T. Lozano-López, A. Maciá-Casas, J. Matías-Fernández, and C. Roncero, "Perceived stress in different countries at the beginning of the coronavirus pandemic," *The International Journal of Psychiatry in Medicine*, 009121742110337, 2021, doi: 10.1177/00912174211033710.
- [12] C. Joaquim, T. Luzia, H. A. Michael, P. M. O. Francisco, D. A. Silvia, A. Pedro, S. H. Aaron, S. Berta, "Negative affect and stress-related brain metabolism in patients with metastatic breast cancer," *Cancer*, **126**(13), 3122-3131, 2020. doi: 10.1002/cncr.32902.
- [13] O. Bălan, G. Moise, L. Petrescu, A. Moldoveanu, M. Leordeanu, and F. Moldoveanu, "Emotion Classification Based on Biophysical Signals and Machine Learning Techniques," *Symmetry*, **12**(1), 21, 2020. doi: 10.3390/sym12010021.
- [14] D. E. Eagle, J. A. Rash, L. Tice, and R. J. Proeschold-Bell, "Evaluation of a remote, internet-delivered version of the Trier Social Stress Test," *International Journal of Psychophysiology*, 2021, doi: https://doi.org/10.1016/j.ijpsycho.2021.03.009.
- [15] C. Hartling, Y. Fan, A. Weigand, I. Trilla, M. Gärtner, M. Bajbouj, and S. Grimm, "Interaction of HPA axis genetics and early life stress shapes emotion recognition in healthy adults," *Psychoneuroendocrinology*, **99**, 28-37, 2019. doi: 10.1016/j.psyneuen.2018.08.030.
- [16] L.M. Glenk, O. D. Kothgassner, A. Felnhofer, J. Gotovina, C. Pranger, A. N. Jensen, and E. Jensen-Jarolim, "Salivary cortisol responses to acute stress vary between allergic and healthy individuals: the role of plasma oxytocin, emotion regulation strategies, reported stress and anxiety," *Stress*, **23**(3), 275-283, 2020. doi: 10.1080/10253890.2019.1675629.
- [17] M. Cohen, and R. Khalaila, "Saliva pH as a biomarker of exam stress and a predictor of exam performance," *Journal of psychosomatic research*, **77**(5), 420-425, 2014. doi: 10.1016/j.jpsychores.2014.07.003.
- [18] G. Giannakakis, D. Grigoriadis, K. Giannakaki, O. Simantiraki, A. Roniotis and M. Tsiknakis, "Review on psychological stress detection using bio-signals," *IEEE Transactions on Affective Computing*, 2019. doi: 10.1109/TAFFC.2019.2927337.
- [19] E. Mejía-Mejía, K. Budidha, T.Y. Abay, J.M. May, and P.A. Kyriacou, "Heart rate variability (HRV) and pulse rate variability (PRV) for the assessment of autonomic responses," *Frontiers in physiology*, **11**, 779, 2020. doi: 10.3389/fphys.2020.00779.
- [20] A. Sch fer, and J. Vagedes, "How accurate is pulse rate variability as an estimate of heart rate variability? A review on studies comparing photoplethysmographic technology with an electrocardiogram," *Int. J. Cardiol.*, **166**, 15–29, 2013. doi: 10.1016/j.ijcard.2012.03.119.
- [21] H. M. Morales-Fajardo et al., "Towards a Non-Contact Method for Identifying Stress Using Remote Photoplethysmography in Academic Environments," *Sensors*, **22**(10), 3780, 2022, doi: https://doi.org/10.3390/s22103780.
- [22] S. Hey, A. Gharbi, B. Von Haaren, K. Walter, N. König, and S. Löffler, "Continuous noninvasive pulse transit time measurement for physiological stress monitoring" In *Proc. 2009 International Conference on eHealth, Telemedicine, and Social Medicine*, Cancun, Mexico, 2009, 113-116. doi: 10.1109/etelemed15088.2009.
- [23] M. Zubair and C. Yoon, "Multilevel mental stress detection using ultra-short pulse rate variability series", *Biomedical Signal Processing and Control*, **57**, 2020. doi: 10.1016/j.bspc.2019.101736.
- [24] A. Sahroni, N. Widiasmara, I. Miladiyah, and H. Setiawan, "Short-Term Pulse Rate Variability to Measure Changes in Emotion during Trier Social Stress Test," *2022 9th International Conference on Information Technology, Computer, and Electrical Engineering (ICITACEE)*, 2022, doi: 10.1109/icitacee55701.2022.9923994.
- [25] C. Kirschbaum, KM. Pirke, DH. Hellhammer, "The trier social stress test a tool for investigating psychobiological stress responses in a laboratory setting", *Neuropsychobiology*, **28**, 76-81, 1993.
- [26] M. A. Birkett, "The Trier Social Stress Test Protocol for Inducing Psychological Stress," *Journal of Visualized Experiments*, **56**, 2011, doi: https://doi.org/10.3791/3238.
- [27] J. A. Seddon et al., "Meta-analysis of the effectiveness of the Trier Social Stress Test in eliciting physiological stress responses in children and adolescents," *Psychoneuroendocrinology*, **116**, 104582, 2020, doi: https://doi.org/10.1016/j.psyneuen.2020.104582.
- [28] J. C. Pruessner, J. Gaab, D. H. Hellhammer, D. Lintz, N. Schommer, and C. Kirschbaum, "Increasing correlations between personality traits and cortisol stress responses obtained by data aggregation," *Psychoneuroendocrinology*, **22**(8), 615–625, 1997, doi: https://doi.org/10.1016/s0306-4530(97)00072-3.
- [29] N. C. Schommer, D. H. Hellhammer, and C. Kirschbaum, "Dissociation Between Reactivity of the Hypothalamus-Pituitary-Adrenal Axis and the Sympathetic-Adrenal-Medullary System to Repeated Psychosocial Stress," *Psychosomatic Medicine*, **65**(3), 450–460, 2003, doi: https://doi.org/10.1097/01.psy.0000035721.12441.17.
- [30] S. Schlatter, L. Schmidt, M. Lilot, A. Guillot, and U. Debarnot, "Implementing biofeedback as a proactive coping strategy: Psychological and physiological effects on anticipatory stress," *Behaviour Research and Therapy*, **140**, 103834, 2021, doi: https://doi.org/10.1016/j.brat.2021.103834.
- [31] A. P. Allen, P. J. Kennedy, S. Dockray, J. F. Cryan, T. G. Dinan, and G. Clarke, "The Trier Social Stress Test: Principles and practice," *Neurobiology of Stress*, **6**, 113–126, 2017, doi: https://doi.org/10.1016/j.ynstr.2016.11.001.
- [32] Brosschot, J. F., Thayer, J. F.: Heart rate response is longer after negative emotions than after positive emotions. *International journal of psychophysiology*. **50**(3), 181-187, 2003.
- [33] A. K. Verma, P. N. Aarotale, P. Dehkordi, J.-S. Lou, and K. Tavakolian, "Relationship between Ischemic Stroke and Pulse Rate Variability as a Surrogate of Heart Rate Variability," *Brain Sciences*, **9**(7), 162, 2019, doi: https://doi.org/10.3390/brainsci9070162.
- [34] E. Gil, M. Orini, R. Bailón, J. M. Vergara, L. Mainardi, and P. Laguna, "Photoplethysmography pulse rate variability as a surrogate measurement of heart rate variability during non-stationary conditions," *Physiological Measurement*, **31**(9), 1271–1290, 2010, doi: https://doi.org/10.1088/0967-3334/31/9/015.
- [35] J.-M. Grégoire, C. Gilon, S. Carlier, and H. Bersini, "Autonomic nervous system assessment using heart rate variability," *Acta Cardiologica*, **1–15**, 2023, doi: https://doi.org/10.1080/00015385.2023.2177371.
- [36] M. G. Ziegler, "Psychological Stress and the Autonomic Nervous System," *Primer on the Autonomic Nervous System*, 291–293, 2012, doi: 10.1016/b978-0-12-386525-0.00061-5.
- [37] H.-G. Kim, E.-J. Cheon, D.-S. Bai, Y. H. Lee, and B.-H. Koo, "Stress and Heart Rate Variability: A Meta-Analysis and Review of the Literature," *Psychiatry Investigation*, **15**(3), 235–245, 2018, doi: 10.30773/pi.2017.08.17.
- [38] M. T. Valderas, J. Bolea, P. Laguna, M. Vallverdu, and R. Bailon, "Human emotion recognition using heart rate variability analysis with spectral bands based on respiration," *2015 37th Annual International Conference of the IEEE Engineering in Medicine and Biology Society (EMBC)*, 2015, doi: 10.1109/embc.2015.7319792.
- [39] F. Shaffer and J. P. Ginsberg, "An Overview of Heart Rate Variability Metrics and Norms," *Frontiers in Public Health*, **5**(258), 2017, doi: 10.3389/fpubh.2017.00258.
- [40] K. Yoo and W. Lee, "Mental stress assessment based on pulse photoplethysmography," *2011 IEEE 15th International Symposium on Consumer Electronics (ISCE)*, 2011, doi: https://doi.org/10.1109/isce.2011.5973841.

## Human-Centered Design, Development, and Evaluation of an Interface for a Microgrid Controller

Mohammed Mahfuz Hossain<sup>1</sup>, Thomas Ortmeyer<sup>\*2</sup>, Everett Hall<sup>2</sup>

<sup>1</sup> *Engineering Science Dept., Clarkson University, Potsdam, NY 13699, USA*

<sup>2</sup> *ECE Dept. Clarkson University, Potsdam, NY 13699, USA*

### ARTICLE INFO

*Article history:*

*Received: 10 February, 2023*

*Accepted: 15 April, 2023*

*Online: 15 May, 2023*

*Keywords:*

*Microgrid*

*Human factors testing*

*Situational awareness*

*Interface design*

### ABSTRACT

*Many millions of people have adverse effects on their lives, both socially and economically, when a power outage occurs. Along with other electrical events, the lack of Situational Awareness (SA) is one of the root causes of power system outages. In order to promote adequate situational awareness, both power system and microgrid interfaces should communicate the necessary information in a helpful format at the right time. It is particularly difficult to present this information to microgrid operators in an accessible and timely manner. A human-centered design approach is used to develop two human-machine interfaces for the Potsdam, NY microgrid project. A detailed description of the process is provided in this extended paper.*

## 1. Introduction

A reliable, quality power supply is vital to our standard of living on a day-to-day basis. Electric power supply interruptions have great negative impact on our social and economic life. Significant research has focused on identifying the root causes of power outages and have reported Situational Awareness (SA) as one of the key causes. In this regard a study has been done to design and develop interface for Potsdam Microgrid. An overview of the main study results is presented in [1]. In this paper, the step-by-step process of conducting the experiment is described in detail.

## 2. SA and its challenges

One of the most widely used SA models can be found in [2]. Where the author defined SA as “the perception of the elements in the environment within a volume of time and space, the comprehension of their meaning and the projection of their “comprehension” of the current situation, and finally, level three is the “projection” of the future state. Further details of the three-level SA model are found in [3].

Power system operations require real-time assessments, monitoring, and activity control. Most importantly, power system operations require the coordination of electricity production at thousands of generators, long transmission line networks, and tens of thousands of electrical buses. All of this is required to ultimately deliver electricity to millions of users by means of the distribution network [4]. The complexity of the power system infrastructure is

continuously rising, and utility companies have been increasingly facing challenges to make decisions in a timely and accurate manner. [5] and [6] identified SA challenges for power transmission and distribution which seriously downgrade operators’ SA.

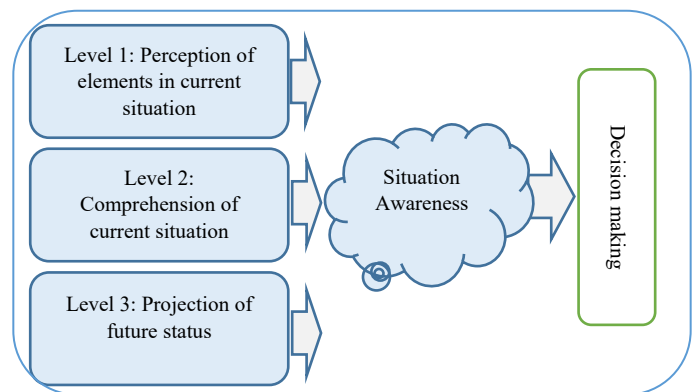


Figure 1: Model of Situation awareness adapted from [3]

*Attentional tunneling* involves situations when even all the needed information is presented, it is not fully attended by the person monitoring the system. The attention narrows as the scanning behavior is dropped.

*Data overload* is related to the volume and rapid change of data that creates an information intake pace that is hard to assimilate. Typically, the operator has to scan through thousands of pages of

\*Corresponding Author: Thomas Ortmeyer, [tortmeye@clarkson.edu](mailto:tortmeye@clarkson.edu)

SCADA data tables. When coupled with weather reports, alarms, contingency analysis data, and state estimator calculations, operators tend to become flooded with data, creating severe losses in SA [7].

*Requisite memory trap.* It is related to the capacity limitations to retain information in the working memory. Control room operators have to monitor more than twenty different pieces of information continuously [8].

*Workload, anxiety, fatigue, and other stressors.* System operators need to seek data, sort through what is available, and integrate information for decision-making in time-pressured environments. This requires high mental workloads, fatigue, and other stressors, leading to an increased number of opportunities for errors.

Misplaced salience occurs when software systems fail to highlight the most critical information. Operators have to visually fight the allure of several flashing lights and a wide variety of colors to identify the relevant information needed.

*Errant mental models.* Mental models tell how to combine information taken from different places. Poor comprehension and projection of the situation result when using incomplete or wrong mental models to interpret information.

*Complexity creep.* The more system features and governing rules, the more difficult it is to understand how the system works, slowing down the ability to extract and interpret information.

*Out-of-the-loop syndrome.* Highly automated systems can leave operators with low awareness of the state of the system. A germane example is the August 2003 blackout [9], where operators did not realize that the diagnostic tools were off-line and not updating in real-time.

There is a need for a good SA design solution to provide support for human limitations and avoid known problems with human information processing. This study developed and tested interface to promote/support operators SA.

### 3. Interface and Simulator Design

Situation Awareness (SA) is the key to user-centered design [10]. Endsley defined SA as “the perception of the elements in the environment within a volume of time and space, the comprehension of their meaning and the projection of their status in the near future” [3] pg. 13. The user interface design process is adapted from [11], shown in Figure 2.

#### 3.1. Requirements analysis

In the first phase of interface design, it is necessary to transform the goals of the project/users into specific system requirements. Typically, the requirements are collected using cognitive task analysis (CTA) [11], [12] presented a form of CTA called a goal-directed task analysis (GDTA) to identify the goals, decisions, and SA requirements of operators. GDTA is used/necessary to understand the interface design specifications with a detail description of not only the specific data operator needs but also indicates the way the operator integrates the data to develop an understanding of the current situation and make a decision [13]. To collect the microgrid specific requirements a set of questions are

prepared. In this study, a number of practicing power system operators were interviewed in preparation for developing these questions. The developed questions are:

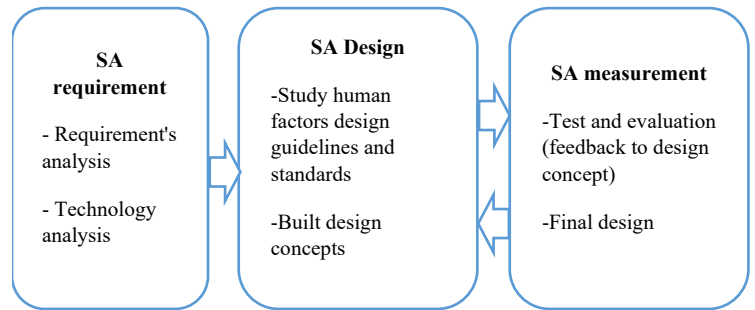


Figure 2: Interface design process [11]

1. What are your main goals during normal operations?
2. What are the functions of the human operator under normal operations? (Daily activity) or what tasks do you need to do to achieve your goals?
3. What do you need to know to achieve your goals? Or what would you ideally like to know? How do you get that information? How do you use that information?
4. What information elements are necessary for properly monitoring the system? How many displays (or any other information sources) do you need to constantly monitor?
5. Do you think these displays (or information sources) are enough for maintaining a safe operation? Or is there anything else that needs to be monitored to improve reliability? What do you do if you do not have the information needed to completely assess the situation (e.g., how do you seek that information and how often does it happen?)
6. Do you think people can make mistakes because the system does not provide all the information needed or the information displays are too complex? If so, what types of mistakes or consequences are likely to occur? Are there any improvements you would like to make?
7. How confident are you that the information you are receiving is reliable and valid? How does that affect your decisions?
8. How do you define normal condition operations? (e.g., what are the threshold values/limits?)
9. How do you identify (or become aware of) a problem/contingency? Does the system alert you in some way? Is there an alarm system (audio, visual, or both)?
10. Do you think these problem identification techniques/methods are good enough? Or do you need better system notifications? Are there any improvement recommendations?
11. If there are multiple types of alarms, is there a prioritization mechanism for addressing problems?
12. How do you determine what actions need to be done to solve the problem? (e.g., do you have to do manual computations? Are there any particular skillset needed or specialized knowledge that helps the decision-making?)

13. What types of problems typically occur? What actions do you perform to solve each type of problem?
14. How much time do you have to (or is expected for you too) solve the problem?
15. Do you think that solving the problem through this method or series of actions are good enough? Or is there anything you need for facilitating your job (e.g., do you have all the information/tools you need to make decisions quicker)? Could you please elaborate on that?
16. What is the workforce needed for smooth operations under normal conditions? (area of operation)
17. Have you ever felt the need for getting information outside of your working area?
18. How would be the ideal way of getting that piece of external information? Via phone? Or Do you think all information should be available for you through electronic communication (e.g., computer software displays)?
19. What is the skill level necessary for the operator (BS, MS or high school grad)?
20. What is the required training for the operator?
21. Do you use any manual operations or documented operation guidelines?
22. Which decisions are automated and, which ones cannot be automated or require final operator input?
23. Do you have anything to support awareness of future projections? (i.e.: that indicates near future worst-case contingencies, trending information)

An interview is not sufficient to create a GDTA table properly. Therefore, this study also relied on literature to identify the goals of power system operators. In [14], the authors interviewed Specialist Reliability Analysis and Operation (SRAO), and the Reliability Coordinator/System Operator (RCSO) positions from two U.S. power companies to develop GDTA. Figure 3 shows the overall goal of the operator: *to keep all elements and voltages within limits in real-time and for first contingency* [14].

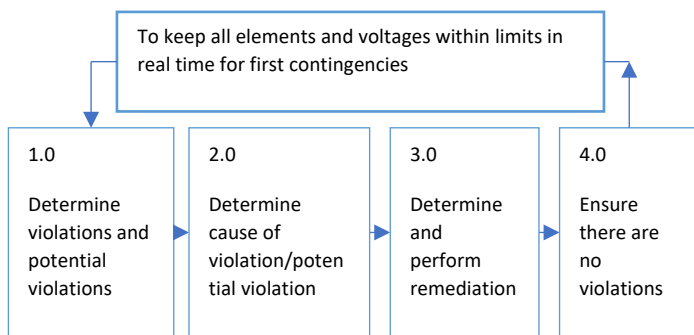


Figure 3: The overall goal of power system operators [14].

Contingencies are an unexpected failure of any system component, for example, transmission line, generator, circuit breaker or other electrical elements. By planning for first contingency means, the operator can attempt to prevent the

uncontrolled cascading loss of system elements that results in widespread load interruption. Four primary goals were identified as well under the overall goal. A primary goal is determining if any violations have occurred. A second primary goal includes the cause of a violation or potential violation. The next two primary goals are to remediation of any violation or possible violation.

### 3.2. Design alternatives

SA is necessary for effective decision making that will lead system operators to take appropriate corrective actions. Initially, four preliminary interface display concepts were developed that were based on the principles and best practices identified from the literature review.

Alternative #1 is shown in Figure 4. Some of the key features are:

- Switches and breakers are shown in a conventional way
- Bus names and pu values are shown to the side of each bus icon
- Loads are shown in MW and MVAR units
- Dynamically sized pie charts show line loading percentages in per cent of the thermal limit.

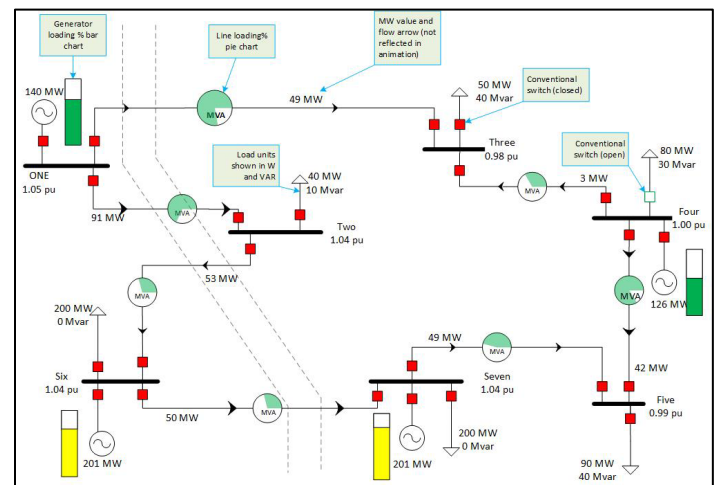


Figure 4: Alternative#1 display overview

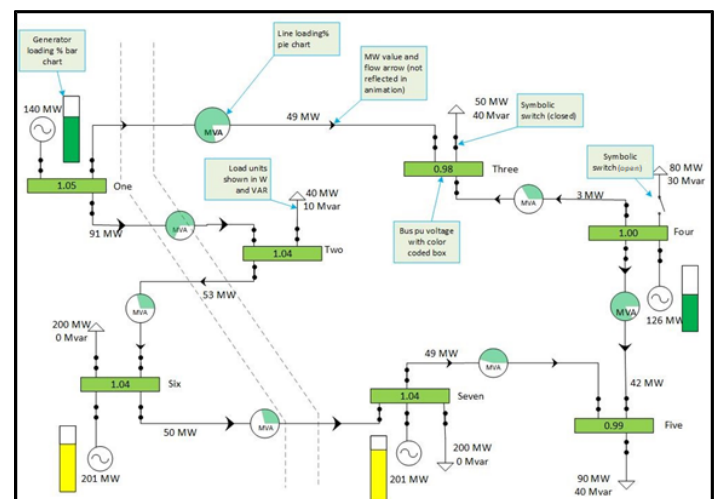


Figure 5: Alternative#2 display overview

Alternative #2 is shown in Figure 5. Key features are:

- Switches and breakers are shown with SPST switch symbols to discern open or close status easily
  - Buses are presented in colored boxes (This color could be reversed based on the operator's choice)
  - Bus per unit values are written inside the box
  - Loads are shown in MW and MVAR units
- Alternative#3 is shown in Figure 6. Some of the key features are:

- An overview box displays key information
- Pie charts show generator loading in percent of rating. The pie chart switches color depending on the situation (normal, alarm, etc.)
- Per Unit bus voltage are shown with a trend line
- Line names are displayed, and the operator has the option to display loading in percent, MVA, or amps.
- The set of overloaded lines are displayed in a single box, as are the set of heavily loaded lines.
- Loads are shown with MW or MVAR trend line
- Last update time is also logged

Alternative #4 is shown in Figure 7. Some of the key features are:

- The overview box has key information, such as overloads, trip and recent alarms
- Selecting an alarm will highlight the fault location/s on the coordinated views
- Generator that are out of service for maintenance are grayed out
- Spinning reserve will be shown in pink color
- Loads are shown with MW or MVAR trend line

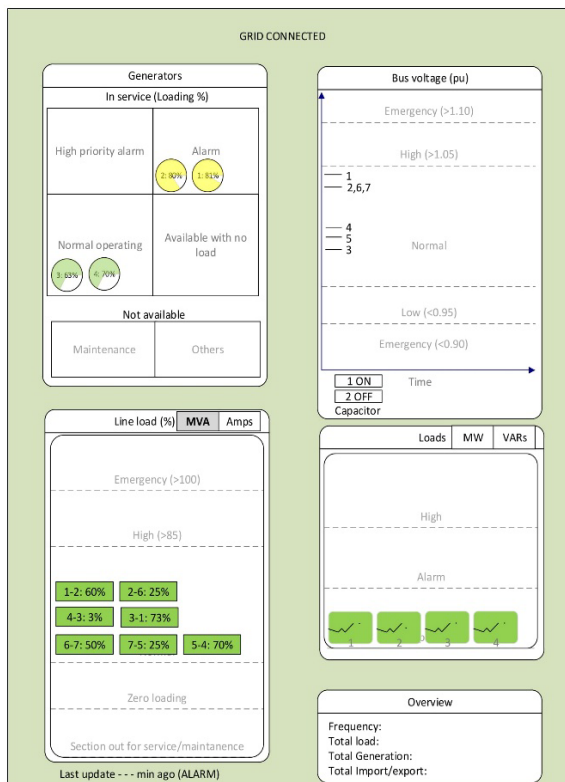


Figure 6: Alternative#3 display overview

### 3.3. Feedback from the experts

These four concepts were presented to power grid operators and supervisors from our industry partners, using simulated screens/animations. A brief feedback survey was done with power system operators. We received four survey responses from these participants. The purpose of this survey was to select one concept

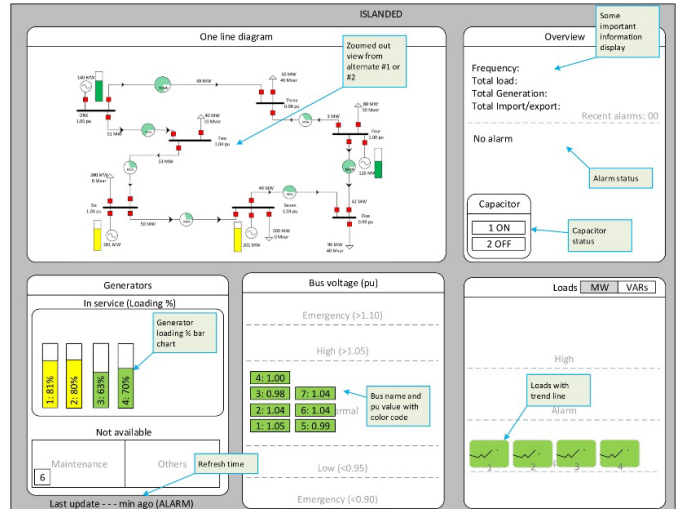


Figure 7: Alternative#4 display overview

and upgrade that interface to integrate it with load flow simulation software to make a fully real time simulation of the microgrid. Survey questions for these four alternatives are as follows:

- How satisfied are you with the interface design?
- Do you think the overview display screen would be appropriate for small screens, e.g. tablet or mobile devices?
- What other important information do you think is necessary to display but is missing in the overview display?
- What other information would be nice to have in the overview display?
- Any suggestions for improvement
- Preference for the design alternatives
- Overall suggestions
- How do you want to view bus voltage values?

Responses: Overall average score of satisfaction for the alternative#1, 2, 3, and 4 are 4, 3.5, 2.25, and 4.25 respectively. As a result of this process, parts of Alternatives #1 and #4 were selected for further study, and revised based on operator feedback. For Alternative #2, it was found that professionals do not want to change from conventional displays for circuit breakers and buses i.e., red for closed, and green for open breakers.

These revised concepts were then developed using LabVIEW software for the HMI and Matlab code for the system state and power flow analysis to develop a real time simulator that was then evaluated using SA measures.

### 3.4. Real Time Simulator

Among the alternatives presented in an earlier section, Alternatives #1 and #4 were selected to move forward for testing. Two HMI's were created for the proposed seven-bus Potsdam, NY.

In both cases, line loading pie charts were replaced with bar charts. The reason behind this is, pie charts are not easy to interpret by the human cognition process. "Pie charts force us to compare either 2-D areas or the angles formed by each pie. Our visual perception handles neither of these comparisons easily or accurately." [15]. Also, operators control each circuit breaker from the one-line diagram. Selection of a given circuit breaker opens a pop-up window to confirm the action. As the status of the microgrid is critical, the one-line also has a block at its center that confirms the status (grid connected or isolated).

Interface A (Figure 8) consists of five blocks of information. These are arranged to provide an intuitive understanding of the status of the microgrid. The first block presents a conventional one-line diagram.

The second block on the right side of the interface presents overview information of the total microgrid. This section provides total microgrid frequency, generation, import/export, and load. In addition, this section presents alarms. One important intended feature of this alarm list is a coordinated view, meaning the selection of one alarm should show/highlight the affected elements in the other blocks of the interface. In the next block (bottom middle) of the interface, the microgrid load is presented in a load curve. The load curve is provided to help in users SA level 3 (projection of the system condition). The load block shows the load curve trend, and includes operator-initiated load shedding capability on the individual busses. Finally, the generator status block presents both generator status and loading as well a capacitor status.

Interface B figure 8, has the same color conventions and diagram symbols as Interface A. Interface B has a single block design, with the one-line diagram enlarged in this block. Load and voltage data are displayed on the one line. Alarms are shown directly on the one line. In Figure 9, the Bus 1 generator is overloaded. As a result, the generator bar graph is red. When it becomes overloaded, the bar graph will pulse, and an audible alarm will sound until it is acknowledged. Operator actions for generator, capacitor and load shedding are initiated directly from the one-line in this interface, rather than from a subpanel. In addition, detailed views of the generator (Figure 10) and bus status (Figure 11) are available for selection by the operator to show additional detail that is in the subblocks of Interface A.

In both HMI's, an overload of violation causes an alarm to sound. For generator and line overloads, the bar graph turns red and blinks. Also, the red "Alarm On" turns on. For bus voltage violations, the bus name turns red and blinks to indicate the alarm state. When the alarm comes on, the operator mutes the alarm by pressing the "Mute Alarm" button. When the alarm is muted, this button turns orange and displays "Unmute Alarm". When the system is in an alarm state, the operator mutes the alarm, and then resolves the contingency by adjusting generator outputs, switching lines or capacitors in or out, or implementing load shedding from

the HMI interface. Contingencies studied include separating from the bulk power grid, line trips and generator trips.

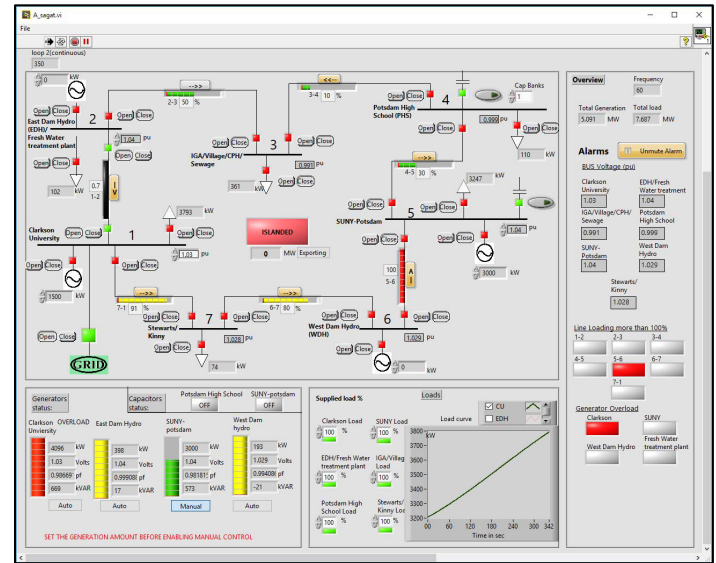


Figure 8: Potsdam microgrid interface-A using LabVIEW software.

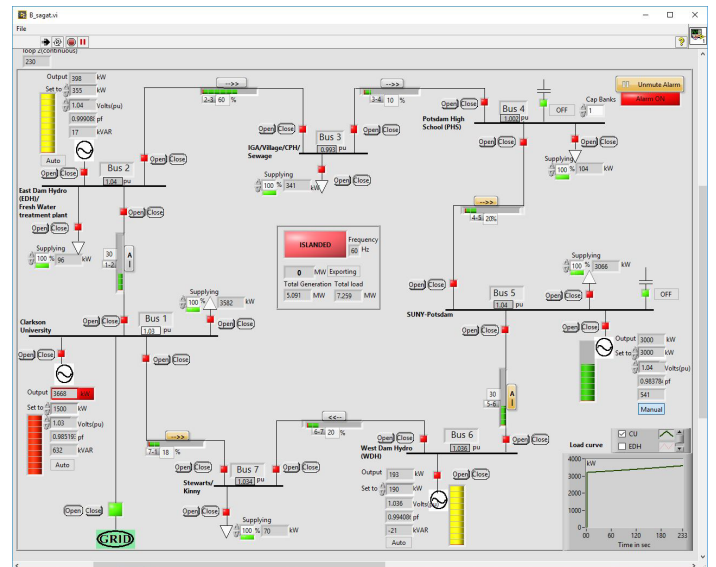


Figure 9: Potsdam microgrid interface-B using LabVIEW software.

These two HMI options were implemented in the LabView software. The Potsdam Microgrid was represented in Matlab with using a Newton-Raphson load flow. TCP/IP communications were used to connect the load flow and HMI interfaces. The load flow had an update rate of 1 second, and it was able to operate in real time. Each second, the load flow algorithm received updated breaker status and generation and load inputs from the HMI. It then ran the load flow, and sent bus voltages and line and generator power flows back to the HMI for display and alarm generation. The user was able to open and close circuit breakers and adjust generator and load settings directly in the HMI.

The next section presents the situational awareness assessment methods evaluation techniques used in this study, and the SA results that provide comparative analysis of the two interfaces.





Figure 10: Detail view of the generator window.

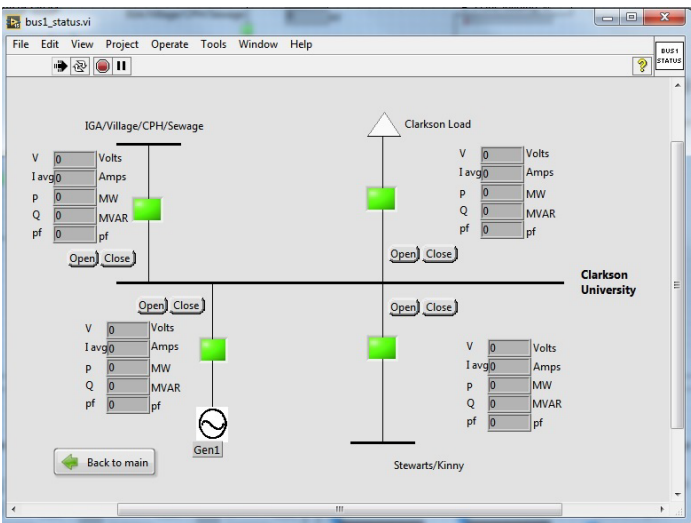


Figure 11: Detail Bus view window.

#### 4. SA assessment/Human factors testing

Assessment or evaluation is an important part of any SA design process. Evaluation is important to avoid any unforeseen issues that can negatively impact an operator's SA. SA is an internalized mental concept, and adequately assessing SA can be difficult. In [16], the authors suggested two evaluation methods: direct and indirect measures of SA (presented in Figure 12). They proposed some techniques for those measures as well. In this study, SAGAT (Situation Awareness Global Assessment Technique) is used as a direct measure and the performance measure method is used as an indirect measure for the microgrid interfaces.

In [17], the authors have used 28 students to participate in their study to assess their simulated interfaces. For the microgrid interface assessment, 28 undergrad and/or graduate students participated in the study. Students were selected from those who have completed or were enrolled in the courses Power Transmission and Distribution, Power System Engineering, High-Voltage Techniques and Measurements, or Energy Conversion. Student subjects are compensated \$20/hr for their participation in the study.

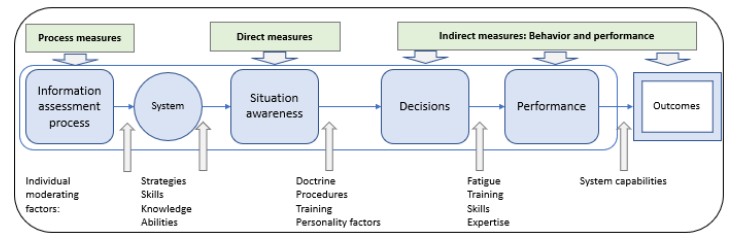


Figure 12: Approaches to SA measurement. Adapted from [16]

#### 4.1. The indirect performance measure of SA

Indirect performance measures consist of techniques that assess SA based on the operators' overall performance. This approach assumes a direct relationship between SA and performance. However, good SA is necessary but not sufficient for good performance. A person might have good SA, but lack the skill, training and/or knowledge that is required for good performance. This section describes the human factors testing methodology used to compare the operators/students' performance between the two interfaces developed using LabVIEW.

In this study, a training manual and video were developed. Participants were given hands-on training with a sequence of 5 trial cases. Half of the participants were trained with interface-A, another half trained with interface-B. Finally, they were tested with 5 trials in each interface (5 x 2 = 10 trials for each participant). Action times were recorded for evaluation as a measure of their performance with the interfaces. Each student received the same contingency (line trip) sequence. In each trial, thirty seconds into the simulation a line trip/outage occurs. This trip causes an overload on one or more of the transmission lines or generators and/or voltage violations. Any of this cause an audible alarm to sound. This event requires three tasks of the user:

- 1- acknowledge the violation
- 2- solve each violation through operator action
- 3- confirm that the system does not have any violation

For the Potsdam microgrid, this study analyzes three measures:

- time taken to acknowledge violation,
- time taken to solve the violation and
- time taken to confirm that there is no violation now/system is a normal state.

Operators/subjects can solve the violations by increasing/decreasing generation kW output, switching capacitors, and/or load shedding. Faster response times for each measure indicate better operator performance.

With each test participant, the time taken to mute the alarm and the time to solve the contingency were recorded. While evaluating responses, the study excludes all the measurements that took 60 seconds or more to solve the contingency. In addition, the test recorded the time to acknowledge no violation scenarios (time is taken to click the unmute button after the system came back to normal state). The study excludes those test points that do not have unmute time (could be for the technical issue) or where participants took more than 20 sec to unmute. Considering all the facts 121

observations for Interface A and 127 observations for Interface B were analyzed.

Table 1: Average times in seconds taken for each interface.

	Interface-A (seconds)	Interface-B (seconds)
Mute time (time between any alarm ON to click MUTE button)	1.73	1.54
Solution time (time between any alarm ON to solve the contingency (all alarm OFF))	19.51	21.51
Acknowledge time (time between all alarm OFF to click the UNMUTE button)	3.63	3.28

From the Table 1 results it is evident that Interface B took less time in both mute time and acknowledgement time. However, Interface A took slightly less time in solving the contingency. Interface A has a dedicated subpanel for alarms to the right side of the screen in Figure 8, with the display having individual indicators for bus voltage and line and generator overload violations. An enlarged version is shown in Figure 13. The Alarm light and the Mute/unmute pushbutton are in this subpanel. Interface B has the Alarm indicator and mute/unmute button in the upper right corner of the one-line diagram that is show in Figure 9. The overloaded device or bus voltage violation are noted by flashing bar graphs or lights on the one line at the location of the violation. An enlarged view of this part of the one-line is also shown in Figure 13. This difference between the alarm display and mute/unmute button location are considered to be the most likely cause of the differences in test results between the HMI's.

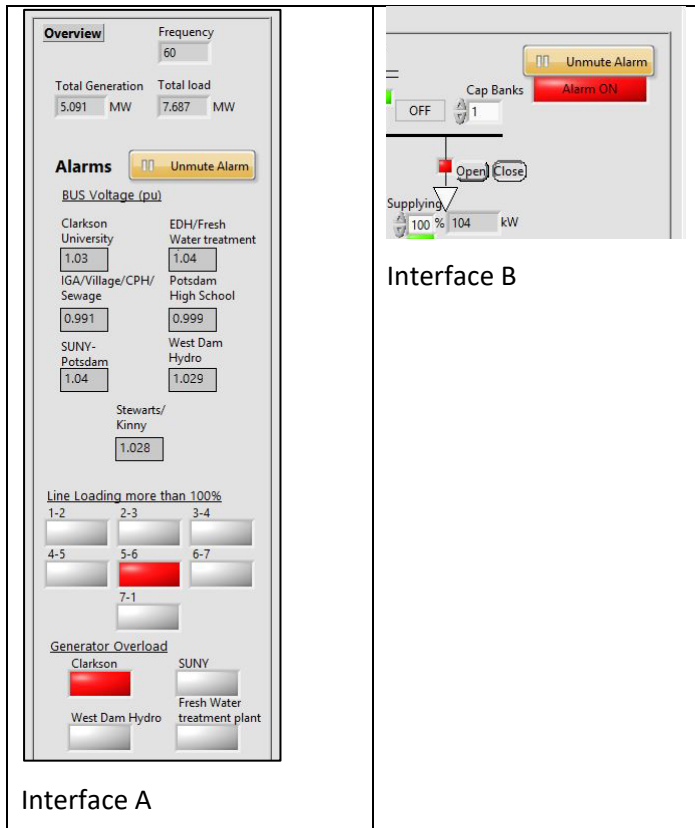


Figure 13: Interface B has an explicit alarm ON/OFF display section.

#### 4.2. The direct measure of SA

SAGAT is a direct measure of SA. This is the human in the loop testing system. The simulation was frozen at several points in time. During this period, a series of questions are asked to the operators to determine his or her knowledge of the situation at the specific moment. Some advantages of the SAGAT technique are:

- it assesses global SA,
- avoids a retrospective recall,
- minimizes biasing,
- performs in a realistic environment.

On the contrary, some disadvantages of the SAGAT technique are that it requires stoppages in the scenarios. This may have a negative impact on the real-time scenarios. As this study is using simulated scenarios, the stoppages are not a factor.

Data were collected using a modified version of the SAGAT technique adopted from [18]. Participants got about five minutes of training to get used to the system/interface. Then simulated scenarios of line trip/outage followed by some voltage/line/generator overload occurred. In these cases, participants were not required to do any activity other than monitoring the system condition/s. A maximum of five halts was used to collect data. Each halt consists of ten queries, with a maximum time limit of two minutes permitted per halt. Each participant was surveyed using an online survey instrument ('Google Forms'). Per standard SAGAT procedure, participants are barred from viewing operational information during the halt. Responses from the first halt were considered a training response. Each query was set based on the goals, decisions, and information requirements of the operators. Selected SAGAT questions and their level of SA's are in (parenthesis):

- Q1. What is the approximate total load in MW? (L1)
- Q2. Is the Microgrid currently importing OR exporting energy? (L1)
- Q3. Are there any lines currently loaded between 80% - 100% (in Yellow condition)? (L2)
- Q4. At this moment which Buses are in voltage violation (pu lower than 0.95 OR higher than 1.05)? (L2)
- Q5. Which buses have capacitor banks? (L1)
- Q6. Currently how many lines are in an outage state? (L2)
- Q7. How many lines are overloaded at this time? (L2)
- Q8. Are there any generators currently loaded over 100% (in Red condition)? (L2)
- Q9. Currently how many generators are set to manual control? (L1)
- Q10. Within the next 10 min, what do you think is going to happen about the load? (L3)

The actual system conditions are recorded at the time of the simulated halt. The accuracy of the responses are compared with the actual scenarios at that time. The time delay from the beginning of the simulation to each halt in different scenarios are presented

in Table 2, 3 and 4 present SAGAT results from the experiment. Total response count is less for halt#1 and halt#5 because each participant with each display faces four halts. The very first response was considered as a training response, regardless of the interface type. Thus, if anyone is presented with ‘interface A’ first then the participants were given 4 more halt (up to 350 - 355 seconds). However, then for the ‘interface B’ the participants were given four halts (up to 268-277 seconds). The following questions were developed and used in this study to conduct the SAGAT measure:

Question 1 (What is the approximate total load in MW) results indicate better performance of ‘interface A’ than ‘interface B’. Total load is displayed in ‘interface B’ right in the middle of the screen whereas in ‘Interface A’ in one corner. It is possible that the positioning of this information on the screen can have an influence on this result.

Question 2 (Is the Microgrid currently importing OR exporting energy) results shows almost the same performance in both interfaces. It is observed that both interfaces have a similar look and positioning of this information. Question 3 (Are there any lines currently loaded between 80% - 100% (in yellow condition?)) ‘Interface A’ has significant preference over ‘interface B’. ‘Interface A’ has a separate section for alarm display. In contrast, participants had to scan all over the ‘interface B’ to get the pieces of information (check Figure 8 and 9. Question 4 At this moment which Buses are in voltage violation (pu lower than 0.95 OR higher than 1.05)?). The results demonstrate that ‘interface B’ better performed than ‘interface A’. ‘Interface A’ has a separate alarm section to display voltage violation information. However, ‘interface B’ displays flashing red light in voltage violation scenarios. Question 5 (Which buses have capacitor banks?) ‘Interface A’ has a clear preference over ‘interface B’. Observations are made that a separate section of capacitors in ‘interface A’ made the privilege over ‘interface B’. Question 6 (Currently how many lines are in an outage state?) same explanation as described under Question 3. Question 7 (How many lines are overloaded at this time?) same explanation as described under Question 3. Question 8 (Are there any generators currently loaded over 100% (in red condition?)) same explanation as described under Question 3. Question 9 (Currently how many generators are set to manual control?) ‘Interface A’ has little better performance over ‘interface B’. Notes are made that ‘interface A’ has the information's displayed together at a place. In contrast, in ‘interface B’ participants had to scan through the full display to get the pieces of information. Question 10 (Within the next 10 min, what do you think is going to happen about the load?). ‘Interface B’ has little better performance over ‘interface A’. Note to be made is that, in terms of responses count this is negligible.

Table 2: Timing of the halts during the experiment

Halt Number	Time delay of a halt in the simulated scenario, (seconds)
1	70-75
2	150-152
3	230-240
4	268-277
5	350-355

Table 4 depicts that both on level 1 and level 2, ‘interface A’ performed better than ‘interface B’. However, level 3 results show almost similar performance on both the interfaces. However, note that there is only one level 3 question (Q10) in this study, and further SA testing at level 3 is indicated.

Table 3: SAGAT Results by Question

Questions	Interface A			Interface B		
	Wrong response	Total response count	% Error	Wrong response	Total response count	% Error
1	3	105	2.9	11	105	10.5
2	15	105	14.3	16	104	15.5
3	21	105	20.0	35	104	33.5
4	22	105	20.9	17	105	16.5
5	9	105	8.6	15	104	14.4
6	12	105	11.4	20	104	19.2
7	14	105	13.3	24	104	23.1
8	3	105	2.9	9	104	8.7
9	18	105	17.1	21	104	20.2
10	17	105	16.1	16	104	15.4

Table 4: SAGAT results showing SA level performance.

SA level	#of Questions	Interface A			Interface B		
		wrong response	Total events	% Error	wrong response	Total events	% Error
L1	4	45	420	10.71	63	417	15.11
L2	5	72	525	13.71	105	521	20.15
L3	1	17	105	16.19	16	104	15.38

5. Conclusion

Both power system and microgrid interfaces should communicate the necessary information in a helpful format at the appropriate time in order to promote adequate situational awareness. For the Potsdam, NY microgrid, four HMI concepts were developed, and two human-machine interfaces were simulated and tested using a human-centered design approach. This paper provides detailed information about the design, development, and evaluation process. Both direct and indirect measures are used to evaluate the designed interface. Study results underscore the importance of both direct and indirect measures while doing human factors testing. The indirect/performance measures showed better performance of Interface A in solving the contingency, while Interface B scored better in the muting and acknowledging time tests. The direct/SAGAT method provided further evidence participant performance was more accurate with Interface A than Interface B.

Acknowledgement

This work was supported by the National Science Foundation, Project 1534035 "PFI:BIC Developing Advanced Resilient Technology to Improve Disaster Response Capability."

## References

- [1] M. H. Mahfuz, T. Ortmeier, and E. Hall, "Development of a Microgrid Controller Interface Using Human-Centered Design Approach," in *IEEE Power and Energy Society General Meeting*, 2022. doi: 10.1109/PESGM48719.2022.9917191.
- [2] P. M. Salmon et al., "What really is going on? Review of situation awareness models for individuals and teams," *Theor Issues Ergon Sci*, vol. 9, pp. 297–323, 2008.
- [3] M. R. Endsley and D. G. Jones, "What Is Situation Awareness?," in *Designing for Situation Awareness*, CRC Press, 2011, 13–30. doi: doi:10.1201/b11371-4 10.1201/b11371-4.
- [4] J. D. Weber and T. J. Overbye, "Voltage contours for power system visualization," *IEEE Transactions on Power Systems*, **15**, 404–409, 2000, doi: 10.1109/59.852151.
- [5] M. R. Endsley and E. S. Connors, "Situation awareness: State of the art," in *2008 IEEE Power and Energy Society General Meeting - Conversion and Delivery of Electrical Energy in the 21st Century*, IEEE, Jul. 2008, 1–4. doi: 10.1109/PES.2008.4596937.
- [6] E. S. Connors, "Situation awareness for the power transmission and distribution industry," in *EPRI's XIII annual power switching safety and reliability conference and seminar*, 2009.
- [7] C. Tu, X. He, Z. Shuai, and F. Jiang, "Big data issues in smart grid – A review," *Renewable and Sustainable Energy Reviews*, **79**, 1099–1107, 2017, doi: <https://doi.org/10.1016/j.rser.2017.05.134>.
- [8] C. Schneiders, J. Vanzetta, and J. F. Verstege, "Enhancement of situation awareness in wide area transmission systems for electricity and visualization of the global system state," in *2012 3rd IEEE PES Innovative Smart Grid Technologies Europe (ISGT Europe)*, 2012, 1–9. doi: 10.1109/ISGTEurope.2012.6465665.
- [9] G. Andersson et al., "Causes of the 2003 major grid blackouts in North America and Europe, and recommended means to improve system dynamic performance," *IEEE Transactions on Power Systems*, **20**(4), 1922–1928, 2005, doi: 10.1109/TPWRS.2005.857942.
- [10] M. R. Endsley and D. G. Jones, "User-Centered Design," in *Designing for Situation Awareness*, CRC Press, 2011, 3–12. doi: doi:10.1201/b11371-3 10.1201/b11371-3.
- [11] M. Endsley and D. Jones, "Design Process," in *Designing for situation awareness*, CRC Press, Taylor and Francis Group, 2011, pp. 43–60.
- [12] S. Chipman, J. M. Schraagen, and V. Shalin, *Introduction to cognitive task analysis*. 2000.
- [13] M. R. Endsley, "A Survey of Situation Awareness Requirements in Air-to-Air Combat Fighters," *Int J Aviat Psychol*, 1993, doi: 10.1207/s15327108ijap0302\_5.
- [14] E. S. Connors, M. R. Endsley, and L. Jones, "Situation awareness in the power transmission and distribution industry," in *Proceedings of the Human Factors and Ergonomics Society Annual Meeting*, SAGE Publications, 2007, 215–219.
- [15] S. Few, *Now You See It: Simple Visualization Techniques for Quantitative Analysis*, 1st ed. USA: Analytics Press, 2009.
- [16] M. R. Endsley and D. G. Jones, "Evaluating Design Concepts for SA," in *Designing for Situation Awareness*, CRC Press, 2011, 259–284. doi: 10.1201/b11371-18.
- [17] A. M. Rich, D. A. Wiegmann, and T. J. Overbye, "Visualization of power systems data: A human factors analysis," *PSERC*, 2001.
- [18] M. R. Endsley, "Measurement of Situation Awareness in Dynamic Systems," *Human Factors: The Journal of the Human Factors and Ergonomics Society*, **37**(1), 65–84, 1995, doi: 10.1518/001872095779049499.

## HistoChain: Improving Consortium Blockchain Scalability using Historical Blockchains

Marcos Felipe, Haiping Xu\*

Computer and Information Science Department, University of Massachusetts Dartmouth, Dartmouth, 02747, USA

### ARTICLE INFO

Article history:

Received: 21 February, 2023

Accepted: 10 May, 2023

Online: 21 May, 2023

Keywords:

Consortium blockchain

Historical blockchain

On-chain big data

Scalable storage

Dynamic load balancing

Healthcare data

### ABSTRACT

Blockchain technology has been successfully applied in many fields for immutable and secure data storage. However, for applications with on-chain big data, blockchain scalability remains to be a main concern. In this paper, we propose a novel scalable storage scheme, called HistoChain, for a consortium blockchain network to manage blockchain data. We use a current blockchain and historical blockchains to store on-chain big data, where the current blockchain and the historical blockchains store data from recent years and earlier years, respectively. Both the current blockchain and the historical blockchains are maintained by super peers in the network; while regular peers manage only the current blockchain and can retrieve historical data by making queries to the super peers. We present procedures for generating historical blockchains, dynamically balancing the data retrieval workload of super peers, and concurrently retrieving historical blockchain data in response to queries. We further provide a case study of healthcare data storage using a consortium blockchain, and the simulation results show that our scalable HistoChain storage scheme supports efficient access and sharing of big data on the blockchain.

## 1. Introduction

In recent years, the use of blockchain technology in many fields has gained increasing interest and popularity [1]. As a distributed and decentralized ledger, blockchain technology allows for the protection of transactions and data while maintaining the data sharing and reliability of a peer-to-peer network [2]. Peers maintain “chains” of blocks consisting of various types of data stored as transactions. Each block contains the hash value of the previous block in the chain, so any attempt to modify one block has a ripple effect on all subsequent blocks in the blockchain. These altered hash values can be easily identified because peers in the network maintain copies of the chain and can independently verify transactions and blocks. Permissioned blockchains allow peers in the network with the required permissions to access recorded transactions, while the key benefits of security, immutability, integrity, and transparency are preserved for transaction records [3]. The reliability and ease of securing and accessing data may explain the growing prevalence of blockchain technology worldwide. Bitcoin, a digital currency that utilizes public blockchain technology, had over 100 million users in 2022. The Bitcoin blockchain grew by more than 400 gigabytes from January 2012 to July 2022, and has even doubled since February 2019. In the face of this incredible growth,

the cost of becoming a full-fledged node in a blockchain network is daunting and could become completely impractical. Similar to public networks like Bitcoin and Ethereum, consortium networks also run into storage problems [4]. In general, applications that require big data storage pose such problems, even if these networks do not consist of many peers or transactions. A wide range of domains, such as healthcare, real estate, insurance, and the Internet of Things (IoT), have adopted blockchain technology, resulting in a variety of data types and applications. While these applications typically use consortium blockchain networks, data-rich applications inevitably face storage issues, which raise significant concern about blockchain scalability.

The concern for blockchain scalability is the main reason for many studies on consortium blockchain storage management [5], [6]. However, most of the proposed solutions employ various off-chain storage strategies such as InterPlanetary File System (IPFS) and cloud storage, where IPFS is a decentralized, secure, verifiable, distributed storage system that can be integrated with blockchain networks [7]. Although off-chain approaches can alleviate the scalability issues of blockchain storage, the benefits of using blockchain technology are lost as the data is moved off the chain and new issues regarding the security and maintainability of off-chain data can be introduced. In this paper, we propose an on-chain approach, called *HistoChain*, to reduce the storage burden on most peers in a blockchain network by

\*Corresponding Author: Haiping Xu, University of Massachusetts Dartmouth, Dartmouth, MA 02747, Email: [hxu@umassd.edu](mailto:hxu@umassd.edu)

[www.astesj.com](http://www.astesj.com)

<https://dx.doi.org/10.25046/aj080311>

splitting the current blockchain (*CB*) and transferring the old data to a historical blockchain (*HB*), thereby reducing the size of the *CB* by half. In the *HistoChain* approach, *HB*s are immutable blockchains containing historical data separate from the *CB*, while the *CB* contains only the most recent years of blockchain data. After a set period of time, the *CB* will have grown further, and it will then be split again, generating another *HB*. In our approach, the nodes in the network are set up as either super peers or regular peers, with a smaller but substantial number of nodes forming a group of super peers, each of which maintains a copy of the *CB* and all *HB*s. Regular peers, which comprise most of the nodes in the network, need only retain the *CB*. This greatly reduces the storage burden on regular peers, which can then access data from the historical blockchains by making queries to the super peer group. In our approach, we use a time-based partitioning method to split the *CB* when it reaches a certain age. For example, if this age is 10 years, an *HB* will be created containing the first 5 years of data, leaving only the most recent 5 years of data in the *CB*. This splitting process can continue over time, resulting in the creation of multiple *HB*s.

Since regular peers are not required to store *HB*s, making query requests to the super peer group is their means of accessing historical data from the blockchain. When a super peer receives a request to search for historical data, it retrieves the requested data from the historical blockchains, and sends a summary report containing all retrieved information back to the requesting regular peer. In our approach, we introduce a meta-block, a mutable block attached to the beginning of the *CB* or each of the *HB*s, which contains index information for all transactions stored in the corresponding blockchain. This index information can facilitate fast and efficient data retrieval from a large blockchain that contains many years of data; therefore, the search time for historical data can be significantly reduced.

This work significantly extends the scalable storage scheme we previously proposed for on-chain big data using historical blockchains, originally presented at the IEEE International Workshop on Blockchain and Smart Contracts in 2022 (IEEE BSC 2022). In our previous work [8], we defined a primary super peer, called *PSP*, as an elected super peer who plays a role in efficiently facilitating access to data in *HB*s by regular peers. However, this approach introduces centralization and requires the necessary trust in a particular super peer (i.e., the *PSP*), which shall be best avoided in a blockchain architecture. In this paper, we allow a query to be sent to any super peer, which is responsible for collecting retrieved historical data and returning a summary report. To ensure temporal efficiency in query execution, query delegation will be performed within the super peer group. We design a dynamic load balancing algorithm to support fulfilling a request in a timely and concurrent manner. Each request for historical data sent to the super peer group is divided into subqueries with a search time of no more than 5 years, which are assigned to super peers based on their current workload. For this purpose, each super peer maintains a Shared Assignment Table (*SAT*) that keeps a record of assignments for all super peers and their completion times. Once an assignment is accepted by a super peer, an update to the *SAT* is broadcast within the super peer group to ensure that the super peers are aware of the latest status of the blockchain network.

The rest of the paper is organized as follows. Section 2 discusses related work. Section 3 presents the *HistoChain* framework for scalable storage using historical blockchains and describes the procedure for generating historical blockchains. Section 4 describes in detail the dynamic load balancing algorithm and the retrieval process of historical blockchain data. Section 5 presents the case studies and their analysis results. Section 6 concludes the paper and mentions future work.

## 2. Related Work

Scalability challenges in blockchain technology, especially in public blockchain systems, remain a persistent issue. In [9], the authors introduced the Bitcoin Lightning Network (BLN), a decentralized system where transactions can be sent off-chain for value transfer through channels. The BLN, through its ability to make micro-payments, has positively impacted the scalability of the global Bitcoin blockchain network by reducing the need to broadcast many transactions. Danksharding is a newer type of sharding architecture proposed to scale the Ethereum network [10]. In the Danksharding proposal, nodes can validate larger data volumes through distributed data sampling across blob; therefore, nodes can avoid processing all data and larger data volumes can be handled by the Ethereum network. Scalability challenges also arise in consortium blockchain networks when large amounts of data need to be stored. In the context of consortium, off-chain strategies to improve the scalability of blockchain applications are the main focus of further research. To reduce the high cost of computation and storage for blockchain-based applications, in [11], the authors investigated a series of off-chain computation and storage approaches. They proposed five off-chain models that move computation and data off the blockchain without violating the trustless property. In [12], the authors proposed an off-chain scalability solution, called ChainSplitter, for Industrial Internet of Things (IIoT) blockchain applications. The proposed approach features a hierarchical storage structure where the recent blocks are stored in an overlay network and the majority of blockchain data is stored in the cloud. Despite being structured as a decentralized cloud storage system, the blockchain data in the cloud is not maintained by peers and thus acts as an off-chain repository for blockchain data. IPFS also offers a scalable off-chain solution for blockchains. In [13], the authors presented a blockchain-based application using IPFS specifically for healthcare systems. They focused on storage of electronic health records (EHRs) and used the IPFS service to transfer data off-chain while retaining hashes of the data on the blockchain. In [14], the authors attempted to reduce the transaction size and increase the transaction throughput of an experimental consortium blockchain network by storing the hash values of encrypted data on-chain and using IPFS to store the encrypted data itself off-chain. They integrated Hyperledger Fabric [15], which is a modular blockchain framework typically using off-chain storage for big data, with IPFS services and provided a solution for secure storage and efficient access to a task-scheduling scheme. While the off-chain approach provides a viable way to mitigate the scalability problem of blockchains, as noted in [11], the fundamental properties of blockchains can be compromised to varying degrees when using the off-chain approach. In contrast, our *HistoChain* approach stores big data in historical blockchains and does not rely on off-chain storage; therefore, all essential

properties of the blockchain data can be strictly maintained using our on-chain storage mechanism.

There are very few on-chain based approaches that address the scalability issues in blockchain networks. In [16], the authors proposed to use Hyperledger Fabric to implement a consortium blockchain for patient access and management of personal health records (PHRs). Although scalability issues remain a major challenge, they concluded that Hyperledger Fabric for on-chain data storage could offer a more practical solution to ensure the privacy of PHRs than the Ethereum public blockchain. In [17], the author introduced the concept of section-blockchain, an on-chain approach for reducing the storage cost of blockchain networks with under-stored devices. In their approach, all nodes store a portion of the complete blockchain and provide incentives for upgrading their local storage. Furthermore, they proposed segmented blockchains to enable nodes to store a blockchain segment [18]. They showed that their approach can help reduce the storage cost of a blockchain without compromising the security requirement of the blockchain. In [19], the authors proposed a framework for cloud-based blockchains to store medical multimedia files on-chain securely and reliably. They used a cloud-based blockchain to store all blockchain data to support data accessibility, redundancy, and security, while a lite blockchain allows local storage of text-based information and metadata for multimedia files. Although the above methods allow for big data storage, data retrieval can be slow because portions of transactions are stored in different blockchains. Conversely, our *HistoChain* approach divides a complete blockchain into a current blockchain and multiple historical blockchains, each of which are full-fledged blockchains containing complete transaction information. Regular peers can then access their local current blockchain and request historical blockchain data from super peers concurrently, making the data retrieval process much more efficient.

One of the main advantages of the *HistoChain* approach is that it supports dynamic load balancing, so requests for historical blockchain data can be retrieved in a timely and concurrent manner. There is a great deal of research efforts in developing dynamic load balancing algorithms in the context of cloud computing and P2P systems. In [20], the authors proposed a load balancing scheduling algorithm for virtual server clusters applied to storage systems to ensure uniform load distribution of virtual server clusters. Their approach is based on the state of the server clusters and periodically sends collected feedback to the load balancer to bring the internal load performance of the system to a more balanced state. In [21], the authors introduced a strategy to use a dynamic hashing scheme to locate data keys based on a structured P2P architecture and maintain the load balance among the peers. They showed that the load balancing of P2P systems can be significantly improved using their proposed method. In [22], the authors proposed a dynamic load management algorithm for cloud computing based on the current state of virtual machines (VM). In their approach, the allocation table is parsed to find each idle and available VM, from which the active load of all VMs under consideration is calculated. Similarly, in our *HistoChain* approach, we utilize a shared assignment table to achieve dynamic load balancing within the super peer group, where the assignment is determined on the basis of the lowest total workload of the super peers. In this sense, our approach complements existing dynamic load balancing mechanisms in cloud computing and P2P systems

and provides a simple yet efficient solution to support concurrent processing of complex query requests for current and historical blockchain data.

### 3. Scalable Storage Using Historical Blockchains

#### 3.1. A Framework for Scalable Blockchain Networks

Data storage technologies such as physical storage and cloud storage each have their inherent advantages, but this meteoric rise in blockchain-enabled applications has led to a great deal of research focused on decentralized storage for managing large amounts of data while maintaining its viability for nodes and networks. To demonstrate this storage requirement, we examine an example of blockchain applications in healthcare. A patient visiting a hospital may generate a certain amount of data, especially in the case of multimedia files such as X-rays or CT scans. If a hospital is to consider adopting blockchain technology for data storage, it must remain scalable because a large number of patients will generate large amounts of data over a long period of time. This issue is further complicated for an entire network of hospitals that utilize a consortium blockchain as a means of sharing medical data. While viable techniques do exist to store off-chain medical data, the benefits offered by using blockchain storage are compromised in this use. In this paper, we propose the *HistoChain* approach that supports the maintenance and sharing of medical data on the chain, with the burden being borne by a smaller group of well-equipped super peers representing large and resourceful hospitals in a local area. Such large hospitals will be able to dedicate more resources to the network to maintain older on-chain data stored in historical blockchains. This makes it feasible for regular peers to participate in the network to maintain the benefits and convenience offered by blockchain technology while having a much lower storage burden without moving their data off-chain. Figure 1 shows the *HistoChain* framework for a scalable consortium blockchain network.

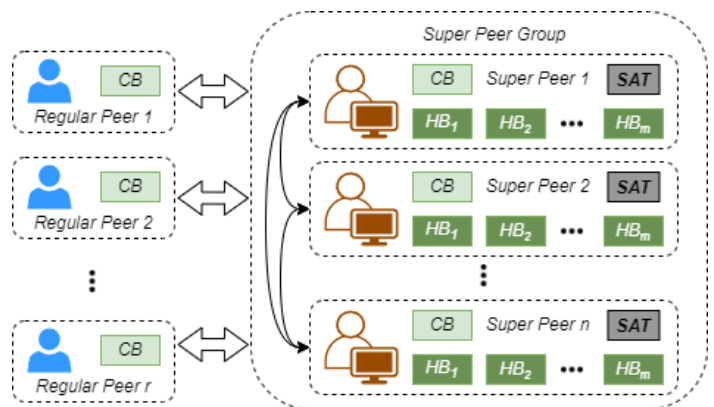


Figure 1: A Framework for a Scalable Consortium Blockchain Network

As shown in Figure 1, a consortium blockchain network consists of  $n$  super peers and  $r$  regular peers. The super peers are tasked with maintaining the current blockchain  $CB$  and all historical blockchains  $HBs$ , as well as creating and verifying new blocks and transactions using a consensus process. Shifting the burden of historical data storage and freeing regular peers from participating in the consensus process allows the introduction of highly lightweight regular peers. Regular peers maintain only the  $CB$ , but can access historical data stored in  $HBs$  through queries

to the super peer group. Upon receiving a query, a super peer splits it into subqueries and assign them to super peers based on the shared assignment table *SAT* as a means of dynamic load balancing to ensure that access to the data remains timely. More importantly, as described in Section 3.4, when the current blockchain reaches a certain age, a super peer can split it into a chain of historical blocks and a reduced chain of current blocks.

### 3.2. The Block Structure

A block, as a building block of a blockchain, can be defined by three parts: the block header, the list of transactions, and the verification section. Figure 2 shows the structure of a block with a list of *m* transactions.

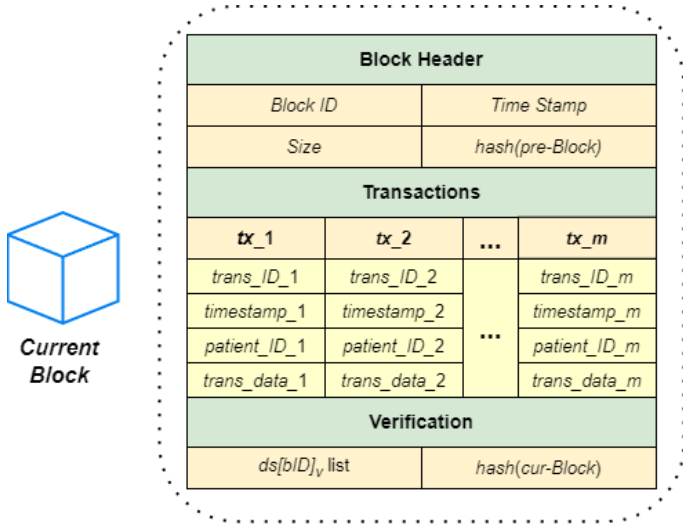


Figure 2: The Structure of a Block with a List of Transactions

As shown in Figure 2, the block header is defined as a 4-tuple  $(B, T, S, H)$ , where  $B$  is the block ID,  $T$  is the timestamp when the block is created,  $S$  is the size of the list of transactions recorded in the block, and  $H$  is the hash value of the previous block. In the context of healthcare, each transaction in the transaction list is defined as a 4-tuple  $(TI, TS, PI, TD)$ , where  $TI$  is the transaction ID,  $TS$  is the timestamp when the transaction is created,  $PI$  is the patient ID, and  $TD$  is the transaction data, including text-based messages and images files. The verification section is essential for the integrity of the blockchain storage, which includes a list of digital signatures,  $ds[bID]_v$ , for a block with ID  $bID$ , where  $v$  is a super peer that approves it as a new block in the consensus process. Any pending block must be approved by the majority of the super peers before it can be added to the blockchain, at which point the hash of the block is computed by applying a hash function to the block file containing all the above components excluding the verification section, and the hash value  $hash(cur-Block)$  is attached to the end of the block file. Note that in order to limit the block size, each block contains no more than 500 transactions and only contains transactions created during the same day. Therefore, the last block created at the end of a day may contain less than 500 transactions.

### 3.3. The Structure of a Meta-Block

To support efficient data retrieval in a blockchain, we define a *meta-block* as a special block that stores metadata for the current

blockchain or each of the historical blockchains. A meta-block is the only mutable block in a blockchain and is attached at the beginning of the blockchain. Figure 3 shows the structure of a meta-block. As shown in the figure, a meta-block consists of two parts: the block header and a HashMap *HM*. The block header is defined as a 4-tuple  $(SD, ED, SB, EB)$ , where  $SD$  is the timestamp of the first transaction in the first block of the blockchain;  $ED$  is the timestamp of the last transaction in the last block of the blockchain;  $SB$  and  $EB$  are the block IDs of the first block and the last block of the blockchain, respectively. In the second part, the HashMap *HM* contains a list of  $\langle key, value \rangle$  pairs, where the key is a patient ID and the value is a list of locations where the patient transactions are stored. Each location is defined as a triple  $(B, A, O)$ , where  $B$  is the block ID,  $A$  is the address of the transaction in the block, and  $O$  is the offset of the transaction size.

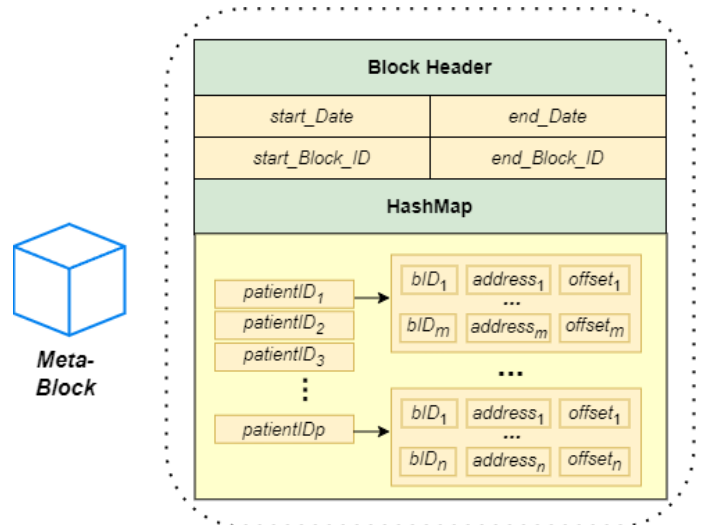


Figure 3: The Structure of a Meta-Block

The use of meta-blocks in a blockchain network provides an additional layer of organization and structure. By placing metadata in a separate block attached to the beginning of a blockchain, searching for information in the blockchain becomes much easier. This metadata allows peers to determine the exact location of transactions in the blockchain that need to be extracted to complete queries on current and historical blockchain data. Thus, the search space is much reduced and the time it takes to execute a query can be minimized. Note that to ensure the integrity of the blockchain metadata, a meta-block can be reviewed, validated and refreshed at any point in time by reading data from the relevant part of the blockchain.

### 3.4. Generation of a Historical Blockchain

At its inception, the current blockchain is the only blockchain in the network. When the current blockchain reaches a certain age, say 10 years, a split occurs. The oldest 5 years of data are transferred to a new blockchain, called a historical blockchain, while the most recent 5 years of data remain in the current blockchain. When a new historical blockchain is generated, a new meta-block containing its metadata is appended to the beginning of the historical blockchain, and the current blockchain's meta-block is refreshed to reflect the movement of that data. This process is repeated 5 years later when the current blockchain again



contains 10 years of data. Figure 4 shows how the current blockchain  $CB$  is split into a historical blockchain and a new current blockchain. Let the block IDs of the first and last block in  $CB$  be  $m$  and  $n$ , respectively. Note that  $m = 1$  if the current blockchain has never been split before. Let block  $k$  be the most recent block in  $CB$  that is at least 6 years old. We establish blocks  $m$  through  $k$  as a historical blockchain  $HB$  and generate a new meta-block  $MB_{HB}$  for it. Blocks  $k+1$  through  $n$  persist as the updated current blockchain, while blocks  $m$  through  $k$  are removed. The meta-block  $MB_{CB}$  associated with the current blockchain is refreshed by scanning the data in the new current blockchain (i.e., blocks  $k+1$  through  $n$ ). We now have an updated current blockchain and a historical blockchain, each containing 5 years of data.

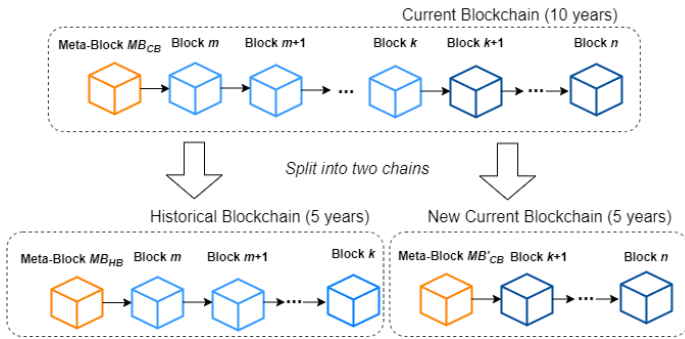


Figure 4: A Blockchain Split into a Historical and a Current Blockchain

A super peer is responsible for splitting a current blockchain with a certain age into a reduced current blockchain and a historical blockchain. When a super peer completes this task, it broadcast the updated current blockchain to all peers and the new historical blockchain to all super peers for updating. Algorithm 1 shows the process of splitting the current blockchain  $CB$  with 10 years of data into a historical blockchain  $HB$  and an updated current blockchain  $CB$ .

**Algorithm 1: Splitting of a Current Blockchain**

**Input:** A current blockchain  $CB$  containing 10 years of data  
**Output:** Historical blockchain  $HB$  with 5 years of old data and an updated  $CB$  with the most recent 5 years of data

1. Let  $m$  and  $n$  be the IDs of the first and the last block in  $CB$
2. Let  $k$  be the most recent block at least 6 years old, where  $n > k$
3. Extract blocks  $m$  through  $k$  from  $CB$  and create a new historical blockchain  $HB$  with the  $k-m+1$  blocks
4. Create an empty meta-block  $MB_{HB}$  associated with  $HB$
5. Set  $SD$  in  $MB_{HB}$  as the date of the first transaction in block  $m$
6. Set  $ED$  in  $MB_{HB}$  as the date of the last transaction in block  $k$
7. Set  $SB$  and  $EB$  in  $MB_{HB}$  to  $m$  and  $k$ , respectively
8. **for** each block  $\beta$  in  $HB$
9.     Scan block  $\beta$  and add each triple  $(B, A, O)$  associated with *patientID*  $\alpha$  to a list  $LS_\alpha$
10. Create a HashMap in  $MB_{HB}$  and add all pairs of  $\langle \alpha, LS_\alpha \rangle$  to it
11. Attach  $MB_{HB}$  to the beginning of  $HB$
12. Remove blocks  $m$  through  $k$  from  $CB$
13. Update  $CB$ 's meta-block  $MB_{CB}$  accordingly, as with  $MB_{HB}$
14. **return**  $HB$  and  $CB$

As shown in Algorithm 1, the meta-block of  $HB$ ,  $MB_{HB}$ , contains the date of the first transaction in the first block of  $HB$ , the date of the last transaction in the last block of  $HB$ , and the

block IDs of the first and last block of  $HB$ . To create a HashMap that contains all  $\langle key, value \rangle$  pairs, each block in  $HB$  is scanned, and each triple  $(B, A, O)$  associated with the patient ID  $\alpha$  is added to a list  $LT_\alpha$ . Once the scanning process is complete, all pairs of  $\langle \alpha, LT_\alpha \rangle$  are added to the HashMap in  $MB_{HB}$ . Now in  $CB$ , all blocks that have been recorded in  $HB$  are deleted, and the meta-block of the updated  $CB$  must be refreshed by removing all triples that reference transactions that have been transferred to  $HB$ . Finally, the new  $HB$  and the updated  $CB$  are returned for broadcasting.

**4. Retrieval of Historical Blockchain Data**

*4.1. Load Balancing Data Retrieval Requests*

In the context of blockchain applications in the healthcare domain, suppose a regular peer (e.g., a doctor) queries patient information from blockchains for multiples of 5 years. When the data to be searched is for the most recent 5 years, the regular peer can search directly from its local current blockchain. When the data to be searched is for the past  $sLen$  years, where  $sLen \in \{5n \mid n \geq 2\}$ , the regular peer can search for patient information for the most recent  $c$  years directly from its local blockchain, where  $c$  is the age of the current blockchain; while the remaining  $(sLen - c)$  years of data must be retrieved from the historical blockchains by making a query to any of the super peers. The request for such a query involves a patient ID (for which data is collected) and the number of years of data being search, called the *search length*. Figure 5 shows the querying process for accessing historical blockchain data.

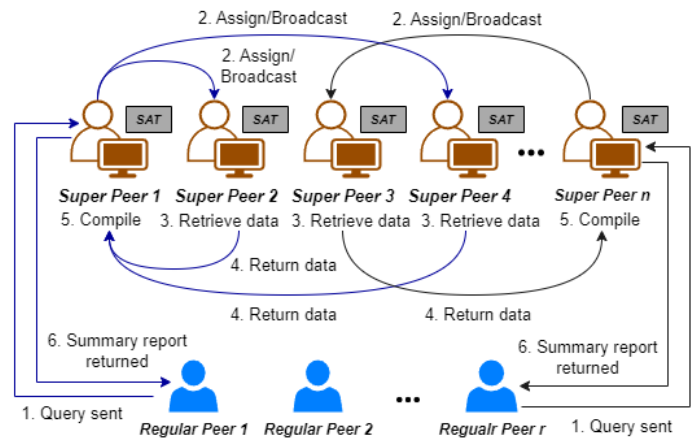


Figure 5: Querying Process for Accessing Historical Blockchain Data

From Figure 5, we can see that when a super peer receives a query from a regular peer, it acts as a director, dividing the query into subqueries and distributing them evenly based on the weights of queries to be completed by the super peers. Each query receives a weight based on the search length. For example, for a blockchain with a current blockchain of 7 years, a query with a search length of 20 years can be split into three subqueries, a 3-year search and two 5-year searches with weights of 3/5 and 1, respectively. Data retrieved from all subqueries are returned to the assigning super peer (if not completed by the assigning super peer) and compiled into a single summary report that is returned to the requesting regular peer. Note that the search for the most recent 7 years of blockchain data must be performed locally by the requesting

regular peer, who is responsible for combining its local report with the summary report received from the assigning super peer into a single summary report.

A new subquery with a 5-year search length is always assigned first to the super peer with the lowest total weight. Subqueries sent to super peers are stored in their query queues, and the total weight of the queries assigned to each super peer must be approximately equal. A super peer processes subqueries in its query queue on a first-come, first-served basis. When a super peer retrieves relevant historical data for a subquery, it compiles the results and returns a response to the assigning super peer, including a summary report of the relevant transactions with links to associated files that a regular peer can download. Note that each super peer maintains its own copy of the historical blockchains; therefore, searches assigned to multiple super peers can be performed by them simultaneously.

#### 4.2. The Structure of Shared Assignment Table

In our proposed *HistoChain* approach, the lightweight nature of regular peers allows for a scalable architecture with the super peers facilitating access to historical data. To this end, queries for patient data are sent from regular peers to the super peers and the summary reports are returned upon completion. To ensure efficient execution of this approach, *dynamic load balancing* is employed, where each super peer retains a copy of *SAT* and broadcasts an updated *SAT* with any assignment changes made by the super peer to the super peer group. These broadcasts contain the current workload and assignment of each super peer as well as estimated time when the subquery must be completed. In case no response is received by the end of the estimated completion time, the task must be completed at the highest priority by the assigning super peer to avoid further delay. Figure 6 illustrates the structure of an *SAT* shared by a group of  $n$  super peers.

Shared Assignment Table (SAT)		
Time Stamp	Publisher ID	
Super Peer ID	Query Queue	Total Weight
Super Peer 1	{ [Query_ID, SubQuery_ID $q_1, sq_1$ , Assigning_ID SP, Receiving_ID $SP_1$ , time_estimate $te_1$ ] ... }	$tw_1$
Super Peer 2	{ [Query_ID, SubQuery_ID $q_2, sq_1$ , Assigning_ID SP, Receiving_ID $SP_2$ , time_estimate $te_2$ ] ... }	$tw_2$
...	...	...
Super Peer $n$	{ [Query_ID, SubQuery_ID $q_n, sq_1$ , Assigning_ID SP, Receiving_ID $SP_n$ , time_estimate $te_n$ ] ... }	$tw_n$

Figure 6: The Structure of a Shared Assignment Table (SAT)

When a query is received by an assigning super peer  $\Psi$ , it will be split into multiple subqueries, each of which can be assigned to a super peer based on the lowest total weight. This ensures the uniform distribution of weights among the super peers and the timely completion of the subqueries. Each subquery consists of a query ID, a patient ID, a requested start date (*SD*), and an end date (*ED*), defined as a 4-tuple ( $qID, pID, SD, ED$ ). Once the assignment is recorded into *SAT*, the updated *SAT* is broadcast within the super peer group. To prevent conflicts, a super peer always uses the latest version of *SAT* for the assignment by checking the publishing timestamp. A super peer may reject a

subquery request due to various reasons. When this happens,  $\Psi$  must update *SAT* and broadcast it again. Algorithm 2 shows the query assignment process done by  $\Psi$ . Let the blockchain be of age 5 or more. Since the age of the current blockchain ranges from 5 to 10 years, the search length of subquery  $sq_1$  can be less than 5 years. To avoid adding network time to the data retrieval time of short subqueries with a search length less than 5 years, the assigning super peer always completes such a subquery by itself rather than assigning it to another super peer.

#### Algorithm 2: Query Assignment by Assigning Super Peer $\Psi$

**Input:** Query  $q$  with a search length  $sLen$  in  $5x$  years,  $x \in [1, 10]$ , current blockchain age  $c$ , shared assignment table *SAT*

**Output:** Updated shared assignment table *SAT*

1. **if**  $sLen \leq c$  **return** *SAT* // only local search is needed
2. Split  $q$  into subqueries  $sq_1 \dots sq_m$ , where  $m = (sLen - c)/5$ , search length  $|sq_1| = 10 - c$ , and  $|sq_i| = 5, 2 \leq i \leq m$ .
3. **if**  $|sq_1| < 5$
4.     Assign  $sq_1$  to  $\Psi$  //self-assign  $sq_1$  for less than 5-year search
5. **else** // when  $|sq_1| = 5$
6.     Assign  $sq_1$  to the super peer with the lowest total weight in *SAT*
7.     **for each** subquery  $\rho$  in  $sq_2 \dots sq_m$
8.         Assign  $\rho$  to the super peer with the lowest total weight in *SAT*
9.     Broadcast updated *SAT* to all super peers
10. **return** updated *SAT*

#### 4.3. Retrieval of Historical Blockchain Data

We now define the procedure for the retrieval of historical data by a super peer *SP*. Let subquery  $\rho$ , defined as a 4-tuple ( $qID, pID, SD, ED$ ), be a subquery assigned to *SP* by an assigning super peer  $\Psi$ , then the search length of the subquery  $|\rho|$  must be no more than 5 years that is covered by one of the historical blockchains. To identify the historical blockchain to be searched, *SP* needs to compare the start date *SD* and end date *ED* of the subquery with those of the historical blockchains by examining their meta-blocks. Once the historical blockchain is identified, the search is facilitated by investigating again its meta-block, which contains indices specifying the exact location of transactions in the identified historical blockchain. Algorithm 3 shows how historical data can be retrieved from historical blockchains by super peer *SP*.

#### Algorithm 3: Historical Blockchain Data Retrieval (Subquery)

**Input:** Subquery  $\rho$  as a 4-tuple ( $qID, pID, SD, ED$ )

**Output:** A summary report with retrieved historical data for  $\rho$

1. Create an empty summary report  $SR_{\rho.qID}$
2. **for each** historical blockchain  $\Pi$
3.     Read  $MB_{\Pi}.SD$  and  $MB_{\Pi}.ED$  from meta-block  $MB_{\Pi}$
4.     **if**  $MB_{\Pi}.SD > \rho.ED \parallel MB_{\Pi}.ED < \rho.SD$
5.         **continue** // outside of the search period, search next  $\Pi$
6.     Get a list of triples  $LTX$  from  $MB_{\Pi}.HM$  with  $pID$  as the key
7.     **for each** triple  $(B, A, O)$  in  $LTX$
8.         Read transaction  $tx$  from block  $B$  at address  $[A, A + O]$
9.         **if**  $tx.TS \geq \rho.SD \ \&\& \ ts.TS \leq \rho.ED$
10.             Add retrieved  $tx$  and links to relevant files to  $SR_{\rho.qID}$
11.     **break** // only one  $\Pi$  needs to be searched for subquery  $\rho$
12. **return** summary report  $SR_{\rho.qID}$

As shown in Algorithm 3, the patient ID in the subquery  $\rho$  is used as the key in the meta-block's HashMap to access the exact locations of relevant transactions in the associated historical blockchain. Super peer  $SP$  then reads the relevant transactions and record them in a summary report  $SR_{\rho,qID}$ . The summary report may contain links to multimedia files, which are hosted by  $SP$ . Finally, the summary report  $SR_{\rho,qID}$  is returned to the assigning super peer  $\Psi$ .

Based on Algorithm 2 and Algorithm 3, we now define the entire process by which the assigning super peer  $\Psi$  completes a summary report for a query  $q$  with a search length  $sLen$ , made by a requesting regular peer. This query completion process done by  $\Psi$  is described in Algorithm 4.

**Algorithm 4: Query Completion by Assigning Super Peer  $\Psi$**

**Input:** Query  $q$  with a search length  $sLen$ , shared assignment table  $SAT$   
**Output:** A completed summary report  $SR_{\Psi}$

1. Invoke Algorithm 2 on  $q$  to create and assign subqueries
2. **if** any assigned subquery  $sq$  is rejected by a super peer
3.     Assign  $sq$  to  $\Psi$  itself
4.     Broadcast the updated  $SAT$
5. **for each** super peer  $SP$  with an assigned subquery  $\rho$
6.     Wait summary report  $SR_{\rho,qID}$  to be received from  $SP$  after  $SP$  invokes Algorithm 3
7.     **if** time estimate of  $\rho$  is exceeded and  $SR_{\rho,qID}$  is not received
8.         Assign  $\rho$  to  $\Psi$  itself and invoke Algorithm 3
9.     Remove subquery assignment for  $SP$  from  $SAT$
10.     Broadcast updated  $SAT$
11. Compile each *summary report* into a complete report  $SR_{\Psi}$
12. **return** summary report  $SR_{\Psi}$

As shown in Algorithm 4, upon receiving query  $q$ , the assigning super peer  $\Psi$  splits it into subqueries and assigns them to super peers by invoking Algorithm 2. If any assigned subquery  $\rho$  is rejected by an assigned super peer  $SP$ ,  $\rho$  is reassigned to  $\Psi$  itself and an updated  $SAT$  is broadcast. Each super peer  $SP$  receiving an assignment then retrieves the historical data requested in the assignment by invoking Algorithm 3. The assigning super peer  $\Psi$  then awaits the summary report from each  $SP$ . When a summary report for a subquery  $\rho$  is returned,  $\Psi$  removes the corresponding assignment in its  $SAT$  and broadcasts this update. If any subquery is not completed by the time estimate,  $\Psi$  assigns the subquery to itself, broadcasts an updated  $SAT$ , and completes the subquery. When all summary reports for the subqueries become available,  $\Psi$  compiles them into a complete final summary report (in chronological order of the subquery start date) and returns it to the requesting regular peer.

Note that a regular peer can perform a local search for a query whose search length is equal to the age of the current blockchain in a similar manner. Remote searches of historical blockchain data by super peers are conducted concurrently with the local search of the current blockchain by a regular peer. The historical data returned from a remote search is then merged with the local search data by the requesting regular peer.

**5. Case Study**

In this section, we present a series of simulations in the context of healthcare to demonstrate the feasibility and effectiveness of the *HistoChain* approach. In our experiments, we assume that

there are 10 large local hospitals participating in a consortium blockchain network. There are also 30 small and medium medical facilities in the network. A consortium blockchain may have a 50-year lifespan, which is enough time to aggregate a substantial amount of data to be useful for experiments. We limit the total number of transactions in each block to 500, where each transaction may contain medical data in the form of image and text files. For simulation purposes, the number of visits per day is between [200, 500] and [50, 200] for large hospitals and small/medium sized medical facilities, respectively.

**5.1. Estimation of Blockchain Size**

To estimate the blockchain sizes along years, we use a time-based partitioning method to generate historical blockchains. A time-based partitioning occurs in the 10th year of the current blockchain; the earliest 5 years of data make up an historical blockchain, while the most recent 5 years of data are retained by the current blockchain. Using this method, super peers representing large local hospitals retain all historical blockchains as well as the current blockchain, while regular peers representing small/medium sized medical facilities store only the current blockchain. Table 1 lists the parameters used in our experiments.

Table 1: Parameters Used for Blockchain Size Estimate

Image occurrence (%)	Image size	Image count	Text occurrence (%)	Text size	File size growth rate (%)	Time to split (year)
5%	1 ~ 3 MB*	1 ~ 5	100%	0.003 ~ 0.007 MB*	0, 1, 3, 5	10

\* File sizes are subject to increase by a 5-year file size growth rate.

As shown in Table 1, for a hospital visit, we assume that there is a 5% probability of including images, such as x-rays, in the doctor's notes. The size of the images is typically between [1MB, 3MB] and the number of images attached is limited to 5. The sizes of text-based medical records are also listed in Table 1. Note that in our experiments, we consider 5-year file size growth rates of 0%, 1%, 3% and 5%, with the file size bound increasing uniformly each year over the 5-year period. For example, when the 5-year growth rate is 3%, the image size increases by 0.6% per year and the maximum image size can reach 4.89 MB in 50 years, which is usually large enough for medical image files.

We now simulate the creation of a 50-year blockchain to estimate the storage burden of regular and super peers in the network. On each day, a large hospital or a small/medium sized medical facility in the network generates a random number of visits within the given range [200, 500] or [50, 200], respectively. A transaction is generated for each visit and stored in a block that can hold up to 500 transactions, independent of the transaction size. Each transaction has a 5% chance of including at least one image file. If a transaction does include image files, the number of image files is chosen randomly within the given range [1, 5]. In addition, the size of each image file or text file is also randomly generated within the certain ranges, as defined in Table 1.

To address the possible growth of image and text file sizes along years, we consider 5-year file size growth rates of 0%, 1%, 3% and 5% in our experiments. For each growth rate, we collected data from a sample of 10 simulations to establish the mean of the evaluation. The 0% growth rate is included as a baseline; while

not a realistic assumption, this establishes the minimum size of the blockchain against which the other growth rates can be considered. Figure 7 shows the change of blockchain storage along the years for the entire blockchain (including both current and all historical blockchains). The experimental results show that the effectiveness of using a historical blockchain structure is evident. After 50 years, the storage volume of the entire blockchain exceeds 33 TB at 0% growth rate, 35 TB at 1%, 38 TB at 3%, and 43 TB at 5%. Due to the storage burden, this would not be a viable solution for regular peers to store the entire blockchain.

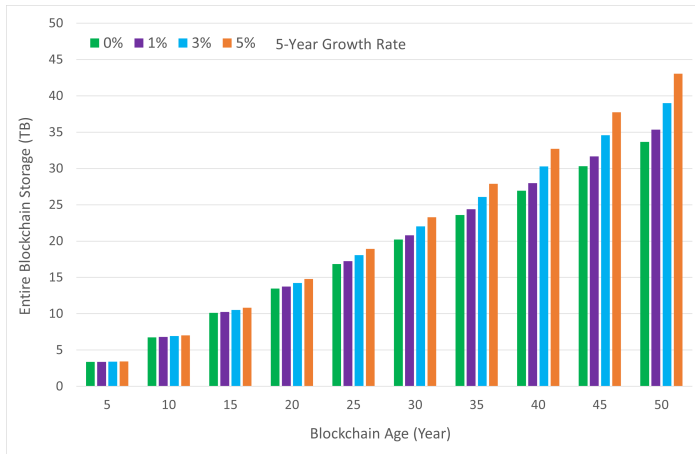


Figure 7: Total Blockchain Size by Year with 5-Year Growth Rates

Now, with the introduction of the historical blockchain structure, the storage load for regular peers can be greatly reduced, as regular peers no longer need to store the entire blockchain. Figure 8 shows the change of blockchain storage along the years for the current blockchain. The experiment records the size of the current blockchain in the year before the current blockchain split (e.g., year 4, year 9, year 14, etc.) to show the approximate maximum size of the current blockchain along the way.

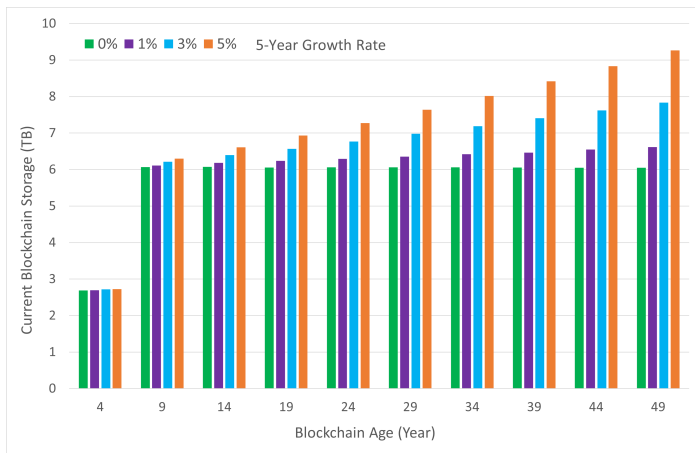


Figure 8: Current Blockchain Size by Year with 5-Year Growth Rates

From Figure 8, we can see that the size of the current blockchain is much smaller than the size of the entire blockchain. At 0% growth rate, the current blockchain size is at most 6.05 TB; at 1%, 6.62 TB; at 3%, 7.83 TB; and at 5%, 9.26 TB. The results show that for a growth rate of 0%, the size of the current blockchain is consistent regardless of the age of the blockchain. At a growth rate of 5%, the size of the current blockchain

increases with the year but remains manageable for regular peers. Note that the size of the current blockchain doubled from year 4 to year 9 because the current blockchain did not need to split during those 9 years.

### 5.2. Data Retrieval Time for a Single Request

In this experiment, we measure the data retrieval time for a single query request for blockchain historical data by a regular peer. The data retrieval request is a search for a patient’s medical records within a specified number of years. For any search within the current blockchain age, the data can be readily retrieved from the current blockchain; however, when the search length is greater than the current blockchain age, a query needs to be sent to a super peer to identify the relevant data and retrieve them from the historical blockchain(s). In this experiment, we let the age of the entire blockchain be 50 years old; therefore, up to 50 years of data can be retrieved from the blockchain. Table 2 lists additional parameters used for data retrieval in the simulations.

Table 2: Parameters for Data Retrieval Used in the Simulations

Search length (year)	Annual patient visits	File size growth rate (%)	Network latency time	Data extraction time	Data export time	Average meta-block size
5, 10, 15, ..., 50	1 ~ 7	3	0.5 seconds	0.02s /MB	0.017s /MB	100MB

Since one of the important factors affecting the search time is in reading meta-blocks of the historical blockchains that contain 5-years of data, we consider search lengths in 5-year intervals up to 50 years. A 50-year blockchain also means that the current blockchain has just been split, so the current blockchain contains only the most recent 5 years of data. This setting helps to show the data retrieval time for the maximum amount of historical data. For a 5-year search, it will only be processed by a regular peer. For any search length of 10 years or more, the most recent years of data will be retrieved by a regular peer and the rest of data must be retrieved by super peers.

We assume a maximum of 7 hospital visits per patient per year and set a file size growth rate of 3% for 5 years, which allows for a reasonable increase in the size of medical image files and text files. Parameters such as image size bounds, image count bounds, text size bounds, and probability of occurrence of images in medical records can be found in Table 1. For search length of 10 years or more, measuring data retrieval time requires consideration of the *network latency time* for searching data in the historical blockchain(s), *data extraction time* for extracting index information from the relevant meta-blocks and the data from relevant blocks, and *data export time* for writing the extracted historical transaction data to a summary file. While the exact location of a transaction in a historical blockchain can be determined in constant time from the index information stored in a meta-block, opening a meta block file and reading the data from the file takes nontrivial time. Based on the average size of the meta-blocks, retrieving the index information from a meta-block can take up to several seconds. Since in our experiments, transactions are generated randomly, the extraction time is dependent upon the size of the transactions. For historical blockchain data, a super peer needs to write the extracted transaction data to a summary file. If a request is split by an

assigning super peer and completed by multiple assigned super peers in parallel, the summary reports returned must be compiled by the assigning super peer and returned to the requesting regular peer. This amount of time is included in the data export time, where a longer query adds more compilation time as it can be split into more subtasks and more reports need to be compiled.

We call our approach *decentralized, fine-grained* because there is no single trusted peer for load balancing; instead, dynamic load balancing is utilized by each super peer in the group based on the SAT. We now compare our decentralized, fine-grained approach to a *centralized, coarse-grained* approach [8], where a search query is processed by a single super peer, regardless of the search length. Figure 9 shows the results of 30 simulations for the centralized and decentralized approaches for each given search length up to 50 years.

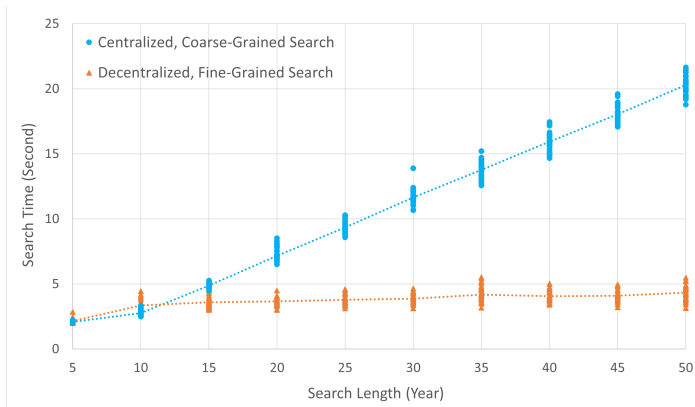


Figure 9: Retrieval Time for Individual Request with Varying Search Length

From Figure 9, we can see that for 5-year search, the average search time for both approaches is about 2 to 3 seconds. This is because the 5-year search can be processed locally by a regular peer and does not require remote data retrieval by super peers. The average 10-year search time with the decentralized approach is slightly larger, which can be attributed mainly to the increase in network time; the assigning super peer may need to delegate a remote 5-year search to another super peer and await its response. Otherwise, the search time would be the same, since the remote search for 5-year data is handled by one super peer in both methods. As the search length increases, the data retrieval time increases accordingly, with a maximum of about 20 seconds in the centralized approach for a 50-year search length. We see this growth is approximately linear, which is expected because the searches in multiple historical blockchains are performed sequentially by a single super peer, rather than in parallel by multiple super peers. In contrast, in the decentralized approach, there is a slight initial increase in search time for a 10-year search, but this increase is flat for longer searches. We see that a 50-year parallel search takes just over 4 seconds on average. The very small increase in time from a 10-year search to a 50-year search can be explained by the time it takes to compile summary reports received from multiple super peers.

Note that the 10-year search time does not increase significantly over the 5-year search time in both approaches because the 10-year search consists of a local search by a regular peer in the current blockchain and a remote search of the remaining data by a super peer, both of which are performed

concurrently. The insignificant increase in the average data retrieval time in the 10-year search in both approaches is due to the additional network time and export time caused by the remote search of the historical data.

### 5.3. Data Retrieval Time for Concurrent Requests

Our approach supports simultaneous processing of multiple query requests. In this experiment, we compute the distribution of weights across a group of 10 super peers for 10, 25, and 50 concurrent requests. Since requests are expected to be received at 5-minute intervals and up to 50 concurrent requests can be processed in this interval (at times of high workload), there is no overflow. Weights are assigned in proportion to the number of years involved in the search. We again consider searches involving up to 50 years of data at 5-year intervals. A 5-year search is not considered, as it can be retrieved locally from the current blockchain by a regular peer. We assume the probability of each search length occurring is equal, forming a uniform distribution. Figure 10 shows the variance of the weights assigned to each super peer in this strategy, where a number of simulations are generated for each number of concurrent query requests.

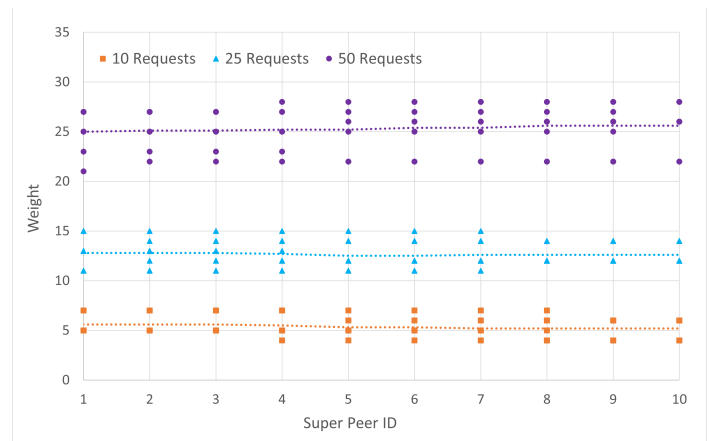


Figure 10: Distribution of Weights for Varying Numbers of Concurrent Requests

In a group of 10 super peers, queries are randomly sent to super peers who split the queries and assign subqueries to others to ensure even load balancing among the super peers. In this way, simultaneous historical blockchain data retrieval requests can be processed concurrently by the super peers. To examine the search time of concurrent data retrieval requests, the requests of regular peers for 10 to 50 years of data are measured. From Figure 10, we can see that the distribution of weights among the super peers is approximately uniform. For 10 concurrent queries, the average weight of the super peers is 5.37; for 25 queries, it is 12.65; and for 50 queries, it is 25.32. This demonstrates the effectiveness of the dynamic load balancing algorithm, which allows for even workload distribution in the super peer group and leads to efficient concurrent data retrieval by the super peers.

We further compare the centralized and decentralized approaches to demonstrate the efficiency of the decentralized, fine-grained approach. Load balancing can also be incorporated in the centralized approach, so weights are assigned to each request according to the length of the request [8]. We assume search lengths of up to 50 years and simulate 10, 20, 30, 40, and 50 concurrent searches at 5-minute intervals to calculate the total

data retrieval time. Note that 50 concurrent requests represent a very high volume of requests in a 5-minute interval, this may occur at certain times of the year, such as a flu season. We calculate the average data retrieval time for completion of all concurrent requests in a 50-year blockchain, which we refer to as the *completion time*. Figure 11 shows the average and individual completion time for the specified numbers of concurrent requests by running 30 simulations of each approach.

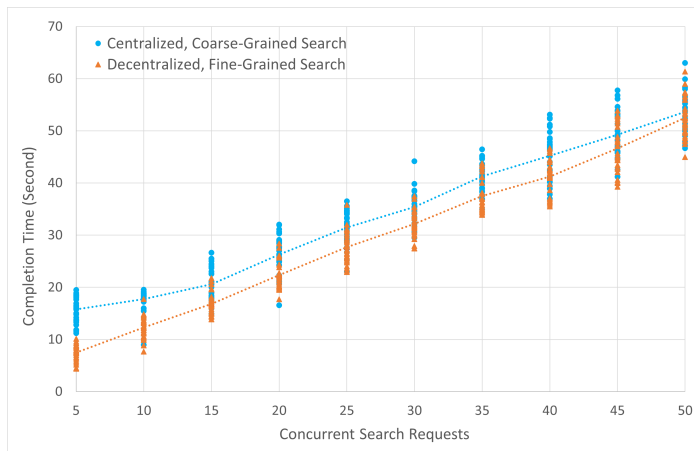


Figure 11: Completion Time for Varying Number of Concurrent Requests

From Figure 11, we can see that employing a decentralized, fine-grained approach is superior to a centralized, coarse-grained load balancing mechanism. Since in the decentralized approach, long queries are split into 5-year subqueries, the dynamic load balancing would result in more even workload distribution among super peers than in the centralized approach. On the other hand, although the average completion time of the centralized approach is higher than that of the decentralized approach for each number of concurrent requests, we note that as the number of concurrent requests increases, the queue completion times of the centralized and decentralized approaches start to converge and are almost equal at 50 concurrent requests. This is because when there are more concurrent requests, the weight distribution of the centralized approach can become more uniform and may approach the performance of the decentralized approach. This finding suggests that the decentralized, fine-grained dynamic load-balancing algorithm could be more effective in the off-season or normal season than in the peak season, although it performs better than the centralized, coarse-grained load-balancing mechanism in general.

## 6. Conclusions and Future Work

To address the scalability issues of consortium blockchains, recent solutions have focused on transferring data off-chain by using IPFS and cloud-based storage structures. In this paper, we propose a novel approach, called *HistoChain*, to improve consortium blockchain scalability using historical blockchains and dynamic load balancing. We introduce a time-based partitioning strategy to generate a historical blockchain, where older sections of the current blockchain are transferred to the historical blockchain after a specified time interval (e.g., 5 years). This approach allows the current blockchain to contain a useful amount of the up-to-date data, while freeing regular peers with limited resources or storage from maintaining the entire data-

intensive blockchain. The historical blockchains are maintained by a group of super peers with greater resources and computing power. In addition, we introduce a meta-block, attached to a historical or the current blockchain, which serves as an index file for facilitating efficient data retrieval. To support concurrent processing of queries, we split a query into subqueries and employ a dynamic load balancing algorithm to assign the subqueries to a group of super peers. This assignment is based on a shared assignment table that records the current workload of each super peer. Once the relevant data for the query has been collected, the assigning super peer sends a summary report of the retrieved data to the requesting regular peer. Finally, we provide a case study of healthcare data storage using a consortium blockchain. The experimental results show that our *HistoChain* approach can effectively reduce the storage burden of data-intensive blockchain applications on regular peers while providing efficient access to historical data through a group of super peers.

In future work, we will implement *HistoChain* and conduct more experiments to illustrate the effectiveness of using historical blockchains to efficiently retrieve historical blockchain data in real scenarios. We will further investigate effective methods to improve the performance of concurrent data retrieval by super peers. One such method to be developed is to analyze the efficiency of parallel searches by a super peer across multiple historical blockchains. This parallelization should allow a super peer to reduce and optimize the search time if the historical blockchains are stored on different hard drives. Furthermore, a hierarchical architecture can be considered to orchestrate multiple consortium blockchains to support blockchain data sharing across cities and states. Finally, to ensure strong data privacy, it is necessary to design access control policies so that users with different roles can access blockchain data with the required permissions [23]. This is especially necessary in applications with multilevel security requirements [24], such as healthcare blockchain applications.

## Conflict of Interest

The authors declare no conflict of interest.

## Acknowledgment

We thank the editors and all anonymous referees for the careful review of this paper and the many suggestions for improvements they provided. We also thank the University of Massachusetts Dartmouth for their financial support to the first author in completing this work.

## References

- [1] H. Guo and X. Yu, "A survey on blockchain technology and its security," *Blockchain: Research and Applications*, **3**(2), February 2022, doi: 10.1016/j.bcr.2022.100067
- [2] S. Nakamoto, "Bitcoin: a peer-to-peer electronic cash system," October 2008. Retrieved on January 15, 2022 from <https://bitcoin.org/bitcoin.pdf>.
- [3] M. J. Amiri, D. Agrawal, and A. El Abbadi, "Permissioned blockchains: properties, techniques and applications," In *Proceedings of the 2021 International Conference on Management of Data (SIGMOD'21)*, 2813-2820, Virtual Event China, June 2021, doi: 10.1145/3448016.3457539
- [4] O. Dib, K.-L. Brousmiche, A. Durand, E. Thea, and E. B. Hamida, "Consortium blockchains: overview, applications and challenges," *International Journal on Advances in Telecommunications*, **11**(1&2), 51-64, 2018.

- [5] S. Liu and H. Tang, "A consortium medical blockchain data storage and sharing model based on IPFS," In Proceedings of the 4th International Conference on Computers in Management and Business (ICCMB 2021), 147-153, Singapore, January 30 - February 1, 2021, doi: 10.1145/3450588.3450944
- [6] X. Chen, K. Zhang, X. Liang, W. Qiu, Z. Zhang, and D. Tu, "HyperBSA: A high-performance consortium blockchain storage architecture for massive data," IEEE Access, **8**, 178402-178413, September 2020, doi: 10.1109/ACCESS.2020.3027610.
- [7] D. P. Bauer, "InterPlanetary File System," In Getting Started with Ethereum: A Step-by-Step Guide to Becoming a Blockchain Developer, 83-96, Apress, Berkeley, CA, July 2022, doi: 10.1007/978-1-4842-8045-4\_7.
- [8] M. Felipe and H. Xu, "A scalable storage scheme for on-chain big data using historical blockchains," In 2022 IEEE 22nd International Conference on Software Quality, Reliability and Security Companion (QRS-C), 54-61, IEEE BSC 2022, Guangzhou, China, December 5-9, 2022, doi: 10.1109/QRS-C57518.2022.00017.
- [9] J. Poon and T. Dryja, "The Bitcoin lightning network: scalable off-chain instant payments," White Paper, 2016. Retrieved on September 1, 2022 from <https://lightning.network/lightning-network-paper.pdf>
- [10] Ethereum Foundation, "DankSharding," White Paper, 2023. Retrieved on May 12, 2023 from <https://ethereum.org/en/roadmap/danksharding/>
- [11] J. Eberhardt and S. Tai, "On or off the blockchain? insights on off-chaining computation and data," In: De Paoli, F., Schulte, S., Broch Johnsen, E. (eds) Service-Oriented and Cloud Computing, ESOC 2017, Lecture Notes in Computer Science (LNCS), **10465**, 3-15, Springer, Cham, 2017, doi: 10.1007/978-3-319-67262-5\_1.
- [12] G. Wang, Z. Shi, M. Nixon, and S. Han, "ChainSplitter: towards blockchain-based industrial IoT architecture for supporting hierarchical storage," In Proceedings of the 2019 IEEE International Conference on Blockchain (Blockchain), 166-175, Atlanta, GA, USA, July 14-17, 2019, doi: 10.1109/Blockchain.2019.00030.
- [13] J. Jayabalan and N. Jeyanthi, "Scalable blockchain model using off-chain IPFS storage for healthcare data security and privacy," Journal of Parallel and Distributed Computing, **164**, 152-167, June 2022, doi: 10.1016/j.jpdc.2022.03.009.
- [14] D. Li, W. E. Wong, M. Zhao, and Q. Hou, "Secure storage and access for task-scheduling schemes on consortium blockchain and interplanetary file system," IEEE 20th International Conference on Software Quality, Reliability and Security Companion (QRS-C), 153-159, IEEE BSC 2020, Macau, China, December 2020, doi: 10.1109/QRS-C51114.2020.00035.
- [15] E. Androulaki, A. Barger, V. Bortnikov, C. Cachin, K. Christidis, A. De Caro, D. Enyeart, C. Ferris, G. Laventman, Y. Manevich, S. Muralidharan, C. Murthy, B. Nguyen, M. Sethi, G. Singh, K. Smith, A. Sorniotti, C. Stathakopoulou, M. Vukolic, S. Cocco, and J. Yellick, "Hyperledger Fabric: a distributed operating system for permissioned blockchains," In Proceedings of the Thirteenth EuroSys Conference (EuroSys'18), Article No. 30, 1-15, Porto Portugal, April 23-26, 2018, doi: 10.1145/3190508.3190538.
- [16] H. Im, K. H. Kim, and J. H. Kim, "Privacy and ledger size analysis for healthcare blockchain," In Proceedings of the 2020 International Conference on Information Networking (ICOIN), 825-829, Barcelona, Spain, 2020, doi: 10.1109/ICOIN48656.2020.9016624.
- [17] Y. Xu, "Section-Blockchain: A storage reduced blockchain protocol, the foundation of an autotrophic decentralized storage architecture," In Proceedings of the 23rd International Conference on Engineering of Complex Computer Systems (ICECCS), 115-125, Melbourne, VIC, Australia, December 12-14, 2018, doi: 10.1109/ICECCS2018.2018.00020.
- [18] Y. Xu and Y. Huang, "Segment blockchain: a size reduced storage mechanism for blockchain," IEEE Access, **8**, 17434-17441, 2020, doi: 10.1109/ACCESS.2020.2966464.
- [19] A. Thamrin and H. Xu, "Cloud-based blockchains for secure and reliable big data storage service in healthcare systems," In Proceedings of the 15th IEEE International Conference on Service-Oriented System Engineering (IEEE SOSE 2021), 81-89, Oxford Brookes University, UK, August 23-26, 2021, doi: 10.1109/SOSE52839.2021.00015.
- [20] X. Yang, H. Shi, S. Yang and Z. Lin, "Load balancing scheduling algorithm for storage system based on state acquisition and dynamic feedback," In Proceedings of the 2016 IEEE International Conference on Information and Automation (ICIA), 1737-1742, Ningbo, China, 2016, doi: 10.1109/ICInfA.2016.7832098.
- [21] Y. Chang, H. Chen, S. Li and H. Liu, "A dynamic hashing approach to supporting load balance in P2P Systems," The 28th International Conference on Distributed Computing Systems Workshops, 429-434, Beijing, China, June 17-20, 2008, doi: 10.1109/ICDCS.Workshops.2008.109.
- [22] R. Panwar and B. Mallick, "Load balancing in cloud computing using dynamic load management algorithm," 2015 International Conference on Green Computing and Internet of Things (ICGCIoT), 773-778, Greater Noida, India, 2015, doi: 10.1109/ICGCIoT.2015.7380567.
- [23] H. Guo, W. Li, M. Nejad, and C. Shen, "Access control for electronic health records with hybrid blockchain-edge architecture," In Proceedings of the 2019 IEEE International Conference on Blockchain (Blockchain-2019), 44-51, Atlanta, GA, USA, July 14-17, 2019, doi: 10.1109/Blockchain.2019.00015.
- [24] R. Anderson, Security engineering: a guide to building dependable distributed systems, 3rd Edition, John Wiley & Sons, Indianapolis, Indiana, USA, December 2020.

## Landmarking Technique for Improving YOLOv4 Fish Recognition in Various Background Conditions

Sutham Sathamsakul, Ari Kuswantori, Witsarut Sriratana, Worapong Tangsirat\*, Taweepol Suesut

Department of Instrumentation and Control Engineering, School of Engineering, King Mongkut's Institute of Technology Ladkrabang (KMITL), Bangkok, 10520, Thailand

### ARTICLE INFO

Article history:

Received: 20 February, 2023

Accepted: 11 May, 2023

Online: 21 May, 2023

Keywords:

Fish classification

Fish recognition

YOLO

Landmarking technique

Computer vision

### ABSTRACT

The detection and classification of fish is a prevalent and fascinating area of study. Numerous researchers develop skills in fish recognition in both aquatic and non-aquatic environments, which is beneficial for population control and the aquaculture industry, respectively. Rarely is research conducted to optimize the recognition of fish with diverse backgrounds. This paper proposes a method for fish recognition that uses the landmarking technique to optimize YOLO version 4 to detect and classify fish with varying background conditions, making it applicable for both underwater and terrestrial fish recognition. The proposed procedure was evaluated on the Brigham Young University (BYU) dataset containing four different fish species. The final test results indicate that the detection accuracy had reached 96.60% with an average confidence score of 99.67% at the 60% threshold. The outcome is 4.94% better than the most common traditional labeling method.

### 1. Introduction

Fish detection and classification, or fish recognition, are exciting and popular research topics [1]. Numerous researchers devise techniques for recognizing fish in underwater and out-of-water environments [2]. Recognition of fish in their underwater condition is beneficial for fish population control and their long-term viability [3-8], especially in light of climate change and global warming [5, 8-10]. It is advantageous for the aquaculture industry to recognize fish in conditions outside the water, such as through automatic classification processes, fish quality control, or other processes [2, 11].

Fish recognition has quite complex and varied challenges, both in conditions in the water and outside the water [1]. The challenges of recognizing fish in underwater conditions are; resolution of the image, swimming freely, camouflaging with other objects and other fish, in various background conditions and lighting conditions, and other challenges such as noise [3, 5, 7-9, 12]. For fish recognition in out-of-water conditions, the challenges that arise are structural deformations of the fish, such as the condition of the eyes, scales, abdomen, and fins that are damaged lightly, moderately, or severely. The condition of random fish positions is also a challenge in this recognition process [11].

Many image processing techniques are used to overcome the challenges, such as; noise filtering by the median filter [11], fish

head detection using convex-hull deficiency [11], Color Multi-Scale Retinex (MSR) to overcome water turbidity [13], orientation correction using MSEE [11], contrast enhancement to find a fish disease [14], and auto segmentation of fish objects with various techniques [9, 11]. Deep learning methods or models are also widely used for fish detection and classification, such as Convolutional Neural Network (CNN) [3, 4, 15-18], YOLO [5, 13, 19-23], few-shot learning for limited training images [6], Alex-Net, ResNet-18, ResNet-50, Inception V3, GoogleLeNet [11], etc.

Numerous strategies have been implemented to overcome the various background challenges and optimize the fish recognition results. CNN was used to classify fish in [3] by training it with the number of species and their environments, including reef substrates and water. They applied their proposed method to 116 videos of fish captured underwater with a GoPro camera. The greatest results were obtained when classifying nine of the twenty fish species that appear most frequently in the videos. Using an ensemble of seven CNN components and two Region Proposal Networks (RPNs) coupled by sequentially jointly trained Long Short-Term Memory (LSTM) units, a multi-cascade object detection network was constructed as described in [4].

They used a collection of 18 underwater fish recordings recorded with a GoPro underwater camera for training and testing. Even though their proposed method can reliably identify and count fish objects in a variety of benthic backgrounds and lighting conditions, it is not used to classify fish. Rather, it is used to locate

\*Corresponding Author: Worapong Tangsirat, worapong.ta@kmitl.ac.th



fish. Using classic CNNs such as these has benefits when applied to other industries, such as agriculture [24] or in other general situations, such as detecting micro scratches [25]. In [12], the foreground extraction was implemented and a CNN-based algorithm with an SVM classifier was created. The instant segmentation on underwater fish images was proposed in [9] and then developed an algorithm based on Res-Net. The recognition of moving fish in [5] used Optical flow, GMM (Gaussian Mixture Models), and ResNet-50, and then combined the output with YOLOv3. The combination of these techniques allowed for the robust detection and classification of fish, which was applied to the LifeCLEF 2015 benchmark dataset from the Fish4Knowledge repository [26] and a dataset collected by the University of Western Australia (UWA) that was described in detail [27]. The GMM and Pixel-wise Posteriors were proposed in [8], and then combined with CNN in [28] for further development. In addition, they utilized a fish dataset extracted from the Fish4Knowledge repository. Similar to the work [4], the approaches proposed in their papers were limited to fish detection without classification.

The fish was divided into three sections: the head, the torso, and the scales [11]. Alex-Net was then utilized to categorize each of these components. The ultimate classification results were then determined utilizing Naive Bayesian Fusion (NBF). This method performed admirably when applied to the Fish-Pak [29] and Brigham Young University (BYU) datasets [20]. Even though the narrative of this work was intended for an automatic classification system, the fish images used were static. The method for detecting fish in aquaculture ponds was developed in [13]. YOLOv3 was utilized to detect the fish after image enhancement was used to improve fish detection in murky water conditions. This method is not intended for classification, but rather for counting and monitoring the trajectory of fish. Faster R-CNN was used to detect and record fish trajectories and compared with YOLOv3 to investigate its behavior and relationship to ammonia levels in pond water [30].

However, the works cited in [3-5, 8, 28] identified moving fish for underwater (ocean) environments, whereas other works merely detected fish without classifying them. In aquaculture, the works of [13] and [30] discovered swimming fish, but it was not used for classification. The work described in [11] classified fish using narration for an automatic classification system, but the datasets used were images that were not dynamic. According to the knowledge of the authors, there is no public dataset for cultured fish that travel on conveyors, and there is no published work to detect and classify moving fish for the fish culture industry, particularly for automatic sorting based on fish species using deep learning and computer vision.

There are numerous versions of YOLO (You Only Look Once) algorithms, such as YOLOv3 [19], YOLOv4 [23], and YOLOv5 [21], that are suitable for real-time applications in terms of detection speed and precision. The optimal algorithm is YOLOv5, but we opted for YOLOv4 on the CiRA-Core platform, which yielded satisfactory results. This study proposes a straightforward method that incorporates the landmarking technique and YOLOv4 for identifying and classifying fish in various background conditions. In the most prevalent labeling technique, the accuracy results will be compared to the conventional “box-squeezing-object” method.

This paper proposes and evaluates a method for detecting and classifying fish using deep learning and computer vision on real videos of aquaculture freshwater fish moving along a conveyor belt for automatic sorting. Consequently, the proposed methodology originates from the following major contributions.

- We created our own database of eight species of cultivated fish. The dataset includes both static images and videos of fish moving at random with two distinct speeds (i.e., low and high) on a conveyor belt.
- This method used YOLOv4, a widely-used recognition algorithm that was optimized using a novel labeling method.
- Additionally, trial research evaluating the efficacy of multiple strategies was conducted. These are training schemes, variants of YOLOv4, and labeling technique comparisons.

The paper is therefore divided into four sections. Section 1 introduces the background of the problem, and approaches from previous researchers. In Section 2, the input datasets, augmentation techniques, landmarking, and algorithms used in this study are discussed. Section 3 contains the outcomes of the experiment. In Section 4, a conclusion and future work are summarized.

## 2. Material and Methodology

### 2.1. Dataset and Image Augmentation

This study aims to detect and categorize fish in a variety of background conditions, such as objects, hues, and others. For this reason, the BYU dataset is deemed highly suitable for use in this work. This dataset was developed by the robotic vision group at Brigham Young University [20], which contains sixteen species of fish photographed under various conditions. Multiple images of fish are captured in the processing unit on a table equipped with an image calibration plate, which provides guidelines for preprocessing and color correction. Other fish photographs were captured in nature and water. Some images have also been altered by means of cropping, recoloring, etc.

Additionally, each species’ image from the sixteen different fish species is quite imbalanced. Due to these factors, only four species were obtained in this study despite the large quantity of image data, unprocessed raw images, and diverse background conditions, i.e., natural and underwater backgrounds. The four fish species listed in Table 1 are B.C. Trout, Kokanee, UT Sucker, and Steal Head. Figure 1 contains illustrations of image data from the BYU dataset. Table 1 shows that the amount of images for the three classes, Kokanee, UT Sucker, and Steal Head, is insufficient and out of proportion to the amount of image data for the entire class. Less than 100 data points reduce validation, and unbalanced data inhibits the algorithm from having the same training chance. Table 2 displays the statistical data for the BYU dataset and image augmentation. This calls for a procedure of augmentation [11]. In this study, the augmentation methods employed include flip, rotation, and translation. This method is thought to be appropriate for fish augmentation [21].

Table 1: BYU dataset and image augmentation

Fish class	No. of images	Multiplication factor	No. of augmented images	New image dataset	For training (80%)	For testing (20%)

B.C. Trout	191	0	0	191	153	38
Kokanee	60	1	60	120	96	24
UT Sucker	87	1	87	174	139	35
Steal Head	25	3	75	100	80	20
Total	363	-	222	585	468	117

Table 2: Statistical data of BYU dataset and image augmentation

No. of images	Fish class				Total	Standard Deviation Value (SDV)	Average
	B.C. Trout	Kokanee	UT Sucker	Steal Head			
Images dataset	191	60	87	25	363	61.91	91
New images dataset	191	120	174	100	585	37.42	146

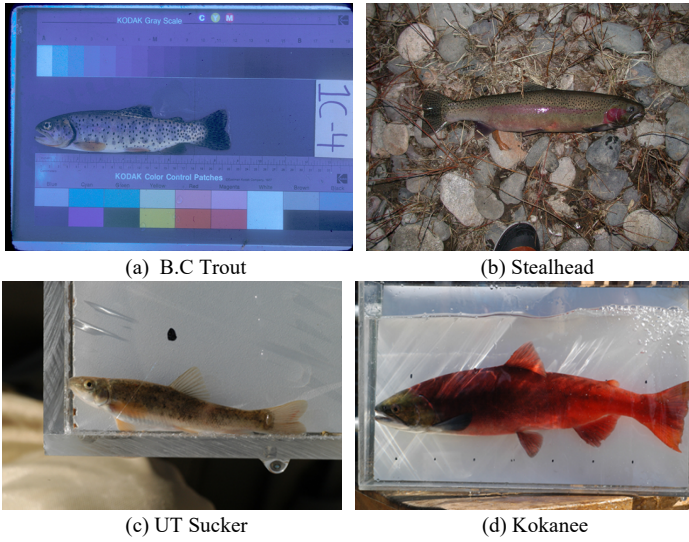


Figure 1: Sample images of BYU dataset

Initially, the number of images ( $N_c$ ) for each class of fish images ( $I_f^c$ ) is determined as shown in (1). The multiplication factor ( $m_f^c$ ) is obtained by comparing the target ( $N_T$ ) with the number of images in each class ( $N_c$ ) as in (2). In this work, the target ( $N_T$ ) is set at 100 for each class. The set of multiplication factors ( $m_f$ ) is obtained by repeating the procedure for each class of fish. The multiplication factor indicates the number of augmented images that need to be created from each image ( $n$ ) in each class of fish. Flip ( $F_a$ ), rotation ( $\theta_a$ ), and translation vector ( $T_a$ ) are selected randomly and generate an augmented image of the  $I_{af}^c$  set obtained from a single image ( $I_f^{N_c}$ ) as in (3). The variances of each of the flip ( $F_a$ ), rotation ( $\theta_a$ ), and translation vectors ( $T_a$ ) were predetermined. Finally, all the augmented image sets ( $I_{af}^{N_c}$ ) are merged with the original image set ( $I_f^c$ ), and a new data set ( $I_{Nf}^c$ ) is formed as in (4).

$$I_f^c = \{I_f^{1c}, I_f^{2c}, \dots, I_f^{N_c c}\} \quad (1)$$

$$m_f = \left\{ m_f^c = \left\lfloor \frac{N_T}{N_c} \right\rfloor, C \in [1, 2, \dots, C], N_c < N_T \right\} \quad (2)$$

$$I_{af}^{nc} = \left\{ H(I_f^{nc}, F_a, \theta_a, T_a) \mid a \in [1, 2, \dots, m_f^c] \right\} \quad (3)$$

and

$$I_{Nf}^c = \{I_f^{1c}, I_f^{2c}, \dots, I_f^{N_c c}, I_{af}^{1c}, I_{af}^{2c}, \dots, I_{af}^{N_c c}\} \quad (4)$$

After the augmentation procedure, the number of images in the new dataset, which ranges from 363 to 585, has increased significantly. The average number of images in each class increased from 91 to 146. In addition, the dataset is now more evenly distributed, as indicated by the decrease in standard deviation from 61.91 to 37.42. The training (80%) and testing (20%) processes were then randomly applied to the images [7].

## 2.2. Occupancy Ratio and Landmarking Technique

The occupancy ratio ( $OR$ ) compares the object area to the overall image area or bounding box, which includes the background, and is measured in  $M \times N$ . The high occupancy ratio reduces the likelihood of an algorithm for deep learning capturing extraneous backgrounds during training. It will increase the effectiveness of deep learning in identifying features unique to objects. The occupancy percentage is represented by the following expression [11]:

$$OR_{bb} = \frac{\sum_{i=1}^M \sum_{j=1}^N I_{bb}(i, j)}{M \times N} \quad (5)$$

The landmarking technique is a relatively new labeling method that is still infrequently employed, particularly on fish objects. This technique is utilized immediately prior to the image being utilized in the training procedure. With this technique, any portion of the object may be marked and become an area that is processed only during training. The  $OR$  will increase to a very high level or even reach unity, resulting in more accurate and efficient extracted feature maps. As a result, the training process will be more efficient, and the recognition results are anticipated to be more accurate and robust.

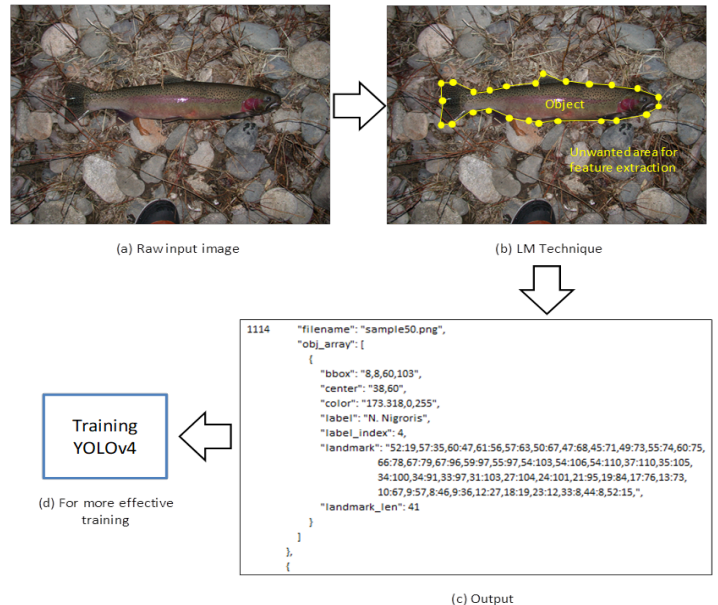


Figure 2: Landmarking technique.

In theory, the landmarking technique will arrange the object's coordinate coordinates into a polygon and create an area on the object. Only objects or portions of objects that have been marked as areas will be extracted later for the training process; disregard other objects outside of the area. This method is utilized concurrently during the labeling procedure (class recognition). In addition to bounding box (bbox), center point, color, label, and index label information, the output of this process includes landmark points and landmark len, which will be utilized to improve the effectiveness of the training process. Figure 2 illustrates the concept of this method of landmarking.

Figure 3 illustrates procedure of the proposed scheme. First, the image data from the BYU dataset were subjected to an image augmentation procedure in order to increase the number of images by means of twisting, rotating, and transitioning. The new fish image dataset was then partitioned into two parts: 80% for the training dataset, which was subjected to the landmarking technique and trained with YOLO v4, and 20% for the testing dataset. Accuracy, precision, recall, specificity, and the F1 score were the outcomes of the classification procedure. Using the CiRA-Core software, this method of landmarking is implemented.

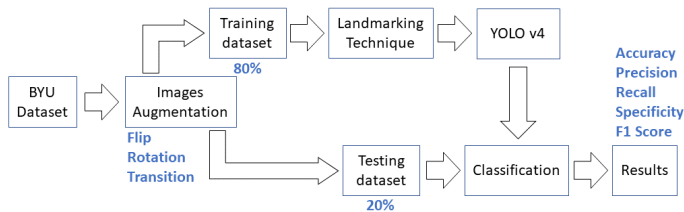


Figure 3: Overview of the proposed scheme.

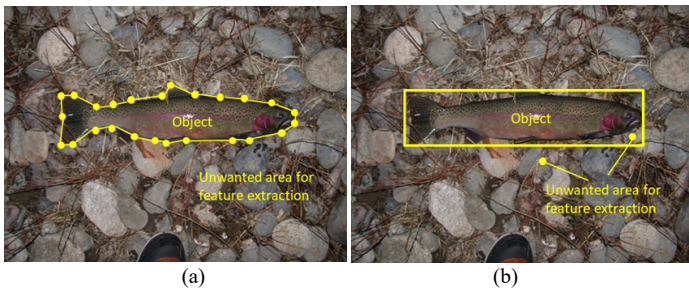


Figure 4: (a) labeling using the landmarking technique (b) conventional and the most commonly labeling technique.

This paper also discusses fish recognition using the most prevalent conventional labeling method, namely the “box squeezing object” method. Figure 4 illustrates the distinction between the landmarking method and the conventional method.

### 2.3. YOLOv4

In this experiment, the detection and classification algorithm is YOLO version 4 (YOLOv4). YOLO is an algorithm for detecting and classifying viral objects. Due to its reasonable detection rate, accuracy, and quick detection time, YOLO has become popular and extensively employed. YOLO operates differently than the majority of other object detection algorithms. A singular neural network is applied to the entire image by YOLO. The network will segment the image into regions, identify the bounding box, and designate a probability value. The probability of classifying each unit within the boundary as an object or not is measured. Finally, the bounding box with the highest value is chosen as the object

separator [23]. It makes the YOLO algorithm suitable for detecting fish as objects in a variety of background conditions, even when the background is in motion or when there are multiple fish in a single image. As depicted in Figure 5 [23], the initial YOLO structure and working system consisted of 24 convolutional layers and two completely connected layers.

The YOLOv4 utilized in this work is the April 2020 release of the fourth development version of YOLO [23]. In this research, YOLOv4 achieves state-of-the-art performance with 43.5% AP operating at 65 FPS in real time on a Tesla V100 with the MS COCO dataset. To achieve these outcomes, they combine Cross-Stage-Partial-connections (CSP), DropBlock regularization, Weighted-Residual-Connections (WRC), Self-adversarial-training (SAT) and Mish -activation, CIOU loss, Cross mini-Batch Normalization (CmBN), and Mosaic data augmentation [31].

As shown in Table 1, YOLOv4 was trained using training data from the BYU dataset and was able to achieve acceptable results with an average loss of 0.01. Training is conducted with 32 data points and 32 subdivisions per iteration. Data enhancement is performed by rotating a threshold between -180° and 180° with 90 steps and comparing it to a threshold between 0.4 and 1.1 with 0.2 steps. Simulating noise and blur during the training procedure is not used to improve data.

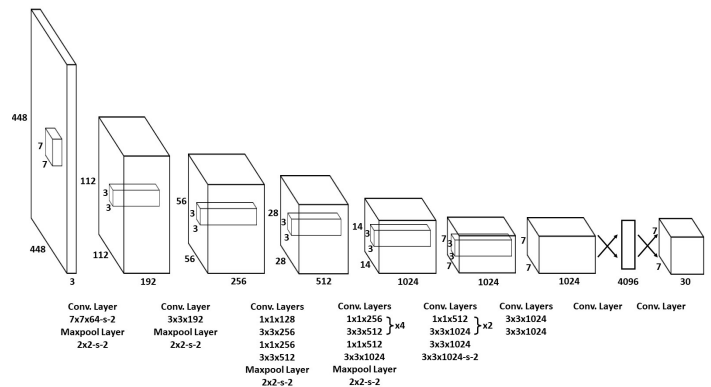


Figure 5: YOLO architecture [22].

### 2.4. Validation Matrix

The confusion matrix is utilized to characterize the model's performance. The confusion matrix is composed of four components: True Positive (TP) and True Negative (TN) for fundamental truth, and False Positive (FP) and False Negative (FN) for fundamental false. TP is when the model correctly detects the object, TN is when the model does not detect because the object does not exist, FP is when the model detects an object incorrectly, including double detecting, and FN is when the model does not detect objects [32].

- Accuracy

One of the evaluation metrics is accuracy. It is defined as the proportion of correctly classified fish to the total number of fish in the test set.

$$\text{Accuracy} = \left( \frac{TP + TN}{TP + TN + FP + FN} \right) \times 100\% \quad (6)$$

Alternately, the following relation represents a comparison between the total number of predictions and the number of accurate predictions as a measure of the model's precision.

$$\text{Accuracy} = \left( \frac{\sum_i^N P_i}{\sum_i^N |Q_i|} \right) \times 100\% \quad (7)$$

In (7),  $\sum_i^N P_i$  is the number of correct predictions, and  $\sum_i^N |Q_i|$  is the total number of predictions.

• Precision

Precision is the ratio of correctly classified fish ( $TP$ ) to positive detection ( $TP + FP$ ). It determines the percentage of precisely classified fish as specified by:

$$\text{Precision} = \left( \frac{TP}{TP + FP} \right) \times 100\% \quad (8)$$

• Sensitivity

Sensitivity is the ratio of correctly classified fish ( $TP$ ) to fundamental truth fish ( $TP + FN$ ), as defined by:

$$\text{Sensitivity} = \left( \frac{TP}{TP + FN} \right) \times 100\% \quad (9)$$

• Specificity

Specificity is determined by the ratio of  $TN$  to the sum of  $FP$  and  $TN$ , as stated below:

$$\text{Specificity} = \left( \frac{TN}{TN + FP} \right) \times 100\% \quad (10)$$

• F1 Score

F1 Score (Measure F) is a metric derived from the average of precision symphony and memory [32], based on the following relationship:

$$\text{F1 Score} = 2 \left( \frac{\text{Precision} \times \text{Sensitivity}}{\text{Precision} + \text{Sensitivity}} \right) \times 100\% \quad (11)$$

### 3. Experimental Results

The proposed method has been evaluated based on the BYU testing data set. The testing data consists of 20% of each image of four fish classes (species) that have been enhanced, as shown in Table 1. At the 50% threshold, the average ultimate detection accuracy is 94.22% and the average classification score for correct detection is 99.42%. The UT Sucker class had the lowest accuracy at 88.57%, while the Kokanee class had the highest accuracy at 100%. Table 3 provides a summary of the results, while Figure 6 depicts the confusion matrix.

Interestingly, the detection continues to run well even though there are actually different types of fish in one class (class BC Trout, Kokanee, and UT Sucker). There are several types of BC Trout, including BC Trout Provo, BC Trout Little Dell, and BC

Trout H Creek in the BC Trout class. These varieties of BC Trout have different colors and scales. As depicted in Figure 7, there are variants of Kokanee Male and Kokanee Female within 1 Kokanee class that have slightly distinct morphologies. Similarly, the UT Suckerfish class includes the fish species UT Sucker, UT Sucker Weber, and UT Sucker Imm Weber, each of which has a slightly unique scale pattern.

Table 3: Experimental results of YOLOv4 with landmarking technique at the 50% threshold.

Threshold: 50%								
Class	Testing data	Correct classification	Wrong classification	Not detect	Double classification	Total prediction	Accuracy (%)	Avg. Classification score (%)
BC Trout	38	35	0	3	0	38	92.11	99.67
Kokanee	24	24	0	0	0	24	100.00	99.93
UT Sucker	35	31	1	0	3	35	88.57	99.20
Steelhead	20	19	0	0	1	20	95.00	99.09
Total	117	-	-	-	-	-	-	-
Average	-	-	-	-	-	-	93.92	99.47

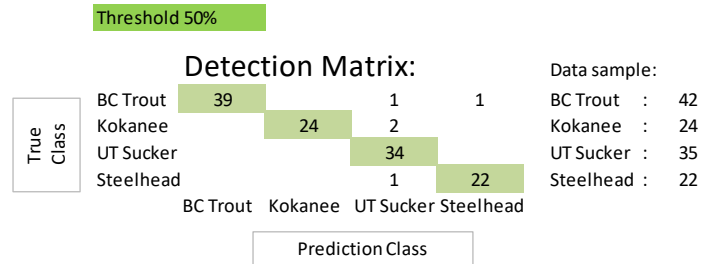
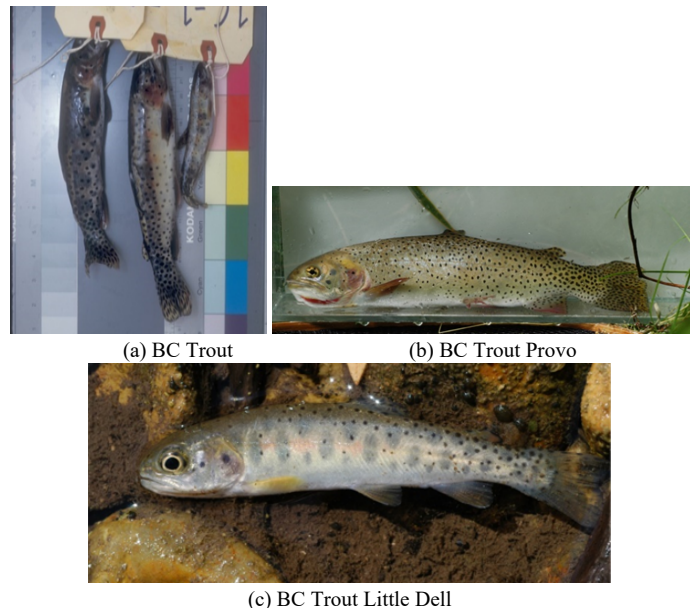


Figure 6: Confusion matrix for experiment results of YOLOv4 with landmarking technique at the 50% threshold.





(d) BC Trout H Creek



(e) Kokanee Female



(f) Kokanee Male



(g) UT Sucker



(h) UT Sucker Weber

Figure 7: Examples of different fish in one class.

The test also revealed that double detection occurs frequently. One fish object was incorrectly identified as two different fish objects with a confidence level below 60% for the incorrect classification. It optimizes the accuracy level by increasing the threshold to 60%, enabling the final average detection accuracy level to reach 96.79% and the average confidence score for correct detection to reach 99.42%. As summarized in Table 4 and Figure 8, the lowest detection accuracy reached 92.86% for the BC Trout class, while the maximum detection accuracy reached 100% for the Kokanee and Steelhead classes. Fish structural deformities are responsible for detection failure. This issue was considered during the development of an algorithm utilizing the Fish-Pak dataset [33].

This work also evaluates the YOLOv4 algorithm model using the conventional “box squeezing object” labeling technique, which is most commonly applied to the same set of test data. With the conventional labeling technique, the final average accuracy is 90.09 % with a confidence score of 99.19 % at the 50% threshold, and the final average accuracy is 92.56 % with a confidence score of 99.19 % at the 60% threshold. At the 50% threshold, the accuracy is 4.59% lower than with the landmarking technique, and at the 60% threshold, it is 4.57% lower. The results of YOLOv4 detection using this conventional labeling technique are summarized in Tables 5 and 6, and Figure 9 depicts the confusion matrix.

Table 4: Experimental results of YOLOv4 with landmarking technique at the 60% threshold.

Threshold: 60%								
Class	Testing data	Correct classification	Wrong classification	Not detect	Double classification	Total prediction	Accuracy (%)	Avg. Classification score (%)
BC Trout	38	35	0	3	0	38	92.11	99.67
Kokanee	24	24	0	0	0	24	100.00	99.93

UT Sucker	35	33	1	0	1	35	94.29	99.24
Steelhead	20	20	0	0	0	20	100.00	99.83
Total	117	-	-	-	-	-	-	-
Average	-	-	-	-	-	-	96.60	99.67

Table 5: YOLOv4 detection results with conventional labeling techniques at the 50% threshold.

Threshold: 50%								
Class	Testing data	Correct classification	Wrong classification	Not detect	Double classification	Total prediction	Accuracy (%)	Avg. Classification score (%)
BC Trout	38	35	1	2	0	38	92.11	99.12
Kokanee	24	21	0	0	3	24	87.50	99.99
UT Sucker	35	27	0	0	8	35	77.14	99.96
Steelhead	20	20	0	0	0	20	100.00	99.87
Total	117	-	-	-	-	-	-	-
Average	-	-	-	-	-	-	89.19	99.74

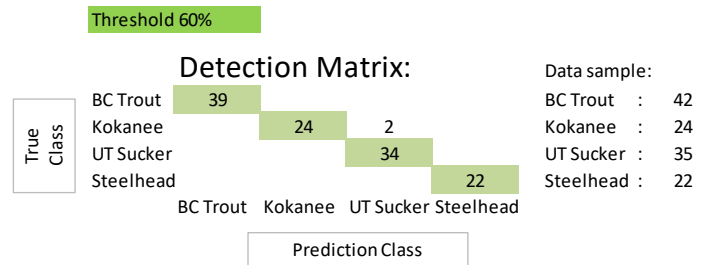


Figure 8: Confusion matrix for experiment result of YOLOv4 with landmarking technique at the 60% threshold.

Table 6: YOLOv4 detection results with conventional labeling techniques at the 60% threshold.

Threshold: 60%								
Class	Testing data	Correct classification	Wrong classification	Not detect	Double classification	Total prediction	Accuracy (%)	Avg. Classification score (%)
BC Trout	38	35	1	2	0	38	92.11	99.12
Kokanee	24	22	0	0	2	24	91.67	99.99
UT Sucker	35	29	0	0	6	35	82.86	99.96
Steelhead	20	20	0	0	0	20	100.00	99.87
Total	117	-	-	-	-	-	-	-
Average	-	-	-	-	-	-	91.66	99.74

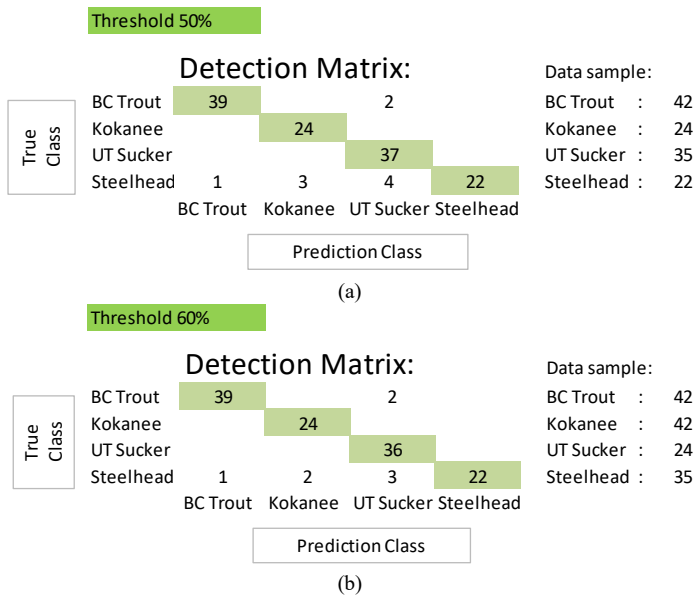


Figure 9: Confusion matrix for experiment result of YOLOv4 with conventional labeling technique (a) at the 50% threshold (b) at the 60% threshold.

#### 4. Conclusion

The purpose of this paper is to propose a method for detecting fish in a variety of background conditions. Combining the landmarking technique with YOLO version 4 is the method. The proposed method was evaluated using the BYU dataset, which contained four different fish species. According to the experimental test results, the detection accuracy is 94.22% at a 50% threshold and 96.79 % at a 60% threshold. This result is greater than the 4.59% at the 50% threshold and 4.57% at the 60% threshold obtained using the conventional labeling method. The results of this trial are considered quite favorable, and the method used is straightforward. The proposed method does not require complicated work steps and is available for implementation.

In future research, it may be possible to automate the landmarking technique in fish using BLOB. Through the implementation of image processing techniques, it is possible to increase precision by adjusting the threshold value. The challenge that will be faced is the ability to detect and separate fish objects from their backgrounds, find the edges of fish objects, and export the coordinate points on the fish edges needed to define the required area.

#### Acknowledgments

This work was financially supported by King Mongkut’s Institute of Technology Ladkrabang, Contract no. 2562-02-01-004. The authors would also like to thank AMI-KMITL for granting the CiRA-Core software license.

#### References

[1] M. K. Alsmadi, I. Almarashdeh, "A survey on fish classification techniques," *Journal of King Saud University - Computer and Information Sciences*, **34**, 1625-1638, 2020, doi: <https://doi.org/10.1016/j.jksuci.2020.07.005>.

[2] S. Zhao, S. Zhang, J. Liu, H. Wang, J. Zhu, D. Li, R. Zhao, "Application of machine learning in intelligent fish aquaculture: A review, *Aquaculture*, **540**, 1-19, 2021, doi: <https://doi.org/10.1016/j.aquaculture.2021.736724>.

[3] S. Villon, D. Mouillot, M. Chaumont, E.S. Darling, G. Subsol, T. Claverie, S. Villéger, "A deep learning method for accurate and fast identification of coral reef fishes in underwater images," *Ecological Informatics*, **48**, 238-244, 2018, doi: <https://doi.org/10.1016/j.ecoinf.2018.09.007>.

[4] A. B. Labao, P.C. Naval, "Cascaded deep network systems with linked ensemble components for underwater fish detection in the wild," *Ecological Informatics*, **52**, 103-121, 2019, doi: <https://doi.org/10.1016/j.ecoinf.2019.05.004>.

[5] A. Jalal, A. Salman, A. Mian, M. Shortis, F. Shafait, "Fish detection and species classification in underwater environments using deep learning with temporal information," *Ecological Informatics*, **57**, 1-13, 2020, doi: <https://doi.org/10.1016/j.ecoinf.2020.101088>.

[6] S. Villon, C. Iovan, M. Mangeas, T. Claverie, D. Mouillot, S. Villéger, L. Vigliola, "Automatic underwater fish species classification with limited data using few-shot learning," *Ecological Informatics*, **63**, 1-6, 2021, doi: <https://doi.org/10.1016/j.ecoinf.2021.101320>.

[7] Z. Ju, Y. Xue, "Fish species recognition using an improved alexnet model," *Optik*, **223**, 1-9, 2020, doi: <https://doi.org/10.1016/j.ijleo.2020.165499>.

[8] A. Salman, S. Maqbool, A.H. Khan, A. Jalal, F. Shafait, "Real-time fish detection in complex backgrounds using probabilistic background modelling," *Ecological Informatics*, **51**, 44-51, 2019, doi: <https://doi.org/10.1016/j.ecoinf.2019.02.011>.

[9] N. F. F. Alshdaifat, A. Z. Talib, M. A. Osman, "Improved deep learning framework for fish segmentation in underwater videos," *Ecological Informatics*, **59**, 1-11, 2020, doi: <https://doi.org/10.1016/j.ecoinf.2020.101121>.

[10] A. B. Hollowed, M. Barange, R. J. Beamish, K. Brander, K. Cochrane, K. Drinkwater, M. G. G. Foreman, J. A. Hare, J. Holt, S. Ito, S. Kim, J. R. King, H. Loeng, B. R. MacKenzie, F. J. Mueter, T. A. Okey, M. A. Peck, V. I. Radchenko, J. C. Rice, M. J. Schirripa, A. Yatsu, Y. Yamanaka, "Projected impacts of climate change on marine fish and fisheries," *ICES Journal of Marine Science*, **70**, 1023-1037, 2013, doi: <https://doi.org/10.1093/icesjms/fst081>.

[11] N. S. Abinaya, D. Susan, R. K. Sidharthan, "Naive bayesian fusion based deep learning networks for multisegmented classification of fishes in aquaculture industries," *Ecological Informatics*, **61**, 1-13, 2021, doi: <https://doi.org/10.1016/j.ecoinf.2021.101248>.

[12] H. Qin, X. Li, J. Liang, Y. Peng, C. Zhang, "Deepfish: Accurate underwater live fish recognition with a deep architecture," *Neurocomputing*, **187**, 49-58, 2016, doi: <https://doi.org/10.1016/j.neucom.2015.10.122>.

[13] H. E. D. Mohamed, A. Fadl, O. Anas, Y. Wageeh, N. ElMasry, A. Nabil, A. Atia, "Msr-yolo: Method to enhance fish detection and tracking in fish farms," in *The 11th International Conference on Ambient Systems, Networks and Technologies (ANT)*, 539-546, 2020, doi: <https://doi.org/10.1016/j.procs.2020.03.123>.

[14] M. S. Ahmed, T.T. Aurpa, M.A.K. Azad, "Fish disease detection using image based machine learning technique in aquaculture," *Journal of King Saud University - Computer and Information Sciences*, **34**, 5170-5182, 2021, doi: <https://doi.org/10.1016/j.jksuci.2021.05.003>.

[15] A. A. D. Santos, W. N. Gonçalves, "Improving pantanal fish species recognition through taxonomic ranks in convolutional neural networks," *Ecological Informatics*, **53**, 1-11, 2019, doi: <https://doi.org/10.1016/j.ecoinf.2019.100977>.

[16] T. Miyazono, T. Saitoh, "Fish species recognition based on CNN using annotated image," in *IT Convergence and Security 2017, Lecture Notes in Electrical Engineering*, **449**, 156-163, 2018, doi: [https://doi.org/10.1007/978-981-10-6451-7\\_19](https://doi.org/10.1007/978-981-10-6451-7_19).

[17] B. S. Rekha, G. N. Srinivasan, S. K. Reddy, D. Kakwani, N. Bhattad, "Fish detection and classification using convolutional neural networks," in *International Conference On Computational Vision and Bio Inspired Computing*, 1221-1231, 2019, doi: [https://doi.org/10.1007/978-3-030-37218-7\\_128](https://doi.org/10.1007/978-3-030-37218-7_128).

[18] A. Taheri-Garavand, A. Nasiri, A. Banan, Y.-D. Zhang, "Smart deep learning-based approach for non-destructive freshness diagnosis of common carp fish," *Journal of Food Engineering*, **278**, 1-9, 2020, doi: <https://doi.org/10.1016/j.jfoodeng.2020.109930>.

[19] K. Cai, X. Miao, W. Wang, H. Pang, Y. Liu, J. Song, "A modified yolov3 model for fish detection based on mobilenetv1 as backbone," *Aquacultural Engineering*, **91**, 1-9, 2020, doi: <https://doi.org/10.1016/j.aquaeng.2020.102117>.

[20] K. D. Lillywhite, D.J. Lee, *Robotic vision lab, brigham young university, fish dataset*, 2013, Available: [http://roboticvision.groups.et.byu.net/Machine\\_Vision/BYUFish/BYU\\_Fish.html](http://roboticvision.groups.et.byu.net/Machine_Vision/BYUFish/BYU_Fish.html).

[21] Z. Liu, X. Jia, X. Xu, "Study of shrimp recognition methods using smart

- networks," *Computers and Electronics in Agriculture*, **165**, 1-10, 2019, doi:<https://doi.org/10.1016/j.compag.2019.104926>.
- [22] J. Redmon, S. Divvala, R. Girshick, A. Farhadi, "You only look once: Unified, real-time object detection," in *2016 IEEE Conference on Computer Vision and Pattern Recognition (CVPR)*, 779-788, 2016, doi:<https://doi.org/10.48550/arXiv.1506.02640>.
- [23] A. Bochkovskiy, C. Y. Wang, H. Y.M. Liao, "Yolov4: Optimal speed and accuracy of object detection," *ArXiv:2004.10934*, 1-17, 2020, doi:<https://doi.org/10.48550/arXiv.2004.10934>.
- [24] C. Li, T. Zhen, Z. Li, "Image classification of pests with residual neural network based on transfer learning", *Appl. Sci.*, **12**, 4356, 2022, doi:<https://doi.org/10.3390/app12094356>
- [25] W. Li, L. Zhang, C. Wu, Z. Cui, C. Niu, "A new lightweight deep neural network for surface scratch detection", *Int. J. Adv. Manuf. Technol.*, **123**, 1999–2015, 2022, doi:<https://doi.org/10.1007/s00170-022-10335-8>
- [26] R. B. Fisher, Y. H. Chen-Burger, D. Giordano, L. Hardman, F. P. Lin, *Fish4Knowledge: Collecting and Analyzing Massive Coral Reef Fish Video Data*; Springer: Berlin/Heidelberg, Germany, 2016.
- [27] S. A. Siddiqui, A. Salman, M. I. Malik, F. Shafait, A. Mian, M. R. Shortis, E. S. Harvey, "Automatic fish species classification in underwater videos: Exploiting pre-trained deep neural network models to compensate for limited labelled data", *ICES J. Mar. Sci.*, **75**, 374–389, 2018, doi:<https://doi.org/10.1093/icesjms/fsx109>
- [28] A. Salman, S. A. Siddiqui, F. Shafait, A. Mian, M. R. Shortis, K. Khurshid, A. Ulges, U. Schwanecke, "Automatic fish detection in underwater videos by a deep neural network-based hybrid motion learning system", *ICES J. Mar. Sci.*, **77**, 1295–1307, 2020, doi:<https://doi.org/10.1093/icesjms/fsz025>
- [29] S. Z. H. Shah, H. T. Rauf, M. Ikram Ullah, M. S. Khalid, M. Farooq, M. Fatima, S. A. C. Bukhari, "Fish-pak: Fish species dataset from Pakistan for visual features based classification", *Data in Brief*, **27**, 104565, 2019, doi:<https://doi.org/10.1016/j.dib.2019.104565>
- [30] W. Xu, Z. Zhu, F. Ge, Z. Han, J. Li, "Analysis of behavior trajectory based on deep learning in ammonia environment for fish", *Sensors*, **20**, 4425, 2020, doi:<https://doi.org/10.3390/s20164425>
- [31] N. D. Marom, L. Rokach, A. Shmilovici, "Using the confusion matrix for improving ensemble classifiers," in *2010 IEEE 26-th Convention of Electrical and Electronics Engineers in Israel*, 555-559, 2010, doi:<https://doi.org/10.1109/EEEL.2010.5662159>.
- [32] D. H. T. Minh, D. Ienco, R. Gaetano, N. Lalande, E. Ndikumana, F. Osman, P. Maurel, "Deep recurrent neural networks for winter vegetation quality mapping via multitemporal sar sentinel-1," *IEEE Geoscience and Remote Sensing Letters*, **15**(3), 464-468, 2018, doi:<https://doi.org/10.1109/LGRS.2018.2794581>.
- [33] A. Kuswantori, T. Suesut, W. Tangsrirat, N. Nunak, "Development of object detection and classification with YOLOv4 for similar and structural deformed fish," *EUREKA: Physics and Engineering*, **2**, 154-165, 2022, doi: 10.21303/2461-4262.2022.002345

## Accuracy Improvement-Based Wireless Sensor Estimation Technique with Machine Learning Algorithms for Volume Estimation on the Sealed Box

Kitipoth Wasayangkool, Kanabadee Srisomboon, Chatree Mahatthanajatuphat, Wilaiporn Lee\*

Department of Electrical and Computer Engineering, Faculty of Engineering, King Mongkut's University of Technology North Bangkok, Thailand

### ARTICLE INFO

Article history:

Received: 22 February, 2023

Accepted: 24 April, 2023

Online: 21 May, 2023

Keywords:

RSSI

Volume Estimation

Machine Learning

Neural Network

### ABSTRACT

Currently, the quality and quantity of product must be inspected before transporting. Currently the popular unsealing box product inspecting is performed by weighing the box where the errors occur according to the tolerance of the weighting machine and tolerance weight of the product. On the other hand, the quantity of product can be inspected automatically using the image processing and recognition where the sealed box needs to be unpacked which is difficult to be implemented in practice. Then, the error in product transportation causes a loss profit of for the vendor and losing the reliability from customers. In this paper, we proposed a new volume estimation technique to estimate the product quantity in the sealed box using RSSI with machine learning for improving the monitoring accuracy. The proposed system includes one transmitter on the top and five receivers at bottom of the package. Based on practical environment, we align the product's pattern inside the boxed package into two cases including horizontal/vertical aligned pattern and random pattern. In the experiment, we compare the volume estimation accuracy of five machine learning techniques including linear regression, logistic regression, Naïve Bayes, KNN, and NN. From the results, the NN method provide the highest volume estimation accuracy among others and consumes the shortest estimation time. NN presents accuracy as 99.4% and consumes 6.51 milliseconds of estimation time. Moreover, for protecting the products from the delivery process, shockproof material must be put to cover the product in the box. Three shockproof types are considered in our experiment such as bubble wrap, paper, and airbag and our proposed system is considered all kinds of shockproof situations. The suggested method can estimate the volume of products without necessitating their opening or destruction. The suggested approach is also resistant to the impacts of packaging cushioning material.

### 1. Introduction

To the COVID-19 situation, the number of online purchases worldwide are grown up to 5.2 trillion US dollars and will reach 8.2 trillion US dollars in 2026. Figure 1 shows the rising trend of online marketing sales [1-3]. In Thailand, online shopping orders have increased by an average of 45% per year and they will rise with the rate steadily [4-5]. According to the new commodity trading behavior, customers order the products via online platform

and the traders stage the products before sending to the customers. Once the number of orders is high, the error easily happens. Therefore, the bounce rate increased from approximately 8% in 2007 to 22% in 2017 and is anticipated to continue rising [6-8]. One of the reasons to return products is the incorrect number of product or a mismatch with the user order. Therefore, the monitoring quantity of the product inside the package before sending it to the customer is an important part of quality control and inspection to prevent mistakes and the associated expenses.

\* Corresponding Author: Wilaiporn Lee, KMUTNB, [wilaiporn.l@eng.kmutnb.ac.th](mailto:wilaiporn.l@eng.kmutnb.ac.th)



There is a requirement for varying quantities of merchandise since the behavioral characteristics of each transaction are distinct. Even though the contents of the parcel are the same, the number of objects in each parcel box will vary.

The entrepreneurs must verify their own cargo before delivering it to the carrier by implementing a quantity verification inspection procedure at the end. However, human error may occur if this strategy is used. In addition to losing energy, manufacturing delays may also result. Therefore, technology has been developed to assist with this verification.

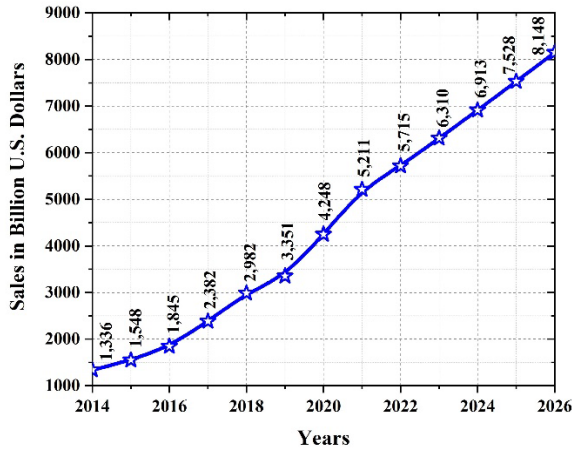


Figure 1: The ongoing expansion of internet shopping in 2014 – 2026.



Figure 2: RFID reader and RFID tag.

The number of products can be verified via many solutions such as directly counting by humans, image processing and recognition, RFID technology or calculate from the volume estimation methods. RFID scheme is one of the common methods used in worldwide. The RFID tag is attached to the products and used to count the number of products within the package. This approach is regarded as used with certain items; however, it cannot be used for some products such as water, seeds or many overlapping products because the RFID tag gets obscured, leading to measurement inaccuracies. In addition, this method is expensive due to the high cost of the RFID reader and the requirement to purchase RFID tags as the number of products. Figure 2 demonstrates an example of an RFID system [9-10]. Another technique is a weight meter. For the industry scale, the high-resolution weight meter is used for a quantity verification inspection procedure at the end that provides a high level of precision, but it is a premium cost that the high-resolution weight meter shows in Figure 3. For local commercial scales, the general

weight meter is commonly used because this meter has low complexity and cost. However, this method has important restrictions the size of the items cannot exceed the scale's capacity, and it requires calibration and maintenance from the specialist inspector. Moreover, some products may have the same weights, but different volumes. Then, the only weight meter method may not be appropriate to check the number of products. On the other hand, if the volume of products can be calculated, the number of products can be exactly determined. Therefore, volume estimation should consider for estimating the number of products.



Figure 3: The inspector weighting machine.

Image-based volume estimation [11-12] is widely used in many researches. This method utilizes image processing techniques with image recognition to estimate the volume of an product. It requires to capture photographs from a variety of perspectives as well as adjust the lighting and clarity of the images. This method necessitates a visual inspection of the object to compute the volume, i.e., the package box must be opened. Consequently, image-based volume estimation method is unsuitable for determining the number of products already packed into a package.

Nowadays, the wireless sensors that operate on WI-FI technologies are unquestionably the most popular and frequently utilized today. It is a technology that is easily accessible and widespread. There are several uses of wireless sensor, such as applications for identifying the position of people or objects in indoor and outdoor environments [13-16], estimation of a person's posture inside a room [17-18], etc. There are several popular techniques for estimating the positions of objects, including the received signal strength indicator (RSSI), the time-of-arrival (TOA), the time difference of arrival (TDOA), and the angle of arrival (AOA) [19-24]. Each method has the unique advantages and disadvantages, including varying degrees of complexity, the precision accuracy, or the energy consumption. Due to its simplicity and low complexity, the RSSI method is the most utilized. The transmitter and receiver are the primary devices used to measure RSSI. The RSSI value delivered from the transmitter to the receiver will vary based on the environment, considering either the distance between the transmitter and receiver or the thickness of objects that obstruct the signal between the transmitter and receiver. These variations in RSSI readings can be utilized to estimate the position of a person or item [25-27]. From the RSSI measurement concept, we apply the RSSI value to estimate the volume of product in the sealed package for verified the quantities of merchandise.

In [28], we proposed the volume estimation method in the sealed package by applying the RSSI measurement. The proposed system installs 1 transmitter and 4 receivers to measure the RSSI value for improving the volume estimation accuracy by utilizing 4 machine learning algorithms including linear regression, logistic regression, Naïve Bayes, and K-nearest neighbors (KNN). From the experimental results, we found that the KNN method presented the highest volume estimation accuracy at 94%. However, regarding the arrangement of objects in the parcel box, only the horizontal arrangement was evaluated in this work. In the practical transit of packages, objects can be arranged in a variety of patterns. In addition, shockproof materials are normally put on the products for protecting it from damage in the delivery process. There are several types of cushioning materials; therefore, the performance and precision of the proposed volume estimation technique must consider the effect of the type of cushioning materials on the RSSI value.

In this paper, an RSSI measurement of wireless sensor and machine learning analysis-based system for estimating the product quantity under three types of sealed packages is presented. According to the RSSI characteristic, the signal is transmitted from the transmitter and the received signal is received by the receiver. Once the received signal strength is attenuated by the object which obstructs the transmission path, then we can utilize the received signal strength for estimating the amount of object in the sealed box without unpacking the box. We also evaluated the quantity of equipment, the number of products, and consider all of pattern of packed inside the package box in all instances. Four protection environments are considered including no cushioning material and the three commonly used cushioning materials: bubble wrap, paper, and airbags. For improving the accuracy, we apply five machine learning (ML) approaches, including linear regression, logistic regression, Naïve Bayes, KNN, and neural network (NN) for estimation of the volume of items in the material box. Based on the results of the experiment, the ML approach could be used to estimate the real volume of products with efficiency and precision. The provided system estimated the product with an accuracy of 99.40% using the NN method. However, the disadvantage is the long training time. On the other hand, the logistic regression is not appropriate to be implemented in volume estimation since it presents the lowest accuracy and consumes long estimation time. Regarding the optimal number of devices, it was determined that one transmitter and five receivers supported the greatest probability of placement. In calculating the number of items, the proposed system will be able to support the packaging of products in the absence of cushioning materials and with all three types of cushioning objects.

## 2. The Related Knowledge

In this section, we describe the RSSI calculation concept and five well-known ML methods. The considered ML methods are very popular on many applications and appropriate for the characteristic of RSSI data.

### 2.1. The Received Signal Strength Indicator (RSSI)

RSSI collecting techniques are utilized for a variety of different environments, including indoor or outdoor positioning systems, and determining distances based on RSSI measurements. In addition [29-32], the RSSI value has a low level of complexity and

a short time to store the data, allowing low-cost and widely available storage devices to be utilized. Identifying the position of a person or object is an example of an application that uses the RSSI value to compute distance using the RSSI's distance measurement equation. The equation for computing the distance measurement from the RSSI level is shown in (1).

$$RSSI = 10 \log_{10} \frac{P}{1mW} \quad (1)$$

where  $P$  is the signal's strength (W) and  $RSSI$  is the RSSI value (dBm). Typically, the RSSI will fluctuate as the distance between the transmitter and receiver changes or when barriers are present.

### 2.2. Machine learning technology

Machine learning is an intelligent system capable of analyzing data to propose or predict outputs to assist in decision-making. As the system accumulates more data, machine learning can help it make better decisions. This research utilizes linear regression, multinomial logistic regression, Naïve Bayes, KNN, and NN. Following is a detailed discussion of each technique.

#### 2.2.1. Linear regression

Regression analysis is the application of machine learning where the prediction line of the learning model is generated by fitting the linear equation with the data. To estimate the output value, the new data is fed to the learning model which predict the output value from the generated prediction line. This technique is straightforward and efficient for studying linear data. It present a high degree of precision, then the linear regression equation is shown in (2).

$$y = \theta_0 + \theta_1 x_1 + \dots + c \quad (2)$$

where  $y$  is the desired output,  $\theta_i$  is the slope of the linear line of  $i$  data,  $x$  is the input feature, and  $c$  is the constant.

The mean square error (MSE) approach is applied as the cost function of the training process. From equation, the sum of the mean errors is shown in (3).

$$J(\theta) = \frac{1}{2m} \sum_{j=1}^m [y(x^{(j)} - y^{(j)})]^2 \quad (3)$$

where  $x^{(j)}$  is the input feature,  $j$  is the point of the, and  $y^{(j)}$  is the desired result.

#### 2.2.2. Multinomial logistic regression

Logistic regression is a technique for predicting the binary output which is normally used in binary classification. In this study, we utilize data with the discrete outputs by implementing the multinomial logistic regression which can be considered as multi-class classification. This regression technique's core concept is to establish a decision boundary between the dataset to classify the type of data. If the data is evenly distributed, it will be difficult to classify it, and the error easily happens. When new data are obtained, the model decides based on previously created data lines. The multi-class logistic regression equation is illustrated in (4).

$$Y = \frac{1}{1 + \exp^{-(\alpha_0 x_0 + \alpha_1 x_1 + \dots + c)}} \quad (4)$$

where  $Y$  is the probability that the input scenario occurs,  $\alpha_i$  is the independent variable of  $i$  data,  $x$  is the clarify variable, and  $c$  is the constant.

The logistic regression equation is therefore modified by applying the cost function from equation (3). Logistic regression's cost function equation is presented as (5).

$$J(\theta) = -\frac{1}{m} [\sum_{j=1}^m y^{(j)} \log(y_{\theta}) + (1 - y^{(j)}) \log(1 - y_{\theta})] \quad (5)$$

where  $y_{\theta}$  is the preceding base for logistic regression, and  $x^{(j)}$  is the considered data, and  $y^{(j)}$  is the average result of the data considered.

### 2.2.3. Naïve Bayes

The Naïve Bayes method classifies the class of input data according to probability-based distribution of the data. In terms of the Naïve Bayes predictions, the conditional probability is determined based in the likelihood function to categorize the data class. The probability that the input data becomes a member of the considered class can be calculated as

$$P(y|x) = \frac{P(x|y)P(y)}{P(x)} \quad (6)$$

where  $P(y)$  is the probability of output class of the new data,  $P(x)$  is the probability in each class of the dataset,  $P(x|y)$  is the probability of the dataset correlating to new data and  $P(y|x)$  is the probability of new data correlating to the dataset.

The solution in the Naïve Bayes method is typically presented as discrete data. According to the considered continuous data, the probability density function (pdf) distribution equation must be used, and it can be expressed as the following equation (7).

$$P(x|\mu, \sigma^2) = \frac{1}{\sqrt{2\pi\sigma^2}} \exp\left(-\frac{(x-\mu)^2}{2\sigma^2}\right) \quad (7)$$

where  $\mu$  is the mean value of the input data, and  $\sigma$  is the standard deviation of the input data.

### 2.2.4. K-Nearest Neighbor (KNN)

K-nearest neighbor compares the new data to the current data in the dataset to determine the similarity based on their distance. By predicting the result, KNN determines the class of new data from K nearest members of the data in the dataset. KNN measures the distance between the new data and the member in the dataset through the Euclidean distance ( $d$ ) which is expressed in (5). In this approach, the processing time depends on the data volume of the dataset.

$$d = \sqrt{(x_2 - x_1)^2 + (y_2 - y_1)^2} \quad (8)$$

where  $d$  is the distance between the new data and the existing dataset,  $(x_1, y_1)$  is the point of the data in dataset,  $(x_2, y_2)$  is the point of the test data or new data.

### 2.2.5. Neural Network (NN)

A neural network is an artificial intelligence technique that trains a machine to process information in a manner base on the human brain. Deep learning is a method of machine learning that utilizes interconnected nodes or neurons, resembling the layered structure of the human brain. This produces an adaptive platform that allows computers to learn from their mistakes and continuously improve. Basically, NN consists of three layers: the input layer, the processing layer, and the output layer. The input layer mainly consists of one layer and delivers data to the hidden levels. The processing layer is a hidden layer that contains the number of neurons. Depending on a particular optimal, the number of neurons on hidden layers can be increased to improve precision. The output layer is the last layer responsible for weighting each neuron or set of outputs using the values from the hidden layer to achieve the most accurate results. The NN structure is seen in Figure 4.

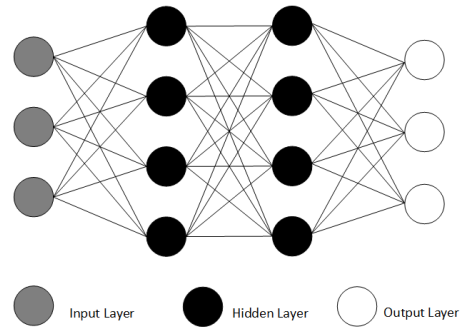


Figure 4: The structure of the neural network

The output of the previous step is fed to the system as the NN training process iterates over the data in the dataset to improve decision-making assume  $L$  is the output of the present hierarchy. In a process known as back propagation, the output of layer  $L$  is transmitted back to layer  $L - 1$ . Stochastic gradient descent is used in this procedure to minimize the error which is illustrated in (9).

$$e = \frac{1}{2} \sum [t_k - a_k]^2 \quad (9)$$

where  $e$  is the error value,  $t_k$  is the average result for node  $k$ , and  $a_k$  is the error of the excitation effect from  $k$  nodes.

The equation for adjusting the decision weight is shown in (10).

$$\theta_{kj} = \theta_{kj} - \alpha \delta_j^l a_j^{l-1} \quad (10)$$

where  $\theta_{kj}$  is an improvement in the hidden layer, and  $\delta_j^l$  is the difference between the error value and the result.

When the sigmoid function is invoked, the equations for orienting the model configuration in the hidden layer appear in (11).

$$\delta_h^l = a_h^l (1 - a_h^l) \sum_j \delta_j^{l+1} \theta_{hj}^{l+1} \quad (11)$$

where  $\delta_h^l$  is the result of considering all nodes in the hidden layer.

### 3. Methodology of the proposed system

In terms of measuring and storing RSSI values, the experiments were done in a noise-free chamber room, as seen in Figure 5. We use MCU ESP32 as a transmitter and the receivers. We install the transmitter on top of the station and the receivers are installed at the bottom of the station, and a test box is placed at the middle of the station. Then, the RSSI values are collected and transmitted to be further processed according to the procedure.

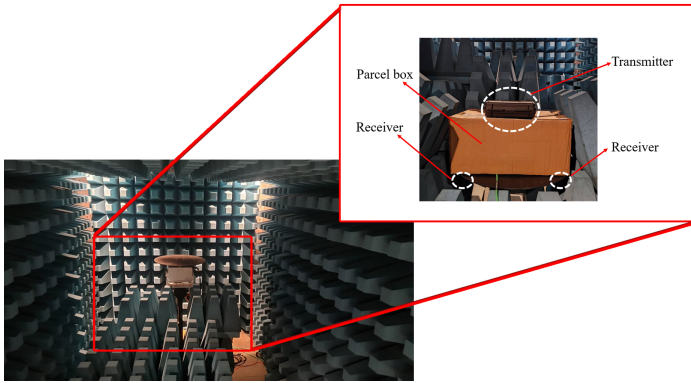


Figure 5: The proposed setup

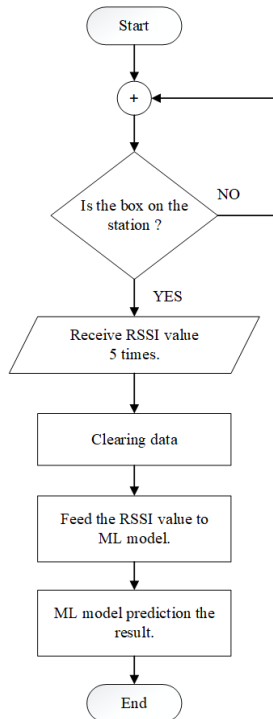


Figure 6: Flowchart of the proposed system

In this research, the RSSI value was collected in accordance with the flowchart depicted in Figure 6, beginning with the determination of whether or not a package was present on the measurement station. When there is a package at the station, the RSSI value will be collected five times from each receiver. Then, the system will transmit it to the clearing data in order to eliminate interference. The value will then be transmitted to a machine learning (ML) model for processing in order to forecast the result. The accuracy of estimation can be determined by

$$Acc = \frac{1}{m} \sum [y_{pred} - y_{actual}]^2 \quad (12)$$

where  $Acc$  is the accuracy rate,  $y_{pred}$  is the result of prediction, and  $y_{actual}$  is the actual value,  $m$  is amount of sample.

#### 3.1. Experimental setup

In this section, we describe the experimental environment of the proposed system. In the experiment, the size of product is 8 cm. x 8cm. x 3 cm with the weight of 100 g. The size of box is 25 cm. x 35 cm. x 25 cm. To estimate the quantity of product in the sealed box, we collect the RSSI values from receivers under different volumes of product in the box where the determined volume are 0%, 20%, 40%, 60%, 80% and 100%. Then, we collect 2000 records of RSSI for each testing volume. Moreover, for weight measuring, we also collect 2000 records for each testing volume.

Firstly, we consider 5 cases of receiver's number that are 1 to 5 of receivers for finding the optimum RSSI value that cover all the object patterns. Secondly, we present the object patterns in which we arrange our object in two cases: pattern alignment and random pattern. Thirdly, we consider four our experimental environments including one non-protection product and three protection products. Additionally, we show the performance comparison of the proposed system under 5 ML methods including linear regression, logistic regression, Naïve Bayes, K-nearest neighbors, and neural network.

##### 3.1.1. Receiver installation and the proportional number of receivers.

In the experiment, we consider the proportional number of receivers. We consider 5 cases by increasing the number of receivers from 1 to 5 receivers. For example, we placed a 4-receivers in each corner of the box, as depicted in Figure 7(a), and a 5-receiver by mounting an additional receiver in the middle of the bottom of the box, as depicted in Figure 7(b), to examine the accuracy when the number of receivers varies.

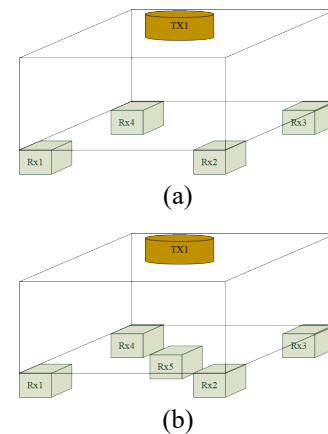


Figure 7: The example of 4 and 5 receivers in our experimental.

As illustrated in Figure 7, five receivers were recorded to establish the optimal number of sensors. For all considered ML methods, it was discovered that the efficiency of each method was better than other cases because a fifth receiver was added to the center of the bottom of the box. Then, we create a system with 1 transmitter and 5 receivers to accommodate all possible scenarios.

The performance comparison of volume estimation accuracy when varying the number of receivers depicted in Figure 8.

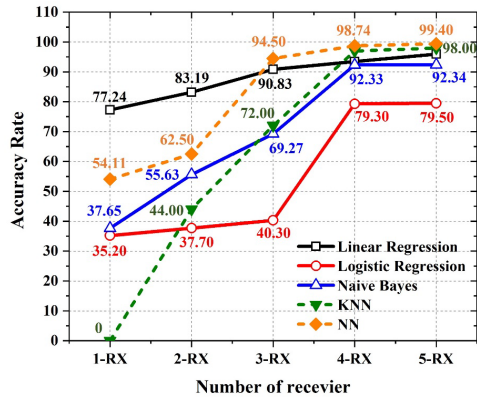


Figure 8: The performance comparison of volume estimation accuracy when varying the number of receivers.

### 3.1.2. The object alignment

In this section, the patterns of the object alignment is described which can be divided into two distinct categories, namely aligned pattern and random pattern. The item is arranged by increasing its volume from 0 to 100 percent in 10 percent increments. For instance, if the item occupies 10% of the box, we align the object in six situations, such as left, right, front, back, bottom, and random pattern, and then measure the RSSI between the transmitter and five receivers.

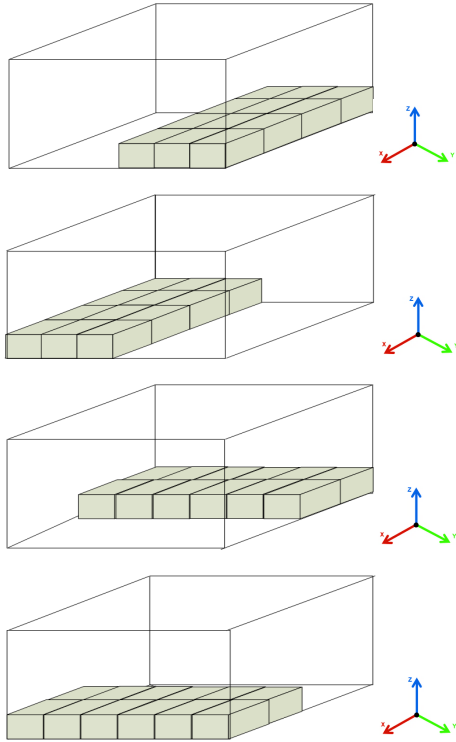


Figure 9: 10% of products' pattern that initial arrangement of items begins in the horizontal plane of the XY plane.

To examine the object layout within the box, we separated the arrangement of objects within the box into three distinct configurations. As illustrated in Figure 9, firstly, we present 10%

of products' pattern that initial arrangement of items begins in the horizontal plane of the XY plane and subsequently increases along the Z axis to achieve 100 percent. The second pattern is to arrange the 10% of items on the YZ or XZ side planes and add up to 100 percent, as seen in Figure 10. In the final form, as seen in Figure 11, 10% of objects are randomly distributed in the box with no alignment between the objects.

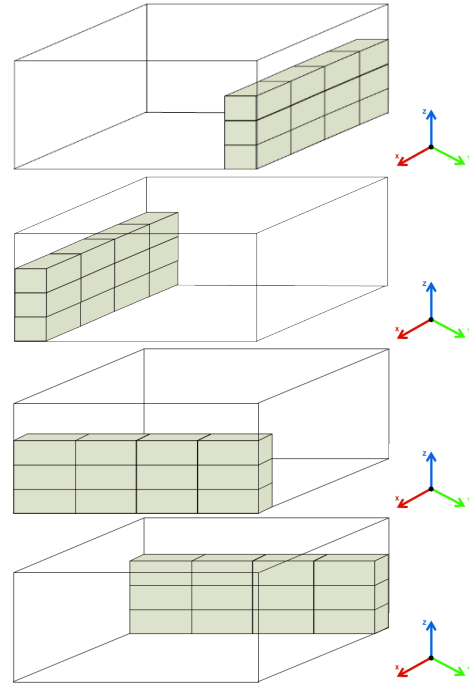


Figure 10: The second pattern is to arrange the 10% of items on the YZ or XZ side planes.

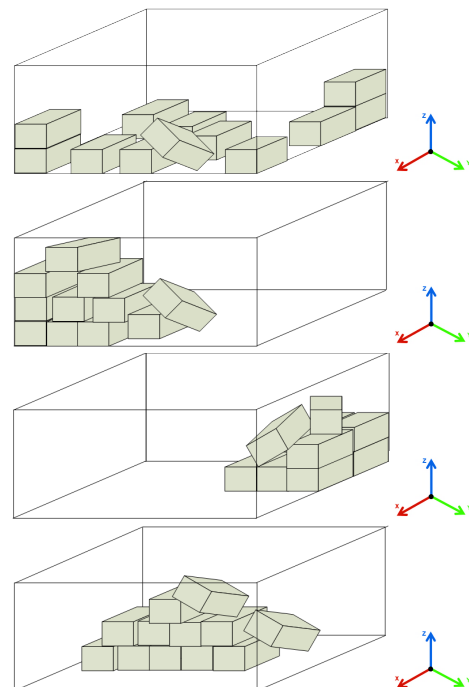


Figure 11: 10% of objects are randomly distributed in the box with no alignment between the objects

3.1.3. Data Cleansing

Before applying the ML techniques to estimate the volume of product, data cleansing is one important step to perform. When we obtain five RSSI values from 1 round of data accumulation, we evaluate the RSSI values, and we clean data by removing the RSSI value that differs from the measurement and replaced with the average from all other values before storing into the database. The clearing data algorithm is shown in Figure 12.

Table 1 shows the effectiveness comparison between the operating on data that was cleaned and not-cleaned. It was discovered that the volume estimation accuracy of the cleaned data is higher than the performance system of not-cleaned data. Moreover, from the results, we can conclude that cleansing data is an important procedure, especially for linear regression, KNN, and NN methods.

Table 1: Data outline clearing.

Techniques	The volume estimation accuracy of non-cleansing data (%)	The volume estimation accuracy of cleansing data (%)
Linear regression	85.70	95.93
Logistic regression	79.10	.7950
Naïve Bayes	82.46	.9240
KNN	94.80	98.00
NN	96.93	99.40

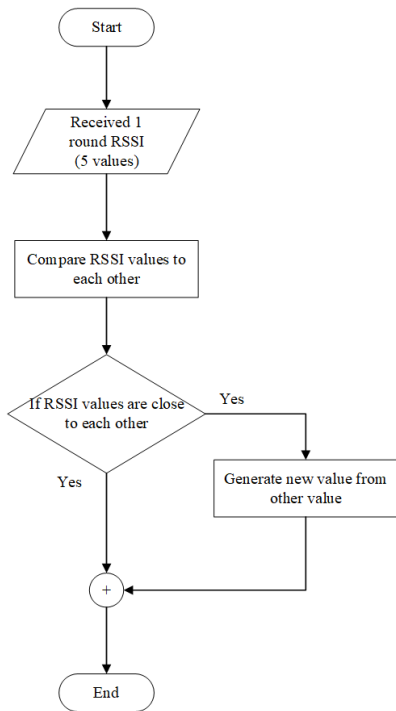


Figure 12: Flowchart of clearing data algorithm.

3.2. Comparison of methods efficiency

In our experiment, the volume estimation in the proposed system is considered under three object alignment including horizontally aligned, vertically aligned, and randomly patterns and we increase the number of items in the sealed package raising from 0% to 100% in 10% increments. The total records are 84,000 records that is separated to 70% for training dataset and 30% for

testing dataset. The quality of the system was evaluated using the following five analytical methods: linear regression, logistic regression, Naïve Bayes, KNN, and NN.

The results of the experiments shown in Table 1 indicated that the efficiency of five receivers yielded the following results: the NN approach shows the highest accuracy, 99.40%, while KNN provides a value of 98.00%. The accuracy of linear regression and Naïve Bayes is 95.93% and 92.4%, respectively. The logistic regression also provides an accuracy of at least 79.50%. The investigation revealed that NN shows the highest accuracy because it learns the characteristic of RSSI information according to the object storing pattern and generates the weights through back propagation algorithm. It can be seen that characteristic of the RSSI values from each transmitter is not correlated to others then NN benefits from data from those transmitters. In the case of KNN, it shows a high accuracy since it estimates the output value by determining all data from the database. Consequently, the system achieves high precision.

In the case of linear regression, it generates a linear equation from an existing dataset and will use this equation to predict the output when the new data is coming into the system. In our experiment, this method gives a high precision of output estimation because the dataset of our system is a nearly linear pattern that proper to this method. Conversely, Naïve Bayes will do a probabilistic analysis of the new data. The new data will be verified that it has a probability to be similar to a group in the data in database and deciding to provide new information to that group based on that comparison, may improve the efficiency of data management. To categorize data types, the logistic regression method divides the data's boundaries using a line. If the data are highly similar, it will be unable to distinguish between the different types. Therefore, this procedure is less accurate than alternative ways.

Additionally, we determine the volume estimation time of each methods. Table 2 shows the time spent on each technique. It was discovered that the KNN approach did not require any training time, i.e. the KNN model measures simply the distance between old and new data to make decisions. On the other hand, it takes a long volume estimation time and will be longer if the database is huge. The Naïve Bayes consumes 14.72 milliseconds of training time since it only determines the average and standard deviation (SD) values to be used as the learning model. The linear regression approach and logistic regression consumes 19.10 milliseconds and 828.00 milliseconds, respectively. Finally, the NN consumes the longest training time, 365,060.00 milliseconds, since its training algorithm is highly complex.

Table 2: Time usage of 5 machine learning techniques.

Techniques	Time of training (ms)	Time of test (ms)
Linear regression	19.10	7.68
Logistic regression	828.00	7.24
Naïve Bayes	14.72	8.42
KNN	-	25.97
NN	365,060.00	6.51

From the aforementioned testing findings, it can be concluded that the approach with the best accuracy was the NN method and consumes the shortest estimation time of 6.51 milliseconds. Since the model will experiment by weighting each variable on the new

data set and generating predictions, it takes longer than other methods to predict. Next, the second most accurate method was KNN, which made predictions in 25.97 milliseconds. This approach used less time than the previous one since it calculated the distance between new and old data. However, if there is a huge quantity of historical data, this method will take a considerable amount of time to predict. The Naïve Bayes technique predicts in 8.42 milliseconds once it calculates the probability that the new data belong to the considered group. Linear regression and logistic regression predict in 7.68 and 7.24 milliseconds, respectively, using the new data mapping method to the linear line and data, respectively.

Based on the results of the experiments, it can be concluded that the NN methodology is the best method since it presents the most accurate and shortest volume estimation time, while logistic regression seems to be the worst. Therefore, the NN methodology can be considered as the most appropriate method to be implemented in the volume estimation application.

3.3. The effect of shockproof to RSSI

3.3.1. Type of shockproof

In addition, this research examines the effects created by shock-resistant materials utilized in transportation. As indicated in Table 3, the impacts of various shockproof materials such as bubble wrap, paper, and airbag are evaluated using RSSI values. In the case of bubble airbags filling the boxes to their maximum capacity, the RSSI values were observed to vary by 1–2 dBm relative to the empty boxes. The measured RSSI difference for the bubble wrap was between 5 and 7 dBm. In the latter instance, the difference was 7–10 dBm, as is the case with paper. The 100% of the capacity of the box has been padded with shock-absorbing material, according to all dimensions. Figure 13 depicts a shockproof material type.

Table 3: The differential of RSSI values with shockproof.

Type of Shockproof	RSSI value: Free space (dBm)	RSSI value: 100% of shockproof (dBm)	The differential RSSI values (dBm)
airbag	-26 to -27	-27 to -28	±1
Bubble wrap	-26 to -27	-31 to -33	±(7 – 5)
paper	-26 to -27	-33 to -36	±(10 – 7)

3.3.2. Accuracy rate with shockproof

Considering the real circumstances of transport that need the use of cushioning material to prevent potential damage to the object during transit, we pack the object with padding. Consequently, at this stage, measurements and processing were conducted to establish the impact that happens when the shockproof material fills the remaining space of the box. Airbag shockproof, bubble wrap and paper shockproof materials are popular to be used and we evaluate these materials in our experiment. The impact was precisely quantified and compared to a casing that lacked a shockproof coating. Table 4 demonstrates that the precision findings are like the previous results, i.e., in the case of the 5 receivers when the paper is used as a shockproof. The NN model has the greatest performance at 98.95%, followed by the KNN model at 97.25% and the linear regression model at

93.67%. The accuracy of Naïve Bayes and logistic regression was 90.22 and 79.03 percent, respectively. The precision of the other two materials, bubble wrap and airbag shockproof, is greater than that of paper. The airbag shockproof has the smallest effect on the RSSI quantification. The accuracy was determined to be (0-1) % different from that in the absence of cushioning material, and (1-2) % different from that in the presence of bubble wrap. In the last instance, the paper had an accuracy variation of (1-3) %. The conclusion is that RSSI measurement still produces accurate results when packing cushioning in shipping boxes.

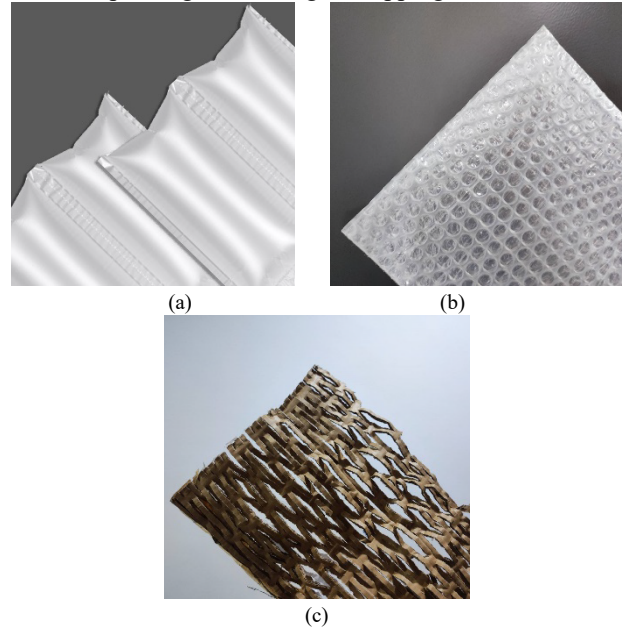


Figure 13: Types of shockproof.

In the previous section, the effectiveness of each cushioning material was evaluated. Different sorts of cushioning materials may be utilized in actual transportation environments. In this consideration, the next part of the experiment includes the situations of quantification without cushioning in comparison to all potential cases. There were 84,000 records of experimental data, which included non-shockproof, item with airbag shockproof, object with bubble wrap, and paper shockproof. The test results are evaluated and shown in Table 4 by analyzing the RSSI data from all instances that were trained on different models. As a result, NN shows the highest performance for all shockproof environment while the logistic regression shows the worst. It can be mentioned that logistic regression and Naïve bayes are the learning algorithms for classification application therefore they show lower performance than others. Moreover, we compare the performance for all situation as depicted in figure 14. It was determined that the accuracy gained from the prediction of case 5 receivers using the NN approach was still the greatest at 99.07%, followed by KNN at 98% and linear regression at 95.10%. The results for Naïve Bayes and logistic regression were 92.20 percent and 79.28 percent.

Moreover, we compare the best and worst performance of the ML implemented techniques to the weight measuring technique which are shown in table 5. From the experimental results, weight

measuring technique presents 91.31% of accuracy where the tolerance value of the weight machine is 5%. As compared to the highest and lowest accuracy of volume estimation by ML techniques, the NN presents higher accuracy than weight measuring where logistic regression presents lower accuracy. It can be noticed that once NN learns the characteristic of RSSI values according to the product quantity, it present higher accuracy. On the other hand, the framework of logistic regression is not appropriate to predict the continuous value of quantity estimation, therefore it presents lower accuracy.

Table 4: The accuracy of volume estimation considering non-shockproof and three shockproof environments.

Techniques	Non-shockproof (%)	Airbag shockproof (%)	Bubble warp (%)	Paper shockproof (%)
Linear regression	95.93	95.45	93.82	93.67
Logistic regression	79.50	79.42	79.29	79.03
Naïve Bayes	92.34	92.14	90.95	90.22
KNN	98.00	98.00	97.55	97.25
NN	99.40	99.23	98.85	98.95

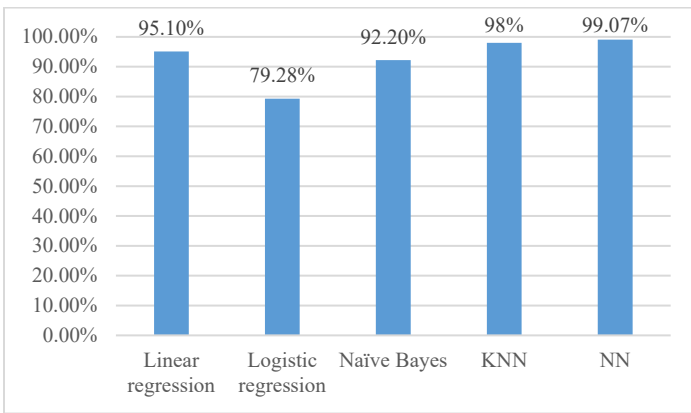


Figure 14: A performance comparison of overall performance

Table 5: Accuracy of unpack boxes volume estimation.

Accuracy rate of weighting machine (%)	Accuracy rate of logistic regression (%)	Accuracy rate of NN (%)	Accuracy rate of weighting machine (%)	Accuracy rate of logistic regression (%)
91.31	79.28	99.07	91.31	79.28

#### 4. Conclusion and future work

In this study, an experiment to measure and estimate the quantity of products in non-open or destroy-sealed box containing different layouts of objects was presented. Using a receiver created from 5 nodes of MCU ESP32, a total of 84,000 records of RSSI are collected under noiseless environment and used to estimate the quantity of product using the ML techniques including linear regression, logistic regression, Naïve Bayes, K-nearest neighbors, and neural network. The impact of the

packaging's cushioning material and various patterns of product in the sealed package are examined. Moreover, we compare the performance of volume estimation without the box unpacking technique which is done by weight measuring to the proposed method. From the experimental results, once the location of receivers are set appropriately where the coverage area of signal covers all area of the box, the measured RSSIs can be used to estimate the quantity of product in the sealed box. Among the determined ML techniques, NN shows the highest accuracy once it learns the characteristic of RSSIs under different product quantity to generate the weights of the algorithm. On the other hand, logistic regression shows the lowest accuracy since the learning characteristic is appropriate to the classification application where the output is discrete. By comparing to the weight measuring, it can be noticed that the proposed method is better than the weight measuring since the accuracy of the weight measuring depends on the device and the specific tolerance. Once the tolerance is high, the error also high. Moreover, the proposed method consumes short product quantity estimation time without unpacking or destructing the box.

In future work, improving the accuracy and adjusting the data processing algorithms to be more resistant to the arrangement of things within the package and to be utilized in a loud environment, as well as developing a system that is adaptable to changing parcel sizes, are the next steps.

#### Acknowledgment

This research was funded by King Mongkut's University of Technology North Bangkok. Contract no. KMUTNB-PHD-63-03.

#### References

- [1] T. Anusha, "Trends and Analysis of E-Commerce Market: A Global Perspective," *International Journal of Applied Marketing and Management*, **6**, 11-22, 2021.
- [2] M. Aghaei, A. Mohammad, R. Sahebi, "Investigating the Change in Customers, Sustainable Consumption Behaviour after the Outbreak of COVID-19," *International Journal of Applied Marketing and Management*, **6**, 34-49, 2021.
- [3] B. Anam, H. Akram, H.M. Basit, A.U. Khan, "E-commerce trends during COVID-19 Pandemic," *International Journal of Future Generation Communication and Networking*, **13**, 2020.
- [4] P. Goyal, K. Goyal, A. Chauhan, "Emerging Trends of E-Commerce perspective in Developing Countries," *Journal of Positive School Psychology*, **6**(4), 7090 – 7096, 2022.
- [5] R. Somdech, T. Sriyakul, K. Jermstittiparsert, "The Era of e-Commerce & Online Marketing: Risks Associated with Online Shopping," *International Journal of Innovation, Creativity and Change*, **8**, 201-221, 2019.
- [6] K. Chueamuangphan, P. Kashyap, C. Visvanathan, "Packaging Waste from E-Commerce: Consumers Awareness and Concern," in Ghosh S. (eds) *Sustainable Waste Management: Policies and Case Studies* Springer, **1**, 27-41, doi: 10.1007/978-981-13-7071-7.
- [7] B. Stöcker, D. Baier, B.M. Brand, "New insights in online fashion retail returns from a customers' perspective and their dynamics," *The Journal of Business Economics (JBE)*, **91**, 1149–1187, 2021.
- [8] T. Rintamäki, M.T. Spence, H. Saarijärvi, J. Joensuu, M. Yrjölä, "Customers' perceptions of returning items purchased online: planned versus unplanned product returners," *International Journal of Physical Distribution & Logistics Management*, **51**(4), 403-422, doi: 10.1108/IJPDLM-10-2019-0302.
- [9] M. Truijens, X. Wang, H. de Graaf, J.J. Liu, "Evaluating the Performance of Absolute RSSI Positioning Algorithm-Based Microzoning and RFID in Construction Materials Tracking," *Mathematical Problems in Engineering*, **2014**(3), 2014.



- [10] K. Bouzaffour, B. Lescop, P. Talbot, F. Gallée, S. Rioual, "Development of an Embedded UHF-RFID Corrosion Sensor for Monitoring Corrosion of Steel in Concrete," *IEEE Sensors Journal*, **21**(10), 12306-12312, 2021.
- [11] Ifmalinda, R.E. Putri, I. Rasinta, "Estimation of Size Volume and Weight of Oranges Using Digital Images Processing," in *The 4th International Conference on Sustainability Agriculture and Biosystem*, **100**(2), 315-321, 2010, doi: 10.1088/1755-1315/1059/1/012016.
- [12] Y. Sun, Z.X. Liu, M. Li, Z.T. Zeng, Z.X. Zong, C.L. Ji, "An Object Recognition and Volume Calculation Method Based on Yolov3 and Depth Vision," *Journal of Physics Conference Series*, **1684**(1), 2020, doi:10.1088/1742-6596/1684/1/012009.
- [13] A. Poulouse, D.S. Han, "Performance Analysis of Fingerprint Matching Algorithms for Indoor Localization," in *2020 International Conference on Artificial Intelligence in Information and Communication (ICAIC)*, 661-665, 2020.
- [14] M. Taha, R. Atallah, O. Dwiek, F. Bata, "Crowd Estimation Based on RSSI Measurements Using kNN Classification," in *2020 3rd International Conference on Intelligent Autonomous Systems (ICoIAS)*, 67-70, 2020.
- [15] K. Coussement, S. Lessmann, G. Verstraeten, "A comparative analysis of data preparation algorithms for customer churn prediction: A case study in the telecommunication industry," *Decision Support Systems*, **95**, 27-36, 2017.
- [16] R. D. Ainul, S. Wibowo, Djuwari, M. Siswanto, "An Improved Indoor RSSI Based Positioning System Using Kalman Filter and MultiQuad Algorithm," in *2021 International Electronics Symposium (IES)*, 558-564, 2021, doi:10.1109/IES53407.2021.9594009.
- [17] P.D. Tinh, T.T.N. Mai, "Mobile Indoor Positioning System Utilizing WiFi RSSI and Motion Data," in *2020 4th International Conference on Recent Advances in Signal Processing Telecommunications & Computing (SigTelCom)*, 98-102, 2021, doi:10.1109/SigTelCom49868.2020.9199021.
- [18] J. Ren, Y. Wang, W. Bai, C. Niu, S. Meng, "An improved indoor positioning algorithm based on RSSI filtering," in *2017 IEEE 17th International Conference on Communication Technology (ICCT)*, 1136-1139, 2017, doi:10.1109/ICCT.2017.8359812.
- [19] W. Wang, Y. Zhang, L. Tian, "TOA-based NLOS error mitigation algorithm for 3D indoor localization," *China Communications*, **17**(1), 63-72, 2020.
- [20] S. Jeong, T.K. Sung, K.E. Lee, J. Kang, "Joint TOA/AOA-based localization in wireless sensor networks," in *2014 8th International Conference on Signal Processing and Communication Systems (ICSPCS)*, 1-5, 2014.
- [21] B. Al-Qudsi, M. El-Shennawy, Y. Wu, N. Joram, F. Ellinger, "A hybrid TDoA/RSSI model for mitigating NLOS errors in FMCW based indoor positioning systems," in *2015 11th Conference on Ph.D. Research in Microelectronics and Electronics (PRIME)*, 93-96, 2015, doi:10.1109/PRIME.2015.7251342.
- [22] F. B. Günay, T. Çavdar, "Mobile fleet localization model via RSSI, TOA and TDOA in wireless sensor networks," in *2014 22nd Signal Processing and Communications Applications Conference (SIU)*, 1431-1434, 2014, doi:10.1109/SIU.2014.6830508.
- [23] M. I. Jais, P. Ehkan, R. B. Ahmad, I. Ismail, T. Sabapathy, M. Jusoh, "Review of angle of arrival (AOA) estimations through received signal strength indication (RSSI) for wireless sensors network (WSN)," in *2015 International Conference on Computer, Communications, and Control Technology (I4CT)*, 354-359, 2015, doi:10.1109/I4CT.2015.7219597.
- [24] K.J. Baik, S. Lee, B.J. Jang, "Hybrid RSSI-AoA Positioning System with Single Time-Modulated Array Receiver for LoRa IoT," in *2018 48th European Microwave Conference (EuMC)*, 1133-1136, 2018, doi:10.23919/EuMC.2018.8541736.
- [25] N. Raj, "Indoor RSSI Prediction using Machine Learning for Wireless Networks," in *2021 International Conference on COMMunication Systems & NETWORKS (COMSNETS)*, 372-374, 2021, doi:10.1109/COMSNETS51098.2021.9352852.
- [26] M. Schroth, T. Etkin, W. Stork, "A novel approach for human activity recognition using object interactions and machine learning," in *2021 IEEE Sensors Applications Symposium (SAS)*, 1-6, 2021, doi:10.1109/SAS51076.2021.9530029.
- [27] B. Zheng, T. Masuda, T. Shibata, "An Indoor Positioning with a Neural Network Model of TensorFlow for Machine Learning," in *2021 International Symposium on Intelligent Signal Processing and Communication Systems (ISPACS)*, 1-2, 2021, doi:10.1109/ISPACS51563.2021.9651131.
- [28] K. Wasayangkool, K. Srisomboon, W. Lee, "The Volume Estimation Technique using RSSI with Machine Learning in Manufacturing Process," in *2022 37th International Technical Conference on Circuits/Systems Computers and Communications (ITC-CSCC)*, 1-4, 2022. doi: 10.1007/978-981-13-7071-7.
- [29] A. Shojafar, "Evaluation and Improvement of the RSSI-based Localization Algorithm: Received Signal Strength Indication (RSSI) Dissertation," *Computing and Intelligent Systems*, **2**, 10-12 2015.
- [30] H. Ahmadi, R. Bouallegue, "Exploiting machine learning strategies and RSSI for localization in wireless sensor networks: A survey," in *2017 13th International Wireless Communications and Mobile Computing Conference (IWCMC)*, 1150-1154, 2017, doi:10.1109/IWCMC.2017.7986447.
- [31] P. Koovimol, S. Pattaramalai, "Experimental Machine Learning for RSSI fingerprint in Indoor WiFi Localization," in *2021 18th International Conference on Electrical Engineering/Electronics, Computer, Telecommunications and Information Technology (ECTI-CON)*, 1018-1021, 2021, doi:10.1109/ECTI-CON51831.2021.9454865.
- [32] D.O. Camacho, L.M. Proaño, "Increasing Accuracy in Positioning by RSSI: an Analysis with Machine Learning Algorithms," in *2019 International Conference on Information Systems and Computer Science (INCISCOS)*, 31-35, 2019, doi: 10.1109/INCISCOS49368.2019.00014.

## Social Financial Technologies for the Development of Enterprises and the Russian Economy

Evgeniy Kostyrin\*, Evgeniy Sokolov

Bauman Moscow State Technical University, Engineering Business and Management, Finance, Moscow, 105005, Russia

### ARTICLE INFO

Article history:

Received: 27 February, 2023

Accepted: 05 May, 2023

Online: 21 May, 2023

Keywords:

Economic and mathematical model

Working citizen

Social state

### ABSTRACT

The main **contradiction** identified in the study is that the existing scientific and methodological solves of economy development management processes does not create prerequisites for improving the efficiency of their work, the introduction of progressive technologies for material and moral stimulation of the work of performers and administrative and managerial personnel, advanced social mechanisms for country's economy development and social security employees. Economic and mathematical modeling of the complex system of social financing of enterprises and the economy of the country, scientifically sound personnel policy and the system of motivation of performers and administrative and management personnel **is an important and urgent problem. The purpose of the study is** to develop and implement an economic and mathematical model of a comprehensive system of social financing of enterprises and the economy of the country, optimizing the wages of the workforce, consistent with revenue growth, deductions for the development of the enterprise (relevant for the employer and the entire workforce), taxation and social contributions (important for the state). **The results** of the studies conducted and presented in this article allow us to conclude that the proposed social financial technologies for the development of enterprises and the economy of Russia, make it possible, at quite achievable rates of growth of gross domestic product (revenue of enterprises) by 3% per year, to ensure an increase in the wages of working citizens for 5 years by 34 %, which will make it possible to practically end poverty, and to increase contributions to the development fund over 5 years by 16%. Starting from 2026, increase receipts from income tax, tax on profit rate and value added tax and bring this growth to 30% by 2041, which will allow the state to solve many social problems.

### 1. Introduction

Social financial technologies for the development of enterprises and the economy of any country in the world are connected with the life of a person and his relationships with other people in society. The realization of the most diverse needs of people in goods, works, services in society is provided only in the process of work, thus, the social financial technologies considered in this study should be perceived as a reflection of labor relations aimed at self-realization of citizens of working age.

For the first time, social protection of the population, including citizens working at enterprises, was issued through collective insurance.

According to the existing legislation of the Russian Federation, all enterprises, companies, organizations must make

contributions: to the Pension Fund of Russia (PFR) – 22% of wages; to the Federal Compulsory Medical Insurance Fund (FCMIF) – 5.1% of wages; to the Social Insurance Fund (SIF) – 2.9% of wages (in case of temporary disability and maternity). Also, according to Federal Law No. 517-FZ of December 19, 2022, depending on the class of occupational risk, contributions in the amount of 0.2% to 8.5% of wages are paid.

All citizens of the Russian Federation are associated with the aforementioned funds. So, working citizens make contributions to the PFR and the FCMIF, and this is 82,678 thousand people, more than 36 million people receive a pension in our country, which means that in total it is already more than 118 million people, i.e. more than 80% of the population of the country, which indicates the importance and urgent need to study issues related to the effective management of funds of social funds and optimization of contributions of enterprises to these funds, so that the relationship with the funds does not lead to a decrease in the efficiency of enterprises and organizations, but on the contrary, is

\*Corresponding Author: Evgeniy Kostyrin, mauntain76@mail.ru

an incentive to the development of the enterprise, the economy of the country, motivation of personnel to work.

On the topic of this study, we analyzed 176 articles by different researchers and specialists. The analysis of articles devoted to the practical implementation of financial and social mechanisms of personnel management and enterprise development, which take into account the interests of the workforce, managers, shareholders and owners of enterprises, as well as the state as one of the stakeholders in the growth of wages of enterprise personnel, its development and increase in tax deductions to the federal and territorial budgets, can be divided into the following groups: Cash Flow Management (30 articles), Investment Efficiency (34 works), Socio-economic Security (23 articles), Welfare, Wage Growth (27 articles), Enterprise Development (12 scientific studies), Economic and Mathematical Modeling (23 scientific articles) and Business Process Management (27 articles). The relative weight of each group in the review is shown in Figure 1.

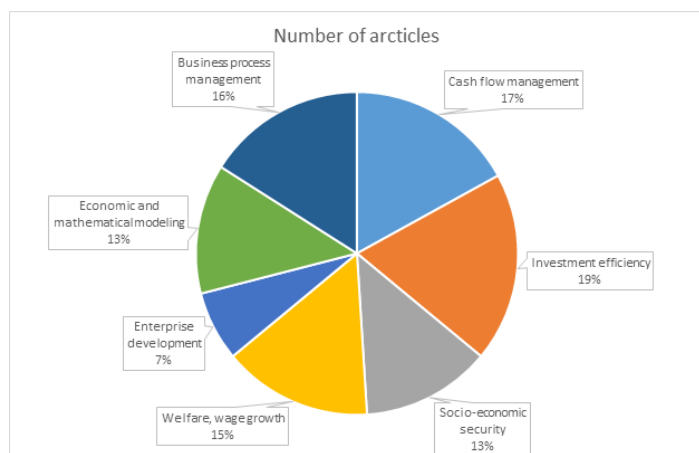


Figure 1: Distribution of Articles by Research Topics

Figure 1 shows that the largest share of the studied articles on the research topic falls on the Investment Efficiency section (34

articles, or a fifth of all works), followed by a problem related to cash Flow Management (Cash Flow Management), with the number of articles 30, which is 17% of the literature review. The group of articles devoted to Business Process Management closes the top three most popular research topics (28 papers, 16% of articles). The smallest group of works belongs to the Enterprise Development section with a total number of articles equal to 12, which is 7% of the list of analyzed articles.

The degree of elaboration of the research problem and its analysis are presented in detail in Table 1.

Table 1: Analysis of works devoted to the problems of this study

Articles directions	Scientists and specialists who have contributed to the subject of the study
Welfare, Wage Growth	[1-27]
Enterprise Development	[28-39]
Investment Efficiency	[40-73]
Socio-economic Security	[74-96]
Cash Flow Management	[97-126]
Economic and Mathematical Modeling	[127-149]
Business Process Management	[150-176]

A comparative analysis of the scientific results obtained by the authors and the results of other scientists and specialists dealing with certain aspects of the problems raised in the article is presented in Table 2.

Table 2: Comparison with Other Studies and Scientific Increment of Knowledge

Number	Research directions	Scientific result	Scientific novelty
1	Welfare, Wage Growth	Social technologies have been developed for the financing of enterprises and the development of the country's economy, maximizing the wages of employees, taxation and social contributions of enterprises, which can significantly increase the welfare of working citizens and ensure the supply of products in accordance with the increased demand for it and practically end poverty.	In contrast to the models of social financing of enterprises used in practice [14; 22] the basis of this social technology of enterprise financing is a breakthrough mechanism for increasing wage growth, material and moral incentives for workers, based on taking into account the needs of working citizens, managers, owners and shareholders of enterprises and the state, which allows the entire workforce to participate in the process of enterprise management, be a full participant in socio-economic relations in society, the development of the country and enterprises by directing part of the company's revenue to its development and the growth of the welfare of citizens of the country, equipping the workplaces of employees, improving their qualifications.

2	Enterprise Development	<p>A unique social technology for financing the economy of the country and its enterprises has been developed, which allows linking profits from the sale of products and services with additional remuneration of personnel, labor, taxation and social contributions of enterprises to the FCMIF, PFR and SIF, as well as contributions to the development of the enterprise.</p>	<p>In contrast to the well-known macroeconomic models of managing the country's economy and microeconomic models of managing the development of enterprises [28-30] the developed method allows us to simultaneously take into account the interests of the labor collective, managers and shareholders of enterprises and the state as a whole through the use of progressive mathematical models aimed at solving the main tasks, the purpose of which is the effective management of social contributions to the PFR, FCMIF, SIF and effective, interrelated relationships with the needs of working citizens in wage growth, by the state and owners on the basis of making complex scientifically based management decisions with a synergistic effect. This approach gives a significant increase in the economic, social and professional efficiency of working citizens and the economy of the country as a whole in comparison with their work, provided that the interests of only one of the parties are taken into account: working citizens, business owners or the state as an institution for data collection. taxes and social contributions of citizens and enterprises. Thus, the difference between the methodology of this scientific research compared to analogues lies in the complexity and comprehensiveness of the management of the enterprise and working citizens, based on the interests of all participating groups of beneficiaries.</p>
3	Investment Efficiency	<p>An approach to the economic assessment of the effectiveness of the development of the country's economy and enterprises, as well as investments in the development of enterprises, equipping the workplace of an employee and improving his qualifications, which consists in making a management decision to redistribute the effect of reducing the cost of products, services, works, goods associated with the growth of income of enterprises per employee, and the direction of this effect on the increase in wages and the development of the enterprise.</p>	<p>This approach differs from other methods of assessing enterprises and the country's economy, as well as the effectiveness of investments [45; 54; 66] in that the criterion for the effectiveness of the management decision is the growth of wages of the workforce and the growth of the welfare of the population, which is ensured by the optimal redistribution of the effect of reducing the cost of goods between wages, enterprise development, social contributions, taxation of enterprises, while taking into account the interests of all beneficiaries. In addition, in the author's approach, additional profit from increased sales is directed to investments in the entrepreneurship development fund, payroll, taxation and social contributions, the amount of which significantly depends on the average monthly revenue of enterprises per working citizen, which motivates him to high effective, high-performance work makes him not in words, but on a participant in labor relations interested in the development of the enterprise where he works and the country in which he lives. Thus, the author's methodology makes such an approach to social technologies for financing enterprises and the country's economy closed, complex and dynamic, increasing the well-being of citizens working at the enterprise.</p>
4	Socio-economic Security	<p>An approach to ensuring the social and financial security of the state and the population is proposed, the essence of which is that the authors propose technologies that ensure wage growth, bringing the pension level to 40% of wages in four years; in 8 years – up to 60% of wages; in 10 years – up to 80% of wages fees, an increase in total FCMIF and PFR receipts, as well as tax on profit, income tax and VAT by 30% of the base level, while reducing FCMIF and PFR receipts by 14.08% over five years.</p>	<p>In contrast to the works [74; 80], the developed technology is aimed at increasing the investment attractiveness of the country's economy and domestic enterprises by applying in practice the progressive system of personnel labor incentives developed by the authors and the optimal distribution of funds from reducing the cost of production and investments between the payroll, development fund and contributions to the PFR, FCMIF, income tax, VAT and tax on profit are based on solving the problem of economic and mathematical modeling and using social technologies of financing to manage enterprises and the economy of the country as a whole.</p>

5	Cash Flow Management	A comprehensive model for managing the cash flows of an enterprise, its income and expenses, cost, unit fixed costs and unit variable costs, the effect of cost reduction, tax and social deductions from the sale of products has been developed.	The proposed model differs from the models used for managing financial flows of enterprises [99; 105; 109; 126], by enabling management decision makers to coordinate investment programs and plans depending on the prices of final products, goods, works, services, their volumes and production costs, which contributes to the growth of profitability of investments in the economy of the country and enterprises, labor productivity of personnel (citizens working at the enterprise) and finance for the development of enterprises.
6	Economic and Mathematical Modeling	A new formulation and approach to solving the problem of nonlinear programming about the optimal combination of labor wages compatible with an increase in company revenue, tax revenues, which is important for the development of the state and the growth of the welfare of its citizens, and to the enterprise development fund, which is important for its management and shareholders, owners, are proposed.	In contrast to the famous researchers devoted to solving the problem of investment allocation [130; 133; 137; 138], in the author's approach, the company's budget is used as a source of financing, which is formed by contributions to the development fund, depending on the effectiveness of each employee's activities. This approach allows the most efficient redistribution of financial flows between the payroll fund, the enterprise development fund, taxation and social contributions and provides sources of financing for equipping the workplace of personnel, improving the skills of employees, involves all personnel in the enterprise management.
7	Business Process Management	An economic and mathematical model of wage maximization consistent with the growth of the revenue, process management of cash flows of enterprises, characterized by a systematic combination of methods of nonlinear programming, economic and mathematical modeling, social financial technologies, has been developed, this makes it possible to create tools for managing the cash flow and development of enterprises and to develop standard projects of management decision support systems with the prospect of their integration into existing and promising information and analytical systems at enterprises that ensure a combination of the interests of the workforce, owners, managers of enterprises and the state.	The developed complex model of nonlinear programming, which maximizes wages consistent with the growth of the company's revenue and the funds that are released from the company by reducing the cost, allows us to find an optimal scientifically based management solution to the complex problem of combining and taking into account the development goals of the state, the enterprise and the needs of the workforce by dividing into smaller subtasks: increasing the wages of the labor collective through the use in practice of material and moral factors to increase productivity and labor efficiency, revenue growth at the enterprise, reduction in the unit cost of production, increase in contributions to the development fund and wages, tax deductions and social contributions to the FCMIF, PFR and SIF, each of which represents a well-known task of economic and mathematical modeling, and then the integration of the results into a comprehensive management decision-making system at the stage of practical implementation by applying additional criteria: market capacity, profit share, aimed at increasing material incentives for personnel, for the development of the economies of countries and enterprises, for investment, etc.

Thus, the literature review presented in Tables 1 and 2 allowed us to conclude that in scientific research there are practically no economic and mathematical models and technologies of social financing of enterprises using methods of nonlinear programming and mathematical optimization, which allow the manager to ensure the relationship of financial indicators of enterprises (revenue, profit, unit cost of production) and a progressive system of material incentives for the labor of citizens working at enterprises, as well as tax and social contributions to the FCMIF, PFR and SIF, which allows for a synergistic effect as a result of taking into account the needs of workers (citizens working at enterprises), owners, managers of enterprises, budgets of all levels (federal and territorial) and the state as a whole. The article [25] shows that social financial technologies are based on the construction of models of economic

and mathematical optimization, flowcharts, tools, algorithms, software products and environments and allow solving two problems:

- 1) Efficient allocation of enterprises' contributions to off-budget funds and their subsequent use (PFR, FCMIF, SIF).
- 2) Effective distribution and accounting at enterprises of the needs of the state, owners, shareholders and the workforce.

The solution to the first problem should be sought in the transition of healthcare and pension insurance to personalized medical and pension accounts of citizens [25-27; 85-95].

The article [25] solves the second problem of optimizing social financial technologies, taking into account various interests

both in the country as a whole and within labor relations at enterprises.

In the same article, using a nonlinear model, it is also proved that in the case of an increase in wages at an enterprise above the average in Russia, it is advantageous for the state to reduce deductions to FCMIF by increasing tax deductions due to wage growth.

In the article [93], using a nonlinear model, it is also proved that when wages increase above the average in Russia (consistent with revenue growth), it is advantageous for state and employer to reduce deductions to the PFR.

In the article [95], using a nonlinear model, it is proved that when switching, starting from 2021, to personalized accumulative pension accounts (PAPA) for 19 years (by 2039), 11,833,027 rubles will accumulate on PAPA of working citizens (with an average salary of 54,175 rubles), which is enough to provide a pension in the amount of 80% of wages for 20 years, which corresponds to the expected period of survival.

In other words, after 2038, every working citizen with a salary of 52,355 rubles (the average salary in Russia in August 2021) will have an amount of 11,099,133.99 rubles on his account, which is enough to receive a monthly pension of 80% of the national average salary for the rest of his life (the survival period). Accordingly, enterprises after 2038 can stop deducting 22% of wages in favor of citizens, which will reduce the unit cost of goods produced in the country, and hence the price of their sale to the population, and this in turn is already an effective method of combating inflation in the country.

***This article shows that the post-retirement transition to a reduction in the percentage of deductions from wages for pension and medical support of citizens from the first (2021), and not from 2038, is much more profitable for the labor collective, employers and the state.***

In this article, the main ***contradiction*** is noted, which consists in the fact that the existing organizational, economic and scientific support for the development of enterprises does not create prerequisites for improving the efficiency of their work, the introduction of progressive technologies for material and moral stimulation of the labor of performers and administrative and managerial personnel, advanced social technologies for financing the economy of the country and the development of enterprises, as well as social security of employees.

The existing processes of socio-financial development of the country's economy and individual enterprises can be characterized as extremely inefficient, since there is no holistic scientific and methodological approach integrated into everyday practice to develop and apply effective management solutions based on optimization tools, models and breakthrough financial management algorithms. The low efficiency of managing the country's economy and the socio-financial activities of enterprises is associated with the fragmentation and imperfection of the mathematical apparatus and tools used in practice, as well as methods of stimulating labor. Attempts to create a full-fledged integrated enterprise development management system, including a progressive incentive system for employees, receipts to the development fund, as well as effective financial resource

management mechanisms based on the methodology of nonlinear programming of enterprise development management processes and their individual assets, organizational and structural units built in this article, are presented in [25-27; 85-95], but their main drawback is that the issues of social financing of the Russian economy and domestic enterprises have not been fully worked out, mutually linking the interests of the state, the labor collective, owners, shareholders, heads of enterprises, problems of enterprise taxation management, social contributions to the PFR, FCMIF and SIF are not fully reflected depending on from the growth of revenue of enterprises, the growth of employee productivity, criteria for making informed management decisions have not been developed, aimed at organizing effective labor relations in the company.

Ambitious goals require advanced social financial technologies and optimization models for the development of enterprises and promising systems for financing their activities, taking into account the optimization of taxation and social contributions to FCMIF, PFR and SIF. Nonlinear processes and computational methods in the management of such systems are becoming increasingly relevant as the most effective tools for making managerial decisions and providing scientifically sound algorithms and models for the development of management objects. When managing complex systems with many interrelated parameters, it becomes necessary to use algorithms and methods of nonlinear programming to achieve the optimal result from the set of possible values of the dependent variable with limited ranges of changes in influencing factors. As a rule, both the objective function and each of the inequalities of the system of constraints of the optimization problem in most modern control models of real processes are nonlinear functions, which imposes additional restrictions on control objects and requires special mathematical models and instrumental methods for solving such problems. Thus, optimization methods, in particular nonlinear programming models, have proven themselves well in macroeconomic problems and problems of managing the development of enterprises using social financing technologies [85; 88; 91].

Thus, economic and mathematical modeling of a complex system of social financing of the country's economy and enterprises, optimization of employees' wages tied to the company's revenue, optimization of the size of the enterprise development fund, which is important for the owners of enterprises and all employees, as well as taxes, which ensures the performance of state functions, a well-thought-out policy towards existing and potential consumers and categories of goods, an instrumental basis for managing the development of enterprises, taking into account promising and effective technologies for their financing and investment in development, structural analysis, system analysis, factors of the internal and external environment, a scientifically sound personnel policy and a system of motivation of performers and administrative and managerial personnel ***is an important problem for the national economy.***

***The purpose of the study is*** to build and implement an optimization model of an integrated system of social financing of the country's economy and enterprises, maximizing the wages of the workforce associated with income for the development of the enterprise, which is important and relevant for owners and

shareholders, the management of the enterprise, increasing revenue, taxation and contributions to off-budget funds, which is relevant for the state.

**The object of the study** is the average Russian enterprise, its financial flows, taxation and social contributions to extra-budgetary funds (FCMIF, PFR and SIF). The article discusses social financial technologies with the average monthly salary of employees according to the Federal State Statistics Service, the share of wages in the structure of gross domestic product (GDP) of Russia in the amount of 44.9% and the profitability of products in the amount of 9.9%.

**The subject of the study** is modeling the optimal distribution of investments in wages of labor, consistent with revenue growth, in the enterprise development fund, taxation and deductions to off-budget funds, which is relevant for the state, using methods of nonlinear programming and process management.

For the purposes of this article, we will define the concepts of "products", "goods", "work", "service". According to Article 38 of the Tax Code of the Russian Federation, by **goods** we will mean any property sold or intended for sale. Without loss of meaning in this article, the terms "products" and "goods" are identified.

**Work** is an activity whose results have a material expression and can be implemented to meet the needs of an organization and (or) individuals.

A **service** is an activity whose results have no material expression, are realized and consumed in the process of carrying out this activity.

## Materials and Methods

The financial system of Russia consists of three subsystems: public finance; finance of enterprises (organizations) and household finance. As shown in [92], the basis of the Russian financial system is working citizens, on whose well-organized and motivated work its condition depends. The personnel of enterprises providing services to the population, performing work, producing products and essential goods also need to create and implement in daily practice an effective motivation system that can become a source of scientifically sound management decisions, involve each employee of the enterprise (organization) in the management system of all divisions of the enterprise. enterprises create the material and moral foundations of responsibility for the quality and efficiency of their work. The foundation of the motivation system can be an economic and mathematical model of enterprise profit management, which is considered in the works [25; 88; 90; 95]. The introduction of this model into the daily activities of enterprises for many years has shown their high efficiency, allows you to manage profits due to the optimal ratio of such economic indicators of enterprises as prices for products, goods, works, services, production volumes and sales of enterprise products, cost. When managing enterprises, optimization models of profit management make it possible to link the reduction in the cost of enterprises' products, which provides additional demand for products and goods, with an increase in their production and sales volumes. Moreover, the growth of volumes allows you to get a double effect. The first is directly related to the growth of volumes. The second is

associated with a reduction in the cost of production, due to a reduction in unit fixed costs with the growth of the company's production.

One of the key tasks of this work is to build a comprehensive system of stimulating the work of personnel of enterprises, analysis and justification of ways to improve the working conditions and workplace of employees of enterprises, without motivation and initiative work of which it is impossible to achieve high financial results.

The work [94] shows that the most important factor in improving the Russian finance system are working citizens, on whose material and moral incentives depend not only household incomes (family budgets), but also the fullness of budgets at all levels of the financial system, namely: the finances of the state and the finances of economic entities (enterprises, organizations). Thus, there is a need to create such an economic and mathematical model that would allow calculating the amount of material incentives for employees of enterprises and all restrictions on the range of changes affecting its size factors. We will build an optimization model that ensures the maximization of material incentives for the work of employees of enterprises and the level of financial contributions for its development is not lower than indicated.

A common practice of managing the development of enterprises is the material stimulation of workers' labor as a percentage of total revenue. Therefore, as a target function of the developed model, we will take the amount of deductions from the company's revenue directed to financial incentives for employees:  $Sal_j = \theta_j \cdot Rev_j / 12 \rightarrow \max$ , where  $Sal_j$  stands for the monthly financial remuneration of employees of the  $j$ -th division of the enterprise in rubles;  $\theta_j$  stands for the percentage of revenue from the revenue of the  $j$ -th division of the enterprise, directed to stimulating the work of performers (employees of the  $j$ -th division) in fractions of units;  $Rev_j$  stands for the revenue of the  $j$ -th division of the enterprise in rubles.

To stimulate the company's employees to increase revenue and productivity of their labor, it is necessary to create a progressive scale of material remuneration. In other words, the percentage of income allocated to the remuneration of employees of the enterprise should depend on the amount of this income, i.e.  $\theta_j(Rev_j)$ . We will assume that all income earned by employees of the enterprise in excess of the base amount is distributed between employees and the enterprise in pre-established ratios. Let's call this ratio the coefficient of redistribution of the financial result between the labor collective and the management, owners, shareholders of the enterprise and denote it  $\xi$ . Then the financial result received by the enterprise will be redistributed between employees and the enterprise in the following proportions:

- 1)  $Sal_j = (Rev_j / 12) \cdot \theta_{bj} + \xi \cdot (FR_j - FR_{bj}) / 12$  – this part of the income will be used to stimulate the work of employees.
- 2) Therefore, the amount of income that will be directed to the development of the enterprise is equal to  $Rev_{dev} = (FR_{bj} / 12) + \xi \cdot [(FR_j - FR_{bj}) / 12] \cdot (1 - Tax_{prof})$ .

From the formulas presented above, it is possible to deduce the dependence of the parameter  $\theta_j$  on the revenue growth of the enterprise, i.e. to create a progressive system of material and

moral incentives for employees, in which the amount of remuneration directly depends on the revenue of the enterprise and at the same time the value of the percentage  $\theta_j$  does not remain constant, but grows with the growth of revenue. This means that the increase in material incentives for employees occurs under the influence of a double effect: a) depending on the growth of revenue; b) on the change in the amount of interest directed to stimulating the work of employees. Thus, the amount of interest allocated to stimulate the work of employees has the following form:  $\theta_j(Rev_j) = \frac{(Rev_j/12) \cdot \theta_{bj} + \xi \cdot (FR_j - FR_{Rb_j})/12}{Rev_{bj}/12}$ , where  $Rev_{bj}$  stands for the base revenue of the  $j$ -th division of the enterprise in rubles;  $\theta_{bj}$  stands for the share of the basic income of the enterprise, which goes to stimulate the work of employees in fractions of units.

Combining all of the above, we will build an optimization model that belongs to the class of nonlinear programming models that maximizes the wages of employees with the growth of the company's income, integrated with income for its development (relevant for the employer and the entire workforce as a whole), taxation and contributions to off-budget funds):

Target Function

$$Sal = Rev \cdot \theta_b + \xi \cdot (FR - FR_b) \rightarrow max, \quad (1)$$

$$Rev_{dev} = FR_b + (1 - \xi) \cdot (FR - FR_b) \cdot (1 - Tax_{prof}), \quad (2)$$

$$\theta = (Rev \cdot \theta_b + \xi \cdot FR) / Rev_b, \quad (3)$$

$$\Delta C = V \cdot \left( C_{var} + \frac{C_{fix}}{\sum_{i=1}^n V_i} \right) - V_b \cdot \left( C_{var} + \frac{C_{fix}}{\sum_{i=1}^n V_i} \right), \quad (4)$$

$$D_{PFR} = Sal \cdot \varphi_{PFR} + (Rev - C_{var}) \cdot VAT, \quad (5)$$

$$D_{FCMIF} = Sal \cdot \varphi_{FCMIF} + Sal \cdot Tax_{inc} + FR \cdot Tax_{prof}, \quad (6)$$

$$D = D_{PFR} + D_{FCMIF}, \quad (7)$$

$$\varphi_{FCMIF} = \varphi_{FCMIF5.1\%} - \Delta\varphi_{FCMIFstim} - \Delta\varphi_{FCMIFcost}, \quad (8)$$

$$\Delta\varphi_{FCMIFstim} = [(Sal - Sal_b) / Sal_b] \cdot \varphi_{FCMIF5.1\%}, \quad (9)$$

$$\Delta\varphi_{FCMIFcost} = [\Delta C / FR_b] \cdot \varphi_{FCMIF5.1\%}, \quad (10)$$

$$\varphi_{PFR} = \varphi_{PFR22.0\%} - \Delta\varphi_{PFRstim} - \Delta\varphi_{PFRtax}, \quad (11)$$

$$\Delta\varphi_{PFRstim} = [(Sal - Sal_b) / Sal_b] \cdot \varphi_{PFR22.0\%}, \quad (12)$$

$$\Delta\varphi_{PFRtax} = [(FR - FR_b) / Sal_b] \cdot \varphi_{PFR22.0\%}, \quad (13)$$

$$FR = Rev - V \cdot \left( C_{var} + \frac{C_{fix}}{\sum_{i=1}^n V_i} \right), \quad (14)$$

$$\omega_{fix} = \frac{\frac{C_{fix}}{\sum_{i=1}^n V_i}}{C_{var} + \frac{C_{fix}}{\sum_{i=1}^n V_i}}, \quad (15)$$

$$\omega_{var} = \frac{C_{var}}{C_{var} + \frac{C_{fix}}{\sum_{i=1}^n V_i}}, \quad (16)$$

when  $Sal$  stands for the salary of employees in rubles;  $Sal_b$  stands for the base salary of employees in the first case simulation in rubles;  $Rev$  stands for the revenue in rubles;  $\theta$  stands for the share of the income of the enterprise, which goes to stimulate the work of employees in fractions of units;  $\xi$  stands for the coefficient of redistribution of the financial result between the labor collective and the management, owners, shareholders of the enterprise;  $\Delta C$  stands for the unit cost reduction in rubles;  $Rev_{dev}$  stands for the value of the development fund in rubles;  $Rev_b$  stands for the base revenue in the first case simulation in rubles;  $\theta_b$  stands for the share of the basic income of the enterprise, which goes to stimulate the work of employees in fractions of units;  $V$  stands for the number of products sold by the enterprise in units;  $V_b$  stands for the base number of products sold by the enterprise in the first case simulation in units;  $C_{var}$  stands for the unit variable costs in rubles;  $C_{fix}$  stands for the total fixed costs in rubles;  $\sum_{i=1}^n V_i$  stands for the total number of products sold by the enterprise in units;  $n$  stands for the total number of divisions of the enterprise in units;  $D_{PFR}$  stands for the amount of value added tax and receipts to the PFR in rubles;  $D_{FCMIF}$  stands for the amount of tax on profit, income tax and receipts in FCMIF in rubles;  $D$  stands for the total deductions of the enterprise in rubles;  $\varphi_{PFR}$  stands for the rate contributions to the PFR in %;  $\varphi_{PFR22.0\%}$  stands for the base rate of deductions to the PFR in the first case simulation, equal to 22.0% of the wage fund (WF) in %;  $\Delta\varphi_{PFRstim}$  stands for the change in the rate of deductions to the PFR related to wage growth in %;  $\Delta\varphi_{PFRtax}$  stands for the change in the rate of deductions to the PFR due to the increase in value added tax in %;  $\varphi_{FCMIF}$  stands for the rate of deductions to the FCMIF in %;  $\varphi_{FCMIF5.1\%}$  stands for the base rate of deductions to the FCMIF in the first case simulation, equal to 5.1% of the wage fund (WF) in %;  $\Delta\varphi_{FCMIFstim}$  stands for the change in the rate of deductions in FCMIF related to wage growth in %;  $\Delta\varphi_{FCMIFcost}$  stands for the change in the rate of deductions to the FCMIF due to the effect of cost reduction in %;  $FR$  stands for the financial result or profit in rubles;  $FR_b$  stands for the base financial result or base profit in the first case simulation in rubles;  $VAT$  stands for the rate of value added tax (VAT), 20%;  $Tax_{prof}$  stands for the tax on profit rate, 20%;  $Tax_{inc}$  stands for the income tax rate, 13%;  $\omega_{var}$  stands for the share of variable costs in fractions of units;  $\omega_{fix}$  stands for the share of fixed costs in fractions of units.

**The main limitations, prerequisites and assumptions used in the development and practical implementation of the optimization model (1)-(16):**

- 1) personalized pension accounts and medical savings accounts are used as a source of financing for pension provision and healthcare of citizens working at the enterprise, which means that part of the social contributions that the enterprise makes to the FCMIF and the PFR go to medical savings accounts and personalized accounts of citizens;
- 2) information about the cost structure, operating and investment activities, as well as financial results provided by the management and employees of the analyzed enterprise is correct, complete and reliable;



- 3) any hidden (not explicitly stated) factors will not have a significant impact on the company and the results of the practical application of the model (1)-(16);
- 4) the company is active and will continue its business activities in the foreseeable future;
- 5) in the future, the responsible attitude of the owners of the enterprise and the competent management of its operational activities will remain;
- 6) the company will comply with all applicable provisions of laws and regulations, especially in terms of taxation and social contributions;
- 7) the enterprise has, will receive or will extend all necessary permits and licenses on which the functioning of the enterprise and the applicability of the economic and mathematical model developed by the authors are based (1)-(16);
- 8) all cash flows received from operating activities occur during the same year to which the corresponding income received and expenses incurred relate.

Figure 2 shows a flowchart of the integrated system of social financing of enterprises, which reflects in detail the main aspects and criteria for making key management decisions and shows the optimal strategy for the practical implementation of the optimization model (1)-(16).

A more detailed algorithm and tools for the practical application of social technologies for financing the Russian economy and enterprises are given in the section "Results".

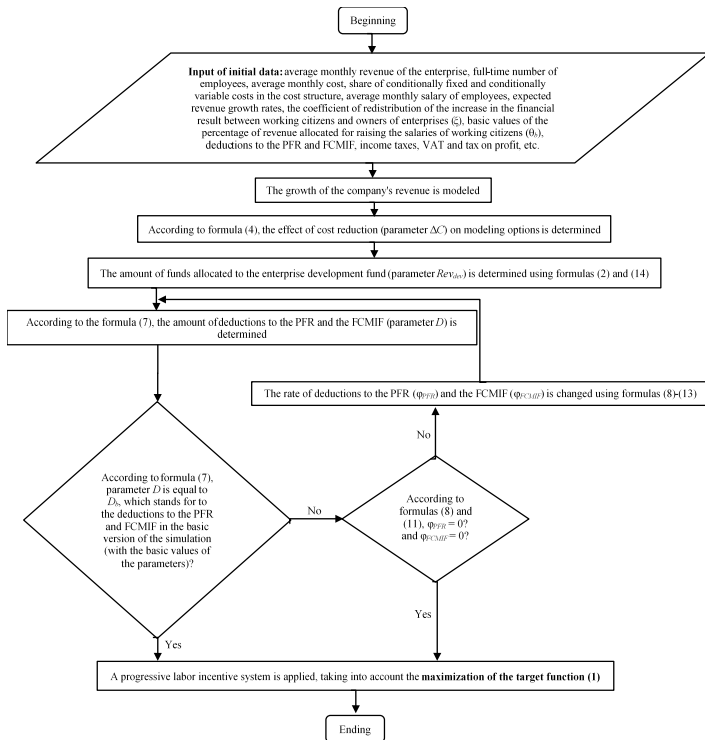


Figure 2: Block Diagram of the Complex System of Social Financing of Enterprises

## Results

Table 3 shows the practical implementation of the optimization model (1)-(16). Column 1 shows the number of the simulation variant, which corresponds to the year shown in

columns 2 and 15 of Table 3. The first simulation variant is the basic one and corresponds to the **2021st year, in which the basic values of the parameters being changed are indicated**. The salary according to the Federal State Statistics Service for November 2023 is 63,060 rubles (see row 1, columns 10 and 13 of Table 3). The share of wages in the structure of Russia's gross domestic product (GDP) is 44.9%, and the profitability of products sold is 9.9%. Formula (1) establishes the basic parameters and the relationship between them, namely: wages (*Sal*), enterprise income (*Rev*) and the share of the income of the enterprise, which goes to stimulate the work of employees. Since  $FR - FR_b = 0$  in the first case simulation, it is possible to determine the revenue of enterprises by dividing wages by the share of wages in the GDP structure ( $Rev = Sal : \theta_b$ ), i.e. 63,060 rubles : 0.449 (44.9%) = 140,445.43 rubles (see column 3 of Table 3).

The cost of production is equal to the revenue of enterprises minus the profit from the sale of products, which is 140,445.43 rubles · 0.099 = 13,904.10 rubles. This means that the cost price will be: 140,445.43 rubles – 13,904.10 rubles = 126,541.34 rubles (see the first row, column 4 of Table 3). Next, we increase the company's revenue by 3% per year, which corresponds to the growth rate of average wages in [95]. As shown above, the revenue of enterprises is equal to the amount of wages divided by its share in the structure of GDP. So, for the second row of Table 1, the income is 63,060 rubles · 1.03 (average wage growth rate) : 0.449 = 144,658.80 rubles, for the tenth modeling option 63,060 rubles · 1.039 : 0.449 = 183,249.44 rubles, etc. In the latest version of the simulation, the revenue of enterprises per employee exceeds the basic version of the simulation by 4.38 times.

In the production of products, the total costs are divided into fixed (63,035.89 rubles, see column 7), which do not depend on the volume of products, and variable (42,023.92 rubles in the basic version of modeling, see column 8 of Table 3). At the same time, the share of fixed costs is equal to 60% of total costs in the basic version of modeling ( $\omega_{fix} = 60\%$ , see line 1 of Table 3), and the share of variables is 40% of total costs ( $\omega_{var} = 40\%$ ). With an increase in production volumes, unit costs decrease, and the share of fixed costs in the cost structure also decreases, which makes it possible to direct the released financial resources to additional material incentives for employees, i.e. to introduce a progressive system of material incentives for labor (see column 13 of Table 3). The meaning of this system is that with an increase in labor productivity increases the share of the income of the enterprise, which goes to stimulate the work of employees ( $\theta$ ), as shown in column 11 of Table 3. The share of fixed costs ( $\omega_{fix}$ ) is determined by the formula (15), and the share of variable costs ( $\omega_{var}$ ) is determined by the formula (16). Variable costs depend on the quantity of products produced, while fixed costs do not.

The progressive system of material remuneration (objective function (1)) makes it possible to increase wages faster (see column 13) compared to the data in column 10 of Table 3, namely: more than eight times compared to the basic modeling option at annual growth rates of the volumes of products, services and works produced and sold, equal to 3.0% (see column 14 of Table 3).

Table 3: Progressive Labor Incentive System

Option number	Year	The revenue of enterprises per employee with a share of wages in its structure of 44.9% in the first (basic) version of the simulation, rubles per month	The cost of production per employee with a profitability of 9.9% in the first (basic) version of the simulation, rubles per month	The share of fixed costs	The share of variable costs	Total fixed costs, rubles per month	Total variable costs, rubles per month	The effect of cost reduction, rubles per month	The average monthly nominal accrued salary, rubles per month	The share of the company's income allocated to wages	Wage growth, rubles per month	Innovative technology of material remuneration of employees, rubles per month	Wage index
1	2	3	4	5	6	7	8	9	10	11	12	13	14
1	2023	140,445.43	126,541.34	60.00%	40.00%	75,924.80	50,616.53	0.00	63,060	44.90%	0.00	63,060	1.000
2	2024	144,658.80	128,059.83	59.29%	40.71%	75,924.80	52,135.03	2,277.74	64,952	45.40%	2,155.89	67,108	1.064
3	2025	148,998.56	129,623.88	58.57%	41.43%	75,924.80	53,699.08	4,623.82	66,900	45.90%	4,376.46	71,277	1.130
4	2026	153,468.52	131,234.86	57.85%	42.15%	75,924.80	55,310.05	7,040.28	68,907	46.40%	6,663.65	75,571	1.198
5	2027	158,072.57	132,894.16	57.13%	42.87%	75,924.80	56,969.36	9,529.23	70,975	46.90%	9,019.45	79,994	1.269
6	2028	162,814.75	134,603.24	56.41%	43.59%	75,924.80	58,678.44	12,092.85	73,104	47.40%	11,445.93	84,550	1.341
7	2029	167,699.19	136,363.59	55.68%	44.32%	75,924.80	60,438.79	14,733.38	75,297	47.90%	13,945.20	89,242	1.415
8	2030	172,730.17	138,176.75	54.95%	45.05%	75,924.80	62,251.95	17,453.13	77,556	48.40%	16,519.45	94,075	1.492
9	2031	177,912.07	140,044.31	54.21%	45.79%	75,924.80	64,119.51	20,254.47	79,883	48.90%	19,170.93	99,053	1.571
10	2032	183,249.44	141,967.90	53.48%	46.52%	75,924.80	66,043.10	23,139.84	82,279	49.40%	21,901.95	104,181	1.652
11	2033	188,746.92	143,949.19	52.74%	47.26%	75,924.80	68,024.39	26,111.78	84,747	49.90%	24,714.90	109,462	1.736
12	2034	194,409.33	145,989.92	52.01%	47.99%	75,924.80	70,065.12	29,172.88	87,290	50.40%	27,612.24	114,902	1.822
13	2035	200,241.61	148,091.88	51.27%	48.73%	75,924.80	72,167.08	32,325.81	89,908	50.90%	30,596.51	120,505	1.911
14	2036	206,248.86	150,256.89	50.53%	49.47%	75,924.80	74,332.09	35,573.33	92,606	51.40%	33,670.29	126,276	2.002
15	2037	212,436.32	152,486.85	49.79%	50.21%	75,924.80	76,562.05	38,918.27	95,384	51.90%	36,836.30	132,220	2.097
16	2038	218,809.41	154,783.71	49.05%	50.95%	75,924.80	78,858.91	42,363.57	98,245	52.40%	40,097.28	138,343	2.194
17	2039	225,373.69	157,149.48	48.31%	51.69%	75,924.80	81,224.68	45,912.22	101,193	52.90%	43,456.09	144,649	2.294
18	2040	232,134.90	159,586.22	47.58%	52.42%	75,924.80	83,661.42	49,567.33	104,229	53.40%	46,915.67	151,144	2.397
19	2041	239,098.95	162,096.06	46.84%	53.16%	75,924.80	86,171.26	53,332.09	107,355	53.90%	50,479.03	157,834	2.503
20	2042	246,271.92	164,681.20	46.10%	53.90%	75,924.80	88,756.40	57,209.80	110,576	54.40%	54,149.30	164,725	2.612
21	2043	253,660.08	167,343.89	45.37%	54.63%	75,924.80	91,419.09	61,203.84	113,893	54.90%	57,929.67	171,823	2.725
22	2044	261,269.88	170,086.47	44.64%	55.36%	75,924.80	94,161.66	65,317.69	117,310	55.40%	61,823.45	179,134	2.841
-----													
50	2072	597,766.59	291,359.88	26.06%	73.94%	75,924.80	215,435.08	247,227.82	268,397	69.40%	234,002.09	502,399	7.967
51	2073	615,699.58	297,822.93	25.49%	74.51%	75,924.80	221,898.13	256,922.39	276,449	69.90%	243,178.04	519,627	8.240

Table 4: Progressive system of reducing the tax burden on enterprises

Option number	Year	Growth of the development fund, rubles per month	Receipts to the development fund, rubles per month	The rate contributions to the PFR	Index of deductions to the PFR	The rate of deductions to the FCMIF	Index of deductions to the FCMIF	Income tax rate	Tax on profit rate	VAT rate	Financial result, rubles per month	Increase in VAT deductions, rubles	Deductions to the PFR + VAT, rubles per month	Deductions to the FCMIF + income tax + tax on profit rate, rubles per month	Deductions to the PFR + deductions to the FCMIF + income tax + tax on profit rate + VAT, rubles per month
1	2	3	4	5	6	7	8	9	10	11	12	13	14	15	16
1	2023	0.00	13,904.10	22.00%	1.00	5.10%	1.00	13.00%	20.00%	20.00%	13,904.10	0.00	31,838.98	14,194.68	46,033.66
2	2024	431.18	14,335.28	19.87%	0.90	3.88%	0.76	13.00%	20.00%	20.00%	14,335.28	538.97	31,838.98	14,194.68	46,033.66
3	2025	875.29	14,779.39	17.93%	0.81	2.77%	0.54	13.00%	20.00%	20.00%	14,779.39	1,094.12	31,838.98	14,194.68	46,033.66
4	2026	1,332.73	15,236.83	16.15%	0.73	1.75%	0.34	13.00%	20.00%	20.00%	15,236.83	1,665.91	31,838.98	14,194.68	46,033.66
5	2027	1,803.89	15,707.99	14.52%	0.66	0.82%	0.16	13.00%	20.00%	20.00%	15,707.99	2,254.86	31,838.98	14,194.68	46,033.66
6	2028	2,289.19	16,193.28	13.02%	0.59	0.00%	0.00	13.00%	20.00%	20.00%	16,193.28	2,861.48	31,838.98	14,230.13	46,069.10
7	2029	2,789.04	16,693.14	11.64%	0.53	0.00%	0.00	13.00%	20.00%	20.00%	16,693.14	3,486.30	31,838.98	14,940.11	46,779.09
8	2030	3,303.89	17,207.99	10.36%	0.47	0.00%	0.00	13.00%	20.00%	20.00%	17,207.99	4,129.86	31,838.98	15,671.39	47,510.37
9	2031	3,834.19	17,738.28	9.17%	0.42	0.00%	0.00	13.00%	20.00%	20.00%	17,738.28	4,792.73	31,838.98	16,424.61	48,263.59
10	2032	4,380.39	18,284.49	8.06%	0.37	0.00%	0.00	13.00%	20.00%	20.00%	18,284.49	5,475.49	31,838.98	17,200.42	49,039.40
11	2033	4,942.98	18,847.08	7.03%	0.32	0.00%	0.00	13.00%	20.00%	20.00%	18,847.08	6,178.73	31,838.98	17,999.51	49,838.49
12	2034	5,522.45	19,426.55	6.07%	0.28	0.00%	0.00	13.00%	20.00%	20.00%	19,426.55	6,903.06	31,838.98	18,822.57	50,661.55
13	2035	6,119.30	20,023.40	5.16%	0.23	0.00%	0.00	13.00%	20.00%	20.00%	20,023.40	7,649.13	31,838.98	19,670.33	51,509.31
14	2036	6,734.06	20,638.16	4.32%	0.20	0.00%	0.00	13.00%	20.00%	20.00%	20,638.16	8,417.57	31,838.98	20,543.52	52,382.50
15	2037	7,367.26	21,271.36	3.53%	0.16	0.00%	0.00	13.00%	20.00%	20.00%	21,271.36	9,209.07	31,838.98	21,442.90	53,281.88
16	2038	8,019.46	21,923.55	2.78%	0.13	0.00%	0.00	13.00%	20.00%	20.00%	21,923.55	10,024.32	31,838.98	22,369.26	54,208.24
17	2039	8,691.22	22,595.32	2.08%	0.09	0.00%	0.00	13.00%	20.00%	20.00%	22,595.32	10,864.02	31,838.98	23,323.42	55,162.40
18	2040	9,383.13	23,287.23	1.42%	0.06	0.00%	0.00	13.00%	20.00%	20.00%	23,287.23	11,728.92	31,838.98	24,306.20	56,145.18
19	2041	10,095.81	23,999.90	0.79%	0.04	0.00%	0.00	13.00%	20.00%	20.00%	23,999.90	12,619.76	31,838.98	25,318.46	57,157.44
20	2042	10,829.86	24,733.96	0.20%	0.01	0.00%	0.00	13.00%	20.00%	20.00%	24,733.96	13,537.32	31,838.98	26,361.09	58,200.07
21	2043	11,585.93	25,490.03	0.00%	0.00	0.00%	0.00	13.00%	20.00%	20.00%	25,490.03	14,482.42	32,448.20	27,435.00	59,883.20
22	2044	12,364.69	26,268.79	0.00%	0.00	0.00%	0.00	13.00%	20.00%	20.00%	26,268.79	15,455.86	33,421.64	28,541.13	61,962.77
-----															
50	2072	46,800.42	60,704.52	0.00%	0.00	0.00%	0.00	13.00%	20.00%	20.00%	60,704.52	58,500.52	76,466.30	77,452.81	153,919.11
51	2073	48,635.61	62,539.71	0.00%	0.00	0.00%	0.00	13.00%	20.00%	20.00%	62,539.71	60,794.51	78,760.29	80,059.47	158,819.76

The developed optimization model makes it possible to increase the salaries of employees, which is beneficial to both the state and shareholders, managers and owners of enterprises. The algorithm of practical implementation of the optimization model is as follows.

Formula (14) is used to calculate the financial result, which is given in column 12 of Table 4, and formula (4) is used to calculate the effect of reducing unit costs (see column 9 of Table 3).

Formula (5) is used to calculate receipts to the VAT and PFR (see column 14 of Table 4), and formula (6) is used to determine the values of column 15 of Table 4. To calculate the data presented in column 16 of Table 4, formula (7) is used. The data in column 16 of Table 4 are equal to the sum of the values in the columns 14 and 15 of Table 4.

Formula (3) is used to calculate the share of the company's income, which is used to increase the salaries of employees. Formulas (1) and (2) are used to calculate the increase in wages and the development fund (column 12 of Table 3 and column 3 of Table 4, respectively). The coefficient  $\xi$  is equal to 0.8, which means that 80% of the increase in the financial result of enterprises from the sale of products is directed to the salaries of employees, and 20% is directed to the development fund. This distribution of the financial result is taken from the ratio of wages and financial result in the basic version (63,060 rubles : 13,904.10 rubles = 4.5). We will show an algorithm for calculating deductions for salary increases and to the entrepreneurship development fund using the example of the second row of column 12 of Table 3 and column 3 of Table 4. According to the formula (14), the financial result is 144 658.80 rubles (the company's revenue per employee, see row 2, column 3 of Table 3) – 128 059.83 rubles (the cost of production per employee) = 16,598.96 rubles. The increase compared to the basic version of the simulation is 2,694.86 rubles = 16,598.96 rubles – 13,904.10 rubles (the financial result in the basic version of the simulation, see row 1, column 12 of Table 4). Then for the second row of column 12 of Table 3, the wage increase according to the formula (1) is equal to 2,155.89 rubles. = 2,694.86 rubles (increase in financial result relative to the base value)  $\cdot$  0.8 (coefficient of redistribution of financial result between employees and owners, managers, shareholders of enterprises), and an increase in contributions to the development fund (see the second row, column 3 of Table 4) is 431.18 rubles = 2,694.86 rubles (increase in financial result relative to the base value)  $\cdot$  (1 – 0.8 (coefficient of redistribution of the increase in financial result between employees and managers of enterprises)  $\cdot$  0.8 (adjustment of the income tax rate, 20%, see formula (2))). Similarly, for the other rows of column 12 of Table 3 and column 3 of Table 4. For the 51st variant of the simulation, the growth of the development fund amounted to 48,635.61 rubles per employee (see the last row of column 3 of Table 4), which is more than the basic option development fund [(48,635.61 rubles : 13,904.10 rubles)  $\cdot$  100% = 350%] by 350%.

In column 4 of Table 4 the average monthly contributions to the development fund are given, determined by adding an increase in contributions to the development fund to the base amount of the financial result (see formula (2)). So, for the

second row of column 4 of Table 4 the value of 14,335.28 rubles = 13,904.10 rubles (see the first row, column 4 of Table 4) + 431.18 rubles (see the second row, column 3 of Table 4). Similarly, for the remaining rows of column 4 of Table 4. In column 5 of Table 4 shows the size of the deduction rate in the PFR, which are determined by the formula (11) of the economic and mathematical model (1)-(16) and include the effect of wage growth and VAT. The VAT rate is 20%, the value is shown in column 11 of Table 4. The article [95] shows that pension funding is carried out from two sources: deductions from the wages of employees (22%) and the federal budget (for 2023 – 4,822.23 rubles on average per pensioner). It was emphasized above that wage growth increases VAT and pension contributions and is not beneficial to the labor collective and the owner.

This article proposes a mechanism of state regulation that encourages enterprises to increase wages, which consists in reducing pension contributions and deductions to the FCMIF depending on wage growth, but at the same time does not allow a reduction in the basic amount of deductions for VAT, pension provision, income tax, income tax and deductions to the FCMIF.

According to the second term of the formula (5) of the economic and mathematical model (1)-(16) for the basic (first variant, Table 4) the value of VAT is equal 17,965.78 rubles = (140,445.43 rubles (the average monthly revenue of enterprises, see the first row, column 3 of Table 3) – 50,616.53 rubles (conditionally variable costs, see the first row, column 8 of Table 3))  $\cdot$  0.20 (VAT rate). Further, according to the first term of formula (5), deductions to the PFR are calculated as the product of wages at the rate of deductions to the PFR (63,060 rubles  $\cdot$  0.22 = 13,873.20 rubles). Total deductions, according to formula (5), will be 17,965.78 + 13,873.20 rubles = 31,838.98 rubles (first row, column 14 of Table 4). On the example of the second row of column 14 of Table 4 we will show a *detailed methodology for calculating* the rate of monthly deductions to the PFR and VAT, taking into account the reduction in the rate of deductions to the PFR (column 5 of Table 4):

**Step 1.** We determine the amount of monthly deductions to the PFR and VAT (formula (5) of the economic and mathematical model (1)-(16)). To do this, we will calculate deductions to the PFR and VAT at the base rate of deductions to the PFR (22.0%). And in the future, we will reduce the deduction rate in proportion to the increased amount of deductions so that in row 2, column 14 of Table 4 get an irreducible amount 31,838.98 rubles, i.e. as in the basic version of the simulation.

**Step 2.** We calculate the amount of deductions to the PFR at a rate of 22.0% (see the first term of formula (5)): 67,108 rubles (the average monthly nominal accrued salary, taking into account the progressive labor incentive system, see row 2, column 13 of Table 3)  $\cdot$  0.22 = 14,763.76 rubles.

**Step 3.** Calculate the amount of VAT deductions. According to the second term formula (5) the amount of VAT deductions is equal to (144,658.80 rubles (the average monthly revenue of enterprises, see the second row, column 3 of Table 3) – 52,135.03 rubles (conditionally variable costs of enterprises in the sale of products, services and works, see the second row, column 8 of Table 3))  $\cdot$  0.2 (VAT deduction rate) = 18,504.75 rubles.

**Step 4.** According to formula (5), to the value obtained in step 3 of the algorithm, we add the amount of deductions to the PFR from wages at a rate of 22.0%, we have 18,504.75 rubles + 14,763.76 rubles = 33,268.51 rubles.

**Step 5.** To calculate the rates of deductions to the PFR, the condition is accepted that the amount of monthly deductions to the PFR and VAT must be at least the amount of these deductions in the basic version of the simulation. Thus, the rate of deductions to the PFR can be reduced with an increased salary level so that deductions to the PFR and VAT amount to 31,838.98 rubles (see row 1, column 14 of Table 4). Then, according to the formula (5) of the economic and mathematical model (1)-(16) the amount of deductions to the PFR it should be 31,838.98 rubles – 18,504.75 rubles (total VAT deductions according to step 3 of the algorithm) = 13,334.23 rubles. In other words, the product of increased wages (67,108 rubles for the second row of column 13 of Table 3) the rate of deductions to the PFR should bring at least 13,334.23 rubles, hence we get the rate of deductions to the PFR in the amount of 13,334.23 rubles : 67,108 rubles • 100% = 19.87%, which is indicated in the second row of column 5 of Table 4. Similarly, for all other rows of column 19 of Table 3.

In other words, with this approach, PFR and the federal budget receive an irreducible amount of 31,838.98 rubles per month from each employee, and the company's deductions to the PFR for modeling options are reduced in accordance with formulas (11)-(13) from 22.00% in the basic version to 0.00% in the 21st version of modeling, which corresponds to the 2043st year (see line 21, column 5 of Table 4). Further, the rate of deductions to the PFR remains unchanged and equal to 0.00% (see lines 21-51, column 5 of Table 4). To calculate the rates of deductions to the PFR, the condition of not reducing the amount of monthly deductions due to VAT and deductions to the PFR (formula (5) of the model) was also taken into account, at least the amounts necessary to accumulate funds for retirement for the period of survival (see Table 3-6 [95]), as can be seen from the analysis of the data presented in column 14 of Table 4. Thus, for column 5 of Table 4 the reduction in the rates of deductions to the PFR occurs due to wage growth and the redistribution of VAT funds from the increased amount of wages of working citizens and VAT from the increased volume of manufactured and sold products, goods, works and services to personalized pension accounts of citizens in banks (see formulas (11)-(13)).

Despite the reduction in the rate of deductions to the PFR, the financing of pension provision is not reduced, since it is fully compensated by the increase in VAT deductions received by the federal budget and directed to personalized pension accounts of employees in banks.

Let's look at this process in more detail. In column 13 of Table 4 shows an increase in deductions from VAT in the PFR, compensating for a decrease in the rate of deductions from wages in the PFR (column 5 of Table 4). In the second version of the simulation (2024), deductions from VAT in the PFR will amount to 538.97 rubles (row 2, column 13), in the tenth version of the simulation 5,475.49 rubles, in 20 option (2042) 13,537.32 rubles (row 20, column 13 of Table 4). In all these variants (from 1 to 20), deductions to the PFR and VAT are constant (31,838.98 rubles, column 14) and correspond to the basic variant. But

already in 21 variants (2043) with the rate of deductions to the PFR equal to 0 (row 21, column 5 of Table 4) deductions to the PFR and VAT begin to increase 32,448.20 (line 21, column 14 of Table 4) and to 51 variants in accordance with formula 5 of the economic and mathematical model (1)-(16) amount to 78,760.29 rubles, exceeding the basic modeling variant in (78,760.29 : 31,838.98 = 2.47) 2.47 times.

It should be emphasized that Tables 3 and 4 is suitable only for citizens who started working in 2023. For those who have already worked, the table is shifted a year ago. That is, for those who have already worked for 1 year, the calculation is carried out by 2023 and zero deductions to the PFR will begin from 2044. For those who have been working for 5 years before the implementation of social financing technologies, zero deductions will begin from 2047 and so on.

Thus, the proposed mechanism contributes to the growth of wages of the labor collective, the growth of deductions for development and the growth of revenues to PFR and the federal budget.

Contributions to the FCMIF are formed as follows. According to the formula (6) for the basic (first variant, Table 4) the amount of income tax is determined (63,060 rubles • 0.13 (income tax rate, see column 9 of Table 4) = 8,197.80 rubles, income tax (13,904.10 (financial result, see column 12 of Table 4) • 0.20 (income tax rate, see column 10 of Table 4) = 2,780.82 rubles) and deductions to the FCMIF (63,060 rubles • 0.051 = 3,216.06 rubles), which in total will be: 8,197.80 rubles + 2,780.82 rubles + 3,216.06 rubles = 14,194.68 rubles (first row, column 15 of Table 4).

In other words, with this approach, the territorial budget and the FCMIF receive an irreducible amount of 14,194.68 rubles per month from each employee, and the company's deductions to the FCMIF for modeling options are reduced in accordance with formulas (8)-(10) from 5.10% in the basic version to 0.00% in the 6th version of modeling, which corresponds to the year 2028 (see row 6, column 7 of Table 4). Further, the rate of deductions to the FCMIF remains unchanged and equal to 0.00% (see rows 6-51, column 7 of Table 4). To calculate the rates of deductions to the FCMIF, the condition of not reducing the amount of monthly deductions due to income tax, income tax and deductions to the FCMIF (formula (6) of the model) at least the amount of monthly deductions in the basic version of the simulation was also taken into account, as can be seen from the analysis of the data presented in column 15 of Table 4. Thus, for column 7 of Table 4, the reduction in the rates of deductions to the FCMIF occurs due to wage growth and the redistribution of income tax funds from the increased amount of wages of working citizens and income tax from the increased volume of manufactured and sold products, goods, works and services to personalized medical savings accounts of citizens in banks.

It should be emphasized that despite the reduction in the rate of deductions to the FCMIF, the financing of medical care is not reduced, since it is fully compensated by the increase in income tax and income tax deductions received by the territorial budget and directed to personalized medical savings accounts of working citizens in banks.

Table 5: The Economic Effect

Line number	Year	The growth index of the revenue of the enterprise	Revenue of enterprises per employee, rubles	Wage growth index	Salary deductions + from wages, rubles	Annual wage growth, thousand rubles	Average annual contributions to the development fund, thousand rubles	The rate of deductions to the PFR,	The rate of deductions to the FCMIF
1	2	3	4	5	6	7	8	9	10
0	2023	1.00	140,445.43	1.000	63,060	62,564,096,160	13,794,756,169	22.00%	5.10%
1	2024	1.03	144,658.80	1.064	67,108	66,579,958,692	14,222,544,098	19.87%	3.88%
2	2025	1.06	148,998.56	1.130	71,277	70,716,297,100	14,663,165,666	17.93%	2.77%
3	2026	1.09	153,468.52	1.198	75,571	74,976,725,661	15,117,005,880	16.15%	1.75%
4	2027	1.12	158,072.57	1.269	79,994	79,364,967,078	15,584,461,301	14.52%	0.82%
5	2028	1.15	162,814.75	1.341	84,550	83,884,855,738	16,065,940,384	13.02%	0.00%

And the total deductions due to income tax, income tax and deductions to the FCMIF (column 15 of Table 4, formula (6) of the economic and mathematical model (1)-(16)), despite the reduction in the rate of deductions to the FCMIF, increase from 14,194.68 rubles (in the basic version and variants 2 to 5), starting from option 6 (14,230.13 rubles) to 80,059.47 rubles in the 51st version of the simulation (5.64 times).

Thus, the proposed mechanism contributes to the growth of wages of the labor collective, the growth of deductions for development and the growth of revenues to FCMIF.

It is worth noting that the total deductions due to income tax, income tax, VAT, deductions to the FCMIF and the PFR (see formula (7)) increase from 46,033.66 rubles in the basic version of the simulation to 158,819.76 rubles in the 51st version of the simulation, i.e. 158,819.76 rubles : 46,033.66 rubles = 3.45 times (see column 16 of Table 4).

The rate of deductions to the FCMIF becomes zero already for the salary of a working citizen of Russia in the amount of 84,550 rubles, which is 34.08% higher than the average salary in the country as of November 2022 (84,550 rubles : 63,060 rubles = 1,341), as can be seen by comparing the data presented in line 6, columns 13 of Table 3 and column 7 of Table 4.

**Discussion**

The use of a progressive labor incentive system and the reduction of deductions to the PFR and the FCMIF with a corresponding increase in revenue from VAT, income tax and profit tax is beneficial to working citizens, business owners and the state. The economic effect for working citizens, owners of enterprises and the state from an annual increase in GDP (revenue of enterprises) by 3.0% over the first five years of the introduction of social financing technology is presented in Table 5.

Column 1 of Table 5 shows the year number, and column 2 of Table 5 shows the year. The first row (year zero) of Table 5 corresponds to the basic modeling variant (2023), i.e. row 1 of Tables 3 and 4. It is assumed that the annual revenue of enterprises will increase annually for 5 years by 3.0% from the baseline (row 1 of Tables 3 and 4). The data presented in columns

2-6, 9 and 10 are taken from similar columns of Tables 3 and 4. Annual wage growth (62,564,096,160 thousand rubles, see the first row, column 7 of Table 3) calculated as the product of wages (63,060 rubles, see row 1, column 13 of Table 3), by 12 (the number of months in a year) and by the population of working age according to Rosstat (82,678 thousand people according to Rosstat). With an increase in the revenue of enterprises by 3.0%, wage growth is 6.4% (see the first year, second row, column 5 of Table 5). With an increase in revenue by 3.0% per year for five years, wage growth per employee is 34.1% (see the last row, column 5 of Table 5), and the cumulative annual wage growth for all workers in Russia is 83,884,855,738 thousand rubles (see the last row, column 7 of Table 5). Thus, the wage increase is almost 20 trillion rubles.

Average annual contributions to the development fund (column 8 of Table 5) are determined by multiplying the amount of contributions to the development fund (column 4 of Table 4) by 12 (the number of months in a year) and by 82,678 thousand people (the population of working age). So, for the basic variant (year zero, the first row of column 8 of Table 5) the value of 13,794,756,169 thousand rubles = 13,904.10 rubles • 12 • 82,678 thousand people. For the second row, column 8 of Table 5 value 14,222,544,098 thousand rubles = 14,335.28 rubles • 12 • 82,678 thousand people. For the owners of enterprises, the use of social technologies developed in this article for financing enterprises leads to an increase in the size of average monthly contributions to the development fund to 16,193.28 rubles (see the sixth row, column 4 of Table 4) and this is only from one employee at the enterprise. There are 82,678 thousand citizens of working age in Russia. Thus, with an increase in the revenue of enterprises by 15%, the average annual contributions to the development fund using social technologies for financing enterprises are equal to 16,193.28 rubles • 12 • 82,678 thousand people = 16,065,940,384 thousand rubles (see the last row, column 8 of Table 5), the growth is 16,065,940,384 thousand rubles : 13,794,756,169 thousand rubles = 1.16 times, i.e. average annual contributions to the development fund increased by 16% compared to the base variant, the zero year.

An important result of the use of social financial technologies is the reduction of the deduction rate in the PFR for 5 years to 13.02% and in the FCMIF to 0 for workers with average wages

who started working in 2023 (columns 9 and 10 of Table 5), which allows owners to significantly reduce social contributions and, accordingly, reduce the cost of all manufactured in Russia, goods, works and services.

### Conclusion

The proposed technology of financing enterprises and the Russian economy, harmoniously combining the interests of working citizens, owners and the state, makes it possible:

1. At quite achievable rates of GDP growth (enterprise revenue) by 3% per year, ensure a 34% increase in wages of working citizens over 5 years (see the last row, column 5 of Table 5), **which will practically end poverty**. Under the current funding system, this has not been done in 30 years.

2. To ensure in four years the level of pension provision for current and future pensioners in the amount of 40% of wages; in 8 years – 60% of wages; in 10 years – 80% of wages. Under the current funding system, this has also not been done in 30 years.

3. To increase contributions to the development fund for 5 years by 16% while reducing social contributions (PFR and FCMIF by 14.08%), which, first of all, the owners of enterprises are interested in, since this ensures the growth of their incomes, a significant reduction in cost and the possibility of constant modernization and updating of technological equipment and the release of new competitive products. In other words, if the owner motivates employees by increasing wages to increase sales volumes, then funds for development will grow at a higher rate than revenue. If the owner takes all the profits for himself, as is currently being done at many enterprises, then he will not be able to increase the volume of sales without motivation due to wage growth of working citizens, and, consequently, there will be much less funds for development. Thus, the motivation of employees by increasing wages, and owners by reducing social contributions is extremely beneficial for the owner. It is also important that wage growth, rigidly linked to an increase in product sales, stimulates the entire workforce to develop the enterprise. In other words, not only the owner and senior management, but the entire workforce becomes interested in the development of their enterprise.

4. First, to stabilize, and starting from 2028, to increase deductions to the PFR and the FCMIF and income tax, income tax and VAT receipts and bring this growth to 30% by 2043, which will allow the state to solve many social problems. Reduce deductions to the PFR and FCMIF by 14.08% by 2028, which will significantly reduce the cost of products, services and works of all enterprises in Russia.

5. The wage growth provided by the proposed social financial technologies contributes to the growth of the purchasing power of citizens of the relevant region (stimulates demand), and this, in turn, allows enterprises to increase products sales, which together ensures their development and subsequent wage growth of workers.

6. At the beginning of this article, it was shown that in social relations, the main thing is not to distribute, but to create, and that all goods, works and services are produced in the process of labor at enterprises. Therefore, state (public) funds should, first of all,

perform the function of enterprise development, and only then will the incomes of working citizens grow and there will be funds for social support. The reduction in the rate of deductions to the PFR proposed in this article at wages above a certain level is, as shown in this article, an effective tool to support the development of enterprises. Why drive money up in the form of taxes and social contributions, and then bring it to enterprises and citizens, creating the ground for corruption along the way, when they can immediately be sent to PAPA and medical bills and to enterprises in the form of a reduction in the rate of deductions to the PFR and FCMIF.

### *The developed optimization model (1)-(16) allows:*

1. To determine the optimal ratios of the main economic indicators of the company's division, such as revenue, the price of products, goods, works, services, discounts on them, which are provided to increase demand for the company's products, cost and profit, as well as to provide a progressive system of material incentives for employees involved in the business processes of the enterprise, in depending on the growth or decline of the specified economic indicators of the unit.

2. To create the necessary economic mechanisms for moral and material encouragement of employees of the enterprise to increase the quality and effectiveness of their work, to involve them in the process of managing the activities of the enterprise, to create incentives for the formation of responsibility for the results of work in the workplace.

3. To form long-term work plans of divisions and the enterprise as a whole, to identify deviations in the work of divisions in order to be able to correct them in a timely manner and provide employees with a clear and understandable information base for self-improvement, self-development, formation of independence and responsibility for decisions made.

4. Calculate the size of consumption funds and accumulation funds. Determine, depending on the results of the work, the amount of material remuneration and the amount of deductions for the development of the enterprise, from which sources can be formed in the future for updating the material and technical base of the division, improving the skills of personnel, increasing the capacity of the division of the enterprise and (or) the equipment of the enterprise, the purchase of new technological and auxiliary equipment and necessary consumables for it, which will further contribute to the growth of the volume of manufactured and sold products of the enterprise, goods, works, services, reducing their cost and, ultimately, increasing the profit of the enterprise.

5. To create additional sources of formation and strengthening of the financial system of Russia, since, as mentioned above, working citizens are the basis of the financial system of Russia. This means that the stability of the entire financial system depends on the organized and well-motivated work of working citizens, and the developed economic and mathematical model is a tool for managing the work of employees, increasing their material and moral remuneration depending on the results of work. At the same time, a distinctive feature of the developed staff motivation system is the dependence of the percentage of deductions from income for

stimulating the work of employees on the amount of this income, which makes it possible to use a progressive scale of material incentives.

The developed economic and mathematical model and the system of personnel motivation, which contributes to the growth of the company's revenue, as well as the system of progressive material and moral incentives for employees is a very important source of their development for enterprises.

An essential factor in the proposed system of material and moral incentives for personnel is their direct participation in the decision-making process, together with managers and owners of enterprises, on the acquisition of technological and auxiliary equipment that improves the quality of products, goods, works, services and the throughput capacity of the enterprise division and (or) equipment from the funds accumulated in each division for its development. Such participation morally stimulates each employee of the enterprise to continuously improve their professional qualifications, increases the prestige and demand for their work and at the same time contributes to the development of this division and the enterprise as a whole.

The developed economic and mathematical model of material incentives for employees, consistent with the growth of the company's revenue, allows you to increase deductions for material incentives for employees, as well as deductions for the development of the enterprise. The indisputable practical significance of the model is the functional scientifically based relationship between the structure of the cost of manufactured and sold products, goods, works, services, financial incentives for employees involved directly in the business processes of the enterprise, the amount of deductions to the development fund and revenue, which allows the model to be used for the analysis and development of optimal long-term work plans of divisions and the enterprise as a whole.

Progressive financial incentives lead to an increase in deductions for the development of the enterprise. These funds, allocated for the purchase of advanced technological and auxiliary equipment and staff training, significantly improve the quality of the company's products and contribute to the influx of new customers.

The economic and mathematical model presented in the scientific study is a development plan for the division and the enterprise as a whole. It models how, depending on revenue growth, the profitability and profit of the division's work increases, the cost and prices of the company's products decrease, the material remuneration of personnel and deductions for the development of the division and the enterprise as a whole increase. Social financial technologies for the development of enterprises allows employees to participate in management, coordinating with management their needs for the purchase of technological and auxiliary equipment, based on the amount of financial resources transferred by each division to the development fund. The proposed mechanism of material and moral incentives contributes to the fact that not only the management and owners of the enterprise and their deputies think about the development of the enterprise, but the entire workforce is interested in increasing professional growth, prestige and demand for their work, which contributes to a significant increase

in the quality and availability of the enterprise's products for citizens of the state.

**Conclusion, recommendations and direction of future research.** The economic and mathematical model of the integrated system of social financing of enterprises and the country's economy developed by the authors can be used to improve the accuracy, efficiency and validity of management decisions in the interests of enterprise development, increase the profitability of its activities, increase employee salaries and contributions to the development fund.

The results of the development of the scientific and methodological apparatus and the implementation of practical tools of this study allow us to conclude that the goal of the study has been achieved. The completed scientific work provides management decision makers with effective tools for social financing of enterprises and the country's economy. **The directions of further research on the problems of the article are:** the introduction of a progressive system of stimulating the work of employees in other fields of activity, for example, the provision of educational services to motivate highly effective work of scientific and pedagogical workers, improving their qualifications and professional level; expansion of the technology of setting and solving the problem of nonlinear programming for prospective investors and the search for optimal sources of financial resources from the point of view of the weighted average price for the implementation of investments in the development of enterprises and the economy of the country; adaptation of the economic and mathematical model developed in the article at enterprises of all sectors of the economy; the inclusion of the developed economic and mathematical tools into a unified information and analytical system for managing the financial flows of the enterprise, its interaction with widely used application software products and others.

### Conflict of Interest

The authors declare no conflict of interest.

### References

- [1] A. Prskawetz, G. Feichtinger, M. Luptacik, A. Milik, "Endogenous growth of population and income depending on resource and knowledge," *European Journal of Population*, **14**(4), 305-331, 1999, doi: 10.1007/BF02863319.
- [2] A. Bellou, B. Kaymak, "The cyclical of job quality and real wage grow," *American Economic Review Insights*, **3**(1), 83-96, 2021, doi: 10.1257/aeri.20190553.
- [3] Y. Avraamova, "The risks of reduced welfare of the population: stratification analysis," *Social Sciences*, **48**(3), 37-50, 2017, doi: 10.21557/SSC.49373409.
- [4] A.R. Cardoso, "Long-term impact of minimum wages on workers' careers: evidence from two decades of longitudinal linked employer-employee data," *The Scandinavian Journal of Economics*, **121**(4), 1337-1380, 2019, doi: 10.1111/sjoe.12327.
- [5] C. Krolage, A. Peichl, "Long-run trends in top income shares: the role of income and population growth," *The Journal of Economic Inequality*, **20**, 97-118, 2022, doi: 10.1007/s10888-021-09520-8.
- [6] C.C. Chao, M.S. Ee, X. Nguyen, E.S.H. Yu, "Minimum wage, firm dynamics, and wage inequality: theory and evidence," *International Journal of Economic Theory*, **18**(3), 2021, doi: 10.1111/ijet.12307.
- [7] Y.Y. Finogenova, "Analysis of new financing opportunities for Russian pension insurance system," *European Journal of Economics and Management Sciences*, **1**, 47-53, 2017, doi: 10.20534/EJEMS-17-1-47-52.
- [8] N. Gavkalova, I. Kolupaieva, M. Barka Zine, "Analysis of the efficiency of levers in the context of implementation of the state regulatory policy,"

- Економічний часопис-xxi, **165**(5-6), 41-46, 2017, doi: 10.21003/ea.V165-09.
- [9] J. Barry, "Real wage growth in the U.S. health workforce and the narrowing of the gender pay gap," *Human Resources for Health*, **19**(1), 2021, doi:10.1186/s12960-021-00647-3.
- [10] J. Adda, C. Dustmann, "Sources of wage growth," *Journal of Political Economy*, **131**(2), 2023, doi: 10.1086/721657.
- [11] E.V. Kabashova, "Statistical methods in the analysis factors of welfare of the population," *Modern European Researches*, **1**, 27-34, 2017.
- [12] J. Končar, R.M. Marić, S. Yučenović, G. Yukmirović, "Employee welfare in the western balkanretail sector: how to improve it through socio-organizational variables," *Revija za Socijalnu Politiku*, **27**(2), 151-170, 2020, doi: 10.15838/esc.2022.1.79.6.
- [13] L. Malcoci, V. Mocanu, "The middle class in the republic of Moldova: determinant factors of formation," *Economie si Sociologie: Revista Teoretico-stiintifica*, **1-2**, 103-111, 2017.
- [14] E. Pelinescu, M. Iordan, M.N. Chilian, "Digitization and population welfare in the new EU member states," *Romanian Journal of Economic Forecasting*, **24**(4), 59-75, 2021.
- [15] J. Pi, Y. Ge, J. Yin, "The impacts of rural property rights on urban unemployment, wage inequality, and welfare in developing countries," *Journal of Economic Analysis & Policy*, **17**(1), 2015-2025, 2017, doi: 10.1515/bejeap-2015-0225.
- [16] P. Litynski, "Living in sprawling areas: a cost-benefit analysis in Poland," *Journal of Housing and the Built Environment*, 2022, doi:10.1007/s10901-022-09986-6.
- [17] S.N. Rastvortseva, I.V. Manaeva, "Modern development of small and medium-sized cities: trends and drivers," *Economic and Social Changes: Facts, Trends, Forecast*, **15**(1), 110-127, 2022, doi: 10.15838/esc.2022.1.79.6.
- [18] G.N. Semenova, E.I. Larionova, O.G. Karpovich, S.V. Shkodinsky, F.M. Ouroumova, "Social integration as a factor of economic growth: experience and perspectives of developing countries," *International Journal of Sociology and Social Policy*, 2020, doi: 10.1108/IJSSP-03-2020-0083.
- [19] R.S.P. Singh, "The 4 quadrants of monthly household budgets," *Research Trends in Multidisciplinary Subjects*, **1** 264, 264-271, 2022.
- [20] E. Sofilda, R. Hamzah, M. Zilal Hamzah, "The effect analysis of minimum regional wages and macroeconomic on poverty level in Indonesia period 2010-2015," *Oida International Journal of Sustainable Development*, **11**(10), 11-24, 2018.
- [21] S. Brunow, S. Losch, O. Okhrin, "Labor market tightness and individual wage growth: evidence from Germany," *Journal for Labour Market Research*, **56**(1), 2022.
- [22] L. Snyayeva, A. Yarchuk, D. Verba, I. Verkhohod, D. Aleksandrov, "Resources of educational and healthcare industries and population welfare: comparative analysis in post-socialist and OECD countries," *WSEAS Transactions on Business and Economics*, **18**, 531-542, 2021, doi: 10.37394/23207.2021.18.54.
- [23] U. Ulugkhan, "Employment of the population on the basis of development and regulation of the labor market, demographic factors and welfare economic development of the region," *Internauka*, **182**(6-2), 66-67, 2021.
- [24] X. Lu, X. Wu, R. Xu, "Why low unemployment rate in the United States has not delivered meaningful wage growth," *Highlights in Business, Economics and Management*, **2**, 2022, doi: 10.54097/hbem.v2i.2386.
- [25] E.V. Sokolov, E.V. Kostyrin, A.B. Balantsev, "Social technologies of enterprise financing," *Economics and Management: Problems, Solutions*, **3**(4), 13-27, 2021, doi: 10.36871/ek.up.pr2021.04.03.002.
- [26] E.V. Sokolov, E.V. Kostyrin, "Justification of expediency of transition of financing of domestic healthcare to medical savings accounts," *Economics and Management: Problems, Solutions*, **4**(8), 194-212, 2018.
- [27] E.V. Sokolov, E.V. Kostyrin, "Justification of the necessity and effectiveness of the introduction of medical savings accounts for all subjects of the Russian Federation and Russia as a whole," *Economics and Management: Problems, Solutions*, **11**(1), 52-65, 2018.
- [28] A.P.B. Etges, V. Grenon, M. Lu et al., "Development of an enterprise risk inventory for healthcare," *BMC Health Serv Res*, **18**, 578, 2018, doi: 10.1186/s12913-018-3400-7.
- [29] J. Horkoff, M.A. Jeusfeld, J. Ralyté et al., "Enterprise modeling for business agility," *Bus Inf Syst Eng*, **60**, 1-2, 2018, doi: 10.1007/s12599-017-0515-z.
- [30] J.E. Vahlne, W.A. Bhatti, "Relationship development: a micro-foundation for the internationalization process of the multinational business enterprise," *Manag Int Rev*, **59**, 203-228, 2019, doi: 10.1007/s11575-018-0373-z.
- [31] A.A. Adamenko, D.V. Petrov, V.V. Markelov, "Effective management of cash flows of an economic entity," *Bulletin of the Academy of Knowledge*, **6**(35), 14-18, 2019.
- [32] K.B. Akhmedjanov, I.S. Musakhonzoda, "Financial performance management system as a factor of efficiency of a balanced financial management system," *Journal of Advanced Research in Dynamical and Control Systems*, **5**(12), 301-310, 2020, doi: 10.5373/JARDCS/V12I5/20201718
- [33] M. Alnaimat, N. Rudyk, A. Al-Naimi, A. Panchenko, I. Turski, "The impact of international economic sanctions on the use of financial technologies," *WSEAS Transactions on Business and Economics*, **20**, 682-693, 2023, doi: 10.37394/23207.2023.20.63.
- [34] L.N. Altunina, I.E. Khorolskaya, A.I. Smirnova, "Evaluation of the effectiveness of cash flow management of a commercial organization," *Bulletin of the Academy of Knowledge*, **4**(39), 41-46, 2020, doi: 10.24411/2304-6139-2020-10435.
- [35] S. K. Azimov, "The development of financial markets and financial theory," *Theoretical & Applied Science*, **8**(112), 2409, 2022, doi: 10.15863/TAS.2022.08.112.3
- [36] L.E. Basovskiy, *Financial management*, Moscow, INFRA-M, 2019.
- [37] M.U. Boboev, D.A. Gaibulloeva, "Baxisobgiri moliyavāi xamchun manbai ittilooti nizomi menejementi moliyavāi," *Bulletin of the Technological University of Tajikistan*, **1**(44), 125, 2021.
- [38] T. Bolgar, V. Varenik, Z. Pestovska, I. Miro, "Innovative information technologies in financial management," *Academic Review*, **2**, 98-110, 2022, doi: 10.32342/2074-5354-2022-2-57-8.
- [39] J.L. Combes, P. Plane, T. Kinda, R. Ouedraogo, "Financial flows and economic growth in developing countries," *Economic Modelling*, **83**(c), 195-209, 2019, doi: 10.1016/j.econmod.2019.02.010.
- [40] A. Aurora Ndelo, Y. Permatasari, I. Harymawan, N. Anridho, "Corporate tax avoidance and investment efficiency: evidence from the enforcement of tax amnesty in Indonesia," *Economics*, **10**(10):25, 1-23, 2022, doi:10.3390/economics10100251.
- [41] A. Ali, "Investment projects portfolio analyses using fuzzy evaluation methods," *Advances in Intelligent Systems and Computing*, **1306**, 685-693, 2021, doi: 10.1007/978-3-030-64058-3\_85.
- [42] K. Amel, "Corporate sustainability disclosure and investment efficiency: the Saudi Arabian context," *Sustainability*, **14**(21):13984, 1-13, 2022, doi: 10.3390/su142113984.
- [43] A. Costăngioară, "Introducing a new requirement in the assessment of the impact of companies on the environment, the multidimensional approach," in *19th International Scientific Geoconference*, 271-278, 2019, doi: 10.5593/sgem2019/4.1/S17.035.
- [44] E. Vasilyeva, T. Kudryavtseva, D.V. Ovsyanko, "Evaluation of the effectiveness of investment in innovation in industry," *Innovation Project Management*, **9**, 13-18, 2019, doi:10.17513/vaael.693.
- [45] M.A. Filina, Z.M. Umarova, "Investment risk: types and evaluation methods," *Era of Science*, **20**, 477-480, 2019, doi: 10.24411/2409-3203-2019-12099.
- [46] I. Golaydo, I. Parshutina, G. Gudimenko, A. Lazarenko, N. Shelepina, "Evaluation, forecasting and management of the investment potential of the territory," *Journal of Applied Economic Sciences*, **2**(48):12, 618-635, 2017.
- [47] M.V. Grenaderova, "Methodological approaches to the evaluation of investment efficiency taking into account environmental factors," in *IOP Conference Series Materials Science and Engineering*, **753**(8):082036, 1-5, 2020, doi: 10.1088/1757-899X/753/8/082036.
- [48] J.J. Heung, M.O. Hyun, "Debt origin and investment efficiency from Korea," *International Journal of Financial Studies*, **8**(3):47, 1-27, 2020, doi: 10.3390/ijfs8030047.
- [49] D.D. Ierkovska, M.Yu. Bugayko, Hryhorak, Yu. Zaloznova, N. Trushkina, S.I. Gritsenko, T.I. Dovgan, V.Z. Ninich, V.A. Kulik, V.Ye. Marchuk, O.M. Harmash, O. Karpun, N.M. Perederii, "Intellectualization of logistics and supply chain management," *Electronic Scientific and Practical Collection*, **9**, 2021, doi:10.46783/smart-scm/2021-9.
- [50] J. Bian, Ya. Shan, G. Zhao, "Evaluation and analysis of environmental protection investment efficiency in China based on DEA model," *Research Square*, 1-16, 2021, doi: 10.21203/rs.3.rs-277471/v1.
- [51] K. Yang, S. Fahad, F. Yuan, "Evaluating the influence of financial investment in compulsory education on the health of Chinese adolescents: a novel approach," *BMC Public Health*, **22**(1):1725, 1-15, 2022, doi: 10.1186/s12889-022-14125-5.
- [52] K. Kim, J. Koo, J. Kim, "Development of an investment efficiency evaluation model for waterworks maintenance through data envelopment



- analysis," *Desalination and Water Treatment*, 73-72, 2018, doi: 10.5004/dwt.2018.21640.
- [53] M.V. Korolkova, T.S. Novikova, "Approaches to the efficiency evaluation for the complex of interrelated investment projects," *World of Economics and Management*, 18(3):66-80, 2018, doi: 10.25205/2542-0429-2018-18-3-66-80.
- [54] P. Kovalenko, A. Rokochinskiy, P. Volk, V. Turcheniuk, N. Frolenkova, R. Tykhenko, "Evaluation of ecological and economic efficiency of investment in water management and land reclamation projects," *Journal of Water and Land Development*, 1-3(48), 81-87, 2021, doi: 10.24425/jwld.2021.136149.
- [55] L. Lijia, X. Guanglong, L. Keyao, H. Juhua, M. Wanzhen, W. Xuejie, Zh. Huiyu, "Investment efficiency assessment of distribution network for the high proportion of renewable energy: a hybrid multiattribute decision-making method," *Mathematical Problems in Engineering*, 2022, doi: 10.1155/2022/2373363.
- [56] L. Wang, J. Liang, J. Liu, "Research on investment efficiency evaluation of wind power projects under supply-side reform," in *IOP Conference Series Earth and Environmental Science*, 508(1):012089, 1-5, 2022, doi: 10.1088/1755-1315/508/1/012089.
- [57] Y. Liu, H. Zhang, Y. Wu, Y. Dong, "Ranking range based approach to MADM under incomplete context and its application in venture investment evaluation," *Technological and Economic Development of Economy*, 5(25), 877-899, 2019, doi: 10.3846/tede.2019.10296.
- [58] M. Luchko, R. Ruska, G. Lew, I. Vovk, "Modelling the optimal size of investment portfolio in a non-state pension fund," *Journal of International Studies*, 1(12), 239-252, 2019, doi: 10.14254/2071-8330.2019/12-1/16.
- [59] S.K. Malhotra, A. Saran, D. John, H. White, N.D. Cruz, J. Eyers, E. Beveridge, N. Blöndal, "Studies of the effectiveness of transport sector interventions in low- and middle-income countries: an evidence and gap map," *Campbell Systematic Reviews*, 4(17), e1203, 2021, doi: 10.1002/cl2.1203.
- [60] M. Nourani, Q.L. Kweh, W.M. Lu, I. Gurrib, "Operational and investment efficiency of investment trust companies: do foreign firms outperform domestic firms?" *Financial Innovation*, 8(79), 2022, doi: 10.1186/s40854-022-00382-1.
- [61] V. Obinna, C. Amarachi, L. Anthony, D. Ajibare, Oladayo, D. Oluleye, "Small and medium enterprises assessment of investment decisions and financial performance of small and medium enterprises in federal capital territory," *Nigeria*, 40-49, 2022, doi: 10.46281/ijsmes.v5i1.1813.
- [62] Y. Qixiong, L. Zhenqiu, C. Yu, Z. Ying, "An investment efficiency evaluation model for distribution network with distributed renewable energy resources," *Frontiers in Energy Research*, 10, 1-4, 2022, doi: 10.3389/fenrg.2022.931486.
- [63] Q. Trung Tran, Q. Dat Tran, "How does national culture affect corporate investment efficiency?" *Global Business Review*, 2022, doi: 10.1177/09721509221088898.
- [64] O. Sumets, "Evaluation of the investments efficiency in the development of the key component of the supply chain," *Electronic Scientific and Practical Publication in Economic Sciences*, 5, 43-61, 2021, doi: 10.46783/smart-scm/2021-5-4.
- [65] S.T. Do, N.N.N. Tran, "An investment willingness assessment model for private sector in PPP transportation," *Public-Private Partnership Transportation Projects in Vietnam*, 2019.
- [66] P. Wang, "Application of cloud computing and information fusion technology in green investment evaluation system," *Journal of Sensors*, 1-13, 2021, doi: 10.1155/2021/2292267.
- [67] X. Wang, W. Chen, W.J. Lekse, "Investment selection and evaluation for china express delivery market," *International Journal of Industrial Engineering: Theory Applications and Practice*, 2(28), 190-208, 2021.
- [68] W. Hao, H. Gao, Z. Liu, "An evaluation study on investment efficiency: a predictive machine learning approach," *Complexity*, 1-9, 2021, doi: 10.1155/2021/6658516.
- [69] X. Tian, Y. Zhang, G. Qu, "The impact of digital economy on the efficiency of green financial investment in China's provinces," *International Journal of Environmental Research and Public Health*, 19(14):8884, 1-18, 2022, doi:10.3390/ijerph19148884.
- [70] G. Xiong, L. Wang, "Factors and economic evaluation of transnational investment risks," *Discrete Dynamics in Nature and Society*, 1030183, 2021, doi: 10.1155/2021/1030183.
- [71] G. Kou, X. Chao, Y. Peng, F. Wang, "Network resilience in the financial sectors: advances, key elements, applications, and challenges for financial stability regulation," *Technological and Economic Development of Economy*, 28(2), 531-558, 2022, doi:10.3846/tede.2022.16500.
- [72] L. Lehoux, T.V. Morozova, E.G. Safonova, A.D. Balashova, M.V. Protasov, "Practical aspects in calculating of impairment of financial assets according to IFRS 9 Financial instruments," in *Proceedings of the 33RD International Business Information Management Association Conference, IBIMA 2019: Education Excellence and Innovation Management Through Vision 2020*, 6624, 2019.
- [73] P. Liu, A. Hendalianpour, "A branch cut/metaheuristic optimization of financial supply chain based on input-output network flows: investigating the Iranian orthopedic footwear," *Journal of Intelligent and Fuzzy Systems*, 41(2), 2561, 2021, doi: 10.3233/JIFS-201068.
- [74] U.S. Aliyu, H.L. Ozdeser, B.L. Çavuşoğlu, M.A.M. Usman, "Food security sustainability: a synthesis of the current concepts and empirical approaches for meeting SDGS," *Sustainability*, 21(13), 2021, doi: 10.3390/su132111728.
- [75] H. El Bilali, "Research on agro-food sustainability transitions: where are food security and nutrition?" *Food Security*, 11(3), 559-577, 2019, doi: 10.1007/s12571-019-00922-1.
- [76] D. Enahoro, K.M. Rich, S.S. Staal, D. Mason-D'croz, M. Mul, T.P. Robinson, P. Thornton, "Supporting sustainable expansion of livestock production in south Asia and sub-saharan Africa: scenario analysis of investment options," *Global Food Security*, 20, 114-121, 2019, doi: 10.1016/j.gfs.2019.01.001.
- [77] D. Hall, "National food security through corporate globalization: Japanese strategies in the global grain trade since the 2007-8 food crisis," *Journal of Peasant Studies*, 47(5), 993-1029, 2020, doi: 10.1080/03066150.2019.1615459.
- [78] S. Li, X. Li, L. Sun, G. Cao, G. Fischer, S. Tramberend, "An estimation of the extent of cropland abandonment in mountainous regions of China," *Land Degradation and Development*, 29(5), 1327-1342, 2018. doi: 10.1002/ldr.2924.
- [79] A. Semin, A. Kibirov, U. Rassukhanov, "Problems and main mechanisms to increase investment attractiveness of agricultural production," *European Research Studies Journal*, 21(2), 378-400, 2018, doi: 10.35808/ersj/1009.
- [80] G.T. Shakulikova, A.S. Baidalinova, A.M. Uakhitzhanova, G.B. Baimuldina, E.B. Ikmatova, "Agriculture financing – a basic premise for ensuring food security in Kazakhstan," *Journal of Applied Economic Sciences*, 13(1), 216-226, 2018.
- [81] M. Svanidze, L. Götz, I. Djuric, T. Glauben, "Food security and the functioning of wheat markets in Eurasia: a comparative price transmission analysis for the countries of central Asia and the south Caucasus," *Food Security*, 11(3), 733-752, 2019, doi: 10.1007/s12571-019-00933-y.
- [82] O.V. Vaganova, N.E. Solovjeva, O.N. Polukhin, V.M. Zakharov, G.G. Zabnina, R.V. Lesovik, S.L. Lesovaya, M.E. Ageykina, "Analysis of supply chain in investment activity in the Russian agricultural complex," *International Journal of Supply Chain Management*, 9(5), 1615-1622, 2020.
- [83] V. Verma, B. Vishal, A. Kohli, P.P. Kumar, "Systems-based rice improvement approaches for sustainable food and nutritional security," *Plant Cell Reports*, 40(11): 2021-2036, 2021, doi: 10.1007/s00299-021-02790-6.
- [84] K. Wakjira, T. Negera, A. Zacepins, A. Kviesis, V. Komasilovs, S. Fiedler, S. Kirchner, O. Hensel, D. Purnomo, M. Nawawi, A. Paramita, O.F. Rachman, A. Pratama, N.A. Faizah, M. Lemma, S. Schaedlich, A. Zur, M. Sper, K. Proschek, K. Gratzer, R. Brodschneider, "Smart apiculture management services for developing countries-the case of SAMS project in Ethiopia and Indonesia," *Peerj. Computer Science*, 7, e484, 2021, doi: 10.7717/PEERJ-CS.484.
- [85] E.V. Sokolov, E.V. Kostyrin, "Medical savings accounts as a tool for increasing doctors' salaries and motivating Russian citizens to high-performance work and a healthy lifestyle," *Economics and Management: Problems, Solutions*, 7(2), 24-31, 2020, doi: 10.34684/ek.up.p.r.2020.07.02.004.
- [86] E.V. Sokolov, E.V. Kostyrin, "Organization of the transition of citizens of the Sverdlovsk region to medical savings accounts," *Economics and Management: Problems, Solutions*, 12(108):1, 39-60, 2020, doi: 10.36871/ek.up.p.r.2020.12.01.007.
- [87] E.V. Sokolov, E.V. Kostyrin, "The economic effect of using medical savings accounts instead of the existing system of healthcare financing," *Economics and Management: Problems, Solutions*, 2(110):1, 16-26, 2021, doi: 10.36871/ek.up.p.r.2021.02.01.003.
- [88] E.V. Sokolov, E.V. Kostyrin, "The mechanism of financing health care on the basis of medical savings accounts," *Economics and Management: Problems, Solutions*, 3(5), 64-85, 2019.
- [89] E.V. Sokolov, E.V. Kostyrin, S.V. Lasunova, "Financial technologies for the development of enterprises and the economy of Russia," *Economics*

- and Management: Problems, Solutions, **10**(118):1, 91-106, 2021, doi: 10.36871/ek.up.p.r.2021.10.01.013.
- [90] E.V. Sokolov, E.V. Kostyrin, P.A. Nevezhin, "Modeling of the insurance and accumulative parts of the old-age labor pension," *Economics and Management: Problems, Solutions*, **9**(1), 132-153, 2018.
- [91] E.V. Sokolov, E.V. Kostyrin, K.V. Rudnev, "Social financial technologies for the development of enterprises and the economy of Russia," *Soft Measurements and Calculations*, **9**(46), 74-96, 2021, doi: 10.36871/2618-9976.2021.09.004.
- [92] E.V. Sokolov, E.V. Kostyrin, "Social financial technologies for the development of large scale healthcare systems and the Russian economy," in *2022 15th International Conference Management of Large-Scale System Development (MLSD)*, 1-5, 2022. doi: 10.1109/MLSD55143.2022.9934748.
- [93] E.V. Sokolov, P.A. Nevezhin, "Breakthrough technologies of old-age labor pension financing," *Economics and Management: Problems, Solutions*, **7**(3), 4-9, 2018.
- [94] E.V. Sokolov, "The main source of development of the financial system of Russia," *Economics and Management: Problems, Solutions*, **9**(2), 158-161, 2016.
- [95] E.V. Sokolov, E.V. Kostyrin, "Breakthrough technologies of old-age labor pension financing," *Economics and Management: Problems, Solutions*, **7**(115):1, 63-80, 2021, doi: 10.36871/ek.up.p.r.2021.07.01.009.
- [96] E.V. Kostyrin, "Progressive system of stimulating the work of doctors," *Economics and Entrepreneurship*, **2**(103), 1122-1131, 2019.
- [97] S. Abbasov, "Improving cash flow management," *Economic Herald of the Donbas*, **33-38**, 2021, doi: 10.12958/1817-3772-2021-4(66)-33-38.
- [98] M. Apsite, D. Belova, "Financial analysis as a cash flow management tool," *Interactive Science*, 2019, doi: 10.21661/r-509061.
- [99] N. Atakul, "Exploring the cash flow management strategies of Turkish construction companies," *Journal of Construction Engineering, Management & Innovation*, **5**, 2022, doi: 10.31462/jcemi.2022.03168180.
- [100] O. Chubka, I. Skoropad, "Features of cash flow management in public finance," *Odessa National University Herald. Economy*, **25**, 2020, doi: 10.32782/2304-0920/2-81-25.
- [101] O. Chubka, R. Zhelizniak, "Cash flow management in banking," *International Humanitarian University Herald. Economics and Management*, 2019, doi: 10.32841/2413-2675/2019-40-21.
- [102] L. Dvořáková, J. Kronych, A. Malá, "Cash flow management as a tool for corporate processes optimization," *Smart Science*, **6**(1-7), 2018, doi: 10.1080/23080477.2018.1505370.
- [103] E. Etim, E. Daferighe, E. Enang, M. Nyong, "Cash flow management and financial performance of selected listed companies in Nigeria," *Indo-Asian Journal of Finance and Accounting*, **3**, 27-46, 2022, doi: 10.47509/IAJFA.v03i01.03.
- [104] Z. Imanbayeva, H. Kusainov, B. Zhakupova, A. Niyazbayeva, B. Bimbetova, "Ways to improve the company's cash flow management," *Reports*, **4**, 177-185, 2020, doi: 10.32014/2020.2518-1483.107.
- [105] K. Ketova, I. Rusyak, E. Kasatkina, E. Saburova, D. Vavilova, "Organizing the cash flow management in the construction industry in the Russian Federation," in *IOP Conference Series: Materials Science and Engineering*, **862**, 042035, 2020, doi: 10.1088/1757-899X/862/4/042035.
- [106] K. Koopman, R. Cumberlege, "Cash flow management by contractors," in *IOP Conference Series: Earth and Environmental Science*, **654**, 012028, 2021, doi: 10.1088/1755-1315/654/1/012028.
- [107] O. Korobova, M. Blum, "Application of digital technologies in cash flow management at a commercial enterprise," *Voprosy Sovremennoj Nauki i Praktiki*, 062-070, 2021, doi: 10.17277/voprosy.2021.02.pp.062-070.
- [108] T. Kucherenko, H. Anishchenko, "Accounting and analytical support of cash flow management of enterprises," *Efektivna Ekonomika*, 2020, doi: 10.32702/2307-2105-2022.2.12.
- [109] O. Kudyrko, I. Kopchykova, "Methodological approaches to cash flow management at the enterprise," *European Journal of Economics and Management*, **8**, 17-22, 2022, doi: 10.46340/eujem.2022.8.3.3.
- [110] A. Nanggala, "Free cash flows, management ownership, dividend policy, and debt policy," *Jurnal Ekonomi Akuntansi dan Manajemen*, **19**, 30, 2020, doi: 10.19184/jeam.v19i1.17544.
- [111] E. Nangih, T. Ofor, O. Joshua, "Cash flow management and financial performance of quoted oil and gas firms in Nigeria," *Journal of Accounting and Financial Management*, **6**, 2020.
- [112] M. Nashkerska, N. Patriki, "Instruments for cash flow management of construction enterprises," *Economic Analysis*, 223-229, 2020, doi: 10.35774/econa2020.01.02.223.
- [113] O. Oladimeji, O. Aina, "Cash flow management techniques practices of local firms in Nigeria," *International Journal of Construction Management*, **21**, 1-9, 2018, doi: 10.1080/15623599.2018.1541705.
- [114] J. Ongpeng, K. Aviso, D. Foo, R. Tan, "Graphical pinch analysis approach to cash flow management in engineering project," *Chemical Engineering Transactions*, **76**, 493, 2019, doi: 10.3303/CET1976083.
- [115] K.V. Oriekhova, O.Hr. Golovko, "Cash flow management strategy," *Economics and Law*, 89-97, 2022, doi: 10.15407/econlaw.2022.01.089.
- [116] X. Peng, Z. Ren, "Design and implementation of electronic commerce cash flow management system," *Agro Food Industry Hi-Tech*, **28**, 2535-2540, 2017.
- [117] T. Phuong, N. Thuy, "Impact of cash flow management on shareholder value of listed real estate companies in Vietnam," *Vnu Journal of Economics and Business*, **1**, 2021, doi: 10.57110/jeb.v1i4.4584.
- [118] N. Piontkovich, E. Shatkovskaya, "An organization's cash flow management in digital economy," in *Proceedings of the Ecological-Socio-Economic Systems: Models of Competition and Cooperation (ESES 2019)*, 2020, doi: 10.2991/assehr.k.200113.099.
- [119] S.T. Dinh, N.C. Phuc, "Foreign financial flows, human capital and economic growth in African developing countries," *International Journal of Finance and Economics*, **27**(5), 2020, doi: 10.1002/ijfe.2310.
- [120] L.N. Dobryshina, "Socio-economic security: essence, evolution, factors," *Transport Business of Russia*, **10**, 5-7, 2011.
- [121] K.V. Ekimova, I.P. Savelyeva, K.V. Kardapol'tsev, *Financial management*, Moscow, Yurayt Publishing House, 2019.
- [122] Explanatory note to the draft federal law "On compulsory medical insurance in the Russian Federation using medical accounts," 2019, URL: <http://sokolov.expert>.
- [123] V.A. Fedorov, "Methodology for assessing the impact of the effect of financial leverage on the total cash flow of the company," *Innovations and Investments*, **10**, 60-62, 2021.
- [124] A.M. Galimova, A.N. Kirpikov, "Perspective economic assessment of financial stability indicators organizations with the use of economic and mathematical modeling of cash flows," *Economic Bulletin of the Republic of Tatarstan*, **1**, 64-72, 2019.
- [125] A.A. Ilyinykh, "The economic essence of the cash flow of the organization," *Young Scientist*, **14**, 103-105, 2019.
- [126] Z. JingJing, "Risk assessment method of agricultural management investment based on genetic neural network," *Security and Communication Networks*, **1-10**, 2022, doi: 10.1155/2022/2373363.
- [127] A. Podgornaya, K. Romanov, "Actual issues of cash flow management in enterprises in Russia," *Género & Direito*, **8**, 2019, doi: 10.22478/ufpb.2179-7137.2019v8n6.49183.
- [128] E.V. Kostyrin, "Economic and mathematical models of financial incentives for the personnel at medical organization departments," *International Journal of Pharmaceutical Research*, **4**(12), 1769-1780, 2020, doi: 10.31838/ijpr/2020.12.04.253.
- [129] E.V. Kostyrin, "Economic and mathematical modeling of financial resource management in medical organizations," *Industrial Engineering and Management Systems*, **3**(19), 716-729, 2020, doi: 10.7232/ie.ms.2020.19.3.716.
- [130] A.V. Kemenov, *Cash flow management*, Moscow, UNITY-DANA, 2015.
- [131] K.V. Ketova, D.D. Vavilova, "Optimization of financial flows in a building company using an escrow account in the Russian Federation," in *Recent Research in Control Engineering and Decision Making*, 427-442, 2021, doi: 10.1007/978-3-030-65283-8\_35.
- [132] A.N. Kirpikov, T.A. Sibgatullin, "Simulation modeling of cash flows in the system of predictive analysis and financial management of an organization," *Scientific Review: Theory and Practice*, **7**(63):9, 1086-1100, 2019, doi: 10.35679/2226-0226-2019-9-7-1086-1100.
- [133] A.E. Kisova, V.K. Zolotareva, "Cash flows as a factor in ensuring financial stability of an organization," *Notes of a Scientist*, **8**, 362, 2021.
- [134] M.A. Magomedov, E.D. Ozdeadzhieva, "Features of managing financial flows of the enterprise," *Economics and Entrepreneurship*, **3**(140), 1038-1041, 2022, doi: 10.34925/EIP.2022.140.03.196.
- [135] S. Mahdi, Z. Grzegorz, A. Arash, E.G. Frateme, "The impact of investment efficiency on firm value and moderating role of institutional ownership and board independence," *Journal of Risk and Financial Management*, **15**(4):170, 1-13, 2022, doi: 10.3390/jrfm15040170.
- [136] M.B. Melikhov, "Methodological foundations of systematic economic and statistical modeling of financial flows," *Bulletin of the Tula branch of the Financial University*, **1-1**, 227-238, 2019.
- [137] S.S. Morozkina, A.V. Rykalo "Analysis of the organization's cash flows," *Natural Sciences and Humanities Research*, **24**(2), 55-59, 2019.
- [138] E.A. Pirogova, V.S. Kirsanova, "Financial flow management," *Development Trends and Actual Problems of Assessment, Management and Regulatory Support of the Financial System of Russia*, **2**, 205, 2020.

- [139] N.S. Plaskova, N.A. Prodanova, E.V. Prokofieva, "Methods of financial analysis of the organization's cash flows and assessment of the effectiveness of cash flow management," *Financial Analysis: Theory and Practice*, 106, 2021.
- [140] A. Ramli, L. Yekini, "Cash flow management among micro-traders: responses to the COVID-19 pandemic," *Sustainability*, **14**, 10931, 2022, doi: 10.3390/su141710931.
- [141] I. Rosemary, I. Abner, A. Jack, O. Fausat, E. Enoch, U. Samuel, "Cash flow management and industrial firms' performance in Nigeria," *Universal Journal of Accounting and Finance*, **9**, 2021, doi: 10.13189/ujaf.2021.090416.
- [142] A. Shash, A. Qarra, "Cash flow management of construction projects in Saudi Arabia," *Project Management Journal*, **49**(2):875697281878797, 2018, doi: 10.1177/8756972818787976.
- [143] M. Sofyan, U. Ludigdo, A.D. Mulawarman, (2021). "The meaning of cash flow management for the non-bank housing developers," *International Journal of Research in Business and Social Science*, (2147-4478), **10**, 195-203, doi: 10.20525/ijrbs.v10i4.1174.
- [144] A. Sulla, D. Slepchenko, I. Kuzmicheva, E. Zaostrovskikh, "Financial logistics and its application in cash flow management", 2021, doi: 10.2991/assehr.k.210322.206.
- [145] O. Vodolazska, K. Petrenko, "Enterprise cash flows: management principles and methods," *Eastern Europe: Economy, Business and Management*, 2019, doi: 10.32782/easterneurope.23-88.
- [146] V. Voloshina-Sidey, I. Rud, O. Portnenko, "Cash flow management at the enterprise during COVID-19," *Market Infrastructure*, 2021, doi: 10.32843/infrastruct54-33.
- [147] K.S. Zaryvakhina, "Cash flow management of the corporation in the conditions of instability," *Scientific Review. Economic Sciences*, **10-15**, 2022, doi: 10.17513/sres.1102.
- [148] U.D. Atmond, V. Vyatkin, Z. Salcic, K.I.K. Wang, "A service-oriented programming approach for dynamic distributed manufacturing systems," *IEEE Transactions on Industrial Informatics*, **1**(16), 151-160, 2020, doi: 10.1109/TII.2019.2919153.
- [149] M. Dehgnani, Z. Montazeri, A. Ehsanifar, A.R. Seifi, M.J. Ebadi, O.M. Grechko, "Planning of energy carriers based on final energy consumption using dynamic programming and particle swarm optimization," *Электротехника і Електромеханіка*, **5**, 62-71, 2018, doi: 10.20998/2074-272X.2018.5.10.
- [150] B. Di, A. Lamperski, "Newton's method, Bellman recursion and differential dynamic programming for unconstrained nonlinear dynamic," *Dynamic Games and Applications*, **413**, 87-102, 2021, doi: 10.1007/s13235-021-00399-8.
- [151] B. Doerr, A. Eremeev, F. Neumann, M. Theile, C. Thyssen, "Evolutionary algorithms and dynamic programming," *Theoretical Computer Science*, **43**(412), 6020-6035, 2011, doi: 10.1016/j.tcs.2011.07.024.
- [152] M.I. Gomoyunov, "Dynamic programming principle and Hamilton-Jacobi-Bellman equations for fractional-order systems," *Siam Journal on Control and Optimization*, **6**(58), 3185-3211, 2020, doi: 10.1137/19M1279368.
- [153] M. Justiz, B. Bychko, S. Soler, V. Frolov, O. Malafeyev, A. Vasileva, "Application of dynamic programming to minimize energy consumption in industrial dryers," *Bulletin de L'academie International Concorde*, **2**, 3-20, 2021.
- [154] T.S. Karaseva, "Genetic programming algorithm for the dynamic systems identification," *Young People. Society. Modern Science, Technology and Innovation*, **19**, 299-301, 2020.
- [155] K. Land, B. Vogel-Heuser, S. Cha, "Applying dynamic programming to test case scheduling for automated production systems," *Communication in Computer and Information Science*, **1262**, 3-20, 2020, doi: 10.1007/978-3-030-58167-1\_1.
- [156] V. Struchenkov, D.A. Karpov, "High-speed dynamic programming algorithms in applied problems of a special kind," *Mathematics and Statistics*, **3**(8), 339-346, 2020, doi: 10.13189/ms.2020.080313.
- [157] A. Yamaganov, A. Agafonov, V. Myasnikov, "An improved map matching algorithm based on dynamic programming approach," *Lecture Notes in Business Information Processing*, **413**, 87-102, 2021, doi: 10.1007/978-3-030-71846-6\_5.
- [158] Y. Zhu, G. Jia, "Dynamic programming and Hamilton-Jacobi-Bellman equations on time scales," *Complexity*, 7683082, 2020, doi: 10.1155/2020/7683082.
- [159] J. Butt, "A conceptual framework to support digital transformation in manufacturing using an integrated business process management approach," *Designs*, **4**(3), 1-39, 2020, doi: 10.3390/designs4030017.
- [160] K.A. Krylyvetz, A.A. Krylyvetz, "Process approach in the quality management system," *Young People. Society. Modern Science, Technology and Innovation*, **19**, 201-203, 2020.
- [161] F. Li, G. Fang, "Process-aware accounting information system based on business process management," *Wireless Communications and Mobile Computing*, **2022**, 7266164, 2022, doi: 10.1155/2022/7266164.
- [162] O. Olshanskiy, "Development of methods of improvement of business process management," *Technology Audit and Production Reserves*, **5**(4), 20-25, 2018, doi: 10.15587/2312-8372.2018.146862.
- [163] P. Saragiotis, "Business process management in the port sector: a literature review," *Maritime Bussiness Review*, **4**(1), 49-70, 2019, doi: 10.1108/MABR-10-2018-0042.
- [164] S.G. Sboeva, Y.A. Klyueva, N.L. Burdaev, M.A. Zaharchenko(2019). "Development of methodical bases for business process management optimization in clinical trials," *Journal of Advanced Pharmacy Education and Research*, **9**(2), 137-142, 2019.
- [165] S. Tabassam, O. Hassan, E. AL-Qahtnae, N. AL-Ahmary, "Question metrics and its application to process management and improvement," *National Journal on Engineering Applications*, **7**(2), 52-58, 2019, doi: 10.15866/irea.v7i2.17013.
- [166] L.A. Taskymbayeva, A.A. Shaikh, R.A. Salimbayeva, "Application of business process management methods in higher education institutions," *Central Asian Economic Review*, **3**(144), 45-55, 2022, doi: 10.52821/2789-4401-2022-3-45-55.
- [167] A.S. Voskovskaya, T.A. Karpova, P.P. Rostovtseva, N.V. Guseva, A.V. Shelygov, "Development of the learning process management in the context of digitization," *Revista Inclusiones*, **7**(S4-5), 240-249, 2020.
- [168] N. Yehorchenkova, O. Yehorchenkov, "Modeling of project portfolio management process by cart algorithm," *Advances in Intelligent Systems and Computing*, **1265**, 353-363, 2021, doi: 10.1007/978-3-030-58124-4\_34.
- [169] M. Saha, K.D. Dutta, "Nexus of financial inclusion, competition, concentration and financial stability: Cross-country empirical evidence," *Competitiveness Review*, 2020, doi: 10.1108/CR-12-2019-0136.
- [170] M.Y. Shakatreh, M.M.A. Orabi, B.R.T. Shammout, "The role of financial vigilance in predicting possible financial distress among foreign banks," *Journal of Management Information and Decision Science*, **24**(5), 1-18, 2021.
- [171] E.G. Spodareva, Ya.V. Sazhnikova, "Monitoring as a way of managing financial flows at the enterprise," *Bulletin of the Ural Institute of Economics, Management and Law*, **2**(59), 4, 2022.
- [172] S. Suhadak, R.S. Mangesti, S.R. Handayani, "GCG, financial architecture on stock return, financial performance and corporate value," *International Journal of Productivity and Performance Management*, **69**(9), 1813, 2019, doi: 10.1108/IJPPM-09-2017-0224.
- [173] L.B. Sungatullina, E.S. Golovchenko, "The economic essence of the company's cash flows as an object of financial management," *Accounting in Budgetary and Non-profit Organizations*, **1**(505), 14, 2021.
- [174] X. Yujing, Z. Qinli, W. Daolin, W. Shihai, "Mining investment risk assessment for nations along the belt and road initiative," *Land*, **11**(8):1287, 2022, doi: 10.3390/land11081287.
- [175] Q. Zhang, F. Li, "Financial resilience and financial reliability for systemic risk assessment of electricity markets with high-penetration renewables," *IEEE Transactions on Power Systems*, **37**(3), 2312-2321, 2022, doi: 10.1109/TPWRS.2021.3115499.
- [176] N.F. Zhokabine, "Cash flows in the financial resources management system of the enterprise," *Bulletin of Lugansk State University named after Vladimir Dal*, **1**(43), 62-66, 2021.

## Tunable Resistorless Phase Shifter Realization with a Single VDGA

Orapin Channumsin<sup>1</sup>, Jirapun Pimpol<sup>1</sup>, Tattaya Pukkalanun<sup>2</sup>, Worapong Tangsrirat<sup>2,\*</sup>

<sup>1</sup>Faculty of Engineering, Rajamangala University of Technology Isan, Khonkaen Campus, Khonkaen 40000, Thailand

<sup>2</sup>School of Engineering, King Mongkut's Institute of Technology Ladkrabang, Bangkok 10520, Thailand

### ARTICLE INFO

Article history:

Received: 30 January, 2023

Accepted: 12 May, 2023

Online: 12 June, 2023

Keywords:

Voltage Differencing Gain

Amplifier (VDGA)

Phase shifter

Electronically tunable

All-pass filter

Voltage-mode circuit

### ABSTRACT

This paper describes the design of a phase shifter with electrically adjustable parameters employing only one voltage differencing gain amplifier (VDGA) and one floating capacitor. This circuit requires no external resistors, resulting in a resistorless design and a low component count. The proposed circuit implements a first-order all-pass filter response with electronic control of its passband gain, pole frequency, and phase difference via bias current modification. Non-ideal effects of the VDGA on the phase shifter circuit are also examined. PSPICE simulation results using TSMC 0.25- $\mu\text{m}$  real process parameters and practical test results using readily available LM13700s are incorporated to validate the theoretical conclusions. The results indicate that the simulations and experiments yielded phase shift deviations of 2.22% and 3.11%, respectively. The pole-frequency errors for simulations and experiments were 0.31% and 0.63%, respectively. The applicability of the suggested phase shifter is illustrated by the design of the voltage-mode quadrature oscillator.

## 1. Introduction

The design and synthesis of the phase shifter circuit, also known as a first-order all-pass filter, has received a great deal of interest [1]. In general, the phase behavior of the phase shifter circuit can be adjusted from  $0^\circ$  to  $180^\circ$  or from  $180^\circ$  to  $0^\circ$ , while its amplitude remains unchanged over the entire frequency range of interest. Due to this, the phase shifter circuit is employed in a number of communication and instrumentation systems, such as universal biquad filters, high quality factor frequency-selective filters, and quadrature and multiphase oscillators [2]-[20]. However, voltage-mode phase shifter circuits with one or more active components are the most often suggested circuits in [2]-[3], [5]-[16], [18]-[20]. Additionally, many of the works in [2]-[3], [5], [10]-[16], [18],[20] are inaccessible electronically. Moreover, all of these configurations are realized with the use of external passive resistors.

The main objective of this contribution is, therefore, to design a simple and compact phase shifter circuit with only one active and one passive component. Without an extra passive resistor, the

suggested structure consists merely of one voltage difference gain amplifier (VDGA) and one floating capacitor. The benefits of the design include the facility, low power consumption, and small integrated chip area. Furthermore, the important features of the proposed phase shifter, including passband gain ( $H_0$ ), pole frequency ( $\omega_p$ ), and phase response ( $\phi$ ), are electronically tunable through the transconductance gains of the VDGA. A thorough investigation is also done into the non-ideal gain effects of the VDGA on the circuit performance. In addition, a new voltage-mode quadrature oscillator is proposed to highlight the advantages of the designed phase shifter. The designed circuit and its application are simulated using PSPICE software using TSMC 0.25- $\mu\text{m}$  CMOS process technology, and the simulation results are consistent with the theoretical analysis. The experimental measurement results from the laboratory breadboard using commercially available LM13600s are also given to prove the features of the proposed circuit. In addition, a summary of the performance comparison of the proposed circuit and those that the previous works [2]-[20] is provided in Table 1. The observations show that the suggested circuit has more features than recently published circuits, which is commendable.

\*Corresponding Author: Worapong Tanasrirat, Email: worapong.ta@kmitl.ac.th

Table 1: Comparative study of the proposed circuit with the similar previous works.

Ref	Year	No. of active components	No. of passive components	Resistorless structure	Variable-gain control	Electronic tunability	Power dissipation (W)	Pole frequency (Hz)	Supply voltages (V)	Technology
[2]	2005	CCII+ = 2	R = 2, C = 2	no	yes	no	NA	15.9 k	±12 (experiment)	AD844
[3]	2006	DDCC = 1	R = 1, C = 1	no	no	no	NA	265.4 k	±3.3 (simulate)	1.2 μm
[4]	2017	MMCC = 1, CFA = 1	R = 1, C = 1	yes	no	yes	NA	9.91 M	NA	AD835, AD844
[5]	2000	CDBA = 1	R = 1, C = 1	no	no	no	NA	1.59 M	±2.5 (simulate)	0.8 μm
[6]	2001	CCCII+ = 1	R = 1, C = 1	yes	no	yes	NA	10 M	±2.5 (simulate)	0.35 μm
[7]	2015	VDGA = 1	R = 1, C = 1	yes	yes	yes	1.45 m	429 k	±1.5 (simulate)	0.35 μm
[8]	2017	VDBA = 1	R = 1, C = 1	yes	no	yes	0.37 m	1.06 M	±0.75 (simulate)	0.25 μm
[9]	2019	LT1228 = 1	R = 2, C = 1	yes	no	yes	NA	100 k	±5 (simulate)	LT1228
[10]	2010	FDCCH = 1	R = 2, C = 1	no	no	no	NA	1.59 M	±3.3 (simulate)	0.35 μm
[11]	2012	DDCC = 2	R = 1, C = 1	no	no	no	NA	15.91 M	±2.5 (simulate)	0.5 μm
[12]	2011	FDCCH = 1	R = 1, C = 1	no	no	no	NA	2.65 M	±1.3 (simulate)	0.35 μm
[13]	2012	DDCC = 2	R = 1, C = 1	no	no	no	NA	1.17 M	±2.5 (simulate)	0.5 μm
[14]	2019	Fig.2: CFOA = 2 Fig.3: CFOA = 3	Fig.2: R = 5, C = 1 Fig.3: R = 6, C = 1	no	yes	no	Fig.2: 0.26, Fig.3: 0.39	7.59 k	±10 (experiment)	AD844
[15]	2020	VCII+ = 2	R = 3, C = 1	no	yes (TM)	no	1.22 m	636.6 k	±0.9 (simulate)	0.18 μm
[16]	2020	EXCCII = 1	R = 2, C = 2	no	no	no	0.7 m	3.18 M	±1.2 (simulate)	0.25 μm
[17]	2021	ICCI+ = 2	Fig.2: R = 1, C = 1 Fig.3: C = 1	Fig.2: no, Fig.3: yes (active resistor)	no	Fig.2: no, Fig.3: yes	3.29 m (simulate)	7.96 M (simulate), 159 k (experiment)	±0.75 (simulate), ±9 (experiment)	0.13 μm, AD844
[18]	2021	CFOA = 2	Fig.1: R = 3, C = 1 Fig.2: R = 4, C = 1	no	yes	no	NA	33.829 k	±8 (simulate/ experiment)	AD844
[19]	2021	FDCCH = 1	C = 1	yes (active resistor)	no	yes	2 m	6.37 M	±1.25 (simulate)	0.25 μm
[20]	2022	DVCC = 2	Fig.1 : R = 1, C = 1 Fig.2 : R = 3, C = 1	no	Fig.1: no Fig.2: yes	no	0.6	62.41 k	±5 (simulate)	AD844
This work	2022	VDGA = 1	C = 1	yes	yes	yes	1.56 m (simulate)	1.59 M (simulate), 159 k (experiment)	±0.75 (simulate), ±5 (experiment)	0.25 μm, LM13600

Abbreviation:

NA = Not Available

CCII = second-generation current conveyor, DDCC = differential difference current conveyor, MMCC = Multiplication Mode Current Conveyor, CFA = current feedback operational amplifier, CDBA = current differencing buffered amplifier, CCCII+ = plus-type current-controlled current conveyor, VDBA = voltage differencing buffered amplifier, FDCCH = fully differential current conveyor, CFOA = current feedback operational amplifier, VCII+ = plus-type second-generation voltage conveyor, EXCCII = extra-X second generation current conveyor, ICCII+ = plus-type second-generation current conveyor, DVCC = differential voltage current conveyor, TM = transimpedance-mode

## 2. Proposed Circuit Configuration

The VDGA was first introduced in [21], as illustrated in Figure 1. The VDGA device is a six-port versatile active building block described by the following matrix equation [21]-[22]:

$$\begin{bmatrix} i_z \\ i_{zc} \\ i_x \\ v_w \end{bmatrix} = \begin{bmatrix} g_{mA} & -g_{mA} & 0 \\ -g_{mA} & g_{mA} & 0 \\ 0 & 0 & -g_{mB} \\ 0 & 0 & \beta \end{bmatrix} \begin{bmatrix} v_p \\ v_n \\ v_z \end{bmatrix} \quad (1)$$

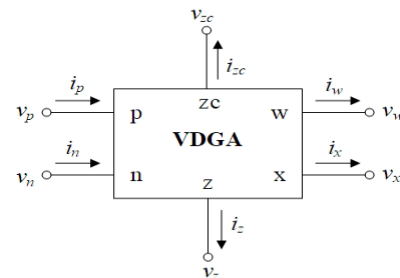


Figure 1: Circuit symbol of the VDGA.

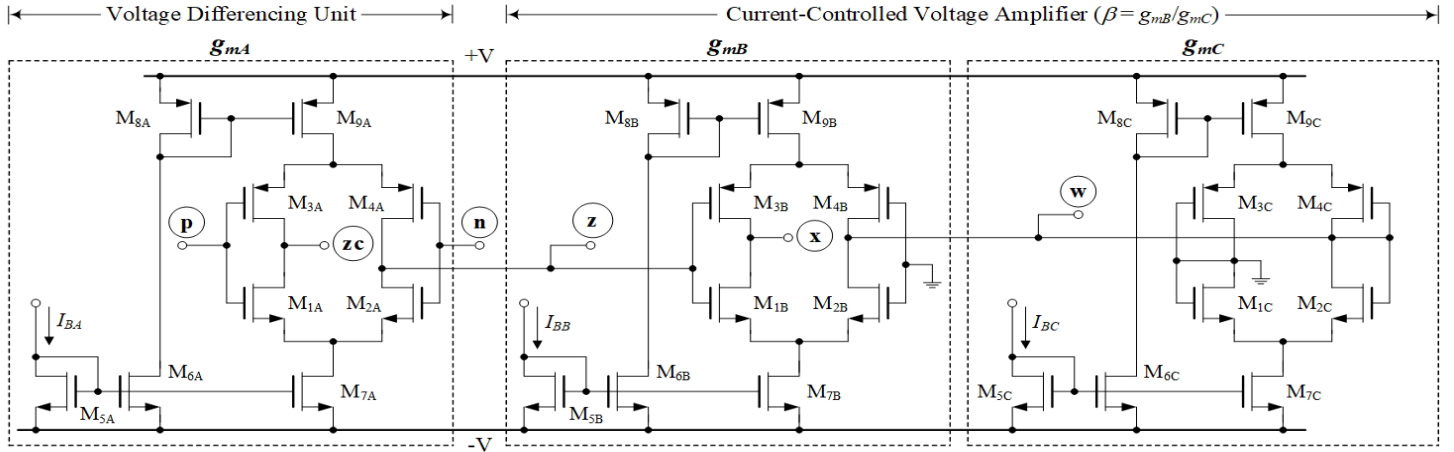


Figure 2: CMOS internal structure of the VDGA.

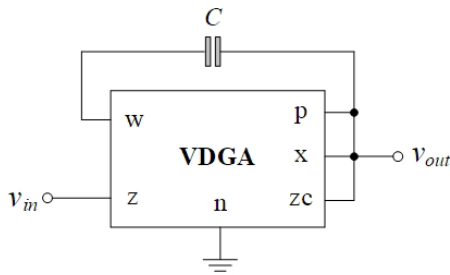


Figure 3: Proposed single VDGA-based resistotless phase shifter circuit.

In (1),  $g_{mk}$  ( $k = A, B, C$ ) and  $\beta$  represent the transconductance gain and the voltage transfer gain of the VDGA, respectively. This element has two high input impedance voltages ( $v_p$  and  $v_n$ ), three high output impedance currents ( $i_z$ ,  $i_{zc}$  and  $i_x$ ), and a zero output impedance voltage ( $v_w$ ).

The values of  $g_{mk}$  and  $\beta$ , when implemented in CMOS technology such as that depicted in Figure 2 [22]-[23], can be expressed as follows:

$$g_{mk} = \sqrt{K \left( \frac{W}{L} \right) I_{Bk}} \quad (2)$$

and 
$$\beta = \frac{g_{mB}}{g_{mC}} \quad (3)$$

where  $K = \mu_0 C_{ox}$  is the transistor transconductance,  $\mu_0$  is the carrier mobility,  $C_{ox}$  is the gate-oxide capacitance per unit area, and  $W/L$  is the width-to-length ratio of the transistor. From Figure 2, the CMOS VDGA is made up of three sections of transconductance amplifiers ( $M_{1A} - M_{9A}$ ,  $M_{1B} - M_{9B}$  and  $M_{1C} - M_{9C}$ ). Each transconductor contributes its own transconductance gain  $g_{mk}$  that is electronically controllable. Consequently, external bias currents  $I_{Bk}$  can be used to adjust the parameters  $g_{mk}$  and  $\beta$  of the VDGA.

Figure 3 depicts the realization of the phase shifter circuit that requires only one VDGA and one floating capacitor without an external resistor requirement. Despite the fact that the capacitor  $C$  employed in this realization is floating, a second poly-layer technique is provided by advanced integrated circuit (IC) technology, making it simple to implement [24]. A preliminary

analysis of the proposed configuration in Figure 3 gives the voltage transfer function shown below

$$\frac{V_{out}(s)}{V_{in}(s)} = \beta \left( \frac{\frac{sC}{g_{mC}} - 1}{\frac{sC}{g_{mA}} + 1} \right) \quad (4)$$

Assuming  $g_m = g_{mA} = g_{mC}$ , the passband gain ( $H_0$ ), pole frequency ( $f_p$ ) and phase response ( $\phi$ ) of the configuration are obtained as:

$$H_0 = \beta \quad (5)$$

$$f_p = \frac{\omega_p}{2\pi} = \frac{g_m}{2\pi C} \quad (6)$$

and 
$$\phi = \pi - 2 \tan^{-1} \left( \frac{\omega C}{g_m} \right) \quad (7)$$

Thus, the transconductances  $g_{mk}$  or by changing the external bias currents  $I_{Bk}$  can be modified to alter the values of  $H_0$ ,  $\omega_p$  and  $\phi$ . Also noticed is the fact that the gain  $\beta$  can be controlled to provide orthogonal  $H_0$  control.

### 3. Effects of Non-Ideal Gains

Ideally, the VDGA features are thought to be perfect. However, due to device mismatch, transfer errors may occur in CMOS implementations of VDGA, deviating from the expected behavior. The impact of the VDGA non-idealities on the functioning of the suggested circuit must thus be investigated. In view of VDGA's non-ideal gains, (1) may be changed and expressed as:

$$\begin{bmatrix} i_z \\ i_{zc} \\ i_x \\ v_w \end{bmatrix} = \begin{bmatrix} \alpha_A g_{mA} & -\alpha_A g_{mA} & 0 \\ -\alpha_A g_{mA} & \alpha_A g_{mA} & 0 \\ 0 & 0 & -\alpha_B g_{mB} \\ 0 & 0 & \delta \beta \end{bmatrix} \begin{bmatrix} v_p \\ v_n \\ v_z \end{bmatrix} \quad (8)$$

where  $\alpha_k = 1 - \varepsilon_\alpha$  represents the transconductance inaccuracy coefficient, and  $\delta = 1 - \varepsilon_\delta$  represents the parasitic voltage transfer

gain. Here,  $\varepsilon_\alpha$  ( $|\varepsilon_\alpha| \ll 1$ ) and  $\varepsilon_\delta$  ( $|\varepsilon_\delta| \ll 1$ ) are the undesirable parameters deviating from unity due to the transfer errors of the VDGA. For the non-ideal analysis of the suggested phase shifter circuit in Figure 3, the modified parameters  $H_0$ ,  $f_p$ , and  $\phi$  can be given by the following expressions:

$$H_0 = \delta\beta \quad (9)$$

$$f_p = \frac{\alpha_A g_m}{2\pi C} \quad (10)$$

and 
$$\phi = \pi - 2 \tan^{-1} \left( \frac{\delta\omega C}{\alpha_B g_m} \right) \quad (11)$$

It is evident from (9)-(11) that the circuit parameters  $H_0$ ,  $f_p$  and  $\phi$  are slightly affected by the unwanted factors  $\alpha_k$  and  $\delta$  of the VDGA. However, this effect can be diminished by modifying the transconductance gain  $g_{mk}$  for the circuit shown in Figure 3. According to (2), the value of  $g_{mk}$  can be modified conveniently by altering the external bias current  $I_{Bk}$ .

#### 4. Simulation Verification

In order to evaluate the performance of the proposed phase shifter circuit in Figure 3, the CMOS-based VDGA in Figure 2 was simulated with the TSMC 0.25- $\mu\text{m}$  transistor model in PSPICE computer simulation program. Symmetrical supply voltages of  $+V = -V = 0.75\text{V}$  were used to bias the VDGA. The transistor sizes ( $W$  and  $L$ ) used in the VDGA realization are listed in Table 2.

Table 2: Transistor sizes used in VDGA realization of Figure 2.

Transistor	$W$ ( $\mu\text{m}$ )	$L$ ( $\mu\text{m}$ )
$M_{1k}\text{-}M_{2k}$	15	0.25
$M_{3k}\text{-}M_{4k}$	23	0.25
$M_{5k}\text{-}M_{7k}$	4.5	0.25
$M_{8k}\text{-}M_{9k}$	5.5	0.25

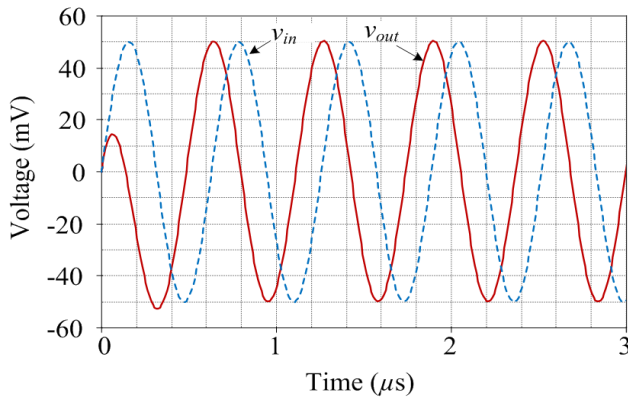


Figure 4: Simulation results of the transient waveforms of the proposed phase shifter in Figure 3.

The active and passive component values are specified as:  $g_{mA} = g_{mB} = g_{mC} = 1 \text{ mA/V}$ , ( $I_{BA} = I_{BB} = I_{BC} = 100 \mu\text{A}$ ), and  $C = 0.1 \text{ nF}$  for the proposed resistorless phase shifter with  $H_0 = 1$  and  $f_p = 1.59 \text{ MHz}$ . Figure 4 shows the simulated transient responses of the proposed circuit for an input signal with a sinusoidal frequency of  $1.59 \text{ MHz}$  and an amplitude of  $50 \text{ mV}$  (peak). In contrast to the

theoretical value of  $\phi = 90^\circ$ , the simulation results show a phase difference between  $v_{in}$  and  $v_{out}$  of  $\phi = 92^\circ$ .

Figure 5 also shows the simulation outcomes for the gain and phase frequency characteristics in comparison to the ideal curves. The simulated  $f_p$  is approximately  $1.585 \text{ MHz}$ , resulting in a frequency error of  $0.31 \%$ . The simulation results clearly show that they closely match the theoretical predictions, demonstrating the usefulness of the suggested circuit. It is discovered that the simulated power dissipation of the circuit is around  $0.82 \text{ mW}$ , when the input  $v_{in}$  is kept grounded.

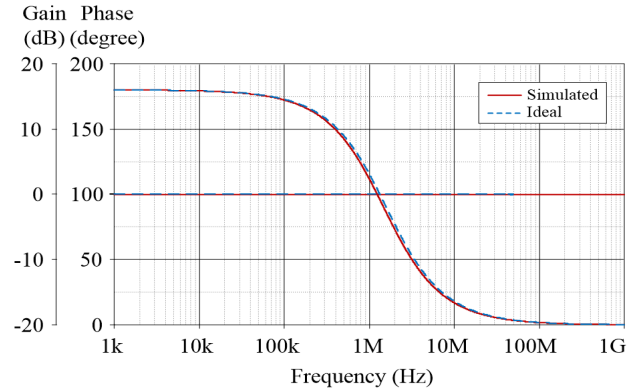


Figure 5: Ideal and simulated frequency characteristics of the proposed phase shifter in Figure 3.

Figure 6 depicts the electronic tuning of  $H_0$  without altering the  $\phi$ -value by controlling the  $g_{mB}$ -value. The values of the circuit components for these settings are listed in Table 3. The sinusoidal input waveform in these figures is  $20 \text{ mV}$  (peak) at  $f = 1.59 \text{ MHz}$ . While  $g_{mA} = g_{mC} = 1 \text{ mA/V}$  ( $I_{BA} = I_{BC} = 100 \mu\text{A}$ ) remains constant, the values of  $g_{mB}$  are altered between  $0.707 \text{ mA/V}$ ,  $1 \text{ mA/V}$ , and  $1.414 \text{ mA/V}$  ( $I_{BB} = 50 \mu\text{A}$ ,  $100 \mu\text{A}$ , and  $200 \mu\text{A}$ ). These facts lead to the  $\beta$ -value being, respectively,  $0.707$ ,  $1$ , and  $1.414$ .

Table 3: Component values for electronic tuning of  $H_0$  with  $I_{BB}$ .

$I_{BB}$ ( $\mu\text{A}$ )	$g_{mB}$ (mA/V)	$I_{BA} = I_{BC}$ ( $\mu\text{A}$ )	$g_{mA} = g_{mC}$ (mA/V)	$\beta$ ( $g_{mB}/g_{mC}$ )
50	0.707	100	1	0.707
100	1.000	100	1	1.000
200	1.414	100	1	1.414

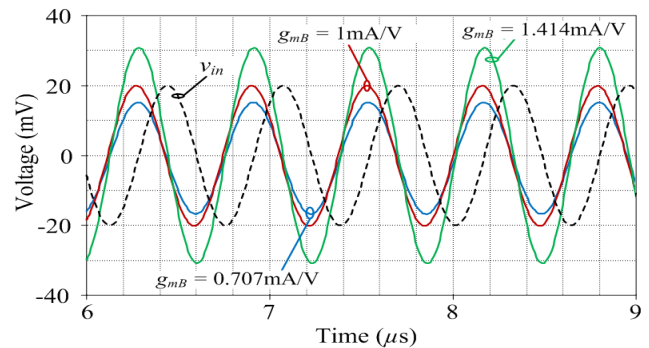


Figure 6: Simulated transient waveforms of the proposed phase shifter with tuning  $g_{mB}$  value.

The simulated transient responses of the circuit and its corresponding phase response are also shown in Figures 7 and 8 for three different values of  $g_m$ , i.e.,  $g_m = g_{mk} = 0.707$  mA/V, 1 mA/V and 1.414 mA/V ( $I_{Bk} = 50$   $\mu$ A, 100  $\mu$ A, and 200  $\mu$ A). The computed values of  $\phi$  were determined to be, respectively, 70.5°, 90°, and 109.4°. The measured  $\phi$  values based on the simulation results were 73°, 92.1°, and 110.2°, respectively, which accord quite well with the estimated values.

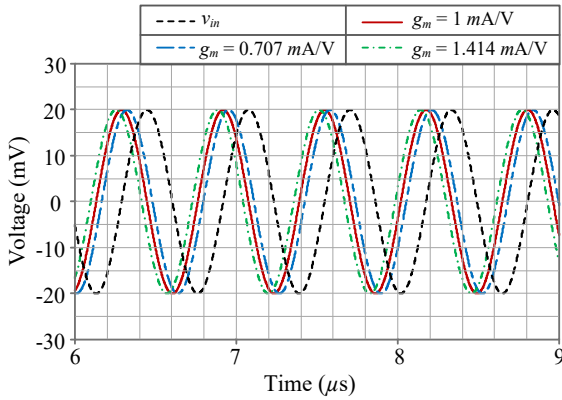


Figure 7: Simulated transient waveforms of the proposed phase shifter with tuning  $g_m$  value.

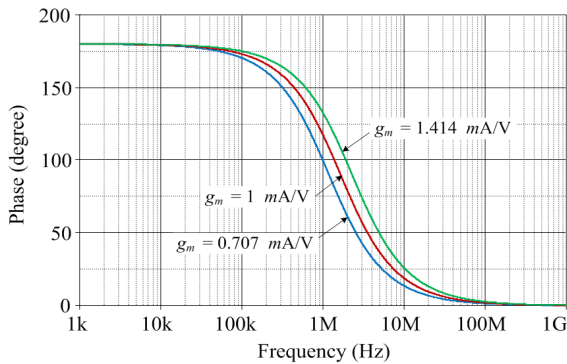


Figure 8: Simulated frequency characteristics of the proposed phase shifter with tuning  $g_m$  value.

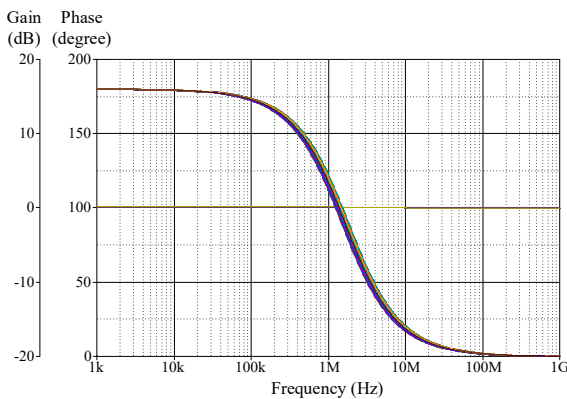


Figure 9: Monte Carlo statistical analysis for the frequency responses of the proposed phase shifter circuit with 5% capacitor tolerance.

In order to demonstrate the impact of capacitor tolerance on the gain and phase responses, a Monte Carlo analysis with a hundred runs is performed for the proposed phase shifter circuit given in

Figure 3. It is supposed that the value of capacitor C will change uniformly by 5%. Figure 9 depicts the simulated frequency responses of Monte Carlo statistical analysis. In addition, the results of the Monte Carlo analysis indicate that the mean and sigma of  $f_p$  are approximately 1.589 MHz and  $2.204 \times 10^{10}$ , respectively. It can be clearly seen from Figure 9 that the capacitance tolerance has a minor effect on the frequency response of the proposed circuit.

### 5. Experimental Measurements

Experimental measurement was used to validate the practicability of the designed circuit in Figure 3. The schematic for the practical implementation of the VDGA is shown in Figure 10 [25], using readily available IC dual-OTA LM13600s from National Semiconductor [26]. For LM13600s, the DC bias voltages are  $+V = -V = 5V$ .

The proposed phase shifter circuit of Figure 3 was constructed with the following component values:  $g_{mk} = 1$  mA/V ( $I_{Bk} = 100$   $\mu$ A) and  $C = 1$  nF. For time-domain analysis, the circuit was applied with a sinusoidal input of frequency 159 kHz and of amplitude 50 mV (peak). The measured waveforms for  $v_{in}$  and  $v_{out}$  are shown in Figure 11. The measured  $\phi$  is 92.8°, which is close to the theoretical  $\phi$  of 90°. Accordingly, the measured phase error is about 3.11%. Figure 12 also shows the measured Fourier spectrum of the output waveform  $v_{out}$  at 159 kHz.

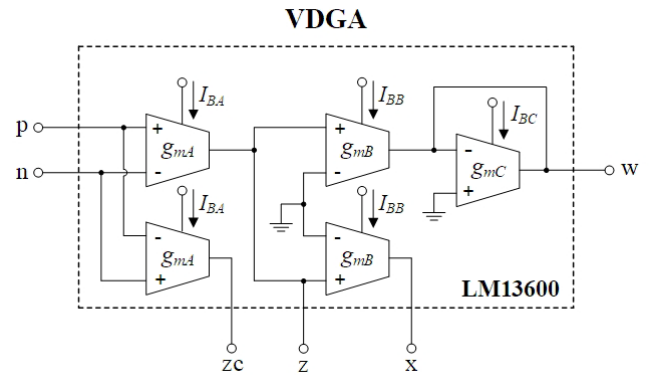


Figure 10: Practical realization of VDGA using readily available IC LM13600s

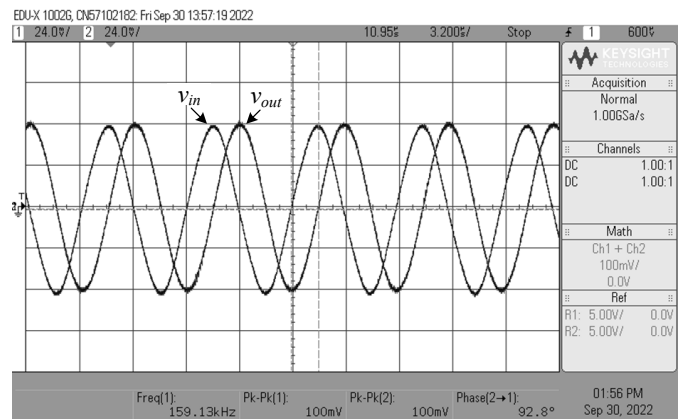


Figure 11: Measured time-domain waveforms of  $v_{in}$  and  $v_{out}$  for the propose circuit in Figure 3.



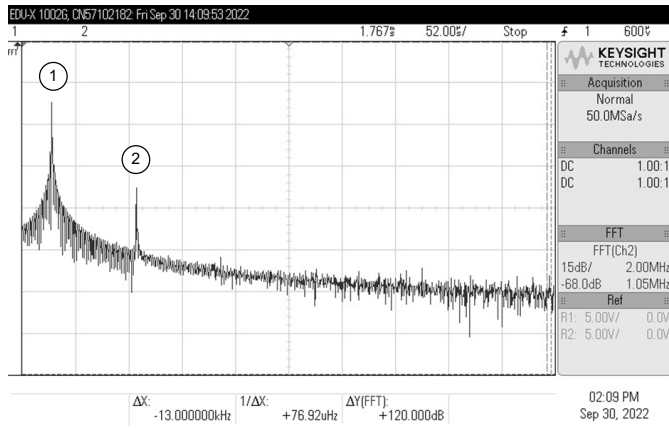


Figure 12: Measured spectrum frequency of  $v_{out}$  at 159 kHz (No.1: Frequency = 159 kHz, Gain = -28.91 dB, and No.2: Frequency = 479 kHz, Gain = -29.13 dB)

The next observation on the circuit is carried out on its frequency response characteristic. The measured frequency responses in comparison to the theoretical responses are given in Figure 13. The measured value of  $f_p$  is found to be 158 kHz, which corresponds to the frequency deviation of 0.63%. The experimental testing results show that while the gain response is essentially constant up to the working frequency of roughly 4 MHz, the phase characteristic is found to change with frequency, as predicted. The difference between measured and ideal curves in the high-frequency region is predominantly attributable to the gain-bandwidth product of the IC OTA LM13600s used to implement the circuit [26]. Obviously, higher-speed active devices could produce superior frequency responses.

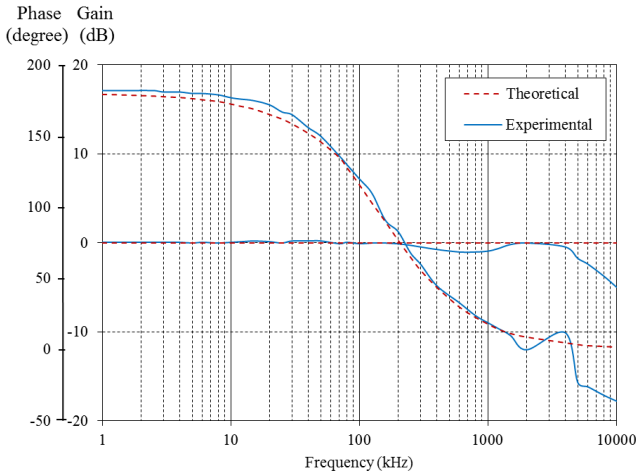


Figure 13: Theoretical and measured frequency responses of the propose circuit in Figure 3.

### 6. Quadrature Oscillator Application

The quadrature oscillator (QO) circuit can be simply implemented by utilizing the proposed phase shifter circuit, as shown in Figure 14. In the configuration, VDGA2 and  $C_2$  create a simple lossless integrator. The following relationship describes the characteristic equation of the QO circuit:

$$s^2 + g_{mA1} \left( \frac{1}{C_1} - \frac{\beta_1}{C_2} \right) s + \left( \frac{g_{mA1} g_{mB1}}{C_1 C_2} \right) = 0 \quad (12)$$

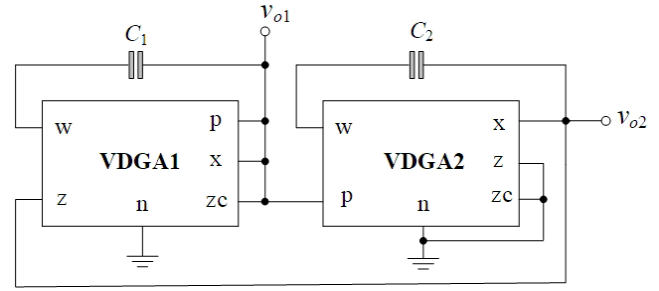


Figure 14: Quadrature oscillator implemented with the proposed circuits.

From the characteristic equation in (12), the condition for oscillation (CO) is satisfied at

$$\frac{\beta_1 C_1}{C_2} \geq 1 \quad (13)$$

and the frequency of oscillation ( $f_o$ ) is obtained as:

$$f_o = \frac{\omega_o}{2\pi} = \frac{1}{2\pi} \sqrt{\frac{g_{mA1} g_{mB1}}{C_1 C_2}} \quad (14)$$

The equation for the relationship between the produced quadrature signals is

$$\frac{V_{o2}(j\omega)}{V_{o1}(j\omega)} = \left| \frac{g_{mA1}}{\omega C_2} \right| e^{j90^\circ} \quad (15)$$

Obviously, both quadrature voltages  $v_{o1}$  and  $v_{o2}$  are ideally shifted by a phase ( $\phi$ ) of  $90^\circ$ . It may also be observed that  $g_{mA1}$  and  $C_2$  have a direct impact on the amplitude ratio of the quadrature voltages. Therefore, it follows that the output voltage amplitude of the QO can be controlled by the values of  $g_{mA1}$  and  $C_2$ . When the frequency is altered, equal voltage amplitudes can be achieved by changing  $g_{mA1}$  while maintaining  $C_2$ .

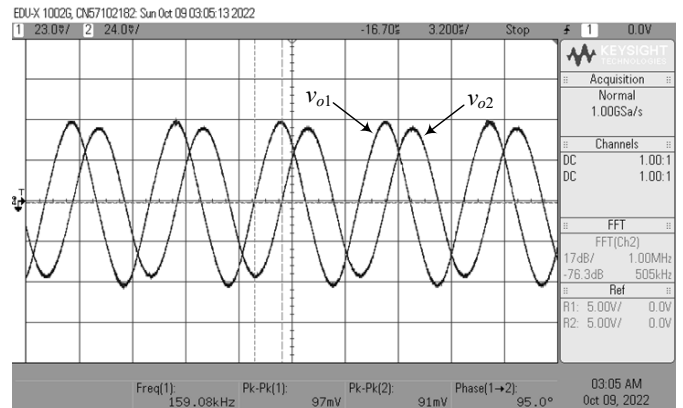


Figure 15: Measured waveforms of the developed QO circuit at  $v_{o1}$  and  $v_{o2}$  outputs.

The following values were chosen for the circuit elements in order to test the functionality of the QO circuit in Figure 14. The selection of  $g_{mk} = 1 \text{ mA/V}$  ( $I_{Bk} = 100 \mu\text{A}$ ) and  $C_1 = C_2 = 1 \text{ nF}$  for all transconductances and capacitances results in  $f_o = 159 \text{ kHz}$ . Figure 15 shows the typical waveforms measured at  $v_{o1}$  and  $v_{o2}$

output terminals with  $f_o = 159.08$  kHz and  $\phi = 95^\circ$ . The resulting deviations for  $f_o$  and  $\phi$  are 0.05% and 5.55%, respectively. The differences from ideal values are mainly attributed to the non-ideal gains and parasitic elements of IC LM13600s, which are described in Section 3. In Figure 16, the corresponding Lissajous figure of the QO circuit is also shown. Figure 17 illustrates the measured spectrum frequency of  $v_{o2}$  of the QO circuit, with the corresponding frequencies and gains at various spectra listed in Table 4. All the results support the practical usefulness of the proposed phase shifter circuit in implementing the quadrature oscillator.

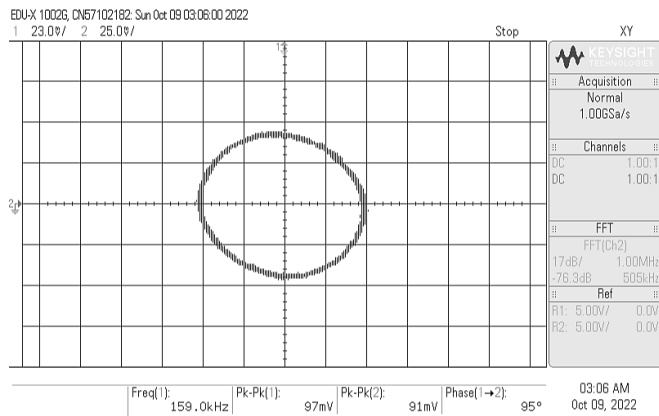


Figure 16: Lissajous figure of the developed QO circuit in Figure 14.

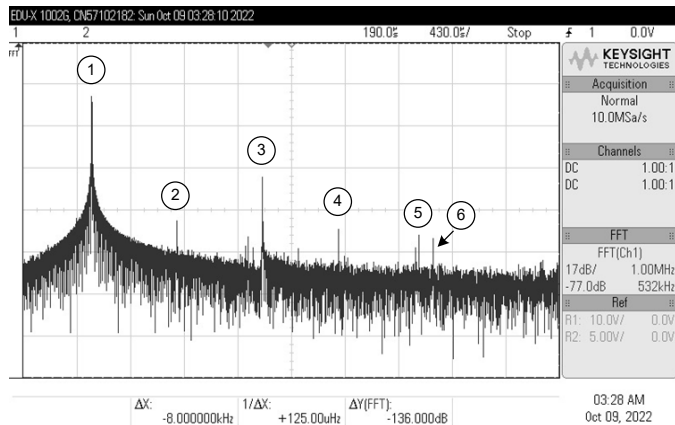


Figure 17: Measured spectrum frequency of  $v_{o2}$  at 159 kHz.

Table 4: Frequencies and gains at different spectrums of Figure 17.

No.	Frequency (kHz)	Gain (dB)
1	159	-30.798
2	318	-79.650
3	478	-63.720
4	620	-86.022
5	770	-88.677
6	796	-89.208

## 7. Conclusions

The paper describes the design of the compact resistorless tunable phase shifter circuit. The described phase shifter circuit requires only one VDGA as an active component and one floating capacitor, resulting in a resistorless architecture and ease of integration. Electronic tuning of the important features of the resulting design, such as the passband gain ( $H_0$ ), pole frequency ( $f_p$ )

and phase response ( $\phi$ ), is possible by modifying the  $g_m$ -values of the VDGA. The non-ideal analysis of the VDGA was also carried out. The voltage-mode quadrature oscillator has been used as an illustrative application for the proposed design. PSPICE simulation data with TSMC 0.25- $\mu$ m CMOS model parameters have been performed to support the theoretical research. In addition to validating the practical circuit behaviors, experimental measurements with commercially available IC LM13600s have been included.

## Conflict of Interest

The authors declare no conflict of interest.

## Acknowledgments

This work was supported by King Mongkut's Institute of Technology Ladkrabang [2566-02-01-041]. The Institute of Research and Development Rajamangala University of Technology Isan, and the Faculty of Engineering, Rajamangala University of Technology Isan, Khonkaen Campus, are also acknowledged for their providing support.

## References

- [1] W. Tangsrirat, T. Pukkalanun and W. Surakamponorn, "Resistorless realization of current-mode first-order allpass filter using current differencing transconductance amplifiers", *Microelectronics Journal*, **41**(2-3), 178-183, 2010, doi.org/10.1016/j.mejo.2010.02.001.
- [2] J. W. Horng, "Current conveyors based allpass filters and quadrature oscillators employing grounded capacitors and resistors," *Computers & Electrical Engineering*, **31**(1), 81-92, 2005, doi.org/10.1016/j.compeleceng.2004.11.006.
- [3] J. W. Horng, C. L. Hou, C. M. Chang, Y. T. Lin, I. C. Shiu, and W. Y. Chiu, "First-order allpass filter and sinusoidal oscillators using DDCCs," *International Journal of Electronics*, **93**(7), 457-466, 2006, doi.org/10.1080/00207210600711481.
- [4] K. Mathur, P. Venkateswaran, and R. Nandi, "All-pass filter based linear voltage controlled quadrature oscillator," *Active and Passive Electronic Components*, **2017**(4), 1-8, 2017, doi:10.1155/2017/3454165.
- [5] A. Toker, E. O. Gune, and S. Ozoguz, "Current-mode all-pass filters using current differencing buffered amplifier and a new high-Q bandpass filter configuration," *IEEE Transactions on Circuits and Systems-II: Analog and Digital Signal Processing*, **47**(9), 949-954, 2000, doi.org/10.1109/82.868465
- [6] A. Toker, E.O. Gune, and S. Ozoguz, "New high-Q band-pass filter configuration using current controlled current conveyor based all-pass filters," in the 8th International Conference on Electronics, Circuits and Systems (ICECS 2001), 165-168, 2001.
- [7] J. Satansup, and W. Tangsrirat, "Single VDGA-based first-order allpass filter with electronically controllable passband gain," in the 7th International Conference on Information Technology and Electrical Engineering (ICITEE 2015), 106-109, 2015.
- [8] O. Channumsin, and W. Tangsrirat, "Single VDBA-based phase shifter with low output impedance," in the 14th International Conference on Electrical Engineering/Electronics, Computer, Telecommunications and Information Technology (ECTI-CON 2017), 427-430, 2017.
- [9] A. Chaichana, S. Siripongdee, and W. Jaikla, "Electronically adjustable voltage-mode first-order allpass filter using single commercially available IC," in International Conference on Smart Materials Applications, Tokyo, Japan, **559**(1), 012009, 2019.
- [10] S. Maheshwari, J. Mohan, and D. S. Chauhan, "Voltage-mode cascadable all-pass sections with two grounded passive components and one active element," *IET Circuits, Devices and Systems*, **4**(2), 113-122, 2010, doi.org/10.1049/iet-cds.2009.0167.
- [11] D. S. Chauhan, G. Garg, J. Mohan, and S. Maheshwari, "Two DDCC based cascadable voltage-mode first-order all-pass filters," in International Conference on Advances in Electronics, Electrical and Computer Science (EEC 2012), 290-294, 2012.

- [12] B. Metin, N. Herencsar, and K. Pal, "Supplementary first-order all-pass filters with two grounded passive elements using FDCCII," *Radioengineering*, **20**(2), 433-437, 2011.
- [13] B. Chaturvedi, and S. Maheshwari, "An ideal voltage-mode all-pass filter and its application," *Journal of Communication and Computer*, **9**, 613-623, 2012.
- [14] E. Yuce, R. Verma, N. Pandey, and S. Minaei, "New CFOA-based first-order all-pass filters and their applications," *International Journal of Electronics and Communications (AEU)*, **103**, 57-63, 2019, doi.org/10.1016/j.aeue.2019.02.017.
- [15] E. Yuce, L. Safari, S. Minaei, G. Ferri, and V. Stornelli, "New mixed-mode second-generation voltage conveyor based first-order all-pass filter," *IET Circuits, Devices & Systems*, **14**(6), 901-907, 2020, doi.org/10.1049/iet-cds.2019.0469.
- [16] J. Jitender, J. Mohan, and B. Chaturvedi, "A novel voltage-mode configuration for first order all-pass filter with one active element and all grounded passive components," in the 6th International Conference on Signal Processing and Communication (ICSC 2020), 2020.
- [17] E. Yuce, and S. Minaei, "A new first-order universal filter consisting of two ICCII+s and a grounded capacitor," *International Journal of Electronics and Communications (AEU)*, **137**, 153802, 2021, doi.org/10.1016/j.aeue.2021.153802.
- [18] R. Senani, D. R. Bhaskar, and P. Kumar, "Two-CFOA-grounded-capacitor first-order all-pass filter configurations with ideally infinite input impedance," *International Journal of Electronics and Communications (AEU)*, **137**, 153742, 2021, doi.org/10.1016/j.aeue.2021.153742.
- [19] J. Jitender, J. Mohan, and B. Chaturvedi, "CMOS realizable and highly cascadable structures of first-order all-pass filters," *Walailak Journal of Science and Technology (WJST)*, **18**(14), 21451, 2021, doi.org/10.48048/wjst.2021.21451.
- [20] A. Raj, D. R. Bhaskar, R. Senani, P. Kumar, "Four unity/variable gain first-order cascaded voltage-mode all-pass filters and their fully uncoupled quadrature sinusoidal oscillator applications," *Sensors*, **22**(16), 6250, 2022, doi.org/10.3390/s22166250.
- [21] J. Satansup, W. Tangsrirat, "CMOS realization of voltage differencing gain amplifier (VDGA) and its application to biquad filter," *Indian Journal of Engineering and Material Sciences*, **20**(6), 457-464, 2013.
- [22] O. Channumsin, T. Pukkalanun and W. Tangsrirat, "Single VDGA-based dual-mode multifunction biquadratic filter and quadrature sinusoidal oscillator," *Informacije MIDEM-Journal of Microelectronics, Electronic Components and Materials*, **50**(2), 125-136, 2020, doi.org/10.33180/InfMIDEM2020.205.
- [23] W. Tangsrirat, T. Pukkalanun, O. Channumsin, "Dual-mode multifunction filter realized with single voltage differencing gain amplifier (VDGA)," *Engineering Review*, **41**(2), 1-14, 2021, doi.org/10.30765/er.1441
- [24] R. J. Baker, H. W. Li, and D. E. Boyce, *CMOS circuit design, layout and simulation*, Chapter 7, IEEE Press, New York, 1998.
- [25] N. Roongmuanpha, W. Tangsrirat, T. Pukkalanun, "Single VDGA-based mixed-mode universal filter and dual-mode quadrature oscillator", *Sensors*, **22**(14), 5303, 2022, doi.org/10.3390/s22145303.
- [26] National Semiconductor. Dual operational transconductance amplifiers with linearizing diodes and buffers. LM13600 datasheet 1998.

## Design and Comparative Analysis of Hybrid Energy Systems for Grid-Connected and Standalone Applications in Tunisia: Case Study of Audiovisual Chain

Saidi Mohamed<sup>1,2,\*</sup>, Habib Cherif<sup>1,2</sup>, Othman Hasnaoui<sup>1,2</sup>, Jamel Belhadj<sup>1,2</sup>

<sup>1</sup>Electrical Systems Laboratory (LSE-LR-11ES15)-ENIT, University of Tunis el Manar, Tunis, 1002, Tunisia

<sup>2</sup>Université de Tunis, ENSIT, BP 56 Montfleury, 1008, Tunisia

### ARTICLE INFO

Article history:

Received: 06 February, 2023

Accepted: 13 May, 2023

Online: 12 June, 2023

Keywords:

Audiovisual chain

Net Present Cost

Micro-grid

Optimization

Renewable energy

### ABSTRACT

*In this research paper, a technical and economic-environmental study was developed to investigate the possibility of establishing various hybrid power systems with different operation modes. Grid-connected and standalone hybrid systems (solar-wind with storage batteries and diesel generators) have been realized in order to carry out a comparative analysis study of two configurations. These systems have been investigated through the Hybrid Multi-Energy Resource Optimization software (HOMER), which calculates pollutant gas emissions, simulates and optimizes energy consumption based on energy demand and resources. As part of the economic analysis, the internal rate of return, the net present value and the payback period were estimated. Both configurations have been developed to meet the power consumption of an audiovisual system. The results obtained show that the first system is the most cost-effective to establish, considering in particular the energy production potential and gas emissions. It can be stated that the proffered grid-connected hybrid system is the most suitable and cost-effective system as it offers several advantage. The total net present cost is \$5.425million and the total energy cost is approximately \$0.0686 per unit.*

## 1. Introduction

Today the most serious problems of the world are the decrease of fossil fuel reserves, and their elevated price, it is therefore necessary to consider a solution to reduce the use of non-renewable resources and to use sustainable alternative energies like solar and wind energy. Renewable energies have progressively substituted nuclear energy and fossil fuels in four different sectors: power generation, heating plants, transports and stand-alone energy production [1]. This is the case of photovoltaic (PV) and wind energy, worldwide, this sector is growing rapidly [2,3], in particular because of the increasing competition of renewable energies, the rise of electricity demand in developing countries and the benefits of this type of energy in terms of pollution reduction. In this regard, it is important to note that gas, oil and coal are always highly popular fuels for power generation. The effects of these energy sources, as well as the increase in the world's population and its energy consumption, have had a negative impact on the environment [4,5]. In addition, among the objectives of the Tunisian state is to limit the impact of environmental damage by exploiting the potential of available renewable resources, which

will help manage the risk. Considering the previous context, in previous years a growing number of studies have been conducted on hybrid grid-connected and standalone generation systems, by mixing different energy resources such as wind, solar, hydro and generators [6–8]. For this reason, a design and a technical-economic and environmental study has been carried out in the development of various systems of solar-wind hybrid systems that incorporate additional generation sources such as diesel generators. To evaluate the proposed design [9–11], the energy consumption of the building of an audiovisual channel in Tunisia was used as a case study. The novelty of this work is the incorporation of the ecological component as well as the technical and economic aspects in order to achieve a consistent analysis [12], which facilitates decision for the development of energy production strategies based on hybrid systems.

As a developing country, Tunisia has energy supply problems to support its economic growth. 30% of energy should be renewable by 2030, according to the national energy strategy. The development of multi-source energy systems for commercial enterprises is crucial, including energy sources such as photovoltaic, wind [13–15]. Tunis is the capital city, geographically located in the north of Tunisia, the coordinates of its geographical site are 36°49.43'north10°09.27'east (Figure 1).

\*Corresponding Author: Saidi Mohamed, Email [msaidi31@yahoo.fr](mailto:msaidi31@yahoo.fr), Tel 0021698924458

Therefore, this site is a good place to design a multi-source renewable energy system, especially for an audiovisual television channel with an available surface area of about 10000 m<sup>2</sup>. In this context, this paper presents a comparative study of two modes micro-renewable energy network [7], in order to choose the right solution to reduce the cost of energy consumption for an audiovisual chain and ensure continuous and regular electricity production.

The paper is based on real project in the Tunisian television, in order to implant a new smart-grid for the Tunisian television, which is a high consumer of energy every year.

Our main objective is to define the optimal sizing based on various configurations, and minimize cost parameters such as, total net present cost (TNPC), cost of energy (COE), and unmet electrical load and CO2 emissions [10] using HOMER software.

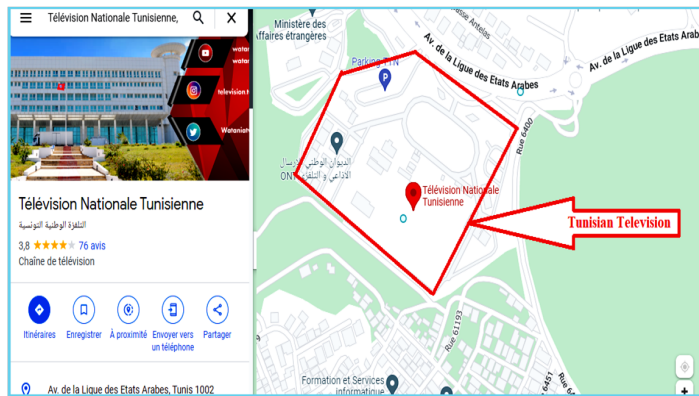


Figure 1: Geographic coordinate of studied area

## 2. Current Power Supply Architecture

Figure 2 shows that the television is supplied from a medium voltage network (10kV) through six transformers (5×1250kVA and 1×800kVA) connected in parallel; two of them are stand-by. Three diesel generators (3×1390kVA) are used to provide emergency power for certain priority equipment. It is very important to ensure the continuity of broadcasting; in this context four (online) inverters (500kVA and 250 kVA) with a park of batteries (12V and 6V) are used [11].

In this study, two types of loads are defined [8]:

- Sensitive loads, also called critical loads (control rooms, broadcasting center, studios, stage lighting)
- Other/normal loads (air conditioner, offices, lighting, pumps)

## 3. Methods and Materials

In this research, two configurations of hybrid micro-grid on-grid and standalone were designed and compared in order to find the optimum for an audiovisual chain located in the north of Tunisia (36°49.43'N, 10°09.27'E). The objective of this micro-grid design is to reduce the cost of the company's electricity consumption and to provide energy supply continuity.

### 3.1. Introduction to HOMER-pro software

The HOMER-Pro software was developed by NREL, USA. It facilitates the process of designing the most economical microgrid in a distributed energy system. It gives precise and independent results. It also investigates all possible configurations and determines the lowest cost solution by combining several system elements and a storage technology.

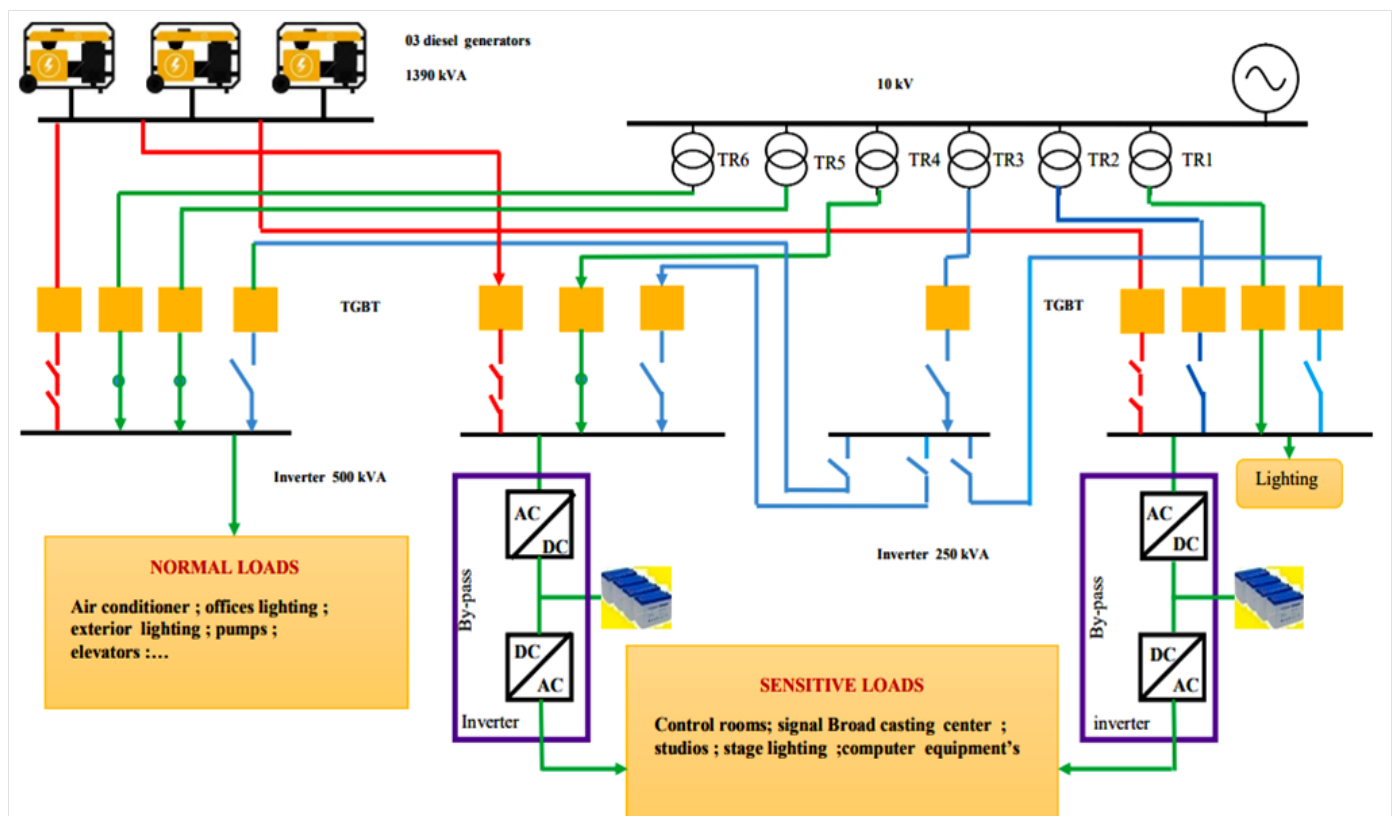


Figure 2: Micro-grid of the power supply and electrical distribution system

Different metrological data are needed to design the hybrid system, in the same way as to describe the possibilities. The workflow in this software is in 3 steps. The process starts with the project input data which includes the load profile, site specific resources and system components, in step 2 HOMER-Pro analyzes the simulation, optimization and sensitive parameters, in step 3 it shows the result which delivers detailed information about the system sizing, performance and financial parameters.

The following Figure 3 presents the diagram of the proposed hybrid energy systems design methodology.

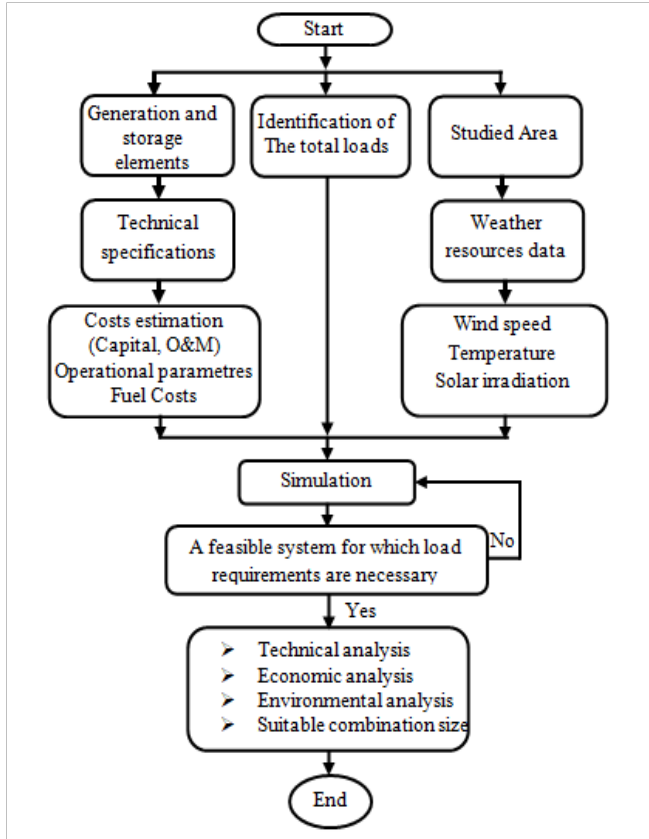


Figure 3: The diagram of the proposed hybrid energy systems design methodology.

In the simulation process, during simulation we define the various system combinations, the number of components needed, the sizes and the dispatch strategy. HOMER-Pro is able to model many system configurations by taking into account any combination of PV panels, hydrogen tanks, wind turbines, hydroelectricity, an electrolyzer, an AC-DC converter and a battery storage. The designed system can be grid-connected or off-grid and can supply different electrical loads. HOMER-Pro analyzes two important aspects: firstly, it evaluates the functionality of the system design and secondly, it determines the life cycle cost of the design, which is the total cost of installation and operation.

The optimization phase defines the most ideal combination, as well as the best configuration that meets the load requirements. In this process, HOMER-Pro simulates different varieties of system configurations, removing those that are not feasible. The feasible configurations are organized according to the lowest net present cost (NPC) and energy cost (COE). This software analyzes

different variables to obtain the most feasible configuration for the desired load [16,17]. The decision variables that are analyzed include: generator size, PV module, AC to DC converter, electrolyzer, hydrogen storage tank, number of wind turbines, number of batteries and dispatch strategy.

The software adopts assumptions that affect the design of the system. These assumptions are called sensitivity variables. Sensitivity variables include solar radiation, diesel cost, wind speed, interest rate, grid price, etc. The software finds many combinations of systems which are feasible under some conditions. A sensitivity analysis illustrates the effect of changing inputs on the results [18]. The software is able to analyze multiple sensitive values at once to find the economically suitable result. The software user can include as much sensitivity as desired for the needs of the analysis.

### 3.2. Energy Potential

In this paragraph, we analyze the wind, solar and ambient temperature resources available in the project area. The ambient temperature and wind values are obtained from the National Institute of Meteorology of Tunisia. The solar radiation is obtained using the HOMER (Hybrid Optimization of Multiple Energy Resources) simulation tool, which is linked to the National Aeronautics and Space Administration (NASA) database.

First, Figure 4 shows the monthly average ambient temperature. The lowest value is indicated in January with 14.5°C and the highest in August with 31.5°C. It is essential to take into consideration the environmental temperature, since it affects the photovoltaic modules' efficiency and performance, which is best achieved at an operating temperature of 25°C.

Figure 5 shows the average monthly solar radiation of the position of the Tunisian TV channel, where we observe that the minimum radiation is presented in december with 2.09 kWh/m<sup>2</sup>/day and the maximum radiation is presented in July with 7.31 kWh/m<sup>2</sup>/day.

Figure 6 presents the monthly average wind speed, where it can be seen that the minimum speed is presented in August with 4.950 m/s and the maximum speed is presented in February with 7.07 m/s.

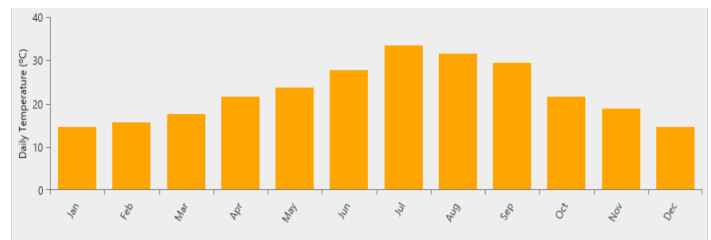


Figure 4: The monthly average of the ambient temperature

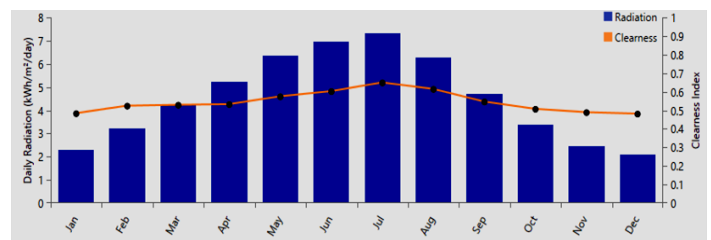


Figure 5: The monthly solar radiation

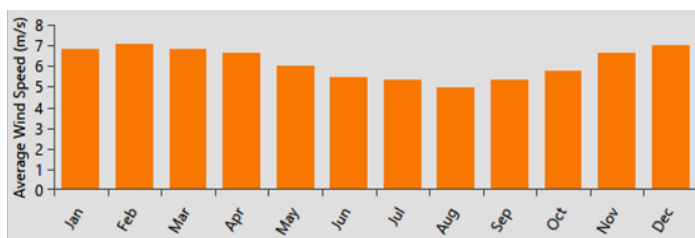


Figure 6: The monthly average wind speed

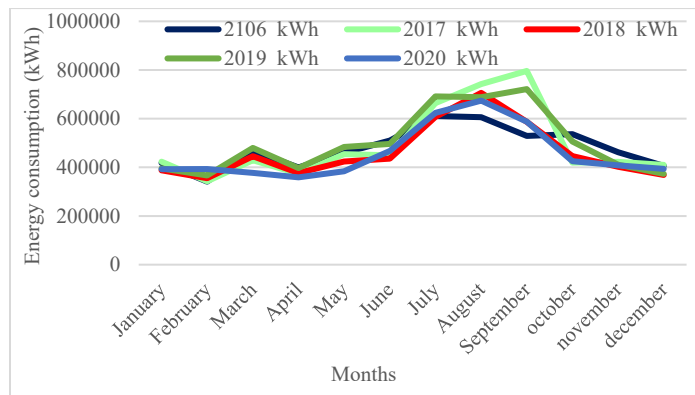


Figure 7: Monthly energy consumption in recent years

### 3.3. Load profile

Based on Figure 7 and Figure 8, in Tunisian television the average monthly consumption in the years (2016-2017-2018-2019-2020) is a function of production emissions during three distinct seasons: winter, summer and the month of Ramadan. Monthly consumption is almost the same during the months of

October to May (an average consumption of 400,000 kWh per month), then a slight increase (20%) in the month of Ramadan (June) and finally three months of high consumption (June-July-August), about 35% of total annual consumption (air conditioning). It was seen that the peak is about 1442 kW and with an average of 626 kW [7], [10].

The investigated area is located in the north of Tunisia; its geographical site co-ordinate is located at 36°49.43' north 10°09.27' east). Consequently, this site is an appropriate place to design a grid connected multisource energy renewable system, especially for an audiovisual television chain.

The options of hybrid systems proposed in this work were designed for energy consumption in broadcasting building of the Tunisian television during 2020. The two hybrid systems were designed for a load of 15000kWh/d. The electrical load profile is shown in Figure 8.

To study the performance of the system over the course of a year, HOMER uses the daily load profile illustrated in Figure 9. The load profile is variable on various days and times due to seasonal and regional time changes for more efficient electricity consumption. The load variations during seasonal changes, and the minimum and maximum loads recorded are illustrated.

### 4. System description and simulation models

Using HOMER, two models of hybrid system have been established: grid-connected hybrid system and off-grid hybrid system.

Figure 10 illustrates the concept of a grid-connected hybrid system, which includes wind turbines, photovoltaic panels, loads, and inverter, with a diesel generator and a park of batteries that are used to maintain the system in its off-grid state. Figure 11 shows the same concept, but a standalone configuration.

The HOMER simulation software gives the possibility of entering the various electrical components that will have to be used for the device to be effective and which automatically carry out all the possible configurations, taking into account only those that satisfy the required load.

To maximize system performance in various situations, HOMER simulates the configurations listed below with the same loads in the same region based on various costs such as estimated installation cost, operation and maintenance cost, replacement cost, interest rates and energy cost, as well as the analysis of pollutant emissions.

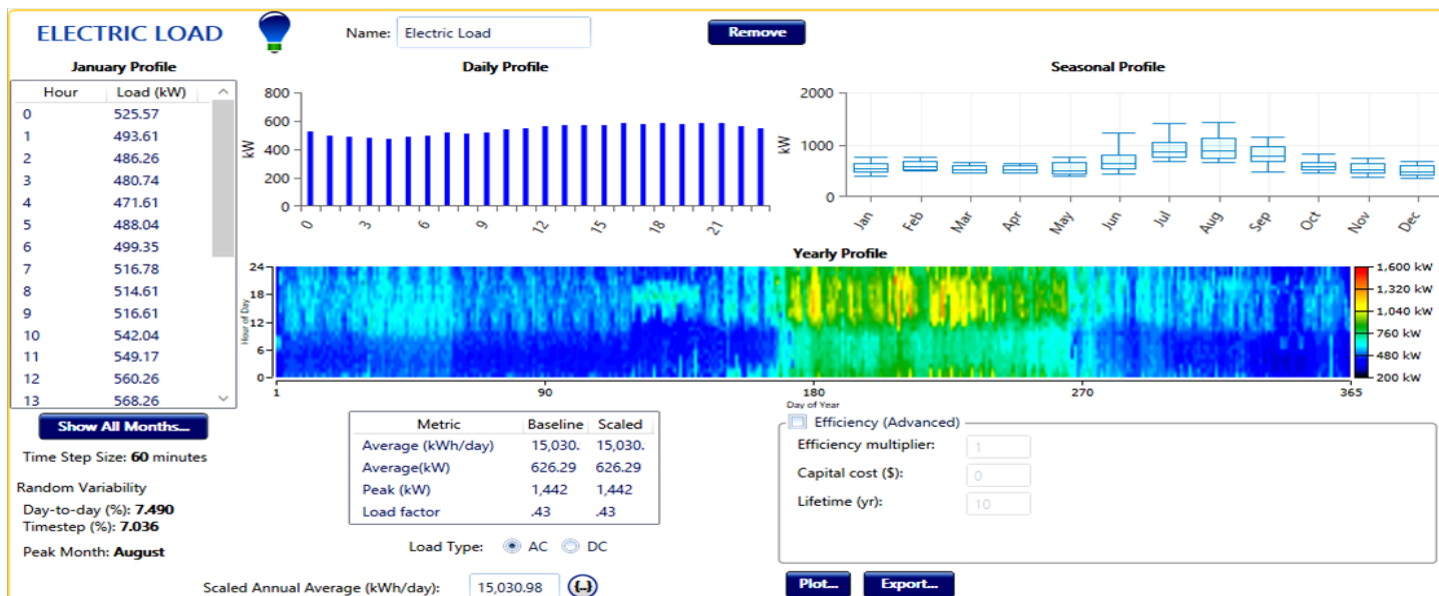


Figure 8: Load profile of audiovisual chain.

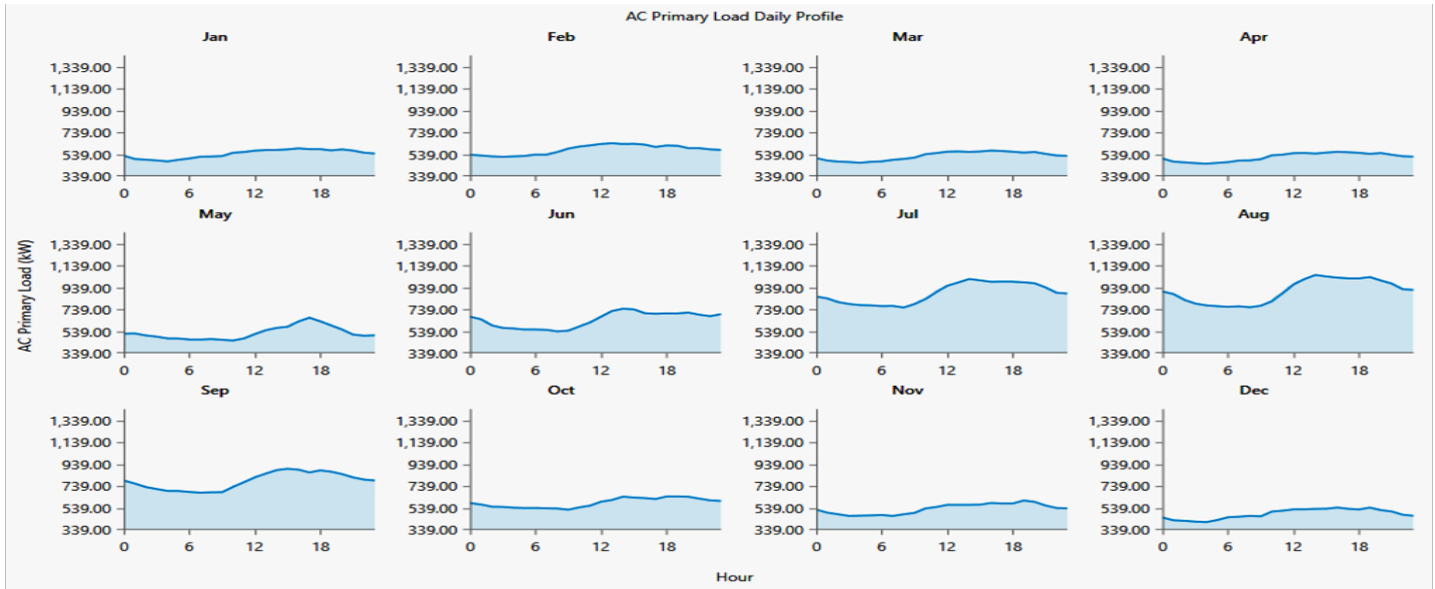


Figure 9: load profile of the studied area

The Figures 10 and 11 are the studied models in this paper which are developed to replace the current power supply configuration illustrated in Figure 2, with the integration of new renewable energy sources.

So, our main task is to design and investigate a new smart-grid based on renewable energy for energy supply of the Tunisian television.

#### 4.1. Wind Turbine

Wind turbine converts the kinetic energy of the wind into AC or DC electricity for particular power curve. The power curve is a graph between power output and wind speed.

Bergey wind power's Excel 10-R model with hub height (30 m) is considered. It has a rated capacity of 10 kW and provides (AC) voltage as an output. The cost of one unit is considered (\$15000) while replacement and maintenance costs are taken as (\$13500) and (\$150/year)

$$P_{wt} = 0.5\rho V^3 S \eta_1 C_p \quad (1)$$

where:

V: the wind speed in m/s,

S: rotor swept area in m<sup>2</sup>,

$\eta_1$ : generator efficiency,

$C_p$ : maximum power coefficient,

$\rho$ : air density in kg/m<sup>3</sup>,

#### 4.2. Solar PV panel

HOMER-Pro develops a PV module that produces DC electricity when the solar radiation incident upon it. It is best to choose a solar panel when the price of diesel fuel is high and wind speeds are low. The capital cost of a 1kW solar panel is approximately\$600; the replacement and operating costs are \$600 and \$10, respectively. The service life of the PV system is 25 years.

$$P_{PV} = C_{PV} \times P_{PV} \times (I_T/I_S) \quad (2)$$

where,

$C_{PV}$ : PV rating factor.

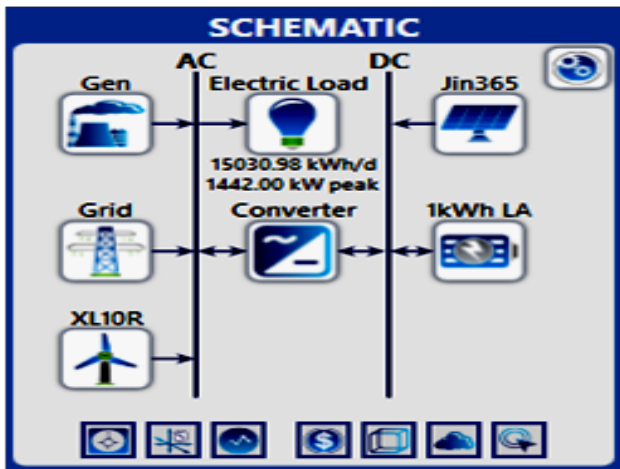


Figure 10: Grid-connected Hybrid System

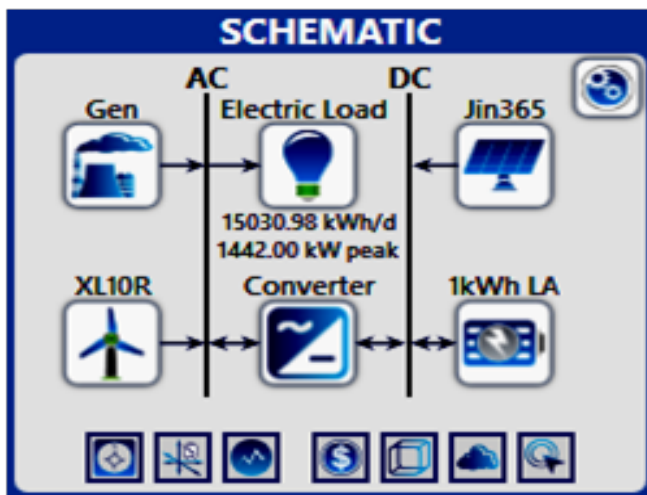


Figure 11: The Standalone Hybrid System.



$P_{PV}$  : PV array rated capacity (kW).

$I_T$ : Solar radiation values that strikes on the surface of the PV Array (kW/m<sup>2</sup>).

$I_S$ : Standard radiation value, 1kW/m<sup>2</sup>.

#### 4.3. Diesel Generator project

Diesel generator is used as alternative power sources when there is no access to the grid or interruption of electrical power. Diesel generator is also preferred as backup power, ensuring a robust energy supply. Generator cost is determined for 1kW output power. The capital cost is \$ 300, the replacement cost is 270\$, O&M cost is 0.03(\$/op. hour) and the lifetime is 15000 hours [4,5]. The fuel consumption per hour of a diesel-fueled diesel generator is calculated by Equation 3.

$$F = F_0 \times Y_{gen} + F_1 \times P_{gen} \quad (3)$$

where,

F: the fuel consumption rate (L/hr.)

$F_0$ : the fuel curve intercept coefficient (L/hr/kW),

$F_1$ : the fuel curve slope (L/hr/kW),

$Y_{gen}$ : the rated capacity of the generator (kW),

#### 4.4. Battery Storage Bank

For a certain hour, the surplus power produced by the hybrid system can be used to charge the batteries, while the stored energy can be discharged at any time when there is a power deficit.

The battery considered is a generic 12v lead acid battery with 1kwh of energy storage. The estimated lifetime is (5 years) and the cost of one battery is (\$250) with a replacement cost of (\$250) while the maintenance cost is estimated at (\$5/year).

$$C_{wh} = (E_L \times AD) / (\eta_{inv} \times \eta_{bat} \times DOD) \quad (4)$$

where,

$E_L$  is the average daily load energy (kWh/day),

AD is daily autonomy of the battery,

DOD is battery depth of discharge,

$\eta_{inv}$  and  $\eta_{bat}$  respectively, represent the inverter and battery efficiency.

#### 4.5. Converter

The energy feed between the AC bus and the DC bus within the microgrid is realized by a bidirectional power converter according to the production, consumption, and storage energy conditions of the micro grid. Converter cost is determined for 1kW output power. The capital cost is 200\$, the replacement cost is 180\$, O&M cost is 5\$ and the life expectancy is 15 years [5–7]. The efficiency of the converter connected to two bus bars is taken as 95%.The inverter changes the DC current at the output of the photovoltaic system and battery to supply the electrical load, which by its nature is alternating current. The design is kept to supply the load 24 hours a day, 7 days a week without any disruption in the

power supply due to the uncertain nature of solar and wind generation.

### 5. Economic analysis

Net Present Cost (NPC): The NPC is the cost of installing and operating of the system over its lifetime which is calculated with the following formula [18,19].

$$NPC = T_{Ann, cost} / CRF (j, R_{Project}) \quad (5)$$

$T_{Ann, cost}$ : It is the sum of the annualized costs of each component of the power system, including capital, operating and maintenance costs. It also includes the replacement cost and the cost of fuel.

j: Interest rate in percentage

$R_{project}$ : lifetime in year

CRF: Capital recovery factor is a ratio which is used to calculate the present value of a series of equal annual cash flow.

$$CRF = j \times (1+j)^n / (1+j)^n - 1 \quad (6)$$

where,

j: Interest rate in percentage

n: number of years

The cost of energy is calculated by the following formula

$$COE = T_{Ann, cost} / (E_{primary} + E_{def} + E_{grid.sell}) \quad (7)$$

$T_{Ann, cost}$ : Total annualized cost

$E_{primary}$ : No of primary load

$E_{def}$ : No of deferrable load

### 6. Optimization and Simulation Results

The supply of a load of 15,030.98kWh/d with a peak value of 1442kW was studied in 2 scenarios. In the first scenario, the power demand was provided by a grid-connected microgrid and in the second scenario by standalone microgrid. For both scenarios, PV, wind turbines, diesel generator and a battery park were used.

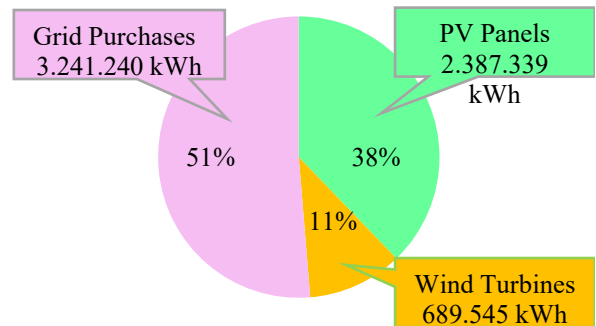


Figure 12: Energy Production summary

#### 6.1. Grid- connected configuration

In this part, the simulation results of grid-connected installations are calculated for different configurations using HOMER. The main energy source is the photovoltaic. In case of lack of energy from PV panels and wind turbines, the electrical

Table 1: Categorized optimization results

Architecture						Cost				
PV (kW)	Wind turbine	Diesel generator (kW)	Batteries	Grid (kW)	Inverter (kW)	NPC (\$)	COE (\$)	Operating Cost (\$/yr)	Initial capital (\$)	Renewable fraction (%)
1,667	30		300	999,999	1000	5.43M	0.0686	285,183	1.74M	47
1,708			300	999,999	1000	5.47M	0.0712	321,218	1.32M	37.6
1,667	30	1600	300	999,999	1000	5.81M	0.0734	277,318	2.22M	47.0
1,708		1600	300	999,999	1000	5.85M	0.0761	313,413	1.80M	37.6
	30		300	999,999	1000	6.15M	0.0867	418,215	740,000	12.6
			300	999,999	1000	6.30M	0.0888	464,519	290,000	0.00372
	30	1600	300	999,999	1000	6.53M	0.0920	410,410	1.2M	12.6
		1600	300	999,999	1000	6.67M	0.0941	456,714	770,000	0.0372

grid, the battery storage system and the diesel generator are used as auxiliary energy sources.

Monthly average electrical power generated by each of the hybrid system elements is illustrated in figure 12, it is clear that the most important quantity of energy is given from the grid (51.3%) whereas photovoltaic generate only 37.8% of overall energy and wind turbine produce about 10.9%. The photovoltaic energy production is 2,387,339 kWh/yr and the wind turbines energy production is 689,545 kWh/yr.

As shown in Table 1, in current simulation of the designed micro-grid, the optimized results demonstrates that the cost of energy have the minimum value COE of \$0.0686/kWh.

Table 2 indicates that pollutant emissions like carbon dioxide, carbon monoxide, and sulfur dioxide are significantly decreased by using the grid-connected hybrid system.

Table 2: Quantity of emission produces by different pollutants

Quantity	Value (kg/yr)
Carbon Dioxide	2,055,538
Carbon Monoxide	0
Unburned Hydrocarbons	0
Particulate Matter	0
Sulfur Dioxide	8,912
Nitrogen Oxides	4,358

According to Table 3, 89.7% of the electricity produced by the renewable system is sent to the AC grid and 10.3% is sold to the grid at specified selling price.

Table 3: Energy consumption summary

component	Consumption kWh/yr	Percentage
AC Primary Load	5,486,307	89.7
Grid Sales	633,321	10.3
Total	6,119,628	100

According to Figure 13 in this micro grid, 48.7% of the total energy is generated from renewable sources. All of this generation is delivered right into the load. The proportion of renewable sources energy directly used by the load is 47%. Thus, 1.16% of the total energy, generation during a year are excess energy confirming to the results of simulation.

Figure 14 illustrates the results of the microgrid evaluation in terms of capital costs and operation and maintenance costs. The PV array system represents the largest capital cost, therefore the grid represents the highest operation and maintenance cost Based on this estimation, the hybrid project will have approximately a \$5.425 million cost over its operating lifetime In Figure 15, we observe the cumulative cash flow of this system over the life of the project, as shown in the curve over 25 years, there are significant changes between the initial system and the proposed system, there is a large decrease in term of cash flow of the final system.

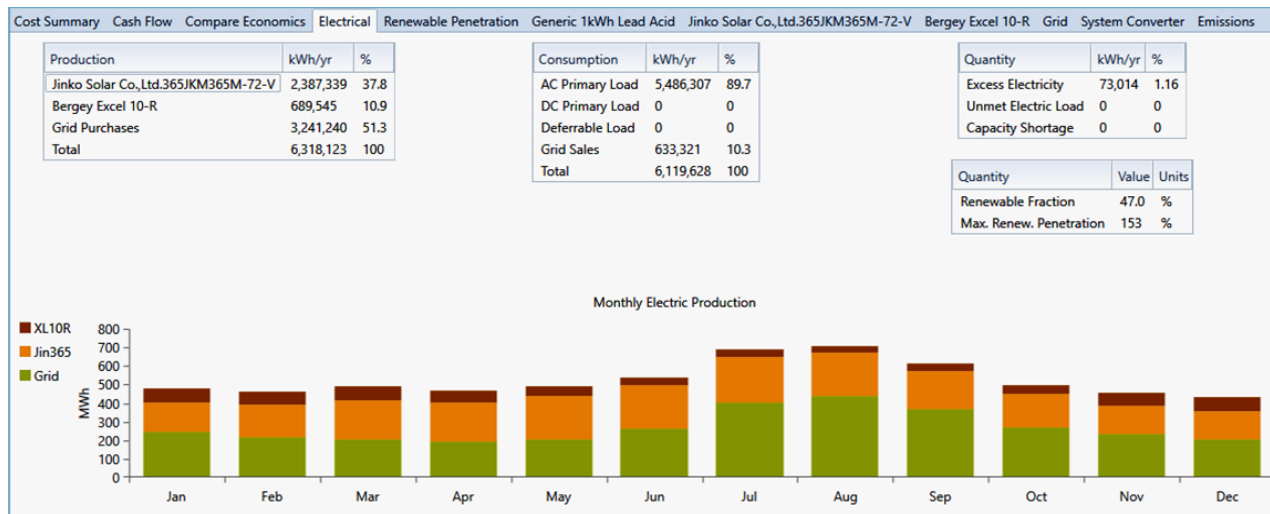


Figure 13: Production and consumption of electricity

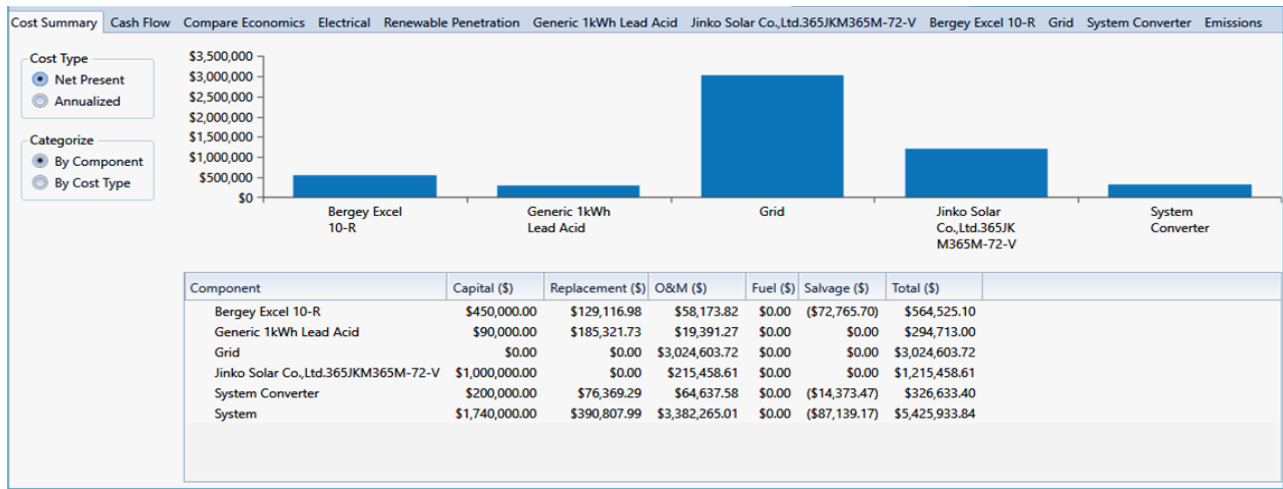


Figure 14: Cost status of the system

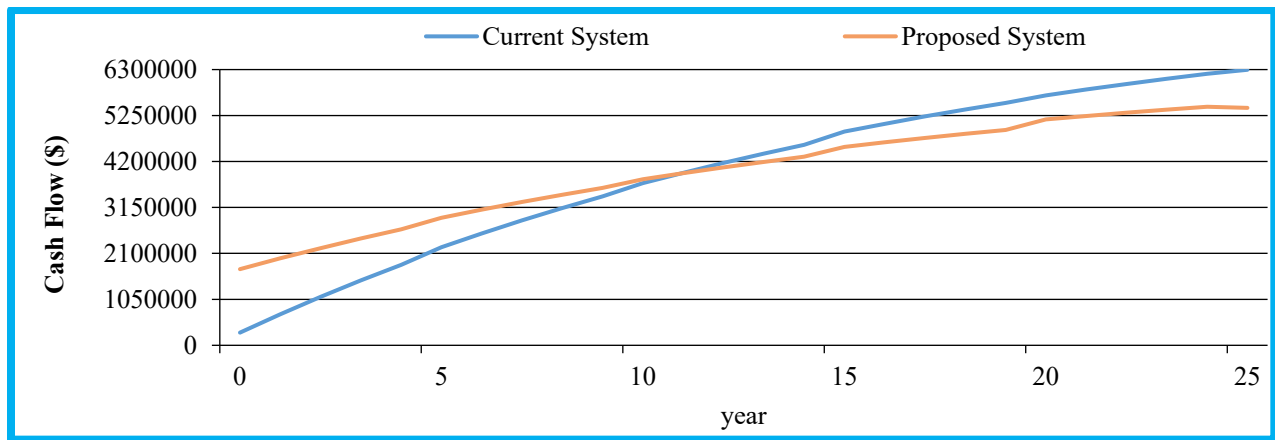


Figure 15: Cumulative cash flow over project lifetime

6.2. Off-Grid configuration

In this section, the simulation results of the different stand-alone combinations are calculated for the various configurations using HOMER. The two main energy sources are photovoltaic and wind turbine. In case of lack of energy from the photovoltaic panels and wind turbines, the diesel generator is used as a complementary energy source, as well as the battery storage system which is used in case of lack of power to ensure the continuity of the TV chain.

Monthly average electrical power generated by each of the hybrid system elements is illustrated in figure 16, it is clear that the most important quantity of energy is given from the diesel generator (49.2 %) whereas photovoltaic generate only 30.5% of overall energy and wind turbine produce about 20.3%. The photovoltaic energy production is 2.283.006 kWh/yr, the wind turbines energy production is 1.522.149 kWh/yr and an energy production of 3.688.661 kWh/yr from the diesel generator.

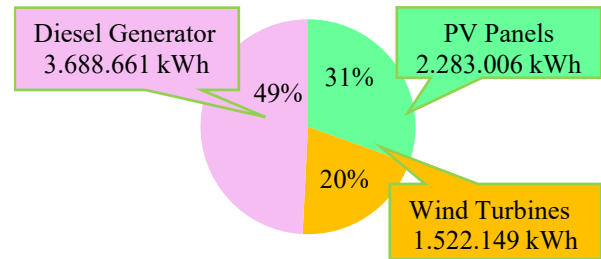


Figure 16: Energy Production summary

As shown in Table 4, in current simulation of the designed micro-grid, the optimized results demonstrates that 1505kW of photovoltaic panels and 58 wind turbines of 10kW are used the cost of energy COE is \$0.258/kWh.

Table 4: Categorized optimization results

Architecture					Cost				
PV (kW)	Wind turbine	Diesel generator (kW)	Batteries	Inverter (kW)	NPC (\$)	COE (\$)	Operating Cost (\$/yr)	Initial capital (\$)	Renewable fraction (%)
1,505	58	1,600	1,200	500	18.3M	0.258	1.21M	2.68M	32.8
270	40	1,600		160	18.4M	0.260	1.33M	1.27M	15.9
	40	1,600			18.5M	0.261	1.35M	1.08M	12.2
	40	1,600	4	1.30	18.5M	0.261	1.35M	1.08M	12.2

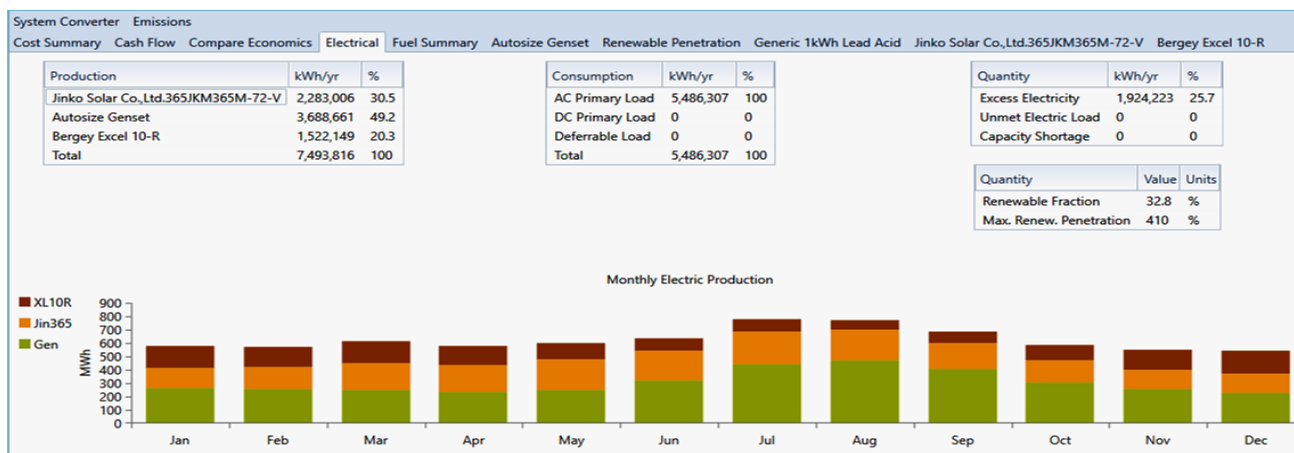


Figure 17: Production and consumption of electricity

In this microgrid, 50.8% of the total energy is produced from renewable sources. All of this generation is delivered directly to the load. According to Figure 17, the proportion of energy from renewable sources directly used by the load is 32.8%. Thus, 100% of the electricity generated by the renewable system is sent to the AC grid and 25.7% of the total energy production during a year is surplus energy confirming the simulation results.

Table 5 illustrates that pollutant emissions such as carbon dioxide, carbon monoxide, unburned hydrocarbons, nitrogen oxides and sulfur dioxide are significantly increased by the use of the stand-alone hybrid system.

Table 5: Quantity of emission produces by different pollutants

Quantity	Value (kg/yr)
Carbon Dioxide	2.779.450
Carbon Monoxide	17.646
Unburned Hydrocarbons	770
Particulate Matter	107
Sulfur Dioxide	6.855
Nitrogen Oxides	16.577

Figure 18 demonstrates the cost status of the off grid hybrid system during its project lifetime. Table 4 shows the results of the evaluation of the isolated micro grid in terms of investment costs

and operation and maintenance costs. The renewable energy system (photovoltaic and wind) represents the high investment cost, therefore the diesel generator represents the highest operation and maintenance cost. Based on this estimate, the hybrid project will have a lifetime cost of approximately \$18.30 million.

In Figure 19 we can see the cumulative cash flow of this system over the project live time, as seen on the curve during 25 years there is no significant change between the based system and the proposed system.

## 7. Conclusion

This working study is a comparative study between off-grid and a grid-connected hybrid electrical system with different modes of operations for an audiovisual chain. The results obtained with the HOMER-pro software show a detailed cost analysis structure, cash flow overview, and energy production yield of the proposed hybrid configuration.

An analysis of the situation was carried out in the Tunisian television chain. The study was conducted taking into account energy use, climatic conditions, current prices for all components and accessible areas within the study area. The optimization results show that the on-grid hybrid system is more efficient and cost-effective than the off-grid hybrid system with the same load.

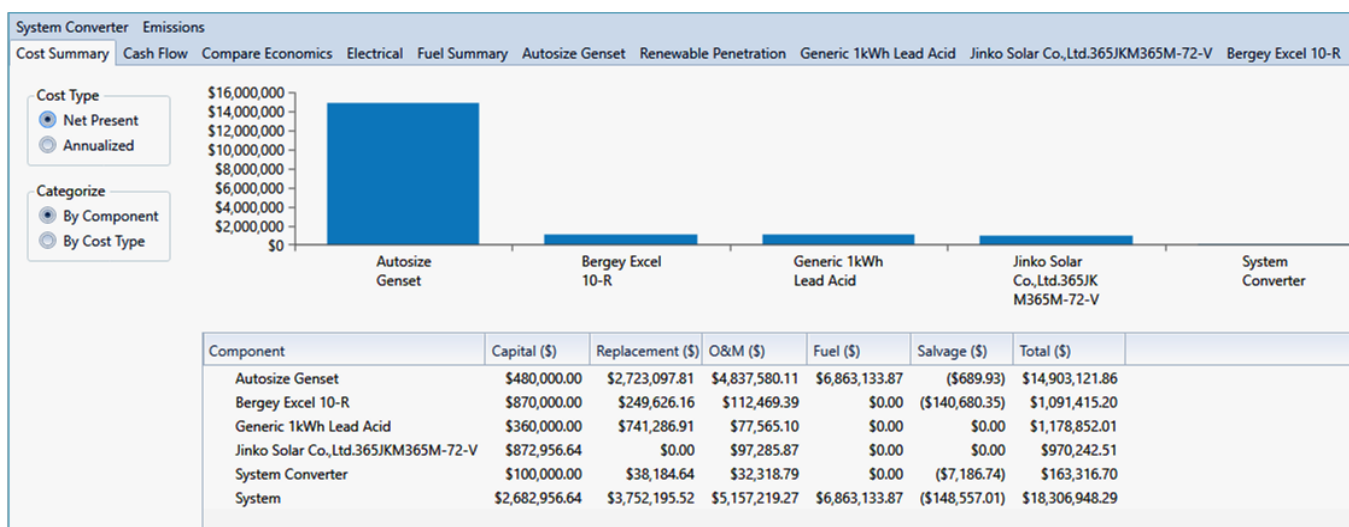


Figure 18: Cost status of the system

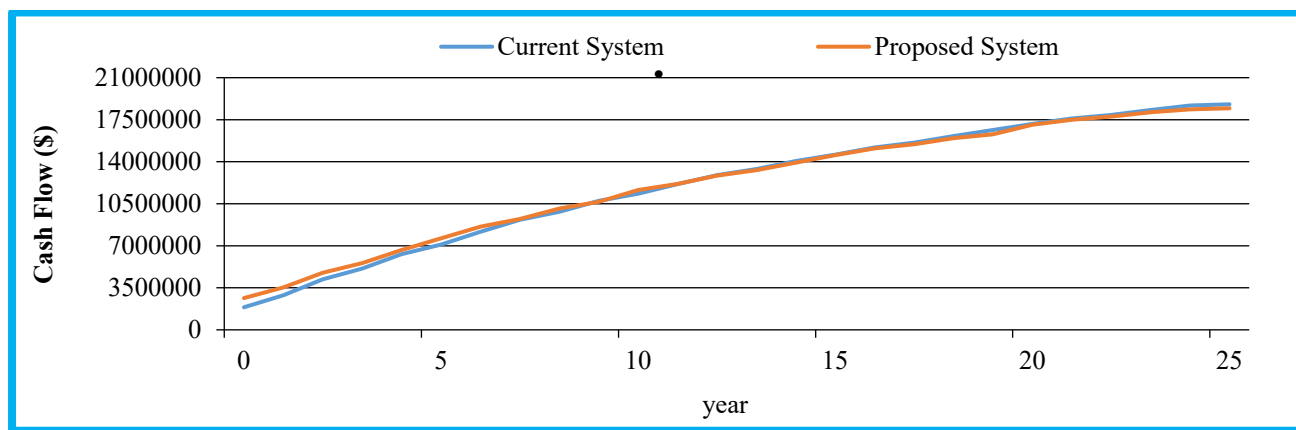


Figure 19: Cumulative cash flow over project lifetime

According to the results of the simulation, it can be observed that of the on-grid hybrid system is the most sustainable hybrid system configuration with the lowest NPC and COE. The total net present cost is \$5.425million and the total energy cost is approximately \$0.0686 per unit. From the simulation results it is clear that the grid-connected configuration is optimal.

### Acknowledgment

This work was supported by the Tunisian Ministry of High Education and Research under Grant LR 11ES15.

### References

- [1] G. Zhang, C. Xiao, N. Razmjoooy, "Optimal operational strategy of hybrid PV/wind renewable energy system using homer: a case study," *International Journal of Ambient Energy*, **43**(1), 3953–3966, 2022, doi:10.1080/01430750.2020.1861087.
- [2] İ. Çetinbaş, B. Tamyurek, M.D. Of, "Design, analysis and optimization of a hybrid microgrid system using HOMER software: Eskisehir osmangazi university example," *Int. Journal of Renewable Energy Development (IJRED)*, **8**(1), 65–79, 2019, doi:10.14710/ijred.8.1.65-79.
- [3] M. Usman, M. Khan, A. Rana, S.A. And, "Techno-economic analysis of hybrid solar-diesel-grid connected power generation system," *Journal of Electrical Systems and Information Technology*, 2017, doi:http://dx.doi.org/10.1016/j.jesit.2017.06.002.
- [4] D. Nachtigall, "Improving Economic Efficiency and Climate Mitigation Outcomes through International Co-ordination on Carbon Pricing-Environment Working Paper No. 147," 2019.
- [5] L. Oliveros-Cano, J. Salgado-Meza, C. Robles-Algarín, "Technical-economic-environmental analysis for the implementation of hybrid energy systems," *International Journal of Energy Economics and Policy*, **10**(1), 57–64, 2020, doi:10.32479/ijee.8473.
- [6] F. Rinaldi, F. Moghaddampoor, B. Najafi, R. Marchesi, "Economic feasibility analysis and optimization of hybrid renewable energy systems for rural electrification in Peru," *Clean Technologies and Environmental Policy*, **23**(3), 731–748, 2021, doi:10.1007/S10098-020-01906-Y.
- [7] A.C. Duman, Ö. Güler, "Techno-economic analysis of off-grid PV/wind/fuel cell hybrid system combinations with a comparison of regularly and seasonally occupied households," *Sustainable Cities and Society*, **42**, 107–126, 2018, doi:10.1016/j.scs.2018.06.029.
- [8] S. Mohamed, C. Habib, H. Othman, B. Jamel, "Comparative Analysis of Hybrid Systems for on-grid and off-grid Applications in Tunisia: case study of Audiovisual chain," in *5th International Conference on Advanced Systems and Emergent Technologies, IC\_ASET*, 450–455, 2022, doi:10.1109/IC\_ASET53395.2022.9765947.
- [9] S. Goyal, S. Mishra, A.B. And, "A comparative approach between different optimize result in hybrid energy system using HOMER," *International Journal of Electrical and Computer Engineering (IJECE)*, **9**(1), 141–147, 2019, doi:10.11591/ijece.v9i1.
- [10] K. Ritu, A. Wadhvani, ... A.R., "Techno-Economic Comparison of on Grid and off Grid Hybrid WT/Solar Photo Voltaic Connected Power Generating Unit Using HOMER," in *International Conference on Advanced Computation and Telecommunication (ICACAT)*, 2018, doi:10.1109/ICACAT.2018.8933685.
- [11] S. Mohamed, C. Habib, H. Othman, B. Jamel, "Electrical Distribution Architecture and Load Curves Analysis of Audiovisual System," in *2021 IEEE 2nd International Conference on Signal, Control and Communication (SCC)*, IEEE, 25–30, 2023, doi:https://dx.doi.org/10.1109/SCC53769.2021.9768369.
- [12] H.S.A.-E. Mageed, "Cost analysis and optimal sizing of PV-Diesel hybrid energy systems," in *American Journal of Renewable and Sustainable Energy*, 47–55, 2018.
- [13] I. Tizgui, F. El Guezar, H. Bouzahir, A.N. Vargas, "Estimation and analysis of wind electricity production cost in Morocco," in *zbw.eu*, 58–66, 2018.
- [14] A. Said, A. Busaidi, H.A. Kazem, A.H. Al-Badi, M. Farooq Khan, "A review of optimum sizing of hybrid PV-Wind renewable energy systems in oman," *International Journal of Students Research in Technology & Management*, **2**(3), 93–102, 2015, doi:10.1016/j.rser.2015.08.039.
- [15] A.S. Almashakbeh, A.A. Arfoa, E.S. Hrayshat, "Techno-economic evaluation of an off-grid hybrid PV-wind-diesel-battery system with various scenarios of system's renewable energy fraction," *Energy Sources, Part A: Recovery, Utilization and Environmental Effects*, 2019, doi:10.1080/15567036.2019.1673515.
- [16] R.T.A. Al-Rubaye, A.T.A. Al-Rubaye, M.M. Al-Khuzai, "Optimal Design of Hybrid Renewable Energy System off grid in Al-Diwaniyah, Iraq," *IOP Conference Series: Materials Science and Engineering*, **454**(1), 2018, doi:10.1088/1757-899X/454/1/012103.
- [17] M. Kamran, M. Mudassar, M. Rayyan Fazal, R. Asghar, S. Rukh Ahmed, M. Irfan Abid, M. Usman Asghar, M. Zunair Zameer, C. Author, "Designing and optimization of stand-alone hybrid renewable energy system for rural areas of Punjab, Pakistan," *Researchgate.Net*, **8**(4), 2018.
- [18] A. Al-Sharafī, A. Sahin, T. Ayar, S. Bekir, "Techno-economic analysis and optimization of solar and wind energy systems for power generation and hydrogen production in Saudi Arabia," *Renewable and Sustainable Energy Reviews*, **69**, 33–49, 2017, doi:https://doi.org/10.1016/j.rser.2016.11.157.
- [19] H. Taghavifar, Z.S. Zomorodian, "Techno-economic viability of on grid micro-hybrid PV/wind/Gen system for an educational building in Iran," *Renewable and Sustainable Energy Reviews*, **143**, 110877, 2021.

## Photoluminescence Properties of Eu(III) Complexes with Two Different Phosphine Oxide Structures and Their Potential uses in Micro-LEDs, Security, and Sensing Devices: A Review

Hiroki Iwanaga\*

*Photoluminescence Material Project, New Business Development Office, Next Business Development Div. Toshiba Corporation, 72-34 Horikawa-cho, Saiwai-ku, Kawasaki 212-8585, Japan*

### ARTICLE INFO

*Article history:*

*Received: 28 February, 2023*

*Accepted: 20 May, 2023*

*Online: 12 June, 2023*

*Keywords:*

*Eu(III) complex*

*Phosphine Oxide*

*Red Phosphor*

*micro-LED*

*Security*

*Sensing*

*Display*

### ABSTRACT

*In the field of micro-LED displays, there is strong demand for red phosphors with high photoluminescence intensity, high color purity, and small particle size. Here, we focus on Eu(III) complexes because they produce sharp photoluminescence spectra with high color purity and can be dissolved in polymer, enabling a reduction in particle size to the molecular level. We have previously established novel molecular design concepts for Eu(III) complexes by coordinating two different phosphine oxide structures to one Eu(III) ion in order to enhance photoluminescence intensity and increase solubility in polymers and solvents. Many Eu(III) complexes have been developed based on these concepts and their photoluminescence properties investigated. Eu(III) complexes with two different phosphine oxide structures are important candidates for red phosphors in micro-LEDs.*

### 1. Introduction

Displays require phosphors with high photoluminescence intensity and high color purity. In addition, in micro-LED displays containing ultraviolet (UV) or blue LED arrays and phosphors, where chips are very small, the particle size of phosphors must be sufficiently small to suppress variation in hues among pixels. Therefore, there is a strong demand for a red phosphor that satisfy these conditions. To this end, novel Eu(III) complexes were introduced in a paper originally presented at the 2022 International Conference on Electronics Packaging as a candidate red phosphor for micro-LEDs [1].

In the case of inorganic phosphors, quantum yields decrease with decreasing phosphor particle size because they are present as fine particles in a polymer (Figure 1). Comparison of properties of the Lanthanide complexes and inorganic phosphors are shown in Table 1. The color purity of inorganic phosphors is low because of the large half widths of emission spectra.

Recently, lanthanide complexes, especially Eu(III) complexes, have attracted increasing attention for their application in emission devices, secure media, sensors, and so on [2–8]. Eu(III) complexes are attractive for display use because they produce

\*Corresponding Author: Hiroki Iwanaga, [hiroki.iwanaga@toshiba.co.jp](mailto:hiroki.iwanaga@toshiba.co.jp)

sharp photoluminescence spectra with high color purity and can reproduce colors in large-area displays.

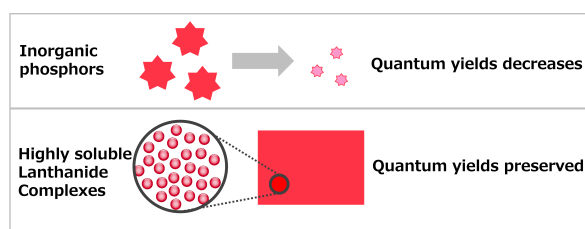


Figure 1: Comparison of inorganic phosphors and highly soluble lanthanide complexes in a polymer.

Table 1: Comparison of properties of the Lanthanide complexes and inorganic phosphors

Phosphors with small particle size	Quantum yield	Color purity
Lanthanide complex	Large	High
Inorganic phosphor	Small	Low

In contrast to inorganic phosphors, particle size is not relevant to the theoretical quantum yield because each molecule of a Eu(III) complex has the function of absorbing and emitting light. From this point of view, Eu(III) complexes are promising candidate red phosphors for micro-LEDs. However, the photoluminescence intensity and solubility of Eu(III) complexes developed to date are insufficient for display use.

An Eu(III) ion itself has very low light absorption and weak emission. However, the emission of lanthanide ions can be enhanced through the antenna effect of ligands.  $\beta$ -diketonates are known to be effective ligands for enlarging photoluminescence intensity of Eu(III) complexes.  $\beta$ -Diketonates absorb light and transfer energy to lanthanide ions efficiently [9, 10]. The photoluminescence intensity of Eu(III) complexes depends largely on the substituents on the  $\beta$ -diketonates because the triplet-state energy levels of  $\beta$ -diketonates are derived from the molecular structures of the substituents. However, it can be difficult to obtain sufficient emission intensity for use in emission devices simply by adjusting the substituents of  $\beta$ -diketonates.

There are two main types in ligands of lanthanide complexes. One is ionic ligands and the other is non-ionic ligands.  $\beta$ -diketonates are prominent ionic ligands and neutralize the charge of lanthanide ions. It is known that photoluminescence intensities are enhanced by the effects of non-ionic ligands in addition to  $\beta$ -diketonates. Phosphine oxide compounds are strong Lewis bases and excellent non-ionic ligands for enlarging photoluminescence intensity [11] (Figure 2).

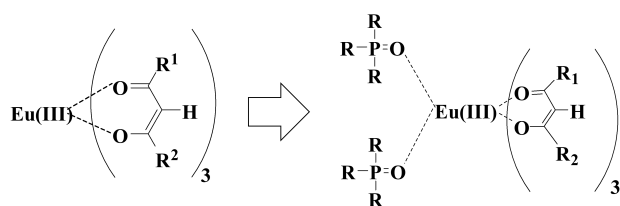


Figure 2: Coordinating phosphine oxides to a Eu(III) ion.

However, there is room for further improvements in emission intensity. At the same time, the solubility of Eu(III) complexes with two identical phosphine oxides are too low to be dissolved in polymers or solvents. For this reason, Eu(III) complexes with low solubility have limited applications.

## 2. Experimental Section

### 2.1 Measurement of photoluminescence and excitation spectra

Photoluminescence and excitation spectra were measured at room temperature using a spectrofluorometer (Fluoromax 4, Horiba Jobin Yvon Inc.). Excitation and emission slit widths were set to 0.5 nm for measurement of emission spectra, and to 0.7 and 0.6 nm for measurement of excitation spectra, respectively. Measurement intervals are 1 nm. Scanning rate are 600 nm/min. Dark offset and corrections were applied to both the emission and excitation sites.

### 2.2 Measurement of emission lifetimes

Measurement of emission lifetimes were performed as follows. Each solution of the Eu(III) complexes was placed in a sealed cell and measured using the spectrofluorometer with the excitation wavelength set to 370 nm. Single exponential functions were used to fit the relative decay curves monitored at the maximum wavelength in order to calculate the emission lifetimes.  $\chi^2$  values were in the range of  $>1.0$  and  $<1.2$ .

### 2.3 Measurement of absolute quantum yields

Total absolute quantum yields ( $\Phi_{TOT}$ ) were measured using a photonic multichannel analyzer (PMA-12 C10027-01,

Hamamatsu Photonics K.K.). An integrating sphere was used for all measurements.

## 3. Results and Discussion

### 3.1. Eu(III) complexes with two different phosphine oxides

Figure 3 shows the relationships between molecular structures and photoluminescence spectra of Eu(III) complexes. The photoluminescence intensity of a Eu(III) complex with no phosphine oxide is usually very small, but when two triphenyl phosphine oxides coordinate, it increases to some extent. Furthermore, when two tributyl phosphine oxides coordinate, photoluminescence intensity increases further, and when both triphenyl and tributyl phosphine oxides coordinate, photoluminescence intensity becomes much higher [12]. The important point here is that coordination of two different phosphine oxide ligands is effective for increasing photoluminescence intensity [12–14]. Eu(III) complexes with two different phosphine oxides can be dissolved and are homogeneous at the molecular level in polymers. Polymers containing our Eu(III) complexes are colorless and transparent under room light but emit a pure color when irradiated with UV and 464-nm light.

### 3.2. Eu(III) complexes with an asymmetric diphosphine dioxide ligand

We detected the ligand exchange of phosphine oxide in Eu(III)- $\beta$ -diketonates by NMR analysis [13]. However, ligand exchange is expected to have an undesirable effect on durability. To overcome this problem, we developed asymmetric diphosphine dioxide ligands (Figure 4). They have molecular structures consisting of two different phosphine oxide parts and methylene units and suppress ligand exchange via the chelate effect. In addition, the photoluminescence intensity of Eu(III)- $\beta$ -diketonates with an asymmetric diphosphine dioxide ligand is higher than that with two different phosphine oxides [15, 16].

Tb(III) complexes with two different phosphine oxides or a single asymmetric diphosphine dioxide were also investigated [17]. It was found that solubilities of Tb(III) complexes were increased by coordination of two different phosphine oxide structures. However, photoluminescence intensities are strongly dependent on the substituents of  $\beta$ -diketonates because of the strong influences of back-energy transfer from excited Tb(III) ions to the ligands.

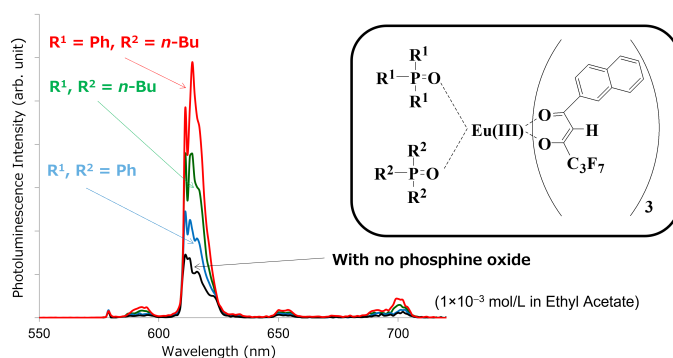


Figure 3: Comparison of the photoluminescence spectra of Eu(III) complexes in ethyl acetate at a concentration of  $2 \times 10^{-4}$  mol/L at room temperature. Showing the effects of phosphine oxides and their combination on photoluminescence intensity [12].

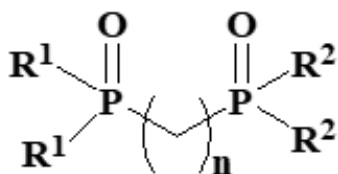


Figure 4: Molecular structures of the asymmetric diphosphine dioxide ligand that increase the photoluminescence intensity of Eu(III) complexes ( $R^1$ =aromatic substituent,  $R^2$ =aliphatic substituent).

### 3-3. Solubility of Eu(III) complexes with phosphine oxide ligands

Relationships between the molecular structures of Eu(III) complexes and solubility in solvents were investigated [18]. Eu(III) complexes with two different phosphine oxides are highly soluble in solvents and can be dissolved even in a fluorinated solvent. However, the solubility of Eu(III) complexes with an asymmetric diphosphine dioxide ligand is lower than that of Eu(III) complexes with two different phosphine oxides. We found that meta-substitution of trifluoromethyl groups ( $CF_3$ ) on the phenyl groups of diphosphine dioxide ligands produces outstanding effects in terms of enhancing the solubility of Eu(III) complexes [19]. Similarly, the solubility of anthraquinone dichroic dyes in fluorinated media are markedly enhanced by the substitution of  $CF_3$  groups [20–22].

### 3.4. Photoluminescence properties of Eu(III) complexes with an asymmetric diphosphine dioxide ligand

Figure 5 shows the optimal diphosphine dioxide ligand for Eu(III) complexes that increases both quantum yields and solubility [23]. Having  $CF_3$  groups at the meta position of phenyl groups is one of the most important characteristics for achieving both high quantum yield and high solubility. Figures 6 and 7 show the relationships between excitation wavelength and quantum yields of Eu(III) complexes with and without diphosphine dioxide ligands, respectively [23].

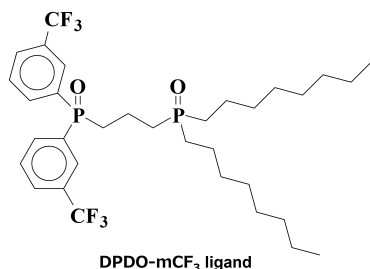


Figure 5: Molecular structure of the asymmetric diphosphine dioxide ligand for Eu(III) complexes that increase the photoluminescence intensity (DPDO- $mCF_3$  ligand) [23].

The maximum total photoluminescence quantum yield ( $\Phi_{TOT}$ ) of Eu(III)(hfnh)<sub>3</sub> is small and the solid-state  $\Phi_{TOT}$  of Eu(III)(hfnh)<sub>3</sub> is smaller than the solution-state  $\Phi_{TOT}$  caused by concentration quenching (Figure 6). In contrast,  $\Phi_{TOT}$  of Eu(III)(hfnh)<sub>3</sub>(DPDO- $mCF_3$ ) is much greater than that of Eu(III)(hfnh)<sub>3</sub>. Furthermore,  $\Phi_{TOT}$  is greater in the solid state than in the solution state. By coordinating the diphosphine dioxide ligands, quantum yields increase eminently. In the solid state, the maximum quantum yield reaches 0.82.

Diphosphine dioxide ligand functions as a separator, maintaining the distance among Eu(III) ions that prevent concentration quenching. In the solid state, there are no solvent molecules to decrease  $\Phi_{TOT}$  of the Eu(III) complexes.

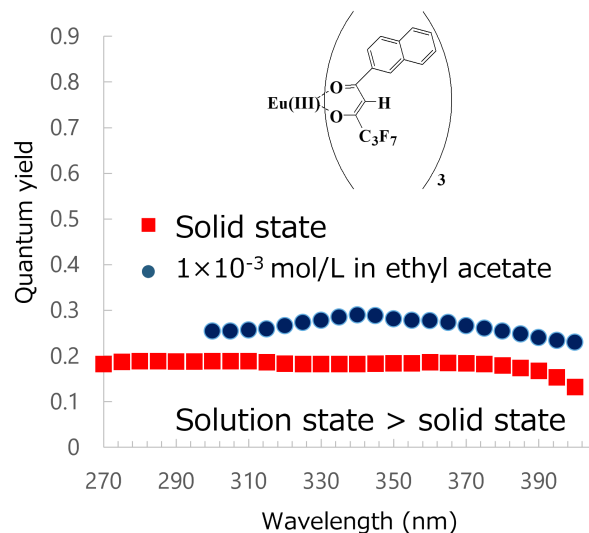


Figure 6: Action spectra (excitation wavelength vs.  $\Phi_{TOT}$ ) of Eu(III)(hfnh)<sub>3</sub> in the solid and solution states [23].

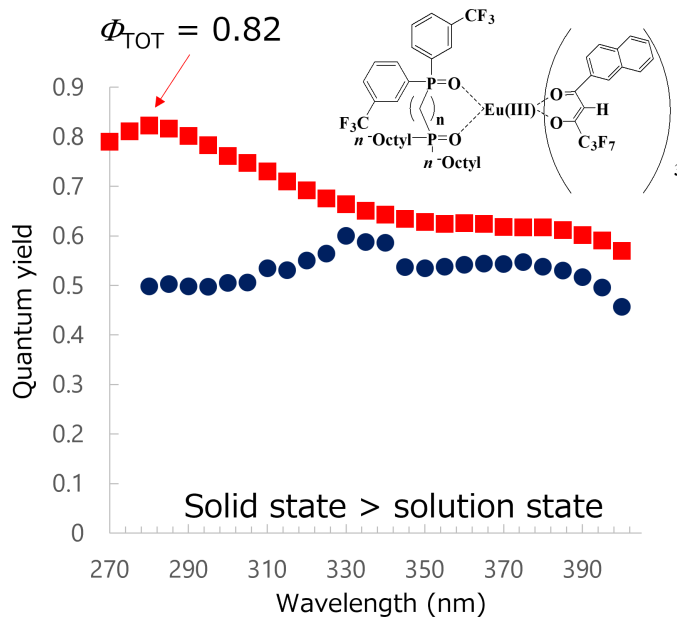


Figure 7: Action spectra (excitation wavelength vs.  $\Phi_{TOT}$ ) of Eu(III)(hfnh)<sub>3</sub>(DPDO- $mCF_3$ ) in the solid and solution states [23].

### 3.5. Quantum yields of Eu(III) complexes with thienyl substituted diphosphine dioxide

Thienyl groups are electron-donating substituents that are expected to enhance the Lewis basicity of the oxygen atoms in diphosphine dioxide ligands. Dithienyl[3-(diethylphosphinyl)propyl] phosphine oxide (DTDOPO) and dithienyl[5-(diethylphosphinyl)pentyl]phosphine oxide (DTDBPO) ligands were developed with the aim of forming stronger coordinate bonds with the Lewis acid Eu(III). A diphenyl[3-(diethylphosphinyl)propyl]phosphine oxide (DPDO) ligand with



phenyl groups instead of thienyl groups was prepared for comparison (Figure 8) [24].

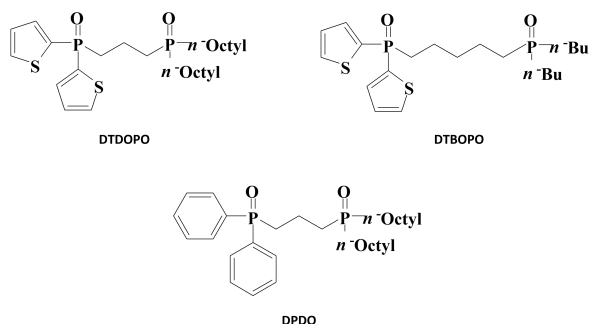


Figure 8: Molecular structures of thienyl-substituted and phenyl-substituted diphosphine dioxides [24].

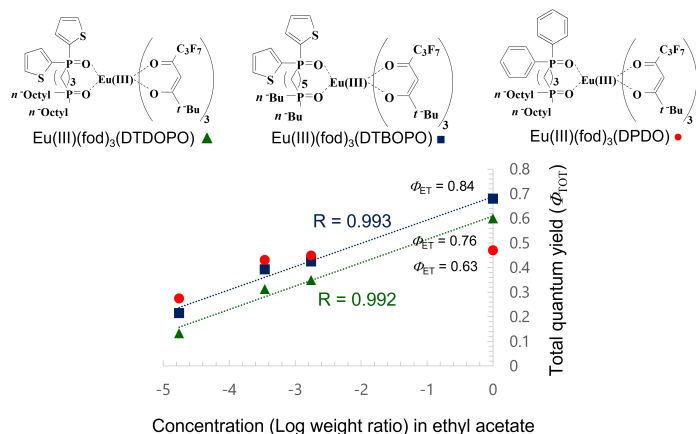


Figure 9: Quantum yields of Eu(III) complexes with thienyl-substituted and phenyl-substituted diphosphine dioxides both in the solid state and in solution (ethyl acetate) [24].

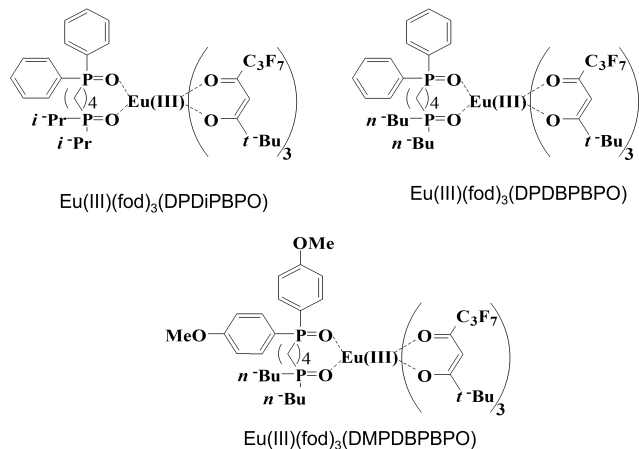


Figure 10: Molecular structures of Eu(III) complexes with a diphosphine dioxide ligand [25]. DPDiPBPO: diphenyl[4-(diisopropylphosphinyl)butyl]phosphine oxide, DPDBPBPO: diphenyl[4-(dibutylphosphinyl)butyl]phosphine oxide, DMPDBPBPO: di(4-methoxyphenyl)[4-(dibutylphosphinyl)butyl]phosphine oxide.

Figure 9 shows the relationships between concentrations in ethyl acetate and quantum yields of Eu(III)(fod)<sub>3</sub>(DTDOPO), Eu(III)(fod)<sub>3</sub>(DTBOPO), and Eu(III)(fod)<sub>3</sub>(DPDO). The concentrations and quantum yields have a strong positive linear correlation and the quantum yields in the solid state (point with concentration [Log weight ratio] 0) are located on the extended line

for Eu(III)(fod)<sub>3</sub>(DTDOPO) and Eu(III)(fod)<sub>3</sub>(DTBOPO) with thienyl groups. No concentration quenching was observed. As the concentration of Eu(III)(fod)<sub>3</sub>(DPDO) increases, the differential coefficients become smaller. Research investigating the special feature of Eu(III) complexes with thienyl groups in the solid state is ongoing.

### 3.6. Effects of alkyl groups in diphosphine dioxide ligands on the photoluminescence properties of Eu(III) complexes

To investigate the effects of the molecular structures of diphosphine dioxide ligands on the photoluminescence properties of Eu(III) complexes, we prepared three Eu(III) complexes with the same molecular structure except for the slight difference in diphosphine dioxide ligands shown in Figure 10 [25].

Eu(III)(fod)<sub>3</sub>(DPDiPBPO) has *i*-propyl groups in a diphosphine dioxide ligand, while Eu(III)(fod)<sub>3</sub>(DPDBPBPO) and Eu(III)(fod)<sub>3</sub>(DMPDBPBPO) have *n*-butyl groups.

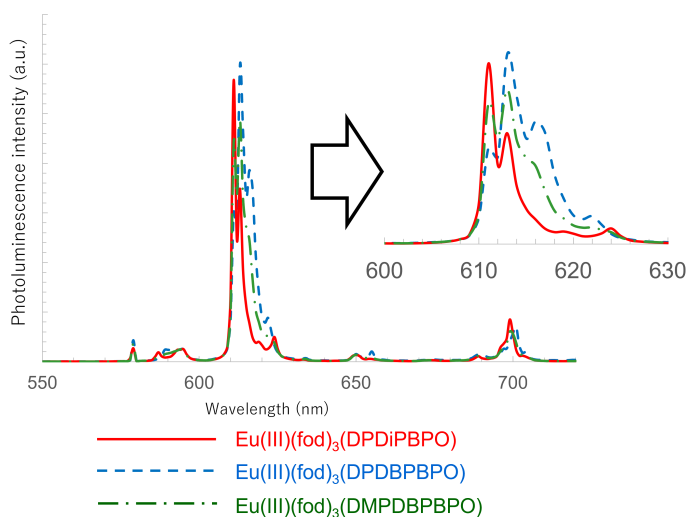


Figure 11: Photoluminescence spectra of the Eu(III) complexes Eu(III)(fod)<sub>3</sub>(DPDiPBPO), Eu(III)(fod)<sub>3</sub>(DPDBPBPO), and Eu(III)(fod)<sub>3</sub>(DMPDBPBPO) in the solid state. They are excited at 370 nm [25].

The photoluminescence spectra of the Eu(III) complexes Eu(III)(fod)<sub>3</sub>(DPDiPBPO), Eu(III)(fod)<sub>3</sub>(DPDBPBPO), and Eu(III)(fod)<sub>3</sub>(DMPDBPBPO) in the solid state are shown in Figure 11. The shapes of the Stark splitting of the <sup>5</sup>D<sub>0</sub>→<sup>7</sup>F<sub>2</sub> transition differ among them. Of note, the half-width of the <sup>5</sup>D<sub>0</sub>→<sup>7</sup>F<sub>2</sub> transition of Eu(III)(fod)<sub>3</sub>(DPDiPBPO) with *i*-propyl (*i*-Pr) substituted for the diphosphine dioxide ligand was 2 nm and conspicuously smaller compared with Eu(III)(fod)<sub>3</sub>(DPDBPBPO) and Eu(III)(fod)<sub>3</sub>(DMPDBPBPO) with *n*-butyl substituted for the diphosphine dioxide ligand. The smaller half-width means the ligand field has a higher symmetry.

Table 2: Photoluminescence properties of the Eu(III) complexes [25]

Ligand	Solid state		
	DPDiPBPO	DPDBPBPO	DMPDBPBPO
$\tau_{exp}$ (ms) <sup>a</sup>	0.99	0.84	0.89
$k_{exp}$ (s <sup>-1</sup> ) <sup>b</sup>	1009	1193	1129

$\tau_{\text{rad}}$ (ms) <sup>c</sup>	1.37	0.99	1.09
$k_{\text{rad}}$ (s <sup>-1</sup> ) <sup>d</sup>	729	1012	992
$k_{\text{nrad}}$ (s <sup>-1</sup> ) <sup>e</sup>	280	181	207
$\Phi_{\text{Ln}}$ <sup>f</sup>	0.72	0.85	0.82
$\Phi_{\text{ET}}$ <sup>g</sup>	0.81	0.83	0.76
$I_{\text{MD}}/I_{\text{TOT}}$ <sup>h</sup>	0.0678	0.0488	0.0537
$\Phi_{\text{TOT}}$ <sup>i</sup>	0.58 (345 nm)	0.70 (350 nm)	0.62 (345 nm)
Ratio $R^j$	11.1	16.7	14.9

<sup>a</sup>Experimental lifetime measured in solid.  $\chi^2$  values were in the range of > 1.0 and < 1.2.

<sup>b</sup>experimental decay rate

<sup>c</sup>Radiative lifetime calculated using the formula

$$\tau_{\text{rad}} = 1/n^3 A_{\text{MD},0} \times I_{\text{MD}}/I_{\text{TOT}} \quad (n = 1.50).$$

<sup>d</sup>Radiative decay rate

<sup>e</sup>Non-radiative decay rate

<sup>f</sup>Intrinsic quantum yield calculated using the formula

$$\Phi_{\text{Ln}} = \tau_{\text{exp}} / \tau_{\text{rad}}.$$

<sup>g</sup>Energy transfer efficiency

<sup>h</sup>Ratio between the integrated intensity of the  ${}^5\text{D}_0 \rightarrow {}^7\text{F}_1$

transition ( $I_{\text{MD}}$ ) and the total integrated emission intensity  ${}^5\text{D}_0 \rightarrow {}^7\text{F}_J$  ( $J = 0-6$ ) ( $I_{\text{TOT}}$ )

<sup>i</sup>Total quantum yield measured in solid state. (Peak wavelength of the action spectrum (wavelength vs. quantum yield)).

<sup>j</sup>Calculated from the formula  $I({}^5\text{D}_0 \rightarrow {}^7\text{F}_2) / I({}^5\text{D}_0 \rightarrow {}^7\text{F}_1)$

Table 2 shows the photoluminescence properties of the Eu(III) complexes. The  $\Phi_{\text{TOT}}$  of Eu(III)(fod)<sub>3</sub>(DPDiPBPO) was smaller than that of others because of the smaller intrinsic quantum yield ( $\Phi_{\text{Ln}}$ ). The smaller ratio  $R$  and larger  $I_{\text{MD}}/I_{\text{TOT}}$  of Eu(III)(fod)<sub>3</sub>(DPDiPBPO) showed that the Eu(III) complex with *i*-Pr groups in the diphosphine dioxide ligand had a higher symmetry in ligand fields compared with the others in the solid state. These results agree well with the result of the smaller half-width of Eu(III)(fod)<sub>3</sub>(DPDiPBPO). These noticeable differences in properties are caused by the difference in molecular structures between the *i*-Pr and *n*-Bu groups in diphosphine dioxides.

Based on the above, we propose a hypothesis about  $\Phi_{\text{TOT}}$  and diphosphine dioxide ligand structures: the steric hindrance of diphosphine dioxide ligands with *n*-Bu groups is larger than that of ligands with *i*-Pr groups, and a larger steric hindrance causes diphosphine dioxide ligands to have lower symmetry of the ligand field, thereby inducing a larger  $\Phi_{\text{TOT}}$ . In the next section, we focus on the effects of steric hindrance in diphosphine dioxide ligands.

### 3.7. Elucidation of the effects of diphosphine dioxide ligands on the quantum yield and photoluminescence intensity of a 6-coordinate Eu(III)- $\beta$ -diketonate complex

To elucidate the coordination effects of phosphine oxide ligands, the following 6-coordinate Eu(III) complex designed to have low luminescence and a large absorption coefficient was synthesized: (Tris{6,6,7,7,8,8,8-heptafluoro-1-[2-(9,9-dimethylfluorenyl)]-1,3-octanedionate}) europium(III) (Eu(III)(hfod)<sub>3</sub>) (Figure 12) [26].

Dimethylfluorenyl groups are bulky aromatic substituents with large absorption coefficients. Partially fluorinated alkyl groups in  $\beta$ -diketonates are also very bulky. The methylene units in partially fluorinated alkyl groups have the function of decreasing the energy transfer efficiency from the ligands to the Eu(III) ion.

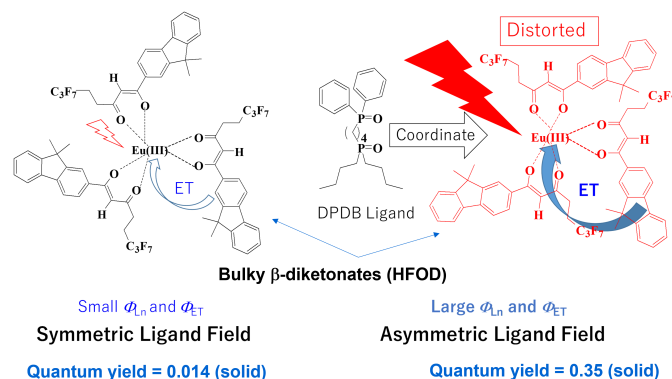


Figure 12: Coordinating effects of DPDB ligand with Eu(III)(hfod)<sub>3</sub> with bulky  $\beta$ -diketonates, “hfod” [26].

The photoluminescence intensity of Eu(III)(hfod)<sub>3</sub> is dramatically enhanced by coordinating a DPDB ligand (generating Eu(III)(hfod)<sub>3</sub>(DPDB)) due to the increased  $\Phi_{\text{TOT}}$ ,  $\Phi_{\text{Ln}}$ , and  $\Phi_{\text{ET}}$  in both the solution and solid states.

We propose the following hypothesis for the increase in  $\Phi_{\text{TOT}}$  of 6-coordinate Eu(III) complex caused by the effects of the DPDB ligand. When a DPDB ligand coordinates with the Eu(III) ion, the positions of the nearest oxygen atoms around the Eu(III) ion are shifted by steric repulsion, and the relative positions of the nearest oxygen atoms become distorted. Ligand field is asymmetricized by the distorted coordination environment, and that increases  $\Phi_{\text{TOT}}$ .

The norm of the effective dipole moment of the ligand field  $\mu$  was defined [26]. We demonstrated that the energy transfer efficiencies from the lowest triplet state of the ligands to the  ${}^5\text{D}_1$  level of the Eu(III) ion ( $\Phi_{\text{ET}}$ ) increases when the ligand fields of the Eu(III) ion become more asymmetric by coordinating the DPDB ligand.

### 3.8. High-sensitivity method for detecting the pesticide dichlorvos by using Eu(III)- $\beta$ -diketonate as a quenching probe

Dichlorvos is a general-purpose insecticide with agricultural, household, and animal applications. However, it is harmful to humans, and thus a high-sensitivity method for detecting dichlorvos that provides results in a short time would be desirable.

We found that  $\text{Eu(III)(hfnh)}_3$  was a highly sensitive luminescent probe for the pesticide dichlorvos. The photoluminescence intensity of  $\text{Eu(III)(hfnh)}_3$  was drastically and rapidly decreased when a dilute solution of dichlorvos was added to the solutions of  $\text{Eu(III)(hfnh)}_3$  (Figure 13) [27].

When a solution of dichlorvos was mixed with a solution of  $\text{Eu(III)(hfnh)}_3$  and shaken,  $\Phi_{\text{ET}}$  drastically decreased ( $0.64 \rightarrow 0.15$ ). The photoluminescence quenching of  $\text{Eu(III)(hfnh)}_3$  by dichlorvos occurred before the energy transfer from  $\beta$ -diketonates to a  $\text{Eu(III)}$  ion between the dichlorvos molecules and the  $\beta$ -diketonates

The photoluminescence of  $\text{Eu(III)(hfnh)}_3$  is not quenched by compounds with similar structures and has a favorable selectivity for dichlorvos. These results indicate that  $\text{Eu(III)(hfnh)}_3$  is a strong candidate for a sensitive, selective, and quick method for detecting dichlorvos. Other organophosphorus pesticides can be selectively detected by other  $\text{Eu(III)-}\beta$ -diketonates.

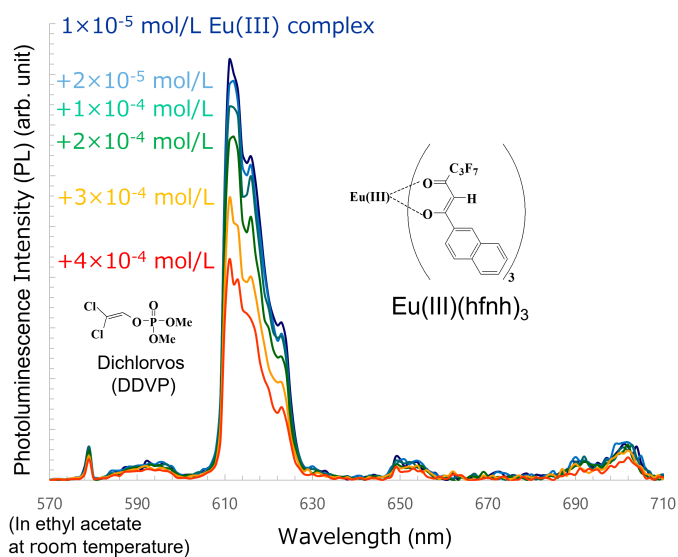


Figure 13: Photoluminescence quenching of  $\text{Eu(III)(hfnh)}_3$  by the pesticide dichlorvos [27].

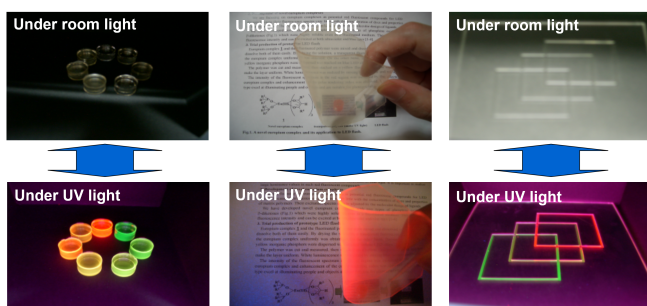


Figure 14: Colorless and transparent photoluminescence materials containing our  $\text{Eu(III)}$  complexes and/or  $\text{Tb(III)}$  complexes in a polymer [16].

### 3.9. Characteristics of colorless and transparent photoluminescence materials involved in our $\text{Eu(III)}$ complexes and/or $\text{Tb(III)}$ complexes in a polymer

We developed multiple lanthanide complexes having two different phosphine oxides or an asymmetric diphosphine dioxide that improved both photoluminescence intensity and solubility. When  $\text{Eu(III)}$  or  $\text{Tb(III)}$  complexes or both are dissolved in a polymer, materials that are colorless and have transparent

[www.astesj.com](http://www.astesj.com)

photoluminescence under room light are produced. These materials emit pure red or green as well as yellow and orange intermediate colors when irradiated with UV or near-UV light (Figure 14) [16].

LED devices comprising a UV-light LED chip and a fluorescent layer consisting of a fluorinated polymer and  $\text{Eu(III)}$  complexes with two different phosphine oxides were prototyped. The developed devices emit a pure red color. The highest luminous flux obtained under optimum conditions, which to our knowledge is the best result reported as of 2007, was 870 m lumen/20 mA, when excited by a 402-nm LED chip (Figure 15) [28].

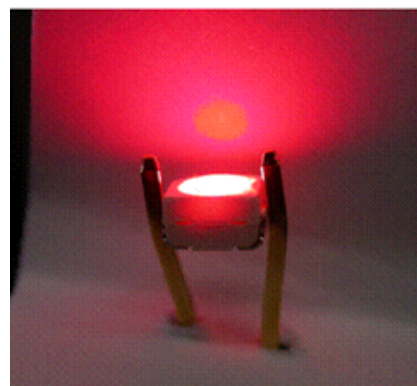


Figure 15: LED devices containing novel  $\text{Eu(III)}$  complexes in the fluorinated layer [28].

## 4. Conclusion

We found that coordination of two different phosphine oxide structures to a lanthanide ion is effective for enhancing the photoluminescence intensity and solubility of lanthanide complexes. An asymmetric diphosphine dioxide ligand consisting of two different phosphine oxide parts and methylene units produce further excellent effects in terms of enhancing the quantum yields and photoluminescence intensity of  $\text{Eu(III)}$  complexes. Asymmetric diphosphine dioxide ligands induce asymmetry in the ligand fields of  $\text{Eu(III)}$  complexes, thereby improving the quantum yields. Colorless and transparent photoluminescence materials can be obtained by dissolving  $\text{Eu(III)}$  complexes in polymers or solvents. These materials show great promise for use in LEDs as well as security and sensing devices.

We believe that our  $\text{Eu(III)}$  complexes have advantages over inorganic phosphors as red phosphors for use in micro-LED displays.

## Acknowledgment

The author would like to thank Okuno Atsushi, Takahisa Kobayashi, Junichi Washizuka, Chiari Shimizu, Naruaki Watanabe, Akiko Yuzawa, and Huang Chingchun for fruitful discussions.

## References

- [1] H. Iwanaga, "Photoluminescence Properties of  $\text{Eu(III)}$  Complexes with an Asymmetric Diphosphine Dioxide Ligand for Potential Uses in LED, Security, and Sensing Devices," 2022 International Conference on Electronics Packaging (ICEP), 17-18, 2022, doi:10.23919/ICEP55381.2022.9795463.
- [2] Q. Xin, W.L. Li, G.B. Che, W.M. Su, X.Y. Sun, B. Chu, B. Li, "Improved

- Electroluminescent Performances of Europium-Complex Based Devices by Doping into Electron-Transporting/Hole-Blocking Host," *Applied Physics Letters*, **89**, 223524, 2006, doi:10.1063/1.2400112.
- [3] Q. Xin, W.L. Lia, W.M. Su, T.L. Li, Z.S. Su, B. Chu, B. Li, "Emission Mechanism in Organic Light-Emitting Devices Comprising a Europium Complex as Emitter and an Electron Transporting Material as Host," *Journal of Applied Physics*, **101**, 044512, 2007, doi:10.1063/1.2655225.
- [4] G. Santos, L.G. Paterno, F.J. Fonseca, A.M. Andrade, L.F. Preira, "Enhancement of Light Emission from an Europium(III) Complex Based-OLED by Using Layer-by-Layer Assembled Hole-Transport Films," *ECS Transactions*, **39**, 307-313, 2011, doi:10.1149/1.3615207.
- [5] S.G. Liu, W.Y. Su, R.K. Pan, X.P. Zhou, "Red Emission of Eu(III) Complex Based on 1-(7-(tert-butyl)-9-ethyl-9H-carbazol-2-yl)-4,4,4-trifluorobutane-1,3-dione Excited by Blue Light," *Chinese Journal of Chemical Physics*, **25**, 697-702, 2012, doi:10.1088/1674-0068/25/06/697-702.
- [6] A.M. Kaczmarek, Y.Y. Liu, C. Wang, B. Laforce, L. Vincze, P.V.D. Voort, K.V. Hecke, R.V. Deun, "Lanthanide "Chameleon" Multistage Anti-Counterfeit Materials," *Advanced Functional Materials*, **27**, 1700258, 2017, doi:10.1002/adfm.201700258.
- [7] X. Li, J. Gu, Z. Zhou, L. Ma, Y. Tang, J. Gao, Q. Wang, "New Lanthanide Ternary Complex System in Electrospun Nanofibers: Assembly, Physico-Chemical Property and Sensor Application," *Chemical Engineering Journal*, **358**(15), 67-73, 2019, doi:10.1016/j.cej.2018.10.003.
- [8] G. Lu, X. Kong, C.M. Wang, L.Y. Zhao, D.D. Qi, Y.Y. Jiang, S. Zhao, Y.L. Chen, J.Z. Jiang, "Optimizing the Gas Sensing Properties of Sandwich-Type Phthalocyaninato Europium Complex Through Extending the Conjugated Framework," *Dyes and Pigments*, **161**, 240-246, 2019, doi:10.1016/j.dyepig.2018.09.062.
- [9] S. Sato, M. Wada, T. Seki, "Some properties of europium  $\beta$ -diketone chelates 1. (Synthesis and fluorescent properties)," *Japanese Journal of Applied Physics*, **7**, 7-13, 1968, doi: 10.1143/JJAP.7.7
- [10] S. Sato, M. Wada, "Relation between intramolecular energy transfer efficiencies and triplet state energies in rare earth  $\beta$ -diketone chelate," *Bulletin of the Chemical Society of Japan*, **43**, 1955-1962, 1970, doi:10.1246/bcsj.43.1955.
- [11] J. Yuan, K. Matsumoto, "Fluorescence Enhancement by Electron-Withdrawing Groups on  $\beta$ -Diketones in Eu(III)- $\beta$ -diketonato-topo Ternary Complexes", *Analytical Sciences*, **12**, 31-36, 1996, doi:10.2116/analsci.12.31.
- [12] H. Iwanaga, "Investigation of strong photoluminescence and highly soluble Eu(III) complexes with phosphine oxides and  $\beta$ -diketonates," *Journal of Luminescence*, **200**, 233-239, 2018, doi:10.1016/j.jlumin.2018.03.070.
- [13] H. Iwanaga, A. Amano, M. Oguchi, "Study of molecular structures and properties of europium(III) complexes with phosphine oxides by NMR analysis," *Japanese Journal of Applied Physics*, **44**, 3702-3705, 2005, doi:10.1143/JJAP.44.3702.
- [14] H. Iwanaga, A. Amano, F. Aiga, K. Harada, M. Oguchi, "Development of Ultraviolet LED Devices Containing Europium (III) Complexes in Fluorinated Layer," *Journal of Alloys and Compounds*, **408-412**, 921-925, 2006, doi:10.1016/j.jallcom.2005.01.138.
- [15] H. Iwanaga, F. Aiga and A. Amano, "The molecular structures and properties of novel Eu(III) complexes with asymmetric bis-phosphine oxides," *Materials Research Society symposia proceedings*, **965**, 211-216, 2006, doi:10.1557/PROC-0965-S03-12.
- [16] H. Iwanaga, "Emission properties, solubility, thermodynamic analysis and NMR studies of rare-earth complexes with two different phosphine oxides," *Materials*, **3**, 4080-4108, 2010, doi:10.3390/ma3084080.
- [17] H. Iwanaga, and F. Aiga, "Novel Tb(III) complexes with two different structures of phosphine oxides and their properties", *Journal of Luminescence*, **130**(5), 812-816, 2010, doi:10.1016/j.jlumin.2009.11.039.
- [18] H. Iwanaga, A. Amano, F. Furuya, and Y. Yamasaki, "Solubility in fluorinated medium and thermal properties of Europium(III) complexes with phosphine oxides," *Japanese Journal of Applied Physics*, **45**, 558-562, 2006, doi:10.1143/JJAP.45.558.
- [19] H. Iwanaga, "Relationships between molecular structures of aromatic- and aliphatic-substituted diphosphine dioxide ligands and properties of Eu(III) complexes," *Optical Materials*, **85**, 418-424, 2018, doi:10.1016/j.optmat.2018.08.071.
- [20] H. Iwanaga, K. Naito, and Y. Nakai, "The Molecular structures and properties of anthraquinone-type dichroic dyes," *Molecular Crystals and Liquid Crystals*, **364**, 211-218, 2001, doi:10.1080/10587250108024989.
- [21] H. Iwanaga, K. Naito, and F. Aiga, "Properties of novel yellow anthraquinone dichroic dyes with naphthylthio groups for guest-host liquid crystal displays," *Journal of Molecular Structure*, **975**, 110-114, 2010, doi:10.1016/j.molstruc.2010.04.003.
- [22] H. Iwanaga, and F. Aiga, "Correlations among molecular structures, solubilities in fluorinated media, thermal properties and absorption spectra of anthraquinone dichroic dyes with phenylthio and/or anilino groups," *Liquid Crystals*, **38**(2), 135-148, 2011, doi:10.1080/02678292.2010.531149.
- [23] H. Iwanaga, "A CF3-substituted Diphosphine Dioxide Ligand that Enhances both Photoluminescence Intensity and Solubility of Eu(III) Complexes," *Journal of Alloys and Compounds*, **790**, 296-304, 2019, doi:10.1016/j.jallcom.2019.03.085.
- [24] H. Iwanaga, "Photoluminescence Properties of Eu(III) Complexes with Thienyl-Substituted Diphosphine Dioxide Ligands," *Bulletin of the Chemical Society of Japan*, **92**(8), 1385-1393, 2019, doi:10.1246/bcsj.20190068.
- [25] H. Iwanaga, "Effects of Alkyl Groups in Diphosphine Dioxide-Ligand for Eu(III)- $\beta$ -Diketonate Complexes on Photoluminescence Properties," *Chemical Physics Letters*, **736**, 136794, 2019, doi:10.1016/j.cplett.2019.136794.
- [26] H. Iwanaga and F. Aiga, "Quantum Yield and Photoluminescence Intensity Enhancement Effects of Diphosphine Dioxide Ligand on a 6-Coordinate Eu(III)- $\beta$ -Diketonate Complex with Low Luminescence," *ACS Omega*, **6**(1), 416-424, 2021, doi:10.1021/acsomega.0c04826.
- [27] H. Iwanaga and F. Aiga, "A Simple and Sensitive Detection Method for the Pesticide Dichlorvos in Solution using Eu(III)- $\beta$ -Diketonate as a Luminescent Probe," *Japanese Journal of Applied Physics*, **59**, SDDF05, 2020, doi:10.7567/1347-4065/ab5c96.
- [28] H. Iwanaga, and A. Amano, "Solid-State  $^{31}\text{P}$ -Nuclear Magnetic Resonance Analysis of Eu(III) Complexes with Phosphine Oxides in Fluorinated Polymer," *Japanese Journal of Applied Physics*, **46**, L495-L497, 2007, doi:10.1143/JJAP.46.L495.

## Design and Implementation of an Automated Medicinal-Pill Dispenser with Wireless and Cellular Connectivity

Chanuka Bandara<sup>1</sup>, Yehan Kodithuwakku<sup>1</sup>, Ashan Sandanayake<sup>1</sup>, R. A. R. Wijesinghe<sup>2</sup>, Velmanickam Logeeshan<sup>\*3</sup>

<sup>1</sup>Department of Electrical, Electronic and Telecommunication Engineering, Faculty of Engineering, General Sir John Kotelawala Defence University, Sri Lanka

<sup>2</sup>Department of Mechanical Engineering, Faculty of Engineering, General Sir John Kotelawala Defence University, Sri Lanka

<sup>3</sup>Department of Electrical Engineering, University of Moratuwa, Sri Lanka

### ARTICLE INFO

Article history:

Received: 01 January, 2023

Accepted: 23 February, 2023

Online: 12 June, 2023

Keywords:

Adherence

IoT

Dispenser

Web Interface

Pills

Regimen

### ABSTRACT

Medical adherence is a major concern globally and is increasing with improved access to medication. Unfortunately, patients taking multiple medications often struggle with confusion about when and how to take each medication. To address this issue, an inexpensive domestic device has been proposed to improve medication adherence. This device uses Wi-Fi and cellular Internet of Things (IoT) integration to dispense medication at the prescribed times, making it suitable for use in both home and long-term care settings. The device also includes a web interface that allows users to control the device and make changes to dosage and other related information. Additionally, the device features an intricate system for sorting pills to ensure accurate and efficient medication delivery. Automating medication taking through this device can improve patient adherence and overall health outcomes, which could significantly impact public health and quality of life for patients struggling with medication adherence.

## 1. Introduction

The purpose of this paper is to present a revised and expanded version of the smart medicinal pill dispenser originally presented at the World AI IoT Congress in 2022 [1]. Additional research and testing have been conducted to further improve the device and to provide more in-depth explanations of its functionality and effectiveness. This paper presents the updated findings and conclusions from the continued research, development and testing of the smart medicinal pill dispenser.

Medicine has evolved alongside humanity, with treatments and technologies constantly improving and advancing. While there are still a handful of currently incurable diseases, the vast majority of illnesses can be treated with some form of medication. Despite numerous medical advances, oral medication remains the most convenient and widely available form of treatment [2]. This is due, in part, to the fact that oral medication is easy to administer and

does not require specialized equipment or training. As a result, oral medication continues to be a crucial aspect of modern healthcare.

The increasing use of oral medication highlights the importance of effective systems for managing and administering these drugs. In the United States, prescription drug usage in 2020 was 6.324 billion, significantly increasing from the 3.953 billion doses used in 2009 [3]. Globally, the IMS Institute for Healthcare Informatics estimates that 4.5 trillion doses of oral medication were used in 2020, a 24% increase over 2015 [4]. These statistics underscore the need for efficient and convenient systems for administering oral medication, particularly for patients taking multiple drugs or those in long-term care facilities. Effective management of oral medication can help improve patient adherence and overall health outcomes, making it a crucial aspect of modern healthcare.

Managing multiple medications can be challenging for patients, especially when multiple types of drugs are prescribed in a single prescription, as is common practice among doctors. This can be especially difficult for patients who are taking multiple medications or who have complex treatment regimens. A study

\*Corresponding Author: Dr. Velmanickam Logeeshan, Department of Electrical Engineering, University of Moratuwa, Sri Lanka. Email: [logeeshanv@uom.lk](mailto:logeeshanv@uom.lk)

conducted by [5] found that a significant percentage of patients struggle with complex medication regimens. In fact, only about 15% of the target group in the study organized their dose times to create a more manageable routine. This can be particularly problematic for patients taking number of medications. In [6], the authors showed that the target group in their study used an average of 8 medications in a single prescription.

Adherence to medications is crucial in healthcare, particularly for those taking oral medications. The World Health Organization (WHO) has determined that if a patient's adherence to medication is generally considered satisfactory if the proportion of prescribed medication taken as directed is greater than 80%. This is determined by calculating the number of pills absent in each time period and dividing it by the number of pills prescribed by the physician in that same time period [7].

Unfortunately, many patients struggle to consistently follow their prescribed treatment regimens, leading to significant problems with non-adherence. The WHO recognized this as a major health issue in 2003 [8], and subsequent studies have further highlighted the prevalence and consequences of non-adherence. For example, a study by Eindhoven et al. [9] found that only 40% of the general population consistently followed their prescribed medical routines. Another study conducted in Sri Lanka [10] revealed that a large majority (84.5%) of 303 patients with high blood pressure at the Teaching Hospital of Jaffna were non-adherent to their medication regimens. This was primarily due to forgetfulness and disruptions in daily routines, but other factors, such as managing multiple medications or feeling that they do not receive sufficient attention (particularly among elderly patients) can also contribute to non-adherence. The consequences of medical non-adherence can be severe, including increased risk of antibiotic resistance, worsening of existing conditions, and falling outside of the therapeutic range [11].

According to [12], over 15% of patients ignore the recommended dosages for over-the-counter (OTC) drugs. OTC medications are widely available and do not require a prescription, making them convenient for treating common ailments. Some common OTC medications include acetaminophen, antihistamines, and antacids [13]. However, the ease of access and lack of direct supervision by a healthcare provider can lead to issues with non-adherence to dosage recommendations. This can have negative consequences for patient health and well-being, as taking too much or too little of a medication can have dire consequences. As such, it is important for patients to follow dosage recommendations for OTC drugs carefully and to seek guidance from a healthcare provider if they have any questions or concerns.

In [14], the authors found that accidental overdose on acetaminophen (also known as paracetamol) is a common problem with OTC medications. The same study states that over 23% of participants accidentally overdosed on acetaminophen products. This is often due to a lack of knowledge about proper dosage and dosing intervals for OTC medications and the fact that different medications have different recommended dosages and dosing intervals. For example, the recommended adult dosage for acetaminophen is two pills every 6 hours [15], while the recommended adult dosage for ibuprofen is 2 pills every 8 hours [16]. This suggests that while many people are aware of common

OTC medications and their intended uses, they may not clearly understand proper dosage and dosing intervals. This lack of knowledge can increase the risk of accidental overdose and other adverse health consequences.

Inadequate adherence to medication regimens is a significant issue that contributes to negative health outcomes and increased healthcare costs. One of the major challenges in ensuring proper medication adherence is the complexity of some regimens, which can involve taking multiple medications at different times of day or administering drugs in unconventional ways. These factors can be confusing for patients and may lead to doses being missed or taken at the wrong times [17]. According to the Centers for Disease Control and Prevention (CDC), the United States experiences over 2.8 million antibiotic-resistant infections annually, and antibiotic resistance is responsible for over 35,000 deaths [18]. Improper medication use, including self-medication with antibiotics and not following dosage instructions, contributes to the growing problem of antibiotic resistance.

## 2. Analysis of Survey and Interview Data on Medicine Usage

### 2.1. Survey analysis

A survey was conducted among a sample of Sri Lankan adults over the age of 40 years to examine patterns of medicine used in this population in 2022. The survey sample was obtained through distribution to university students, resulting in a total of approximately 320 participants.

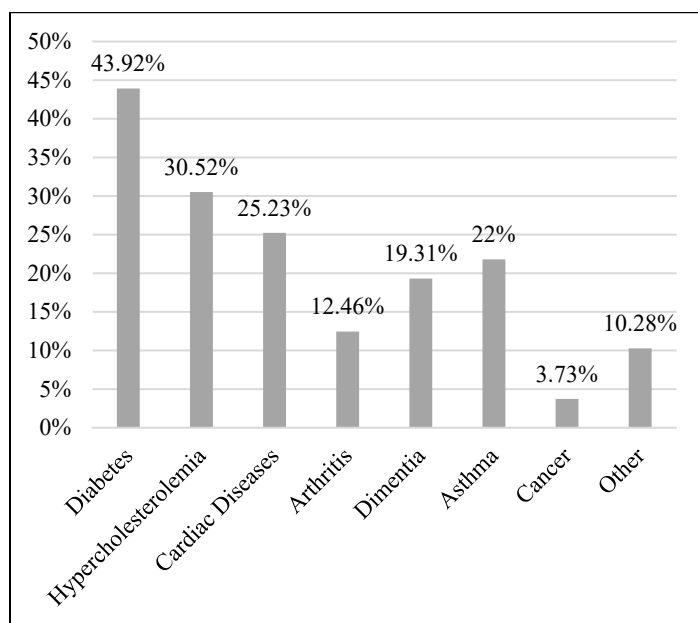


Figure 1: Proportion of long-term illnesses in the survey sample population

The survey results revealed a high prevalence of chronic diseases among Sri Lankan adults (Figure 1). In particular, it was found that over 95% of the target group had at least one chronic condition, with diabetes being the most common at over 40%. Additionally, the survey revealed that over 30% of Sri Lankan adults had high blood cholesterol or hypercholesterolemia. In addition to the high prevalence of diabetes and hypercholesterolemia among Sri Lankan adults, the survey also

identified other common chronic conditions. Cardiac diseases, such as hypertension, were prevalent among a significant percentage of the target group. Additionally, a significant number of participants reported suffering from arthritis. Cancer was also reported among a small percentage of the sample. The findings of the 2022 survey are consistent with those obtained in a previous survey on the same topic in 2021 by Bandara C. et al. [1].

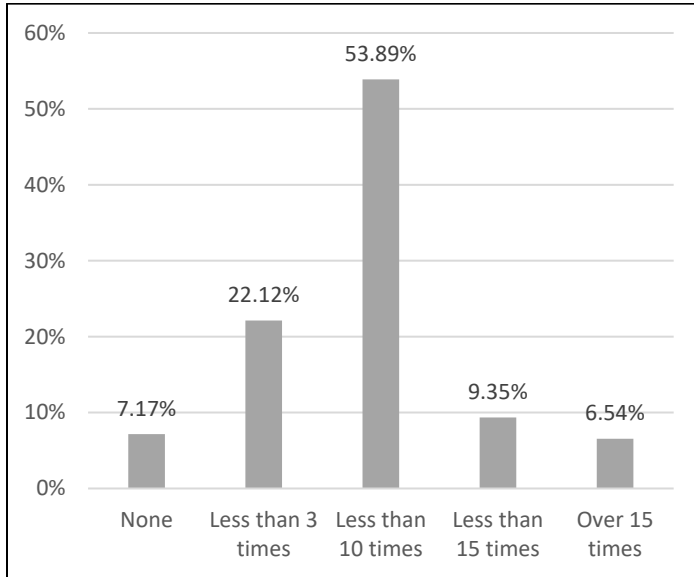


Figure 2: Proportion of sample population reporting medication non-adherence within a month

In addition to examining the prevalence of chronic diseases among the survey sample, the survey also assessed participants' adherence to their medication regimens (Figure 2). The results showed that under 30% of the population consistently took their medication without missing doses or rarely lacking. All other participants reported frequently forgetting to take their medication. These findings suggest that medication adherence is a significant issue among the Sri Lankan adult population, with the majority of participants struggling to consistently follow their prescribed treatment regimens.

### 2.2. Interview findings

A series of interviews were conducted with professionals in the medical sector to explore the issue of medication adherence. The interviews confirmed that patients are often prescribed multiple medications to treat their underlying diseases, manage symptoms, and control pain. It was noted that similar drugs are often included in the same regimen, which can lead to confusion for some patients. The professionals interviewed emphasized the importance of clear communication between healthcare providers and patients to ensure that patients fully understand their prescribed treatment regimens and the potential risks and benefits of each medication.

One potential source of confusion and non-adherence among patients taking multiple medications is the similarity in the appearance of certain drugs. For example, diabetes medications such as Metformin and Gliclazide may be easily mistaken for one another, particularly if they are taken at different frequencies (e.g., Metformin once daily and Gliclazide twice daily). Similarly, hypertension medications like Hydrochlorothiazide and Losartan

Potassium, which may be taken at different frequencies (e.g., Hydrochlorothiazide twice daily and Losartan Potassium once daily), may also be confusing for some patients.

The interviews also revealed that patients may neglect their medication dosages due to busy schedules and may simply ignore their medication altogether. Additionally, older patients may not receive sufficient care to remind and administer their medication at home. These findings suggest that time constraints and lack of support may contribute to non-adherence among certain patient populations.

Although medical professionals are actively working to minimize the issue of non-adherence to medication regimens, the lack of resources and lack of patient cooperation are significant challenges. Despite efforts to educate patients about the importance of adherence and to provide support to help patients follow their prescribed treatment regimens, many patients continue to struggle with non-adherence.

### 3. Existing Approaches

#### 3.1. The traditional approach to managing multiple medications.

The traditional method of accessing and administering prescribed medications (Figure 3) typically involves manually checking the prescription and individually taking each type of medication in the prescribed dosage. This process can be tedious and time-consuming, and it can also lead to errors. For example, if the patient becomes distracted or fatigued while following their medication regimen, they may accidentally skip a dose or take an incorrect dosage. Additionally, if the patient has multiple medications with different dosing instructions, it can be easy to confuse or mix up the instructions, leading to further errors in medication adherence. This can have serious consequences for the patient's health, as incorrect dosages or missed doses can lead to ineffective treatment or negative side effects.

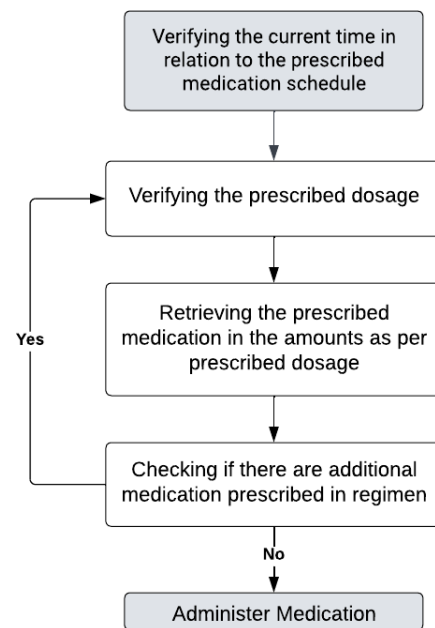


Figure 3: Flowchart of managing multiple medication by hand.

### 3.2. Prevailing products

To address these challenges, a number of products have been developed and are currently available on the market where each of these products has its own limitations and challenges. Some major examples include, Pointells Automatic Pill Dispenser, Hero Medication Manager, e-Pill Voice Pro, MedaCube, and RxPense.

The Pointells Automatic Pill Dispenser requires users to manually sort and store each dose in a separate compartment, which can be time-consuming and inconvenient [19]. The Hero Medication Manager offers a user-friendly interface but is only available in certain regions and requires a subscription fee in addition to its high cost [20]. The e-Pill Voice Pro has many features, but also shares the limitations of the Pointells Automatic Pill Dispenser and includes an alarm feature that may disrupt users' daily routines [21]. The MedaCube is a highly advanced medication dispenser but is expensive and not widely available [22]. The RxPense is a more compact alternative to the MedaCube, but also has a subscription-based payment model and limited global availability [23].

### 3.3. Comparable prototypes

The automated pill dispensing device by Ramkumar et al. [24] proposes a solution to the problem of medication non-adherence in patients using an automated pill dispenser that is connected to the Internet of Things (IoT). The proposed solution leverages the IoT to provide patients with medication reminders, dispense the right pills at the right time, and enable healthcare professionals to monitor their patients' medication adherence in real-time. However, the device by Ramkumar et al. lack the ability to provide connectivity when the Wi-Fi connectivity is absent.

In [25], the researchers proposes an autonomous bot to administer medication to elderly patients. The bot uses line-following mechanism to track the patient's location and dispenses the required medicines based on user-programmed instructions. The system store information in the cloud for future reference. However, the device does not present a mechanism for the sorting and dispensing of pills in accordance with a predetermined schedule. Rather, its function lies in the delivery of medication to the patient and dispensing the pre-sorted pills as required.

The smart automated pill dispenser by Kumar [26] proposes a Wi-Fi enabled device with a smart app and a pill dispensing mechanism to address medication non-adherence. The device uses four separate cartridges for different sized pills. Which could limit the usability of the device.

To overcome the limitations of the implementations, it is suggested that a Global System for Mobile Communications (GSM) module be integrated into the system, a mechanism for automated sorting of medication without manual pre-sorting should be proposed, and the design of cartridges must also be optimized to accommodate pills of varying sizes and function seamlessly with the proposed sorting mechanism.

## 4. Proposed Device

The proposed device is designed to dispense medication at the prescribed times and remind the patient or guardian to administer the medication. This device conveniently stores the medications

and manages the dosage, eliminating the need for the patient or guardian to worry about finding and correctly dosing the medications. With this device, users simply need to take the medication at the prescribed times, with the device managing all other aspects of the medication regimen. This feature allows for increased convenience and ease of use for the patient or guardian.

The proposed device is designed with several key components, including an ESP32 microcontroller, infrared sensors, a GSM module, a real-time clock module, and motors and motor drivers. These components work together to ensure that the device can dispense medication accurately at the prescribed times and provide reminders to patients or guardians as needed. Advanced technologies such as the ESP32 microcontroller and GSM module allow for integration with the IoT, enabling control of the device through a web interface. The inclusion of infrared sensors and a real-time clock module allow for precise timing and accuracy in the dispensing process. The motors and motor drivers ensure that the device is able to dispense the required medication doses efficiently. Overall, these components are essential for the effective functioning and performance of the proposed device.

### 4.1. Operation

The proposed device is designed to ensure that patients are able to take their medication on schedule and avoid missing doses (Figure 4). To accomplish this, the device uses a real-time clock module to track the current time and a GSM module to send reminders to the patient if they are behind schedule for their medication. Additionally, the device is equipped with infrared sensors and motors to dispense the appropriate dosage of medication based on the prescribed schedule. If the patient has not taken their previous dose, the device will not dispense the next one, but will instead send a reminder and reset its status so that the next dosage can be issued at the appropriate time.

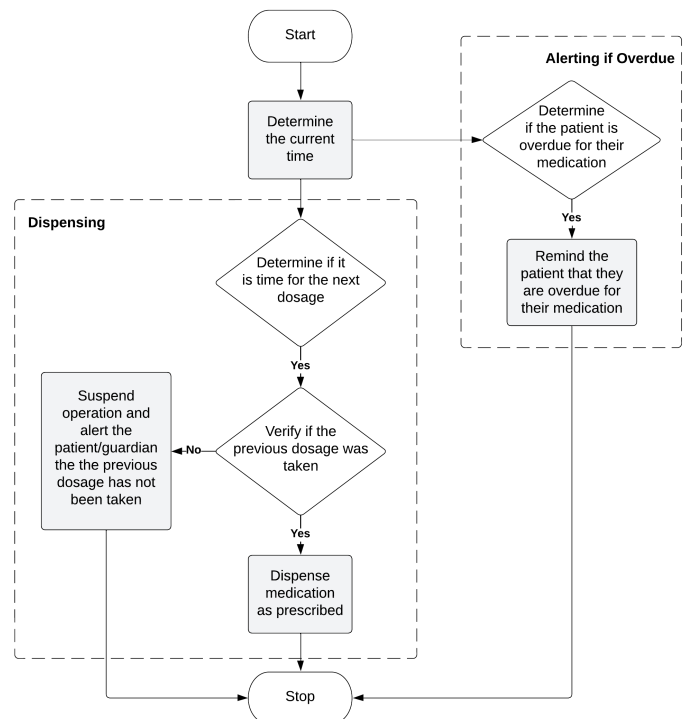


Figure 4: Operation diagram of the proposed device



#### 4.2. Physical design

The proposed device includes several compartments designed to dispense a specific medication. The design of these compartments includes a handle, an arm, a funnel, an infrared sensor space, a pill exit, and a disk (Figure 5).

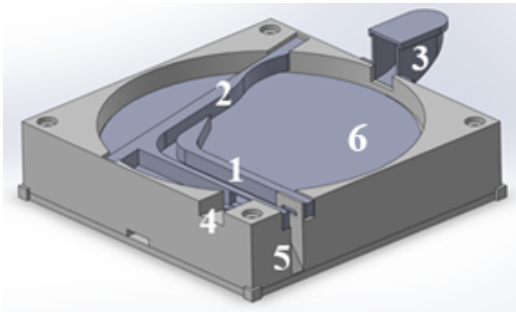


Figure 5: 3D model of a compartment. 1. Handle 2. Arm 3. Funnel 4. IR sensor space 5. Pill exit 6. Disk

The proposed device is designed to dispense medication using a rotating disk and an arm mechanism. Medication is inserted into the device through a funnel, and then the disk rotates to separate a single pill. The pill is then passed through a gap between the arm and handle, and an infrared sensor detects its movement and signals the microcontroller to stop the rotation and dispense the pill. The motor used to rotate the disk is located within the compartment and attached to the disk. An additional infrared sensor is included to detect when the cup, which holds the dispensed medication, has been moved by the user, indicating that the medication has been taken.

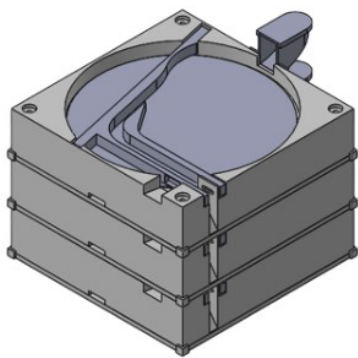


Figure 6: Compartments stacked

The proposed device includes individual compartments for each type of medication, with each compartment being approximately 15 cm by 15 cm in size. This allows for proper storage and organization of medications, ensuring that patients or caregivers can easily access the correct medication at the appropriate time. Multiple compartments can be stacked on top of each other for efficient storage and organization of multiple medications (Figure 6). The device also includes motors and infrared sensors to facilitate the dispensing process and track medication intake.

#### 4.3. Working mechanism

The proposed device utilizes a rotating disc mechanism to dispense individual pills. The rotational speed of the disc is

calculated to ensure that only a single pill is dispensed at a time. This is achieved by considering the relationship between angular velocity and linear velocity. The linear velocity of a rotating disc increases as it moves further away from the center, and by carefully controlling the angular velocity, the device is able to accurately dispense single pills. This mechanism allows for the device to effectively dispense a wide range of pill sizes and shapes.

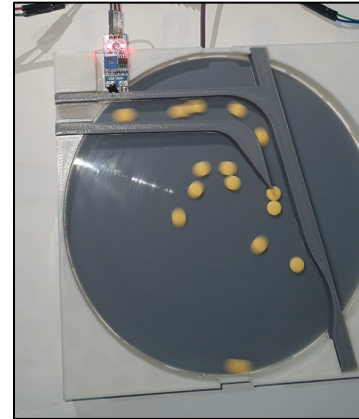


Figure 7: Extracting a single pill

Figure 7 illustrates a momentary snapshot of the rotation of the disk in an open compartment unit. Pills closer to the center of the disc experience a lower linear velocity, while those further from the center experience a higher linear velocity. This can be observed in the differential blur of pills in the center versus those at the edges of the disc in Figure 7. This method allows for efficient and accurate dispensing of medication.

The pill separation is achieved by first rotating the disk in a backward direction (clockwise in Figure 7) at varying speeds to disperse the pills across the surface of the disk. The disk is also rapidly oscillated back and forth to further spread out the pills. After this initial shaking process, the disk is then rotated in the forward direction through the path between the arm and handle of the device. As the pills are guided through this path, the linear velocity helps to create a gap between each pill. This method allows for the efficient separation of individual pills for accurate and reliable dispensing.

To optimize the dispensing process, the proposed device includes a dynamic adjustment feature for the rotation time and speed of the disk. This allows for the proper isolation of individual pills and ensures that they are dispensed accurately. The user can also manually reset and calibrate the rotation time using the provided controls. If a pill is not dispensed after two attempts, the rotation time and speed is adjusted, and the process is repeated. The updated rotation time and speed are then recorded in the microcontroller for future use.

It is important to consider the potential for damaging medication when spinning pills at high speeds. While high speeds may be effective in isolating individual pills, they may also cause pills to break or crumble. This can result in reduced efficacy of the medication or even potential harm to the patient if they ingest broken or damaged pills. It is essential to carefully consider the appropriate speed range for spinning pills in order to minimize the risk of damage while still effectively isolating individual doses. Additionally, the material and construction of the spinning

mechanism should be carefully considered to ensure that it is strong enough to handle the forces involved without causing damage to the pills.

#### 4.4. IoT implementation

A cellular IoT module was implemented to provide reminders to users via short message service (SMS). This allows users to be reminded of their medication schedule even when they are not at home, simply by using their mobile device. For example, if a user's medication time is set for 8 pm, they will receive an SMS at 8.30 pm reminding them that they are half an hour past their medication time and encouraging them to take their medication as soon as possible. The delay in sending reminders for medication is intended to provide patients with a grace period to self-administer medication, if they recall it, without being prompted unnecessarily. This approach is aimed at minimizing the potential inconvenience. This implementation in overall adds convenience for users without the need for additional equipment.

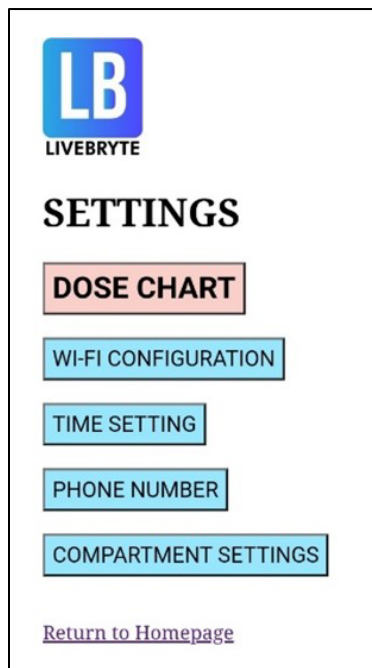


Figure 8: Settings page of the web-interface

The inclusion of the ESP32 microcontroller offers numerous benefits, including its lightweight design and 4 MB of SPI flash memory for permanent data storage [27]. The ESP32 microcontroller and Wi-Fi IoT capabilities to enable access to device configurations through an HTML and CSS based web interface in Figure 8. This interface can be accessed through a local Wi-Fi network or through the microcontroller's own soft access point.

The web interface for the proposed device allows users to easily enter and modify their medication prescription information, including dosage and timing. This interface also allows users to customize device settings such as the device time, phone number for reminder messages, and Wi-Fi network to which the device is connected. By leveraging the IoT through the use of the ESP32 microcontroller, this interface can be accessed remotely, providing users with greater convenience and flexibility. It is important to

note that utilizing an internet-connected network is recommended to enhance the user experience. Additionally, this web interface can be easily updated by linking additional information through URLs, allowing developers to easily make changes to the device without the need for hardcoding data directly into the device.

The proposed device includes a microprocessor with the capability to record and notify the user of any errors that may occur during device operation. This feature is implemented through the ESP32 microcontroller and its ability to store data in flash memory, even during a power interruption. This ensures that the device remains functional and able to provide necessary medication to the user [28].

#### 4.5. User operation

To initiate the operation of the device, To use the device for the first time, the user must access the device's own soft access point (AP) address using the provided instructions. Then, they should enter the Service Set Identifier (SSID) and password for their current local network into the device. This will allow the device to connect to the local network and be accessible for further configuration and use.

Afterwards, the patient or guardian must first the user must load the appropriate medications into compartments using the provided funnel and input relevant information, such as the type of medication pills being stored in each container and their prescribed dosages using the "Dose Chart" page in the web-interface settings page shown in Figure 8. The "calibrate" feature should then be run using the "Compartment Settings" page, during which the device will dispense a single pill from each container to determine the optimal settings, including time and rotation speed, for the specific type of pill. The user may also need to adjust the timing and provide a phone number for alert notifications.

In the event of an error, whether due to missed medication or a technical malfunction of the device, the device ceases operation and alerts the user via SMS. The guardian or nurse must then confirm that the issue has been resolved and instruct the device to resume operation. This helps to ensure that any errors or disruptions in the medication regimen are promptly addressed and corrected.

Each dose must be double-checked before administration due to the sensitivity of the device's operation.

## 5. Final Device Design

The completed product, named "LIVEBRYTE," was made primarily of wood, with 3D printed parts made of polylactic acid (PLA).

### 5.1. Accuracy

There are several limitations to the current design of the proposed device. The device is currently limited to pills. Another limitation is the reliance on infrared sensors to detect pills as they are dispensed. This can be problematic as some pills may not be properly detected, as pills are passing the sensor at high velocities leading to inaccurate dispensing. In addition, the device is not able to handle pills that are particularly large or oddly shaped, as they may not pass through the dispensing path correctly. The device is also limited in its ability to handle many medications, as it can only

store a limited number of pills in each compartment. Finally, the device relies on the user to accurately input information about the medications and their prescribed dosages, which can lead to errors if the user is not careful or if there are changes to the prescription. Despite these limitations, the device has shown significant improvement in accuracy during the troubleshooting phase, increasing from 40% to its current level through algorithmic improvements.



Figure 9: The final product

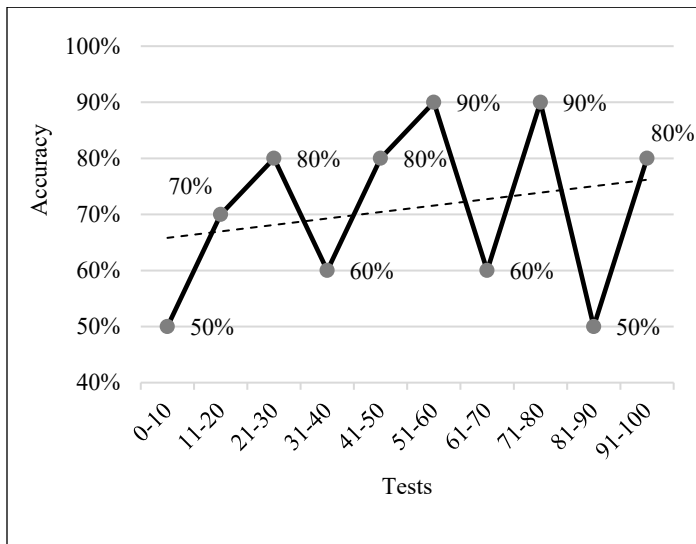


Figure 10: Accuracy for 100 tests

The accuracy of the LIVEBRYTE device was evaluated through a series of tests in which the device was instructed to dispense a single pill. First, the number of successful dispenses, defined as instances in which only a single pill was released, was recorded, and compared to the total number of dispense attempts. Next, unsuccessful dispenses, defined as instances in which no pills or more than one pill were released, were also recorded. The device's accuracy was then calculated as the percentage of successful dispenses out of the total number of dispense attempts.

This indicated the reliability and precision of the device in accurately fulfilling prescribed dosage regimens.

The results of these tests, conducted 100 times with an average accuracy of 71%, are depicted in Figure 10. The trendline illustrates that the accuracy of the device improved dynamically with dynamic adjustments.

The use of an infrared sensor as a proximity sensor ensures that the accuracy of the device is not affected by the color of the medication. However, it has been observed that pills with a glossy outer coating tend to be less responsive to the infrared sensor. Despite this, it can be ensured that there will not be any confusion between different medications, as each medication is stored in a separate compartment.

### 5.2. User feedback

The final product was provided to 10 long-term patients with varying levels of proficiency in using technology for a period of 10 weeks, or approximately 2.5 months. The patients were instructed to carefully review their medication doses and prescriptions before taking their medications, and the device was used to dispense and track their medication adherence. A survey was conducted at the end of the trial to gather feedback on the patients' experiences with the device.

The results of the survey indicated that the majority of the participants were satisfied with the LIVEBRYTE device and believed that it aided in their medication adherence. On a scale of 1 to 5, the majority of participants rated the product as 4 out of 5. They reported that the device improved their medical adherence and that they experienced few errors during the week-long trial period. On average, participants experienced errors 6.09 times per week. This is consistent with the expectations for the device, given that the device was expected to produce 7.1 errors in average.

## 6. Conclusion

The proposed device is a smart pill dispenser designed to help patients and their caregivers manage and adhere to their prescribed medication regimens. The device stores multiple medications and dispenses them at the prescribed times, providing a convenient and reliable solution for those who struggle with medication management. In addition to dispensing medication, the device also sends reminders to the patient or caregiver to take their medication as prescribed. This can be especially helpful for those who take multiple medications and may have difficulty remembering which medications to take and when. The device is also equipped with a web interface that allows users to easily access and control the device, making it suitable for use in both home and long-term care settings. Overall, the automation of medication taking through this device has the potential to improve patient adherence and overall health outcomes, which could have a significant impact on public health and quality of life for patients struggling with medication adherence.

To further assess the usability and effectiveness of the device, it was given to 10 long-term patients for a period of 10 weeks (about 2 and a half months). These participants were instructed to always double-check their medication doses and their prescription before taking their medications. The results of a survey conducted after this trial period showed that most participants were satisfied

with the product, with most rating it 4 out of 5. They reported that the device had helped with their medication adherence and that they had experienced few errors, with an average expected error rate of 6 per participant.

Despite the efforts made to improve accuracy, it is important to note that the proposed device is not intended to replace the role of a nurse or guardian in ensuring that patients take their medication as prescribed. The device is simply intended to assist in the process of medication adherence and should be used in conjunction with supervision to ensure the safe and effective administration of medication. It is also important to note that the device is not foolproof and may still be subject to errors or malfunctions. Therefore, it is essential that patients and guardians continue to carefully monitor their medication use and seek medical advice if any concerns arise.

It is important to consider the ethical implications of using this device. One potential concern is the potential for patients to rely too heavily on the device and neglect their own responsibility to manage their medication. It is essential that patients are educated on the importance of self-management and encouraged to take an active role in their own healthcare. Additionally, it is important to ensure that the device is used in accordance with the patient's prescription and that any changes to the dosage or medication schedule are made in consultation with a healthcare provider.

Overall, the proposed device has the potential to significantly improve medication adherence and overall health outcomes for long-term patients. As outlined above, the device has successfully addressed the limitations of the compared devices and has incorporated additional features, thus enhancing its overall functionality.

There are several potential future improvements that could be made to the device to make it even more effective at improving medication adherence and overall patient health outcomes. One potential improvement could be to integrate more advanced sensors, such as weight sensors, to track medication usage and detect any potential issues with pill dispensing more accurately. Moreover, improvements for the physical compartment designs can be done to elevate the device efficiency and to accommodate a wider range of medications. The device could be developed to accommodate medication for multiple patients, providing the device much more capable in long-term care facility administrators. Additionally, incorporating machine learning algorithms into the device's software could allow it to better adapt to individual patient needs and preferences, as well as optimize the timing and frequency of medication reminders based on user data. Other potential improvements could include integrating more advanced communication capabilities, such as voice recognition and virtual assistant functionality, to make the device more user-friendly and accessible for patients with limited technology skills. Finally, incorporating more robust data storage and analysis capabilities could allow the device to track patient medication usage and provide insights to healthcare providers on how to optimize treatment plans more effectively. Furthermore, implementing automatic refill reminders could help to ensure that patients never run out of their medication, while the ability to track and record medication intake could provide valuable information for healthcare professionals to use in managing their patients'

treatment. Additionally, integrating the device with healthcare systems could facilitate better communication and collaboration between patients and healthcare professionals. To ensure that patients are able to effectively use and benefit from the device, developing user-friendly interfaces and providing instructional materials could be helpful. Finally, it is important to conduct further testing and evaluation of the device to understand its potential impact and ensure that it is being used safely and appropriately.

## References

- [1] C. Bandara, A.D. Sandanayake, Y. Kodithuwakku, V. Logeeshan, "Automated Medicinal-Pill Dispenser with Cellular and Wi-Fi IoT Integration," in 2022 IEEE World AI IoT Congress (AIIoT), IEEE: 692–698, 2022, doi:10.1109/AIIoT54504.2022.9817226.
- [2] M.S. Alqahtani, M. Kazi, M.A. Alsenaidy, M.Z. Ahmad, "Advances in Oral Drug Delivery," *Frontiers in Pharmacology*, **12**, 62, 2021, doi:10.3389/FPHAR.2021.618411/BIBTEX.
- [3] Medicines Use and Spending in the U.S., 2017.
- [4] Global Medicines Use in 2020, Mar. 2022.
- [5] M.S. Wolf, L.M. Curtis, K. Waite, S.C. Bailey, L.A. Hedlund, T.C. Davis, W.H. Shrank, R.M. Parker, A.J.J. Wood, "Helping Patients Simplify and Safely Use Complex Prescription Regimens," *Archives of Internal Medicine*, **171**(4), 300–305, 2011, doi:10.1001/ARCHINTERNMED.2011.39.
- [6] D. Garfinkel, D. Mangin, "Feasibility Study of a Systematic Approach for Discontinuation of Multiple Medications in Older Adults," *Archives of Internal Medicine*, **170**(18), 2010, doi:10.1001/archinternmed.2010.355.
- [7] M.T. Brown, J.K. Bussell, "Medication Adherence: WHO Cares?," *Mayo Clinic Proceedings*, **86**(4), 304–314, 2011, doi:10.4065/mcp.2010.0575.
- [8] S. de Geest, E. Sabaté, "Adherence to long-term therapies: evidence for action," *European Journal of Cardiovascular Nursing: Journal of the Working Group on Cardiovascular Nursing of the European Society of Cardiology*, **2**(4), 323, 2003, doi:10.1016/S1474-5151(03)00091-4.
- [9] D. Ile C. Eindhoven, A.D. Hilt, T.C. Zwaan, M.J. Schalij, C.J.W. Borleffs, "Age and gender differences in medical adherence after myocardial infarction: Women do not receive optimal treatment The Netherlands claims database," *European Journal of Preventive Cardiology*, **25**(2), 181–189, 2017, doi:10.1177/2047487317744363.
- [10] S. Pirasath, T. Kumanan, M. Guruparan, "A Study on Knowledge, Awareness, and Medication Adherence in Patients with Hypertension from a Tertiary Care Centre from Northern Sri Lanka," *International Journal of Hypertension*, **2017**, 2017, doi:10.1155/2017/9656450.
- [11] A.F. Yap, T. Thirumoorthy, Y.H. Kwan, "Medication adherence in the elderly," *Journal of Clinical Gerontology and Geriatrics*, **7**(2), 64–67, 2016, doi:10.1016/J.JCGG.2015.05.001.
- [12] N. Kheir, M.S. el Hajj, K. Wilbur, R.M.L. Kaissi, A. Yousif, "An exploratory study on medications in Qatar homes," *Drug, Healthcare and Patient Safety*, **3**(1), 99, 2011, doi:10.2147/DHPS.S25372.
- [13] M.S. Rsfā, J.A.C. Perera, P.P.R. Perera, The usage of over the counter (OTC) medicines and traditional medicines (TMs) for common ailments in selected urban and rural areas in Sri Lanka, 2015.
- [14] M.S. Wolf, J. King, K. Jacobson, L. di Francesco, S.C. Bailey, R. Mullen, D. McCarthy, M. Serper, T.C. Davis, R.M. Parker, "Risk of Unintentional Overdose with Non-Prescription Acetaminophen Products," *Journal of General Internal Medicine*, **27**(12), 1587, 2012, doi:10.1007/S11606-012-2096-3.
- [15] Adult Acetaminophen Dosage Chart | GET RELIEF RESPONSIBLY®, Apr. 2022.
- [16] Ibuprofen Dosing Table for Fever and Pain - HealthyChildren.org, Apr. 2022.
- [17] B. Jimmy, J. Jose, "Patient Medication Adherence: Measures in Daily Practice," *Oman Medical Journal*, **26**(3), 155–159, 2011, doi:10.5001/omj.2011.38.
- [18] Centers for Disease Control and Prevention, Antibiotic resistance threats in the United States, 2019, Atlanta, Georgia, 2019, doi:10.15620/cdc:82532.
- [19] Amazon.com: Pointells Automatic Pill Dispenser – 28-Day Portable Medication Planner and Organizer – Dispense Vitamins and Tablets Up to 6 Times Per Day – Includes Flashing Light, Alarm and Safety Lock : Health & Household, Apr. 2022.
- [20] Hero Health - A dose of calm for the whole family, Apr. 2022.
- [21] Voice Pro, Apr. 2022.
- [22] PharmAdva MedaCube™, Apr. 2022.

- [23] Medipense » RxPense the best pill dispenser for seniors, chronic care, +, Apr. 2022.
- [24] J. Ramkumar, C. Karthikeyan, E. Vamsidhar, K.N. Dattatraya, Automated Pill Dispenser Application Based on IoT for Patient Medication, 231–253, 2020, doi:10.1007/978-3-030-42934-8\_13.
- [25] K.R. Karthikeyan, E. Dharan Babu, S. Ranjith, S. Arunkumar, “Smart Pill Dispenser for Aged Patients,” in 2021 International Conference on Advancements in Electrical, Electronics, Communication, Computing and Automation (ICAECA), IEEE: 1–5, 2021, doi:10.1109/ICAECA52838.2021.9675784.
- [26] R.H. Kumar, Design and Prototype of Smart Automated Pill Dispenser, VISVESVARAYA TECHNOLOGICAL UNIVERSITY, 2021.
- [27] ESP32WROOM32, 2022.
- [28] N. Koumaris, Using ESP32’s Flash Memory for data storage - Electronics-Lab.com, Apr. 2022.

## Smart Healthcare Kit for Domestic Purposes

Yehan Kodithuwakku<sup>1</sup>, Chanuka Bandara<sup>1</sup>, Ashan Sandanayake<sup>1</sup>, R.A.R Wijesinghe<sup>2</sup>, Velmanickam Logeeshan<sup>\*3</sup>

<sup>1</sup>Department of Electrical, Electronic and Telecommunication Engineering, Faculty of Engineering, General Sir John Kotelawala Defence University, Sri Lanka

<sup>2</sup>Department of Mechanical Engineering, Faculty of Engineering, General Sir John Kotelawala Defence University, Sri Lanka

<sup>3</sup>Department of Electrical Engineering, Faculty of Engineering, University of Moratuwa, Sri Lanka

### ARTICLE INFO

Article history:

Received: 01 January, 2023

Accepted: 20 March, 2023

Online: 12 June, 2023

Keywords:

COVID-19

Beats per Minute

SpO<sub>2</sub>

Electrocardiogram

Telemedicine

Telehealth

Vital signs

Healthcare Kit

### ABSTRACT

The COVID-19 pandemic has caused a substantial death toll throughout the world. The pandemic has created a threat to public health, the economy, food systems, and the workplace. An increased reprioritization of health expenditure towards COVID-19 vaccines will impact on allocations to other medical facilities. In developing countries, hospitals shortage the infrastructure to facilitate patients. Therefore, traditional checkups and clinics are not practical. According to research done in this article, 95 percent would prefer telemedicine and telehealth rather than conventional inspections. Even though smart healthcare technology has been implemented, it does not show adequate effectiveness when commercialized. Therefore, in this paper, a microcontroller-based, low-cost, automated, real-time system has been proposed to give a convenient solution for measuring the vital signs of the body. In this project, Multiple sensors with a microcontroller were intended to measure heartbeats per minute, Oxygen Saturation, body temperature and electrocardiogram of a patient at home without going to a hospital. The developed system indicated very less percentage error in temperature measurement and was able to maintain high accuracy on Beats per Minute, Oxygen Saturation and Electrocardiogram. This approach provides a feasible solution for both patients and medical professionals.

## 1. Introduction

The goal of this article is to propose a revised and expanded version of the IoT-based Healthcare Kit for Domestic Use, which was first presented at the World AI(Artificial Intelligence) IoT(Internet of Things) Congress in 2022 [1]. Additional research and testing have been carried out in order to improve the device and provide more detailed explanations of its performance and efficiency. This document summarizes the most recent findings and conclusions from the smart healthcare kit's ongoing research, development, and testing.

Since the start of the Coronavirus Disease 2019 (COVID-19) outbreak in early Wuhan in December 2019, it has spread to every country, including those with a low income [2]. It is possible that all nations will be vulnerable to this catastrophe as the world

becomes a smaller, more integrated "global village." As a result, the entire world is at risk if a pandemic cannot be stopped in one nation. Not only has a pandemic had a harmful impact on the health sector, but it has also caused difficult economic, social, and political crises that, if they are not resolved quickly, will leave lasting scars [3].

Recent analysis shows that patients with COVID-19 frequently have an increase in severity or death due to related illnesses like hypertension, diabetes, obesity, cardiac diseases etc[2]. The prevalence of chronic diseases is higher in low and middle-income countries due to several risk factors, including dietary habits, physical inactivity, and alcohol consumption[4]. According to a World Health Organization study, 4.9 million people pass away from lung cancer as a result of snuff usage, 2.6 million people die from being overweight, 4.4 million people are dying from excessive cholesterol, and 7.1 million deaths occur from high blood pressure [4].

\*Corresponding Author: Dr. Velmanickam Logeeshan, Department of Electrical Engineering, University of Moratuwa, Sri Lanka. Email: logeeshanv@uom.lk

Traditional examinations in specialized medical facilities were the standard for many years when it came to keeping an eye on heart rhythm, blood pressure, and glucose levels. Because of the rising global population and the increased demand for healthcare resources, there is an increasing burden on medical services. As a result, Healthcare availability in developing countries is already in crisis, and they are seeking to establish a new strategy to distribute medical resources.

In the management of COVID-19 over the world, the terms "Telehealth" and "Telemedicine" are frequently used in public and scholarly research to refer to techniques for providing healthcare remotely [5]. The provision of healthcare remotely via telecommunications technologies is known as telehealth. Telemedicine is the technique of transferring medical information from one location to another using electronic connections in order to enhance a patient's clinical health state [5].

Telehealth services can help in managing COVID-19 by screening high-risk populations and identifying probable cases, assisting with hospitalized patient care and remotely monitoring people on self-quarantine. In addition, Systems for telehealth can be used to avoid congestion in hospitals and other healthcare facilities. Telehealth can also be utilized to reduce the number of physical clinic visits for patients with chronic illnesses like diabetes or cardiac conditions who are at high risk for COVID-19-related problems [5].

By virtually tying patients and healthcare professionals together around-the-clock, seven days a week, the internet of things provides a new approach. The most crucial factors in a disease diagnosis are vital signs [4]. That is common for Chronic illnesses and Covid-19. Therefore, an inexpensive Healthcare kit on hand would save both time and money, especially who are vulnerable to above-mentioned diseases. Additionally, contactless monitoring and telemedicine capabilities ensure the safety of the both medical staff and patients against Covid-19. Therefore, home monitoring of those indicators will offer a better method for resolving those problems. The smart healthcare kit described in this paper allows both the patient and the doctor to view real-time data at any moment.

**2. Literature Review**

Vital signs are clinical assessments of a person's basic body functions that indicate the healthiness of their vital physiological systems. Biological aspects related to this article are mentioned below.

**2.1. Vital Signs**

Body temperature, Pulse Rate, respiration rate and blood pressure are the vital signs of a human. Medical officials express that vital signs such as blood pressure, temperature, heart rate, oxygen saturation(SpO<sub>2</sub>), and respiration rate are key indicators of a patient's present health and must be routinely and precisely recorded [6]. Often, the first evidence of aberrant physiological body changes is seen in the vital signs [6].

**2.2 Beats per Minute (BPM)**

The number of heart contractions per minute, or heart rate, is a measure of how frequently the heart beats. A pulse is the tactile

arterial palpation of the cardiac cycle in medicine (heartbeat). A suitable area to feel the pulse is anywhere on the body where an artery may be squeezed near the skin, such as the neck, wrist, groin, behind the knee, close to the ankle joint, and on the foot [7].

**2.3 Oxygen Saturation**

The ratio of hemoglobin currently bound to oxygen still unbound is known as oxygen saturation. There are countless numbers of these tiny air sacs in the lungs. They are crucial in bringing carbon dioxide and oxygen molecules into and out of the bloodstream. The body's tissues receive oxygen when hemoglobin binds to it during circulation.

**2.4 Body Temperature**

The body uses its temperature as a measure to produce and release heat. The blood vessels on the skin enlarge when someone is overheated to transfer extra heat to the skin [8]. Conversely, a person's blood vessels narrow when they become too cold, reducing blood flow to the skin and increasing heat production. A person's average body temperature may be determined via the mouth, ear, underarm, and scrotum.

**2.5 Electrocardiogram (ECG)**

The electrical activity of the heart during a specific time period is recorded on a graph called an electrocardiogram (ECG) using an electrograph. An ECG is a diagnostic test that examines the cardiac conduction system and provides the doctor with information about the patient's potential illness processes as well as the health of the patient's heart.

The heart, a two-stage electrical pump, can have electrodes placed on its surface to assess its electrical activity. The ECG can track the rate and rhythm of the heartbeat as well as give an imprecise indication of blood flow to the cardiac muscle [7]. The PR and QT intervals are the two fundamental intervals of an ECG. The fundamental ECG segments are shown in Figure 1.

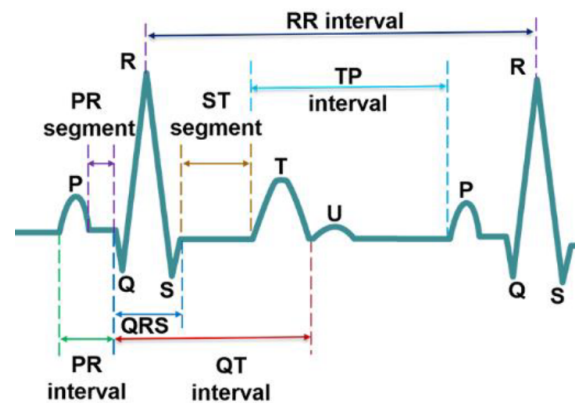


Figure 1: Standard ECG Pulse. Reprinted with permission from [9]

Currently, hospitals use appropriate devices to keep track of their patient's health. However, doctors must be present in such situations. Researchers came up with various IoT models for

healthcare and forecasted various diseases to address this issue. The following are some of the research works done by the authors.

2.6 Wireless Sensor Network-based Smart Healthcare

In the proposed system, a Body Area Network is created by attaching a variety of wireless sensors to the patient's body to measure important body metrics like temperature, blood pressure, and heart rate. The data is wirelessly gathered and shown on the Patient Bed Monitor (PBM). In addition, the room Server (RS) is connected to it for data archiving and analysis [10].

Three tiers make up the suggested system architecture. Tier-1 comprises wireless sensor nodes fastened to the patient's temperature and pulse rate to monitor essential body functions. Tier 2 is the intermediate receiving unit that receives the data that has been transmitted. Alert systems and data transmission over larger distances using the right internet connections are the focus of Tier 3 [10].

2.7 Raspberry-pi based smart healthcare

Sensors have been connected to the proposed system in appropriate ways. The unit integrates the data from the sensors with the board after receiving it from the sensors [11].

This device connects with the temperature, heart rate, ECG, acceleration, and pressure sensor. In addition, the user's and doctor's devices are connected to the internet, and the generated results are shown on a Liquid Crystal Display(LCD) monitor at regular intervals [11].

There are two ways to connect and operate the raspberry device: the first is directly attaching peripherals and the second is connecting the computer after installing the putty program with a IP address, subnet mask, and gateway to that system [11]. If any irregularities in the patient's health are detected, they will be promptly reported to the authorized or guardian via the Global system for mobile communication (GSM) via the network.

2.8 Arduino-based smart healthcare

The design considered detecting temperature, humidity, and blood pressure. Remote patient monitoring is possible for the aforementioned metrics by medical personnel. The goal of this project was to build a patient health monitoring system that could measure ECG, blood pressure, pulse rate, and temperature[4]. The "ThingView" application displays the ECG, temperature, and pulse rate characteristics visually, and the readings are conveyed to a phone through SMS(Short Message Service).

2.9 GSM-based smart healthcare

Sensors are used to measure vital signs, and Zigbee and GSM are also used to send the parameters wirelessly. An SMS is sent to the doctor in an emergency. In an emergency, a SMS is delivered to the doctor. The patient's family and the medical community are the key users of the GSM-based health monitoring system [12]. On the "Thingspeak" website, the results are

displayed. The output is produced using the sensor data. An LCD shows the computed heartbeat rate.

2.10 Shortcomings of the available products

The majority of the aforementioned versions do not monitor BPM, SpO2, body temperature, and ECG at the same time. Currently, available items require a significant amount of power to operate. The various models' precision was insufficient for accurate measurements [13]. Despite the plans being implemented, they were unable to distribute the final products because of the absence of internal resources and a late market launch. These architectural designs may have some privacy issues. People might not want to be completely watched over. They can be concerned that crucial information, including their whereabouts or health status, could be disclosed to other parties with the proper authorization [14].

This project takes an innovative approach to health monitoring by creating a small and affordable system that can measure ECG, blood oxygen, BPM, and body temperature. While similar tools are available, they are frequently pricey and lack the versatility required for daily use. Existing products for measuring ECG, blood oxygen, BPM, and body temperature have limitations that make them unsuitable for usage in the home. For instance, hospital equipment is large and requires qualified personnel to operate. Similarly, most home-based monitoring systems are inaccurate and have a limited feature set. The kit produced in this study, on the other hand, solves these disadvantages by adding modern sensors and microcontrollers which have better accuracy on the body parameters. The kit is intended for home usage, which is both affordable and portable, making it ideal for remote patient monitoring.

3. Product Survey

Several data-gathering approaches were used to get information from the general public and doctors on the smart healthcare kit for home use.

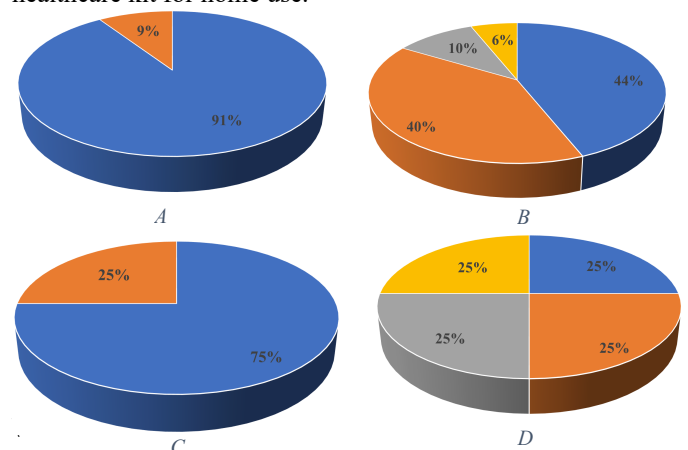


Figure 2: A,B for general people C,D for doctors



3.1 Study for the general public

The authors conducted the research using a Google form. The study enlisted the participation of 120 persons. The experiment lasted for three weeks. Questions that had been asked for the survey are attached below.

- A. Do you prefer to test your vital signs at home rather than visiting a hospital, and consult a doctor online when you are sick?
- B. What are your thoughts on the 'smart-Medicare kit for home usage'?
- C. Are you willing to monitor patients' vital signs online, especially in the midst of a pandemic?
- D. Are you likely to be able to diagnose an illness by taking a patient's temperature, pulse, SpO2, and ECG?

Figure 2 chart A illustrates that when suffering from a disease, 91% of individuals would prefer to evaluate their vital signs at home than go to a hospital and visit a doctor online. However, 9% would consider going to a hospital physically.

Figure 2 B displays the general public's perception of the Smart Medicare kit for household use. Almost 45 percent of individuals thought it was a great idea. Approximately 40% voted as 'Good'. Nevertheless, around 6% think that the idea of a healthcare kit is poor.

3.2 Survey for doctors

If the patient is in critical condition, the system sends an emergency message to a healthcare professional. To calculate vital sign threshold values, a Google form is given to 50 family doctors. Numerous interviews were also done in order to acquire critical information, such as selecting the optimal places of the body to achieve the most exact results. Additionally, the user handbook includes all of the best locations for sensor placement. According to Figure 2, C, almost 75% of doctors are ready to monitor vital signs remotely.

Figure 2, D shows that about a quarter of doctors would be able to detect a basic illness by evaluating the kit's measurement. Half of those polled believe they can diagnose a sickness to some amount by reading values.

3.3 Survey on Hospitals

Telehealth has been available in the country for a decade, but adoption among the general public has been modest [5]. The Information and Communication Technology Agency of Sri Lanka inaugurated the first IoT project in Sri Lanka in 2015, with 25 state hospitals participating. Following it, various numerous were carried out over the nation [15]. The Ministry of Health has also created mobile applications to help increase Telehealth services in Sri Lanka [5]

IoT Usage in Sri Lankan Hospitals

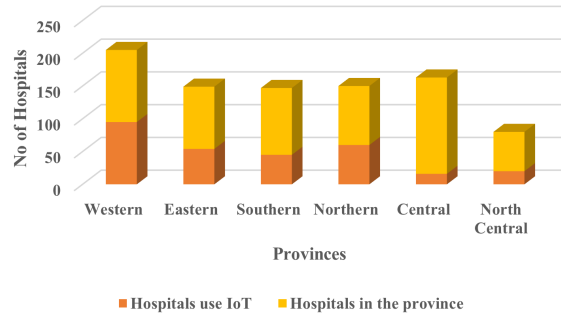


Figure 3: IoT Usage in Sri Lankan Hospitals

An analysis was conducted to determine IoT usage in Sri Lankan hospitals. Personal communications and statistical records were used to obtain data from the Ministry of Health and the Health Informatics Society of Sri Lanka. Figure 3 shows that IoT technology is utilized in practically every province. Medical data management systems, Mhealth apps, and personal health numbers are some examples of IoT applications used in Sri Lankan hospitals [15]. As a result, hospitals will find it easier to integrate IoT.

According to studies, hospitals may leverage Internet of Things technology to improve the efficiency of healthcare services. IoT technology is transforming the healthcare industry; by incorporating IoT, hospitals may enhance professional efficiency while also offering higher-quality medical treatment. Remote patient monitoring technologies allow medical personnel to minimize fatigue while saving patients the trouble of traveling. This is a huge advantage, particularly for persons with restricted mobility.

4. Flowchart

First and foremost, the Wi-Fi name and Passcode should be supplied in the code. The NodeMCU will attempt to link up to Wi-Fi after connecting the micro-USB to the PC. The Message Queuing Telemetry Transport protocol will be attempted if the device is connected.

The system will then check the MAX30102 sensor's availability. If the sensor is present, the kit begins reading data from the MAX-30102, AD-8232, and Temperature sensors. It will then sort out and upload the records to the Serial Monitor and the "Ubidots" cloud platform.

Lastly, any deviations from previously defined threshold values will be detected by the microprocessor. If any of the abnormalities are found, the system will send a message to a doctor based on previously given data, as shown in figure 4.

5. Methodology

The project's purpose is to create a smart Medicare system that can alert a doctor when a patient is in a severe condition. The project's aims are to assess a person's BPM, SpO2, and temperature from home if the person is unwell, to plot an ECG and have it evaluated by a doctor if the person is in a critical

condition, and to safeguard both patients and medical staff against Coronavirus.

The different circuits were tested and validated before being merged onto a single breadboard, as shown in Figure 5. The codes created for each circuit were concatenated to form a single code. This code was then transferred to the esp-8266 module and thoroughly tested for accuracy and faults. To achieve precise readings, special steps were taken, such as configuring the max30102 sensor to take an average of four data points and setting the AD8232 sensor to record 400 samples per second.

"Ubidots" was chosen as the cloud service for the application. To begin, each sensor's data was transmitted to the cloud service and reviewed for errors. Second, the sensors were combined, and data was transferred to the cloud. Real-time data was used to discover faults.

A poll of doctors was conducted to determine the temperature, pulse rate, and blood oxygen level thresholds. If the measured values deviate from the threshold value, an email is automatically sent to the relevant family doctor. This was done through the "Ubidots" website. This cloud platform housed medical records. The ECG was slightly off due to network latencies. Hence, the readings from an ECG were exported to Microsoft Excel utilizing the data streamer option. A caretaker then plotted the graph and sent it to a doctor.

The printed circuit board was designed using Autodesk-Eagle. Separate footprints were created for AD-8232 and MAX-3012. The schematic diagram was then created. Third, all of the components were carefully arranged to reduce the length of the copper cables. After the placement, the routing was completed. The trace width was calculated using 'EE web PCB trace width calculator online tool. Finally, the Gerber files were created and delivered to the manufacturer.

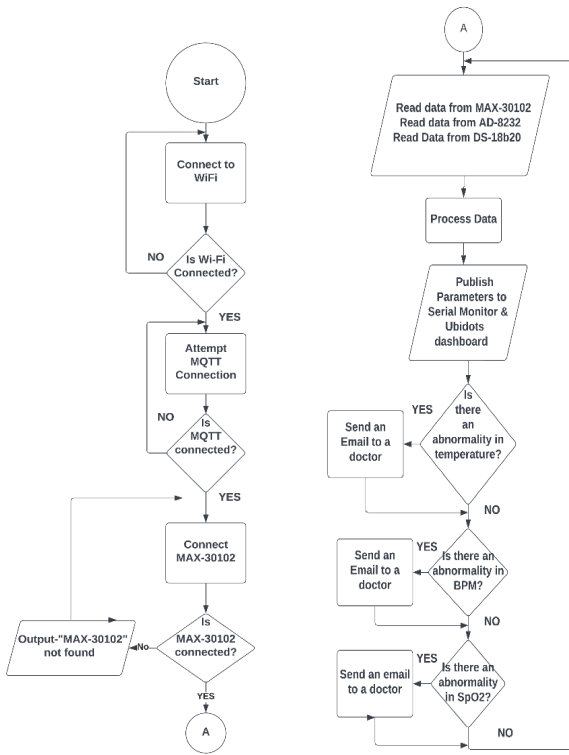


Figure 4: Flowchart of the proposed model

The esp-8266 offers various functionalities that are extremely useful when working with IoT. The Wi-Fi antenna on the module allows embedded devices to connect to networks and send data. Figure 5 depicts the integration of three sensors. Furthermore, the processor handles fundamental inputs from analog and digital sensors in order to perform significantly more sophisticated calculations. As the "Ubidots" cloud platform is accessed here, the esp-8266 can browse websites written in Hyper Text Markup Language(HTML) or any other development language.

The process began with the purchase of required circuits from shops. Individual codes were then written for each circuit. Following that, all circuitries were rigorously tested for flaws and defects to ensure precise and reliable performance.

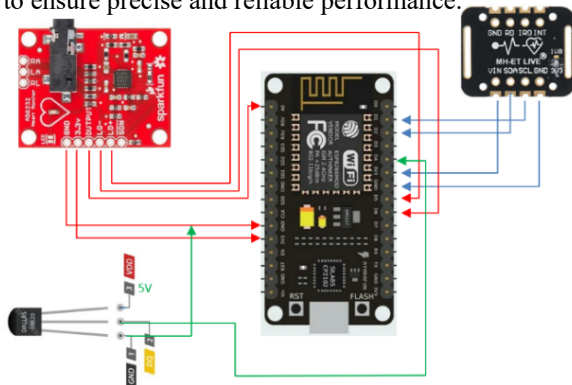


Figure 5: Wiring Diagram

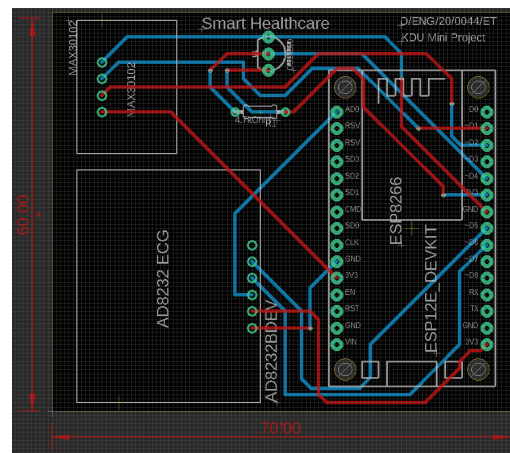


Figure 6: PCB (Printed Circuit Board) Design

The PCB was received and tested for quality after a three-week wait. On the PCB, female header pins were attached, and all sensors were connected to these pins. The sensors' operation was checked and verified when they were put into the board. A second Vero board was required to fit the Max-30102 sensor. To provide reliable readings, the sensor was positioned on top of the plastic stage and isolated from the other sensors to reduce interference. Since the photoplethysmography (PPG) technique is used in

MAX-30102, the sensor was positioned in a dark area to reduce noise and improve measurement accuracy. The configuration was double-checked to confirm that all sensors were working properly.



Figure 7: End Product

Finally, the 3D model was created with AutoCAD. The 3D model was then fed into a laser cutter, which sliced the plastic into the desired shape. Finally, everything was fitted together to make the final product seen in figure 7.

## 6. Validation of Experimental Results

The complete results of the model implementation are shown below. The model's output was validated using a temperature and an oximeter. The experiment was carried out on a healthy middle-aged man.

### 6.1 Body Temperature

Below equation was used to calculate the percentage error.

$$\text{Percentage error} = \frac{|\text{actual value} - \text{experimetal value}|}{\text{experimetal value}} \times 100\%$$

Equation 1 percentage error

$$\text{Percentage error} = \frac{|35.7-35.005|}{35.005} \times 100\% = 1.9\%$$

The percentage of body temperature was calculated, as shown in the preceding equation. The experimental value was determined as the average of seven consecutive 30-second observations. The exact value was determined by averaging seven successive "aeg FT4904" thermometer readings taken within 30 seconds.

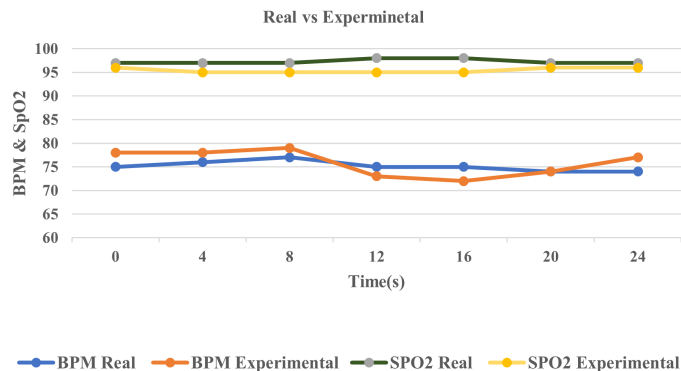


Figure 8: Experimental values from the kit vs real values from the oximeter

### 6.2 Bpm & SpO2

The real and experimental data were displayed for a time of 24 seconds, as illustrated in figure 8. Real measurements were taken with a "ROHS ABH23" fingertip pulse oximeter. The X-axis depicts the time with four consecutive periods, while the Y-axis reflects BPM and oxygen saturation. There is a slight difference between the real and experimental numbers.

### 6.3 Electrocardiogram

Figure 9 depicts a tested graph taken from the system. When compared to a standard graph (figure 1), the key segments (PR,ST) and intervals (PR,QT) can be seen. Likewise, it is observed that the experimented data has high accuracy.

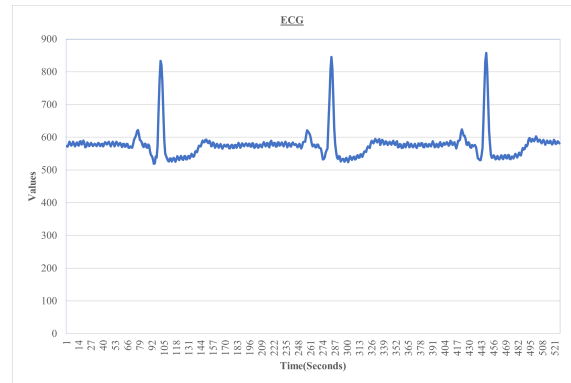


Figure 9: Obtained ECG from the kit

## 7. Discussion

### 7.1. Strengths

The model has a number of strengths. The device can assess body temperature, pulse rate, oxygen level, and ECG. (Four in one). As a result, there is no need to acquire a pricey oximeter, thermometer, and ECG machine individually (Cost-effectiveness). If the values differ, it automatically sends a notification to a doctor. Furthermore, it consumes less electricity and can be carried anywhere (Easily equipped). Finally, the model saves time by storing past data.

### 7.2 Accuracy Improvements

Accuracy enhancement approaches were used to decrease the constraints. For SpO2 and BPM, an average of four data points were collected, while 400 samples were collected every second for ECG and the application of filtering algorithms.

### 7.3 Issues experienced

The first issue encountered was with the MAX-30102. Pullup resistors were the source of the problem. To make it pull up, they were connected to 1.8v. The microcontrollers, on the other hand, ran on 3.3V. As a result, the three pull-up resistors were taken out with a soldering iron.

The second issue was cloud-based monitoring of the ECG. The real-time graph varied from its conventional graph due to network latency issues. As a response, the values were exported to Microsoft Excel, where the graph was created.

7.4 Price Assessment

The smart healthcare kit was expected to cost 8500.00 LKR in total. In contrast, purchasing the medical equipment individually would cost roughly 50,000 LKR. As a result, there is a large amount of difference that is financially favorable.

7.5 IoT Security Design

Because of the fast development and integration of the Internet of Things in various sectors of our everyday lives, Internet of vulnerabilities has emerged. Cyber-attacks risk the security and privacy of IoT device users. IoT devices don't have the adequate processing power, energy, storage capacity, and memory[16]. The best method for protecting communications between IoT devices is still being developed.

Security issues are a continual threat to IoT. Because of a large number of Internet-connected IoT devices, the Internet of Vulnerabilities has emerged. "Symantec" reports stated that IoT threats increased 600% in 2017[16]. The criteria for safeguarding IoT systems are authentication, authorization, communication, and device identification. The most secure authentication techniques concentrate on three characteristics: network assumptions, communication sessions, and users.

The "Ubidots" login information is unique to each individual. The password is only known to one person. This is how authentication is protected. The account token, according to the proposed technique, should be sent to someone's family doctor so that they may verify their live data. As a result, only those people have access to particular information.

Table 1: The comparison of vital signs to the existing systems

Vital signs and systems	Body Temp. (°C)	BMP (BPM)	SpO2 (%)	ECG
Proposed kit	35.005	76	96	Similar to fig1
Available system-1 [17]	28	86	76	Vertically shifted
Available system-2 [18]	29.81	108	63	unclear
Available system-3 [19]	30.45	69	-	Dissimilar to fig1

Table 2: Percentage errors of the existing systems

	Percentage error of Body Temp(%)	Percentage error of BPM(%)	Percentage error of SpO2(%)
Proposed Kit	5.6	5.2	1.0
system-1	32.21	16.27	27.6
system-2	24.11	33.33	53.9
system-3	21.5	4.3	-

To assess the efficacy of our IoT-based healthcare equipment, the accuracy of industry benchmarks was compared. As presented in table 1 BPM, SpO2, ECG, and body temperature results were compared to the previous similar studies.

According to the findings in table 2, the proposed healthcare kit had fewer percentage errors. The percentage error was calculated according to equation 1. Actual values were considered as 37°C, 72 and 97% for body temperature, BPM and SpO<sub>2</sub> respectively which are general truths. When compared to currently commercialized products, our healthcare kit outperformed the above systems in terms of body temperature and SpO<sub>2</sub> accuracy. The ECG of the available system 1 was shifted vertically. Therefore, the vertical measurements were affected. ECG of the available system 2 was unclear and the diagnosis procedure is quite hard. By mitigating the drawback of each existing product mentioned in 2.10, these findings indicate that our healthcare kit has the potential to deliver precise and accurate vital sign measurements for home users.

8. Future Directions and Concluding Remarks

Future enhancements include adding blood pressure equipment to the smart healthcare unit, developing a model utilizing Machine Learning Algorithms to assess ECG data, and sending an automated message to an ambulance service. Furthermore, security enhancements should be implemented to tighten privacy and reduce cyber-attacks.

Artificial Intelligence (AI) in healthcare combines computation with the viewpoints of doctors to build better healthcare technologies. Using NLP, knowledge representation, automated reasoning, and machine learning, AI attempts to make computers more practical and intelligent. Understanding patient health status by a pre-trained model from symptoms could be a future advancement.

Some of the product's primary features include keeping a patient's medical records, alerting a doctor in an urgent emergency, four in one, and many more. The combination of these features makes it a great tool for both individuals looking to monitor their health from the comfort of their own homes and healthcare professionals looking for an accurate solution for remote patient monitoring.

The goal of this research is to develop an IoT-based smart healthcare kit for people suffering from Covid and Chronic diseases. The project was completed and tested with people successfully. We'd like to thank everyone who took the time to fill out the survey. The information obtained was useful in determining a continuing problem and a long-term remedy.

References

[1] Y. Kodithuwakku, A.D. Sandanayake, C. Bandara, V. Logeeshan, "IoT Based Healthcare Kit for Domestic Usage," 2022 IEEE World AI IoT Congress, AIIoT 2022, 760-765, 2022, doi:10.1109/AIIoT54504.2022.9817235.

[2] A.K. Singh, A. Misra, "Impact of COVID-19 and comorbidities on health and economics: Focus on developing countries and India," Diabetes and

- Metabolic Syndrome: Clinical Research and Reviews, **14**(6), 1625–1630, 2020, doi:10.1016/j.dsx.2020.08.032.
- [3] E. Workie, J. Mackolil, J. Nyika, S. Ramadas, “Deciphering the impact of COVID-19 pandemic on food security, agriculture, and livelihoods: A review of the evidence from developing countries,” *Current Research in Environmental Sustainability*, **2**, 100014, 2020, doi:10.1016/j.crsust.2020.100014.
- [4] K. Latha, G. Sravanth, N.V.P. Kumar, ..., “An IoT based patient monitoring system using arduino uno,” ... *Research Journal of ...*, 2020.
- [5] G.G. Kulatunga, R. Hewapathirana, R.B. Marasinghe, V.H.W. Dissanayake, “A review of Telehealth practices in Sri Lanka in the context of the COVID-19 pandemic,” *Sri Lanka Journal of Bio-Medical Informatics*, **11**(1), 8, 2020, doi:10.4038/sljbm.v11i1.8090.
- [6] W.Q. Mok, W. Wang, S.Y. Liaw, “Vital signs monitoring to detect patient deterioration: An integrative literature review,” *International Journal of Nursing Practice*, **21**(S2), 91–98, 2015, doi:10.1111/ijn.12329.
- [7] R. Mahajan, D. Bansal, “Identification of heart beat abnormality using heart rate and power spectral analysis of ECG,” *International Conference on Soft Computing Techniques and Implementations, ICSCIT 2015*, 131–135, 2016, doi:10.1109/ICSCIT.2015.7489555.
- [8] M.U.H. Al Rasyid, B.H. Lee, A. Sudarsono, “Wireless body area network for monitoring body temperature, heart beat and oxygen in blood,” *2015 International Seminar on Intelligent Technology and Its Applications, ISITIA 2015 - Proceeding*, 95–98, 2015, doi:10.1109/ISITIA.2015.7219960.
- [9] L. Xie, Z. Li, Y. Zhou, Y. He, J. Zhu, “Computational diagnostic techniques for electrocardiogram signal analysis,” *Sensors (Switzerland)*, **20**(21), 1–32, 2020, doi:10.3390/s20216318.
- [10] U. Gogate, J.W. Bakal, “Smart Healthcare Monitoring System based on Wireless Sensor Networks,” *International Conference on Computing, Analytics and Security Trends, CAST 2016*, 594–599, 2017, doi:10.1109/CAST.2016.7915037.
- [11] N. Arunpradeep, G. Niranjana, G. Suseela, “Smart healthcare monitoring system using iot,” *International Journal of Advanced Science and Technology*, **29**(6), 2788–2796, 2020, doi:10.22214/ijraset.2020.5101.
- [12] K. Aziz, S. Tarapiah, S.H. Ismail, S. Atalla, “Smart real-time healthcare monitoring and tracking system using GSM/GPS technologies,” *2016 3rd MEC International Conference on Big Data and Smart City, ICBDS 2016*, 357–363, 2016, doi:10.1109/ICBDS.2016.7460394.
- [13] A. Rahaman, M.M. Islam, M.R. Islam, M.S. Sadi, S. Nooruddin, “Developing iot based smart health monitoring systems: A review,” *Revue d’Intelligence Artificielle*, **33**(6), 435–440, 2019, doi:10.18280/ria.330605.
- [14] D. Ding, M. Conti, A. Solanas, “A smart health application and its related privacy issues,” *Proceedings of the 2016 Smart City Security and Privacy Workshop, SCSP-W 2016*, 11–15, 2016, doi:10.1109/SCSPW.2016.7509558.
- [15] R. Rajmohan, P.D.D.M.G.M. Johar, “Adoption of the Internet of Things in the Healthcare Services of Sri Lanka,” *International Journal of Recent Technology and Engineering (IJRTE)*, **9**(1), 1095–1104, 2020, doi:10.35940/ijrte.a2260.059120.
- [16] M.A. Obaidat, S. Obeidat, J. Holst, A. Al Hayajneh, J. Brown, “A comprehensive and systematic survey on the internet of things: Security and privacy challenges, security frameworks, enabling technologies, threats, vulnerabilities and countermeasures,” *Computers*, **9**(2), 2020, doi:10.3390/computers9020044.
- [17] A.D. Acharya, S.N. Patil, “IoT based Health Care Monitoring Kit,” *Proceedings of the 4th International Conference on Computing Methodologies and Communication, ICCMC 2020, (iccmc)*, 363–368, 2020, doi:10.1109/ICCMC48092.2020.ICCMC-00068.
- [18] M.R.R. Akash, Yousuf, K. Shikder, “IoT Based Real Time Health Monitoring System,” *Proceedings of International Conference on Research, Innovation, Knowledge Management and Technology Application for Business Sustainability, INBUSH 2020*, 167–171, 2020, doi:10.1109/INBUSH46973.2020.9392163.
- [19] M.R. Ruman, A. Barua, W. Rahman, K.R. Jahan, M. Jamil Roni, M.F. Rahman, “IoT Based Emergency Health Monitoring System,” *2020 International Conference on Industry 4.0 Technology, I4Tech 2020*, 159–162, 2020, doi:10.1109/I4Tech48345.2020.9102647.

## A Numerical Study on The Change in Safety Factor (FOS) According to Slope Angle Change for The Establishment of Photovoltaic Facilities Using SRM (Strength Reduction Method)

Seungjea Lee<sup>1,\*</sup>, Moonwoo Park<sup>2</sup>

Fire Insurers Laboratories of Korea, Research & Development Strategy Team, Korea Fire Protection Association, Yeosu, 12661, Republic of Korea

### ARTICLE INFO

Article history:

Received: 24 April, 2023

Accepted: 12 May, 2023

Online: 12 June, 2023

Keywords:

Strength reduction method

Solar power generation

FEM analysis

Factor of safety

### ABSTRACT

As the significance of new and renewable energy is highlighted, land-based solar power generation has seen remarkable progress. This study utilizes the Strength Reduction Method in DIANA, a numerical analysis software, to assess the stability concerning various variables, such as slope angle, water level, water depth, and changes in material properties, with a focus on the factor of safety (FOS). This research aims to address the safety concerns of land-based solar power generation facilities installed on varying terrains. The standardized slope permit criteria for solar panels in mountainous areas were revised to a steeper 15 degrees, however, this shift necessitates further investigation as it is not grounded on ample research. Findings from this study revealed a decreasing trend in the factor of safety (FOS) with the increasing slope angle and an inverse proportionality between the factor of safety (FOS) and groundwater level. Moreover, we analyzed the factor of safety (FOS) concerning water level and soil strength. Future studies will incorporate additional factors for a more comprehensive safety factor (FOS) assessment.

## 1. Introduction

Over the years, South Korea has experienced a significant increase in solar power capacity, rising from 1,362 MW in 2017 to 4,658 MW in 2020 [1]. However, the expansion came with challenges, most notably damage to panels installed without adhering to the recommended guidelines. In many cases, these installations were on varying soil types, each of which presents unique challenges and considerations when it comes to stability. To combat this, the Ministry of Environment and the Korea Forest Service tightened regulations, reducing the permissible slope angle for installations from 25 degrees to 15 degrees [2].

These changes, although crucial for safety, led to concerns within the industry regarding their potential impact on operations and a lack of sufficient precautions for accidents. Moreover, the Korea Environment Institute (KEI) proposed even stricter slope criteria, recommending an angle of 10 degrees or less [1], without differentiating between soil types. Given these diverging guidelines, the need to verify the appropriateness of the slope criteria for different soil types became apparent.

In response to this, the current study aims to evaluate the validity of these guidelines for different soil types. We plan to analyze the standardized slope permit criteria of 15 degrees, compare it with the serviceability analysis result (slope 10 degrees or less), and assess them against the "minimum safety factor" and "safety factor for collapse" for each soil type under study.

## 2. Factor of Safety (FOS) and Theoretical Background

### 2.1. Scope of Research

This study can be broadly divided into three parts, as follows: 1) analyzing slope stability based on the location of the groundwater table, 2) analyzing slope stability based on the groundwater level, and 3) analyzing slope stability based on the degree of soil hardness. Each of these parts will utilize the Factor of Safety (FOS), a critical indicator in slope stability analysis which measures the capacity of a system to resist failure. The exact range of the FOS considered will be determined based on a thorough survey of the relevant literature to ensure that our study reflects the most up-to-date and the most relevant data.

While some studies highlight the potential risks and challenges of installing solar panels on steep slopes, others present innovative solutions and strategies for overcoming these challenges. Together,

\* Corresponding Author: Seungjea Lee, 1030, Gyeongchung-daero, Ganam-eup, Yeosu-si, Gyeonggi-do, Republic of Korea, +82\_31\_887\_6712 & [sjlee@kfpa.or.kr](mailto:sjlee@kfpa.or.kr)

these case studies underscore the importance of proper site evaluation, strategic planning, and rigorous safety measures.

These analyses will be conducted using the commercial finite element program TNO DIANA [3]. TNO DIANA was selected because it provides excellent material models for damage and collapse modelling implementation compared to other finite element packages. Additionally, it provides a robust platform for implementing the calculation of FOS, thereby enhancing the reliability and validity of our study.

Equation (1) for calculating the factor of safety (FOS) in slope stability analysis using numerical analysis is as follows [4], [5]:

$$FOS = \frac{\text{Shear Strength}}{\text{Shear Stress}} = \frac{c + (\rho g H \cos \theta - \rho_w g W) \tan \phi}{\rho g H \sin \theta} \quad (1)$$

\*  $c$  : Adhesiveness,  $\rho$  : Density of Topsoil,  $g$  : Acceleration of Gravity,  $\rho_w$  : Density of Water,  $\phi$  : Internal Friction Angle

The following tasks will be performed in this study:

- Conducting slope stability analysis simulations based on the location of the groundwater table.
- Performing slope stability analysis simulations for slope angles ranging from 10° to 30°.
- Dynamic analysis, which considers infiltration, requires a significant amount of time and accurate data [5]-[6].  
\* Due to the substantial time consumption in generating appropriate input data and simulations, along with physical time constraints, a static analysis will be conducted.
- Before conducting dynamic analysis, static analysis will be performed to understand the basic principles of slope collapse mechanisms.
- Subsequently, the basic theory will be applied to find ways to maintain the structural integrity of slopes by addressing collapse scenarios that may occur in actual terrain.

## 2.2. Method for Slope Stability Analysis

Slope stability analysis refers to the calculation of stability concerning slope failure based on shear stress and shear strength. There are three main methods for slope stability analysis, and in this study, we conducted slope stability analysis using the strength reduction method. The advantages and disadvantages of each slope stability analysis method are explained as follows.

### 2.2.1. Limit Equilibrium Method

The conventional method for slope stability calculation involves defining a sliding surface in advance and dividing the ground within the surface into segments based on the equilibrium of forces in each segment's limit state to calculate the factor of safety. This method can be computed through classical mathematical equations, but for more accurate calculations, it requires dividing the segments into many parts, making it more suitable for numerical analysis using computers.

### 2.2.2. Stress Analysis Method

The stress analysis method is similar to the limit equilibrium method in that it calculates the factor of safety based on the ratio of stress and strength generated on the sliding surface. However, it differs from the limit equilibrium method in that it derives the

stress state of the sliding surface using the results of finite element analysis, rather than by balancing the forces of each segment. Like the limit equilibrium method, it has the disadvantage of requiring the definition of a failure surface in advance.

### 2.2.3. Strength Reduction Method

The strength reduction method is developed based on the finite element method that divides the material properties of the ground into the factor of safety and analyzes them, considering cases where failure occurs. Even if the failure surface is not defined in advance, it is possible to calculate the factor of safety, and it is possible to calculate the factor of safety regardless of the arbitrarily generated failure surface. Furthermore, it can analyze even slopes with complex 3-dimensional shapes and can consider reinforcing materials, groundwater, dynamic behavior, etc., making it a recently highlighted analysis method.

However, the Strength Reduction Method tends to have excessively long analysis times compared to the Limit Equilibrium Method, and when applied to dynamic analysis, calculations must be performed for every time step, requiring analysis times in days. However, with recent advancements in computer technology, analysis times have become much shorter, and except for analyzing dynamic behavior, analysis times are not significantly restricted. The strength reduction method is a numerical analysis method that calculates the factor of safety by repeatedly reducing the strength while reaching the slope failure state based on the safety coefficient. By dividing the strength ratio by the factor of safety, as in equations (2) and (3) [7], the shear strength of the soil is gradually reduced, and when the analysis does not converge, it is assumed that the slope has failed with the minimum factor of safety based on the strength reduction at that point [8]-[9].

$$c^{trial} = \frac{1}{FS^{trial}} \times c \quad (2)$$

$$\phi^{trial} = \arctan \left( \frac{1}{FS^{trial}} \times \tan \phi \right) \quad (3)$$

\*  $FS^{trial}$  : Test Safety Factor,  $c$ ,  $c^{trial}$  : Adhesive Strength Considering Actual Adhesion and Factor of Safety,  $\phi$ ,  $\phi^{trial}$  : Internal friction angle considering actual internal friction and factor of safety.

While the Limit Equilibrium Method is straightforward and provides meaningful results, it struggles with complex scenarios and requires the pre-definition of a failure surface. The Stress Analysis Method offers a more detailed analysis through the use of finite element analysis but shares the limitation of needing to pre-define a failure surface.

On the other hand, the Strength Reduction Method does not require a pre-defined failure surface and is more flexible for complex 3D shapes. It provides a comprehensive analysis considering various factors but requires longer computation times, although recent technological advancements have improved this.

In short, simpler slopes may benefit from the Limit Equilibrium or Stress Analysis methods, while more complex situations may warrant the use of the Strength Reduction Method, despite longer analysis times.

2.3. Analysis of pre-existing research on slope stability

Through a review of existing literature, we aim to understand the characteristics of various methods for slope stability analysis by examining domestic and international numerical analysis research cases on slope stability [10].

2.3.1. Particle Finite Element Method (PFEM)

The Particle Finite Element Method (PFEM) has the advantage of being able to handle large deformations as an extension of the traditional Finite Element Method (FEM) [9]. This method simulates the entire evolution of landslides from initiation to deposition, and before applying the PFEM model to real landslides, it examines the collapse mechanism of small landslides on homogeneous soil slopes [4], [11], [12].

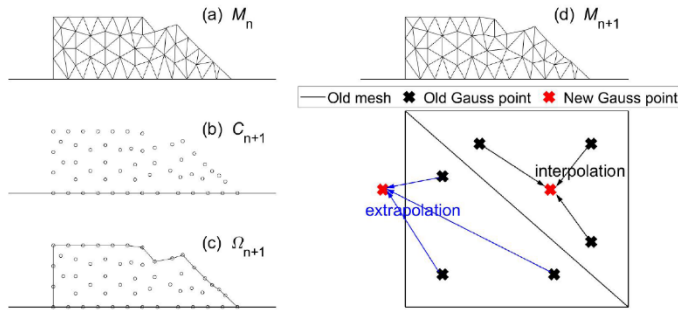


Figure 1: Steps for PFEM technology at time interval [tn, tn+1]

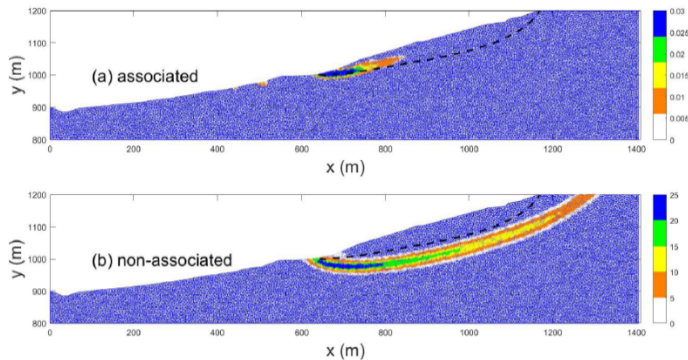


Figure 2: FEM model based on the use of Mohr-Coulomb plastic model

Dynamic analyses of landslides are associated with dynamic processes such as the dynamic behavior of materials and the re-distribution of sliding in the landslide. Several slip surfaces with a critical condition of RF=1.545 identify stages that allow for internal yielding and sliding.

2.3.2. Stress analysis method and strength reduction method.

When comparing the stress analysis method and the strength reduction method, the principle of analysis differs. While the strength reduction method reduces the strength integer until it reaches the failure state, the stress analysis method calculates the shear force and shear strength of the virtual failure plane based on the stress analysis result of the finite element method to calculate the factor of safety [4], [5], [13].

When comparing the advantages and disadvantages of the stress analysis method and the strength reduction method, the

strength reduction method has a relatively simple theory and does not require additional programs for interpretation. However, because it requires repetitive numerical analysis, the calculation time for interpretation may be relatively long, and there are some things that could be improved in terms of convergence and accuracy in the state of destruction.

In stress analysis methods, the calculation time for interpretation is relatively short, and the analysis is for the current stress state rather than the state of destruction, so the convergence and accuracy are relatively good. However, an additional stability evaluation program is required.

2.4. Numerical analysis using FEM

In a numerical analysis using FEM for soil analysis, the Mohr-Coulomb and Drucker-Prager models are commonly used, and in particular, the Mohr-Coulomb model is widely used in slope stability analysis. The equation for the Mohr-Coulomb model is shown in equation (4).

$$\frac{1}{2}(\sigma_1 - \sigma_3) = -\frac{1}{2}(\sigma_1 - \sigma_3)\sin\phi + c \cdot \cos\phi \quad (4)$$

$\phi$ : the internal frictional angle,  $c$ : the cohesion

The Drucker-Prager yield model is commonly used for soil and rock material modelling.

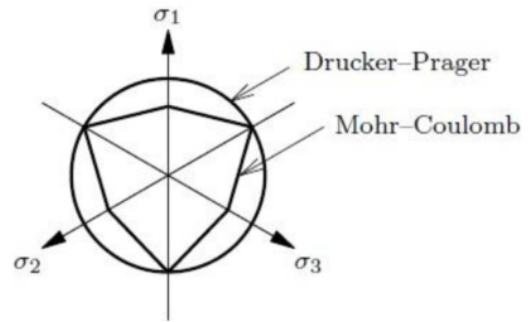


Figure 3: Drucker-Prager and Mohr-Coulomb plastic model & destructive surface by main stress

As can be seen in Figure 3, the Drucker-Prager yield model is a smooth approximation of the yield surface of the Mohr-Coulomb yield model, and the failure surface equation is given by the following equation (5).

$$A + B(\sigma_1 + \sigma_2 + \sigma_3) = \sqrt{\frac{1}{6}[(\sigma_1 - \sigma_2)^2 + (\sigma_2 - \sigma_3)^2 + (\sigma_3 - \sigma_1)^2]} \quad (5)$$

$$* A = \frac{6 \cdot c \cdot \cos\phi}{\sqrt{3}(3 + \sin\phi)}, B = \frac{2 \cdot \cos\phi}{\sqrt{3}(3 + \sin\phi)}$$

Slope stability analysis using the finite element method provides a numerical analysis method capable of calculating the minimum safety factor of a slope and meticulously analyzing the failure behavior of a slope for various shapes, loads, and boundary conditions. The strength reduction method, in particular, enables automatic simulation of the failure process without requiring prior assumptions about the slope's failure activity [6].



The safety factor in slope stability analysis, termed the Factor Of Safety (FOS), is calculated through an iterative calculation routine, as depicted in Figure 4 below.

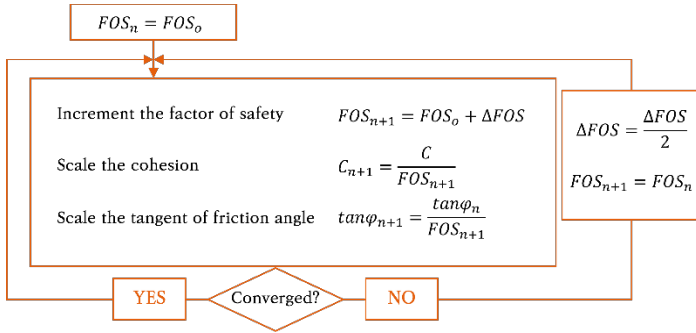


Figure 4: Flowchart of recurring calculations for SRM Method

The algorithm sequence is as follows:

- The primary physical properties of soil and ground, such as cohesion and internal friction angle, are reduced by the currently presumed FOS value.
- The diminished strength (indicated by the red solid line in Figure 5 below) is examined through the Mohr-Coulomb yield surface. If it results in failure, the safety factor is lowered to a value beneath the currently assumed value. If it converges, the process repeats, increasing the safety factor beyond the current safety factor value.

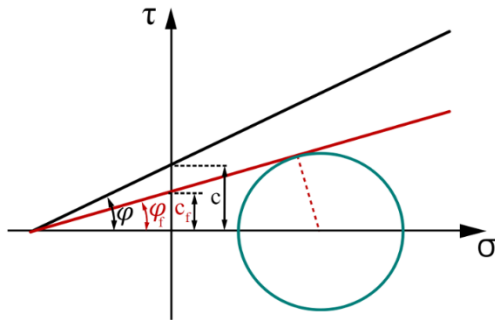


Figure 5: Mohr-Coulomb yield surface after strength reduction

### 3. Research Method

In order to explore and research the potential of the mesh-free method, the PFEM approach was employed in this study. The dynamic behavior, merging traditional finite element analysis with element-based techniques, was primarily concentrated on simulating shallow deformations of landslides [14]. The behavior of soil materials was delineated, and a variety of soil material simulation models were reviewed and evaluated [15]. All simulations were conducted using the DIANA program [12]. Moreover, the strength reduction method was employed for slope stability analysis in this study.

#### 3.1. FEM Numerical Modelling

To generate data, the basic model is schematically illustrated as follows.

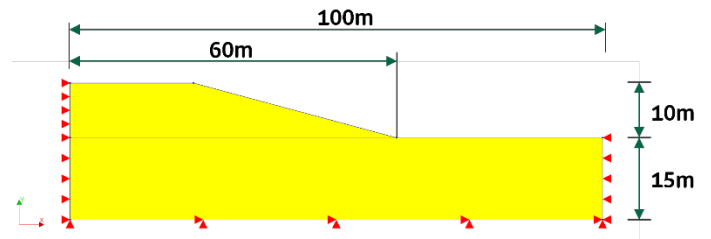


Figure 6: Schematic illustration of the basic model for performing numerical analysis

Based on the analysis of research case studies in existing literature, material properties were assumed to be uniform and the values were adopted from these studies (refer to Table 1). The default position of the water surface was presumed to be inside the slope. Slope stability analysis was conducted under the assumption that the groundwater level was situated 5 meters above ground level and was parallel to the ground level line.

Table 1: Material properties of soil applied to simulation

Material Properties	Value
Young's modulus	1,000,000 N/m <sup>2</sup>
Poisson's ratio	0.3
Density	1814.37 kg/m <sup>3</sup>
Cohesion	10,000 N/m <sup>2</sup>
Friction angle	20 rad (°)
Dilatancy angle	20 rad (°)

For the purposes of examining mesh sensitivity, a slope stability analysis was performed under plain strain conditions for 2D analysis, utilizing higher-order elements. These elements have been found to provide a more accurate calculation of the safety factor. In situations where a groundwater level exists, external water pressure should be applied to areas outside the ground surface where water is present. Given that the strength reduction method carries out an analysis of total stress, pore pressure was defined for the submerged area within the ground surface [16].

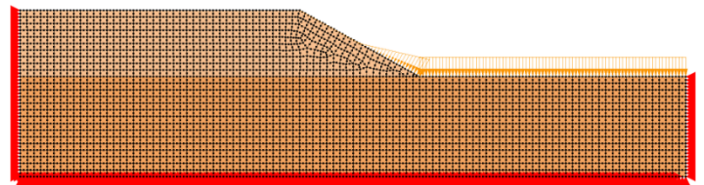


Figure 7: Modelling for mesh sensitivity study

The following is a discussion on the model's mesh sizes and their implications for the results. The boundary conditions were fixed in both the X and Y directions at the bottom, while only X was constrained on the sides. The analysis was performed using the Strength Reduction Method.

In our mesh sensitivity study, we calculated nine different mesh sizes ranging from 5 m × 5 m to 0.1 m × 0.1 m. It was observed that decreasing the mesh size led to stable convergence of the safety factor values. However, this also resulted in an increase in the analysis time. These findings highlight the impact of mesh size on the accuracy and computational efficiency of our model. Smaller mesh sizes provide more precise results but require additional computational time. Table 2 illustrates the changes in safety factors corresponding to different mesh sizes.

Table 2: Comparison of FOS and time required according to mesh size change

Mesh size (m)	FOS	Time (min)
5 m × 5 m	2.5317	1
4 m × 4 m	2.0125	2
3 m × 3 m	1.9500	2.5
2 m × 2 m	1.9500	4
1.4 m × 1.4 m	1.9500	4.5
1 m × 1 m	1.9469	5
0.75 m × 0.75 m	1.95	7.5
0.5 m × 0.5 m	1.9625	10
0.25 m × 0.25 m	1.9361	35
0.1 m × 0.1 m	2.0526	255

Figure 8 illustrates that stable values are achieved when using mesh sizes ranging from 2 m × 2 m to 1 m × 1 m. However, when the mesh size is further reduced, unstable values are once again obtained. The most stable result was obtained when utilizing a mesh size of '1.4 m × 1.4 m'.

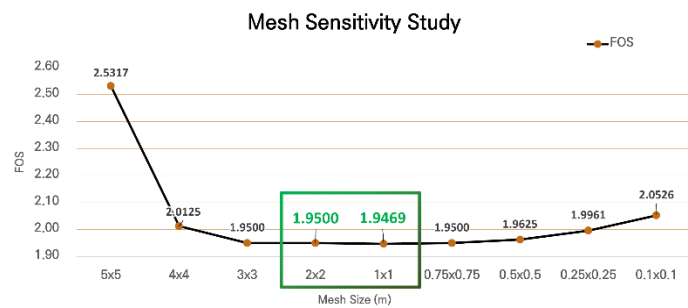


Figure 8: Changes in FOS according to mesh size

#### 4. Analysis of FEM numerical analysis results.

The content presented in this chapter represents a preliminary study aimed at addressing uncertainties regarding the suitability of a 15-degree slope for implementing solar power generation in a production area [17]. The study incorporates variable research involving four factors: angle, water level, water depth, and

alterations in material properties. Its purpose is to investigate the influence of these variables on the feasibility of solar power generation installation.

#### 4.1. FEM Numerical Modelling

A total of ten models were analyzed, considering slopes with angles ranging from 10° to 30°. The safety factor was calculated for each slope to assess its stability. The analysis included slopes with and without groundwater to evaluate their respective influences on stability. The material properties employed in the FEM numerical modeling, as described in section 3.1, were consistently utilized for this analysis.

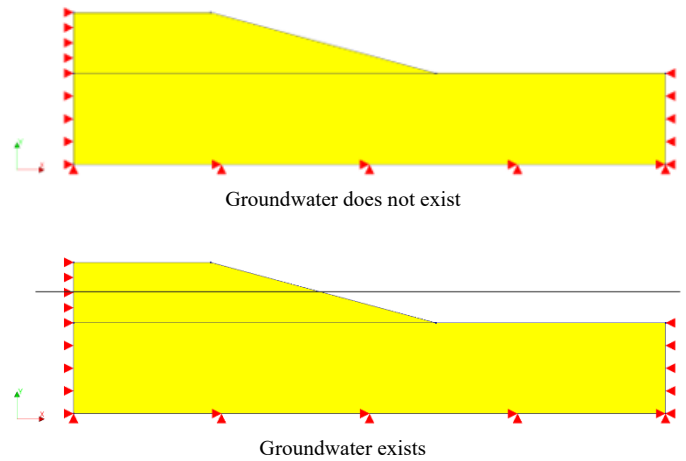


Figure 9: Model and internal deformation according to slope angle change.

To ensure appropriate numerical analysis, all variables except for changes in slope angle and the presence of groundwater used the same values. It was inferred from changes in safety factor that as the slope angle increased, the stability of the slope decreased.

As shown in Table 3, the safety factor was lower when groundwater was present, indicating that groundwater has a negative impact on slope stability. Conversely, when groundwater was absent, it was observed that the stability of the slope was improved.

Therefore, the slope safety factor simulation data and linear regression analysis results for both conditions are shown in Figure 10, and the linear trend lines for the change in safety factor are obtained as Equation (6) for the condition without groundwater and Equation (7) for the condition with groundwater.

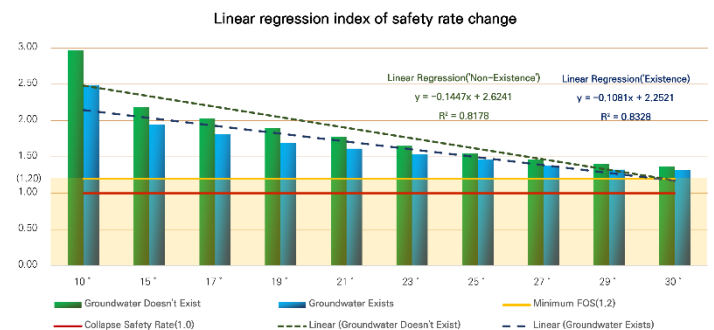


Figure 10: Linear regression index of safety rate change

Table 3: An indicator of the change in safety ratio according to the change in slope angle

Slope angle	Groundwater Not-Existing		Groundwater Exists	
	FOS	Change Rate	FOS	Change Rate
10 °	2.97	136%	2.49	128%
15 °(Standard)	2.19	(Standard)	1.95	(Standard)
17 °	2.03	93%	1.81	93%
19 °	1.89	87%	1.70	87%
21 °	1.77	81%	1.61	83%
23 °	1.65	75%	1.54	79%
25 °	1.55	71%	1.46	75%
27 °	1.46	67%	1.38	71%
29 °	1.40	64%	1.33	68%
30 °	1.37	63%	1.32	68%

$$y = -0.1447x + 2.6241, R^2 = 0.8178 \quad (6)$$

$$y = -0.1081x + 2.2521, R^2 = 0.8328 \quad (7)$$

#### 4.2. Location of Water

The position of the groundwater was changed to be parallel to the ground surface and parallel to the slope surface, and the safety factor was calculated accordingly.

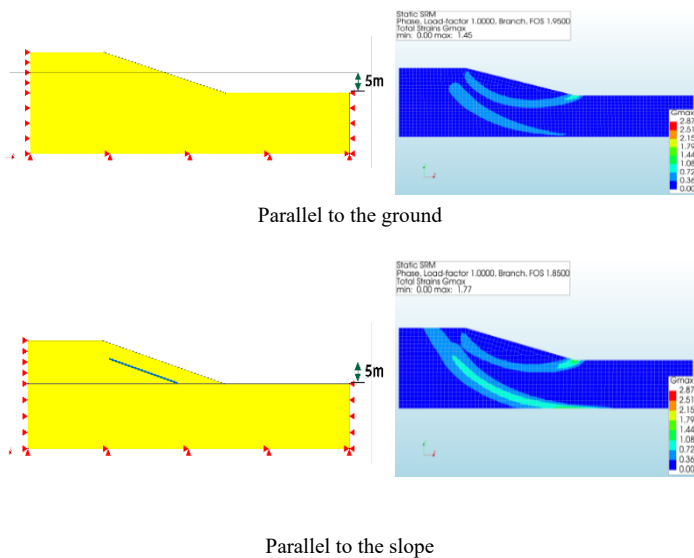


Figure 11: Model and internal deformation according to changes in surface position

The safety factor simulation data for each position of the groundwater level in both conditions can be observed in Figure 12, and Table 4 shows that when the groundwater level was parallel to the ground surface, the safety factor was 0.1 higher (1.95) than in the other condition.



Figure 12: Schematic model for water level changes

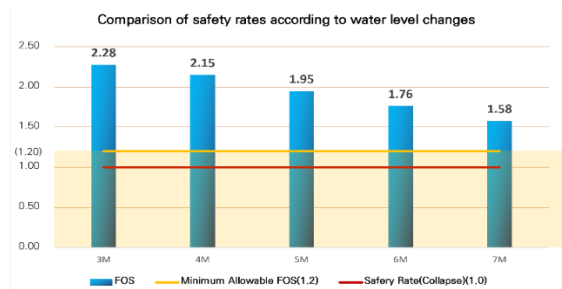


Figure 13: Comparison of safety rates according to water level changes

#### 4.3. Level of Water

The height of the groundwater level was varied (3m, 4m, 5m, 6m, 7m), and a change in the safety factor was observed.

The slope angle was set to 15 degrees, and other material properties were the same as those used in the slope angle variable study. The simulation results showed that the safety decreased as the water level increased, as shown in Figure 14, indicating an inverse relationship between water level and safety.

As the water level increased, the internal deformation rate of the slope increased, which can be confirmed through Table 5.

Table 4: Changes in the safety ratio according to the change in the position of the water surface

Location of Water (m)	FOS	Change Rate
Parallel to the ground	1.9500	(Standard)

Parallel to the slope	1.8500	95%
-----------------------	--------	-----

Table 5: Changes in safety and strain according to water level changes

Level of Water (m)	FOS	Change Rate
3 m	2.2750	117%
4 m	2.1500	110%
5 m	1.9500	(Standard)
6 m	1.7625	90%
7 m	1.5750	81%

#### 4.4. Changes in Material Properties

After setting the slope to 15 degrees, we checked the safety factor using the physical characteristics of the weakest ground in South Korea. These physical characteristics were based on the experimental results from previous literature [12], and we compared the safety factor by considering four types of soil strength (very weak, weak, moderate, and strong).

After incorporating the physical characteristics mentioned above, we simulated the safety factor and obtained results similar to Figure 15. Table 7 provides more detailed information on the variation of safety factors and internal deformation analysis data.

Table 6: Variation of parameters according to changes in soil type for numerical analysis

	Very fragile $c < 0.15$	Fragile $0.15 < c < 0.3$	Common $0.3 < c < 0.6$	Solid $c < 0.6$	Default Opt.
Average $E_f$	27c	30c	31c	34c	-
Modulus of elasticity	2.025	6.75	13.95	30.6	10.197
Cohesion [kgf/cm <sup>2</sup> ]	0.075	0.225	0.45	0.9	0.10197

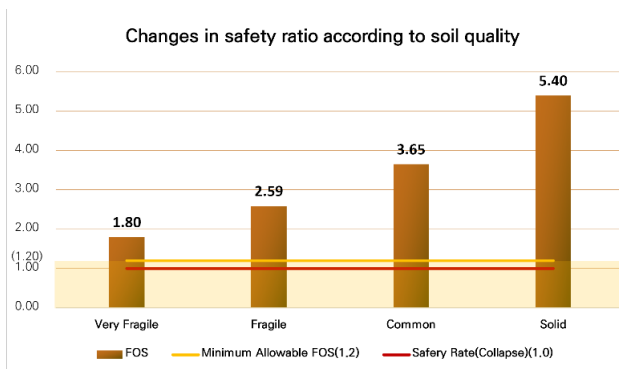


Figure 14: Changes in safety ratio according to soil quality.

Table 7: Safety and strain changes in soil type

Soil Type	FOS	Change Rate
Very fragile	1.7969	49%
Fragile	2.5875	71%
Common	3.6500	(Standard)
Solid	5.3969	148%

### 5. Conclusion and Suggestion

The study conducted a variable analysis to examine the influence of different factors on mountain slope stability. The results indicated that a decrease in slope angle led to an increase in the safety factor. When the slope angle was changed from 15° to 10°, the safety factor changed by 136%, with a gradual decrease as the angle increased. Moreover, variations in groundwater level had an impact on the safety factor when the slope angle was fixed at 15°. The safety factor was slightly lower when the groundwater level was parallel to the slope compared to when it was parallel to the ground surface, suggesting an increase in infiltration. The study also observed that changes in the water level affected the safety factor. A decrease from 5 m to 3 m resulted in a 17% increase in the safety factor, while an increase to 7 m led to a 19% decrease. Additionally, altering the soil characteristics, specifically the elastic modulus and adhesion, showed notable effects on the safety factor. For instance, when compared to moderate soil, the safety factor decreased by approximately 50% for very weak soil and increased by about 50% for hard soil.

The findings confirm that the safety factor increases with a decrease in slope angle, when the groundwater level is parallel to the ground surface, when the water level is lower, and when the soil possesses higher physical characteristics such as elastic modulus and adhesion. The study suggests that strengthening the criteria for solar panel installation on slopes to account for heavy rainfall is reasonable, as heavy rainfall has been linked to solar panel damage. However, it emphasizes the need for considering various factors rather than solely relying on the slope angle criterion. Factors such as groundwater level, soil characteristics, and precipitation should be taken into account when formulating solar panel installation guidelines.

The study also examined the influence of groundwater orientation on slope safety. The Factor of Safety (FOS) was found to be 1.95 when the groundwater level was parallel to the ground and decreased to 1.85 when parallel to the slope. This represents a 95% change rate compared to the standard scenario, highlighting the significant impact of groundwater orientation on the safety of solar panel installations on slopes.

Although the study assessed safety factors based on slope angle, groundwater level, water level, and soil characteristics, it acknowledged limitations in comprehensively applying each factor and analyzing real-time infiltration rates. The study highlighted the need for further research to establish a more precise engineering basis for the current legal criterion of a slope angle of 15° or less when installing photovoltaic facilities. Future studies should analyze the relationships between various factors, including those explored in this study, and develop models that consider real-time infiltration rates.

Overall, this study aims to contribute to the development of the photovoltaic industry in Korea by providing a foundation for further research and the establishment of accurate legal criteria for slope angles.

### Conflict of Interest

The authors declare no conflict of interest.

### References

- [1] K.-I. Chin, "Problem Analysis and Improvement Measures of Rural Area Development for PV Power Plant Project," *KIEAE Journal*, **21**(5), 83–90, 2021, doi:10.12813/kieae.2021.21.5.083.
- [2] C. Kim, "Strengthen of the gradient permit standard was decided prior to the presentation of the service results of the National Research Institute, and 12 mountain solar power plants that suffered damage due to torrential rain were permitted before the gradient s," *Ministry of Trade, Industry and Energy.*, **3**, 2020.
- [3] J. Manie, "DIANA user's manual," TNO DIANA BV, 2009.
- [4] L. Brezzi, E. Carraro, D. Pasa, G. Teza, S. Cola, A. Galgaro, "Post-collapse evolution of a rapid landslide from sequential analysis with FE and SPH-based models," *Geosciences (Switzerland)*, **11**(9), 364, 2021, doi:10.3390/geosciences11090364.
- [5] S.-J.A. Choon-Sik Park, "An Analytical Study on the Slope Safety Factor Considering Various Conditions," *JOURNAL OF THE KOREAN GEOTECHNICAL SOCIETY*, **35**(5), 31–41, 2019, doi:10.7843/kgs.2019.35.5.31.
- [6] Y.-C. Hsu, Y.-L. Chang, C.-H. Chang, J.-C. Yang, Y.-K. Tung, "Physical-based rainfall-triggered shallow landslide forecasting," *Smart Water*, **3**(1), 3, 2018, doi:10.1186/s40713-018-0011-8.
- [7] Q.-A. Gian, D.-C. Nguyen, D.-N. Tran, D.-T. Tran, "Monitoring of Landslides in Mountainous Regions based on FEM Modelling and Rain Gauge Measurements," *International Journal of Electrical and Computer Engineering (IJECE)*, **6**(5), 2106, 2016, doi:10.11591/ijece.v6i5.10482.
- [8] S. Ravindran, I. Gratchev, "Prediction of Shallow Rainfall-Induced Landslides Using Shear Strength of Unsaturated Soil," *Indian Geotechnical Journal*, **51**(4), 661–672, 2021, doi:10.1007/s40098-020-00468-6.
- [9] J.S. Lee, C.G. Song, S.O. Lee, "Analysis of Characteristic of Debris Flow with Angle of Slope," *Journal of the Korean Society of Safety*, **31**(2), 49–56, 2016, doi:10.14346/JKOSOS.2016.31.2.49.
- [10] J.-Y.K. Joon-Seok Kim, "Study on Characteristics of Numerical Analysis Method for Stability Analysis of Reinforced Slope," *Korean Geosynthetics Society*, **8**(No.3), 17 ~ 23, 2009.
- [11] W.Z. Savage, R.L. Baum, M.M. Morissey, B.P. Arndt, "Finite-element analysis of the Woodway landslide, Washington," *Geomorphology*, **2180**(3–4), 9, 2000.
- [12] H.-S. Seo, *A Study the Relationship Fofmula of Elastic Modulus and Axcial Stress of clay*, Changwon National University, Changwon, 2010.
- [13] J. Si-Yi, L. Hai-Liang, "Disaster Mechanism and Safety Evaluation of Sihong Landslide," in *IOP Conference Series: Earth and Environmental Science*, IOP Publishing Ltd, 2021, doi:10.1088/1755-1315/768/1/012061.
- [14] L. Wang, X. Zhang, S. Tinti, "Shallow landslides modeling using a particle finite element model with emphasis on landslide evolution," *Earth Surface Dynamics Discussions*, **2019**(May), 1–19, 2019, doi:10.5194/esurf-2019-17.
- [15] W.-S. Bae, B.-J. Lee, K.-T. Jang, "Slope Stability Assessment for Colluvial Soil Slumps of the Danyang Region," *Journal of the Korean Society of Safety*, **22**(3), 74–80, 2007.
- [16] K. Su, "Slope Stability Analysis of Levee," in *IOP Conference Series: Earth and Environmental Science*, 2020, doi:10.1088/1755-1315/474/6/062023.
- [17] J.-W.M. Tae-Hyun Kim, Sang-Beom Lee, Hyun-Ju Park, Tae-Hyun Kim, *A Study on the Establishment of Environmental Review Guidelines for Solar Power Generation Projects*, 2018.

## Forecasting Bitcoin Prices: An LSTM Deep-Learning Approach Using On-Chain Data

Yu-Jin An<sup>1</sup>, Ha-Young Oh<sup>\*2</sup>, Hyun-Jong Kim<sup>3</sup>

<sup>1</sup>Department of Fintech, Sungkyunkwan University, Seoul, 03063, Korea

<sup>2</sup>College of Computing & Informatics, Sungkyunkwan University, Seoul, 03063, Korea

<sup>3</sup>Department of Artificial Intelligence Convergence, Sungkyunkwan University, Seoul, 03063, Korea

### ARTICLE INFO

Article history:

Received: 09 November, 2022

Accepted: 30 May, 2023

Online: 25 June, 2023

Keywords:

Bitcoin

On-chain

Blockchain

Cryptocurrency

Deep Learning

RNN

LSTM

Price

### ABSTRACT

Over the past decade, Bitcoin's unprecedented performance has underscored its position as the premier asset class. Starting from an insignificant value and reaching an astounding high of around 65,000 U.S dollars in 2021 - all without a central controlling authority - Bitcoin's trajectory is undoubtedly a historical feat. Its intangible nature, initially a subject of skepticism, has turned into an attractive quality, leading many investors to allocate a significant portion of their portfolios to Bitcoin. The traditional banking and investment sectors have also turned their attention to Bitcoin's exponential growth. Concurrently, research on macro-economic variables and investor sentiment explaining Bitcoin's price fluctuations has seen considerable development. However, there is a notable absence of studies leveraging On-Chain Data, information derived from transaction data in Bitcoin's blockchain network. This paper fills this gap by using LSTM (Long Short-Term Memory), a technique widely utilized for time-series data prediction, in conjunction with On-Chain Data, to predict Bitcoin prices.

## 1. Introduction

In recent years, Bitcoin has been in the spotlight not only of investors, but also in fields such as politics and media. Ever since its advent in 2008, Bitcoin has appreciated exponentially in U.S dollar terms, reaching a price of \$20,000 in January of 2017. The dramatic increase in the price of Bitcoin formed an atmosphere among the public that Bitcoin may be a good means to store value. Governments around the world, on the other hand, expressed deep concerns about Bitcoin's volatile nature. Despite the concerns of financial regulators and governments, in 2021 Bitcoin once again pumped over \$64,900, though it did cool-off after Elon Musk's negative tweets on Bitcoin.

The Bitcoin rally that was seen during 2020 and 2021 drew more attention to Bitcoin than ever before. Huge financial investment firms and multinational corporations such as Tesla started to accept Bitcoin as means of payment. According to the article[1], Moreover, rumors behind Apple accepting Bitcoin as a means of payment based on its Apple Pay seems likely to become a reality. Such interest from multinational corporations is making

even those doubtful about Bitcoin enter or re-enter the crypto space.

Many estimate that Bitcoin has potential to break its all-time high in the near future and argue that its fundamentals seem to be strengthening as time passes [2]. However, as seen in the recent 50% drop, the Bitcoin market is still very volatile and can be risky to many, especially retail investors. Firms such as Tesla and Micro Strategy, unlike retail investors, have the financial stability to seek longer term returns and can manage the risks accompanied with downside volatility. The fundamental differences between the so-called Bitcoin "whales" and retail investors lead retail investors to be more elastic to downside price movements and loss from investing in Bitcoin. Considering how the crypto-currency market is unregulated compared to traditional assets such as real estate and equity, the fear of loss can be much bigger for retail investors than big firms [3].

There have been numerous research projects that attempted to predict the movement of this unstable market using the methods that were used to predict the price of traditional assets such as stocks. However, these studies seem to neglect the fact that there are data on Bitcoin itself that contain more information about the

\* Corresponding Author: Ha-Young Oh, [hyoh79@gmail.com](mailto:hyoh79@gmail.com)

potential movement of Bitcoin’s price [4]. Thus, this research attempts to use data that are obtained directly from Bitcoin’s blockchain, called on-chain data. This attempt may be conducive to providing guidelines to retail investors on which data an investor should focus when investing in Bitcoin. We review related work in Section 2, discuss the background of our data and theory in Section 3, and present our data preprocessing and test analysis in Section 4. Finally, we conclude in Section 5.

**2. Related Works & Literature**

As Bitcoin solidifies its position as a mainstream asset class, various studies regarding Bitcoin’s price have been conducted. Early research on Bitcoin concentrated on looking for the factors that determine Bitcoin’s price. These factors include the macroeconomic variables gold price, inflation, employment rates, and stock index. Other factors that were shown to influence Bitcoin’s price include twitter and news sentiment.

Corporate interest to own Bitcoin to hedge against inflation gave Bitcoin the famous alias ‘digital gold’. The firms that entered the Bitcoin market sparked interest in trading algorithms like it did in the equity market[5]. The use of trading algorithms in the crypto currency market also resulted in many researchers and traders making use of machine learning and deep learning algorithms to predict the price movements of Bitcoin to improve the returns of the trading algorithms in use. The studies can be categorized based on the variables that were used and the goals of each research [6].

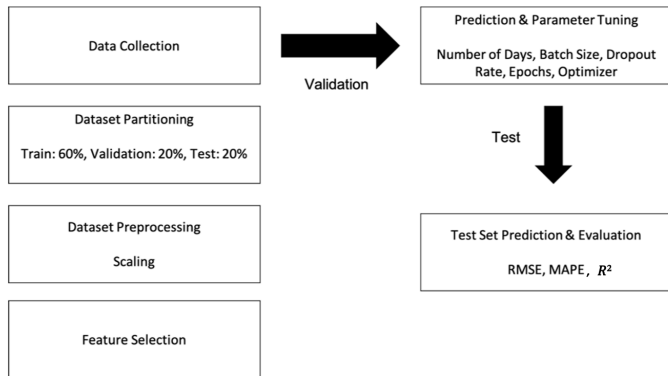


Figure 1: The flow of the experimentation process

The studies listed in Table 1 mainly used data such as trading volume that were obtained from crypto currency exchanges, macro-economic variables, and sentiment analysis of social networking services such as Twitter. There are studies that conduct their research using blockchain data such as hash rate and mining difficulty. However, such data are what is written explicitly on the blocks and are not what are obtained using thorough analysis of the transactions recorded in the blocks. Thus, to make better use of the data from Bitcoin’s chains, this research aims to make use of LSTM (Long Short-Term Memory) based on on-chain data obtained through thorough analysis of transaction data recorded in Bitcoin’s blockchains. We predicted the price of Bitcoin based on various data such as price forecasts from FOMC announcements[7], [8]. In particular, a recently published study [9] utilized on-chain data and used LSTM, which is similar to our work. However, the data, time period, and features we used are different. We utilized market data to consider the "Kimchi

Premium," which is unique to the Korean coin market and is different from other coin exchange data.

Our research will proceed as illustrated in Fig. 1. First, an explanation of the on-chain data that will go through feature engineering will be followed by an explanation of the LSTM. Next, the process of how the features were scaled and selected will be explored. Finally, the preprocessed data will be used to predict Bitcoin’s future price and will be evaluated based on certain performance measures.

Table 1: summary of related works on bitcoin prediction

	Name of Thesis	Research Topics & Goals	Characteristics
1	Deep Learning Approach to Determine the Impact of Socio-Economic Factors on Bitcoin Price Prediction	Predicting Bitcoin price based on gold price and tweet sentiment	- Use of high-frequency Data (5-minutes) - Compared prediction performance of bitcoin price with variables from the traditional market and investor sentiment
2	Do FOMC and macroeconomic announcements affect Bitcoin prices?	Look into the impact FOMC announcement have on Bitcoin price	- Use of announcement about traditional economic factors such as employment rate, PPI, and CPI - Implemented traditional statistical methods such as regression t-statistics and p-value to figure out the impact the announcements have
3	Empirical Analysis on Bitcoin Price Change by Consumer, Industry and Macro-Economy Variables	Look into impact of diverse factors that might potentially have effects on Bitcoin price	- Implemented diverse hypotheses not only about economic variables, but also search traffic on certain keywords such as ‘war’ or ‘ransomware’ that might have relation to bitcoin’s security. - Implemented traditional statistical methods
4	The Determinant of Bitcoin Prices in Korea	Investigate the determining factors that contribute to Bitcoin price in Korea	- Used diverse factors that affect Korea domestically such as inflation, industrial supply, unemployment, KOSPI index, and Naver trend - Use of traditional statistical methods
5	The Prediction model of cryptocurrency price using news sentiment analysis and deep learning	Predicting Bitcoin price using news sentiment	- Use of news instead of social networking services such as twitter to measure sentiment - Used deep learning methods such as RNN and compared with ARIMA
6	Price clustering and sentiment in Bitcoin	Showing the impact of investor sentiment on Bitcoin price clustering	- Utilized various traditional trading data such as price, volume, and number of trades and find relation to sentiment online - Use of traditional statistical methods
7	Bitcoin price forecasting with neuro-fuzzy techniques	Predicting Bitcoin price using a hybrid Adaptive Neuro-Fuzzy Inference System	- Compared the performance between diverse deep-learning models such as artificial neural network and fuzzy logic - Devised a hybrid architecture of already existing ANFIS to predict Bitcoin price

		(ANFIS)	
8	Predicting the Price of Bitcoin Using Machine Learning	Predicting the direction of Bitcoin daily closing price	<ul style="list-style-type: none"> <li>- Compared performance of deep learning sequential models such as RNN and LSTM in Bitcoin prediction with the ARIMA method</li> <li>- Used only price data</li> </ul>
9	Bitcoin price prediction using machine learning: An approach to sample dimension engineering	Predicting the direction of Bitcoin daily and 5-minute interval price	<ul style="list-style-type: none"> <li>- Used On-chain data such as block size, hash rate, and mining difficulty</li> <li>- Compared performance between statistical, machine learning, and deep learning methods</li> </ul>
10	Predicting the direction, maximum, minimum, and closing prices of daily Bitcoin exchange rate using machine learning techniques	Predicting various prices using machine learning techniques	<ul style="list-style-type: none"> <li>- Utilized diverse data from Bitcoin chain and traditional financial markets</li> </ul>
11	A Streaming Data Collection and Analysis for Cryptocurrency Price Prediction using LSTM	Full data analysis steps from data collection to model evaluation using Long Short-Term Memory (LSTM) for predicting cryptocurrency prices	<ul style="list-style-type: none"> <li>- Data Collection via Web Crawling at coinmarketcap.com</li> <li>- BTC, ETH, and LCT price prediction through LSTM based on collected data</li> </ul>

### 3. Data and Background

The most important aspect of this research is the use of on-chain data, a type of data that was not utilized in earnest in previous studies on predicting the price of Bitcoin. Therefore, section A of Part 3 will be an explanation of on-chain data for a better understanding of the overall research. The data are subdivided into six categories.

#### 3.1. On-Chain Data Explanation

##### 1) Exchange Flows Data

Exchange flow data play a major role in explaining potential movements in the Bitcoin price. Unless Bitcoin is traded over the counter, most of its trading takes place in the Bitcoin exchange [10]. In this category, total reserves, reserve net flow, address count, and transaction count data will first be considered as potential factors that influence the predictability of the model. In any asset class, it is considered that the more assets there are in the market, the less valuable. ‘Total reserve’ and ‘total reserve net flow’ are data that show the amount of Bitcoin in the Bitcoin exchanges and the amount of Bitcoin that came into the exchange and went out. It can be inferred from the famous adage from economics, ‘the more the supply, the lower the price’, more stocks of Bitcoin in exchanges and more inflow into exchanges can lead to a lower price. The ‘address count’ and ‘transaction count’ data show the number of addresses participating and the number of transactions made in the exchange.

##### 2) Flow Indicator

Flow indicators help assume the risks of holding Bitcoin and give insights on the value of holding Bitcoin. ‘Exchange whale ratio’ and ‘stablecoins ratio’ are two indicators that fall into this category. ‘Exchange whale ratio’ is calculated by dividing the sum of the top 10 inflows by the sum of the total inflows into exchanges. Several Bitcoin traders think that whales, who own more than a thousand bitcoins, have enough control over the market and can decide the movement of Bitcoin’s price. The ‘stablecoins ratio’ is calculated by dividing the total bitcoin reserve in exchanges by the total stablecoins reserve. Stablecoins such as USD Tether is what participants in the market use to buy cryptocurrencies. Thus, the reserve of stablecoins in exchanges can signify the amount of demand pressure in the market.

##### 3) Market Indicator

Indicators such as ‘estimated leverage ratio’ and ‘MVRV (Market Value to Realized Value)’ fall into this category [11]. Market indicators concentrate on showing how much the market’s investors are heated or cooled off. To be specific, ‘estimated leverage ratio’, which is calculated by dividing the open interests of exchanges by the exchanges’ Bitcoin reserves, represents the average amount of leverage of the market participants. MVRV, calculated by dividing the market value by the realized value, illustrates the relationship between short-term and long-term investors.

##### 4) Miner Flow

Miner flow data focus on showing the flow of Bitcoin from the miners’ wallets. Miners are critical players in the Bitcoin ecosystem in that they are the ones who secure the network and confirm transactions and get paid with Bitcoin in return. ‘Miner’s total reserve’ and ‘miner’s net flow’ are the total amount of Bitcoins in the miner’s wallets and the net change in the miners’ reserves in a given time horizon, respectively [12].

##### 5) Market Data

Market data are comprised of the open, close, low, and high U.S dollar value of Bitcoin in each time period

##### 6) Network Data

Network data consist of information recorded in each block of the Bitcoin chain, such as transaction fees, mining difficulty, and hashrate [13], [14]. Network data were previously used along with other macro-economic metrics and social networking sentiment data to predict the price of Bitcoin. ‘Transaction fee’ shows the amount of fees that incurred from the transactions in a block. Mining difficulty shows how difficult it was to mine the specific block. Lastly, hash rate shows how quickly the miners solve hash problems to mine Bitcoin.

#### 3.2. LSTM Background

##### 1) RNN (Recurrent Neural Network)

An RNN [15], unlike an ANN (Artificial Neural Network), forms a loop so that information persists throughout the network. As illustrated in [Fig. 2], if there is a neural network **A**, **x** and output **o**,



the RNN consistently inputs the element in  $x_t$  to the successor output  $o_t$ . Therefore, RNNs are adequate to process data in the form of chains or lists. Due to this trait, RNNs are frequently used in speech recognition and language modeling.

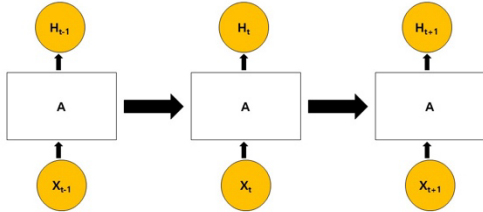


Figure 2: Structure of an RNN

2) LSTM (Long Short-Term Memory)

An LSTM [16] can be considered as a sub-category of RNNs. Although RNNs make use of the output  $o_{t-1}$ , as the output gets processed and the gap gets wider, RNNs can't connect current information and the information input in the distant past.

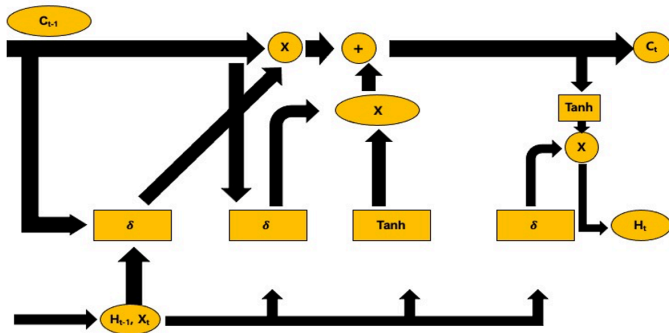


Figure 3: LSTM structure

An RNN, unlike an ANN (Artificial Neural Network), forms a loop so that information persists throughout the network. As illustrated in [Fig. 2], if there is a neural network A,  $x_t$  and output  $o$ , the RNN consistently inputs the element in  $x_t$  to the successor output  $o_t$ . Therefore, RNNs are adequate to process data in the form of chains or lists. Due to this trait, RNNs are frequently used in speech recognition and language modeling.

To deal with this problem, LSTMs have a rather complex structure and involve diverse linear interactions compared to their simple counterpart [17]. Fig. 3. shows the  $H_t$  of LSTMs. The upper arrow is where the cell state  $C_{t-1}$  is inputted. The upper arrow seems more straightforward than the arrows below. This shows that  $C_{t-1}$  faces minor interactions. Cell states are also passed through gates, structures that control whether to remove or add information to the cell state. Gates, which consist of a sigmoid layer and a pointwise multiplication operation, output values between 0 and 1. The higher the value, the more of its components are let through. An LSTM network has three such gates. To be

specific, the first layer, known as the 'forget gate layer', receives  $h_{t-1}$ , which is the output of the previous LSTM and  $x_t$ , the t-th input and returns values between 0 and 1, which shows how much of  $C_{t-1}$  should pass through. Next, another sigmoid layer, which is also known as the input gate layer, determines the values that will be updated. The tanh layer then makes new values  $\tilde{C}_t$ , which are candidates that can be added to the state. The sigmoid layer and the tanh layer are combined to create an update to the state. After going through the layers, the output that went through the first sigmoid layer  $f_t$  is multiplied by the old cell state  $C_{t-1}$ . Moreover, the output of the second output layer and the tanh layer are multiplied as well. The two outputs from the multiplications are then added. Finally, to decide the output, the final sigmoid layer and tanh decide which part of the cell state will be the outcome of the process.

The fact that LSTMs consistently make use of the necessary information is the key to making predictions. Time-series data, such as the data used in this research, can make good use of the LSTM characteristic in that they do not abandon data with a large enough time gap. Moreover, since they drop the information that doesn't seem vital to the prediction process, LSTMs suit well with Bitcoin prediction, which can contain noise in the data [18].

4. Experimentation & Evaluation

4.1. On-Chain Data Explanation

1) Data Preprocessing & Engineering

The necessary on-chain data and price data were extracted from CryptoQuant (www.cryptoquant.com) via an api access. CryptoQuant provides not only 'Reserve' and 'Exchange' data, but also provides data on the Bitcoin network and miners. However, it is important to note that the time frame of each datum can be different. Low-frequency (day) data were provided for most features, but high-frequency data such as hourly data were not provided for many features. Therefore, the experiment was based on low-frequency data to avoid having different time frames in the features. The data were first split into training, validation, and test sets. The training set consists of data from April 19th, 2019, to July 5th, 2020, which is a total of 444 days. The validation set and the test set are the data from July 6th, 2020, to November 30th, 2020, and December 1st, 2020 to April 27th, 2021, respectively, which sums up to 144 days each.

The most important part of the experiment was the scaling method. If the whole dataset is scaled at once, the 2-year length of data would be incapable of capturing the short-term trends which are apparent in the data. Thus, the scaling of the training data and the test data were done separately. The specific methodology to implement the scaling is illustrated in [Algorithm 1].

**Algorithm 1:** Algorithm for the scaling method

**Requirements:** Scaled Training Dataset, Test Dataset, Look Back Days

split features(X) and target(y) for both training and test datasets

make two new lists for features and target

# Making Training Dataset Suitable for LSTM

```

for i in range(from=lookback days, to=dataset length):
    append features[i-lookback:i] to features list
    append target[i] to target dataset

# test set scaling
make new empty an empty list for features and two new lists for target

for i in range(from=len(training data), to=len(whole data length)):
    standard scaling for features[i-look back:i]
    append to new features list
    standard scaling for target[i-lookback:i]
    append to new target list(for inverse-scaling)
    append target[i] to new target list2
    
```

#### 4.2. Hyperparameter Tuning & Validation

Table 2 shows the features that were selected after scaling the training set. The 10 features were selected using sklearn.model\_selection’s Select K Best setting the score function to mutual information. The prediction was done using Python’s Keras library. The data was scaled so that all values were between 0 and 1.

Table 2: 10 selected features

Feature	Definition	Feature Type
Exchange Reserve	Total Number of Bitcoins in Exchanges	Exchange Flows
Exchange Transactions Count Outflow	Total Number of Transactions flowing out of Bitcoin Exchanges	Exchange Flows
Addresses Count Inflow	Total Number of Addresses involved in Inflow Transactions	Exchange Flows
Fund Flow Ratio	The total BTC amount flowing into or out of exchanges divided by the total BTC transferred on the whole Bitcoin network	Flow Indicator
Estimated Leverage Ratio	Open Interest of Exchange divided by Exchange’s Bitcoin Reserve	Market Indicator
Stablecoin Supply Ratio	Ratio of the stablecoin supply in the whole cryptocurrency market.	Market Indicator
Miner’s Reserve	Total Number of Bitcoins Miners hold	Miner Flows
Miner’s Reserve in USD	USD total of Bitcoins Miners hold	Miner Flows
Open Interest	BTC Perpetual Open Interest from derivative exchanges.	Market Data
Hashrate	The mean speed at which miners in the network solve hash problems.	Network Data

Moreover, hyper-parameter tuning was done to make the results as accurate as possible. The model’s performance is evaluated using RMSE, MAPE, and R-squared, all of which are used frequently to measure the performance of regression models.

$$RMSE = \sqrt{\frac{\sum_{i=1}^n (y_{true(i)} - y_{pred(i)})^2}{n}} \tag{1}$$

$$MAPE = \frac{100}{n} \sum_{i=1}^n \left| \frac{y_{true(i)} - y_{pred(i)}}{y_{true(i)}} \right| \tag{2}$$

$$R^2 = 1 - \frac{\sum_{i=1}^n (y_{true(i)} - y_{pred(i)})^2}{\sum_{i=1}^n (y_{true(i)} - y_{mean})^2} \tag{3}$$

To optimize the model’s performance, hyperparameter tuning was performed using a grid search method. Specifically, we used scikit-learn’s GridSearchCV function to systematically search through different combinations of hyperparameters, including lookback day, epoch, batch size, unit, dropout rate, and optimizer, in order to identify the combination that produced the best results. GridSearchCV performs a search over a pre-defined parameter space, and returns the best combination of parameters based on cross-validation scores. In our study, the best combination of hyperparameters was found to be a lookback day of 3, an epoch of 30, a batch size of 128, a unit of 1, a dropout rate of 0.4, and the optimizer set to Nadam, which produced the highest scores for all three metrics.



Figure 4: Prediction Result (Full Data Length)

#### 4.3. Test Results & Evaluation

Table 4 shows the performance of the validation and test predictions. During the validation process, the RMSE, MAPE, and R<sup>2</sup> results were 457, 2.267%, and 0.968, respectively. In the test set prediction, the RMSE, MAPE, and R<sup>2</sup> results were 2344, 4.316%, and 0.971, respectively. There was some gap between the performance between the validation and the test prediction. A possible

explanation for this would be the variation of the Bitcoin price during the validation set's data and the test set's data. Starting from December of 2020, Bitcoin's price started its rally and almost tripled from 20,000 U.S dollars to 65,000 U.S dollars, while during July to November of the same year, Bitcoin price was in the price range between 10,000 U.S dollars to 20,000 U.S dollars. Moreover, the participation of institutions in the market might have influenced the data during the test set's time-period.

Table 4: validation/test evaluation

Evaluation Metrics	Validation	Test
RMSE	436.894	2162.380
MAPE	2.074%	3.993%
R <sup>2</sup>	0.971	0.976

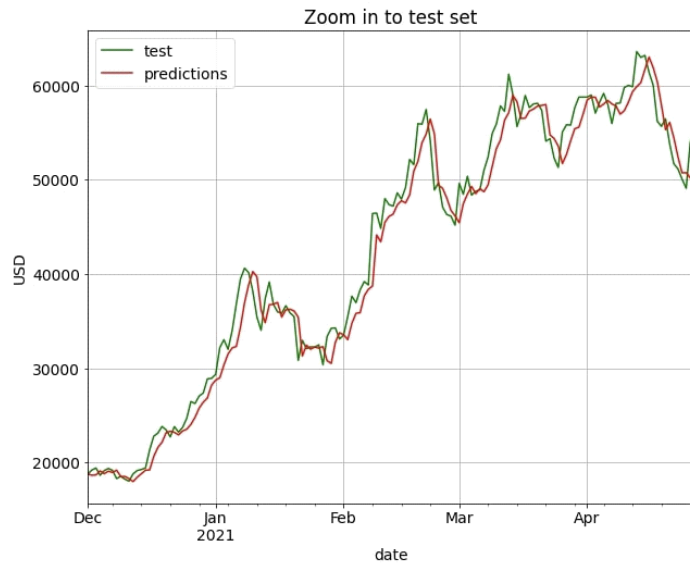


Figure 5: Comparison Between Prediction Results and Actual Data

### 5. Conclusion

This research was based on Bitcoin's on-chain data provided by CryptoQuant. The results show that on-chain data might be of good use when predicting the movement of Bitcoin's price rather than traditional factors such as macro-economic data. Although data such as hashrates were used in previous studies, better performance might be drawn from the movement of Bitcoin in the exchange's reserve or the miners' wallets, which were data that were not previously used to forecast Bitcoin's price movement. Although, such data are not yet utilized as much, the use of deep-learning algorithms such as LSTM with on-chain data might provide a good guideline of where Bitcoin's price will be in the near-future. However, this work should be extended in some way, e.g., by comparing the performance of different deep learning models and/or classical non-deep learning-based models.

This research made use of various on-chain data, but there still are some on-chain data that were not available because of

budget restraints but might be useful for prediction. Especially, the movement of 'whales' who hold more than 1,000 bitcoins is suspected to have a tremendous impact in Bitcoin's price and can be subject to further research. Furthermore, if on-chain data and macro-economic variables are used together for prediction, there is a possibility of improvement in the prediction performance.

In addition, prediction using high-frequency data can also be a valid research topic. Especially when day-trading is such a huge part of the Bitcoin market. Using high-frequency data for prediction can lead to higher profits for those who invest in Bitcoin.

Finally, using other cryptocurrencies and their on-chain data for price prediction needs further research as well. Other cryptocurrencies have important data of their own. Cryptocurrencies that use Proof of Stake as a validation method do not have data such as hashrate and difficulty. Thus, other data in their blockchains need to be extracted to make a solid prediction of their prices.

### Acknowledgment

This work was supported by the National Research Foundation of Korea (NRF) grant funded by the Korean government (MSIT) (No. NRF-2022R1F1A1074696).

### References

- [1] T. Bradshaw, "Apple ad for 'alternative payments' job signals cryptocurrency interest", *The Financial Times*, May 27, 2021.
- [2] A. Inamdar; A. Bhagtani; S. Bhatt; P. M. Shetty, "Predicting Cryptocurrency Value using Sentiment Analysis", *International Conference on Intelligent Computing and Control Systems (ICCS)*, 2019, doi:10.1109/ICCS45141.2019.9065838
- [3] J. Lee, K. Kim, and D. Park, "Empirical Analysis on Bitcoin Price Change by Consumer, Industry and Macro-Economy Variables", *Journal of Intelligence and Information Systems*, **24**, 2018, doi:10.13088/jiis.2018.24.2.195
- [4] A. Aggarwal, I. Gupta, N. Garg and A. Goel, "Deep Learning Approach to Determine the Impact of Socio Economic Factors on Bitcoin Price Prediction", *Twelfth International Conference on Contemporary Computing (IC3)*, 2019, doi:10.1109/IC3.2019.8844928
- [5] S. Ilie DRAGOE, C. OPREAN-STAN, "BITCOIN, THE MOTHER OF ALL BUBBLES OR THE FUTURE OF MONEY?", *International Conference KNOWLEDGE-BASED ORGANIZATION*, 2020, doi:10.2478/kbo-2020-0046
- [6] A. Baig, B. M. Blau and N. Sabah, "Price clustering and sentiment in bitcoin", *Finance Research Letters*, **29**, 2019, doi:10.1016/j.frl.2019.03.013
- [7] S. Pyo, J. Lee, "Do FOMC and macroeconomic announcements affect Bitcoin prices?", *Finance Research Letters*, vol. **37**, 2020, doi:10.1016/j.frl.2019.101386
- [8] K. Lee, S. Cho, G. Min and C. Yang, "The Determinant of Bitcoin Prices in Korea", *Korean Journal of Financial Studies*, **47**, 2019, doi:10.26845/KJFS.2019.08.48.4.393
- [9] Kim, Gyeongho & Shin, Dong-Hyun & Choi, Jaegyong & Lim, Sunghoon. "A Deep Learning-Based Cryptocurrency Price Prediction Model That Uses On-Chain Data." *IEEE Access*. **10**. 56232-56248, 2022, doi:10.1109/ACCESS.2022.3177888.
- [10] G. S. Atsalakis, I. G. Atsalaki, F. Pasiouras, C. Zopounidis, "Bitcoin price forecasting with neuro-fuzzy techniques", *European Journal of Operational Research*, **276**, 2019, doi:10.1016/j.ejor.2019.01.040
- [11] S. Oikonomopoulos, K. Tzafilkou, D. Karapiperis and V. Verykios, "Cryptocurrency Price Prediction using Social Media Sentiment Analysis," *International Conference on Information, Intelligence, Systems & Applications (IISA)*, Corfu, Greece, 2022, doi:10.1109/IISA56318.2022.9904351.
- [12] S. McNally, J. Roche and S. Caton, "Predicting the Price of Bitcoin Using Machine Learning," *2018 26th Euromicro International Conference on Parallel, Distributed and Network-based Processing (PDP)*, 2018,

doi:10.1109/PDP2018.2018.00060

- [13] D. C. Mallqui and R. A. Fernandes, "Predicting the direction, maximum, minimum and closing prices of daily Bitcoin exchange rate using machine learning techniques", *Applied Soft Computing*, **75**, 2019, doi:10.1016/j.asoc.2018.11.038
- [14] Z. Chen, C. Li and W. Sun, "Bitcoin price prediction using machine learning: An approach to sample dimension engineering", *Journal of Computational and Applied Mathematics*, **365**, 2020, doi:10.1016/j.cam.2019.112395
- [15] M. Schuster and K. K. Paliwal, "Bidirectional recurrent neural networks," in *IEEE Transactions on Signal Processing*, **45**, 1997, doi:10.1109/78.650093.
- [16] Tehseen Zia and Usman Zahid. "Long short-term memory recurrent neural network architectures for Urdu acoustic modeling." *Int. J. Speech Technol*, **22**, 21–30, 2019, doi:10.1007/s10772-018-09573-7
- [17] F. Valencia, A. Gómez-Espinosa, B. Valdés-Aguirre, "Price Movement Prediction of Cryptocurrencies Using Sentiment Analysis and Machine Learning", 2019, doi:10.3390/e21060589
- [18] A Kim, Jongyeop & Wimmer, Hayden & Liu, Hong & Kim, Seongsoo, "A Streaming Data Collection and Analysis for Cryptocurrency Price Prediction using LSTM.", in *2021 IEEE/ACIS 6th International Conference on Big Data, Cloud Computing, and Data Science (BCD)*, 45-52. 2021, doi:10.1109/BCD51206.2021.9581491.

## Investigation of Swimming Behavior and Performance of the Soft Milli-Robots Embedded with Different Aspects of Magnetic Moments

Xiuzhen Tang, Laliphat Manamanchaiyaporn\*

Center of Excellence in Creative Engineering Design and Development, Department of Mechanical Engineering, and Research Unit of Multi-Scale Robotics, Thammasat School of Engineering, Faculty of Engineering, Thammasat University, Thailand

### ARTICLE INFO

Article history:

Received: 28 February, 2023

Accepted: 05 May, 2023

Online: 25 June, 2023

Keywords:

Magneto-elastic actuator

Soft-robotics

Magnetic manipulation

### ABSTRACT

Among the development of technology, a large number of medical devices have been implemented in various forms for therapy and treatment. Remote controllability, real-time response, small size, and non-toxicity of the devices are the critically requirement to be operated in the blind, unstructured and fluidic environments of biomedical regions. Untethered soft swimming milli-robots have been developed to fulfill the remote operation in such that region under magnetic navigation. A motor-less mechanism of the soft robots utilizes a high degree of freedom provided by magnetic compliance of the deformable structure with a minimal control of the oscillating magnetic field. Theoretically, magnetic property of the soft robots is defined by magnetic moments consisting of orientation and strength. Orientation of magnetic moments can be defined by magnetizing technique, and strength of magnetic moments is obtained by their quantity in the magnetic structure. Herein, this work investigates how magnetic moments through the details of magnetic orientation and quantity affects swimming behavior and performance. The soft robots are fabricated with elastomer embedded with NdFeB microparticles to obtain three types of distinguish magnetic property in the deformable structure; the I robot has non-uniform magnetic orientation and uniform magnetic strength, the II robot has uniform magnetic orientation and non-uniform magnetic strength, and the III robot has non-uniform magnetic orientation and non-uniform magnetic strength. The results interestingly report that each type of robot's property functions mechanism and benefits swimming performance differently under the same magnetically control parameters. The I robot does not have any exceptional potential, but the II robot can be operated at the higher control frequency even reaching the step-out point. The III robot shows the greatest performance in swimming and maneuverability. These results would be useful to design a swimming soft-robot capable of applying for various purposes, especially when the demand concerns non-harm, small-scale size, soft interface and remote controllability.

### 1. Introduction

This paper is an extension of work originally presented in the eighth (8<sup>th</sup>) edition in the series of the International Conference on Control, Decision and Information Technologies, CoDIT'22 [1], in order to clarify how orientation and quantity of magnetic moments affect the in-fluid swimming potential of the soft robots.

Our body inside is a fantastic and complex system consisting of the circulation of diverse biological fluids and unstructured

environments. Untethered miniature robots with millimeter scale or less have been promising to access the hard-to-reach biomedical regions for minimally invasive treatments (e.g., targeted drug delivery, biopsy) [2]. Due to the small size of the robot, the battery and motion mechanism were unable to set up inside the robot's structure. In order to function locomotion of the robots, active elements to respond with the external power sources were embedded in their body instead, during the fabrication process. Some types of the robots received the light emission pulse to transform its structure for mobility. Another type of robots employed the chemical reaction with the surrounding

\* Corresponding Author: Laliphat Manamanchaiyaporn, [mlalipha@engr.tu.ac.th](mailto:mlalipha@engr.tu.ac.th)

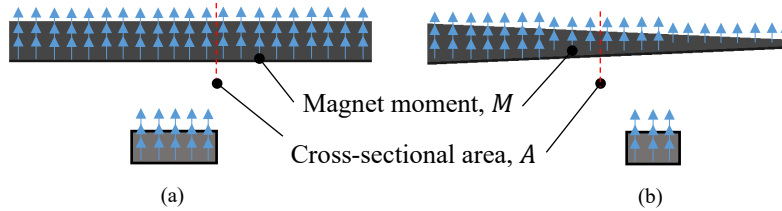


Figure 1: The different magnetic property of magnetic-soft structure between previous works and this work (a) uniform distribution of magnetic moments, (b) non-uniform distribution of magnetic moments

environment for propulsion. Other types of robots holding magnetic property were active after experiencing the actuating magnetic field. Each of robots has own mechanism functioned by particular active elements to create locomotion in environments.

The use of magnetic field was proved no harm to human tissue, especially affording the clinical imaging (e.g., MRI). It was one of the most selective sources to remotely manipulate robots. In order to generate magnetic energy to manipulate the robots, magnetic actuation systems were specifically designed in diverse configurations with a variety of control techniques (e.g. magnetic navigation in a large workspace) [3]. Once the actuation system generated magnetic field, the magnetic property of the robots as called magnetization responded with such that actuation through magnetic alignment. This concept allowed the robot to have effective locomotion via motor-less mechanism [4].

In life, environments are mostly viscous, which is hard for matters to perform motion, but microorganism-inspired robots adopt the asymmetric body movement with solid components as a key of success in fluidic maneuverability to swim effectively (e.g. beating or waving of flagella or cilia, helical propulsion) [5, 6], but having a solid structure limits safe interaction. The transition from a hard structure to a soft structure is wide-opening to fabricate swimming tiny robots by using materials embedded with functional elements. The integration of magnetic particles into the deformable structure enables controllability, leading to continuous and controllable movement under magnetic actuation due to magnetic alignment of magnetic moments within specimens of the structure. This aspect allows medical tools and medical robots to become more deformable and dexterous in various types of biomedical application (e.g. compliant-soft

medical tools, flexible wearable devices) [7]-[10]. Moreover, having a deformable structure benefits a soft interface to greatly deal with uneven terrains and unstructured geometry without harmfulness [11, 12]. Such that soft structure with additional matters (e.g., drug molecule, chemical nanoparticles) still fulfil the remote applications in medicine, such as drug delivery, biopsy, detoxification [13]-[16].

In previous research, there were soft robots employing only anisotropic magnetization or non-uniform magnetic orientation to generate the body movement based on the continuous alignment of magnetic moments with the dynamic magnetic field. The deformation degree of each specimen of the robot’s structure is equal and uniform because the distribution of magnetic moments is uniform across the whole soft structure, resulting in uniform magnetic strength. However, property of magnetic moments embedded in the soft structure still remains a challenge in the core detail. Magnetic moment typically comprises of orientation and strength, and what if they are not uniform across the whole deformable structure. In this paper, effect of orientation and strength of magnetic moments in the deformable structure of the soft robot is investigated in term of swimming behavior and performance based on lateral undulation. Three types of soft milli-robots are fabricated; the I robot: uniform magnetic strength and non-uniform magnetic orientation, II: non-uniform magnetic strength and uniform magnetic orientation, and III: non-uniform magnetic strength and orientation.

Those robots having the magnetically deformable structure utilizes high-degree of freedom provided by magnetic compliance as if motor-less mechanism set up inside, and they become more dexterous, especially in the applications of biomedicines (e.g.

Table 1: Raw materials and tools

Material	Property	Function
Liquid silicone rubber: LSR (SIMTEC)	Density: 1.13 g/cm <sup>3</sup> , Young modulus: 300 kPa, temperature resistance: -50 to 250 °C, tensile strength: 1.5 MPa, elongation at break: 700%	Base material to form a soft structure
NdFeB (Neodymium) magnetic microparticles	Particle size: 4 μm to 40 μm, density: 7.57 g/cm <sup>3</sup> , Remanence: 720-760 mT, coercivity: 360-480 A/m, magnetic energy: 80 to 98 kJ/m <sup>3</sup>	Active elements; base material to respond to magnetic actuation
A stainless-iron plate	30 mm x 100 mm with 80 μm ± 10 μm cavity	A mold doe the mixture to fabricate a magnetic-soft sheet
A shape guider	PLA (Polylactic Acid) 3D-printed parts with sinusoidal profile* ( $\sin(\frac{2\pi l}{\lambda})$ ) at the inner surface	To constraint a magnetic-soft sheet before applying a magnetizing magnetic field to specific magnetic orientation of magnetic moments

\* Profile to specify orientation of magnetic moments can be adjusted to any form.

compliant robotics, flexible medical tools). In particular, in order to operate the robot for treatment and therapy, potential of the robot to swim in fluidic and wet environments is a critical requirement.

Methods and materials are detailed in the next section. Next, experiments are conducted to test performance in swimming of the robots in fluid under the change in controlled parameters. Finally, the conclusion is issued.

## 2. Material and Method

### 2.1. Conceptual design

In the case that the size of a matter moving in media is millimeter or less, inertia term is dominated over viscous term, resulting in low Reynold number condition ( $Re < 1$ ). Purcell stated that one of feasible motion patterns for small objects to effectively move in fluid was the use of the asymmetric body deformation under time-reversal [17]. Consequently, liquid silicone rubber (LSR) as a base material is used to obtain a deformable property, and magnetic particles is filled in order to respond with magnetic actuation. The combination of them leads to a controllable-deformable structure under magnetic field. This aspect results a motor-less mechanism in a soft small-scaled robot remotely controlled by the dynamic magnetic field to serve as a medical device.

Theoretically, magnetic moment or magnetic dipole is a vector that consists of magnitude and direction. It can be played in the detailed to define a specifically magnetic property. The soft milli-robot is designed to have three types of distinguish magnetic property; the I robot is with uniform magnetic strength and non-uniform magnetic orientation, the II robot is with non-uniform magnetic strength and uniform magnetic orientation, and the III

robot is with non-uniform magnetic strength and orientation. Based on the modeling of magnetism [18], magnetic moment in a structure can be expressed by

$$\vec{m} = \iiint M dV = \iiint M dAdl \tag{1}$$

where  $A$ ,  $l$ ,  $M$  are respectively the cross-sectional area, length of the structure, and magnetization which is a quantity of magnetized magnetic moment in a concerned volume,  $V$ . Thus, the existence of magnetic moment, according to Figure 1a and the definition of the eq. (1), can expressed that each specimen of the soft rectangular structure has the uniform magnetic orientation which points upward, and the uniform magnetic strength due to having equal number of the moments.

Otherwise, in Figure 1b, the existence of magnetic moment expresses that each specimen of the soft triangular structure has the uniform magnetic orientation which directs upward, but magnetic strength is non-uniform due to unequal number of magnetic moments along the length of the structure. The specimen where is the biggest cross-sectional area contains the strongest magnetic strength, but at the smallest area, magnetic strength is the weakest. Thus, the eq. (1) is rewritten to

$$\vec{m}(x) = \iiint M(x) dV(x) = \iiint M(x) dA(x) dl \tag{2}$$

Eq. (2) expresses that at a position,  $x$ , on the length,  $l$ , if cross-sectional area across the length of the structure is unequal, magnetic moments at each position is different along the length, resulting in non-uniform magnetic strength.

### 2.2. Fabrication process

In this work, three-type property of the soft robot is modified with the existence of magnetic moments in the soft structure. List

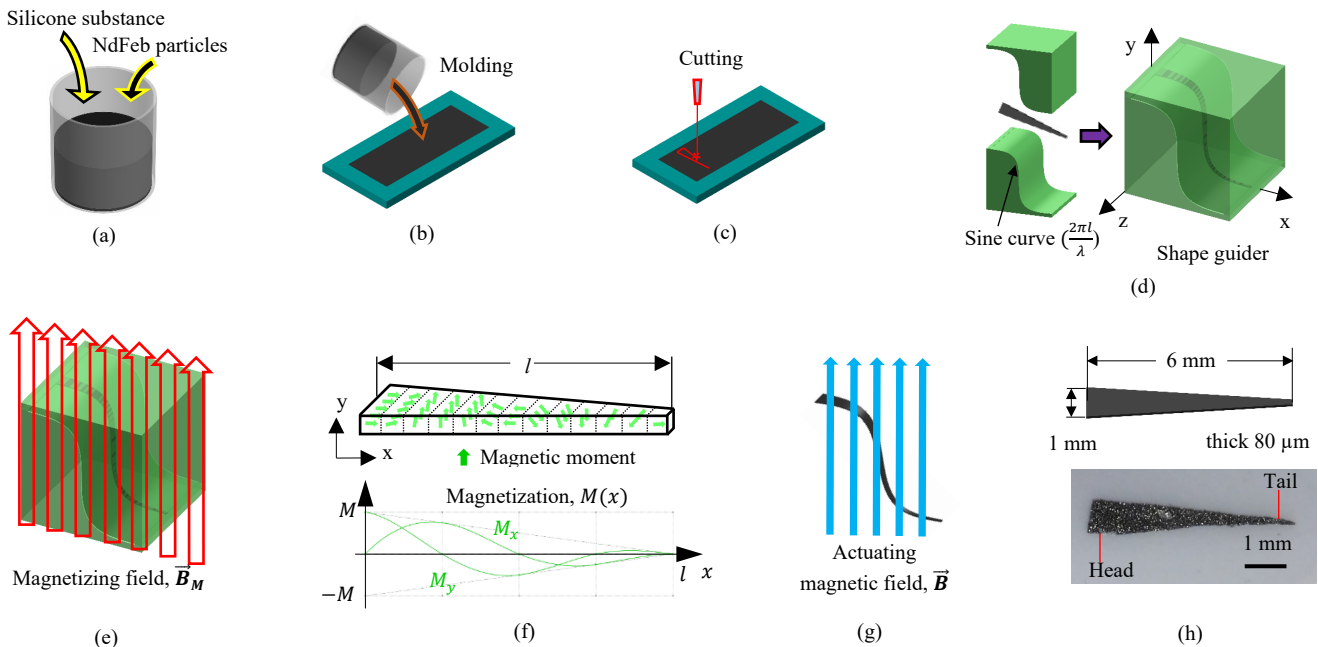


Figure 2: Example of fabricating the III robot. (a) Liquid silicone substances and NdFeb particles with 1:1 of mixing ratio. (b) molding on the stainless-steel plate, then subjects it to heat curing. (c) cutting into a triangular shape. (d) inserting into the sinusoidal-surface shape guider. (e) 700 mT of uniform magnetizing magnetic field. (f) magnetization profile of the film robot: (upper) magnetic orientation. (lower) magnetic strength decreases by increasing the body length. (g) the robot responding to the actuating magnetic field. (h) the triangular body: 1 mm × 6 mm × 80 μm.

Table 2: Three types of soft swimming milli-robots

Type	Width ( $w$ ) Length ( $l$ ) Thick ( $h$ )	Shape	Profile of magnetic direction*	Magnetic strength**	Magnetic response***
I	1 mm 6 mm 80 $\mu$ m	Triangular	Sine 	Uniform 	
II	1 mm 6 mm 80 $\mu$ m	Rectangular	Transverse 	Non-uniform 	
III	1 mm 6 mm 80 $\mu$ m	Triangular	Sine 	Non-uniform 	

\* A set of arrows depicts the direction of magnetic moments, and its quantity refers to magnetic strength in the robot's structure.

\*\* A graph shows the relation of magnetic strength and magnetic orientation of magnetic moments as a function of body length.

\*\*\* Blue hidden line represents the original shape of teach robot before magnetic deformation due to alignment of magnetic moments with respect to the direction of the actuating magnetic field.

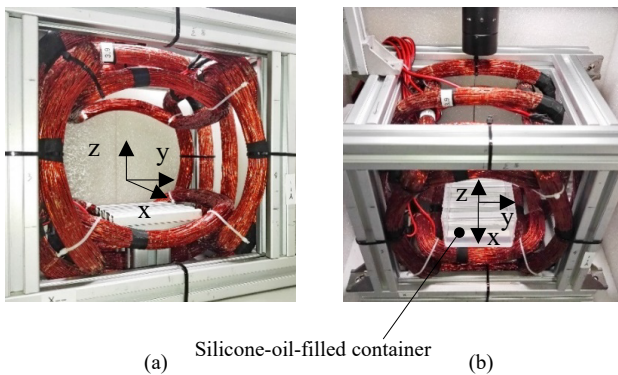


Figure 3: Magnetic actuation system. (a) It generates uniform-based field across the large bore. (b) a silicone-filled container as a workspace inserted into the bore.

of the main materials is reported on Table 1. In Figure 2, the robot fabrication starts from the mixing of liquid silicone rubber and NdFeB magnetic microparticles with the 1:1 mass ratio. Later, pouring the mixture into a stainless-steel mold with 80  $\mu$ m cavity to form a magnetic soft sheet with 80  $\mu$ m thickness, and putting the mold to cure at 250  $^{\circ}$ C about 8-10 minutes. Finally, getting a magnetic soft sheet to prepare for making a magnetic-soft robot.

At this step, the finishing is the sheet embedded with magnetic elements across the whole volume, but its magnetic property is still not defined. In order to specify the direction of all magnetic moments, the sheet must be subjected to the 700-mT magnetizing magnetic field,  $\vec{B}_M$ . For example, if the direction of magnetic moments is similar to a wave, the sheet must be confined into the wave pattern, and then placing it into the  $\vec{B}_M$  for permanent direction. Once removing it from the  $\vec{B}_M$ , the direction of magnetic moments follows as the wave across the whole volume permanently.

According to the eq. (2), uniform or non-uniform magnetic strength across the whole volume can be defined by the shape of the structure. For example, if the structure is symmetric as a rectangle, quantity of magnetic moments at each specimen will be equal across the whole length, resulting in uniform magnetic strength of magnetic moments. Otherwise, if being triangular, the cross-sectional area is not equal across the length, resulting in non-uniform magnetic strength of magnetic moments. As depicted in Figure 1, at the same position on the length, quantity of magnetic moments is different between two shapes. In Figure 3, after getting a desire shape, the sheet is cut into a triangular shape. Then, it is placed into a shape guider to form a sine-based



curve, and subjected into the  $\vec{B}_M$  to profile the magnetic orientation of magnetic moments embedded in the triangular sheet. In this case, if it is actuated by magnetic field, the triangular sheet self transforms into a wave shape or a body wave deformation. Finally, the magnetic-soft sheet becomes a magnetic-soft robot. In this work, the robot is fabricated into three types to have different property of magnetic moments according to the Table 2.

### 2.3. Actuation and control procedure

The magnetic actuation system shown in Figure 3 consists of seven electromagnetic coils to achieve 3D-magnetic field in order to cover 6-DOF motion of the soft robot. It provides three directions of homogeneous magnetic field across a cylindrical workspace (radius: 7.5 cm and length: 18 cm). This aspect guarantees a pure magnetic torque exerted to actuate the soft robots without any drifting caused by the wrench of magnetic force. Each coil is individually operated by seven current drivers (Dimension engineering; 25 kHz, 30V/10A), and electrically supplied by SIEMENS GR60 (40A/48V). A custom controller with 8-bit-packeted-serial communication commands the drivers to pass electrical current into the coils to generate magnetic field. A stationary CMOS camera with zoom lens (working distance: 6-120 mm and 1.6-mm depth-of-field) is mounted to observe locomotion of the robot, and localize the robot's position to feedback the coordinate into the control algorithm in order to adjust a proper magnetic field. Maximum magnetic field is 25 mT and 100 T/m at 15 A input electrical current, measured by a gaussmeter GM-08 Hirst.

The magnetic-soft robot responds to magnetic actuation due to having magnetic moments,  $\vec{m}$ , as active elements embedded in the soft structure. It acts as a motor-less mechanism to make the robot swim in fluid. Depicted in Figure 3, the electromagnetic actuation system [3] is specifically designed to power the robot by using three-dimensional magnetic field,  $\vec{B}$ , which is

$$\vec{B} = [B_x \ B_y \ B_z] \quad (3)$$

Once the robot is under magnetic field, its soft body is deformed toward the direction of the magnetic field due to an

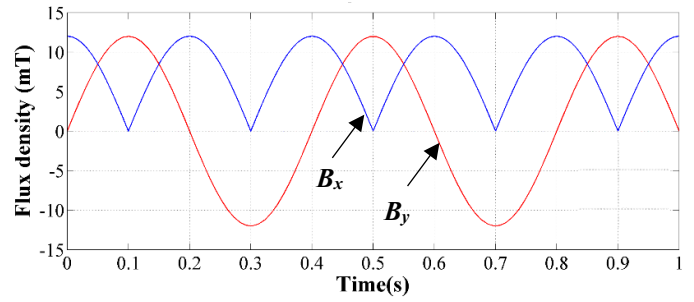


Figure 4: Signal sample of the x- and y-magnetic field,  $B_x$  and  $B_y$ , generates oscillating magnetic field with 2.5 Hz.

alignment of magnetic moments across the volume. Magnetic torque,  $\vec{T}$ , and force,  $\vec{F}$ , are exerted to the robot, expressed by

$$\vec{F}(x) = \nabla(\vec{m}(x) \cdot \vec{B}) \quad (4)$$

$$\vec{T}(x) = \vec{m}(x) \times \vec{B} \quad (5)$$

Magnitude and direction of magnetic field is adjustable by using the superposition technique resulting from sources of magnetic field. In this work, the oscillating magnetic field is applied to manipulate the deformable structure of the robot continuously, leading to the body wave propagation or undulation as if swimming. The oscillating magnetic field is a product of the superposition of the magnetic field in the x- and y-direction,  $B_x$  and  $B_y$ , which oscillates with frequency,  $f$  (Hz: cycle number in a second). As shown in Figure 4 of the signal sample, the eq. (3) is rewritten by

$$\vec{B}(t) = B[\cos(2\pi ft) \ \sin(2\pi ft) \ 0]^T \quad (6)$$

Frequency and magnitude of the oscillating magnetic field in the eq. (6) are adjustable by varying magnitude and direction of the electric input current supplied into each electromagnetic coil.

### 2.4. Modeling of deformation

Regarding the soft property of robots, Euler-Bernoulli beam theory is adopted to determine the local body deformation caused by magnetic field, depicted in Figure 5. Once magnetic torque,  $T$ , as bending moment,  $M_b$ , is exerted to the robot, expressed by

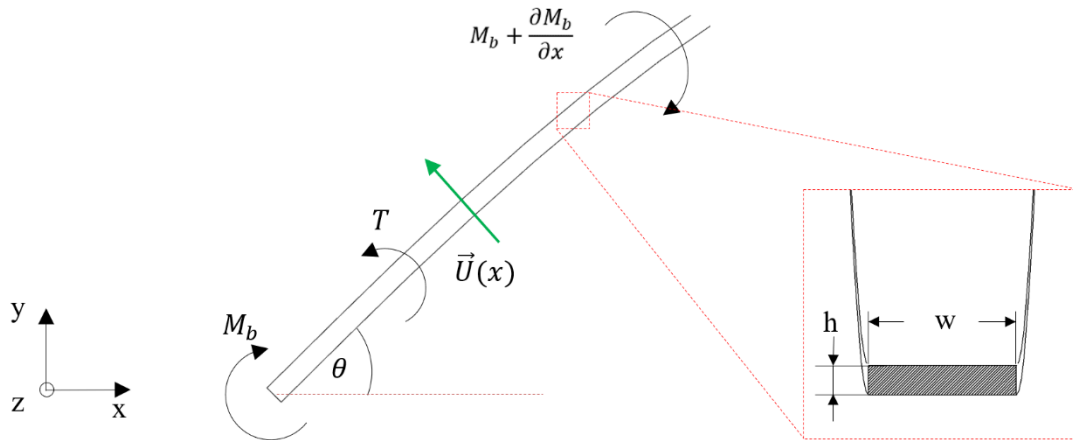


Figure 5: Physical interpretation of a deformable structure. When magnetic torque is exerted to deform a soft robot long,  $l$ , its local body segment,  $x$ , with thickness,  $h$ , and width,  $w$ , is bent with angle,  $\theta$ , resulting in the moving of each local segment with velocity,  $\vec{U}(x)$ .

$$\mathbf{T}(x) = \mathbf{M}_b = -EI \frac{\partial^3 \theta}{\partial x^3} \quad (7)$$

where  $E$  is Young modulus of the robot (Pa),  $\theta$  is bending angle defined by deformation degree over length estimated by  $\theta = \frac{\partial y}{\partial x}$ , and  $I$  is area moment of inertia ( $m^4$ ) which is a function of the thickness,  $h$ , and width,  $w$ . When the body of robot is long,  $l$ , the area moment of inertial at each local body becomes a function of the unit length,  $x$ , of the full length,  $l$ , expressed by

$$I(x) = \frac{h^2 h w}{12} = \frac{h^2 A}{12} \quad (8)$$

where  $A$  is cross-sectional area at the  $x$  position on the body length  $l$ . Substituting the eq. (5) and the eq. (8) in the eq. (7), so

$$(\overline{\mathbf{m}}(x) \times \overline{\mathbf{B}}) = -E \frac{h^2 A}{12} \frac{\partial^3 y}{\partial x^3} \quad (9)$$

$$y(x) = - \iiint \frac{12}{h^2 E A} (\overline{\mathbf{m}}(x) \times \overline{\mathbf{B}}) \partial x^3 \quad (10)$$

As mentioned, considering that the whole body of the robot consists of many magnetic domains. Magnetic moment,  $\overline{\mathbf{m}}$ , at a specimen or a local is a function of magnetization and cross-sectional area. The eq. (10) expresses that deformation of a specimen at the position  $x$ , on the body length depends on magnitude and direction of magnetic moment significantly. Differentiating the eq. (10) over time to obtain swimming velocity,  $\overline{\mathbf{U}}$ , at that local, is expressed by

$$\begin{aligned} \overline{\mathbf{U}}(x) &= - \frac{3fBM\lambda^3}{\pi^2 h^2 EA} \left[ \sin \left( \frac{2\pi x}{\lambda} - 2\pi ft \right) \right] \\ \text{and} \quad \overline{\mathbf{U}}(x) &= + \frac{3fBM\lambda^3}{\pi^2 h^2 EA} \left[ \sin \left( \frac{2\pi x}{\lambda} + 2\pi ft \right) \right] \end{aligned} \quad (11)$$

where  $f$ ,  $B$ ,  $M$ ,  $\lambda$ ,  $E$ ,  $t$  is the oscillating frequency, magnetic field, magnetization, body wavelength, Young modulus of material, oscillating time respectively. Positive and negative sign express the deformation direction of a specimen of the body. From the eq. (11), in short, the swimming velocity,  $\overline{\mathbf{U}}$ , is proportional to magnitude and direction of magnetic moment which is a function of magnetization,  $M$ , at that specimen.

### 3. Experiments and Results

As mentioned, a key to have an effective swimming in fluid for a small-scaled robot is the use of an asymmetric body deformation, and the robots in this work follow such that concept utilizing a deformable structure triggered by magnetic field. The magnetic-soft robots are fabricated into three types, according to Table 2, and they are experimentally investigated in the term of swimming behavior and performance.

Experiments are all set up under the same parameters and conditions. Three types of the robots are all fabricated under the same process, but different in the post-fabrication, which is the cutting process to define quantity of magnetic moments via the final shape, and the magnetizing process to program the orientation of magnetic moments. A tank contains silicone oil to simulate viscosity of biological fluid, and it is inserted into the bore of the magnetic actuation system, depicted in Figure 3b. The system generates the oscillating magnetic field with three numbers of magnitude (5, 10, 15 mT) and fifteen numbers of

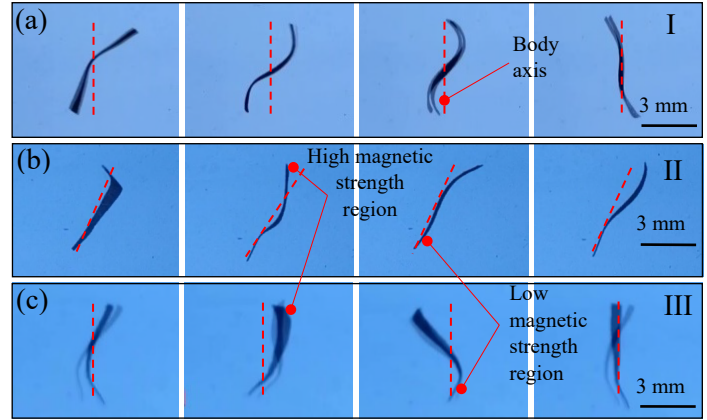


Figure 6: Swimming behavior of three robots holding different magnetic property. (a) The I robot symmetrically deforms as a wave. (b) The II robot sweeps at a specimen of high magnetic strength. (c) The III robot propagates a body wave along the body length.

frequency (1 to 15 Hz) to manipulate three types of the soft milli-robot.

#### 3.1. The I robot

The I robot has a property of uniform magnetic strength and non-uniform magnetic orientation due to having a rectangular film shape ( $1 \text{ mm} \times 6 \text{ mm} \times 80 \text{ }\mu\text{m}$ ) and being magnetized with the sine profile, detailed in Table 2. Thus, its magnetic property is modeled by

$$\overline{\mathbf{M}}_I(x) = [M_x \quad M_y \quad 0]^T = M_I \left[ \cos \frac{2\pi x}{\lambda} \quad \sin \frac{2\pi x}{\lambda} \quad 0 \right]^T \quad (12)$$

The eq. (12) clearly details that magnetic orientation of the robot follows the sine profile depicted by the direction of arrows varying as a wave, and magnetic strength is uniform, depicted by number of arrows which is symmetric at each column along the body length.

Depicted in Figure 6a, once the I robot is actuated by the oscillating magnetic field, the magnetic moments embedded in the soft structure aligns with respect to the direction of the magnetic field, leading to the body deformation, and the deforming shape of the robot turns to be a sinusoidal curve. Next, when the direction of magnetic field oscillates with a frequency, the body of the robot is continuously deformed with respect to the oscillation of magnetic field under the same frequency, resulting in a lateral undulation, leading to swimming in fluid. It is noticed that the deformation of the robot is symmetric, and all of magnetic specimen in the structure simultaneously responds to the magnetic field at the same time because magnetic strength in each specimen is uniform.

#### 3.2. The II robot

The II robot holds a property of non-uniform magnetic strength and uniform magnetic orientation, due to having a triangular shape ( $1 \text{ mm} \times 6 \text{ mm} \times 80 \text{ }\mu\text{m}$ ), detailed in Table 2. Number of magnetic moments in the triangular shape decreases along the body length, according to the eq. (2), resulting in non-

uniform strength across the whole structure. The larger the volume, the stronger the magnetic strength. It is magnetized to have the direction of magnetic moments aligned in the same direction, resulting in uniform magnetic orientation. Its magnetic property is expressed by

$$\vec{M}_{II}(x) = [0 \quad M_y \quad 0]^T = M_{II}[0 \quad 1 \quad 0]^T \quad (13)$$

The eq. (13) expresses that magnetic strength of the II robot is a function of a position along length  $l$ , and the magnetic moments all point to the y direction. Under this condition, once the robot is magnetically actuated, a specimen has a stronger magnetic strength firstly respond, and when the magnetic field is stronger, a specimen has a lower magnetic strength orderly follows. Thus, under the oscillating magnetic field with constant magnitude, the robot sweeps its body with respect to the oscillation of the magnetic field, making the robot propel as shown in Figure 6b.

### 3.3. The III robot

The III robot has a property of both non-uniform magnetic strength and orientation. Same to the II robot, number of magnetic moments varies along the body length due to having a triangular shape. It is maximum at the largest cross-sectional area, but minimum at the smallest area, resulting in non-uniform magnetic strength. The direction of magnetic moments aligned with respect to a sine curve, same to the I robot, resulting in non-uniform magnetic orientation. Its magnetic property can be expressed by

$$\vec{M}_{III}(x) = [M_x \quad M_y \quad 0]^T = M_{III} \left[ \cos \frac{2\pi x}{\lambda} \quad \sin \frac{2\pi x}{\lambda} \quad 0 \right]^T \quad (14)$$

The eq. (14) explicitly expresses that both magnetic orientation and strength are varying along the body length. Once the III robot is actuated by magnetic field, its body deforms as a curve, but the magnetic response of specimen where contains a higher magnetic strength is prior to another specimen where contains a lower magnetic strength. Under the oscillating magnetic field, it propagates the body as if a body waving for swimming interestingly and smoothly, depicted in Figure 6c.

### 3.4. Comparison in swimming behavior and performance

Under the actuation of oscillating magnetic field, each of robots (I, II, III) shows its own specific mechanism to swim in fluid. Magnetic alignment of magnetic moments embedded in the soft structure of each robot draws the deformable pattern differently due to being magnetized with the different profile. Sine profile magnetization causes a body wave propagation for the robot, resulting in more effective swimming, as appeared in the I and III robot. However, in experiments, one more interestingly magnetic aspect in the soft structure is figured out that quantity of magnetic moments has an influence to define the response degree to external magnetic actuation. If higher, magnetic strength is stronger, resulting in a fast response. If lower, magnetic strength is weaker, resulting in a slow response. When both high and low magnetic strength are together in one soft structure, leading to unequal magnetic strength of each specimen. Magnetic response of the entire body is different, and active orderly from the high to low magnetic strength. As apparent in the magnetic response of the I and III robot, both is profiled by sine pattern, but magnetic strength is different. The I robot transforms the entire soft body to

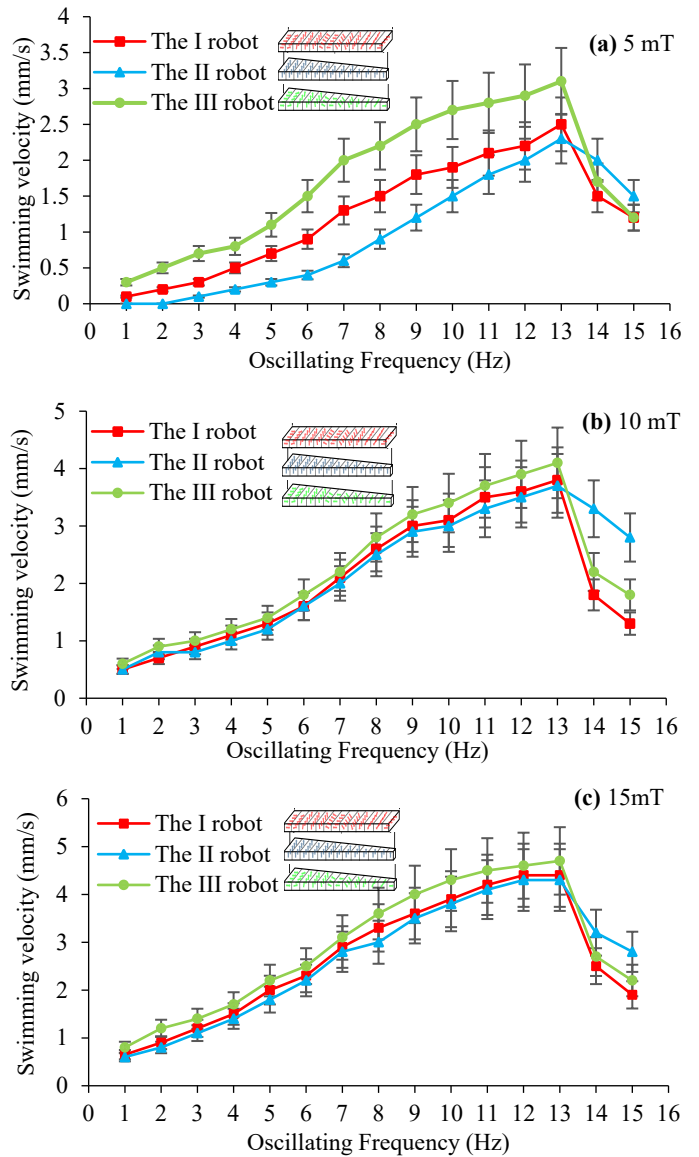


Figure 7: Under (a) 5 mT, (b) 10 mT, (c) 15 mT of magnetic field, the plot of swimming velocity against the different numbers of the oscillating frequency (ranged from 1 to 15 Hz). Three robots are powered by those input parameters to swim in fluid. The robots all swim faster with the increase of the actuating frequency, and drops after reaching the step-out point at 13 Hz.

a curve pattern immediately, but of the III robot, a specimen containing a higher magnetic strength is firstly attractive to magnetic field, but another with a lower strength follows orderly. Moreover, the III robot is better in manipulation because it allows another control of dynamic magnetic field. The rotating magnetic field can drive the robot to swim curvilinearly along clockwise or counter-clockwise direction. (Supplementary video 01)

In order to compare performance of three robots embedded with the distinguish magnetic property, swimming velocity is plotted against actuating input parameters; three numbers of magnetic field (5 mT, 10 mT and 15 mT) with fifteen numbers of the oscillating frequency (from 1 to 15 Hz), shown in Figure 7. The results report that velocity tends to continuously increase by an increase of the gaining frequency. The plot still expresses that the III robot can swim fastest at any magnitude of magnetic field,

including the oscillating frequency. All of the robots have the step-out point of the oscillating frequency about 13 Hz at all ranges of magnetic field. At this point, the robot lost in synchronization to the actuating magnetic field, resulting in lack of control and dramatical decrease in velocity. However, swimming velocity of the II robot does not drop fast interestingly if comparing with the others because its body deformation caused by magnetic alignment is the simplest, pointing toward only one direction. Compared with the I and III robot profiled with the sine-curve manner, the II robot's deformation has least lost in synchronization to the magnetic field. After the step out point at 13 Hz, it turns to be a better swimmer than others. Interestingly, at the lowest magnetic field; 5 mT, the III robot still shows a better control and performance than others at all ranges of the actuating frequency, including having the fastest response and performance even at the low oscillating frequency whereas the others cannot swim out due to lost in the magnetic synchronization.

#### 4. Conclusion

In the research of biomimetic robots, fish-like swimming relies on a flexible body to achieve the higher performance, but this mechanism aspect is limited with the size of the robot down to millimeter or less. The use of magnetic field can be a solution to such that problem promisingly. Remotely magnetic manipulation of tiny robots is an effective and non-harmful technique to deal with biomedical applications in which the small-scaled swimming robots can contribute tremendous results as medical devices. In this works, the combination of both magnetic actuation and flexible structure is presented with the purpose of medical application. It enables the wireless power of the external magnetic field generated by the magnetic actuation system. This concept is beneficially applicable to the small-scale robot to employ motor less-mechanism. Three types of soft swimming robots are fabricated with distinguish magnetic property. Their swimming behavior and performance is investigated under the actuation of the oscillating magnetic field. The magnetic alignment of magnetic moments embedded in the deformable structure of the robot leads to maneuverability in fluid under the minimal control of the oscillating magnetic field. The experimental results report that the swimming performance of the robot mainly relies on two parameters; firstly, the strength of magnetic field to adjust the amplitude of the body deformation, and secondly, the frequency to gain the rate of the body deformation. Finally, we found out that quantity and orientation of magnetic moments in the soft structure function in swimming behavior and performance differently. Either of them can be employed solely to create a motion mechanism of the small-scaled robots. The contribution of this study is wide-opening and promising for a soft small-scaled robot to serve multi-purposes towards biomedical applications.

#### 5. Discussion

There are several concerns to avoid error of the data collection, and prepare the robot to be ready for the application. During the experiments, the swimming velocity data of each robot at all input parameters is critical and needs a precise measurement in order to compare the swimming performance between those robots properly. Object tracking is applied to the camera mounted on the

top of the magnetic actuation system, and the center of robot is captured to obtain the coordinate. Another issue of the work would be about the future work. According to the fabrication process, the robot allows us to add more functions to make the robot greater in performance. We definitely plan to extend this study to an advance experiment such as in-vitro and in-vivo experiment. Even though the results of the study are reliable, the robot still needs to improve biocompatibility. Typically, the magnetic active element used as a main component to fabricate the soft robot is not biocompatible. Consequently, the robot is partially biocompatibility. However, the use of biocompatible polymer (e.g., PEG, hydrogel) to wrap the robot is possible, and it does still not constraint the deformation degree actuated by magnetic field. Another would be about how to image the robot inside the blind area. There are two possible methods; Ultrasound imaging using a probe to detect the robot and PA (Photoacoustic) imaging visualizing the robot via the excited signal from additional components. Both imaging techniques can track the robot accurately. If these issues are managed properly, the robots will be ready for the medical applications.

#### Conflict of Interest

The authors declare no conflict of interest.

#### Acknowledgment

This work is supported by the Research Fund of Faculty of Engineering, Thammasat School of Engineering, Thammasat University, the Thammasat University Research Fund No. TUFT 49/2566, the Thammasat Postdoctoral Fellowship No. TUPD 19/2565, and the Thailand Science Research and Innovation Fundamental Fund fiscal year 2023.

#### References

- [1] X. Tang, L. Manamanchaiyaporn, "Magnetic-Powered Swimming Soft-Milli Robot Towards Non-Invasive Applications," The eighth (8th) edition in the series of the International Conference on Control, Decision and Information Technologies (CoDIT'22), 1562-1566, 2022, doi: 10.1109/CoDIT55151.2022.9804108.
- [2] B.J. Nelson, I.K. Kaliakatsos, J.J. Abbott, "Microrobots for Minimally Invasive Medicine," *Annual Review of Biomedical Engineering*, **12**, 55–85, 2010, doi: 10.1146/annurev-bioeng-010510-103409.
- [3] L. Manamanchaiyaporn, T. Xu, X. Wu, "An Optimal Design of an Electromagnetic Actuation System towards a Large Homogeneous Magnetic Field and Accessible Workspace for Magnetic Manipulation," *Energies*, **13** (4), 911, 2020, doi: 10.3390/en13040911.
- [4] L. Manamanchaiyaporn, T. Xu, X. Wu, "Magnetic soft robot with the triangular head-tail morphology inspired by lateral undulation," *IEEE/ASME Transactions on Mechatronics*, **25** (6), 2688-2699, 2020, doi: 10.1109/TMECH.2020.2988718.
- [5] S. Palagi, P. Fischer, "Bioinspired microrobots," *Nature Review Materials*, **3**, 113-124, 2018, doi: 10.1038/s41578-018-0016-9.
- [6] L. Zhang, J.J. Abbott, L.X. Dong, B.E. Kratochvil, D.J. Bell, B.J. Nelson, "Artificial bacterial flagella: fabrication and magnetic control," *Applied Physics Letters*, **94**, 2009, doi: 10.1063/1.3079655.
- [7] H. Huang, M.S. Sakar, A.J. Petruska, S. Pane, B.J. Nelson, "Soft micromachines with programmable motility and morphology," *Nature Communication*, **7**, 12263, 2016, doi: 10.1038/ncomms12263.
- [8] E. Diller, J. Zhuang, G.Z. Lum, M.R. Edwards, M. Sitti, "Continuously distributed magnetization profile for millimeter-scale elastomeric undulatory swimming," *Applied Physics Letters*, **104**, 2014, doi: 10.1063/1.4874306.

- [9] G.Z. Lum, Y. Zhou, X. Dong, H. Marvi, O. Erin, W. Hua, M. Sitti, "Shape-programmable magnetic soft matter," *PNAS*, **113**(41), 6007–6015, 2016, doi: 10.1073/pnas.1608193113.
- [10] W. Hu, G.Z. Lum, M. Mastrangeli, M. Sitti, "Small-scale soft-bodied robot with multimodal locomotion," *Nature*, **554**, 81-85, 2018, doi: 10.1038/nature25443.
- [11] M. Cianchetti, C. Laschi, A. Menciassi, P. Dario, "Biomedical applications of soft robotics," *Nature Review Materials*, **3**, pp.143-153, 2018, doi: 10.1038/s41578-018-0022-y.
- [12] M. Sitti, "Miniature soft robots - road to the clinic," *Nature Review Materials*, **3**, 74–75, 2018, doi: 10.1038/s41578-018-0001-3.
- [13] L. Manamanchaiyaporn, X. Tang, X. Yan, Y. Zheng. "Molecular Transport of a Magnetic Nanoparticle Swarm Towards Thrombolytic Therapy," *IEEE Robotics and Automation Letters*, **6**(3), 5605-5612, 2021, doi: 10.1109/LRA.2021.3068978.
- [14] E. Gultepe, J.S. Randhawa, S. Kadam, et. al, "Biopsy with Thermally-Responsive Untethered Microtools", *Advanced Materials*, **25**, 514–519, 2013, doi: 10.1002/adma.201203348.
- [15] W. Zhu, J. Li, Y. J. Leong, et. al, "3D-Printed Artificial Microfish", *Advanced Materials*, **27**, 4411–4417, 2015, doi: 10.1002/adma.201501372.
- [16] C.W. de Silva, S. Xiao, M. Li, C.N. de Silva, "Telemedicine-Remote Sensory Interaction with Patients for Medical Evaluation and Diagnosis," *Mechatronic System and Controls*, **41**, 2013, doi: 10.2316/Journal.201.2013.4.201-2536.
- [17] E.M. Purcell, "Life at low Reynolds number," *American Journal of Physics*, **45**, 3-11, 1977, doi: 10.1119/1.10903.
- [18] N. A. Spaldin, "Magnetic Materials Fundamentals and Applications," 2<sup>nd</sup> ed. Cambridge University Press, USA, 2010.

## Three-phase Continuously Variable Series Reactor – Realistic Modeling and Analysis

Mohammadali Hayerikhiyavi\*, Aleksandar Dimitrovski

Department of Electrical and Computer Engineering, University of Central Florida, Orlando, 32816, USA

### ARTICLE INFO

#### Article history:

Received: 28 February, 2023

Accepted: 11 May, 2023

Online: 25 June, 2023

#### Keywords:

Continuously Variable Series Reactor (CVSR)

Magnetic Amplifier

Gyrator-Capacitor model

Hysteresis

DC bias control

### ABSTRACT

Continuously Variable Series Reactor (CVSR) is a device that can vary the reactance in an ac circuit by controlling the magnetization of a ferromagnetic core, shared by ac and dc windings. The bias dc current can change the equivalent ac reactance (inductance) in order to, for example, control load flow, damp oscillations, or fault current limitation. Gyrator-Capacitor (G-C) approach in modeling electromagnetic devices provides a strong and practical way in simulating an integrated system composed of magnetic and electric/electronic circuits. The G-C model provides key advantages in analysis of electromagnetic devices, including CVSR. Understanding the performance and the operational characteristics of the CVSR is essential for its proper utilization in the power grid. This paper presents a detailed G-C approach that includes the ferromagnetic core nonlinearities, namely, hysteresis and saturation. The approach has been applied in modeling the electromagnetic coupling between the ac and dc circuits of a three-phase CVSR. Analysis of the effect of different control dc circuit types on the equivalent ac inductance is presented, during operating conditions at different ferromagnetic states. In addition, induced voltages across the windings and the power exchange with the control circuit are presented.

### 1. Introduction

This article augments the underlying work introduced in the 2022 IEEE Kansas Power and Energy Conference (KPEC) [1]. The major contributions and improvements to that work included here are the following:

- 1) Comprehensive analysis of the performance of the CVSR in terms of the induced voltages across the dc winding, to assess the counter impact of the power system on the control circuit.
- 2) Modeling of hysteresis in order to capture the effect of the phenomenon on the induced voltages in the windings and make the model as realistic as possible.
- 3) Power exchange between the controlled and control circuits.

Contemporary power grids operate under increased stress and strain due to the growing demand for electric energy, along with the growing penetration of variable renewable sources. The primary concern system operators have in running the power system and satisfying the demand is to deal with the contingencies in generation and transmission, system oscillations and other events that may result in instabilities and result with blackouts [2].

This is mainly due to the absence of a comprehensive load flow control. Traditionally, load flow control has been implemented using phase-shifting transformers, shunt capacitors and reactors, generator controls, switching system elements on and off and, in the past few decades, various types of power electronics-based controllers [3]. However, these devices either provide only limited control or they come at very high cost. In addition, the meshed topologies of the power systems, make it quite complicated for some of these control means to be effectively employed. More recently, continuously variable series reactor (CVSR) technology was proposed as an alternative option [3-5].

CVSR is a series-connected reactor in the ac power circuit that can continuously vary its reactance within the design boundaries. It is characterized with high reliability and low maintenance, installation, and operating costs [4,6]. Continuous control is achieved by varying a bias control current. Whereas in FACTS controllers, power flows through the high-rated power electronic components, the CVSR control circuit is isolated from the power system and can use low-rated power electronic converters.

Line decongestion and overload relief are easily accomplished by the CVSR through inserting additional impedance in the power circuit in series with its ac winding. Furthermore, CVSR can also

\*Corresponding Author: Mohammadali Hayerikhiyavi ; Email: Mohammad.ali.hayeri@knights.ucf.edu

be used in dynamic applications such as oscillations damping and fault currents limiting by varying the impedance accordingly. Due to the versatility of applications, it is essential to study the mutual impact of the CVSR and the power grid under different operating conditions [4,5].

Gyrator-Capacitor (G-C) modeling approach is a suitable and effective method for modeling magnetic circuits in detailed analyses of power magnetic devices. It directly links electrical and magnetic circuits for comprehensive studies of complex hybrid devices which are part of the power system. In this approach, the analogy between the magnetomotive force (MMF) and the electromotive force is preserved, however the electrical current is analogous to the rate of change of the flux. As a result, the permeance (inverse reluctance) becomes analogous to capacitance.

In a basic representation of the CVSR, as is usual, the magnetic circuit is generally modeled with no core losses, hysteresis in particular. However, some research has been done to include this effect in the analysis [7]. The Jiles-Atherton method can have convergence problems which can be detrimental in transient studies. Furthermore, in some cases, it may result with high percentage error. In [8], alternative models have been examined, with their accuracy and ease of computation compared. The study indicates that Rayleigh model offers sufficient accuracy for cores with high coercivity. On the other hand, Potter model employs simpler mathematical expressions but may lead to significant errors in certain cases. The Frölich and Preisach models provide results that are consistent with experimental findings, although they may not be suitable for dynamic analysis due to their high computation burden. It should be stated that another characteristic of these methods is parameter sensitivity which may also lead to significant errors.

The G-C model represents hysteresis by adding a resistor. The value of this resistor depends on the core geometry, and specific losses [9].

In most studies of electromagnetic devices with controlled bias flux, for simplicity, the source in the control circuit of the device is considered as an ideal current source. This, of course, is not realistic. Three other bias control sources are considered here that have quite different internal impedances. One is an ideal voltage source with zero internal impedance, as opposed to the infinite impedance of the ideal current source. The other two are typical power electronics-based sources: H-bridge converter and buck converter. Their internal impedance values are realistic, in between the two extremes of the ideal sources.

Accurate modeling and simulation of power system elements is fundamental to enhance our understanding of the behavior of the components and their interaction with the power system. This is true in general, but it is also essential in the analysis of the CVSR – a device in which the power circuit is magnetically coupled with a control circuit of much lower ratings. The usual approximations that are justified at the power system level can lead to significant errors and oversights of detrimental conditions on the sensitive controls. Hence, to investigate the impact that the power system has on the CVSR itself, it is important to take all the details into account. The goal of this paper is to provide comparison between idealistic and realistic models of the CVSR and highlight the differences in its performance as a result of the improved accuracy.

The rest of the paper is structured as follows: the concept of three-phase CVSR is discussed in Section 2. The G-C model general concept, expanded to include nonlinearities from core saturation and hysteresis, and applied to the three-phase CVSR is introduced in Section 3. Section 4 introduces the different types of bias dc sources. Section 5 provides a case study with results from simulations with different models and presents the impact on the CVSR in terms of equivalent ac inductance, induced voltages, and the power exchange with the control bias winding. The conclusions are drawn in Section 6.

## 2. Three-phase CVSR

A three-phase CVSR with a five-legged magnetic core, as shown in Fig. 1, includes three-phase ac winding wound on the inner legs that is part of a three-phase ac power circuit that delivers power to the load. Typically, the three inner legs have air gaps to achieve the desired nominal reactance in unsaturated conditions, and to prevent core saturation even at small ac currents. In this particular case, five dc coils are wound on each leg, connected in series and fed by a dc source. The outer legs are gapless in order to provide unimpeded return path for the bias flux. To balance the bias MMFs, the number of turns in the outer dc windings is 1.5 times the number of turns on the inner ones [1]. The controlled bias dc current creates a flux passing through the entire core, hence controlling the ac inductance of the three-phase CVSR. The induced voltages on the coils are proportional to  $d\Phi_{leg}/dt$  and the voltage across the whole dc winding is their algebraic sum:  $V_{bias} = \sum_{i=1}^5 V_{dc,i}$ .

The core can be heterogeneous whose specifications are taken from [1].

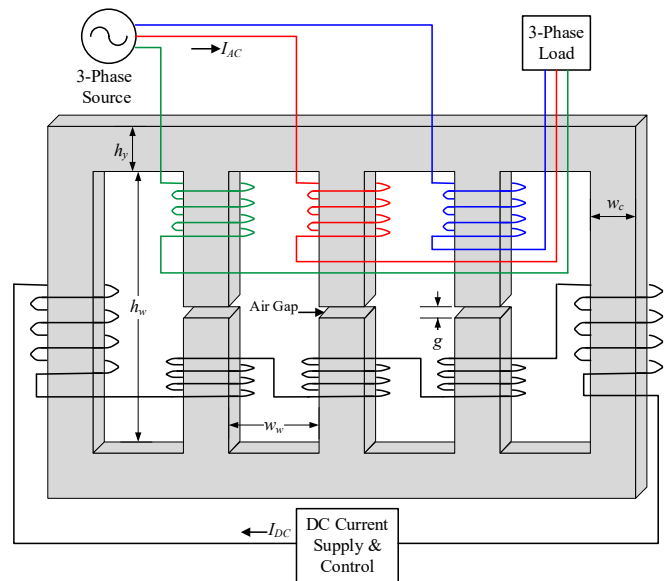


Figure 1: Three-phase CVSR [1]

## 3. Gyrator-Capacitor Model

### 3.1. General Concept

Magnetic circuits are typically represented using the electric circuit analogy [10]. The corresponding circuits are constructed using resistors. Magnetic circuits store energy and they are not

suitably modeled by resistors which only dissipate energy. The G-C modeling concept illustrated in Fig. 2 maintains the power equivalence and is energy/power invariant [11,12].

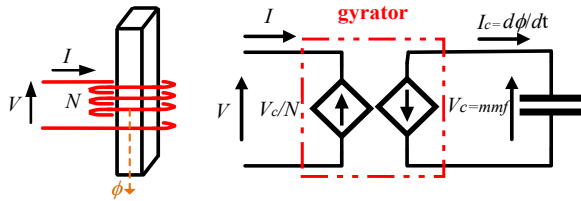


Figure 2: Magnetic circuit and its equivalent gyration-capacitor model

These expressions lead to representation of magnetic permeances, reciprocal values of magnetic reluctances, (magnetic conductances) with capacitances. Nonlinear magnetic paths with nonlinear permeances are represented with nonlinear capacitors. Each coil is represented by a gyrator that relates voltage and current with the number of turns  $N$ .

The reluctances can be expressed approximately with (1):

$$\mathcal{R}(\Phi) = (\mu_r(\Phi)\mu_0 l)/A \quad (1)$$

where:  $\mathcal{R}$  is the magnetic reluctance which depends in general on the magnetic flux  $\Phi$ ;  $\mu_0 = 4\pi \times 10^{-7} \mu_r$  is the relative magnetic permeability of the material;  $A$  is the cross-sectional area;  $l$  is the mean length of the core path.

### 3.2. Hysteresis Modeling

Hysteresis is modeled on one of the most common electromagnetic devices—a two-winding transformer shown in Fig. 3. The hysteresis is modeled by adding a resistor in series with the core capacitance, which represents the magnetic circuit shared by the two windings. The modeling of hysteresis is explicit, meaning that it is reflected in the core B-H characteristic [9]. Besides modeling the ensuing hysteretic losses, more importantly, it captures the other effects of the hysteretic nonlinearity on the performance of the CVSR, as shown later in the case study.

In Fig. 3,  $L_1, R_1, L_2,$  and  $R_2$  represent the primary and secondary winding impedances on the electrical side. The core saturation is modeled by a nonlinear capacitor on the magnetic side. This concept can be extended to the three-phase CVSR.

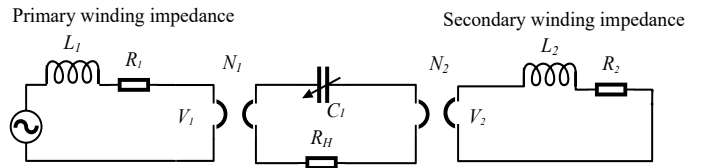


Figure 3: G-C model of a two-winding transformer with hysteretic losses

### 3.3. Three-phase CVSR

An improved G-C model of the physical configuration of the CVSR from Fig.1, with nonlinear core in MatLAB /Simulink® is represented in Fig. 4.

The nonlinear magnetic paths are modeled with variable capacitors, and linear permeances  $C_g$  model the air gaps in the inner legs. They can also include the fringing effect by an effective increase in the cross-sectional area. As described, the coils of the ac and dc windings are modeled with gyrators. The hysteresis in the core is modeled with corresponding resistors ( $R_1 - R_{13}$ ) [10].

The capacitances that represent leakage permeances can be divided into two primary categories: leg leakage permeances ( $C_{14} - C_{18}$ ) and yoke leakage permeances ( $C_{19} - C_{26}$ ).[13]

The dc electric control circuit is connected to the dc source via five gyrators that represent each dc windings.

## 4. Bias Dc Sources

As stated before, four different methods to control the current in the dc winding are assumed. They are applied to explore how different types of the dc electric control circuits impact the operation of the three-phase CVSR in terms of equivalent ac inductance, induced voltage across dc winding, ac terminal

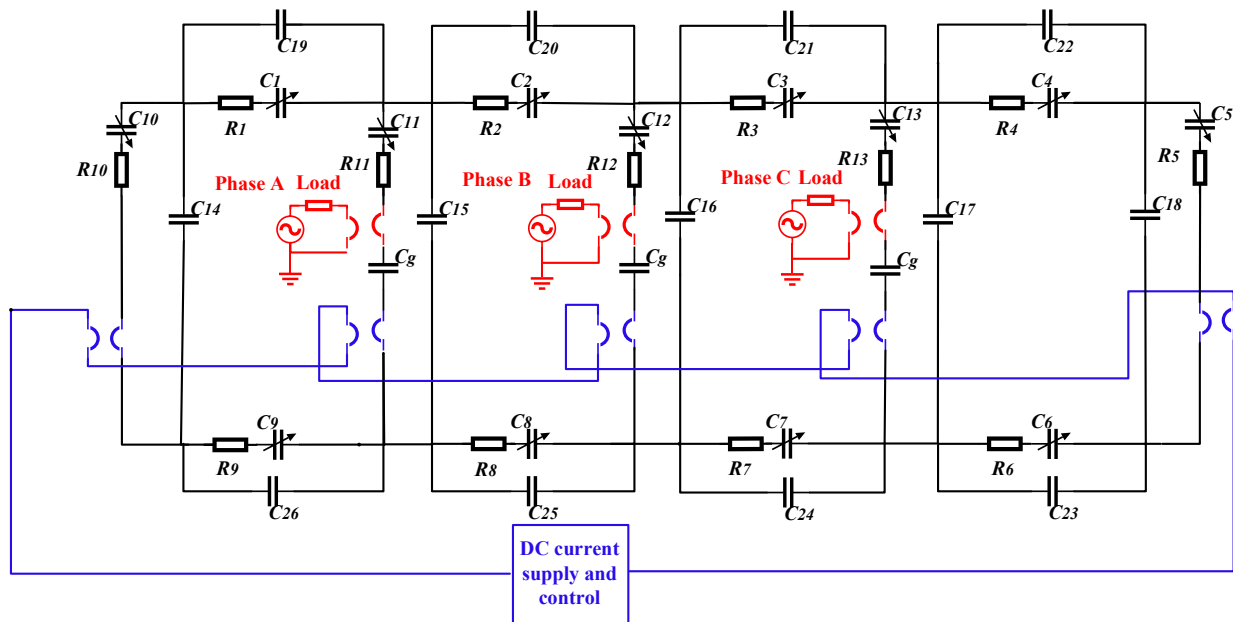


Figure 4: Gyrator-capacitor model of three-phase CVSR



voltage, and power interchange with the dc control circuit during different operating conditions.

All of the dc circuit controllers (DCCs) are simulated to supply the dc winding with five coils at a set of desired current values. The ideal current source has an infinite internal impedance, while the ideal voltage source has no impedance. H-bridge and buck converter are more realistic sources, with an internal impedance value between zero and infinity [1].

Fig. 5 illustrates an H-bridge converter composed of four IGBTs and a front-end rectifier. The PI controller coefficients are selected to ensure standard overshoot, settling time, and ripple in a steady state. A simple buck converter (step-down converter) is illustrated in Fig. 6. It operates in two modes: a) charging and b) discharging. During the charging mode, the IGBT turns on, and the dc winding current ramps up. During the discharging mode, the IGBT turns off, and the dc winding current ramps down [1].

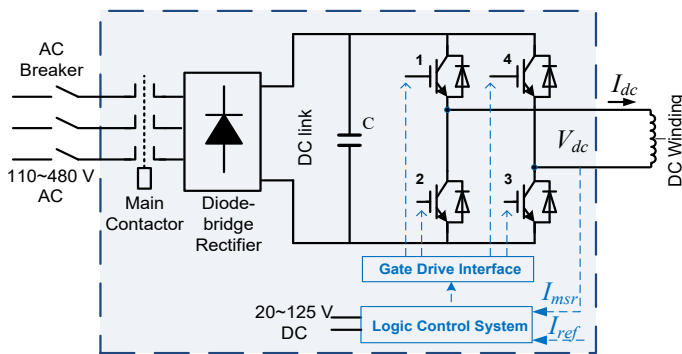


Figure 5: H-bridge converter

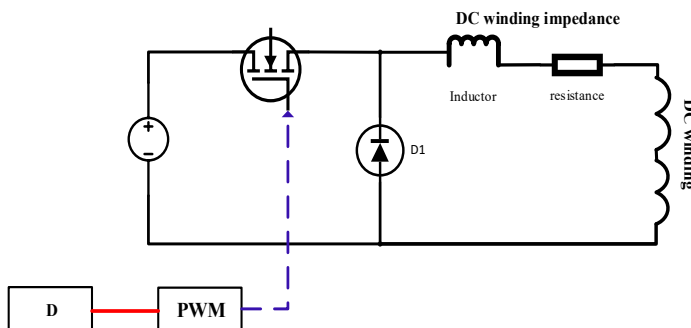


Figure 6: Buck converter

### 5. Case Study

To explore the three characteristic operating states of the CVSR with unsaturated, partially saturated, and fully saturated core, simulations have been conducted for three different dc bias currents: 0 A, 15 A, and 45 A. The simulation results include waveforms for the terminal voltages and currents for each dc source type, at each characteristic bias value. Based on these waveforms, the effective impedances are computed.

Fig. 7 shows the equivalent circuit on the controlled ac power system side with source, load, and CVSR's inductance in series.

The ac equivalent inductance is obtained from the current through the ac winding and the terminal voltage (Fig. 7). Based on the G-C model definition, the terminal voltage across the  $L_{CVSR}$  (ac

variable equivalent inductance of the CVSR) is equal to the gyrator induced voltage on the primary side. It is obtained from the basic Ohm's Law (2):

$$Z_{ac} = V_{ac} / I_{ac} \tag{2}$$

where:  $V_{ac}$  is the terminal voltage, and  $I_{ac}$  is the load current.

For simplicity, it has been supposed that the power system is balanced. Consequently, all of the simulation results shown here are for one phase.

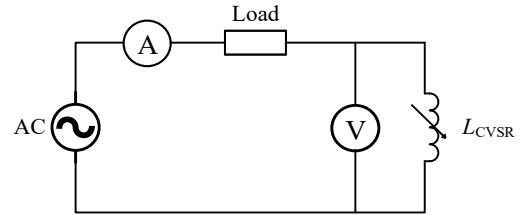


Figure 7: Ac electric circuit

#### 5.1. CVSR without hysteresis

Fig. 8 illustrates the B-H characteristic for the inner legs of the CVSR at 0 A [14].

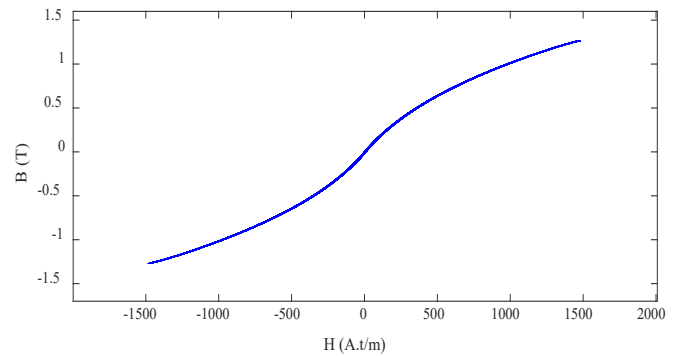


Figure 8: B-H characteristic of the inner legs without hysteresis

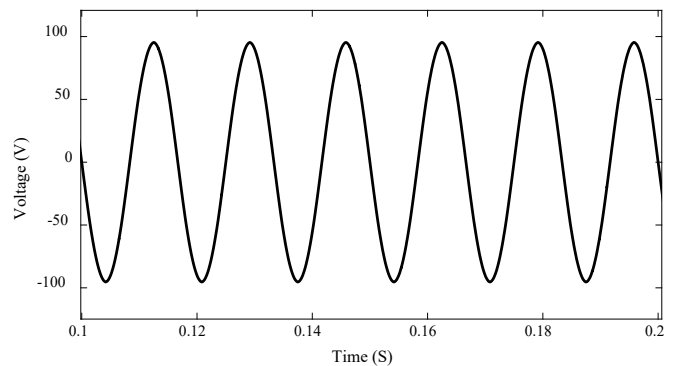


Figure 9: Terminal voltage ( $I_{dc} = 0$  A)

##### 5.1.1. 0A dc bias

The terminal voltage and current through the ac winding (load current) in one phase, from the G-C model at 0 A, are shown in Figs. 9 and 10, respectively. At no bias, the voltage and current waveforms are identical for all source types. In all operational circumstances and for every control source, the current passing through the AC winding is approximately equivalent to the nominal load current value of 20.9 A. This is because, in

comparison to the device's equivalent inductance, the load impedance holds more significance. Thus, the analysis will now shift its focus solely on the terminal voltage.

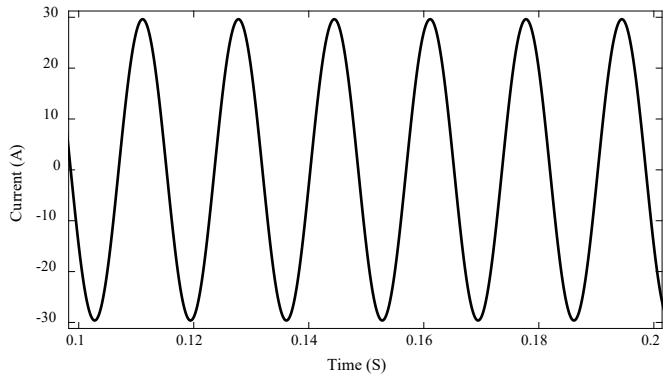


Figure 10: Load current ( $I_{dc} = 0$  A)

The induced voltage across the dc winding in this case is shown in Fig. 11.

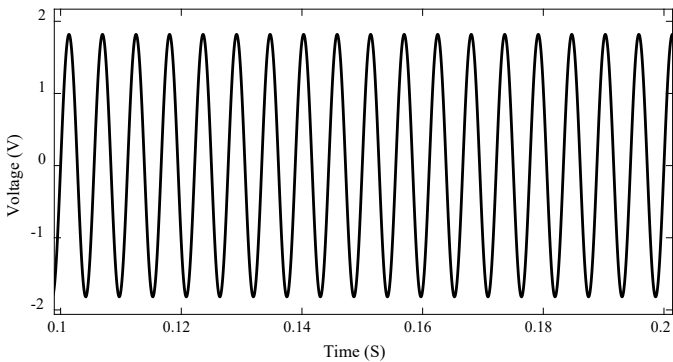


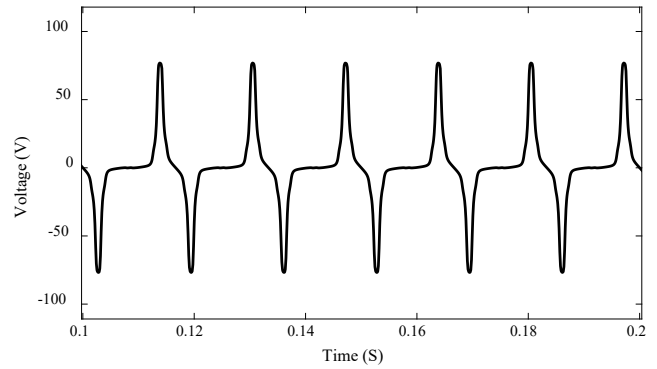
Figure 11: Voltage across dc winding ( $I_{dc} = 0$  A)

5.1.2. 15A dc bias

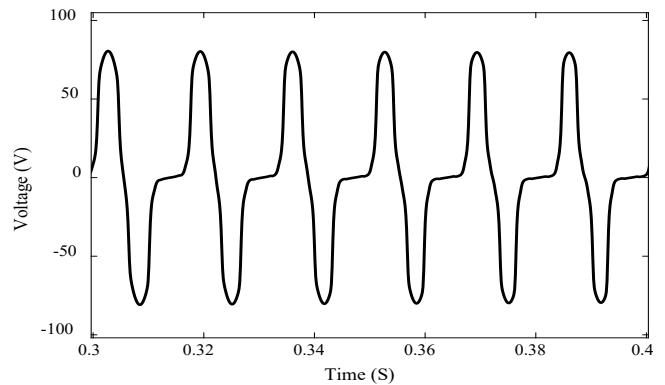
Figs. 12 (a)-(d) depict the terminal voltage on one phase of the CVSR for different dc controlled circuits, when the dc bias is raised to 15 A, the inner legs go into partial saturation, while the others are unsaturated. The flat regions in the voltage waveforms are caused by the saturation. The thick parts in the last two figures are the ripple effect of the PWM frequency (2.5 kHz). The controls move back and forth through the nonlinear B-H characteristic during the transition between the unsaturated and saturated region. This effect does not occur with an ideal current source. It can be seen that the induced voltage with the H-bridge converter is smoother with smaller fluctuations than that with the buck converter due to the closed-loop control. The figures show steady-state conditions, which depend on the settling time of the DCCs, hence the different time periods.

Figs. 13 (a)-(b) show the induced voltages across the dc winding for an ideal current source and an H-bridge converter. The voltage for a buck converter is roughly identical to the latter in terms of shape. The induced voltage is distorted at times when parts of the core enter saturation and it has triple the fundamental frequency of the system. Therefore, the ripple effect on the voltage

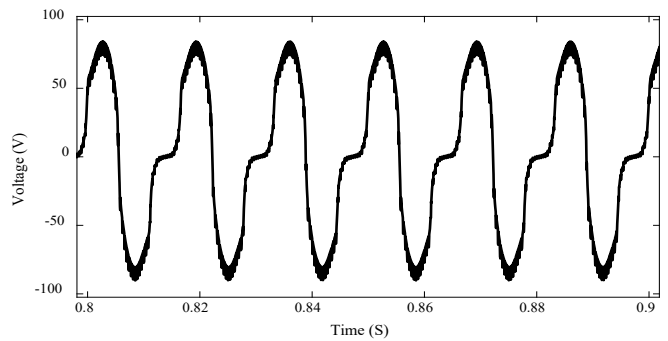
waveforms is even more exaggerated with realistic DCCs. This effect aside, they tend to have the same shape and peak values.



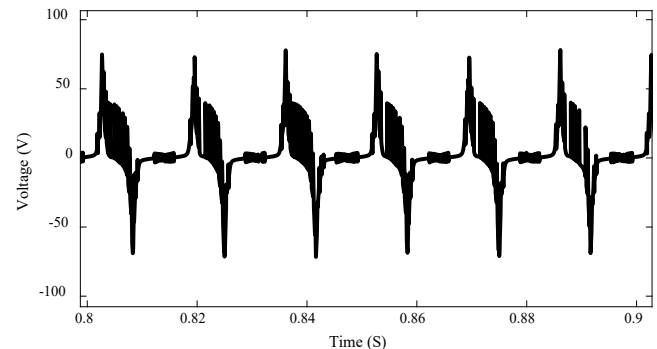
(a) Ideal current source



(b) Ideal Voltage source

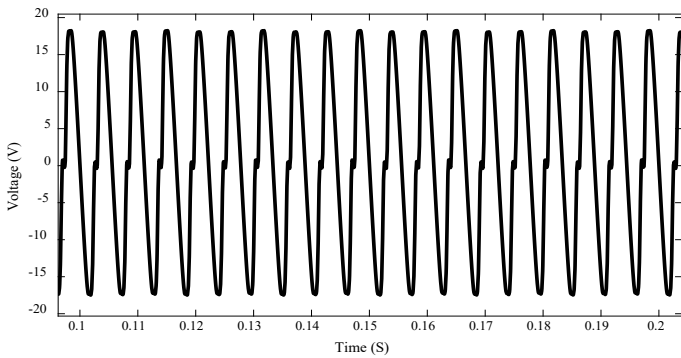


(c) H-bridge converter

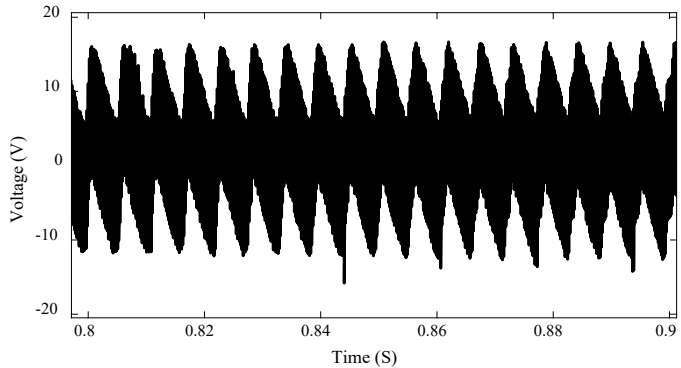


(d) Buck converter

Figure 12: Terminal voltages for different dc bias sources ( $I_{dc} = 15$  A)



(a) Ideal current source



(b) H-bridge converter

Figure 13: Induced voltage across dc winding for different dc sources ( $I_{dc} = 15$  A)

The power exchange with the dc winding is calculated using a “rolling window” approach. Starting at the beginning of the simulation, a window with  $m$  consecutive samples in time is chosen. The window then moves with each next sample. The power is calculated for each rolling window subset. The window size  $m$  depends on the fundamental period  $T$  and the sampling frequency of the data (step size). A longer window size produces smoother results.

The power transferred to the dc winding for an ideal current source is shown in Figure 14. After the initial transient, there is no real power exchange, apart from the small ripple. However, there is a noticeable apparent power transfer present.

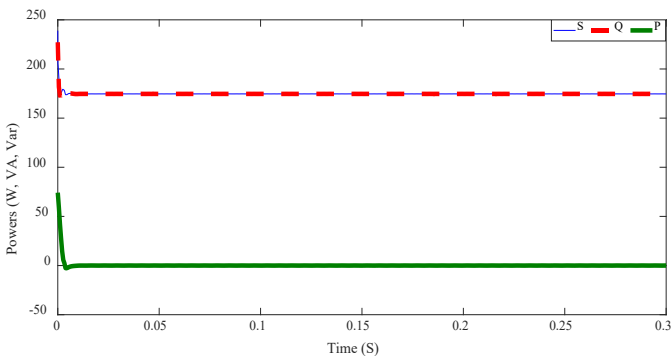


Figure 14: Power transfer to dc winding ( $I_{dc} = 15$  A)

### 5.1.3. 45A dc bias

At a high dc offset of 45 A, the CVSR core goes into complete saturation. Hence, the fluxes through the legs decrease. Also, the [www.astesji.com](http://www.astesji.com)

terminal voltage and the voltage across the dc winding are very low. Fig. 15 shows the terminal voltage on one phase for the ideal dc current source.

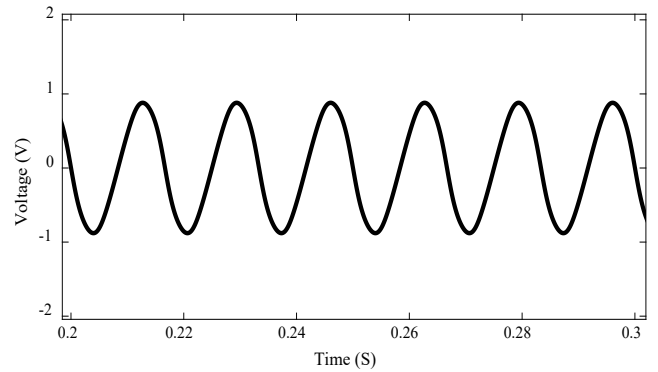


Figure 15: Terminal voltage ( $I_{dc} = 45$  A)

Figs. 16(a)-(c) on the next page show the voltage across the dc winding for an ideal current source, an H-bridge converter, and a buck converter, respectively.

The power transferred to the dc winding for an H-bridge converter is shown in Fig. 17. After the transient, there is no real power and a smaller than before apparent power exchange.

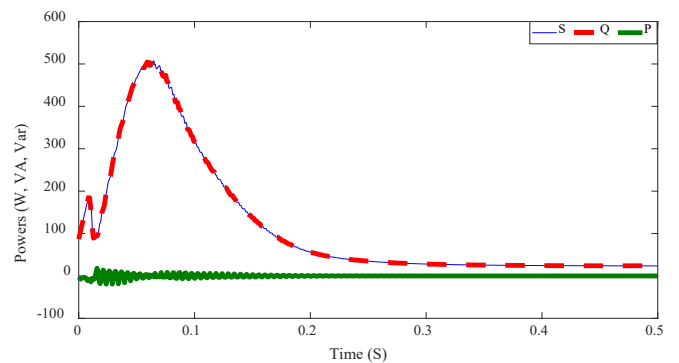
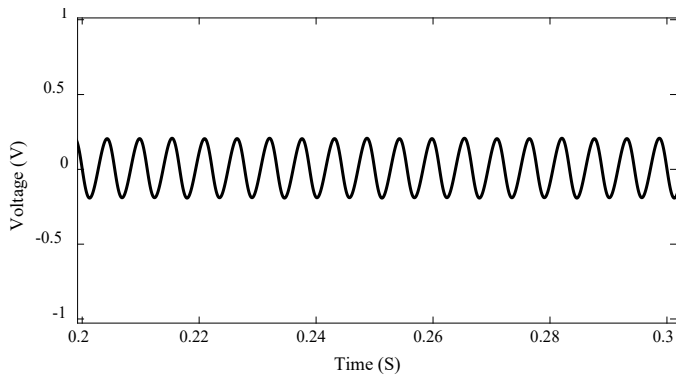


Figure 17: Power transfer to dc winding ( $I_{dc} = 45$  A)

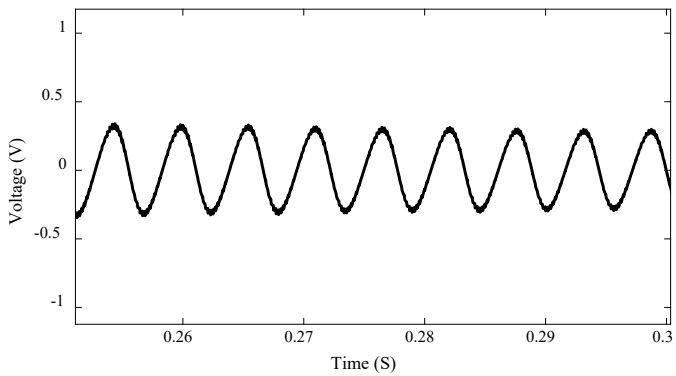
### 5.2. CVSR with hysteresis

The B-H characteristic for the inner legs at 0A is presented in Fig. 18. The hysteresis is small, but visible. The assumed material for the core is soft ferromagnetic and has small hysteretic characteristic. This is consistent with the practice how power electromagnetic devices are built to reduce the core losses. Still, it is of interest to see how this effect will influence the performance of the CVSR.

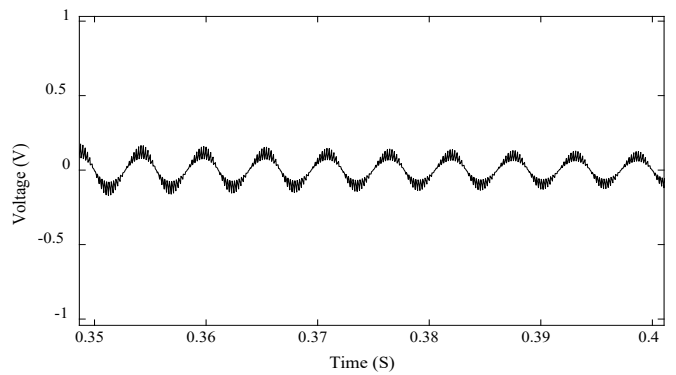
Again, like in the case without considering hysteresis, three different dc bias currents are considered: 0A, 15A, and 45A. The same analyses as before are performed and the results are compared with the previous case.



(a) Ideal current source



(b) H-bridge converter



(c) Buck converter

Figure 16: Voltage across dc winding for different dc sources ( $I_{dc} = 45$  A)

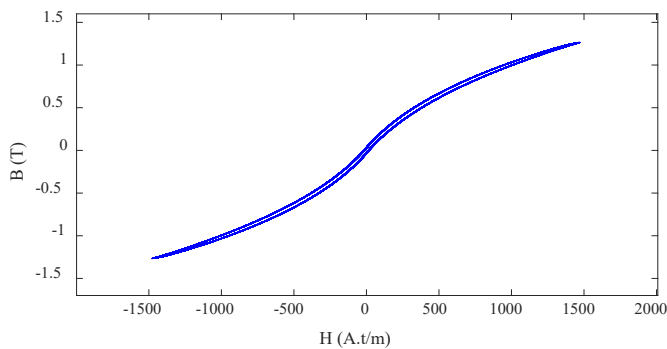


Figure 18: B-H characteristic of the inner legs with hysteresis

5.2.1. 0A dc bias

Fig. 19 shows the terminal voltage on one phase of the CVSR for an ideal current source. Because of the hysteresis, the voltage is not purely sinusoidal. The effect is not obvious and, for comparison, a pure sinusoid is plotted with a dashed red line. The same also for the voltage across the dc winding in Fig. 20.

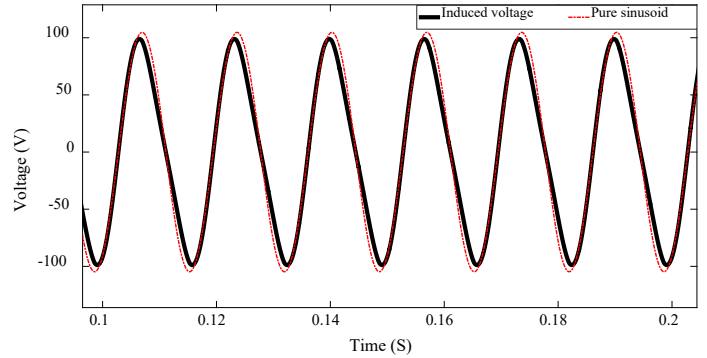


Figure 19: Terminal voltage ( $I_{dc} = 0$  A)

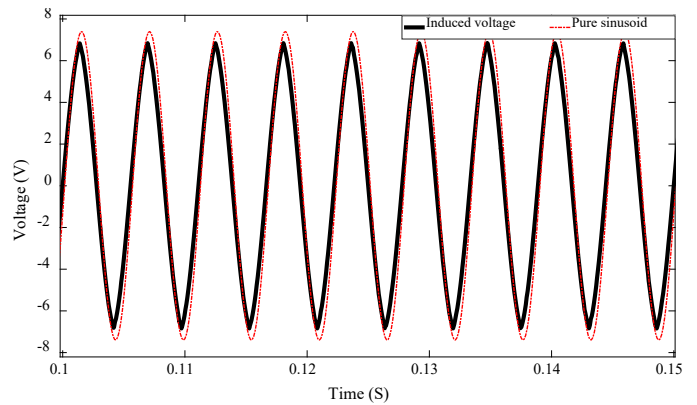


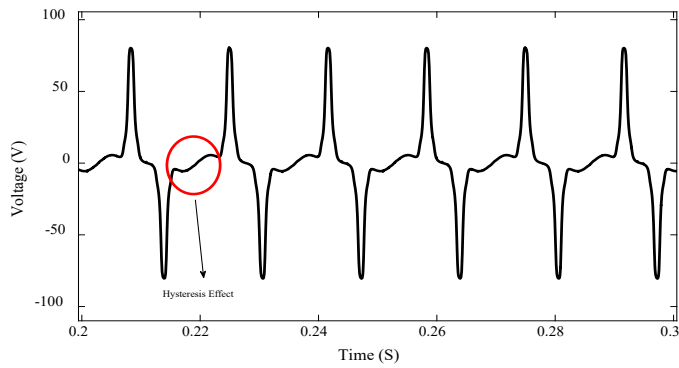
Figure 20: Voltage across dc winding ( $I_{dc} = 0$  A)

5.2.2. 15A dc bias

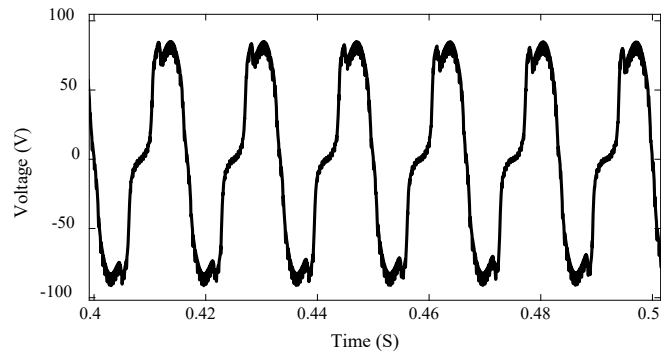
In Figs. 21 (a)-(b), the terminal voltage across one phase for an ideal current source and an H-bridge converter are shown, respectively, at dc bias equal to 15 A. At this bias current, the inner legs go into partial saturation, while the others are unsaturated. The hysteresis effect is encircled in red.

Figs. 22 (a)-(b) show the voltage across the dc winding for the same dc source types. Again, the effect from the hysteresis on the voltage waveform is encircled in red. It can also be seen that, although the hysteresis is quite small, the peaks of the induced voltages are significantly higher than those in the previous case for the same scenario and vary. This shows the value of the improved modeling in analysis of a device like CVSR.

The power transferred to the dc circuit for an ideal current source, shown in Fig. 23, is also significantly higher than in the previous case due to the higher induced voltages from including the hysteresis effect.

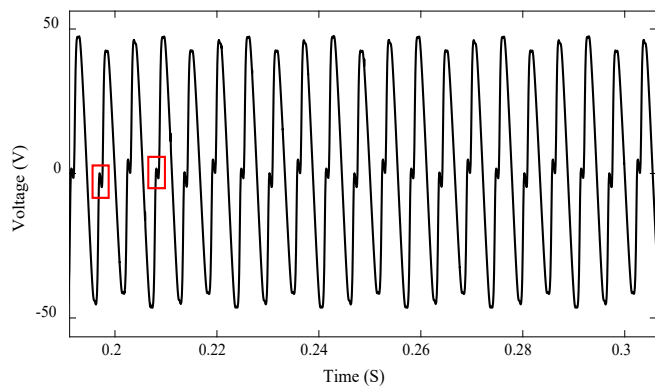


(a) Ideal current source

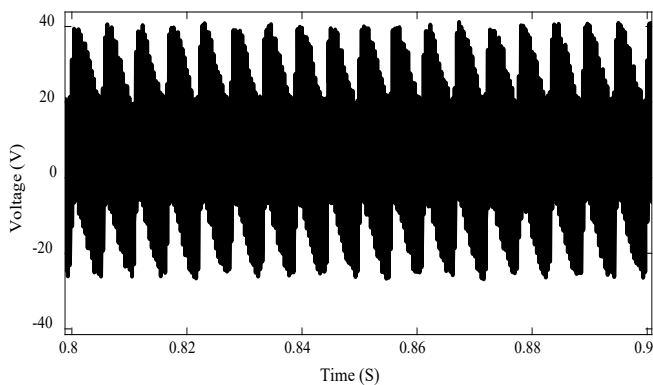


(b) H-bridge converter

Figure 21: Terminal voltage for different dc electric control circuits ( $I_{dc} = 15\text{ A}$ )



(a) Ideal current source



(b) H-bridge converter

Figure 22: Induced voltage across dc winding for different dc sources ( $I_{dc} = 15\text{ A}$ )

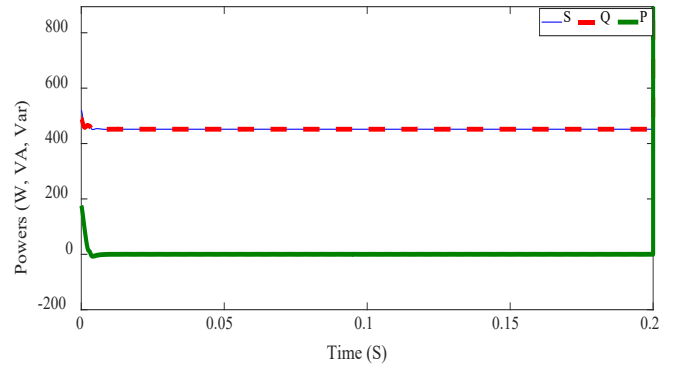
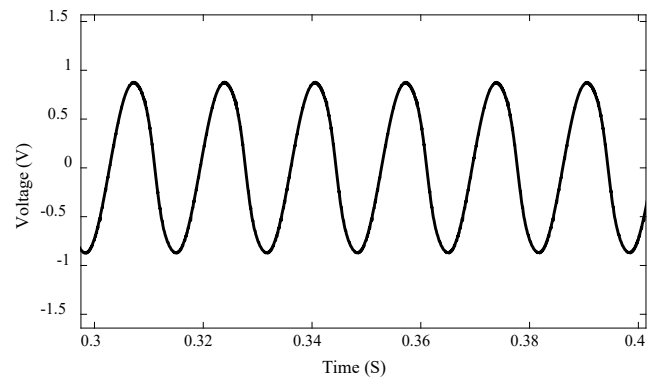


Figure 23: Power transferred to dc winding ( $I_{dc} = 15\text{ A}$ )

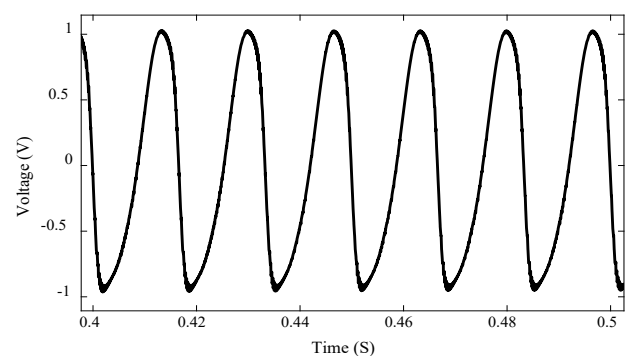
### 5.2.3. 45A dc bias

At a high dc offset of 45 A, the CVSR core again goes into complete saturation. The fluxes through the legs decrease due to core fully saturation. Hence, the terminal voltage and the voltage across the dc winding are very low. Figs. 24 (a)-(b) show the terminal voltage on one phase of the CVSR for an ideal current source and an H-bridge converter, respectively.

Figs. 25 (a)-(b) show the induced voltage across the dc winding for the same dc source types. In Fig. 25, the distorted peaks encircled in red, due to the hysteresis effect, are still visible.

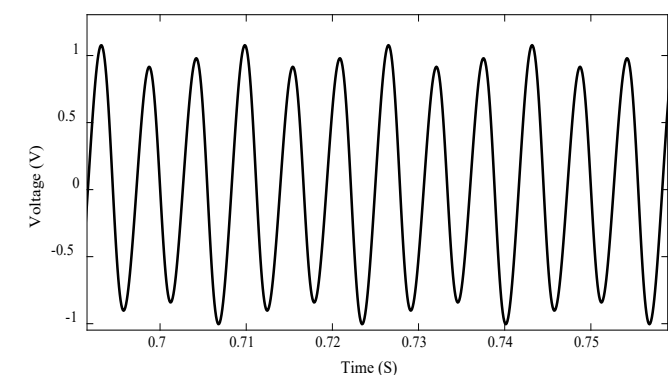


(a) Ideal current source

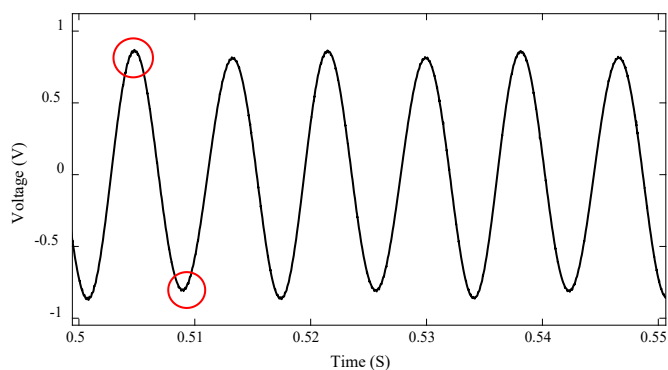


(b) H-bridge converter

Figure 24: Terminal voltage ( $I_{dc} = 45\text{ A}$ )



(a) Ideal current source



(b) H-bridge converter

Figure 25: Induced voltage across dc winding for different dc sources ( $I_{dc} = 45$  A)

The power transferred to the dc winding for a Buck converter in this case is shown in Fig. 26.

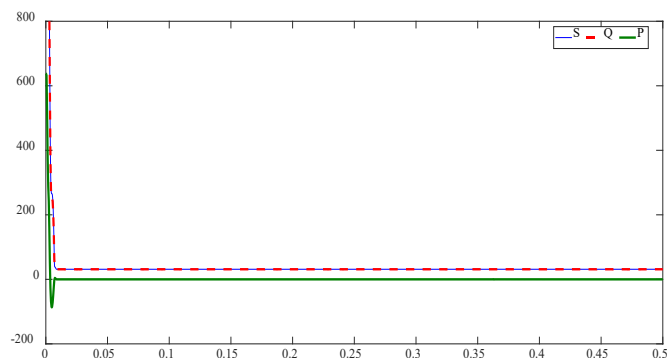


Figure 26: Power transferred to dc winding ( $I_{dc} = 45$  A)

Tables I and II summarize the terminal voltage values and the resulting effective CVSR impedance values derived from the results of the analysis. The differences in the impedance reveal that both the dc source type and the hysteresis effect significantly impact the effective AC reactance of the CVSR.

## 6. Conclusion

The paper presents an improved realistic model of a three-phase CVSR, based on the gyrator-capacitor modeling approach. To improve the accuracy for an electromagnetic device that operates in the whole range of its B-H characteristic like the CVSR, hysteresis and core saturation nonlinearities are considered. Capacitors model permeances (magnetic conductances), and nonlinear capacitors can model core saturation. Additionally, a resistor connected in series with the core capacitor represent core hysteresis. Simulations of the improved G-C model of three-phase CVSR under different conditions and at different values of the bias dc current have been performed. Different dc control source types have also been considered. Results from the comprehensive analysis show significant impacts on the performance of the CVSR from a more realistic model.

Table 1: AC impedance and terminal voltage for different DC sources and currents – no hysteresis

Bias current \ Bias source	0A (No saturation)		15A (Partial saturation)		45A (Full saturation)	
	Impedance	Voltage	Impedance	Voltage	Impedance	Voltage
Ideal current	3.185 $\Omega$	66.64 V	1.31 $\Omega$	27.3 V	0.060 $\Omega$	0.88 V
Ideal voltage	3.196 $\Omega$	66.81 V	1.82 $\Omega$	38.1 V	0.119 $\Omega$	1.85 V
Buck converter	3.192 $\Omega$	66.73 V	1.56 $\Omega$	32.4 V	0.080 $\Omega$	1.21 V
H-bridge	3.192 $\Omega$	66.74 V	1.69 $\Omega$	35.4 V	0.077 $\Omega$	1.15 V

Table 2: AC Impedance and Terminal Voltage for Different DC Sources and Currents – With Hysteresis

Bias current \ Bias source	0A (No saturation)		15A (Partial saturation)		45A (Full saturation)	
	Impedance	Voltage	Impedance	Voltage	Impedance	Voltage
Ideal current	3.57 $\Omega$	74.64 V	1.97 $\Omega$	41.3 V	0.070 $\Omega$	1.07 V
Ideal voltage	3.73 $\Omega$	77.82 V	2.51 $\Omega$	52.3 V	0.145 $\Omega$	2.07 V
Buck converter	3.71 $\Omega$	77.73 V	2.24 $\Omega$	46.4 V	0.092 $\Omega$	1.33 V
H-bridge	3.71 $\Omega$	77.74 V	2.23 $\Omega$	46.8 V	0.088 $\Omega$	1.24 V

## References

- [1] M. Hayerikhiyavi and A. Dimitrovski, "Impact of Different Types of DC Bias Sources on the Effective Impedance of a CVSR," in 2022 IEEE Kansas Power and Energy Conference (KPEC), 1-6, 2022, doi: 10.1109/KPEC54747.2022.9814785.
- [2] A. Dimitrovski, Z. Li, B. Ozpineci, "Applications of saturable-core reactors(SCR) in power systems," in 2014 IEEE PES T&D Conference and Exposition, 1-5, 2014, doi:10.1109/TDC.2014.6863404.
- [3] A. Dimitrovski, Z. Li, B. Ozpineci, "Magnetic Amplifier-Based Power-FlowController," IEEE Transactions on Power Delivery, **30**(4), 1708-1714, 2015, doi:10.1109/TPWRD.2015.2400137.
- [4] M. Hayerikhiyavi and A. Dimitrovski, "Gyrator-Capacitor Modeling of A Continuously Variable Series Reactor in Different Operating Modes," in 2021 IEEE Kansas Power and Energy Conference (KPEC), 1-5, 2021, doi: 10.1109/KPEC51835.2021.9446236.
- [5] M. Hayerikhiyavi and A. Dimitrovski, "Comprehensive Analysis of Continuously Variable Series Reactor Using G-C Framework," in 2021 IEEE Power & Energy Society General Meeting (PESGM), 1-5, 2021, doi: 10.1109/PESGM46819.2021.9637971.
- [6] M. Young, A. Dimitrovski, Z. Li and Y. Liu, "Gyrator-Capacitor Approach to Modeling a Continuously Variable Series Reactor," in IEEE Transactions on Power Delivery, **31**(3), 1223-1232, 2016, doi: 10.1109/TPWRD.2015.2510642.
- [7] Valadkhan S, Morris K, Khajepour A. "Review and Comparison of Hysteresis Models for Magnetostrictive Materials". Journal of Intelligent Material Systems and Structures. 2009;**20**(2):131-142.
- [8] M. F. Jaafar and M. A. Jabri, "Study and modeling of ferromagnetic hysteresis," in 2013 International Conference on Electrical Engineering and Software Applications, 1-6, 2013, doi: 10.1109/ICEESA.2013.6578426.
- [9] M. Hayerikhiyavi and A. Dimitrovski, "Improved Gyrator-Capacitor Modeling of Magnetic Circuits with Inclusion of Magnetic Hysteresis," in 2022 IEEE/PES Transmission and Distribution Conference and Exposition (T&D), 1-5, 2022, doi: 10.1109/TD43745.2022.9816976.
- [10] S. D. Sudhoff, B. T. Kuhn, K. A. Corzine, B. T. Branecky, "Magnetic Equivalent Circuit Modeling of Induction Motors," IEEE Transactions on Energy Conversion, **22**(2), 259-270, 2007, doi:10.1109/TEC.2006.875471.
- [11] G. M. Shane, S. D. Sudhoff, "Refinements in Anhysteretic Characterization and Permeability Modeling," IEEE Transactions on Magnetics, **46**(11), 3834-3843, 2010, doi:10.1109/TMAG.2010.2064781.
- [12] D. C. Hamill, "Gyrator-capacitor modeling: a better way of understanding magnetic components," Proceedings of 1994 IEEE Applied Power Electronics Conference and Exposition - ASPEC'94, Orlando, FL, USA, 1994, pp. 326-332 vol.1, doi: 10.1109/APEC.1994.316381.
- [13] S. Pokharel and A. Dimitrovski, "Modeling of An Enhanced Three-phase Continuously Variable Reactor," in 2020 IEEE Power & Energy Society General Meeting (PESGM), 1-5, 2020, doi: 10.1109/PESGM41954.2020.9282074.
- [14] M. Hayerikhiyavi and A. Dimitrovski, "Voltage Balancing Using Continuously Variable Series Reactor," in 2023 IEEE Texas Power and Energy Conference (TPEC), 1-5, 2023, doi: 10.1109/TPEC56611.2023.10078529.

## Minimum Static VAR Compensation Capacity for Bad Voltage Drop Buses in Power Systems

Hermagasantos Zein\*, Ahmad Deni Mulyadi, Achmad Mudawari

Jurusan Teknik Konversi Energi, Politeknik Negeri Bandung (Polban), Bandung, Kotak Pos 1234, Indonesia

### ARTICLE INFO

Article history:

Received: 28 February, 2023

Accepted: 11 May, 2023

Online: 25 June, 2023

Keywords:

Quality

Bad voltage

Compensation

Power flow

Compensating modeling

### ABSTRACT

The quality of the electric power system must be maintained properly, one of which is voltage. Under certain operating conditions, the bus voltage may drop below its minimum level, called bad voltage. A large reactive load can cause a voltage drop across the bus or the location of the bus is far from the generator stations, so that the line impedance has a large value. One technique to increase the voltage is through compensation technique. This paper presents the determination of the minimum statistical VAR compensation for increasing the voltage to the minimum safety limit. The methodology creates a compensating model for bad bus voltages. Electrical quantities (voltage, power and system losses) are calculated through the power flow technique. The compensating capacity is increased until the voltage rise reaches its minimum security limit. The simulation results on the IEEE 9 bus system show that the voltage increases on all buses with minimal compensation on buses 5 and 8, and can save up to 1.37 MW of power

### 1. Introduction

The electric power system must maintain its quality. One of its qualities is voltage, where voltage must be kept within its safety limits (minimum and maximum limits). In addition, the operation of the electric power system is highly desirable to be safe, efficient, and economical.

The existence of reactive power flow in the network will worsen the quality of service because it will cause voltage drops. An improved voltage profile by controlling the reactive power flow needs to be considered. Reactive power compensation (RPC) in power systems can increase voltage in addition to improving power factor [1]. However, determining the amount of effective compensation needs to be considered in maintaining voltage security. Maintaining voltage stability through reactive power control has been extensively discussed in [2–4]. This work succeeded in controlling the voltage at the desired level to improve the quality of the voltage to the customer. In electric power, the voltage must not drop below its minimum level. Voltage correction through compensation must consider the voltage limit. The effect of compensation can effects voltage fluctuations and it is an option to support reactive power flow into the network [5–7]. The reactive power flow in the network can be shown to decrease when it is compensated. However, the effect of reactive power flow on the voltage drop has not been clearly formulated.

Intelligent algorithm to control voltage has been studied in [8–10]. The [8] has developed an intelligent algorithm to control voltage. Meanwhile, controlling the flow of reactive power through the application of intelligent algorithms has been implemented in [9]-[10]. These works have successfully applied artificial methods to control the voltage on the demand side.

Whereas in [11–16], compensation techniques are used to control the voltage in the distribution system. The voltage control strategy to maintain the continuity of the distribution network [11] and for optimizing the voltage coordination [12]-[13]. Generally, the centralized voltage control is a good option. Multi-agent techniques can be used for centralized voltage control in power systems as discussed in [14]. The coordinated voltage control for fast location determination is a problem and the solution has been developed in the scheme in [15]. Meanwhile, the voltage control globally in a coordinated online system has been proposed in [16]. One of the problems in the operation of electric power is how to keep the voltage from going out of bounds. If there is a voltage below the minimum level, it must be increased to the minimum level.

Compensation technique can repair voltage drop in the medium voltage feeder [17,18] The voltage drop monitor of the load side can be implemented by using compensation [17]. The simple voltage drop calculation is presented in [18]. The methodology uses the feed current approach. While in [19–22] has studied the optimal compensation to voltage control. The [19-20] presents the

\*Corresponding Author: Hermagasantos Zein; herмага\_s@yahoo.co.id



formulation to control the optimal reactive power. Repair power factor and optimal saving losses depend on the location of capacitor bank in the line feeder [21]. Power system large losses can be repaired by compensation. Optimal compensation to get minimum system losses has been clearly formulated in [22]. Considering that the cost of compensation in high-voltage networks is quite expensive, it is necessary to pay attention to the minimum compensation option so that voltage security can be maintained.

This paper proposes a method to improve voltage quality through minimum compensation in power systems using SVC devices on buses that have bad voltage. The methodology is based on compensation modeling on the observed bus, where the power supply comes from the network, generator and SVC to meet the load.. The compensating capacity is updated until the voltage level has reached the minimum security limit. Each process changes in compensation capacity, the voltage value is calculated using the Newton-Rapson technique. This technique has proven to be robust in power flow calculations in power systems.

This SVC device will act as a reactive power generator that supplies the network. The reactive power flow before the SVC device is installed will be compensated by the reactive power generated by the SVC device. In addition to increasing the voltage, this compensation technique also reduces system losses. In theory, the loss vs compensation curve is as a saddle horse. System losses will decrease towards optimal compensation, but system losses will increase if compensation is greater than optimal compensation. While the voltage tends to rise when compensation increases. The proposed method formulation has been tested with an IEEE 9-bus power system. The test results can increase the voltage to the minimum security limit (0.9 pu) on bad voltage buses (buses 5 and 8) and save system losses of 1.37 MW.

The systematics of this paper consists of 5 parts. The first session explained the state of the art regarding voltage repair through compensation techniques. The third paragraph from the end of this section explains the contribution of the work done.. The second paragraph at the end of this section describes the contribution of the work performed. The second session is to define the problem formulation. This section consists of Newton-Rapson technique, modeling of SCV and effect SCV to system losses. The third part contains procedures for solving problems in the form of a flowchart. The fourth session discussed the simulation results of the IEEE 9-bus power system. The last, fifth session, is to provide conclusions based on the findings in this work.

## 2. Problem Formulation

### 2.1. Newton-Raphson Technique

Refer to [22], the power flow problem is to solve the work network equation in (1).

$$\begin{bmatrix} \Delta P \\ \Delta Q \end{bmatrix} = \begin{bmatrix} J_1 & J_2 \\ J_3 & J_4 \end{bmatrix} \begin{bmatrix} \Delta \delta \\ \Delta V \end{bmatrix} \quad (1)$$

where  $P$  and  $Q$  are the active and reactive powers.  $\delta$  and  $V$  are the complex voltage.  $J_1, J_2, J_3,$  and  $J_4$  are Jacobean matrices. By using the Newton-Raphson technique, the solution to the network

equation through an iteration process will converge when the power balance is reached. The power balance is expressed in (2) and (3).

$$\Delta P = P^{fix} - P^{count} \leq \varepsilon \quad (2)$$

$$\Delta Q = Q^{fix} - Q^{count} \leq \varepsilon \quad (3)$$

where  $\varepsilon$  is the smallest number, it represents the degree of accuracy.

### 2.2. Modeling of SVC

The SVC model is shown in Figure 1. Assumed that the active and reactive power flows from the grid are  $P_{gd-i}$  and  $Q_{gd-i}$ , respectively. From the figure, the convergent power flow will satisfy (4) and (5).

$$P_{d-i} = P_{g-i} + P_{gd-i} \quad (4)$$

$$Q_{d-i} = Q_{g-i} + Q_{gd-i} + Q_{SVC-i} \quad (5)$$

The current and capacity of capacitor can be derived from Figure 1, namely:

$$I_{SC-i} = 2\pi f C_{SC-i} V_i \quad (6)$$

$$Q_{CSVC-i} = B_{SVC-i} V_i^2 \quad (7)$$

Where  $f$  is the system frequency,  $C_{SC-i}$  is capacitance of SCV and  $B_{SVC-i}$  is the susceptance of SVC with the formulation is,

$$B_{SVC-i} = 2\pi f C_{SC-i} \quad (8)$$

Changes in voltage can be caused by the SCV capacity. The value of this voltage change can be derived from (7) and yield,

$$\partial V_i = \frac{\partial Q_{CSVC-i}}{2Q_{SVC-i}} V_i \quad (9)$$

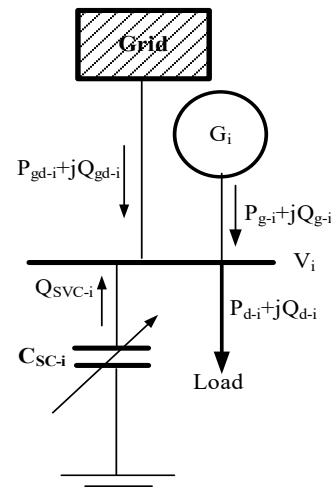


Figure 1: SCV model

While the susceptance change is,

$$\partial B_{CSVC-i} = \frac{B_{SVC-i}}{Q_{CSVC-i}} \partial Q_{CSVC-i} \quad (10)$$

From (9) and (10), the value of the voltage change is obtained,

$$\Delta V_i = \frac{V_i}{2B_{SVC-i}} \Delta B_{CSVC-i} \quad (11)$$

When the bus voltage drops below the minimum security limit, it must be increased at least to the lower limit to maintain the quality of the power flow. In this paper, the voltage increase is limited to the lower limit so that a minimum SCV capacity is required.

$$V_i^{new} = V_i^{old} + \Delta V_{i-min} = V_{i-min} \quad (12)$$

In this proposed method, the value of  $V_i^{new}$  already meets the minimum-security limit voltage ( $V_{i-min}$ ), where previously ( $V_i^{old}$ ) is below the minimum-security limit voltage.

From (9) and (12) it can be derived the change in the minimum SCV capacity to increase the voltage to the minimum-security limit, namely:

$$\Delta Q_{CSVC-i-min} = 2 \frac{Q_{SVC-i}}{V_i} \Delta V_{i-min} \quad (13)$$

### 2.3. Effect SVC to Losses

Calculation of the effect SVC to losses refer to [22]. The line representation is shown in Figure 2. SCV generates reactive power in the network so that it will have an impact on line losses.

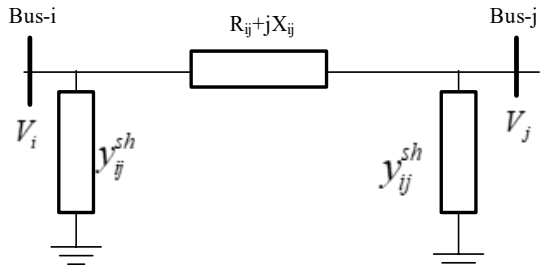


Figure 2: Phi equivalent circuit of line i-j

From Figure 2, line losses can be derived and yield,

$$Pl_{ij} = \frac{R_{ij}}{|z_{ij}|} (V_i^2 - 2V_i V_j \cos \delta_{ij} + V_j^2) \quad (14)$$

So for power system with n-buses, the total losses in power systems is,

$$Pl = \sum_{i=1}^n \sum_{\substack{j=1 \\ j>i}}^n \frac{R_{ij}}{|z_{ij}|} (V_i^2 - 2V_i V_j \cos \delta_{ij} + V_j^2) \quad (15)$$

Or,

$$Pl = \sum_{i=1}^{n_g} P_{g-i} - P_d \quad (16)$$

where  $P_{g-i}$  is the power generated by generator i, and  $P_d$  is the total load. The effect of the voltage on the bus k on the minimum

system losses is shown in Figure 3. Increasing the voltage  $V_j$  in (15) will reduce losses.

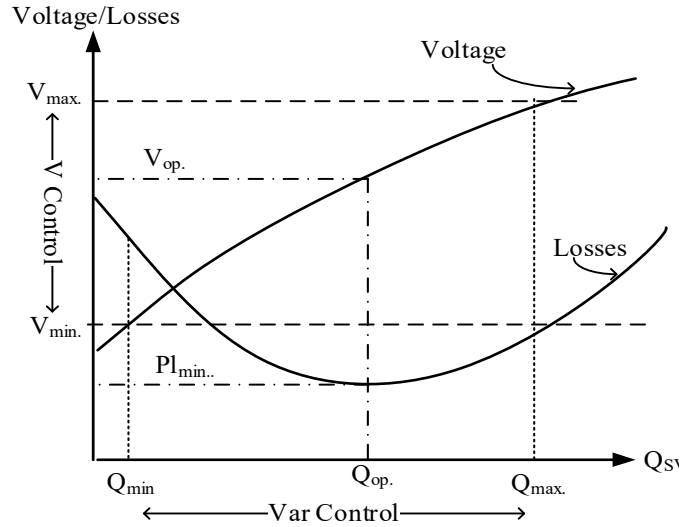


Figure 3: Bus voltage control

From Figure 3 it can be seen that the addition of SCV capacity will increase the voltage. Raising the voltage to the minimum safety limit ( $V_{min}$ ) requires the SCV capacity of  $Q_{min}$ . The effect of the voltage on the bus k on the system losses can be derived from Equation 15 and yield,

$$\frac{\partial Pl}{\partial V_k} = \sum_{\substack{i=1 \\ i \neq k \\ i \in k}}^n \frac{R_{ik}}{|z_{ik}|} (-2V_i \cos \delta_{ik} + 2V_k) \quad (17)$$

Meanwhile based on Equation 7 for  $Q_{SVC}$  compensation on bus k can be defined,

$$X = \frac{Q_{SVC}}{B_{SVC}} = V_k^2 \quad (18)$$

Substitute  $V_k$  for  $X$  from Equation 18 to Equation 16 and yield,

$$\partial X = \frac{\partial Pl}{\sum_{\substack{i=1 \\ i \neq k \\ i \in k}}^n \frac{R_{ik}}{|z_{ik}|} (X - \cos \delta_{ik})} \quad (19)$$

Then obtained  $\Delta X$  through Equations 16 and 19, namely:

$$\Delta X = \frac{\sum P_{Gt}^{old} - \sum P_{Gt}^{new}}{\sum_{\substack{i=1 \\ i \neq k \\ i \in k}}^n \frac{R_{ik}}{|z_{ik}|} (1 - \frac{V_i}{\sqrt{X}} \cos \delta_{ik})} \quad (20)$$

Finally the value of X can be updated,

$$X^{new} = X^{old} + \Delta X \quad (21)$$

Minimum compensation is reached if,

$$X_{k-min}^{SVC} = V_{k-min}^2 \quad (22)$$

where  $X_{k-min}^{SVC}$  is the minimum compensation.  $V_{k-min}^2$  is the lower voltage limit at bus k.

### 3. Flowchart of Proposed Method

The procedures for completing this work will follow the step by step diagram in Figure 4. Base case is determined by the results of calculating the power flow without SVC. Initial conditions are obtained from the base case. The voltage value is calculated from the updated compensation (X). This process is repeated until the voltage has reached the value of the minimum limit security ( $V_{min}$ ). Repeat for bad voltage drop on other buses. Finally, the calculation results are obtained: the minimum SCV capacity.

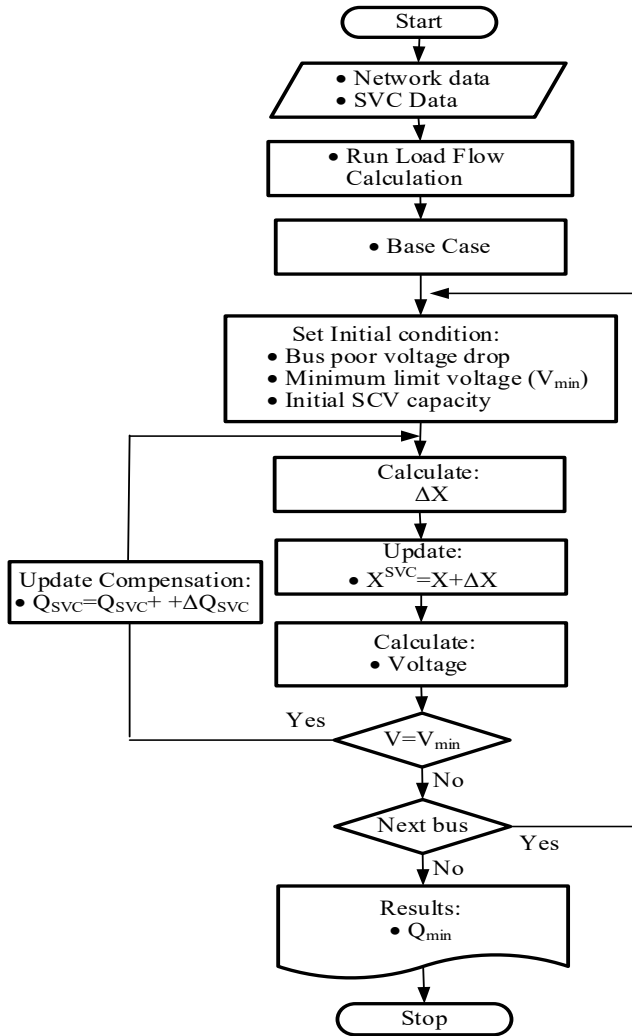


Figure 4: Flowchart of the proposed method

### 4. Simulation, Results and Discussion

The simulation is carried out through application software based on the flowchart in Figure 4 using the FORTRAN language. The software application is run using an Asus Core i3 laptop.

#### 4.1. Simulation

The proposed method has been tested through simulations on electric power systems in order to validate it. This simulation uses an IEEE 9-bus system with a one-line diagram in Figure 5. The data for this system are presented in Tables 1 and 2. In particular, Table 1 is the result of load flow based on the IEEE standard and

is used as a basis for calculations. While Table 2 shows the line characteristics. From the base case the voltage at buses 5 and 8 is below the minimum-security limit (0.90 pu). For this reason, minimum compensation is needed on these two buses to increase the voltage to the minimum-security limit.

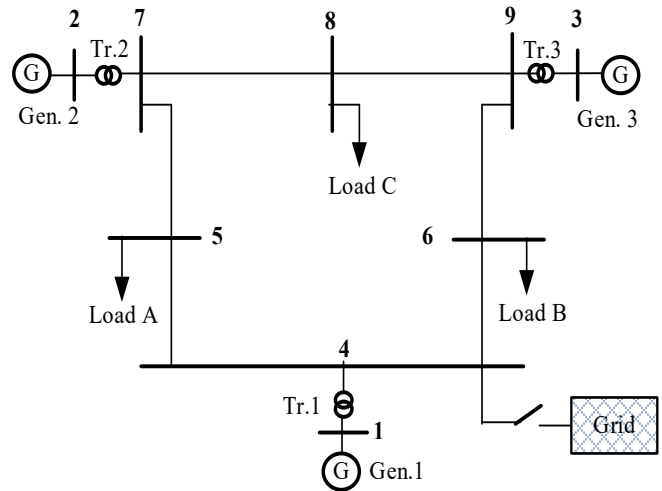


Figure 5: IEEE 9-bus power system

Table 1: Base case

No bus	V [pu]	P <sub>g</sub> [MW]	Q <sub>g</sub> [MVAR]	P <sub>d</sub> [MW]	Q <sub>d</sub> [MVAR]
1	0.950	0	0	0	0
2	1.025	163.00	130.75	0	0
3	1.025	85.00	192.92	0	0
4	0.953	0	0	0	0
5	<b>0.872</b>	<b>0</b>	<b>0</b>	<b>200.0</b>	<b>100.0</b>
6	0.909	0	0	90.0	30.0
7	1.040	391.84	203.21	0	0
8	<b>0.884</b>	<b>0</b>	<b>0</b>	<b>150.0</b>	<b>95.00</b>
9	0.916	0	0	180.0	130.0
Total		639.84	526.88	620.0	335.0

Table 2: Line characteristic

From bus	To	R(pu)	X(pu)	1/2Y(pu)
1	2	0	0.0625	1.000
2	8	0	0.0625	1.000
3	6	0	0.0586	1.000
4	5	0.0085	0.0720	0.0745
4	9	0.0320	0.6110	0.1530
5	6	0.0170	0.0920	0.0790
6	7	0.0170	0.0920	0.0790
7	8	0.0170	0.0920	0.0790
8	9	0.0320	0.6110	0.1530

#### 4.2. Results

The comparison of the results of the base case simulation without the SCV device is shown in Table 1. This table indicates the need for compensation for buses 5, and 8 because low voltage. From the results of the simulations carried out to increase the

voltage on buses 5 and 8, the minimum compensation values are obtained as shown in Table 3.

Table 3: Minimum compensation

#	Before Compensation			After Compensation		
	V (pu)	B <sub>scv</sub> (pu)	Q (MVar)	V (pu)	B <sub>scv</sub> (pu)	Q (MVar)
Bus 5	0.872	0	0	0.9	0.1978	21.0
Bus 8	0.884	0	0	0.9	0.0942	10.0
$f_d$	0.771958			0.803636		
Losses	19.84 MW			18.47 MW		

Note:  $f_d$  is the system power factor.

The load flow simulation results after compensation are presented in Table 4. The gain from this compensation is that the system loss drops by 1.37 MW.

Table 4: Power flow after compensation

No bus	V [pu]	P <sub>g</sub> [MW]	Q <sub>g</sub> [MVAR]	P <sub>d</sub> [MW]	Q <sub>d</sub> [MVAR]
1	0.961	0	0	0	0
2	1.025	163.00	112.77	0	0
3	1.025	85.00	179.83	0	0
4	0.965	0	0	0	0
5	0.900	0	0	200.0	79.0
6	0.921	0	0	90.0	30.0
7	1.040	390.47	180.21	0	0
8	0.900	0	0	150.0	85.00
9	0.923	0	0	180.0	130.0
Total		638.47	472.81	620.0	324.0

### 4.3. Discussion

The proposed method has successfully simulated the IEEE 9 bus system, which is presented in Tables 3 and 4. Table 3 presents the results of the minimum compensation on buses 5 and 8. The previous voltages (based on the base case) were below the minimum safety limits of 0.872 and 0.884 pu, all marked in bold. In the simulation using voltage security 0.9-1.1 pu, so the voltage on the bus becomes bad. To increase the voltage on buses 5 and 8 installed SCV. The SCV capacities required to increase the voltage to the minimum safety level (0.9 pu) are 0.1978 pu and 0.0942 pu, respectively.

The effect of Compensation (see Table 3) is to increase the voltage, not only at the bus being compensated but also at other buses. For example Bus-1 has a voltage of 0.95 pu (see Table 1) before compensation increasing to 0.961 (see Table 4) after compensation. In addition, shown by Table 3, the system power factor increased from 0.803636 to 0.771958 and losses decreased from 4MW to 3 MW or losses were saved by 6.9%.

This increase in voltage needs to be watched out for when it exceeds its maximum limit. If there is an overvoltage due to compensation, the compensation capacity is stopped until one/several bus voltages reach their maximum limit. Furthermore, the load shedding operation needs to be considered to increase the voltage on buses that have the bad voltage.

Besides that, compensation has advantages because it reduces losses. The load flow simulation after compensation in Table 4 states that total power production decrease from 639.84 MW to 638.47 MW or saving 1.37 MW. When these savings are converted to costs, the value is quite large.

Comparison with other results from [23] is shown in Table 5, where compensation on bus 8. The amount of compensation based on the reference is 27.46 MVar to increase the voltage at bus 5 by 0.993 pu compared to the proposed method requiring compensation of 10.00 MVar and the voltage at bus 5 increases to 0.921 pu.

Table 5: comparison results with another method

Item	Base Case	Reference Method	Proposed Method
		SVC at Bus 8	SVC at Bus 8
Losses (MW)	5.300	4.773	4.5389
Q <sub>scv</sub> (MVar)	0	27.46	10.00
Bus	V(pu)	V(pu)	0.961
1	0.950	1.040	1.025
2	1.025	1.025	1.025
3	1.025	1.025	0.965
4	0.953	1.024	0.900
<b>5</b>	<b>0.872</b>	<b>0.993</b>	0.921
6	0.909	1.010	1.040
7	1.040	1.023	0.900
8	0.884	1.000	0.923
9	0.916	1.027	0.961

This proposed method should be supported by fast and robust power flow calculations. There are three power flow methods that should be considered, namely the Gauss-Seidel, Newton and Fast Decouple methods, The Gauss-Seidel method uses an elimination technique that involves all parameters and variables so that the calculations at each iteration step will process large power system data. In addition, it takes many iteration steps to reach convergence. However, this method will be effective for small power system sizes. Newton's method is called the complete power flow method because it uses a complete Jacobean matrix. This causes a large memory usage. The fact that the changes in the calculation results to reach the solution point are quite small so that many iteration steps are needed. Whereas the Fast Decoupled method works by ignoring the out diagonal sub matrix of the Jacobean matrix and the element values of the Jacobean matrix are constants through the approach  $\cos \delta=1$  and  $\sin \delta = 0$  for  $\delta \leq 15^0$ . Through the Fast Decoupled method approach, it can work very quickly with a few iteration steps. The condition needed by this method is that each line must meet  $r/x < 1$ , where line impedance is  $z = r + jx$ .

The IEEE 9 bus system simulation results for the three methods are shown in Table 6. The Fast Decoupled method can work very fast, so it is very advantageous to apply it to real time calculations. However, this method does not work well for the line impedance conditions  $r/x > 1$ . If the Fast decoupled method cannot work, it is necessary to consider the full method option (Newton method).

Table 6: Comparison of three load flow methods

Item	Gauss-Seidel	Newton	Fast Decoupled
Process	Iteration	Iteration	Iteration
Technique	Elimination	Full Jacobean	Ignore out diagonal of sub-Jacobean. Approximate sin and cost values for small angles.
Accuracy	0.00000001	0.00000001	0.00000001
Iteration step	28	25	9.5
Running time	3.715s	3.125s	0.5s

## 5. Conclusion

The method of calculating the minimum compensation in the electric power system has been presented in this paper. Formulation validation has been tested through simulation of electric power systems in section 4 of this paper.

This work uses the IEEE 9-bus power system, based on the base case there are bad voltages on buses 5 and 8. SCV capacities of 0.19 and 0.9 pu are required to increase the voltage to the minimum safety level (0.9 pu) on bus 5 and 8 respectively. The effect of compensation is to increase the voltage across all buses. It should be noted that the voltage increase at the bus does not exceed the maximum-security limit. The addition of compensating capacity must be stopped if the bus voltage reaches its maximum safety limit.

The advantage of compensation is the reduction of system losses. This is caused by a decrease in reactive flow in the network so that the current is reduced. From the simulation results obtained a power saving of 1.37 MW to increase the voltage to the minimum limit level (0.9), where the voltage on bus 5 and 8 is 0.872 pu and 0.884 pu.

## References

- [1] T. Gonen, *Electrical Power Distribution System Engineering*, McGraw-Hill, 1986.
- [2] X. YE, J. LE, Y. LIU, W. ZHOU, K. LIU, "A coordinated consistency voltage stability control method of active distribution grid," *Journal of Modern Power Systems and Clean Energy*, **6**(1), 85–94, 2018, doi:10.1007/s40565-017-0294-z.
- [3] J. Dixon, L. Moran, J. Rodriguez, R. Domke, "Reactive Power Compensation Technologies: State-of-the-Art Review," *Proceedings of the IEEE*, **93**(12), 2144–2164, 2005, doi:10.1109/JPROC.2005.859937.
- [4] P. Kundur, *Power System Stability and Control*, McGraw-Hill, New York, 1994.
- [5] D. Quoc Hung, Y. Mishra, "Voltage fluctuation mitigation: fast allocation and daily local control of DSTATCOMs to increase solar energy harvest," *IET Renewable Power Generation*, **13**(14), 2558–2568, 2019, doi:10.1049/iet-rpg.2019.0223.
- [6] M. Alrashidi, "Community Battery Storage Systems Planning for Voltage Regulation in Low Voltage Distribution Systems," *Applied Sciences*, **12**(18), 9083, 2022, doi:10.3390/app12189083.
- [7] M. Aybar-Mejía, J. Villanueva, D. Mariano-Hernández, F. Santos, A. Molina-García, "A Review of Low-Voltage Renewable Microgrids: Generation Forecasting and Demand-Side Management Strategies," *Electronics*, **10**(17), 2093, 2021, doi:10.3390/electronics10172093.
- [8] R. Anilkumar, G. Devriese, A.K. Srivastava, "Voltage and Reactive Power Control to Maximize the Energy Savings in Power Distribution System With Wind Energy," *IEEE Transactions on Industry Applications*, **54**(1), 656–664, 2018, doi:10.1109/TIA.2017.2740850.
- [9] K.-D. Kim, W.-K. Yu, E.-J. Lee, I.-S. Wang, H.-J. Kang, J.-H. Shin, H.-J. Lee, "Development of an Intelligent Voltage Control System for Jeju Island in Korea," *Journal of International Council on Electrical Engineering*, **1**(2), 156–162, 2011, doi:10.5370/JICEE.2011.1.2.156.
- [10] H. Van Pham, S.N. Ahmed, *Multi-Agent based Approach for Intelligent Control of Reactive Power Injection in Transmission Systems*, John Wiley & Sons, Ltd, Chichester, UK: 269–282, 2018, doi:10.1002/9781119214984.ch13.
- [11] Y. Zhang, A. Srivastava, "Voltage Control Strategy for Energy Storage System in Sustainable Distribution System Operation," *Energies*, **14**(4), 832, 2021, doi:10.3390/en14040832.
- [12] A.K. Ali, M.M. Mahmoud, "Coordinated Distributed Voltage Control Methods for Standalone Microgrids," *International Journal of Robotics and Control Systems*, **2**(2), 262–276, 2022, doi:10.31763/ijrcs.v2i2.612.
- [13] M. Hojati Tabatabaei, H. Siahkali, J. Olamaei, "A quick solution to optimal coordinated voltage-control, based on dimension-reduction of power system via Modified Ward-PV," *Scientia Iranica*, **0**(0), 0–0, 2021, doi:10.24200/sci.2021.56970.4999.
- [14] H. Shahbazi, F. Karbalaei, "Decentralized Voltage Control of Power Systems Using Multi-agent Systems," *Journal of Modern Power Systems and Clean Energy*, **8**(2), 249–259, 2020, doi:10.35833/MPCE.2018.000628.
- [15] J.Y. Wen, Q.H. Wu, D.R. Turner, S.J. Cheng, J. Fitch, "Optimal Coordinated Voltage Control for Power System Voltage Stability," *IEEE Transactions on Power Systems*, **19**(2), 1115–1122, 2004, doi:10.1109/TPWRS.2004.825897.
- [16] K. Alzaareer, M. Saad, H. Mehrjerdi, D. Asber, S. Lefebvre, "Development of New Identification Method for Global Group of Controls for Online Coordinated Voltage Control in Active Distribution Networks," *IEEE Transactions on Smart Grid*, **11**(5), 3921–3931, 2020, doi:10.1109/TSG.2020.2981145.
- [17] C.K. Wachjoe, H. Zein, "A Method for Voltage Drop Monitoring on Load Sides in Medium Voltage Feeder," in *2020 7th International Conference on Control, Decision and Information Technologies (CoDIT)*, IEEE: 1215–1220, 2020, doi:10.1109/CoDIT49905.2020.9263852.
- [18] R. Thakur, P. Chawla, *Voltage Drop Calculations & Design of Urban Distribution Feeders*.
- [19] X.Y. Xu, P. Zhou, Q.Z. Huang, C.M. Deng, M.M. Shi, G. Xue, "Optimization of Voltage and Reactive Power in Regional Power Network Based on MCR," *Advanced Materials Research*, **986–987**, 394–399, 2014, doi:10.4028/www.scientific.net/AMR.986-987.394.
- [20] S.-I. Go, S.-Y. Yun, S.-J. Ahn, J.-H. Choi, "Voltage and Reactive Power Optimization Using a Simplified Linear Equations at Distribution Networks with DG," *Energies*, **13**(13), 3334, 2020, doi:10.3390/en13133334.
- [21] H. Zein, E. Dermawan, "Optimal Location of a Capacitor Bank in a Primary Feeder to Load up Linearly," *IPTeK Journal of Proceedings Series*, **0**(1), 2014, doi:10.12962/j23546026.y2014i1.370.
- [22] H. Zein, S. Saodah, S. Utami, C.K. Wachjoe, "Static VAR Compensation Capacity for Bus Voltage Setting in Electric Power Systems," in *2022 International Conference on Technology and Policy in Energy and Electric Power (ICT-PEP)*, IEEE: 1–6, 2022, doi:10.1109/ICT-PEP57242.2022.9988871.
- [23] J.V. and S.A.S. Parate, "Reactive Power Control and Transmission Reduction with Realization of SVC and TCSC," *International Journal of Engineering Science and Technology (IJEST)*, **4**(7), 3592–3600, 2012.

## How a Design-Based Research Approach Supported the Development and Rapid Adaptation Needed to Provide Enriching Rural STEM Camps During COVID and Beyond

Rebecca Zulli Lowe<sup>1</sup>, Adrienne Smith<sup>1,\*</sup>, Christie Prout<sup>1</sup>, Guenter Maresch<sup>2</sup>, Christopher Bacot<sup>2</sup>, Lura Murfee<sup>2</sup>

<sup>1</sup>Cynosure Consulting, Apex, 27502, USA

<sup>2</sup>North Florida College, Madison, 32340, USA

### ARTICLE INFO

Article history:

Received: 28 February, 2023

Accepted: 20 May, 2023

Online: 25 June, 2023

Keywords:

STEM

Summer Enrichment

Virtual Instruction

### ABSTRACT

Like many STEM research projects, the members of the National Science Foundation-funded STEM SEALS project dramatically shifted from in-person delivery of a summer institute to distance-learning with minimal time for preparation. However, the daunting challenge also offered the unique opportunity to apply Design-based Research within an exploratory study to inform and document the progression and supply counsel to other STEM providers contemplating a shift to a virtual platform. The goals of this exploratory study include (1) to make apparent the barriers to transitioning to virtual STEM enrichment programming in rural spaces during the COVID-19 pandemic, (2) detail important decisions made in the move online, along with the reasoning behind those decisions, and (3) share best practices that arose during the inaugural effort. Methods included the review of multiple data sources, including project meeting minutes, educator reviews of materials, and pre/post institute student and teacher surveys. to inform rapid-paced learning cycles. As a result, the team adopted a mindset that focused on high-quality STEM experiences. Strategies supported by the research include effective substitutes for in-person demonstrations, leveraging existing platforms, employing mechanisms for troubleshooting, and framing failure in ways that encouraged the development of a positive STEM identity.

## 1. Introduction

This paper is an extension of work originally presented at the 2021 Integrated STEM Education conference [1]. It utilizes state of the art research methods in the employment of an exploratory research study to understand best practices in transitioning high quality STEM learning environments from in-person to virtual.

Due to the COVID-19 outbreak, and the World Health Organization (WHO) officially labeling COVID-19 as a pandemic [2], K-12 education in the United States would change dramatically. When stay-at-home orders started going into effect in many states, many public schools were forced to close their doors and move from in-person instruction to online teaching. Soon after, many STEM educators and researchers, including the National Science Foundation-funded STEM Sea, Air, and Land (SEALS) team from North Florida College (NFC) in Madison, Florida, began to realize the pandemic would not be easily or quickly be curbed.

In early 2020, the STEM SEALS team was planning for some highly engaging educational activities for both educators and students in their six-county service region. The STEM SEALS team was led by STEM experts from NFC, a rural community college. The team included educational researchers from Cynosure Consulting, LLC (Cynosure). These activities included opportunities for participants to build rovers, boats, and drones, which they would learn to code and then maneuver to complete fun, yet rigorous engineering design challenges as part of a weeklong STEM camp hosted on the NFC campus. This inaugural camp would expose rural middle school students to hands-on engineering and computer science experiences. Earlier in the fall of 2019, the STEM SEALS team recruited nine middle school educators from the surrounding counties. This group formed the design team and spent one Saturday a month together, where they tested out the curriculum and shared input on the structure and design of the student experience.

As the pandemic began to unfold, it interrupted the project's spring plans in which the STEM SEALS team was in the middle of organizing. In March of 2020, the STEM SEALS team was

\* Corresponding Author: Adrienne Smith, 1302 Applethorn Drive, Apex, NC 27502, 919-616-1565, [adrienne.ann.smith@gmail.com](mailto:adrienne.ann.smith@gmail.com)

scheduled to host a large group of educators on the NFC campus to participate as a review team. As review team members, local educators would learn about the STEM SEALs experience content, give ratings as part of the feasibility testing, and offer critiques that would continue to inform curriculum development and revision. With the date of the on campus large review team meeting approaching, it was clear the impacts of COVID-19 were only increasing. Each day was met with considerable conversations and discussions, which started as predictions about when in the spring the review team would meet as planned to whether it would meet virtually or not at all. Sadly, the STEM SEALs team had to accept that holding a virtual review team was not a viable alternative. The decision was made to postpone the spring review team meeting altogether. As the COVID-19 numbers surged in the US and Florida's own cases began to spike, it became evident that the inaugural STEM SEALs summer camp was in jeopardy of cancellation.

Finally, on April 24<sup>th</sup>, the STEM SEALs team was compelled to make a decision about the fate of the inaugural STEM SEALs enrichment camp that was planned for June. From a national perspective, it became clear that the COVID-19 pandemic was affecting many informal STEM experiences scheduled for the summer. Despite months of developing curriculum materials, testing out prototypes, and carefully arranging an in-person STEM SEALs camp with safety as a priority, it became evident STEM SEALs could not overcome the effects of the pandemic. Knowing the importance of the project goals to learn about best practices in offering high quality STEM exposure and interest for middle grades students in rural areas, the STEM SEALs team reluctantly made the decision to go virtual.

### 1.1. *The Need to Push Forward*

#### **Underrepresentation of Rural Students in STEM**

The underrepresentation of rural students in STEM is not a recent phenomenon, but in the past two decades, the issue has been receiving greater attention. Studies and literature reviews have advanced the field's understanding of the barriers that rural students face. Rural students struggle with issues of geographic separation and insufficient internet bandwidth to support online access and complete access to many technological advances [3]. They face limited opportunities to engage in advanced coursework in mathematics and science [4], and financial obstacles that limit future employment and educational prospects [5]. School administrative data have shown low participation in advanced coursework among low income, rural students in comparison to students from high-income families. The result is an excellence gap that is evidenced as early as elementary school and persists through high school [6]. Education researchers assert that this excellence gap "represents a growing crisis requiring programmatic intervention" [7]. Students in rural schools, particularly those that are under-resourced, are less likely to reach advanced levels of academic achievement compared with their urban peers, even when they demonstrate high potential [8].

#### **Challenges and Strategies for Rural Students**

Rural students that show high potential for academic success confront barriers that limit options for academic acceleration, putting them at risk of becoming part of the "persistent talent underclass" [9]. Researchers studying this excellence gap have identified innovations that can mitigate access to advanced

coursework in high school. They point to programming outside of school time designed for middle school students as a potential stop gap measure [7]. These kinds of programs are advantageous for multiple reasons [6]. Spending time socializing outside of school increases positive peer interactions and stimulates social development, in addition to academic learning for middle school students [10, 11]. These benefits are larger for at-risk students, for whom researchers have documented a link between extracurricular programming and educational success [12].

Not only do informal educational experiences serve as mitigating factors for poor academic outcomes, but they can also serve as a catalyst for the decision to seek advanced coursework in high school [6]. Researchers voice that for the strategy of improving high-potential rural students' STEM achievement through extracurricular programming to work, implementers "must also consider the inclusivity of identification models for such programming" [7]. This STEM SEALs project set out to model the potential efficacy of a widely inclusive outreach strategy with the purpose of reaching a broad pool of rural, high-potential students who are ready for STEM development opportunities.

### 1.2. *Guiding Framework*

The STEM SEALs project was always designed to be more than the creation of a high-quality STEM camp. The work of STEM SEALs was nested within a larger research design focused on efforts to develop rural STEM education pathways and building an evidence base for the emerging strategies and materials with the larger vision of creating broader access to high quality STEM experiences for students in rural parts of the country. The STEM SEALs project was not simply an outreach or STEM enrichment project, but instead, STEM SEALs was from the outset framed as Design-based Research [13, 14]. Design-based Research has been widely used in education, and curriculum development, in particular, where research and design activities are often inseparable parts of improving current practices and refining design theories and principles [15]. It has also been used extensively for researching and improving professional development [16]. This systematic methodology aims to improve educational practices through a cyclical process that involves iterative periods of design, testing, evaluation, and reflection between researchers and practitioners conducted in real-world environments [17].

Design-based Research has its roots in a larger movement near the beginning of the 21<sup>st</sup> century that looked to more effectively bridge the gap between research and practice. It acts as a practical methodology which serves dual roles for both developing and informing learning theory and the means designed to support that learning [13, 14, 18, 19, 20, 21]. In fact, it has been used to improve STEM education in a variety of ways, including developing new curricula and instructional materials for teaching science online to middle students [22]. In this example, the new curriculum was designed to engage students, including English-language learners and students with a disability. The Design-based Research process utilized data from multiple sources, including teacher logs, student and teacher surveys, and focus groups. Results showed the developed curriculum to be feasible, useful, and effective with a diverse student population. It also demonstrated that Design-based Research is a practical framework in such settings. The Design-based Research method has also been used in designing forensic science games for middle school students [23] and developing assessment tools for measuring

students' science critical thinking skills [24]. Supporting teachers in implementing new STEM curricula and instructional materials is another context that has utilized Design-based Research methods. In a recent example, a study by the authors in [25] used Design-based Research to develop a professional development program for supporting teachers in developing children's spatial reasoning. The professional development program was designed to help teachers understand the principles of the curriculum and to develop the skills they needed to implement it effectively. Researchers found Design-based Research to be a catalyst for epistemic change. Overall, Design-based Research is a promising methodology for improving STEM education. It is a flexible and iterative approach that allows for the development and refinement of interventions in real-world settings.

The structure of this Design-based Research study was bolstered through the use of a modified version of the Successive Approximation Model (SAM) [26] to ensure the iterative development process (a) occurs in small steps in association with ongoing evaluation that informs iterative changes, (b) supports productive collaboration among project team members, (c) directs energy and resources effectively in order to move efficiently with intervention development, and (d) allows for manageable completion of high quality projects both on time and on budget. Developers cycle through phases of analysis, design, and development supported by embedded research that routinely provides formative assessment and input to inform the ongoing development efforts. Central to this approach is the use of an iterative "development-revision-testing" process with teachers and students to ensure materials and activities are understandable, appropriate, and engaging.

Design-based Research has been heralded as a research approach that could help those looking to fill the research-practice gap by bringing educational research closer to the needs of educators in the field. The use of this approach by the current project provided clear evidence that supports this contention, with the STEM SEALs use of the Design-based Research approach emerging as a highly effective model for promoting the rapid innovation and adaptation needed to develop, implement, and build momentum under the spectra of the COVID-19 pandemic. Ultimately, the STEM SEALs research project outcomes and findings provide significant evidence in support of the effectiveness of Design-based Research framework for bolstering innovation. This article will provide an illustration of emergent innovations that resulted from its use by STEM SEALs to foster innovation within STEM enrichment in rural counties and a discussion of the key mechanisms of the approach associated with the bolstering of project success.

### 1.3. The Phases of Design-Based Research

The Design-based Research process "consists of four phases: (1) analysis of practical problems by researchers and practitioners working in collaboration; (2) development of new solutions informed by existing design principles; (3) iterative cycles of testing and refinement of solutions in practice; and (4) reflection to produce design principles and enhance solution implementation [27]. Each of these phases was operationalized by the project. See overview in Figure 1.

#### Phase 1: Analysis of practical problems by researchers and practitioners working in collaboration

*Assemble Diverse Team of Researchers and Practitioners.* To address the practical problems that emerged, a project leadership team was assembled with individuals bringing different expertise and skillsets. The STEM SEALs team included members with first-hand experience as STEM teachers in the rural area, education researchers, and content experts from a rural community college representing the fields of Physics, Engineering, Biology, and Advanced Manufacturing.

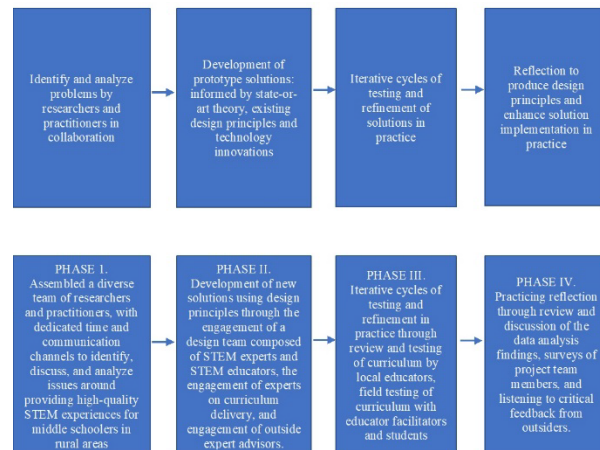


Figure 1: Design-based Research Process Operationalized

*Routine and Ongoing Communication with Diverse Team around Issue of the Need for High-quality STEM Experiences in Rural Spaces at the Middle Grades Level.* Through weekly meetings and ongoing project communication and activities, the team engaged in analysis of the existing problems of practice of access to STEM enrichment and capacity deficits in rural areas to come up with the multi-faceted model for addressing those issues within the context of designing a STEM experience that serves the needs of both students and teachers.

#### Phase 2: Development of new solutions informed by existing design principles

The second phase was addressed by the collaborative STEM SEALs team through engaging in iterative intervention development guided by the SAM model.

*Design Team Collaboration for Curriculum Development.* A key task for the project was creating instructional content that leverages an additional and important group of collaborators – current middle school educators within the rural area. To do this, a design team was comprised of nine rural educators with expertise in middle grades STEM instruction who hail from the five counties within the NCF service area. Design team members attended three day-long meetings where they listened to STEM experts, offered input, engaged with materials, and provided recommended changes in the development of the student institute experience. Design team members provided written and verbal feedback and observation of their use of the materials served as additional data to inform the design. Evaluators and research members from the STEM SEALs team spoke with members of the design team to further understand and be responsive to the ideas raised. The specific input received from content experts, best-practice research, and individuals who work with students in authentic education settings provided a strong foundation for the full scope of curriculum, although the details were subject to change during iterative development.



*Engagement of Different Experts to Inform Curriculum Delivery Design.* Social psychology research provides a wealth of information on techniques and strategies for supporting underrepresented groups in STEM. Led by Cynosure's social science and education researchers, the research team, a subset of the STEM SEALs project team, identified opportune moments within the sequence of the module delivery to elicit conversations and address misconceptions related to who does STEM and what a STEM career looks like. Additionally, activities supported by best practices in the education research literature were incorporated into the modules delivery to bolster the confidence and self-efficacy of rural students as well as develop a growth mindset and sense of identity within STEM. For example, students will watch as the experts troubleshoot, seeing productive failure as an integral part of the engineering design process.

*Consultation with External Advisors.* The project leaders also consulted with advisory board members to solicit feedback on the process of developing high quality materials and designing engaging STEM experiences. Advisory board members brought a wealth of expertise on informal STEM and the intersection between faculty, practitioners, and rural populations. Their feedback was used to refine drafts to maximize implementation with fidelity.

### **Phase 3: Iterative cycles of testing and refinement of solutions in practice**

*Feasibility Testing with Local Educators.* To ensure the curriculum materials were understandable, appropriate, and useful for the intended population, middle grades teachers from the region were recruited to review and react to several of the developed modules planned for the institute. Reviewers were given the physical supplies and curriculum materials associated with each module to work through independently (with a STEM SEALs team member available for questions and trouble shooting.) After each module review, the reviewers completed a form where they rated the module, reflected on the feasibility of the module within a real-world summer institute with middle school students, and provided big picture and detailed feedback along with recommendations to improve the materials. Within the feedback, participants rated the intervention (from 1=Strongly disagree to 5=Strongly agree) to assess: (a) ease of use, (b) innovation, (c) value and need, (d) feasibility, (e) potential effectiveness for achieving intended goals, (f) usability, (g) advantages over existing methods; and (h) overall quality. Educators also rated the degree to which they: (a) would recommend the proposed intervention to schools, (b) would use the intervention themselves, (c) believe the intervention would be effective for preparing students in STEM, and (d) recommend continued development and testing.

As part of the review process, all reviewers were invited to the NFC campus to take part in the module activities during a day-long, more in depth exploration of the materials with the content experts. The purpose was two-fold. First, by implementing pieces of the institute with middle school educators the STEM SEALs team could gather feedback on the appropriateness of the language used as well as the assumptions made about students' pre-requisite content knowledge. Implementers would glean a stronger understanding of the extent to which guidance is needed for handling lab equipment and hear strategies for helping students stay on task and support them in their learning. Second, through the reactions and questions of teachers to the modules, implementers could assess the extent to which teachers have

mastered the content and gain a better awareness of the content information that will be needed in module curriculum facilitator guides.

Lastly, review team members were invited to attend a focus group to gather quantitative and qualitative evaluation data. These data helped the team ascertain whether educators (a) view the intervention as demonstrating high quality, innovation, and value; (b) advocate use of the intervention as feasible and needed for schools; and (c) recommend continued development and testing. During the focus group sessions, the project team member also led group discussion to gather specific comments and suggestions, including review of the implementation guidelines to gather information on potential feasibility and fidelity challenges.

Data were analyzed by the research team to assess the degree to which the curriculum materials are acceptable. If any module failed to meet the team's standards, it was revised accordingly based upon feedback. Examples of revisions included removing confusing elements or adding clarifying directions for equipment use or assembly, substitution of more simplified code, and addition of videos or other resources to extend the learning.

*Field Testing with Educator Facilitators.* Local middle school educators were invited to serve as facilitators of the summer institute, under the direction and support of the community college content experts. During and upon the conclusion of the summer institute, facilitators provided feedback on the experience. Mechanisms were in place to collect data by researchers, evaluators, and content experts and designers. These feedback mechanisms allowed for just-in-time adjustments to the experience and served as a record for changes and recommendations for future institutes.

*Field Testing with Students.* To assess the usability of the materials, students in middle grades were recruited to participate in summer institutes that allowed them to engage with the STEM SEALs materials and culminate with a design challenge. Feedback from students was gathered through informal interviews with students during the institute, observation of their affect and behaviors during the institute, a survey soliciting written ratings and recommendations at the end of the experience, and analyses of pre- and post-institute assessments of key anticipated outcomes.

The iterative design-develop-test process involved multiple testing cycles. Early tests allowed the STEM SEALs team to enact the module curriculums (and design challenge) with the intention of gathering feedback to inform further revisions. Later tests serve more as a pilot, that is, is a more formal testing of the revised modules (and design challenge) to examine whether the intervention elicits the intended outcomes.

### **Phase 4: Reflection to produce design principles and enhance solution implementation**

*Review and Discussion of Data Analysis Findings.* Data from all the processes described were analyzed and then shared with the STEM SEALs team, who reflected and shifted as needed based on the data. This phase involved the use of deliberate reflection activities to ensure that sensemaking happens routinely around the contributions, insights, recommendations, and lessons learned.

*Surveying Project Members as Mechanism for Reflection.* For example, STEM SEALs team members completed reflection forms separately. These data were analyzed, and common themes

shared during team meetings to solicit further discussion and to form the basis for revisioning efforts.

*Reviewing Outside Reactions to Further Stimulate Reflection.* Additionally, the convening of an advisory board and an Expert Teacher Material Reviewer helped to engage in further synthesis, sharing, and outside review and reflection based on experts from the field.

## 2. Method

While Design-based Research was a lens woven into the fabric of our study originally, its application was indispensable during the fast-shifting events that followed the advent of the COVID-19 pandemic. The designers and implementers of the innovation had to make rapid decisions. It was unclear whether the situation would be replicated, and it felt important to be mindful when cataloguing decisions and their rationale under the current context. Suddenly, there were new questions raised, ones whose answers could quickly and meaningfully contribute to the field. The researchers on the STEM SEALs team chose to adapt the Design-based Research approach to create a rapid learning process to align with the quick pace of the pivots made by those implementing. The results were an approach that situated rapid cycles of iteration within a modified Phase IV Design-based Research strategy, with the aim of engaging in strategic data-informed efforts to successfully navigate the pandemic-mandated pivot from an in-person STEM enrichment event to a virtual offering. What ultimately resulted was a series of rapid Design-based Research cycles. Within each cycle the barrier is identified, solutions explored, alternatives analyzed, and a decision is made. See Figure 2.



Figure 2: Design-based Research Rapid Cycle Iteration Process

Ultimately, Design-based Research, on overdrive, if you will, became the methodological mechanism for both informing and capturing the important learning during this time.

Thus, the over-arching research question guiding this effort was, “To what extent does a Design-based Research approach support the development and rapid adaptation needed to provide enriching rural STEM experiences?”

To answer this question, an exploratory study (described next under “Exploratory Approach”) was developed, guided by Design-

based Research, in which existing data (that is, data collected for other purposes) were leveraged along with the collection of additional data, tailored to addressing the specific needs of the Design-based Research rapid cycle iterative design effort (described under “Data Sources”).

### 2.1. Exploratory Approach

The findings presented in this article were generated utilizing a qualitative framework at the level of exploratory analysis with the goal of garnering insights on the emergent success of the approach at promoting adaptation and innovation associated with the project’s success at navigating the challenges and barriers presented by the sudden shutdown of schools and bans on gathering associated with the initial months of the COVID-19 pandemic. Exploratory studies are a type of preliminary research that provides initial information and sense-making. It serves as a foundation for later efforts poised to yield more conclusive findings [28]. Selecting an exploratory design offers several advantages aligned to the goals of this study, including: 1) affording researchers flexibility to adjust and adapt as research advances; 2) permitting researchers to recognize parts of a phenomenon that merit additional study earlier in the process; and 3) assisting other researchers by identifying potential causes of and solutions to a problem, that may be more intensively studied in the future. Additionally, the potential to encourage rapid learning, increase uptake, and share knowledge with the field means the study approach can be responsive to the larger national need for expertise on how STEM enrichment providers can transition from traditional approaches to innovations such as virtual, asynchronous, or blended content delivery models.

### 2.2. Design-based Research Rapid Cycle Data Sources

Data were collected from various sources to make explicit and unpack the STEM SEALs team’s reasoning before, during, and after making the decision to pivot to on online delivery. The utilized data sources include the following:

#### Project Team Meeting Participation and Minutes

The STEM SEALs team convened on a weekly basis in order to document the project’s activities and accomplishments, discuss challenges and issues, make key decisions, and plot out upcoming tasks. Discussions were recorded and meeting notes summarized to document important decisions and their rationale.

#### Project Team Reflection Survey Responses and Transcript

The STEM SEALs team members were each given a reflective survey that they completed individually. These surveys were compiled and analyzed by the research team and shared formally through a group reflection activity. The analysis and the transcript from the reflection activity meeting served as data sources for this study.

#### Internal Review of Virtual Delivery Methods and Materials

Instead of engaging an outside review team during the rapid cycle, the research team asked the STEM SEALs members who had developed the materials to engage in a virtual walk through of the rover experience. This included facilitating a session where the research team coded the Micro:bit, assembled the rover, and manipulated the rovers to accomplish tasks. The review was conducted through the online Zoom platform for two days, March

27<sup>th</sup> and April 3<sup>rd</sup>. It served as a critical initial field test of the material implementation virtually.

### Research Team Facilitated Group Review, Analysis and Decision-making

Data that were collected related to barriers identified were routinely analyzed and presented at STEM SEALs team meetings. Typically, the analysis summaries were provided in advance and explored together during a facilitated virtual meeting. Ultimately, the meetings ended with a decision on a solution or response to the identified barrier.

### 2.3. Design-based Research Rapid Cycle Product Test Stage (the Camp) Data Sources

Data were leveraged from several sources to serve as evidence of success of the product of the Design-based Research rapid cycle process. In this case, the product was the camp itself. An inventory of these data sources included:

#### Observation of Virtual Camp Experiences

The virtual STEM SEALs experience was held July 8<sup>th</sup> through 17<sup>th</sup> of 2020. The virtual camp involved resources cataloged and accessible to participants using the Google Classroom platform. Support was offered by NFC staff through live in-person demonstrations and discussions and as-needed asynchronous support. These support sessions were recorded as part of the observation data collection.

#### Data from Teachers

Data generated from pre- and post-camp surveys captured information on educator backgrounds and perceptions of STEM. Teachers also completed reflection surveys at the end of activities during the STEM SEALs summer camp. The purpose of these reflections was to better understand how teachers and their students experienced the materials and to collect any recommendations for improvement.

#### Data from Students

Data was also collected through student surveys. These surveys asked students about their background and knowledge of STEM at the end and the beginning of the camp. Students also completed end of module assessments to document their learning. Lastly, students took part in an end-of-camp reflection exercise where they were asked to look back on their time at the camp and provide their impressions of the experience as well as offer any recommended changes.

### 2.4. Data Analysis

This exploratory study, situated within the larger project, involved multiple layers of data analysis. Three different perspectives were adopted to address the research question: 1) to delineate the role that emerged for Design-based Research within rapid applications, 2) to describe the contributions and outputs of the rapid Design-based Research cycles on the resulting product, and 3) to test the resulting product. In addressing these aims, qualitative data analysis techniques were predominantly employed. The data analysis strategy varied based on its purpose within the rapid Design-based Research cycle. The data were synthesized systematically and then objectively analyzed using mechanisms that identified key themes. In some cases,

quantitative analysis techniques were further incorporated through summarizing program tracking and survey assessment data. Survey data were analyzed with the statistical software Stata (Version 13) and descriptive statistics were computed. Data verification strategies were incorporated within and across the data analysis activities. Triangulation of findings was conducted such that meeting documentation, field records, and transcripts were referenced as the researchers on the team utilized an iterative process of detecting and categorizing emerging themes, then cross-checking those themes with the various sources of data for confirming evidence.

## 3. Results and Discussion

In early 2020, the STEM SEALs team began to finalize the first inaugural enrichment camp where student participants would be immersed in autonomous and remotely controlled robotic devices. The event was scheduled to reside on the NFC campus and would serve up to 48 participants. Then the pandemic struck. The team looked to regroup with the uncertainty of how to implement the camp while also complying with safety provisions that required social distancing. To even attempt, the STEM SEALs team narrowed in on the robotic rovers and decided to focus specifically on the activities that would culminate in a Land Challenge. Figure 3 displays an image of the rover students would assemble, code, and operate. To lessen obstacles in an already challenging time, recruitment for the first camp was restricted to those educators who had been involved with STEM SEALs as a member of the design or review team. For those educators, the student participant pool was assembled. The student pool was restricted to those individuals who resided with the educator or those whom the educator was in regular close contact (e.g., a grandchild).



Figure 3: Image of Assembled Rover

The camp activities were organized into six modules (see Figure 4). These modules included lessons that introduced students to the overarching engineering design challenge which was the focus for the weeklong summer experience. Following the curriculum timeline, next students would be exposed to coding using the Micro:bit and then begin their construction of the rover. Once built, the students would learn how to use the Micro:bit to control and navigate the rover. The week culminated with a competition tied to the engineering design challenge.

STEM SEALs staff mailed to all participants kits that contained pieces of the rover and assembly tools, as well as binders that served as manuals for the camp. The camp officially began on July 8<sup>th</sup> and lasted until July 17<sup>th</sup>. A total of 29 teachers and students participated. The camp included online meetings each day. These meetings provided a space for students to receive help from the NFC expert team as desired. Teachers were also available

to support and aid students as best they could while also working through the STEM SEALs learning modules.

<b>Module 1: Introduction to the LAND Challenge</b>	
1.1	Student Guide
1.2	Google Classroom Orientation
1.3	Sharing with Flipgrid
1.4	Getting to Know Your Survey
1.5	Your Perceptions
1.6	Getting Warmed Up
<b>Module 2: Introduction to the Micro:bit</b>	
2.0	Student Guide
2.1	What is a Micro:bit?
2.2	What function does the Micro:bit serve in the STEMSEALs Design Challenges?
2.3	Unpacking your Micro:bit
2.4	Exploring the Features and Functions of the Micro:bit
2.5	Use the Micro:bit to Introduce Yourself
2.6	Use the Micro:bit to Play a Game
2.7	Understanding the Micro:bit LEDs
<b>Module 3: Chassis Assembly and Propulsion</b>	
3.0	Student Guide
3.1	Rover Kit and Assembly Tips
3.2	Assembling the Rover
3.2	Assembly Flipgrid
3.3	Making the Rover Move
3.4	Reverse Motion and Speed Test
C1:	Check Your Understanding
<b>Module 4: Controlling the Rover</b>	
4.0	Student Guide
4.1	Using the Micro:bit Radio Functions
4.2	Steering with a Remote Control
4.3	Is your Head on Straight?!
4.4	Steering Calibration
C2:	Check Your Understanding
<b>Module 5: Rover Navigation</b>	
5.0	Student Guide
5.1	What is an Ultrasonic Sensor?
5.2	Sonar Calibration
5.3	Navigating Obstacles
5.4	Navigating Obstacles with Artificial Intelligence
C3:	Check Your Understanding
<b>Module 6: Design Challenge Competition</b>	
Event 1:	Creativity Expo
Event 2:	Race to the Limit
Event 3:	Barrel Race Challenge (Remote Control)
Event 4:	Cutting Corners
Event 5:	Race the Wall-E
Event 6:	Freestyle Course Challenge
C4:	Check Your Understanding

Figure 4: STEM SEALs Camp Content Overview

Individually, students met at the competition site and had a chance to show off their rovers and compete in the challenge.

Feedback on the camp was offered in multiple ways, mutually supporting the value of the experience on student STEM learning.

For example, students said:

*I personally liked learning the coding processes that went into coding the Micro:bit. Learning the code and seeing it work was really satisfying.*

[www.astesj.com](http://www.astesj.com)

*I learned a bit more about the electromagnetic scale and got a more in-depth description of how radio waves communicate with each other.*

*I learned about how even computers use a simulated sense of echolocation to decide how far an object is from it and the patterns it uses to get around the obstacle.*

### 3.1. Findings

The findings section includes a presentation of the iterative design process outcomes along with documentation of the emergent Design-based Research roles and activities at each point in the process. The goal was to document the key decisions at each point in the process and the underlying STEM best practices that were instrumental in the success of the pilot. Ultimately, the findings are in service to a larger question of whether Design-based Research is a good fit for developing high quality STEM experiences, and especially so in situations that require rapid decision-making and significant pivots over time.

### Making the tough call

*Recognizing that it was now or never.* Eventually, the time came when a decision would be needed before the window of opportunity for holding a virtual camp would close. Fortunately, the entire project team recognized that there was no more time to wait or debate. They made the final decision to abandon the idea of an in-person event and instead, move forward with a virtual camp.

Although the pandemic forced US schools to close their doors in late March and early April of 2020, the idea that offering an in-person summer camp opportunity might be in jeopardy was not a consideration, at first. The STEM SEALs team initially thought the county and schools would open in plenty of time to move forward with an in-person summer camp. However, as the pandemic dragged on, the STEM SEALs team began to doubt whether an in-person event would be feasible. When no break in the social distancing restrictions was visible on the horizon the team started to acknowledge that virtual might, in fact, be the only option available. Reluctantly, the team accepted that the inaugural STEM SEALs camp offering would be held as a virtual event.

Early in this process the research team recognized that they were going to be entering into uncharted territory. The traditional approach with well-laid out, pre-determined research activities would need to be paused in favor of strategies that would align to the rapid switch and emerging needs of the new design efforts. As had been the structure of the partnership since the beginning of the grant period, the research team continued to engage in weekly meetings with NFC expert team. It was through these meetings that the new Design-based Research approach began to provide support aligned to the rapidly shifting design efforts. Within these meetings, the research team would identify a welcomed and impactful role as an external sounding board as the NFC expert team collectively began confronting the realization that the social distancing mandates put in place to slow the spread of COVID, might potentially prevent them from hosting an in-person camp as planned. With so much work completed already and so much excitement building to kick off the seminal activities of the project, it was understandable how reluctant the NFC expert team was to accept that the event could not happen as planned.

The research team helped to nudge the STEM SEALs team toward what they recognized as a necessary pivot during the

meetings, sharing about other groups that they were working with who had already made the decision to pivot and providing encouragement that it could be done with STEM SEALs as well. Perhaps more importantly, the research team listened to the thoughts and concerns that were being voiced by the team members and adopted a formal role of providing formative feedback that redirected focus back to areas where issues had been raised, but not yet fully addressed. Ultimately, it was in this role of re-voicing that the research team significantly contributed to the making of a timely decision. The research team recognized that the logistical needs and timeline concerns frequently raised by the project manager needed to be highlighted. This Design-based Research activity was simple, but it proved essential through helping to direct the NFC expert team's focused attention on fast approaching deadlines before they passed. For example, the research team brought up the required timeline needed to successfully engage in recruitment - along with highlighting the long list of activities that would need to occur beforehand.

### Expectation setting

*Avoiding the "Anything is Better than Nothing" Mindset.* Initially, when the STEM SEALs team realized that there was no way that the pandemic conditions would resolve in time to host an in-person event, two competing mindsets emerged: 1) *If we can't do it the way we envisioned, then there is no point in doing it*, and 2) *We need to do something and anything we do is better than nothing*. The team gradually began to embrace the notion that flexibility in the original vision was necessary. However, the team was also firm in not wanting to water down the student experience or alter the main activities that had been so carefully selected. Ultimately, it was the team's deep-rooted commitment to find ways to preserve the foundational elements of STEM SEALs, that propelled them to be able to do what at times seemed impossible, rather than reluctantly shifting toward the second mindset. The commitment to this mindset was an essential component of their persistence and willingness to innovate and adapt to find ways to engage students in a virtual experience that would afford opportunities for them to assemble a rover and to write and run the code that would allow it compete in a real challenge course.

As done previously, the research team engaged with the NFC expert team members weekly with the intention of documenting the process, collecting formative data, creating feedback loops for sharing back findings, and supporting the use of findings to inform continued adaptation and revision. Consistently, but in a much more fast-paced manner, the Design-based Research team had to sacrifice some aspects of rigor to ensure that thoughts were shared in time for decisions to be made. During this time, the research team listened and asked questions, trying to understand more about points of disconnect and indecision and quickly recognizing that the project had yet to engage in the best practices to establish a collective vision. The steps taken to elicit that vision were ultimately very worthwhile, because while many similar efforts pivoted with the "anything is better than nothing" mindset guiding their work, avoiding that mindset was a very important goal of the STEM SEALs team.

The fear that their inaugural effort would be something that lacked the flavor and rigor of what the team had been excited to offer in the original format, was something that permeated their early planning conversations. It was not until they recognized that there were central aspects of the STEM SEALs engagement that would have to be incorporated, or else the team preferred to

abandon the idea rather than try to offer something less. Through questions designed to identify the components of the vision that individuals valued and for which there was significant consensus, the research team supported the NFC expert team in identifying the elements that were believed to be fundamental to the project:

- 1) Providing an opportunity for student participants to construct their own rovers,
- 2) Teaching them how to program a Micro:bit to use in controlling the rover, and
- 3) Allowing them to use their acquired skills to complete a challenge course in competition of some form with others in the camp.

### Identification of the key challenges

*Keeping Students on Track and Maintaining Pace.* Quickly the STEM SEALs team noted how the shift from an in-person to virtual delivery would affect student pace and their ability to note slowdowns and intervene. In the face-to-face delivery as originally envisioned, students could work at their own pace, but that pace would be watched by the teachers and the NFC expert team so they might intervene with support when students got stuck or off-task. The teacher facilitators could assist in making sure all students were successfully able to complete the camp's essential elements. But, the virtual environment did not have the same level of oversight. The team wondered how the organization of the camp content could be structured in such a way that all students were able to follow along, stay on track, and proceed at their own pace.

*Finding an Effective Substitute for In-Person Demonstrations.* In the original, in-person design, the NFC experts planned to provide additional scaffolding for the teacher facilitators and their students through on-demand demonstrations. Thus, the STEM SEALs team had to grapple with the issue of defining and crafting further resources to set students up for success, but without the benefit of on-the-spot, step-by-step, in-person demonstrations. Another related loss was that the in-person demonstrations also afforded students the opportunities to watch other participants and learn through watching and benefiting from other students' efforts to progress through the process. Finding ways for students to receive the instruction needed for them to build their rovers successfully in lieu of the in-person strategies would be a challenge the project would need to overcome.

*Providing Students with the Personalized Support Needed to Stay Engaged.* The activities and learning tasks associated with the STEM SEALs modules are designed to be novel and challenging. In a face-to-face setting, students would be monitored and supported, but the team recognized that the virtual format potentially left students unprepared and without sufficient support to experience the desired level of success. Without a sufficient level of support, the STEM SEALs team feared the students would not stay engaged or be successful. This facet was complicated because the team recognized that the rigor of STEM exposure that was envisioned provided opportunities for students to grapple and problem-solve and with appropriate support to thrive. Without appropriate support most would likely end up frustrated or, even worse, quit in the face of what they perceived to be their failures. Ensuring sufficient support and scaffolding for students engaging in STEM is challenging in any format, but during a pandemic, through a virtual interface, within a rural setting, and maintaining

social distancing guidelines providing suitable support posed an enormous barrier.

As the team forged forward, much of the early conversations were around concerns about what would not work or what needs students would have that would not be easy to meet in a virtual format. In some ways, these conversations sounded a bit like a listing of the top ideas why there was no way to offer the STEM SEALs vision in a virtual format. Eventually, there would be recognition that all most all their concerns and what ifs emanated from four primary hurdles that the team would need to overcome to have confidence that the vision for the STEM SEALs camp could be carried out successfully in a virtual format.

The research team continued to engage in routine conversations with the group, listening to the discussions about moving forward with an ear toward extracting the core set of actionable barriers that were being alluded to by the team members across the discussions. Often in the team discussions, team members tended to talk about different challenges they could foresee:

- What if some students struggle and are not able to keep up while others may try to jump ahead before they are ready?
- We can't be there to be one-on-one with the students and so how are they going to be supported when they struggle?
- Not everybody might be able to be online at the same time, so what if some of the students need to engage asynchronously?
- How are they going to be able to follow along with a virtual demonstration and either do it at the same time or go back and do it later?

Employing a qualitative lens in analyzing the list of challenges that had been voiced, the research team was able to extract a much smaller number of key challenges to maintaining the foundational elements of STEM SEALs as a virtual offering; ultimately helping distilling concerns to identify the four key challenges listed above.

### Identifying promising strategies to address the core challenges

*Placing Significantly Greater Importance on Student Curricular Materials.* The STEM SEALs team worked through each of the challenges, drawing on research, holding discussions, and providing time for reflection. First, how would the team provide the foundational elements remotely? There would need to be very close attention to the materials. STEM SEALs team members would have to think like a student and what would be available to students. For example, students will not have dual monitors. If students were using the computer to talk with an expert or watch a video, they would need directions, durable directions, to follow and track their progress for the rover assembly. The team used cards with detailed pictures to give students the support they would need for the technical assembly.

In the words of a dyad leader...

*Activity cards pictures really helped clarify the steps of each activity and the coding required. Anywhere that more pictures can be added at the various stages of the rover building would help improve understanding of the required activity. The students tended to use the images on activity cards instead of instructions.*

*Taking Advantage of Existing Virtual Platforms.* Ensuring students stayed on track when working independently through online materials seemed like a large issue initially, but ultimately the team

noted it was likely a familiar challenge for anyone offering remote learning. Therefore, the team consulted existing platforms for virtual environments. They landed on Google Classroom, which had the advantage of being designed for students of this age and which students may already be familiar. As the team worked to integrate their materials into the Google Classroom platform, they noted a number of helpful features. There were features for presenting content in modules, similar to the design on the original face-to-face camp, and it possessed tools for controlling how far students could progress (e.g., the team set controls for what students could see and click on) and built-in monitoring to track students efforts (e.g., the team could see what students have clicked on and viewed as well as set mini-assignments that showed what had been completed).

*Provision of Numerous Videos.* Given the critical need for teachers and students to see and observe how to perform certain elements, the team turned first to existing, publicly available videos. Videos would be needed to explain and extend the camp content and could be used to demonstrate the larger context and relevance of the camp by featuring real-world applications. They culled videos from a number of various sources to create a video library for participants. They would also need videos to demonstrate camp-specific activities, so they began shooting videos of themselves performing STEM SEALs activities. These videos would be strategically placed within the STEM SEALs materials so that students could view the relevant videos as they navigated through the STEM SEALs experience.

In the words of dyad leaders ...

*The resources are very thorough. Dr. Maresch's video on propulsion was very interesting but the manual programming of the pins was a little confusing considering the knowledge wasn't necessary for the programming tasks in this module...The remainder of the video was very helpful, especially the speed and steer demo and explanation.*

In fact, the research team received feedback that more and shorter videos would be helpful. In their words,

*To keep the student's attention, the video length needs to be kept at a length of 10 minutes or less. For those struggling, a suggested more detailed tutorial video can be uploaded at the end of each module.*

*More short videos to explain what is happening at each step and what to expect would be great if available to instructors.*

*Using Dyads.* Part of the goal of the STEM SEALs experience was to interest students in STEM careers. To do so, it was important to get and keep students highly engaged throughout the camp. Additionally, students' perception of the camp might be unfavorable if they do not perform well in the culminating Land Challenge. The camp activities were designed to build upon each other, so it was vital that students successfully complete every activity. The STEM SEALs team also recognized that with most of the student participants being middle-school aged, they would need to have a consistent adult to consult with when problems arose and to intervene when their pace slowed. In response to these factors, the team decided to use dyads, that is, each student was paired with an adult, preferably within their household, who could provide that more intimate, just-in-time support and encouragement, and who would help connect them with the experts and other resources needed to be successful.

*Expert Office Hours.* While the selection of a dyad deliver model addressed many of the issues around student engagement, the teacher facilitators could not be expected to have the technical expertise to solve all the potential challenges that could surface. Experts must be accessible to support the dyads, and available in a timely fashion for students to stay on pace. The team had to think through how to provide the technical expertise and flesh out a schedule of their availability to align with the workflow of students.

In the words of a dyad leader on the strengths of the camp...

*The willingness of the team to assist with correcting programming. It takes a village:)*

Armed with a clearer understanding of the challenges that threatened their ability to successfully engage students in a virtual STEM SEALs event, the team was positioned to move forward in rapid fashion. The research team lent their hands to the effort, increasing their role and contributions as design team members helping to search out aligned best practices, identifying existing web resources that could be leveraged, trying out PowerPoint for sharing instructional tutorials, and most notably, suggesting one of key strategies that would ultimately prove most critical to the success of the effort: the dyad model. In December of 2019, when the project was happily proceeding as originally proposed, one of the research team leads, engaged in an observational visit to attend the final meeting of the design team that had been convened to support the NFC expert team in developing curriculum materials aligned to middle school standards and students. At this meeting, a research team member spent the day interacting with the design team members and getting to know more about their backgrounds, interests, and motivations for participating. Several of the members were motivated to participate both by professional and personal desires wanting to be able to provide the best opportunities for their students while also wanting to learn more about ways they could position their own children to be more STEM-able. During the downtime, the researcher noted that several were looking at Amazon and placing orders for things that they had been using at the camp. When asked about the purchases, the researcher learned that they were things they were buying because they thought they would be great for their own children. Grounded in these observations, the research team recognized that one of the most significant threats to being able to provide a positive experience in a virtual camp was a lack of sufficient support for students as they grappled with very new and challenging content, would be best addressed by moving to a model that looked to recruit individuals who resembled the design team members. Individuals who possessed the instructional ability to support students and a desire for their children to have greater access to STEM enrichment. This practice of recruiting paired participation of a teacher/educator and a child was the foundation of the dyad approach that was utilized for the virtual offering.

### **Taking the virtual camp out for a test run**

*Having Mechanisms for the Expert Team to Troubleshoot would be Essential.* After figuring out the strategies and refining the materials, the project team was ready to try out some of the planned camp activities with a group of novices who could provide feedback about what was working and where more development efforts could be directed. The process worked well and provided some good feedback. The initial review, however, was much more influential in preparing the project team for success by making sure

they were prepared to address a need that had not previously been fully illuminated, "How could the team troubleshoot in a virtual environment?"

The research team, which typically includes expert review and feedback gathering as a key step in the Design-based Research process, recognized that providing an opportunity for the project team to engage in a test-run and collecting review feedback would go a long way toward strengthening the efficacy of the planned effort. With very little time and significant barriers to getting outsiders materials, sufficient contextual information, and requisite content knowledge, the research team, who did not have prior firsthand exposure to the actual rover materials, signed up as novices to engage in a virtual run through of the rover construction process. Starting with the same unassembled materials that would be provided to participants, the expert instructors led the research team members who were working at remote sites independent from one another in constructing the rovers. The session proved immediately fruitful as one reviewer struggled to easily identify the front of the rover body frame from the back, and as the challenges of trying to screw in the tiny screws were addressed with some additional tips that would be added to the materials before the camp. Gathering feedback of this nature is an explicit reason for engaging in the review and provided the value-add that was anticipated.

However, the ultimate value of the review would quickly surpass the value envisioned with disaster striking and from that disaster an extremely significant innovation would quickly take form. During the test-run review session that was conducted, when one of the two reviewers was testing out recently programmed code that had been transferred to the Micro:bit controlling the rover, the reviewer had the rover placed on their desk in front of them, but as soon as the code sequence was initiated the rover's motors controlling the wheels engaged and the rover quickly drove itself off the desk surface and came crashing to the floor. The rover was rendered inoperable, and panic started to set in for both the expert team and the reviewer. Solidified in this moment would be a need for the expert team and the participants to connect in ways that afforded opportunities to troubleshoot and come up with solutions when things did not work or go as planned. In this case, the panic quickly subsided as the expert instructor who was connecting with the reviewer via Zoom instructed the reviewer to position their camera such that he could survey the damage. After which, the instructor using the white board feature and his own camera position on his rover helped to talk the reviewer through the steps that would be needed to return the rover to working order. Ultimately, the review effort helped to solidify a need and strategy for how expert instructors would be able to connect with participants to provide the one-on-one technical assistance that would be needed to help diagnose problems and scaffold solutions.

### **Fulfilling the promise of a design challenge event**

*Finding an answer for, "Where is the Challenge in that?."* With the relief that strategies had been incorporated to address all the barriers to success that that had once made a virtual STEM SEALs seem destined to fail, the project leadership did not pause to celebrate, noting that the full STEM SEALs vision centered around the entire experience of learning being grounded in the pursuit of competing with peers in tackling a related design challenge. So, they continued to iterate, recognizing that the virtual format would make it very challenging for students to compete on a similar course and really have the opportunity to apply and test out their

new learning and skills in pursuit of a context embedded design challenge. The design team noted that, to drive the rovers, students would need large, flat, smooth surfaces; something that is much harder to locate in rural areas. The team was greatly concerned that building rovers that could not be successfully driven would leave students disheartened. Ultimately, they believed that learning that does not culminate in a real-world application was below the rigor that they wished to ensure, and they further recognized that completing the camp and competing in isolation would further limit the impact of being part of a cohort of participants who had a shared experience. With that in mind, the team identified a strategy to ensure every student was positioned to be able to successfully engage in the design challenge competition, they arranged for students to compete individually at a parking lot, but live streamed so that students could watch each other and share in the excitement.

#### Documenting the unintended benefits and lessoned learned

In this step, the focus was on reflective learning toward documenting, 1) emergent benefits that were beyond those originally targeted by the STEM SEALs summer enrichment activity, and 2) emergent best practices that have merit for moving beyond just the current offering and incorporated into future project design and development efforts. As such, this process of taking stock to synthesize learning was one that was initiated and led by the research team which synthesized data from their observation of virtual camp activities, student surveys, dyad teacher surveys and focus groups, and project team reflections. From this work, important outcomes in the form of emergent benefits and best practices were identified and documented.

*Increased Versatility.* The shift to an online delivery model made the STEM SEALs land experience instantly more versatile and resulted in quicker progress towards leveraging virtual platforms. Access to a STEM SEALs experience remotely would be very beneficial given its goal of appealing to students in rural areas.

*Strengthening the K-12 Education Connection.* The dyad framework also had unintended advantages. By providing STEM exposure and professional development through the virtual camp, had led to a stronger continued engaged by educators who maintain interested in the STEM SEALs grant and larger mission to build a STEM ecosystem in the area. By connecting directly with teachers and then connecting teachers to each other and the STEM SEALs development work, the project has made swifter progress in creating a core group of educators who can serve as ambassadors as the College looks to strengthen its connection to regional K-12 institutions.

Emergent best practices identified to include in future development efforts were:

*Elevating the Framing of Failure.* Frustration can intensify quickly in virtual spaces when students are not able to observe others experiencing the same challenges or are spending more time grappling before they are able to receive support or technical assistance. The move to an online offering placed a larger spotlight on addressing failure and led to more proactive work to frame failure as normal and positive. In the words of a dyad leader ...

*Consider that middle schoolers' need consistency across directions, platforms, and materials. It is hard for them to have materials vary in information when in truth the purpose is for the material to match. Many of them get so frustrated they shut down.*

*They love learning computer applications, doing their assignments online. coding is interesting to them; however, many get very frustrated. They do not understand that frustration is good/ a part of real learning.*

*New Approach to Differentiation.* The STEM SEALs had known that the participants would be a diverse group, regardless of whether the camp was delivered in-person or remotely. This diversity would mean that students would be bringing different sets of pre-existing knowledge and experience and would vary in the kind and amount of support needed. Given the virtual format and much of delivery asynchronously, there was a need to keep instruction shorter, and more condensed. While in-person delivery might have allowed instructors to shepherd students down a more common pathway, the student pathway through the materials would likely be more disparate in the pivot to online. The team saw how alternate pathways that culminate in a singular outcome would need to be crafted. With multiple pathways available, instructors would have the opportunity to steer students toward the appropriate pathway so all students could feel successful progressing in a way that was aligned to their particular prior knowledge and current expertise.

*Need to Connect Students to Each Other.* The research team had noted the importance of belonging and community in fostering a sense of STEM identity and interest in STEM, leading to student choices to pursue STEM careers, a goal of the project. But, supporting emerging friendships and creating bonds between participants in a virtual environment was an anticipated challenge. While the team had great success in connecting students to facilitators with the dyad support model and in connecting students to experts with the videos and virtual meetings, they had less success connecting students to each other. The team tried to use participant self-introduction videos, videos to showcase participant work, and other strategies to promote team building and student to student connectivity, but these attempts ultimately fell short. New adaptations are currently being considered. In the words of a dyad leader ...

*With the online program this year, there was not a lot of peer student interaction which many teachers felt would have helped the students to work through the many difficulties they had. Most instructors agreed that the materials provided opportunities for students to express, clarify, justify, interpret, and represent their ideas (i.e., making thinking visible) and to respond to (some limited) peer and teacher feedback.*

#### 4. Conclusion

The contributions of this exploratory study of applying the Design-based Research approach within rapid change efforts in STEM enrichment resulted in important contributions to the field in two areas. The first of which is advancing best practice strategies for taking in person hands on STEM enrichment into asynchronous virtual delivery applications. The context of providing high quality STEM enrichment in isolated rural schools areas where connecting students with opportunities and expertise to promote rich engagement in STEM are limited and where creating greater access for rural students is further hampered by transportation and connectivity barriers. Ultimately overcoming these barriers may necessitate expanding opportunities for rural student participation asynchronously in virtual STEM offerings. Research reviews have shown that studies of both synchronous and asynchronous methods of online learning can be effective [29]. The findings of this exploratory study identify emerging best



practices for offering virtual STEM opportunities in a rural setting that are able to meet this high standard have many important implications. The findings lend evidence to support the success of STEM SEALs in offering a highly engaging and successful inaugural summer enrichment experience in an asynchronous and virtual format, and more importantly, provide rich insights to expand the literature on best practices for virtual STEM enrichment programming.

Secondly, the findings of this study are significant because they also provide initial evidence of the viability and value of expanding the knowledge base around best practices for embedding Design-based Research within rapid design efforts. While Design-based researchers have established well-supported best practices and a strong evidence base to promote its routine inclusion in STEM enrichment design efforts, the application of Design-based Research in rapid cycle initial design efforts has not been as well researched [30, 31]. While the pandemic forced widespread pivoting throughout the STEM landscape, the hope is that it will remain an isolated event and that no similar mass need for pivoting will occur. Yet, the rapidly advancing technological will constantly push for rapid development and rapid innovation within STEM enrichment offerings, amplifying the need for greater exploration of Design-based Research methods within rapid cycle design efforts similar to the example provided in this manuscript. The STEM SEALs project efforts to engage Design-based Research to support rapid change efforts represents an important contribution to the field with the findings from the initial test of the offering strongly supporting its effectiveness. The evidence gathered showed Design-based Research as a valuable tool for program improvement, even in the most extreme situation of a global pandemic, and in important contribution to best practices in developing STEM learning experiences.

### Conflict of Interest

The authors declare no conflict of interest.

### Acknowledgment

This material is based upon work supported by the National Science Foundation under grant no. 1812913.

### References

- [1] R. Zulli Lowe, A. Smith, C. Prout, G.G. Maresch, C. Bacot, L. Murfee, & B. Eustace, "Taking STEM enrichment camps virtual: Strategies & reflections from quick pivot due to COVID-19" In 2021 Integrated STEM Education Conference, 83-90, 2021. DOI: 10.1007/s11423-020-09811-3
- [2] World Health Organization, "WHO Coronavirus Disease (COVID-19) Dashboard[Online].," [https://COVID19.who.int/?gclid=CjwKCAjwiMj2BRBFiEiwAYfTbCod9hYnKI6jtuqIoHEVnStP\\_VrjFu3NFnfkKJSgh9rZcBul7mtmfDhoCuYcQAvD\\_BwE](https://COVID19.who.int/?gclid=CjwKCAjwiMj2BRBFiEiwAYfTbCod9hYnKI6jtuqIoHEVnStP_VrjFu3NFnfkKJSgh9rZcBul7mtmfDhoCuYcQAvD_BwE), 2020.
- [3] K. Spencer, "Not all towns are created equal, digitally: How a Colorado school district struggles to give its students a technology boost (The Hechinger Report)," Teachers College at Columbia University, 2017.
- [4] National Science Board, "Science and engineering indicators 2014," National Science Foundation, 2014.
- [5] R. Lapan, M. Aoyagi, M. Kayson, "Helping rural adolescents make successful postsecondary transitions: A longitudinal study," *Professional School Counseling*, **10**, 266-272, 2007, doi: 10.5330/prsc.10.3.u6j3j64h48p27w25
- [6] J. Plucker, B. Harris, "Acceleration and economically vulnerable children," In *A nation empowered: Evidence trumps the excuses holding back America's brightest students*, Belin-Blank Center for Gifted Education and Talent Development, 181-188, 2015.
- [7] S.G. Assouline, L.M. Ihrig, D. Mahatmya, "Closing the excellence gap:

[www.astesj.com](http://www.astesj.com)

- Investigation of an expanded talent search model for student selection into an extracurricular STEM program in rural middle schools," *Gifted Child Quarterly*, **61**(3), 250–261, 2017.
- [8] T. Kittleson, J.T. Morgan, "Schools in balance: Comparing Iowa physics teachers and teaching in large and small schools," *Iowa Science Teachers Journal*, **39**(1), 8-12, 2012.
- [9] J. Plucker, J. Giancola, G. Healey, D. Arndt, C. Wang, "Equal Talents, Unequal Opportunities: A Report Card on State Support for Academically Talented Low-Income Students," Jack Kent Cooke Foundation, 2015.
- [10] J.S. Eccles, B.L. Barber, M. Stone, J. Hunt, "Extracurricular activities and adolescent development," *Journal of Social Issues*, **59**, 865-889, 2003, doi:10.1046/j.00224537.2003.00095.x
- [11] P. Olszewski-Kubilius, S.Y. Lee, "The role of participation in in-school and outside-of-school activities in the talent development of gifted students," *Journal of Secondary Gifted Education*, **15**(3), 107-123, 2004.
- [12] R. Gira, "The challenge: Preparing promising low-income students for college," In *Overlooked gems: A national perspective on low-income promising learners: Conference proceedings from the national leadership conference on low-income promising learners*, National Association for Gifted Children, 69-74, 2007.
- [13] T. Anderson, J. Shattuck, "Design-based research: A decade of progress in education research?" *Educational Researcher*, **41**(1), 16–25, 2012, doi:<https://doi.org/10.3102/0013189X11428813>
- [14] T. Štemberger, M. Cencić, "Design-based research in an educational research context," *Journal of Contemporary Educational Studies*, **65**, 90-104, 2014.
- [15] E. Oh, T.C. Reeves, "The implications of the differences between design research and instructional systems design for educational technology researchers and practitioners," *Educational Media International*, **47**(4), 263-275, 2010.
- [16] D. Zinger, A. Naranjo, I. Amador, N. Gilbertson, M. Warschauer, "A design-based research approach to improving professional development and teacher knowledge: The case of the Smithsonian learning lab." *Contemporary Issues in Technology and Teacher Education*, **17**(3), 388-410, 2017.
- [17] F. Wang, M.J. Hannafin, "Design-based research and technology-enhanced learning environments," *Educational technology research and development*, **53**(4), 5-23, 2005.
- [18] T. Amiel, T. Reeves. "Design-based research and educational technology: Rethinking technology and the research agenda," *Educational Technology & Society*, **11**, 29-40, 2008.
- [19] A. Bakker, "An introduction to design-based research with an example from statistics education," *Approaches to qualitative research in mathematics education: Examples of methodology and methods*, 429-466, 2015, doi:10.1007/978-94-017-9181-6\_16, 2014
- [20] S. Barab, K. Squire, "Design-based research: Putting a stake in the ground," *Journal of the Learning Sciences*, **13**, 1-14, 2004, doi:10.1207/s15327809jls1301\_1.
- [21] C. Pardo-Ballester, J.C. Rodríguez, "Using design-based research to guide the development of online instructional materials." *Developing and evaluating language learning materials 86012*," 2009.
- [22] F.E. Terrazas-Arellanes, L.A. Strycker, E.D. Walden, C. Knox, "Development of a middle school online science curriculum: Lessons learned from a design-based research project." In *Handbook of Research on Diverse Teaching Strategies for the Technology-Rich Classroom*, ICI Global, 2020, doi: 10.4018/978-0238-9.
- [23] D.M. Bressler, M. Shane Tutwiler, A.M. Bodzin, "Promoting student flow and interest in a science learning game: a design-based research study of school scene investigators," *Education Technology Research Development*, **69**, 2789–2811, 2021, doi:10.1007/s11423-021-10039-y
- [24] A. Savran Gencer, H. Doğan, "The assessment of the fifth-grade students' science critical thinking skills through design-based STEM education," *International Journal of Assessment Tools in Education*, **7**(4), 690-714, 2020, doi: 10.21449/ijate.744640
- [25] S. Fowler, S.N. Leonard, "Using design based research to shift perspectives: a model for sustainable professional development for the innovative use of digital tools," *Professional Development in Education*, 1-13, 2021, doi: 10.1080/19415257.2021.1955732
- [26] M. Allen. *Leaving ADDIE for SAM: An agile model for developing the best learning experiences*, ASTD Press, 2012.
- [27] M.W. Easterday, D.R. Lewis, E.M. Gerber, "Design-based research process: Problems, phases, and applications," *International Society of the Learning Sciences*, 2014.
- [28] C. Jackson, "The advantages of exploratory research design," eHow, [https://www.ehow.co.uk/info\\_8525088\\_advantages-exploratory-research-design.html](https://www.ehow.co.uk/info_8525088_advantages-exploratory-research-design.html), 2020.
- [29] F. Amiti, "Synchronous and asynchronous e-learning," *European Journal of*

Open Education and E-Learning Studies, **5**(2), 2020.

- [30] C. Hoadley, F.C. Campos, "Design-based research: What it is and why it matters to studying online learning," *Educational Psychologist*, **57**(3), 207-220, 2022.
- [31] T.C. Reeves, L. Lin, "The research we have is not the research we need," *Education Technology Research Development*, **68**, 1991–2001, 2020, doi: [DOI: 10.1007/s11423-020-09811-3](https://doi.org/10.1007/s11423-020-09811-3)

## Waterfall: Salto Collazo. High-Level Design of Tokenomics

Sergii Grybniak<sup>1</sup>, Yevhen Leonchyk<sup>2</sup>, Igor Mazurok<sup>2</sup>, Oleksandr Nashyvan<sup>1</sup>, Alisa Vorokhta<sup>\*2</sup>

<sup>1</sup>Institute of Computer Systems, Odesa Polytechnic State University, Shevchenko av. 1, Odesa, 65044, Ukraine

<sup>2</sup>Faculty of Mathematics, Physics and Information Technologies, Odesa I.I. Mechnikov National University, Dvoryans'ka St 2, 65082, Odesa, Ukraine

### ARTICLE INFO

Article history:

Received: 28 February, 2023

Accepted: 20 May, 2023

Online: 25 June, 2023

Keywords:

Tokenomics

Incentive System

Distributed Protocol

Transaction Fee

Directed Acyclic Graph

Blockchain

### ABSTRACT

This article explains the fundamental principles of the economic policy that are integrated into the decentralized public platform Waterfall. The platform has a DAG (Directed Acyclic Graph) based system architecture and is designed to develop decentralized applications and financial services. The main goal of this work is to create a favorable environment that incentivizes positive behavior from each network participant and from the system as a whole. Economic leverages ensure general equilibrium to provide an optimal data replication ratio, attack protection, and affordable transaction fees. Although this model of tokenomic is designed explicitly for the current version of the Waterfall platform named Salto Collazo, the presented approaches possess the potential to be applied across a broad spectrum of decentralized public platforms, owing to their inherent transparency and a set of tuned parameters.

## 1. Introduction

### 1.1. Problem Statement

This paper is an extension of work originally presented in the proceedings of the IEEE International Conference on Blockchain, Smart Healthcare, and Emerging Technologies [1] and presents a high-level economic design of decentralized public networks such as blockchains, blockDAGs (Directed Acyclic Graphs consisting of linked blocks), etc.

The emergence of blockchain technology has transformed modern society and businesses, primarily thanks to the attributes of its transparency, tamper-proof safety of data, and logical consistency [2]-[4]. However, its subpar network performance and exorbitant commissions make it unsuitable for many enterprise-class applications. On the other hand, DAG technology is considered the next generation of blockchain due to its optimized validation mechanism, high scalability, efficient provenance, and multiparty involvement [5]-[7]. A DAG-based architecture can provide the necessary functions to develop a variety of decentralized finance (DeFi) services [8], [9], including payment systems, non-fungible tokens (NFTs), web3 gaming [10], new

solutions in logistics [11] and real estate sector [12], identity documents [13], and e-voting services [14]. The success of this approach depends on the establishment of ad-hoc economics for a decentralized storage system that is both high-speed and scalable, while also ensuring low-cost transaction fees. The primary focus of this article is on the core economic principles embedded within the Waterfall DAG-based protocol [15] and its efficacy in fulfilling these specific requirements.

### 1.2. An Exposition of the Waterfall Platform: A Short Survey

Waterfall is a decentralized platform designed for developing a variety of decentralized applications (Dapps). The platform features high scalability and is built on DAG technology, a distributed ledger system that differs from traditional blockchain technology in that it does not rely on a single chain of blocks. Instead, DAG technology uses a graph-like structure, enabling the platform to process transactions in parallel, without the need for central authority.

Waterfall leverages a fast finality Proof-of-Stake (PoS) [16] consensus algorithm to ensure the integrity of its transactions. The platform is built to rely on Coordinating and Sharding networks, enabling a significant volume of transactions via parallelized block generation. The Coordinating network processes transactions and communicates with the Validator network to ensure consensus on the validity of each block. Meanwhile, the Sharding network

\*Corresponding Author: Alisa Vorokhta, Dvoryans'ka St 2, 65082, Odesa, Ukraine, +380951641320 & [alisa.vorokhta@stud.onu.edu.ua](mailto:alisa.vorokhta@stud.onu.edu.ua)

divides the workload across multiple nodes, improving the platform's overall scalability.

Each node in the Waterfall network is composed of 2 components: a Coordinator and a Validator, representing their respective roles within the system. The Sharding network is responsible for processing incoming transactions and ensuring their validity. Transactions are combined into blocks that refer to other blocks to form a DAG. Information about the created blocks enters the Coordination Network for structure linearization and finalization based on consensus. The blockchain of the Coordinating network records data on the finalization of blocks in all shards.

Overall, the Waterfall platform is a highly-scalable smart contract platform. DAGs in decentralized technologies facilitate scalability, addressing one of the key challenges faced by such systems, and allow for the parallel processing of transactions, which can be verified and confirmed quickly and efficiently. This feature of the platform enables it to process a high volume of transactions per second, making it a viable option for decentralized applications.

The Waterfall consensus protocol Gozalandia [17] has established a time-based system to ensure efficient and secure block production. This timeline is composed of distinct time intervals, including slots, epochs, and eras. The Coordinating network assumes responsibility for registering Validators and assigns roles such as block producers, committee members, and leaders during the commencement of each epoch. In addition, the Coordinating network maintains information regarding the validated blocks generated on the Sharding network. The honest producer is required to include links to all the known tip-blocks of the DAG to its created block. Furthermore, the Coordinating network performs ordering and finalization of the distributed ledger, enhancing the synchronization and overall network security.

The Waterfall platform incorporates and refines the most advantageous properties of Ethereum 2.0 [18], augmenting its performance and extending its functionality. The platform's inherited coin serves as a primary digital asset within the network, facilitating the transfer of transactions and governance voting, executing smart contracts, and providing for the creation of auxiliary tokens, thereby creating an ecosystem with the potential for mutually beneficial interaction among all its components. Nonetheless, the structure of the DAG platform requires new approaches to tokenomics and economic incentives, as traditional mechanisms may be incompatible or insufficient to support the platform's decentralized nature and ensure its sustainable growth. Therefore, the Waterfall team must continually research and implement new solutions to empower its users and incentivize positive behavior, thereby promoting the longevity and stability of the system.

### *1.3. Tokenomics Strategies: Achieving Sustainable Development in Decentralized Systems*

Tokenomics is a fundamental concept in decentralized systems that leverages economic incentives to encourage desired behaviors from participants, such as users, developers, and Validators [19]. The goal is to create a self-sustaining and self-regulating ecosystem that maximizes benefits for all stakeholders. Tokenomics involves the use of native tokens or coins that serve as the currency of the decentralized network and facilitate transactions and interactions within the system. A well-designed

tokenomics model can incentivize positive actions, such as network participation, governance voting, and contribution to the development of the network. It can also disincentivize malicious behavior by imposing penalties for non-compliance with network rules and regulations. Additionally, tokenomics can facilitate the effective allocation and use of existing and new resources on the network, resulting in a variety of affordable services for users. Therefore, a robust and balanced tokenomics model is crucial for the successful operation and growth of public decentralized networks [20], [21].

The concept of Waterfall tokenomics is a set of economic principles and mechanisms designed to support the growth and functionality of distributed networks, with a particular emphasis on DAG structures. Waterfall tokenomics has specific goals aimed at creating economic conditions that promote scalability, speed, security, and reliability.

One of the primary objectives of Waterfall tokenomics is to establish economic conditions that enable the network to expand to a size that provides an optimal data replication coefficient and a maximum speed of mempool synchronization. This objective is especially critical for networks that utilize edge networking, which entails a high volume of transactions that must be processed and propagated efficiently.

Another important goal of Waterfall tokenomics is to promote fast finality [22], which plays a pivotal role in facilitating payment systems and decentralized applications (Dapps). Fast finality ensures that transactions are secure and reliable by preventing any alteration or reversal once a transaction is confirmed.

It is worth noting that the DAG structure of the network presents unique challenges and vulnerabilities that differ from those of traditional blockchain architectures. Therefore, Waterfall tokenomics must provide proper protection and security in intimate collaboration with the technical network architecture.

In summary, the concept of Waterfall tokenomics is a vital economic framework for distributed networks, with an emphasis on DAG structures. Its goals are aimed at creating economic conditions that promote scalability, speed, security, and reliability, and it plays a crucial role in supporting payment systems and Dapps. Finally, it must work closely with the technical network design to ensure appropriate protection against possible attacks.

The vertices in bold are spine blocks in Figure 1. These blocks precede all other blocks in their slots after linearization. We used methods of statistical analysis and simulation to study the probability of successfully executed attacks (considered below) and the degree of damage caused by them. This allows us to evaluate the effectiveness of developed countermeasures and analyze the statistical properties of the acquired graph.

The set of rules and guidelines that govern the network economics is implemented through software that encompasses all the essential features required for its operation. These economic rules are autonomously enforced and transparently visible to the general public. This feature increases user confidence in the platform and makes it more resilient. Additionally, there must be mechanisms in place to adapt specific rules dynamically to changing situations. This approach ensures that the network's ability to sustain desirable behavior over its entire lifespan, fostering overall economic equilibrium and systematic development aligned with the network's objectives. Achieving this goal poses a considerable challenge within the scope of this endeavor.

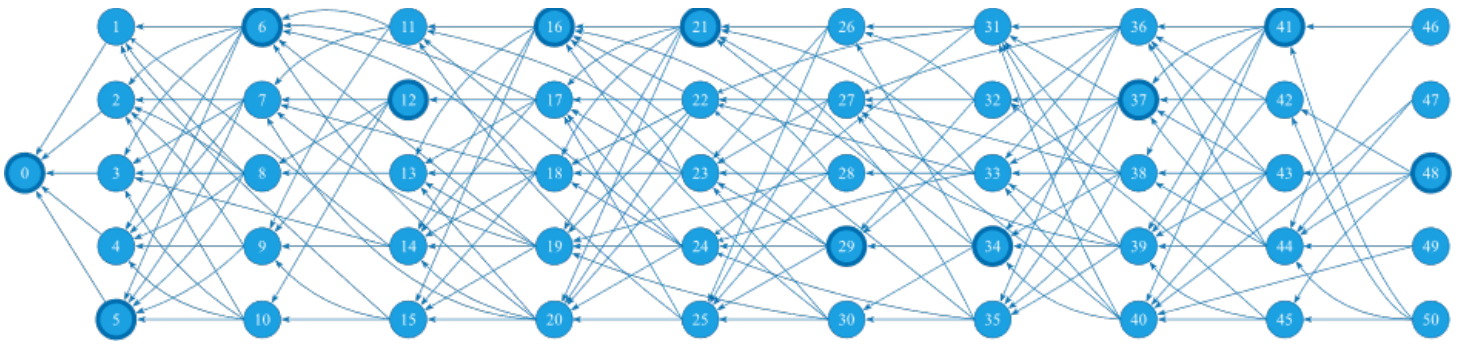


Figure 1: An example of a starting fragment of a DAG network created using simulation

## 2. Related Works

The evolution of economic blockchain models has been a subject of intense research in recent years. The choice of consensus protocol has important implications for the economic model of a blockchain network [23], [24]. For example, the development of Proof-of-Work (PoW) decentralized networks like Bitcoin and Ethereum 1.0 represents a significant milestone in the history of blockchain technology (as evidenced by numerous studies including [19], [25], [26]). In a PoW system, nodes compete to solve cryptographic puzzles, with the first node to solve the puzzle being rewarded with a new block and the corresponding amount of cryptocurrency. This creates an economic, incentivizing network node participation and contributes to the overall security of the system. This type of system is known for its simplicity but has also been criticized for its high energy consumption and vulnerability to 51% attacks. Early models were characterized by relatively simple economics compared to more modern PoS models, which have since emerged as a promising alternative that can potentially enhance network maintenance [27]. PoS systems use a different mechanism to achieve consensus, whereby nodes are selected to create new blocks based on their ownership of a certain amount of cryptocurrency. In such models, network participants are incentivized to hold a certain amount of cryptocurrency as collateral, and transactions are validated based on the stake they hold. Compared to PoW models, PoS models are less energy-intensive and less vulnerable to 51% attacks.

Overall, the development of economic blockchain models has been driven by the need to incentivize network participants to act in ways that contribute to the overall health and sustainability of the system. While early models like PoW and PoS have been successful in achieving this goal, research is continued on new consensus algorithms and economic models that can potentially offer even better performance and security. For example, there are also approaches to achieving consensus that have been proposed in the literature, such as the use of Byzantine Fault Tolerant (BFT) algorithms [28], DAGs [29], and Delegated Proof-of-Stake (DPoS) [30]. However, these approaches often require ad-hoc methods to incentivize network participants [31], which can make them more difficult to implement and manage.

Despite the differences among these models, they all share a common goal: incentivizing network participants to behave in a way that benefits the network as a whole. This challenge requires a deep understanding of game theory [32], [33] and the underlying properties of blockchain technology. By designing economic models that reward good behavior and penalize bad actors, these models aim to ensure the smooth and sustainable functioning of decentralized networks.

In response to modern demands, various economic models have been developed to support PoS-based systems ([34], [35], [36]). These models aim to address the challenges faced by decentralized systems, such as decreasing transaction costs, increasing transaction frequency, and reducing finalization time. Additionally, a few approaches have been proposed by incorporating economic principles into BFT-like consensus mechanisms, these systems aim to achieve a balanced internal economy that aligns with specific objectives ([37], [38], [39]).

After analyzing related works, it has been revealed that one of the primary challenges facing decentralized systems is the need to decrease transaction costs, increase transaction frequency, and reduce finalization time. This is particularly important for the mass adoption of Distributed Ledger Technology (DLT) in real-world applications. In Messari's report for 2023 [8], one can find a comprehensive examination of current prospects and significant trends in the development of tokenomics.

Therefore, our aim is to develop a tokenomics model that addresses these challenges, with a focus on limiting the increase in transaction fees while maintaining the Worker's economic viability, which includes blockchain Validators and block producers. To achieve this, we propose a flexible and transparent architecture that can be easily modified with a set of adjustable parameters. This is especially important for emerging public platforms, as they must be able to successfully meet formation requirements.

However, important to highlight that most of the already existing economic models are developed for established systems such as Ethereum 2.0 [18]. As such, there is a need for new and innovative models that take into account the specific requirements and limitations of emerging decentralized systems.

The Waterfall model incorporates and enhances the most favorable aspects of Ethereum tokenomics. Furthermore, it presents notable benefits owing to its novel consensus protocol [17] and horizontal scaling, with subnetworks necessitating economic incentives [40]:

- **Dynamic adjustment.** A mechanism for dynamic adaptation of system parameters is in place to ensure optimal network behavior, particularly by automatically adjusting the optimal number of Workers. This approach enables the system to attain self-sufficiency throughout its complete lifespan.
- **Low transaction fees.** In various scenarios, the architecture and tokenomics of the system are structured to maintain low transaction fees. The protocol scales dynamically with the increasing network load, which leads to the simultaneous publication of more blocks within the same slot and

consequently reduced transaction fees as the system expands. Thus, transaction processing during peak times remains efficient, while the number of pending transactions in the transaction pool remains low.

- **Supporting high transaction throughput.** The Waterfall platform achieves high transaction throughput via the use of system-scalable DAG-based block structures. These structures allow multiple blocks to be published simultaneously, forming a DAG that provides finality for all transactions, as long as the blocks do not conflict with each other. In recent intermediary lab tests, our protocol demonstrated the ability to process up to 3,600 transactions per second. The tokenomics model effectively supports this architecture.

In the world of public blockchain networks, the presence of corrupt and malicious nodes leads to an environment of complete distrust. To address this issue, a reputation system could be implemented to enhance the security of interactions. Several approaches have been proposed for building a reputation system based on blockchain data, as discussed in existing literature (e.g. [41], [42]).

In [43], a detailed discussion is presented on the reward distribution scheme among honest Workers for their role in block production and validation, as well as on the determination of penalties for faulty Workers, with particular attention paid to the consensus achievement mechanism of the Waterfall platform. The key principles underlying the proposed scheme are that Workers should be rewarded in proportion to the significance of their contributions, and that the penalties imposed on them should outweigh the potential benefits of any malicious actions. The tokenomics of the system is analyzed at a macro level, without delving into the specific functional roles of individual nodes. As such, the proposed approach is independent of any particular PoS-based consensus algorithm that opens up the possibility of its adaptation to a broad range of platforms for macroeconomic design, owing to a multi-parameter configuration.

### 3. Macroeconomic Design

This section delves into the analysis of the decentralized Waterfall platform from an economic standpoint, using a holistic approach that avoids focusing on the specific behaviors or contributions of individual participants. It covers the platform's governance framework, which includes core principles of network economic policy that shape the interactions of community groups and affect various economic indicators such as cryptocurrency rates, inflation, and deflation. The system architecture and coin circulation are visually represented in Figure 2 and are discussed in-depth later in this section.

#### 3.1. Pre-mining Strategy

In the early stages of a network, the initial coin distribution is a critical element for ensuring system security. As such, a recommended approach is to create a set of  $N_{opt}$  Workers at the beginning, each with a fixed stake divided into nodes that share a ledger and IP address. The stake amount is denoted by  $s$  coins per Worker, and any increase in the total amount of the stake is achieved solely through the addition of new Workers. This strategy helps to ensure a secure and stable system during the network's initial phase.

Typically, the entire token supply is not immediately available at the outset. Assume  $\alpha$  represents the proportion of the current

supply ( $C$ ) to the total staked amount  $S_{opt} = s \cdot N_{opt}$ . The value of  $N_{opt}$  should be determined as the present optimal number of Workers necessary to ensure a secure and efficient network. A restricted number of Workers in a network raises the risk of a majority holding attack. Conversely, a larger total stake results in a decrease in free funds in circulation, which can impede effective network operations. To maintain the desired level of available funds and the optimal number of Workers, it is crucial to uphold the ratio  $\alpha$ . In other words if the current supply  $C$  is lower than the total stake multiplied by  $\alpha(1 - \epsilon_1)$ , a proportional amount of coins is released. Conversely, if the current supply  $C$  exceeds the total stake multiplied by  $\alpha(1 + \epsilon_2)$ , an appropriate number of Workers is added using the Foundation's funds.  $\epsilon_1$  and  $\epsilon_2$  are relative values, expressed as fractions of the base value  $\alpha$ , which define the lower and upper limits of the range respectively. In the first scenario mentioned in the text, the Foundation has the ability to revoke its Workers if they were created using a specific protocol. This means that instead of releasing additional coins into circulation, the Foundation can choose to remove Workers from the system. To ensure that this condition is met and that the system remains in balance, a smart contract is used. This smart contract monitors the balance between the current coin supply and the number of Workers in the system. This balance is adjusted periodically to ensure that it remains within acceptable limits. Determining the optimal values of  $\alpha \geq 2$ ,  $\epsilon_1 > 0$ , and  $\epsilon_2 > 0$  to achieve effective and secure network functioning is an unresolved matter that relies on various factors. These factors include the total and current supplies, required available funds, security level, and network operating goals. We consider the initial values of parameters:  $\alpha = 2.5$  and  $\epsilon_1 = \epsilon_2 = 0.25$  as a starting point for the Waterfall case. During the initial stage of the Waterfall platform, it is expected that the foundation will control approximately 2/3 of the total number of tokens in circulation. With the current value of the parameter  $\alpha$ , a network capture attack, also known as a majority attack [44], would inflict losses on both the attackers and the attacked parties, making such an attack economically infeasible. As the platform continues to grow and the number of nodes increases, the value of  $\alpha$  will decrease accordingly, while maintaining a sufficiently high level to guarantee the platform's security.

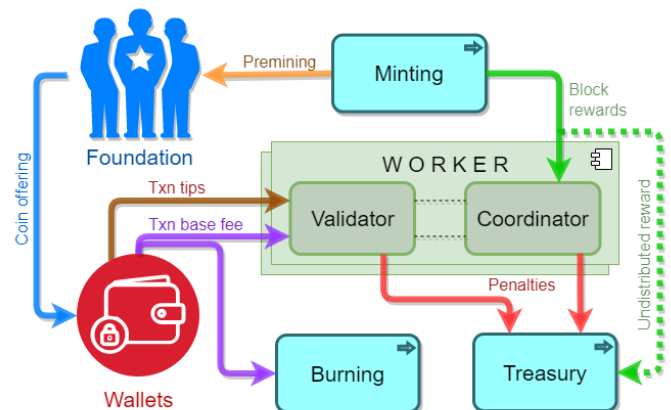


Figure 2: The circulation of coins on the platform

#### 3.2. Understanding the Technical Aspects of Coin Mining and Its Challenges

The proposed tokenomics model incentivizes block production by offering minted rewards for every finalized block in the Coordinating network. This means that new coins will be issued to

compensate Coordinators for ensuring the required security guarantees, which is referred to as "Minimum Necessary Issuance". Earned coins are accrued to Workers every epoch. The annualized minted amount ( $V$ ) is influenced by the total amount of staked coins ( $S$ ):

$$V = k \cdot \sqrt{S},$$

where a coefficient  $k$  will be subsequently defined. As a result, the maximum annualized return rate ( $R$ ) is determined as follows:

$$R = V / S = k / \sqrt{S}.$$

This non-linear relationship proposed in [18] implies that a decrease in the amount of staked coins leads to increased incentivization, and vice versa. This balance between the volume of minted coins and network security ensures that all initial stakes, which are initially uniform (although some may be reduced due to penalties), remain proportional, and

$$S = s \cdot N,$$

the coefficient  $k$  can be obtained through the desired value of  $R_{opt}$  at a certain total stake ( $S_{opt}$ ) as well as at a certain optimal number of Workers ( $N_{opt}$ ). In our case, the coefficient  $k$  is derived from a condition that the maximum annualized return rate equals  $R_{opt}$  with  $N_{opt}$  Workers:

$$k = R_{opt} \cdot \sqrt{S_{opt}} = R_{opt} \cdot \sqrt{s \cdot N_{opt}}.$$

Therefore, considering any given number of Workers, we obtain:

$$V = R_{opt} \cdot s \cdot \sqrt{N_{opt} \cdot N},$$

$$R = R_{opt} \cdot \sqrt{\frac{N_{opt}}{N}}.$$

During the initial stages of coin release, the current supply  $C$  experiences a rapid surge, necessitating the expansion of the optimal number of Workers to ensure network security. Consequently, the value of  $N_{opt}$  should also be substantially increased:

$$N_{opt} = \frac{C}{\alpha \cdot s}.$$

The coefficient  $k$  and the annual minted amount  $V$  are crucial factors that need to be adjusted to ensure the proper release of all coins. Recalibration is necessary to keep the system efficient and engaging for new Workers by increasing the rewards available for minting. However, if the number of Workers in the network exceeds a certain threshold, the platform may overpay for security, leading to inflation that could have detrimental effects on the tokenomics of the system. To prevent this, the value of  $\alpha$ , which represents the percentage of total minted coins allocated for the development fund, should not be too low. It is important to note

that the number of coins yet to be released can be approximated by subtracting the current amount in the releasing account ( $C$ ) from the total coin supply. This approximation provides valuable insights into the state of the system and informs decisions about adjusting the minting process to optimize its performance. The overall rate of return ( $R$ ), may be reduced due to the occurrence of faults or malicious behavior by certain Coordinators. Despite this, honest Workers who make investments at the outset can expect to receive rewards of approximately  $R_{opt}$  per year. This represents the minimum return rate that can be achieved by honest Workers. To illustrate this concept, we present Figure 3, which depicts the maximum annualized return rate that stakeholders can earn as block rewards under varying conditions of the number of Workers and different values of  $R_{opt}$  and  $N_{opt}$ . With the expansion of the Worker count, the return rate diminishes; however, the rewards could potentially be augmented by tips resulting from heightened network activity.

When evaluating the reward for a produced block in a blockchain network, it is crucial to consider various factors that contribute to the overall value of the reward. Two critical elements to consider are the annualized minted amount and the slot times. The annualized minted amount refers to the total number of tokens that will be minted during the year, assuming the network continues to operate at its current capacity. This value is essential because it determines the overall supply of tokens, and therefore impacts their value in the market. Additionally, the annualized minted amount can affect the incentive structure for network participants, such as block producers, who may receive a portion of the newly minted tokens as a reward. The slot times, on the other hand, refer to the time it takes to produce each block in the network. In most blockchain networks, a new block is produced at regular intervals, which are determined by the slot times. The shorter the slot time, the more blocks can be produced within a given timeframe, and the higher the potential rewards for block producers. To evaluate the reward for a produced block, these two factors must be taken into account. By multiplying the annualized minted amount by the slot times, we can calculate the value of each block produced in the network. This information is essential for understanding the incentives and rewards available to network participants and can inform decisions regarding the network's governance and economic policies. Overall, the evaluation of block rewards is a critical aspect of blockchain network design and operation. By considering various factors such as the annualized minted amount and slot times, we can ensure that the network is functioning efficiently and providing appropriate incentives to all participants. To determine the minted reward for a generated block, one can consider the values of the annualized minted amount and slot times. Let  $i$  represent the slot number within the Coordinating network. Then the annualized number of blocks:

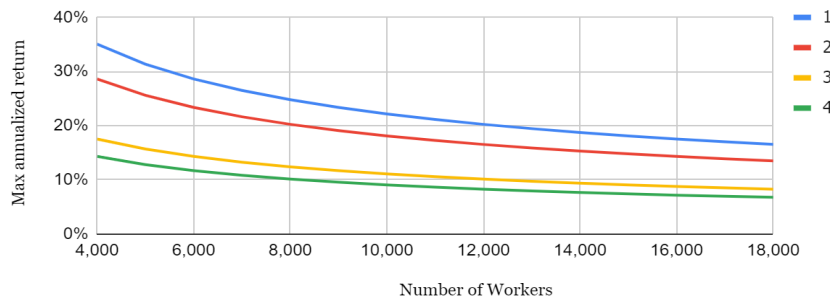


Figure 3: The maximum annual return rate of Workers (case 1 with  $R_{opt} = 0.20$  and  $N_{opt} = 12,288$ ; case 2 with  $R_{opt} = 0.20$  and  $N_{opt} = 8,192$ ; case 3 with  $R_{opt} = 0.10$  and  $N_{opt} = 12,288$ ; case 4 with  $R_{opt} = 0.10$  and  $N_{opt} = 8,192$ )

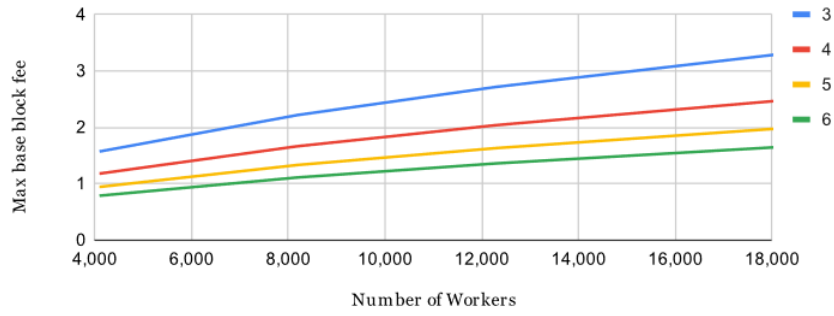


Figure 4: The maximum base block fee ( $W_i^c$ ) with  $N_{opt} = 8,192$  Workers,  $R_{opt} = 0.20$ ,  $s = 32,000$  coins,  $p = 1$ ,  $t_i^s = 4$  sec, and  $b_i = 3...6$  blocks per slot

$$B_i^c = \frac{T}{t_i^c}$$

where  $t_i^c$  is its time in seconds, and constant  $T = 60 \cdot 60 \cdot 24 \cdot 365.25$  represents the number of seconds per year.

Consequently, the reward that is minted per block in the  $i$ -th slot in the Coordinating network is:

$$W_i^c = \frac{V}{B_i^c}$$

It is important to note that the total sum over all slots of the Coordinating network per year ( $Y$ ) is equivalent to:

$$\sum_{\forall i \in Y} W_i^c = V \cdot \sum_{\forall i \in Y} \frac{t_i^c}{T} = V.$$

Further, the amount  $W_i^c$  is divided among the Committee leader and members who have created  $i$ -th block in the Coordinating network.

### 3.3. Understanding Base Transaction Fees

In the context of DLT, any transaction included in a block requires the payment of a base transaction fee. This fee is determined based on a mechanism similar to that used for obtaining a minted reward and depends on the annualized minted amount. Let  $i$  be the slot number of the Sharding network. Then the annualized number of blocks:

$$B_i^s = \frac{T \cdot b_i}{t_i^s}, \quad W_i^s = \frac{V}{B_i^s}$$

where the number of blocks per slot in the Sharding network  $b_i > 1$  and  $t_i^s$  is its time in seconds.

It is worth noting that if the block number and time slot remain constant throughout the year, the annual number of blocks  $B^s$  can be obtained by a simple calculation. By summing up the values of slots and blocks across the Sharding network for the entire year, we arrive at the following expression:

$$\sum_{\forall i \in Y} \sum_{j=1}^{b_i} W_i^s = V \cdot \sum_{\forall i \in Y} \frac{t_i^s}{T} = V.$$

And then, a base transaction fee in  $i$ -th slot is defined as:

$$f = \frac{G}{G_{max}} \cdot W_i^s \cdot p,$$

where  $G$  represents the required gas amount to process the transaction,  $G_{max}$  denotes the maximum permissible gas amount per block, and  $p > 0$  is a price multiplier. The cumulative sum of all base transaction fees across the  $j$ -th block of the  $i$ -th slot:

$$F_{ij} = \sum_{txns} f \leq W_i^s \cdot p.$$

In the case of a regular transaction, the proportion:

$$\frac{G}{G_{max}} = \frac{1}{10,000}$$

ensures quite low base fees, even for quite high values of the multiplier  $p$ .

Clearly, the value of  $W_i^s$  depends on the current number of Workers as well (see Figure 4).

### 3.4. Coin Burning Procedure

The act of permanently removing a certain number of coins from circulation to reduce the current supply is commonly referred to as "coin burning." This process is often carried out by sending tokens to an account that can receive them but cannot withdraw them, rendering the coins useless and irretrievable. In the context of Ethereum, the Ethereum Improvement Proposal EIP-1559 has introduced a mechanism whereby base transaction fees are burned [45], effectively improving the tokenomics of the platform. However, Validators are permitted to retain the tips from transactions, providing an additional incentive for their participation. An alternative approach to coin burning involves deducting a fixed percentage of each transaction fee and sending it to an inaccessible account, thereby reducing the total supply of tokens over time. This method has been adopted by several blockchain platforms as a means of managing their token supply and improving their tokenomics [46]. Our economic model follows a similar approach, wherein the base transaction fee is divided into two portions using a burning multiplier denoted as  $l \in [0; 1]$ :

$$f = l \cdot f + (1 - l) \cdot f.$$



The first component is burned but the second one is left for a Validator. It is clear that  $l$  not equal to 1 increases the total Workers' rewards and reduces the burned coin amount. The value of  $l$  can be the same for all blocks and changed only by the network voting, or it depends on a particular block or the reputation of a block producer to incentivize it.

One of the possible approaches is discussed in [47]:

$$l = l_0 + (1 - l_0) (1 - q(b))$$

for each block  $b$ , where  $q(b) \in [0; 1]$  is a measure of its referential structure "quality" (here 1 means the best quality), and the parameter  $l_0$  not less than 0 signifies the minimum proportion of the transaction fees that are subjected to burning. To make this happen, the DAG topology created by honest Validators was examined and their typical behavior was described in [43]. Therefore, the function  $q(b)$  could be built on the basis of comparing the existing referential structure of block  $b$  with its theoretical reference (ideal) version. Incentivizing the encouragement of the establishment of a well-structured system of references can be highly beneficial in preserving the accuracy and safeguarding the confidentiality of data within the Sharding network. This practice serves as a means of incentivization, motivating users to adopt and adhere to a standardized method of referencing information, which in turn promotes better organization and security throughout the network.

Furthermore, in this system, all penalties incurred are effectively removed from circulation. A Worker who holds less than 50% of his/her initial stake forfeits the privilege to validate and produce blocks in the future, irrespective of any rewards he/she may have received. Any violation of the system's rules or any misbehavior on the part of a Coordinator or a Validator attracts an automatic penalty, which includes the following scenarios: (1) a Coordinator, acting as a committee member, deliberately omits a series of votes; (2) a Coordinator, acting as a committee member, issues conflicting messages or double votes; (3) a Coordinator, acting as a block producer, fails to create a block in the Coordinating network; (4) a Coordinator, acting as a block producer, generates more than 1 block within the same slot of the Coordinating network; (5) a Validator produces more than 1 block in the same slot of the Sharding network, and these blocks are subsequently confirmed in the Coordinating network; (6) a Coordinator submits an invalid proof of any of the aforementioned offenses. Penalties accumulate; for example, if three blocks are produced instead of one, the penalty doubles.

All Coordinators collectively make decisions based solely on the information provided by the coordinating ledger, without requiring any additional network consensus. If a whistleblower identifies an offense, they record proof of it in a block when it is their turn to produce one. Therefore, there is no need for an extra consensus mechanism. For instance, in case 4, a whistleblower, who detects two blocks generated in the same slot receives 50% of the penalty amount as a reward. In case 6, another Coordinator can report malicious activity by providing a reference to such a block, doubling the penalty imposed on such a leader in comparison to their potential benefits.

### 3.5. Treasury

In the blockchain ecosystem, a treasury refers to a reserved pool of digital assets that serve a specific purpose (e.g. [48], [49],

[50]). This allows stakeholders to make decisions, usually through a decentralized governance process, on how to allocate funds. The blockchain treasury can be used for a wide range of purposes, e.g. to finance the development of new features or improvements in network protocols, to cover the costs associated with operational expenses, to fund marketing initiatives aimed at increasing awareness and mass adoption of decentralized services, to acquire other projects, for charitable activities, etc. Replenishment of the treasury can be carried out through various means. The most common methods include coin issuance and the accrual of a portion of transaction fees. Additionally, penalties and donations in the form of cryptocurrency can also be used to fund treasuries.

In the Waterfall platform, if committee members fail to vote in the  $i$ -th slot, they will not receive their share of the minted reward  $W_i^c$ , and a slot leader will not receive the reward for including such missed votes in the block. Any undistributed funds are accumulated every epoch in keeping with the overall system design and can be used to replenish the treasury. In addition, a whistleblower that reports misconduct is rewarded with 50% of the penalty amount, with the other half being transferred to the treasury. If a Validator is unable to synchronize before producing their block and relies on outdated blocks, their reward may be diminished, and the resulting losses are also added to the treasury account.

The main advantage of this approach is that financing the treasury at the expense of undistributed funds and penalties does not create any additional inflationary pressure on the system. Under the consensus protocol assumptions [17], the percentage of faulty Workers does not exceed one-third of their total number. Therefore, the number of funds transferred to the treasury cannot exceed one-third of all minted coins, since at least two-thirds of Workers are well-behaved and fully rewarded. This design ensures a balanced and stable system, promoting fairness and transparency for all participants.

## 4. Examining Attacks on Tokenomics

Waterfall is a public decentralized and open-source peer-to-peer platform, which means that any individual or group can participate in the network, regardless of their motivations or intentions. Unfortunately, this open nature also makes the network vulnerable to bad actors who may choose to deviate from network protocols or even commit malicious acts against other platform participants.

To better understand these threats, we must first define what we mean by an "attack". In this context, an attack refers to any set of actions that results in a violation of the correct operation of the entire system or its components, leading to a deterioration in technical and economic indicators. However, not all attacks are created equally. Some may cause minor disruptions or receive insignificant benefits for a particular network participant, while others can result in irreversible violations and a complete disruption of the platform. In the case of Waterfall, we are particularly interested in attacks that are aimed at the economy of the platform and/or carried out with the help of economic leverage. These types of attacks leverage the financial incentives and structures of the platform to achieve malicious goals. They can take many forms, including, but not limited to, double-spending, Sybil, majority attacks, and other types of manipulation or exploitation.

Given the importance of economic incentives and structures in the functioning of tokenomics networks like Waterfall, it is very important to categorize these attacks based on the amount of damage or potential damage they can cause. Doing so can help us better understand the risks associated with different types of attacks and inform strategies for mitigating those risks. Ultimately, the goal is for the platform to remain secure, stable, and reliable for all involved.

Our next step is to classify attacks according to the extent of damage or potential harm they can inflict. This ranges from minor gains made by certain network participants at the expense of others, to severe violations that may lead to the complete disruption of the platform and irreversible consequences.

#### 4.1. Typology of Node and User Behavior

In the context of the platform, users can be classified into three distinct groups based on their behavioral patterns. The first group comprises users who always abide by the network protocols without exception. The second group consists of users who seek opportunities to increase their income or decrease their expenses by flouting the rules, such as by altering the software. The third group is composed of users who engage in activities that harm the network as a whole or the other users, ultimately leading to financial losses for those involved.

Both the second and third groups of users can act either individually or collectively, forming homogeneous or mixed subgroups. For instance, users from the third group might bribe members of the second group to carry out an attack. While users who inadvertently violate the protocols due to hardware or software failures do not intentionally collude, they may still act synchronously for various reasons. Such users will also be classified under the third group, as they are not seeking to gain any benefit by violating the rules.

#### 4.2. Reputation System

One promising indicator of reliable Worker performance is the number of earned tokens, which can be easily tracked using data from the blockchain ledger. This approach avoids the need for complex calculations that could overburden the network. Notably, we focus only on a "positive" reputation system, as a negative reputation system could be circumvented by a misbehaving Worker who could create a new account and start afresh (known as "zeroing").

It is worth highlighting that, in our scenario, each Worker starts with an equal stake. Consequently, those Workers who are more productive, particularly in block production, earn a higher income. However, the current approach can lead to an advantage for those Workers who joined the network earlier. Moreover, a Worker's productivity and efficiency may fluctuate over time. To address these concerns and ensure that node reputations are continuously updated, a depreciation mechanism can be implemented, such as a weighted moving average of rewards over several eras. This approach considers only tokens earned within a recent timeframe, ensuring that the most up-to-date information is used to determine a Worker's reputation.

The reputation system we propose can have broader applications beyond tracking Worker performance. For example, it could be utilized in peer-to-peer node interactions to prioritize communication with established nodes with a strong reputation. Moreover, we envision offering additional incentives and benefits

to Workers with exceptional reputations as a means of motivating and rewarding their high level of performance.

#### 4.3. Principles for Countering Economic Attacks

The principles for countering economic attacks on a network must be carefully considered to ensure maximum economic benefit to all users who comply with network rules. A unique Nash equilibrium [51] should be established in which it is most beneficial for all users to follow network protocols honestly and refrain from attacking the system. To achieve this, a thorough analysis of the system's functioning must be undertaken, taking into account the best rational behavior of malicious users. The behavior of users in the second group, who seek to increase their income by breaking the rules, must be rendered ineffectual in the absence of external funding for attacks.

It is also essential to estimate the cost of possible attacks by representatives of the third group, which actively disrupt the network to the detriment of individual users' economic interests. Network protocols should be designed to offset any damages caused by network disruptions with the necessary amount of funds. It should be noted that it is impossible to prevent attacks entirely in the operation of any public platform. The very concept of PoS assumes that by investing a certain amount of funds, a group of people gains control over a decentralized platform (a majority attack) [45].

To mitigate the impact of attacks on the network, protocols should be established to detect and promptly respond to any malicious activity. A mechanism for punishing attackers should also be implemented, which could involve the confiscation of tokens or other economic sanctions. Additionally, the use of staking mechanisms could provide incentives for network participants to act honestly, as they would possess a personal interest in the prosperity of the network. In summary, it is essential to build a network that is resistant to economic attacks and promotes honest behavior by all participants.

#### 4.4. Economic Attack Vector

The Waterfall consensus protocol [17] plays a crucial role in countering attacks, including economic attacks. A consensus protocol has to have the following two features [52]:

- **Liveness:** once a valid block becomes available to network nodes, it will be appended to the distributed ledger, and all valid transactions will be accepted after a certain period of time;
- **Safety:** the consensus decision is consistent among all honest nodes.

In other words, the consensus protocol coordinates the current state of the distributed ledger to provide the necessary economic information to all network participants. Then, the directions of typical attacks and possible prevention mechanisms within the framework of high-level design are considered.

**Double-spending** is an attack where a certain number of coins is used multiple times [53]. A situation may arise where a transaction for spending the same amount is published in different blocks of the DAG network. To enhance security, a new PoS-oriented blockDAG linearization algorithm was presented in [17]. Here, security means that if an honest Worker proposes an order of a blockDAG part in its turn, all other honest Workers will also

approve the same block order to be further finalized. Therefore, after running the linearization and finalization procedure, only the first transaction is considered correct, and later conflicting transactions are ignored.

A common argument against PoS is that it favors the rich over time and reduces the rewards for those who start with fewer coins, the so-called **Rich-Get-Richer** problem [54]. To a greater extent, this is inherent in systems with a high financial entry threshold. Rich stakeholders receiving more income have the opportunity to increase their presence in the network by creating new nodes.

On the Waterfall platform, the number of Workers is given preference, setting a low financial entry threshold. Therefore, having earned even a relatively small amount, a new Worker can be created, thereby increasing future earnings. Additionally, there is an opportunity to generate income without staking by providing processing power for the operational platform. One can create a network node and, e.g., for a monthly fee, deploy Workers at the request of other users.

**Nothing-at-stake** is a security issue in PoS-based systems where nodes have no financial risks to support or generate mutually exclusive proposals (e.g. voting for different blockchain forks, producing a certain amount of blocks per slot) to gain extra benefits [55]. Such malicious behavior can disrupt the consensus, reducing system performance.

With Waterfall, as with most other public platforms, there are penalties for the misbehavior of Workers, and simultaneous validation/production of conflicting blocks/messages leads to the loss of locked coins [43]. Based on data recorded in the ledger, these penalties are levied automatically. Since data in the ledger is always the same and available, all honest Workers can make judgments based exclusively on that information without overloading the network or reducing its performance.

**Maximal Extractable Value (MEV)** attacks can occur on cryptocurrency platforms when a block producer is able to incorporate its own transactions and reorder users' transactions in the block to maximize its profit.

In traditional financial systems, this type of attack is only available to a narrow circle of people who have privileged/priority access to confidential information of financial institutions, since any algorithmically predictable behavior in finance is a vulnerability that can be exploited, for example, to conduct arbitrage [56]. However, in public platforms, such information is available to all users, primarily due to the openness and variety of smart contracts that implement financial instruments. Thus, there are ample opportunities for block producers to implement MEV. Strictly speaking, these attacks are not carried out directly on decentralized platforms but are seen in DeFi services deployed on their basis [9].

By definition, MEV provides a way to counteract this type of threat directly, eliminating or significantly reducing the possibility of block producers' influence on the order of transactions written to the ledger. Here, DAG-based protocols have certain advantages over blockchain-based systems [57]. In the future, we plan to implement additional MEV-resistant features into our consensus protocol.

## 5. Modeling Tokenomics

### 5.1. Inflation and Deflation

In traditional economics, the monitoring of currency issuances enables transparency in overseeing different financial aspects.

Within tokenomics, an expansion and contraction in the circulation of coin supply are referred to as inflation and deflation, respectively. The distinction between minted and burned coin quantities is a significant network economic attribute, which can automatically be calculated in real-time. Therefore, the predetermined algorithm of the coin issuance should be carefully examined and simulated, considering specific transaction workloads that impact burned coin quantities as base transaction fees. We have examined several scenarios to gain a more comprehensive understanding of the economic dynamics within the Waterfall platform. Therefore, we were able to optimize and protect it.

Consider a value represented by the occupancy of  $j$ -th block of  $i$ -th slot in the Sharding network (see subsection 3.3):

$$r_{ij} = \frac{F_{ij}}{W_i^s \cdot p} \in (0; 1].$$

If  $r_{ij} = r$  remains constant over a year, then the amount of burned coins ( $U$ ) over a year can be calculated as follows:

$$U = \sum_{\forall i \in Y} \sum_{j=1}^{b_i} F_{ij} l = \sum_{\forall i \in Y} \sum_{j=1}^{b_i} r_{ij} W_i^s p l = r V p l.$$

If the slot time and the number of blocks are constant throughout the year, then the number of burned coins can be calculated using the following formula:

$$U = \sum_{\forall i \in Y} \sum_{j=1}^{b_i} r_{ij} \frac{V}{B^s} p l = r_0 V p l,$$

where  $r_0$  is the average value of  $r_{ij}$  across all blocks per year. The annualized burned amount  $U$  with a price multiplier  $p = 1$  never surpasses the emitted amount  $V$  anyway, since  $r_{ij} \leq 1$ . It is possible to modify the value of  $p$  through network voting in the future.

The calculation of the annual inflation rate involves determining the ratio between the difference between the total coin supply and the burned coins ( $V - U$ ) and the current coin supply, which is approximately equal to the constant  $\alpha$  multiplied by the total coin supply  $\alpha \cdot S$ . Figure 5 illustrates several potential scenarios with varying degrees of block occupancy and number of Workers, all of which are based on the assumption of a constant  $\alpha = 2.5$ , a price multiplier  $p = 1$ , and a burning multiplier  $l = 1$ .

As more transactions take place, more coins are burned as transaction fees, which can help offset the inflationary effects resulting from the creation of new coins. Obviously, there is no inflation when  $r_0 \cdot p \cdot l = 1$ , and the deflation process can be observed when  $r_0 \cdot p \cdot l > 1$ . Thus, the parameters  $p$  and  $l$  can be used to select the scenario of the economic dynamics. For example, when  $l = 1$  and  $p = 2$ , at the level of 50% average block occupancy, the inflation rate equals zero (Figure 6). However, with a higher block occupancy corresponding to more transactions per second, a deflationary trend can occur.

The economic model can exhibit both inflationary and deflationary tendencies, as the number of coins burned in the Sharding network depends on its workload, and is closely tied to the number of coins minted in the Coordinating network. To identify the optimal configuration of parameters for a given set of

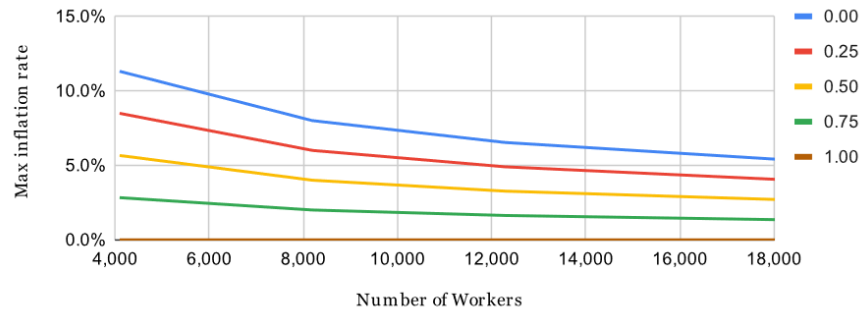


Figure 5: The relationship of the upper limit of the inflation rate per year from the block occupancy  $r_0$  with  $p = 1$  and  $l = 1$

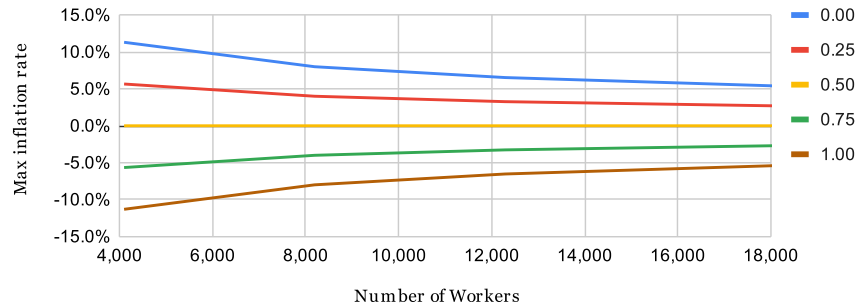


Figure 6: The relationship of the upper limit of the inflation rate per year from the block occupancy  $r_0$  with  $p = 2$  and  $l = 1$

network specifications, it is possible to leverage both structural and mathematical modeling techniques, with a defined objective function tailored to the specific strategy pursued in platform development. By carefully fine-tuning the values of key parameters, it may be possible to achieve a balanced economic system that supports sustainable growth and stability over time. Ultimately, the ability to achieve the desired economic outcomes will depend on a range of factors, including the prevailing market conditions, the actions of network participants, and the overall level of demand for the platform's services.

## 5.2. Faulty Work Simulating

In [43], the theoretical underpinnings of the Waterfall incentive system were elaborated in detail, including the distribution of rewards and the imposition of penalties, all designed to achieve a state of general economic equilibrium. The key principle governing the calculation of penalties is that they should be significantly higher than any potential gains that could be realized through a potential attack on the system. To achieve this, a multiplier of  $\lambda \geq 1$  is used to amplify the scale of the penalties. One of the core objectives of the simulation was to determine an optimal value  $\lambda$  that would be suitable for different scenarios of Worker misconduct. The overarching goal of this process is to ensure that faulty or idle Workers are eventually excluded from the consensus, thus preventing the accumulation of a critical mass of defective nodes that could hinder consensus. At the same time, temporary equipment failures or inadvertent shutdowns of Workers should not result in a permanent ban from the system.

The following scenarios for Worker failures were considered:

1.  $h_{online}$  hours working reliably and  $h_{offline}$  hours off;
2. the shutdown duration distributed according to the normal law with mean  $t_{mean}$  and standard deviation  $t_{std}$ ;

3. the probability of failure when performing one or another action is  $P \in (0; 1)$ .

During the experiments, a fixed time interval was used, and different values were assigned to the various parameters mentioned above. After this interval, Workers were removed from participation in the work, and the topology of the resulting DAG was analyzed. Based on the findings, it was determined that a relatively high value of  $\lambda = 100$  should be set for penalty rates. For instance, failing to produce two consecutive blocks or submitting conflicting messages during the voting process incurs a penalty 100 times greater than the corresponding reward. In addition to the penalty, the Worker's participation in the network is temporarily suspended for the current and next eras so that the necessary equipment settings can be made. This helps to preserve the value of the Worker's stake, as subsequent failures would cause the stake to fall below the 50% threshold, leading to permanent exclusion from the network. While the Worker is suspended, they do not take part in committee work or block production, which in turn reduces the percentage of faulty nodes in the network.

## 6. Implementation and Experimental Study of the Waterfall System

The development of the Waterfall system required a comprehensive approach, starting with the experimental study of its functioning. Initially, we focused on a small but increasing number of nodes, where we studied the system's behavior using simulation tools. As we gained more insights, we moved on to conduct full-scale tests in a test network with a smaller number of nodes.

Currently, we have implemented the main initial elements of our protocol and are conducting load experiments using t3.small and t3.medium AWS Servers with a 2-core CPU and 2 or 4 GB RAM respectively [58]. These tests are being conducted to evaluate the tokenomics model's ability to serve the Waterfall

Table 1: Network load test results

Number of				Loading							
				Idling		1st day			3rd day		
Servers	Nodes	Workers	Total	CPU	RAM	CPU	RAM	Spending	CPU	RAM	Spending
t3.medium	32	32	1024	1.91	0.59	2.51	1.3		2.2	1.8	
	32	16	512	2.32	0.69	2.32	1.3	3.44 USD	0.56	2.2	1.25 USD
	8	32	256	1.91	0.59	2.51	1.3				
	8	16	128	2.32	0.71	2.32	1.3		0.53	2.66	2.33 USD
	8	8	64	2.32	0.51	2.32	1.3				
t3.small	8	8	64	1.91	0.51	2.21	1.3				

platform with high transaction throughput. We are optimistic about the system's performance since it has demonstrated the desired behavior.

However, to ensure optimal performance, we continuously check the values of the system parameters and study further optimization opportunities. Our approach has been focused on caution and thoroughness to ensure that the Waterfall system is developed to the highest standards and is capable of serving its intended purpose.

The outcome of the test that measured the amount of work a server can handle (refer to Table 1) indicated that there was no meaningful connection between the CPU or RAM load and the number of Workers running on a single server. Concurrently, there is a shift in the load structure over time. At the same time, there is a shift in the load arrangement over time. By the third day of operation, the influence of software adaptation mechanisms was observable. A part of the data necessary for work was cached in shared memory. As a consequence, the processor's burden was reduced by 75-77%. Only when the amount of available memory allowed for saving the necessary information for all the Workers running on the node was such a significant reduction in CPU load achieved. Also, an experiment was conducted to evaluate hashing of data with insufficient RAM for 32 Workers. Despite the 38% increase in memory consumption, only 12% savings in CPU resources were observed. Observations show that doubling the minimum required amount of RAM results in more than four times less load on the processor on the third day of operation. This, combined with automatic optimization of communications and the corresponding reduction in traffic, leads to an average 64% reduction in server maintenance costs at Amazon Web Services prices since the third day.

The table demonstrates that entry to the Waterfall network is more accessible compared to other popular networks of a similar nature. A lower entry threshold is made possible by less demanding software and a lower computational load, with everything else being equal.

One can notice that the test network with fewer nodes requires more costs per server. This is due to the overall cost of maintaining the TestNet infrastructure. When distributing these costs over 32 nodes, we naturally get a smaller amount compared to 8 nodes. In this regard, we make a comparative analysis of expenses only within the rows of the table, but not between different rows.

The cost of user-nodes with a transfer rate of 2 standard transactions per second amounted to 28.7 and 35.2 coins per day, on average, where the optimal number of Workers  $N_{opt}$  was equal to 8,192 and 12,288 respectively  $R_{opt} = 0.2$ .

The implementation of the Waterfall System provides for the possibility of deploying several autonomous Workers on each node with a common ledger and a pool of transactions. Having as many Workers as possible in one node provides an economic benefit, but it negatively affects network decentralization. Their number must have an upper boundary, taking into account technical limitations. A large number of Workers deployed on a single device may not have adequate time to create and process blocks. This leads to a shortfall in rewards and the imposition of penalties.

## 7. Conclusion

The multishard DAG-based platform Waterfall is a sophisticated yet efficient amalgamation of diverse pre-existing and unique solutions. Tokenomics serves as the tool to maintain coherence among the distinct components and optimize their operations. Although the presented tokenomics framework is tailored for the Waterfall platform, the methods, and approaches outlined in the document could be valuable for creating economic support systems for other decentralized networks.

The conclusions drawn from the article suggest that the general model designed for Waterfall tokenomics can bring about an economic balance that caters to the concerns of all participants within the platform. This equilibrium is achieved while keeping transaction fees at a low level, which is essential for implementing DLTs and smart contracts into applications designed for enterprise-level use. The advantages of this model become apparent when dealing with a high volume of transactions, making the platform more reliable and promoting digital transformation through transparency and trust.

By offering an affordable transaction fee, the Waterfall platform can be utilized for a broad spectrum of services, such as DeFi, IoT, Web3 gaming, digital identity, medical screening systems, and peer-to-peer energy trading, etc. The foundational principles of Waterfall tokenomics align with its DAG-based architecture design, and dynamically adapting macroeconomic mechanisms ensure that the platform performs optimally and sustainably in rapidly changing situations.

Both inflationary and deflationary tendencies can be observed in the economic model depending on initial parameters and further network management. A few possible scenarios of the system evaluation were mathematically simulated and experimentally studied in the testnet.

Future work on Waterfall tokenomics will focus on researching the economic aspects of interactions between various homomorphic Sharding networks, forming transaction fees based on the external exchange rate, voting for economic parameters, and

developing the mechanics required for implementing different incentivization strategies. Additionally, the economic issues of on/off-boarding process will also be explored, and simulations will be conducted to evaluate the effectiveness of various strategies. Overall, the article highlights the potential benefits of Waterfall tokenomics in promoting decentralized technologies and creating a more transparent and trustworthy digital environment.

### Conflict of Interest

The authors declare no conflict of interest.

### References

- [1] S. Grybniak, Y. Leonchik, R. Masalskiy, I. Mazurok, O. Nashyvan, "Waterfall: Salto Collazo. Tokenomics," 2022 IEEE International Conference on Blockchain, Smart Healthcare and Emerging Technologies (SmartBlock4Health), Bucharest, Romania, 2022, doi: 10.1109/SmartBlock4Health56071.2022.10034521
- [2] M. N. M. Bhutta, A. A. Khwaja, A. Nadeem, H. F. Ahmad, M. K. Khan, M. A. Hanif, M. Alshamari, Y. Cao, "A survey on blockchain technology: evolution, architecture and security," *IEEE Access*, **9**, 61048-61073, 2021, doi: 10.3390/s22145274.
- [3] A. T. Sherman, F. Javani, H. Zhang, E. Golaszewski, "On the origins and variations of blockchain technologies," *IEEE Security & Privacy*, **17**(1), 72-77, 2019, doi: 10.1109/MSEC.2019.2893730.
- [4] S. Grybniak, Y. Leonchik, R. Masalskiy, Igor Mazurok, Oleksandr Nashyvan, Ruslan Shanin "Decentralized platforms: goals, challenges, and solutions," 2022 IEEE 7th Forum on Research and Technologies for Society and Industry Innovation (RTSI), 62-67, doi: 10.1109/RTSI55261.2022.9905225.
- [5] H. Pervez, M. Muneeb, M. U. Irfan, I. U. Haq, "A comparative analysis of DAG-based blockchain architectures," 12th International Conference on Open Source Systems and Technologies (ICOSST), 27-34, 2018, doi: 10.1109/ICOSST.2018.8632193.
- [6] F. M. Benčić, I. P. Žarko, "Distributed ledger technology: blockchain compared to directed acyclic graph," *IEEE 38th International Conference on Distributed Computing Systems*, 1569-1570, 2018, doi: 10.1016/j.technovation.2023.102711.
- [7] Q. Wang, J. Yu, S. Chen, Y. Xiang, "SoK: diving into DAG-based blockchain systems," preprint arXiv:2012.06128, 2020, doi: 10.48550/arXiv.2012.06128.
- [8] R. Selkis, A Messari report: Crypto theses for 2023, 2023, <https://messari.io/crypto-theses-for-2023>.
- [9] S. M. Werner, D. Perez, L. Gudgeon, A. Klages-Mundt, D. Harz, W. J. Knottenbelt, "Sok: decentralized finance (DeFi)," preprint arXiv:2101.08778, 2021.
- [10] L. Dam, What is Web3 Gaming? How is it different from Traditional Gaming? 2023, <https://ekoios.vn/web3-games-and-traditional-games-comparison>.
- [11] E. Tijan, S. Aksentijević, K. Ivanić, M. Jardas, "Blockchain technology implementation in logistics," *Sustainability*, **11**(4), 1185, 2019, doi: 10.3390/su11041185.
- [12] R. M. Garcia-Teruel, "Legal challenges and opportunities of blockchain technology in the real estate sector," *Journal of Property, Planning and Environmental Law*, 2020, doi: 10.1108/JPEL-07-2019-0039.
- [13] J. Lee, "BIDaaS: Blockchain based ID as a service," *IEEE Access*, **6**, 2274-2278, 2018, doi: 10.1109/ACCESS.2017.2782733.
- [14] N. Kshetri, J. Voas, "Blockchain-enabled e-voting," *IEEE Software*, **35**(4), 95-99, 2018, doi: 10.1109/MS.2018.2801546.
- [15] S. Grybniak, D. Dmytryshyn, Y. Leonchik, I. Mazurok, O. Nashyvan, R. Shanin, "Waterfall: a scalable distributed ledger technology," in 2022 IEEE 1st Global Emerging Technology Blockchain Forum: Blockchain & Beyond (iGETblockchain), 1-6, 2022, doi: 10.1109/iGETblockchain56591.2022.10087112.
- [16] C. T. Nguyen, D. Thai Hoang, D. N. Nguyen, D. Niyato, H. T. Nguye, E. Dutkiewicz, "Proof-of-stake consensus mechanisms for future blockchain networks: fundamentals, applications and opportunities," *IEEE Access*, **7**, 85727-85745, 2019, doi: 10.1109/ACCESS.2019.2925010.
- [17] S. Grybniak, D. Dmytryshyn, Y. Leonchik, I. Mazurok, O. Nashyvan, R. Shanin, "Waterfall: Gozalandia. Distributed protocol with fast finality and proven safety and liveness," *IET Blockchain*, 1-12, 2023, doi: 10.1049/blc2.12023.
- [18] K. Lau, Ethereum 2.0. An introduction, Crypto.com, 25 p, 2020.
- [19] S. Au, T. Power, Tokenomics: the crypto shift of blockchains, ICOs, and tokens, Packt Publishing Ltd, 2018.
- [20] L. W. Cong, Y. Li, N. Wang, "Tokenomics: dynamic adoption and valuation," *The Review of Financial Studies*, **34**(3), 1105-1155, 2021, doi: 10.1093/rfs/hhba089.
- [21] G. A. Pierro, H. Rocha, "The influence factors on Ethereum transaction fees," *IEEE/ACM 2nd International Workshop on Emerging Trends in Software Engineering for Blockchain (WETSEB)*, 24-31, 2019, doi: 10.1016/j.bcr.2022.100074.
- [22] E. Anceaume, A. D. Pozzo, T. Rieutord, S. Tucci-Piergiorgio, "On finality in blockchains," preprint arXiv:2012.10172, 2020, doi: 10.4230/LIPIcs.OPODIS.2021.6.
- [23] P. Freni, E. Ferro, R. Moncada, "Tokenomics and blockchain tokens: a design-oriented morphological framework," *Blockchain: Research and Applications*, **3**(1), 2022, doi: 10.1016/j.bcr.2022.100069.
- [24] O. Letychevskiy, "Creation of a self-sustaining token economy," *The Journal of The British Blockchain Association*, **5**(1), 2022, doi: 10.31585/jbba-5-1-(4)2022.
- [25] J. A. Kroll, I. C. Davey, E. W. Felten, "The economics of Bitcoin mining or, Bitcoin in the presence of adversaries," 12th Workshop on the Economics of Information Security, 2013, doi: 10.36484/liberal.662625.
- [26] S. Davidson, P. de Filippi, J. Potts, "Economics of blockchain," *Public Choice Conference*, 2016, doi: 10.2139/ssrn.2744751.
- [27] L. W. Cong, Y. Li, N. Wang, "Blockchain and tokenomics," *COJ Reviews & Research*, **1**(1), 2018, doi: 10.1093/rfs/hhz007.
- [28] A. Yakovenko, Solana: a new architecture for a high performance blockchain v0.8.13, Whitepaper, 2018, <https://solana.com/solana-whitepaper.pdf>.
- [29] W. Silvano, R. Marcelino, "Iota Tangle: a cryptocurrency to communicate Internet-of-Things data," *Future Generation Computer Systems*, **112**, 307-319, 2020, doi: 10.1016/j.future.2020.05.047.
- [30] J. J. Reuben, A. Joshua, "Blinkchain - a regulation friendly proof-of-speed blockchain v0.1," available at SSRN 4267038, 2022.
- [31] S. Bano, A. Sonnino, M. Al-Bassam, S. Azouvi, P. McCorry, S. Meiklejohn, G. Danezis, "SoK: consensus in the age of blockchains," 1st ACM Conference on Advances in Financial Technologies, 183-198, 2019, <https://arxiv.org/pdf/1711.03936.pdf>.
- [32] Z. Liu, N. C. Luong, W. Wang, D. Niyato, P. Wang, Y. Liang, D. I. Kim, "A survey on applications of game theory in blockchain," preprint arXiv:1902.10865, 2019, doi: 10.13868/j.cnki.jcr.000287.
- [33] K. Iyer, C. Dannen, "Crypto-economics and game theory. Building Games with Ethereum Smart Contracts," *Apress Berkeley*, 129-141, 2018, doi: 10.1007/978-1-4842-3492-1\_6.
- [34] Z. Chang, W. Guo, X. Guo, Z. Zhou, T. Ristaniemi, "Incentive mechanism for edge-computing-based blockchain," *IEEE Transactions on Industrial Informatics*, **16** (11), 7105-7114, 2020, doi: 10.1109/TII.2022.3163550.
- [35] S. Motepalli, H. Jacobsen, "Reward mechanism for blockchains using evolutionary game theory," *IEEE 3rd Conference on Blockchain Research & Applications for Innovative Networks and Services (BRAINS)*, 217-224, 2021, doi: 10.1109/BRAINS52497.2021.9569791.
- [36] A. Salau, R. Dantu, K. Morozov, S. Badruddoja, K. Upadhyay, "Making blockchain validators honest," 2022 Fourth International Conference on Blockchain Computing and Applications (BCCA), 267-273, IEEE, 2022, September, doi: 10.1109/BCCA55292.2022.9921952.
- [37] I. Mazurok, V. Pienko, Y. Leonchik, "Empowering fault-tolerant consensus algorithm by economic leverages," *ICTERI Workshops*, 465-472, 2019, doi: 10.1049/blc2.12023.
- [38] Y. Amoussou-Guenou, A. Pozzo, M. Potop-Butucaru, S. Tucci-Piergiorgio, "Correctness and fairness of tendermint-core blockchains," preprint arXiv:1805.08429, 2018, doi: 10.4230/LIPIcs.OPODIS.2018.16.
- [39] P. Chafé, A. Mashatan, A. Munro, B. Goncalves, D. Cameron, J. Xu, Dandelion network whitepaper, 22 p, 2022, [https://dandelionnet.io/wp-content/uploads/2022/09/dandelion\\_whitepaper.pdf](https://dandelionnet.io/wp-content/uploads/2022/09/dandelion_whitepaper.pdf).
- [40] O. Antonenko, S. Grybniak, D. Guzey, O. Nashyvan, R. Shanin, "Subnetworks in BlockDAG," 2022 IEEE 1st Global Emerging Technology Blockchain Forum: Blockchain & Beyond (iGETblockchain), 1-6, doi: 10.1109/iGETblockchain56591.2022.10087101.
- [41] R. Dennis, G. Owen, "Rep on the block: a next generation reputation system based on the blockchain," *IEEE 10th International Conference for Internet Technology and Secured Transactions (ICITST)*, 131-138, 2015, doi: 0.1109/ICITST.2015.7412073.
- [42] Z. Zhou, M. Wang, C. Yang, Z. Fu, X. Sun, Q. Wu, "Blockchain-based decentralized reputation system in E-commerce environment," *Future Generation Computer Systems*, **124**, 155-167, 2021, doi: 10.1016/j.future.2021.05.035.

- [43] I. Mazurok, Y. Leonchik, S. Grybniak, O. Nashyvan, R. Masalskyi, "An incentive system for decentralized DAG-based platforms," *Applied Aspects of Information Technology*, **5**(3), 196–207, 2022, doi: 10.15276/aait.05.2022.13.
- [44] W. Li, S. Andreina, J. Bohli, G. Karame, "Securing proof-of-stake blockchain protocols," *Data privacy management, cryptocurrencies and blockchain technology*, 297-315, Springer, Cham, 2017, doi: 10.1007/978-3-319-67816-0\_17.
- [45] T. Roughgarden, Transaction fee mechanism design for the Ethereum blockchain: an economic analysis of EIP-1559, 2020, doi: <https://timroughgarden.org/papers/eip1559.pdf>.
- [46] Solana Foundation, Transaction fees, 2022, [https://docs.solana.com/ru/transaction\\_fees](https://docs.solana.com/ru/transaction_fees).
- [47] R. Masalskyi, "DAG Distributed Ledger Modeling," *The 1st Student Sci. Conf. of Joint Res. Cooperation between Odesa I.I. Mechnikov National University and Huaiyin Institute of Technology*, 171–175, 2022.
- [48] Polkadot, Understanding the Polkadot treasury, *Medium*, 2021, <https://polkassembly.medium.com/understanding-the-polkadot-treasury-816821ffe589>.
- [49] Cardano, Monetary policy, *Cardano docs*, <https://docs.cardano.org/explore-cardano/monetary-policy>.
- [50] NEAR, Ecosystem treasury DAO, 2021, <https://gov.near.org/t/near-ecosystem-treasury-dao/2946>
- [51] J. F. Nash Jr., "Equilibrium points in n-person games," *Proceedings of the national academy of sciences*, **36**(1), 48-49, 1950, doi: 10.1515/9781400884087-007.
- [52] L. Lamport, "Proving the correctness of multiprocess programs," *IEEE Transactions on Software Engineering*, **SE-3**(2), 125–143, 1977, doi: 10.1109/TSE.1977.229904.
- [53] A. Begum, A. Tareq, M. Sultana, M. Sohel, T. Rahman, A. Sarower, "Blockchain attacks analysis and a model to solve double spending attack," *International Journal of Machine Learning and Computing*, **10**(2), 352-357, 2020, doi: 10.18178/ijmlc.2020.10.2.942.
- [54] Y. Huang, J. Tang, Q. Cong, A. Lim, J. Xu, "Do the rich get richer? Fairness analysis for blockchain incentives," *International Conference on Management of Data*, 790-803, 2021, doi: 10.1145/3448016.3457285.
- [55] D. Rose, E. Machery, S. Stich, M. Alai, A. Angelucci, R. Berniūnas, E. Buchtel, A. Chatterjee, H. Cheon, I. Cho et al., "Nothing at stake in knowledge," *Noûs*, 224–247, 2019, doi: 10.1111/nous.12211.
- [56] K. Qin, L. Zhou, A. Gervais, "Quantifying blockchain extractable value: How dark is the forest?" *2022 IEEE Symposium on Security and Privacy (SP)*, 198-214, 2022, May, doi: 10.1109/SP46214.2022.9833734.
- [57] D. Malkhi, P. Szalachowski, "Maximal extractable value (MEV). Protection on a DAG," preprint *arXiv:2208.00940*, 2022, doi: 10.48550/arXiv.2208.00940.
- [58] Waterfall, Waterfall testnet 3. Test 9, 2022, [https://waterfall.foundation/testnet\\_3\\_test\\_9](https://waterfall.foundation/testnet_3_test_9).

## Simulation of Obstacle Detection Based on Optical Flow Images for Avoidance Control of Mobile Robots

Mai Ngoc Anh\*

Le Quy Don Technical University, Hanoi, Vietnam

### ARTICLE INFO

Article history:

Received: 20 April, 2023

Accepted: 14 June, 2023

Online: 25 June, 2023

Keywords:

Noise-free optical flow

Obstacle detection

Mobile robot control

### ABSTRACT

The article presents a simulation of obstacle detection based on noise-free optical flow images for motion control of mobile robots. The detection of hazardous areas in optical flow images is accomplished by dividing multiple layers of optical flow vectors into equal parts. Based on the results of calculating the average magnitude of the vectors in the divided parts and using a solution of comparing these average magnitudes with each other, the robot can figure out obstacle position to avoid and guide the robot to a safe direction. The experiments are simulated on Matlab program to test the performance of the system. The simulated office environment with many obstacles randomly arranged along the corridors is used to test the ability to recognize obstacles to avoid. Simulation results related to different obstacle density scenarios are analyzed to demonstrate the stability of obstacle detection from the noise-free optical flow images.

### 1. Introduction

There are many solutions for reconstructing 3D structure based on optical flow vectors of 2D images taken by camera(s) mounted on mobile robot. However, the proposed solutions are not be feasible if the optical flow image contains noise vectors. One of the approaches to remove noise in optical flow vectors introduced at the conference ICECCME-2022 [1] makes it possible to study optical flow images on unstable light conditions based on an optical flow noise filter with dynamic thresholds computed by relatively comparing between the average magnitude value of optical flow vectors and an outlier magnitude value. After removing noise vectors, optical flow imaging can be used for mobile robots to observe the working environment and perform complex tasks. Derived from noise-free optical flow images, this article is the next extension of [1] in aspect of experimental simulation of obstacle detection from the noise-free optical flow images to help mobile robots move safely in a simulated indoor office environment.

Over the past decades, mobile robots have been widely used in many production areas such as industry [2] and agriculture [3], in service activities such as search and rescue [4] and in offices [5]. Mobile robots have proven to be effective in supporting humans through their ability to move flexibly and safely in various ways such as by wheels [6], crawlers [7], omnidirectional wheels [8]. Many kinds of sensors such as infrared [9], ultra-sonic [10] and

laser [11] have been applied to help mobile robots recognize the surrounding context and make corresponding decisions according to the set requirements. Among the studies of the sensor-based recognition on mobile robots, image-based recognition solutions have been studied a lot thanks to their ability to recognize many objects with different shapes, sizes and distances [12].

Based on the acquired images, the robot performs 2D or 3D scene reconstruction to identify objects to distinguish between a target (to approach) and an obstacle (to avoid). However, image processing often has to deal with the difficult problems of processing time and noise in captured images [13]. The optical flow vector-based identification solution is researched on the idea of biomimetic mimicry of bees in observing, acquiring and processing dynamic image information [14]. Technically, classical techniques of optical flow recognition usually use the method of comparing the difference in vector density of the left half with that of the right half to determine the direction of the obstacle [15].

In this study, the obstacle detection solution based on optical flow images filtered out noise vectors will be tested on a simulated environment with some situations related to different density of obstacles. The movement trajectory of the robot is automatically recorded to analyze and evaluate the safe movement when passing through the areas arranged many obstacles randomly.

The next content is organized as follows: Firstly, the optical flow processing is introduced. Then, the solution of locating obstacle from noise-free optical flow images is analyzed. After that, the simulation of optical flow-based mobile robot moving and

\*Corresponding Author: Mai Ngoc Anh, [maingocanh.atc@mta.edu.vn](mailto:maingocanh.atc@mta.edu.vn)



avoiding obstacles in a simulated office is depicted and analyzed. Finally, the conclusion are drawn.

## 2. Optical flow processing

The processing of real optical flow vectors is shown in Figure 1a and that of simulation noise-free optical flow vectors is illustrated in Figure 1b. The multi-layer segmentation of the optical flow vectors depicted in Figure 1 can be explained as the following schedule:

In the first processing stage, the optical flow image is divided into four equal parts  $Q_1$ ,  $Q_2$ ,  $Q_3$  and  $Q_4$ . Mathematically, the average magnitude matrix of optical flow vectors in the first processing stage is formulated as follows:

$$\mathbf{Q}^1 = \begin{bmatrix} Q_1 & Q_2 \\ Q_3 & Q_4 \end{bmatrix} \quad (1)$$

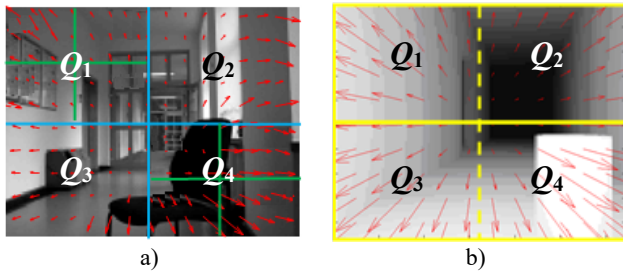


Figure 1: Segmentation of real (a) and simulation (b) noise-free optical flow images.

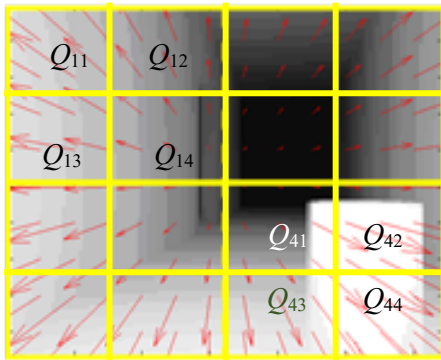


Figure 2: Segmentation in the second processing stage.

Figure 2 illustrates the second stage of multi-layer segmentation of optical flow vectors. In this stage, the four first processing parts are divided into four smaller parts  $Q_{1i}$ ,  $Q_{2i}$ ,  $Q_{3i}$  and  $Q_{4i}$ , where  $i = 1 \dots 4$ . The average intensity matrix of the optical flow vectors in the second processing stage has the following form:

$$\mathbf{Q}^2 = \begin{bmatrix} Q_{11} & Q_{12} & Q_{21} & Q_{22} \\ Q_{13} & Q_{14} & Q_{23} & Q_{24} \\ Q_{31} & Q_{32} & Q_{41} & Q_{42} \\ Q_{33} & Q_{34} & Q_{43} & Q_{44} \end{bmatrix} \quad (2)$$

By the similar way, in the  $n^{\text{th}}$  processing stage, the four parts of the  $(n-1)^{\text{th}}$  processing stage are divided into four smaller parts of the deeper layer of the processing, that means  $Q^1$ ,  $Q^2$ , ... and  $Q^n$  are matrices of average magnitude of optical flow vectors in processing stage 1, 2, ... and  $n$ , respectively.

## 3. Locating obstacle from noise-free optical flow images

To detect obstacle position during robot movement, various depth-based recognition methods [12] and [16] are implemented by processing images captured by a single camera mounted on the mobile robot. Similarly, optical flow vector images are analysed after multi-layer segmentation to locate the obstruction areas and obtain depth information through qualitative calculations. In other words, the basic principle of determining the location of obstacles is to identify a part of the image having the average  $Q_i$  bigger than the others in the magnitude matrix of optical flow vectors.

Figure 3 illustrates the way for locating the obstacle based on the multi-layer segmentation of optical flow vectors. It is easy to see in Figure 3a that in the first processing stage, part  $Q_4$  has the biggest magnitude due to covering the obstacle. In the second processing stage shown in Figure 3b, parts  $Q_{42}$  and  $Q_{44}$  have the biggest magnitudes because the obstacle fills all these parts compared to half filling in parts  $Q_{41}$  and  $Q_{43}$ .

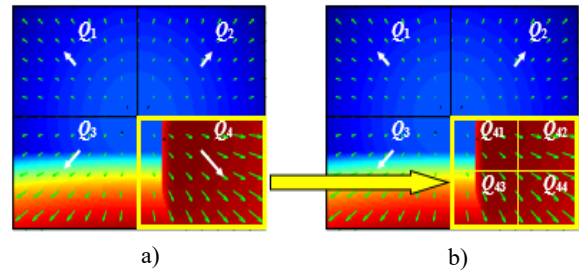


Figure 3: Locating obstacle from optical flow image: a) layer-1; b) layer-2.

As shown in Figure 4, an optical flow vector  $\vec{r}_{ij}$  contains two components projected onto axes OU and OV as follows:

$$\vec{r}_{ij} = u_{ij} \cdot \vec{e}_U + v_{ij} \cdot \vec{e}_V \quad (3)$$

where  $\vec{e}_U$  and  $\vec{e}_V$  are unit vectors,  $u_{ij}$  and  $v_{ij}$  are amplitudes of a vector  $\vec{r}_{ij}$  projected on axes OU and OV, respectively.

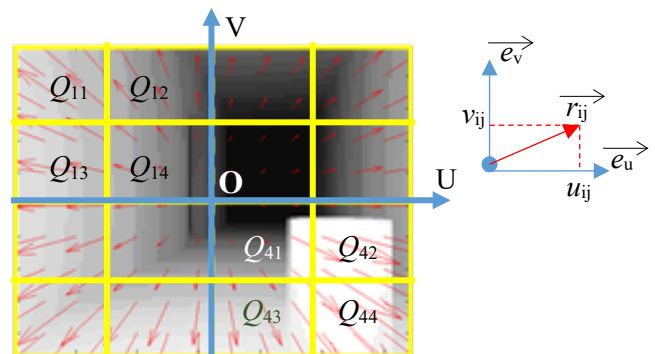


Figure 4: Projecting an optical flow vector  $\vec{r}_{ij}$  onto axes OU and OV

Let consider  $Q_{44}$  containing 16 optical flow vectors arranged in four rows and four columns by the following matrixes:

$$\mathbf{u}_{44} = \begin{bmatrix} u_{11} & u_{12} & u_{13} & u_{14} \\ u_{21} & u_{22} & u_{23} & u_{24} \\ u_{31} & u_{32} & u_{33} & u_{34} \\ u_{41} & u_{42} & u_{43} & u_{44} \end{bmatrix} \quad (4)$$

$$\mathbf{v}_{44} = \begin{bmatrix} v_{11} & v_{12} & v_{13} & v_{14} \\ v_{21} & v_{22} & v_{23} & v_{24} \\ v_{31} & v_{32} & v_{33} & v_{34} \\ v_{41} & v_{42} & v_{43} & v_{44} \end{bmatrix} \quad (5)$$

By averaging all amplitudes  $u_{ij}$  and  $v_{ij}$  in each column, we have the average value  $\mu_{Uj}$  and  $\mu_{Vj}$  as follows:

$$\mu_{Uj} = \frac{1}{n} \sum_{i=1}^n u_{ij} \quad (6)$$

$$\mu_{Vj} = \frac{1}{n} \sum_{i=1}^n v_{ij} \quad (7)$$

where  $n$  is number of components at column  $j$ . As the illustration in Figure 4,  $n = 4$  and  $j = 1 \dots 4$ .

From equation (4) and (6), let compare the average value  $\mu_{Uj}$  of all  $u_{ij}$  in one column and replace the biggest average by 1, we have the matrix of obstacle direction as follows:

$$\mathbf{obstacle}_{U44} = \begin{bmatrix} 0 & 0 & 0 & 0 \\ 0 & 0 & 0 & 0 \\ 0 & 0 & 0 & 1 \\ 0 & 0 & 0 & 1 \end{bmatrix} \quad (8)$$

Similarly, from equation (5) and (7), let compare the average value  $\mu_{Vj}$  of all  $v_{ij}$  in one row and replace the biggest average by 1, we have the following matrix of obstacle direction as follows:

$$\mathbf{obstacle}_{V44} = \begin{bmatrix} 0 & 0 & 0 & 0 \\ 0 & 0 & 0 & 0 \\ 0 & 0 & 0 & 0 \\ 0 & 0 & 1 & 1 \end{bmatrix} \quad (9)$$

Based on the equation (8) and (9), the mobile robot can locate the most dangerous area in the noise-free optical flow image.

## 4. Simulation

### 4.1. Simulation setup

The mobile robot control system with a camera is simulated on the Matlab program and organized into functional modules as illustrated in Figure 5. The two coordinate systems including the [www.astesj.com](http://www.astesj.com)

mobile robot's coordinate system (body frame) related to the motion parameters of the simulated mobile robot and the office's coordinate system (inertial frame) related to the office environment are shown in Figure 6.

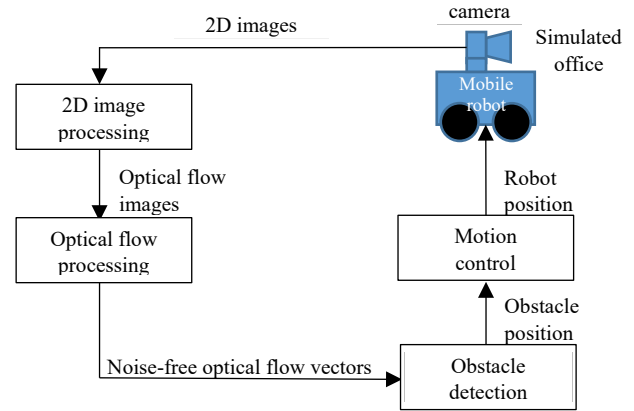


Figure 5: Simulated control system of mobile robot

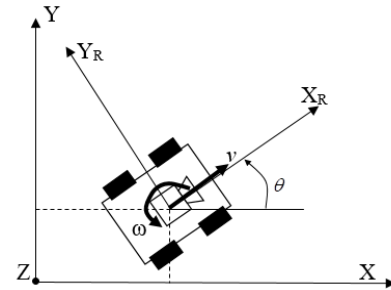


Figure 6: Two coordinate systems and motion parameters of mobile robot

The motion in the simulated mobile robot's coordinate system  $(OXYZ)_R$  can be defined from the office's coordinate system  $(OXYZ)$  as follows:

$$\begin{bmatrix} \dot{x} \\ \dot{y} \\ \dot{\theta} \end{bmatrix} = \mathbf{R}_z(\theta) \cdot \begin{bmatrix} v \\ \omega \end{bmatrix} = \begin{bmatrix} \cos \theta & -\sin \theta & 0 \\ \sin \theta & \cos \theta & 0 \\ 0 & 0 & 1 \end{bmatrix} \cdot \begin{bmatrix} v \\ \omega \end{bmatrix} \quad (10)$$

where

-  $v$ ,  $\omega$ , and  $\theta$  are the linear velocity, angular velocity, and rotational angle of the robot's coordinate system related to the office's coordinate system, respectively.

-  $\dot{x}$ ,  $\dot{y}$ , and  $\dot{\theta}$  are the linear velocities and the rotational angular velocity, respectively because the variable  $x$ ,  $y$  and  $\theta$  are positions and rotational angle of the robot, respectively.

-  $\mathbf{R}_z$  is the rotation matrix on the Z-axis.

The simulated robot has a width of 50 cm and a length of 60 cm. The office is simulated as shown in Figure 7 to test the robot's ability to move through the recorded camera images. The top view of the simulated office in Figure 7a shows that there are four rooms in the central area and some doors connecting the rooms to the corridor surrounding the office. The side view of the office in

Figure 7b provides door (entrance) and ceiling height information. The width of the entrance is 130 cm and the height of the ceiling is 350 cm. A typical camera image is extracted to visualize the robot's view of the work area as the illustration in Figure 7c.

The main objective of the experiments is to test robot's ability to avoid obstacles randomly arranged along the road in different situations based on the result of noise-free optical flow recognition.

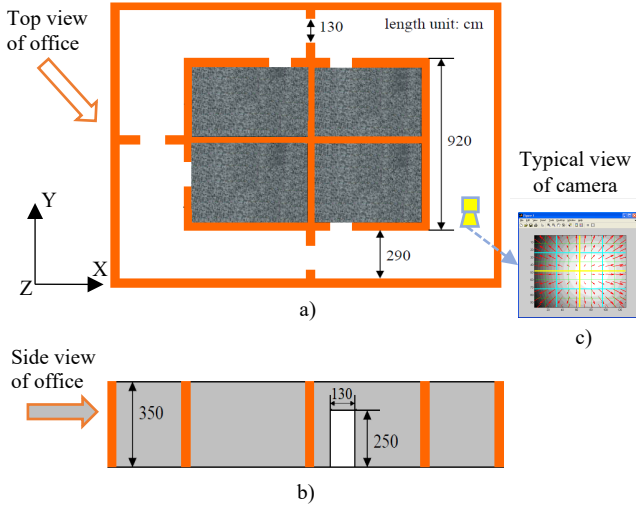


Figure 7: Simulated office for testing obstacle avoidance of mobile robot

4.2. Simulation results

The simulation is performed by the Matlab program with the computer speed 3.40GHz of Intel(R) Pentium(R) 4 CPU and the image processing is carried out by the GPU NVIDIA GeForce GTX 260 1.24GHz with segment size 32 x 32 pixels.

a) Simulated environment image without obstacles

Before testing the robot's ability of obstacle detection, we should review the typical contexts without obstacle in the simulated office situations related to walls, corners, doors and corridors.

Optical flow images are shown in Figure 8 when the robot copes with the walls: the straight view of the camera to a wall (Figure 8a) and the slanted view of the camera to the wall (Figure 8b).

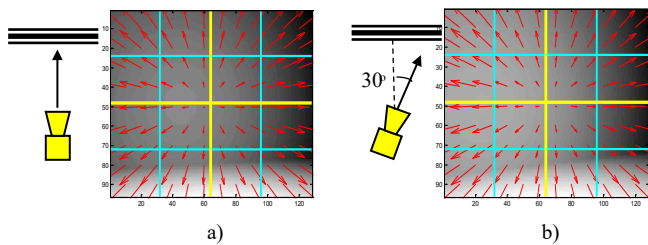


Figure 8: Optical flow images of wall: a) straight view, b) slanted view

Optical flow images are depicted in Figure 9 as the robot approaches the corners of the office: straight view of the corner (Figure 9a) and slanted view of the corner center (Figure 9b).

center (Figure 9a) and slanted view of the corner center (Figure 9b).

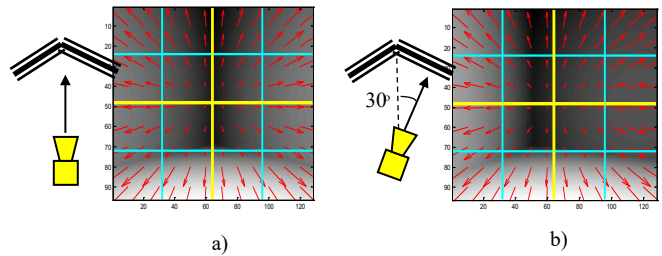


Figure 9: Optical flow images of corner: a) straight view, b) slanted view

Optical flow images are illustrated in Figure 10 as the robot approaches the doors of the office: straight view of the door center (Figure 10a) and slanted view of the door center (Figure 10b).

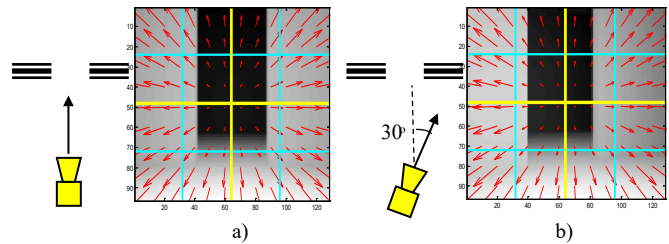


Figure 10: Optical flow images of door: a) straight view, b) slanted view

Optical flow images are sketched in Figure 11 during the robot following the corridors of the office without any obstacle: straight view of the corridor (Figure 11a) and slanted view of the corridor (Figure 11b).

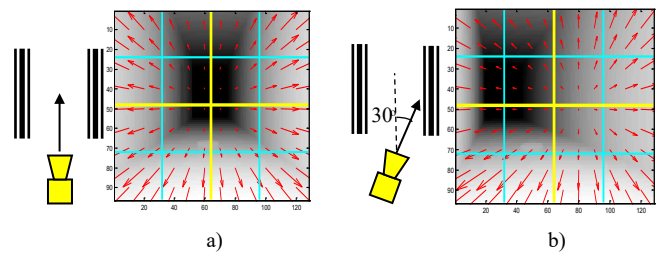


Figure 11: Optical flow images of corridor: a) straight view, b) slanted view

The statistical data of optical flow images are shown by colorful 3D histograms in Figure 12 for different distances (right horizontal axis) including near (blue), middle (yellow) and distal (red) for different objects including walls (A1), corners (A2), doors (A3) and corridors (A4) in 4 depth stages of optical flow vector processing (vertical axis) to evaluate tilt angles between the camera and the observed object by measuring the ratio of the mean value between the left optical quadrant and the right optical quadrant (nearest horizontal axis).

It is easy to see that the optical flow vectors in these situations are distributed differently between images despite the absence of obstructions. However, in the cases of close distances to the objects, the robot still has to avoid the nearest object as if avoiding

an obstacle. Based on the ratio between the left parts and the right part, the principle for avoiding obstacle is that the robot travels to the direction containing the smaller average value between left and right optical flow parts.

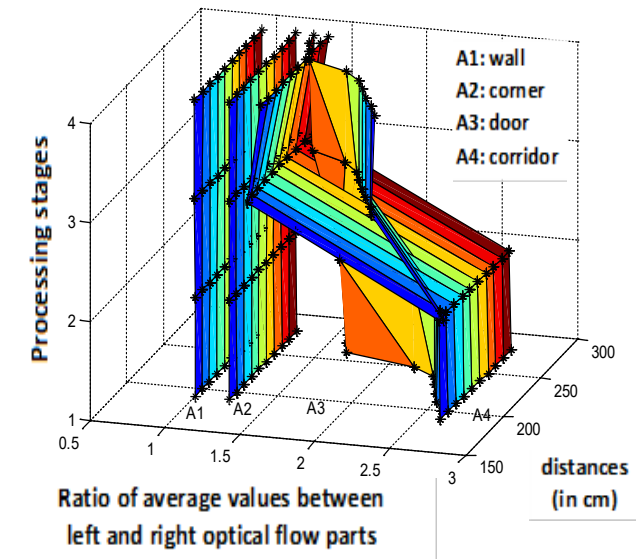


Figure 12: Ratio of average values between left and right optical flow parts.

*b) Simulation test with low obstacle density*

In the first test, the robot moved along a corridor containing several obstacles randomly arranged along the path illustrated in Figure 13. On the moving trajectory, the robot has to detect obstacles through the noise-free optical flow vectors.

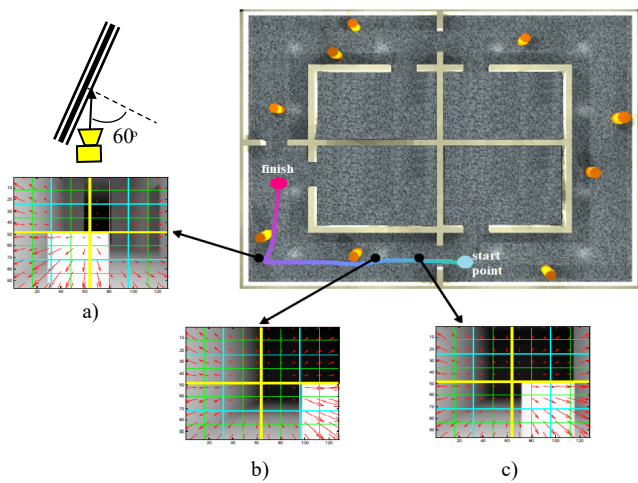


Figure 13: Robot avoids single obstacles

The robot movement is automatically recorded and depicted by a colorful truth-ground line. Along this line, several images are extracted to demonstrate that the robot has moved from the right to the left of the corridor and avoided a close front obstacle (Figure 13a), a close right obstacle (Figure 13b), and a far front right obstacle (Figure 13c). The line with the three extracted optical flow images show the obstacle positions detected from the

optical flow vectors and the robot succeeded in moving safely by avoiding the two detected obstacles.

In the second test, the robot travelled along a different part of the corridor. It has to avoid not only a single obstacle but also a pair of obstacles on the corridor. The robot movement trajectory is automatically recorded by a colorful truth-ground line as shown in Figure 14. Along the line, several images are taken out to prove that the robot has moved from the right to the left of the corridor. The robot avoided a close front obstacle (Figure 14a), a pair of obstacles (Figure 14b) in far distance, and a pair of obstacle and wall (Figure 14c).

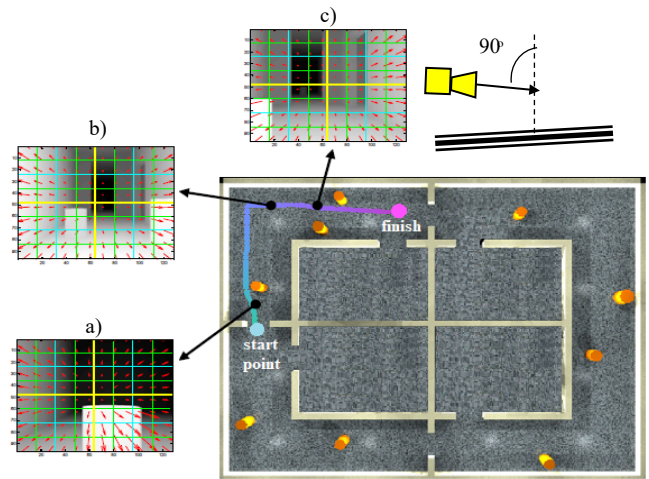


Figure 14: Robot avoids a pair of obstacles

The successful movements of the robot in the two first tests verify the robot's ability of obstacle detection based on the optical flow vectors taken from the simulated images.

*c) Simulation test with high obstacle density*

In the third test, the robot performed the more difficult task of safe movement through the corridor containing much more obstacles randomly arranged in a cramped area.

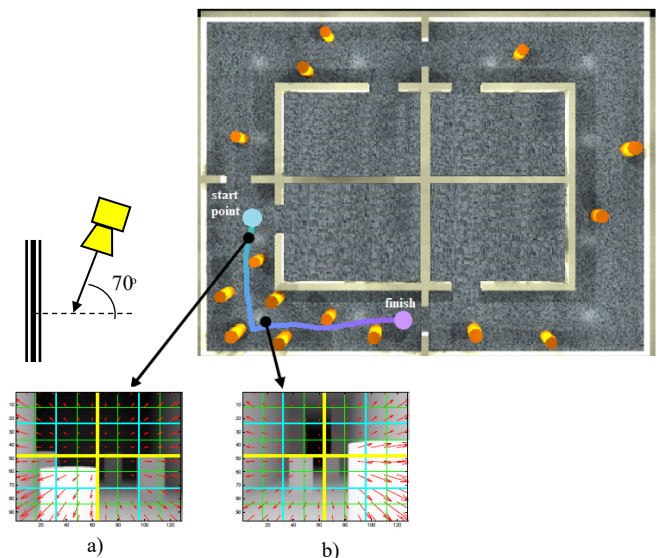


Figure 15: Robot avoids many obstacles in a cramped area

Technically, the solution of dividing the optical flow vector into multiple layers allows the robot system to compare the average magnitude of a part with other parts in the same layer. That means it can detect multiple obstacles at the same time and estimate the distance through the magnitude of the average vector. As a result, the robot can choose the appropriate (possibly suboptimal) movement direction to avoid obstacles.

The moving trajectory of the robot through the narrow area with many obstacles is automatically recorded by the colored line illustrated in Figure 15. Along this line, two images are extracted to represent the movement trajectory of the mobile robot after avoiding the closest obstacle on the left (Figure 15a), passing the area with high obstacle density, and avoiding another close obstacle on the right (Figure 15b) before leaving the danger area successfully.

## 5. Discussion and Conclusion

The above simulation results not only show the stability of optical flow perception in different situations, but also show that the obstacle position detection based on optical flow is independent of the robot's speed. Thanks to the simple calculation method based on the average vector comparison method, the robot does not need large memory to store complex database of obstacle characteristics such as shape and size.

In other words, the simulation results of obstacle detection based on optical flow free-noise images for mobile robot demonstrate that the recognition of dangerous area in the optical flow image is able to perform through the multi-layer processing of optical flow vectors in to many equal parts. By simply comparing the average magnitude values of the divided parts, the mobile robot can figure out obstacle positions to guide the robot follow a suitable safe way.

The limitation of the simulation results is that the mobile robot copes with static obstacles, but not dynamic obstacles. This indicates that in the next phase, the research team need to build an actual mobile robot to test in real environments with dynamic obstacles to more accurately assess the stability of the optical flow-based recognition method.

Furthermore, in the future the real tests will be performed in a complex indoor environment with unstable lighting conditions to estimate the ability of optical flow-based recognition.

## Conflict of Interest

The author declares no conflict of interest.

## References

- [1] N. Anh Mai, "Multi-layer segmentation solution to filter the noise of optical flow vectors to assist robots in object recognition inside buildings," *International Conference on Electrical, Computer, Communications and Mechatronics Engineering, ICECCME 2022*, (November), 16–18, 2022, doi:10.1109/ICECCME55909.2022.9988355.
- [2] A. Markis, M. Papa, D. Kaselautzke, M. Rathmair, V. Sattinger, M. Brandstotter, "Safety of Mobile Robot Systems in Industrial Applications," *Proceedings of the ARW & OAGM Workshop 2019*, 26–31, 2019, doi:10.3217/978-3-85125-663-5-04.
- [3] S.S.H. Hajjaj, K.S.M. Sahari, "Review of research in the area of agriculture mobile robots," *Lecture Notes in Electrical Engineering*, **291 LNEE**(January 2018), 107–118, 2014, doi:10.1007/978-981-4585-42-2\_13.
- [4] N. Ruangpayoongsak, H. Roth, J. Chudoba, "Mobile robots for search and

- rescue," *Proceedings of the 2005 IEEE International Workshop on Safety, Security and Rescue Robotics*, **2005**(July), 212–217, 2005, doi:10.1109/SSRR.2005.1501265.
- [5] W. Chung, G. Kim, M. Kim, C. Lee, "Integrated Navigation of the Mobile Service Robot in Office Environments," *International Conference on Control, Automation, and Systems (ICCAS)*, 2033–2038, 2003.
- [6] M. Trojnecki, P. Dąbek, "Mechanical properties of modern wheeled mobile robots," *Journal of Automation, Mobile Robotics and Intelligent Systems*, **13**(3), 3–13, 2019, doi:10.14313/JAMRIS/3-2019/21.
- [7] A. Dobrokvashina, R. Lavrenov, E. Magid, Y. Bai, M. Svinin, R. Meshcheryakov, "Servosila Engineer Crawler Robot Modelling in Webots Simulator," *International Journal of Mechanical Engineering and Robotics Research*, **11**(6), 417–421, 2022, doi:10.18178/ijmerr.11.6.417-421.
- [8] K. Kanjanawanishkul, "Omni-directional wheeled mobile robots: Wheel types and practical applications," *International Journal of Advanced Mechatronic Systems*, **6**(6), 289–302, 2015, doi:10.1504/IJAMECHS.2015.074788.
- [9] M. Al-Mallah, M. Ali, M. Al-Khawaldeh, "Obstacles Avoidance for Mobile Robot Using Type-2 Fuzzy Logic Controller," *Robotics*, **11**(6), 2022, doi:10.3390/robotics11060130.
- [10] S. Adarsh, S.M. Kaleemuddin, D. Bose, K.I. Ramachandran, "Performance comparison of Infrared and Ultrasonic sensors for obstacles of different materials in vehicle/ robot navigation applications," *IOP Conference Series: Materials Science and Engineering*, **149**(1), 2016, doi:10.1088/1757-899X/149/1/012141.
- [11] J. Cai, T. Matsumaru, "Human detecting and following mobile robot using a laser range sensor," *Journal of Robotics and Mechatronics*, **26**(6), 718–734, 2014, doi:10.20965/jrm.2014.p0718.
- [12] T.A.Q. Tawiah, "A review of algorithms and techniques for image-based recognition and inference in mobile robotic systems," *International Journal of Advanced Robotic Systems*, **17**(6), 1–25, 2020, doi:10.1177/1729881420972278.
- [13] Y. Zhu, C. Huang, "An Improved Median Filtering Algorithm for Image Noise Reduction," *Physics Procedia*, **25**, 609–616, 2012, doi:10.1016/j.phpro.2012.03.133.
- [14] M. Egelhaaf, "Optic flow based spatial vision in insects," *Journal of Comparative Physiology A: Neuroethology, Sensory, Neural, and Behavioral Physiology*, (0123456789), 2023, doi:10.1007/s00359-022-01610-w.
- [15] Y. Zhang, R. Huang, W. Nönerberg, A.B. Arrenberg, "A robust receptive field code for optic flow detection and decomposition during self-motion," *Current Biology*, **32**(11), 2505–2516.e8, 2022, doi:10.1016/j.cub.2022.04.048.
- [16] Z. El Kadmiri, O. El Kadmiri, L. Masmoudi, "Depth estimation for mobile robot using single omnidirectional camera system," *Journal of Theoretical and Applied Information Technology*, **44**(1), 29–34, 2012.

## The Influence Analysis of Internet Finance on China's Banking Industry Development

Yangshichi<sup>1</sup>, Hayoung Oh<sup>\*2</sup>, HyunJong Kim<sup>3</sup>

<sup>1</sup>Department of Economics, Sungkyunkwan University, Seoul, 03063, Korea

<sup>2</sup>College of Computing & Informatics, Sungkyunkwan University, Seoul, 03063, Korea

<sup>3</sup>Department of Artificial Intelligence Convergence, Sungkyunkwan University, Seoul, 03063, Korea

### ARTICLE INFO

Article history:

Received: 21 January, 2023

Accepted: 28 May, 2023

Online: 25 June, 2023

Keywords:

Internet finance

electronic payment

VAR model

### ABSTRACT

*This article presented an overview of the evolution of China's internet financial industry, emphasizing the critical importance of fintech, a novel economic sector improving the efficiency of financial services through innovative technology applications. The systems referred to encompass those technologies, applications, and tools that enhance the efficiency and accessibility of financial services. The historical trajectory of fintech, recent developments, and potential risks were thoroughly examined. A case study was conducted focusing on the significant factors influencing electronic payment in China. The study identified and analyzed key elements shaping China's electronic payment landscape using the VAR model. The results offered insights into the future development of the electronic payment system in China.*

## 1. Introduction

At the turn of the 21st century, the internet finance industry developed rapidly, following more broad technological improvements of the Internet. Fintech, a brand-new economic industry composed of systems that use technology to improve the efficiency of financial services, has commanded attention in both the United States and China. According to this research [1] defined internet finance as a system that is distinguished from both indirect commercial financing and direct financing in the capital market. This research [2] maintained that internet finance is an extension of traditional financial services to the internet that enhances existing business models and internet technologies that play only supporting roles in financial activities.

This article mainly focuses on analyzing the development of the internet finance industry in China. In 2019, the People's Bank of China published a Notice by the People's Bank of China of Issuing the Fin Tech Development Plan (2019-2021) (AKA the "Fin Tech Development Plan"), underscoring the importance that the Chinese government placed on Fintech. Internet third-party payment options such as WeChat Pay have disrupted traditional means of payment, such as credit cards and cash. In addition, internet-based finance companies also threatened to overtake the fundamental functions of saving and loan intermediation through traditional banking.

The flourishing development of internet finance has dramatically changed the banking industry in China. For instance, many banks have developed P2P online lending businesses to attract clients. Also, according to the official China Financial Stability report, published by the People's Bank of China, China's internet finance development has been tepid. Although there are landmark events almost every year (see Figure 1), such as the advent of Alipay in 2004 and the establishment of Alibaba Microfinance in 2011, they have not been broadly accepted by the Chinese public. Until 2013, taking the YueBao as the special mark, the scattered funds and fragmented needs of the public were starting to be met. The year 2013 marks the beginning of Internet finance in China. Not only did the new products emerge and thrive, but they reached an unprecedented level of popularity with consumer groups.

In addition, the COVID-19 situation has made people prefer to transact through contactless services, leading to increased digital experience and maturity.

Internet finance has played an active role in increasing methods of investment, improving the efficiency of capital allocation, promoting financial product innovation, advancing the process of interest rate marketization, and stimulating economic development. However, China's Internet finance is still in the initial phase, relevant laws and regulations are lagging behind, and various risks remain. Therefore, risk control has become an

\*Corresponding Author: Ha-Young Oh, Email: [hyoh79@gmail.com](mailto:hyoh79@gmail.com)

important factor in China’s financial stability. For this reason, on March 5, 2014, Premier Li Keqiang noted in a government work report: “To promote the healthy development of Internet Finance, we need to enhance the financial supervision and must maintain the bottom line to prevent systemic financial risks.”

This article references the latest research about Fintech from Chinese core journals, the Wall Street Journal, Mycaijing, and related websites to analyze and summarize current Chinese research and progress from multiple aspects such as the internet financial market and specific Fintech company development analysis. It then predicts the future development tendencies of Chinese international finance markets (P2P) in the context of Fintech.[3], [4],[5] and [6]

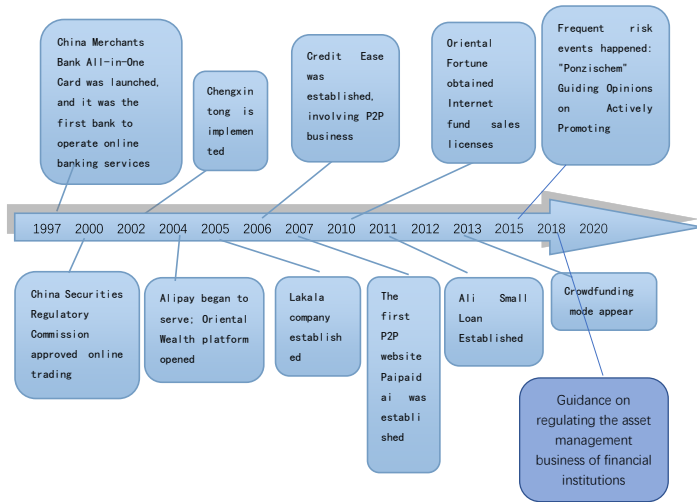


Figure 1: Development of China's Internet Finance Industry  
Source: Liu Wei. The Beautiful Era of Internet Finance in China

The first part of this article will introduce the essential attributes of internet finance development in the banking industry from different perspectives, thus explaining multiple forms of internet finance. It provides a clear scheme describing the whole Internet finance industry while analyzing drawbacks and highlighting risks in the internet finance industry.

This article will focus on the specific influence of third-party payment on the traditional banking industry, which has been a hot issue in Chinese society. Revenue that traditional banks rely on is highly disrupted by this new technology. Since Chinese citizens have started to use electronic payment for daily expenses, even traditional banks are starting to offer this new payment system. Therefore, it is necessary to illustrate the real effects that third-party payments have on traditional banks to propose useful solutions to help them to adapt to this new payment model.

**2. Recent Fintech Development**

Following the increasing popularity of the Internet and development of the related science, the influence of modern informational technology, represented by Internet technology, has had an increasing impact on traditional finance. This technology [3] has prompted the growth of internet finance to accelerate and become more reliable. China’s internet finance has developed over a period of about 20 years and has spawned the electronic banking model, online financial management model, third-party

payment model, and virtual currency model. These models usually have their beneficials and the models themselves depend on different basements.

**2.1. E-banking Model**

Electronic banking refers to electronic services that financial institutions provide to consumers and include but are not limited to telephone banking, mobile banking, and online banking. China’s online banking service [4] was first developed by China Merchants Bank in 1997. Mobile banking has emerged and become popular very fast in recent years. According to a survey conducted by iResearch, online banking accounted for 90% of the whole financial technology market trading volume. Figure 1 shows that whether measured in the proportion of corporate online banking users or the proportion of personal mobile banking users, the number of people using mobile banking has increased each year.

**2.2. Online Financial Management**

In online financial management [5], financial planners may independently choose different financial management methods such as financial insurance, banking services, and funds using online financial platforms. The most important aspect of online financial platforms [6] is that there are no space restrictions for online financial management, which means users may conduct their financial business anytime, anywhere. In addition, because services are available 24 hours per day, 7 days per week, online financial management has become more popular with users than offline financial management. Internet financial companies have also frequently launched online wealth management products. Yuebao, Baidu Wealth Management, and Tiantianfu are all popular online financial management platforms. Taking Yuebao as a specific example, Table 1 shows that from the end of June 2018 to the beginning of March 2021, Yuebao's capital scale expanded from 47 billion to 73.5 billion, and the number of users increased from 68.8 million to 108 million. Such achievements indicate the appeal of online finance and also highlight the good prospects of online financial management.

Table 1: Yuebao's capital scale and numbers of users during different periods  
Source: 2018-2021 Yu'e Bao User Analysis Report

Date	Fund size (100 million)	Number of users (10,000)
2018 6.30	4725	6980
2018 9.30	4980	8100
2018 12.30	5200	8950
2020 6.30	5620	9250
2020 9.30	6305	9670
2020 12.30	6950	10025
2021 1.30	7200	10420
2021 3.30	7350	10800

2.3. Third-Party Payment Model

The whole scheme of third party payment can be illustrated using Alipay as an example [7]. After a buyer selects goods to purchase, their money is sent to an Alipay account. Then the Alipay platform informs the seller to ship the goods. Finally, the buyer confirms receipt of the goods and Alipay pays the seller. If the consumer is dissatisfied and seeks to return the goods, the third-party payment platform transfers payments back to the consumer’s account after it confirms that the seller has received the returned goods. The major domestic Chinese third-party payment platforms include Alipay, Tenpay, Epay, and Kuaiqian.

According to a survey [8] conducted by iResearch, third-party payments accounted for 94.4% of transactions in 2015, and therefore became the most widely recognized Internet financial model (iResearch). Among Internet financial products/services in China, third-party payment accounted for 95.6% of transactions, becoming the most commonly used pattern. Table 2 shows that by the end of 2020, the transaction scale of China’s third-party payment market was expected to reach 50 trillion yuan, while in 2009 it was only 3.1 trillion yuan.

Table 2: Third-party payment market transaction scale from 2009 to 2020  
Source: Third-party payment in 2020 Internet Finance Year-end Report

Table 2 Third-party payment market transaction scale from 2009 to 2020	Table 2 Third-party payment transaction scale from 2009 to 2020	Table 2 Third-party market transaction scale from 2009 to 2020	Table 2 Third-party payment market transaction scale from 2009 to 2020
Table 2 Third-party payment market transaction scale from 2009 to 2020	Table 2 Third-party payment transaction scale from 2009 to 2020	Table 2 Third-party market transaction scale from 2009 to 2020	Table 2 Third-party payment market transaction scale from 2009 to 2020

2.4. Internet Lending Model

Online lending refers to the process of authentication [9], accounting, clearing, and delivery through online platforms for both parties. In 2007, China's first online loan company was founded, while in 2018, there were about 1021 online loan platforms with a total transaction volume of more than 230 billion yuan. However, in 2020, there were only about 343 online loan platforms with a transaction volume of 86 billion yuan (Table 3). Here, this article will mainly focus on P2P microfinance financial platforms.

Simply speaking, the P2P financial platform [10] is a new online financial model, in which the payer lends funds to the borrower in the form of a credit loan through an intermediary agency. P2P has low entry barriers and involves mostly small loans, which allows customers to easily conduct online financial trading while diversifying loan risks. Representative domestic P2P

online financial platforms include Renrendai, Yirendai, Papadai, and Helidai. The main target customers for these platforms are investors with small funding needs, such as small business owners, poor rural farmers, and college students. These groups were not well served by traditional financial institutions. The growth of P2P in China has been quite rapid. China's first P2P website, Paipaidai, was launched in August 2007. In October of the same year, Yixin's online loan platform was launched. In 2015 the number of platforms reached its peak at 3814, while as of 2019, the number of loan companies decreased to 343. This trend indicates that in recent years, the drawbacks of the p2p platform have become clear. The first is that there are no entry barriers, and the second is that there are no operating rules. Finally, there is no external supervision. For example, in October 2019, Wang Longyu, the head of the Angel Project website, lost contact without omen and directly lead to thousand millions losses. In June 2018, the Gold Rush Loan service that had been launched only 5 days prior defrauded more than 100 domestic investors. Although Table 3 shows that the transaction scale and number of companies involved in Chinese P2P loans increased from 2012 to 2015, Figure 2 shows that Internet lending platforms and China’s bad debt rate continued to increase from 2014 May to 2020. In addition, according to a survey conducted by iResearch, in 2015 the P2P platform accounted for 32.2% of Chinese Internet user’s perceptions. Among Chinese Internet financial services, the P2P platform accounted for 2.2% of transactions. Even the result has big gap between offline and online payment.

Table 3: Source: Statista Number of online peer-to-peer lending platforms in China from 2010 to 2019

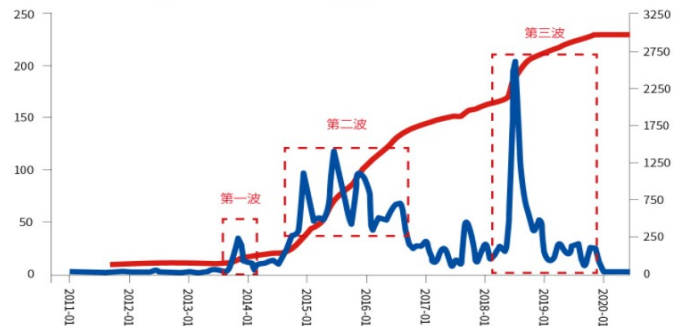
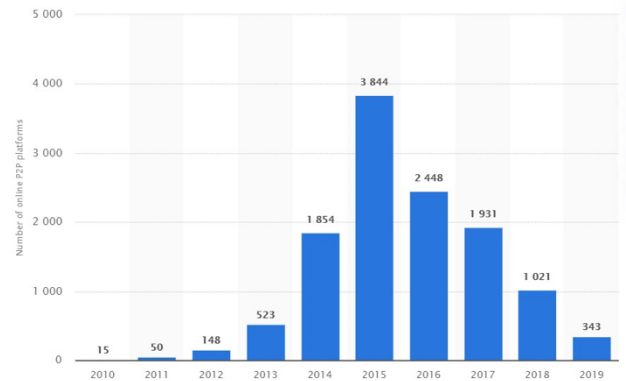


Figure 2: Bad debt rate in China’s P2P platform (red: cumulative number of problem platforms; blue: month statistical quantity)

Source: WangDaiZhiJia



### 3. Risks of China’s Internet finance industry

There are many risks involved in China’s internet finance industry. Some of these risks may only cause limited losses in one aspect of internet finance, but others may be catastrophic. However, whether the risk is systematic or unsystematic, there are some effective strategies to prevent risk.

#### 3.1.1. Run risk

Run risk [11] is a very uncertain factor, because emergencies shake people’s confidence in financial investment. Some internet finance platforms are connected to monetary finance, which means that when a run risk occurs in monetary finance, internet finance will be affected. Taking Yuebao as an example, once the declining amount of Yuebao’s rate of return exceeds consumer expectations, run the risk is very likely to happen. As the risk occurs, whether it is a rumor or real, it will spread through the internet very quickly. Yu'eobao can only use deferred payments to address such a situation, and this is why a run risk is inevitable. The most serious potential result is that Yuebao withdraws from the internet finance area. As risk occurs, internet financial institutions may encounter a shortage of funds for a few days or even collapse in the worst case scenario.

#### 3.1.2. Internet technology management risks

No matter the period, science and technology are the primary productive forces. To maintain the high development speed of Internet finance, it is important to carefully decide in which technology to invest in terms of both safety and reliability. Internet finance is vulnerable to hackers, while systemic failures (both hardware and software), power failures, and computer viruses can all lead to serious losses to financial institutions. Therefore, a stable system itself is the core of internet finance [12].

At the same time, the importance of technology management is also reflected in product support. A mature or popular technology will promote positive marketing extension. Google Wallet launched in the UK in 2011 using a very advanced technology called NFC that is supported neither upstream nor downstream. Because the technology was so sophisticated, with less than 15 kinds of smartphones on the market supporting such technology, it was difficult for merchants to accept payments through NFC. Eventually, this problem led to the inability of the service to become more widespread [13].

Figure 3 shows that even in recent time periods, the service did not acquire sufficient market share.

#### 3.1.3 Institutional risk

China’s Internet finance industry is insufficiently supervised and regulated, which has led to exposure to more problems. Since there are no clear laws or regulations for this market, internet finance-related industries are free to engage in immoral operating behaviors, which provides benefits to the companies themselves while hurting consumers and the whole internet finance market. In addition, inadequate supervision in the whole market makes it difficult for law-abiding internet financial institutions to manage their companies effectively [14]. Because there are no clear boundaries between legal and illegal internet finance behaviors, internet financial institutions can easily wander among legal-blind

spots, which may cause unintentional irregularities. In other words, some companies may implement behaviors that are seen as negative under unrealized situations. If unintentional irregular behaviors were defined as violations, many Internet finance institutions would suffer huge losses.

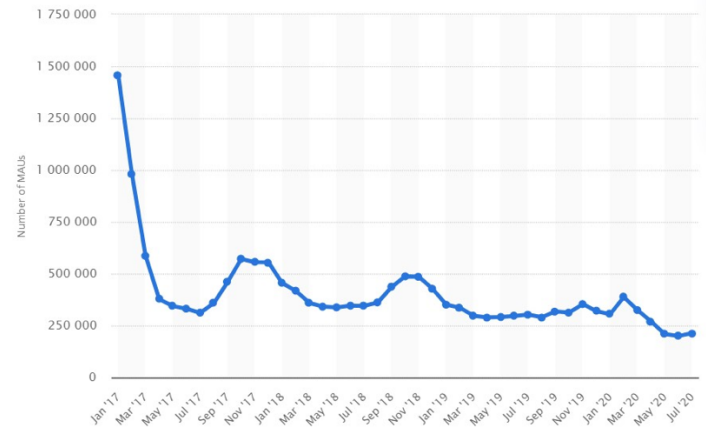


Figure 3: From January 2019 to July 2020 (United Kingdom)

Source: Statista

#### 3.1.4 Credit risk

In terms of target consumer selection, Internet finance platforms are at a disadvantage because access to Internet financial platforms is not strict, which means users can simply register on platforms provided by internet institutions. The requirements for obtaining an Internet loan are very low, usually only a very simple identification test, after which consumers may freely conduct transactions. Even if a customer is required to fill out a basic form to collect basic information, this cannot prevent users from falsifying or concealing important information. Additionally, there is great difficulty evaluating user credit. All of these elements make it very difficult to ensure that online traders complete transactions in good faith in the absence of a credit system. Taking online lending as an example, if a borrower deliberately escapes from bearing the obligation of repayment after accepting a loan from the lender, the loss is borne by the Internet financial institution.

#### 3.1.5 Crime risk

China’s Internet finance currently lacks laws, regulations, and regulatory systems. Moreover, most Chinese Internet finance companies lack self-discipline, causing many employees to commit crimes for personal benefit. For law-abiding institutions, the risk of crime mainly comes from surrounding cooperating companies.

Since the development of Internet finance technology, illegal fund-raising, private capital pool abuse, and money laundering have continued to occur. Furthermore, if nepotistic organizations in the same industry violate the law due to poor management, organizations suffer great losses. According to the Global Economic Crime Survey published by PricewaterhouseCoopers on March 18, 2019, Internet crime has become one of the four

major economic crime categories in 2018, and has become the second most serious economic crime type affecting the financial services industry.

At the same time, data from the Ministry of Public Relations shows that in recent years, the number of Internet crime cases in China has increased at an annual rate of 30%, and the amounts of crime and hazard continue to expand. An average amount of more than several hundred thousand yuan per criminal case (with a maximum of more than 14 million yuan involved), in the internet financial sector accounted for 61% of China's online cases. All of these cases have led to losses of nearly 100 million yuan every year.

### 3.2. Risks faced by users

#### 3.2.1. Operational risks of financial institutions

The interests of Internet finance users are closely related to financial institutions. If internet financial institutions fail due to poor management or dishonest operating, users are vulnerable to losses. Dishonest operations mainly include illegal behaviors, such as managers absconding from the company, concealing risks, exaggerating returns, and providing false information. Taking P2P as an example, from the beginning of 2015 to 2019, more than 70% of P2P platforms went bankrupt (Figure 4). These events involved a total of more than 1.2 billion yuan. Among them, in October alone, 40% of P2P platforms announced that their capital chain was broken or closed. Meanwhile, due to the weak sense of self-discipline in the industry, Internet finance institutions frequently engage in dishonest operations driven by their own interests that seriously jeopardize the interests of users.



Figure 4: Decreasing number of P2P platforms  
Bar: The Number of P2P platforms  
Line: Increasing Rate (Year)  
Source: WangDaiZhiJia

#### 3.2.2. Information security risk

The scope of information security is separated into two main categories. The first is malicious intrusion into internet financial websites, which leads to information leakage. The second involves Internet financial institutions secretly and illegally stealing, buying, and selling the personal information of users. Regardless of whether Internet financial institutions have the right to collect personal information, if it is leaked it can lead to great losses to users. According to the 2020 China Internet Security Report, in 2020, 84.8% of China's Internet users encountered network information security incidents, with a total of 456 million incidents

such as personal data leakage and insecure online shopping or payment. Among these netizens, 77.7% suffered losses, and 7.7% of the events caused economic losses, involving direct economic losses of up to 19.4 billion yuan.

#### 3.2.3. Rights protection risk

The drawback of China's Internet financial laws and regulations is not only reflected in the lack of clear provisions to restrict behavior, but also in the failure to protect the rights and interests of users. For instance, some Internet financial companies conceal risks deliberately, exaggerate returns, and intentionally provide false information. Furthermore, some companies even deliberately sell or uncover customers' private information, which infringes on their right to information, right to fair deals, right to choose freely, and privacy. Among China's Internet supervision laws, there are flaws in special regulations regarding the protection of users' rights and interests. The current basic civil laws in China cannot provide Internet financial users with enough protection, nor can they effectively recover user losses, which are caused by illegal financial behaviors.

## 4. Risk Analysis: Predicting development of electronic payment in China

Risk Analysis: Predicting the Development of Electronic Payment in China

Given the complexities and dynamism inherent in internet financial data, it was essential to employ a model capable of accurately capturing and reflecting these aspects. Therefore, this article used the VAR (Vector Autoregressive) model [15] to conduct specific data analysis. The VAR model was selected for its unique capacity to handle multiple interrelated time series and its allowance for each variable to be a function of past lags of all variables in the system. Furthermore, in contrast to traditional regression models, the VAR model allowed us to directly examine the relationships between economic variables under the time series, effectively sidestepping issues of mistaken endogeneity or exogeneity [16].

Improvements were made to the traditional VAR model based on lessons drawn from previous research [17]. The article first introduces the VAR model, then proceeds to make reasonable assumptions and explain variable selection to ensure accuracy and interpretive power of the results. The stability of the data used in model building and data fitting was ensured through unit root tests. The EG-test was employed to ascertain that the residual terms in the model would not negatively impact the results, thus ensuring that the time series data were suitable for the research.

During the construction of the VAR model, selection criteria including AIC, HQ, SC, and FPE tests were applied to identify the most suitable VAR model, yielding the most reliable model. Following an impulse response analysis, a forecasting analysis was carried out – a step often omitted in previous studies. The forecasting results were then leveraged to provide valuable insights and recommendations for the future of the Chinese internet finance industry.

### 4.1. Introduction to the VAR model

#### 4.1.1. Introduction to the VAR model

Traditional regression models are mostly dependent on basic economic theorems, which can help to explain the behavior of economic agents. Then, researchers can also use the model to analyze how exogenous variables affect endogenous variables. However, traditional regression models have drawbacks, such as mistakenly taking some variables as endogenous, exogenous, or predetermined. Such decisions are often subjective because variables may be highly correlated. Another drawback is that when constructing a joint cubic model, in order to make the model identifiable, certain variables must be abandoned from the original economic equation.

The VAR model can solve such problems because the core idea of the VAR model is to disregard economic theory and directly consider the relationships between economic variables under the time series.

The normal general form of VAR is:

$$Y_t = \alpha + \sum_{i=1}^p \beta_i Y_{t-i} + \varepsilon_t \tag{1}$$

In addition, in the VAR model we assume that:

$$E(\varepsilon_t) = 0, \quad E(\varepsilon_t, Y_{t-i}) = 0, \quad i = 1, 2, \dots, p;$$

$Y_t$  is a linear stochastic process with homoskedasticity consisting of  $(n \times 1)$  vectors.

$\beta_i$  is a coefficient matrix of  $(n \times n)$ .

$Y_{t-i}$  is  $i$ th lagged variable of  $Y_t$  vector.

$\varepsilon_t$  is an error term and can be considered as a random disturbance term in this model.

#### 4.1.2. Ensure the optimal lagging parameter for the VAR model

Since the establishment of the lagging parameter for the VAR equation is strongly influenced by multiple variables, it is necessary to conduct stability tests for the target dataset. Through the Box-Jenkins test, we defined that, basing on the autocorrelation coefficient graph, if the coefficient decreases rapidly as the value of the autocorrelated lagging parameter increases, the time series is a stable series. If the conditions are not met, it is an unstable series. However, this testing method is highly dependent on subjective decisions. Therefore, Dickey and Full proposed using the DF statistic to test whether the data are a stable series, and later modified and improved it by introducing the ADF statistic to perform the test.

The ADF test model is as follows:

$$\Delta y_t = \gamma y_{t-1} + \sum_{i=1}^p \beta_i \Delta y_{t-i} + \varepsilon_t \tag{2}$$

where  $t$  is the time trend term;  $\gamma, \beta$  is the parameter, and  $\varepsilon$  is the error term.

The original hypothesis of the test is  $H_1 : \gamma = 0$ , and the opposing hypothesis is  $H_0 : \gamma < 0$ .

If the original data cannot reject the original hypothesis, one-time difference will be required and the differenced series will be subjected to the ADF test again. We perform this process until the series becomes stable and then build the VAR model. Currently, more than one test can be used to determine the lagging parameter for the model, but the most commonly used criteria are AIC and SIC. The optimal lagging parameter is determined based on the values of the AIC and SIC criteria.

The AIC criteria are calculated as:

$$AIC = \ln \frac{SSR_k}{T} + \frac{2k}{T} \tag{3}$$

Schwarz's SIC criteria, defined as follows:

$$SIC = \ln \frac{SSR_k}{T} + \frac{k(\ln T)}{T} \tag{4}$$

where  $k$  is the lagging parameter,  $T$  is the sample size and  $SSR_k$  is the sum of the squared residuals.

#### 4.1.3. Impulse response function of the VAR model

In order to directly observe the interactions between variables, Sims suggests that the Wald decomposition can be quantitatively converted into a moving average representation.

The whole processes are shown below:

$$Y_t = \alpha + \sum_{i=1}^p \beta_i Y_{t-i} + \varepsilon_t \tag{5}$$

$$Y_t - \sum_{i=1}^p \beta_i Y_{t-i} = \alpha + \varepsilon_t \tag{6}$$

$$(1 - \beta_1 L - \beta_2 L^2 - \dots - \beta_m L^p) Y_t = \alpha + \varepsilon_t \tag{7}$$

$$Y_t = \alpha(1 - \beta_1 L - \beta_2 L^2 - \dots - \beta_m L^p)^{-1} + (1 - \beta_1 L - \beta_2 L^2 - \dots - \beta_m L^p)^{-1} \varepsilon_t \tag{8}$$

$$Y_t = \alpha + \sum_{i=0}^{\infty} A_i \varepsilon_{t-i} \tag{9}$$

From equation (4.9), we conclude that within the VAR model, every variable can be expressed as a linear combination of random shock terms in the current and lagging variables. However, these random shock terms do not have the property of serial correlation, while they may have the property of current correlation. As a result, Sims chose orthogonalization to remove the current correlation.

As we translate the equation (4.9):

$$Y_t = \alpha + \sum_{i=0}^{\infty} A_i C C^{-1} \varepsilon_{t-i} \tag{10}$$

We assumed:

$$D_i = A_i C \quad U_{t-i} = C^{-1} \varepsilon_{t-i}$$

Then:

$$Y_t = \alpha + \sum_{i=0}^{\infty} D_i U_{t-i} \tag{11}$$

Based on equation (4.11), it can be observed that each variable can be expressed as a linear combination of the random shock terms in the current and lagging periods, in other words, the impulse response function (IRF). The impulse response function is used to measure the effect of one standard deviation shock from a random disturbance term on the current and future values of the endogenous variables, which can portray the dynamic interactions between variables and their effects in a more intuitive way.

#### 4.2. Prepare for building the model

##### 4.2.1. Some assumptions:

- a) The effectiveness of internet finance is explained by how many users use the service.
- b) The influence of internet finance service on the traditional banking system is measured by the differences in user numbers compared to traditional banking.
- c) We only consider relationships between third-party market scope and traditional banking service market.

##### 4.2.2. Selection of model indicators

###### 1. Third-party payment amounts

To better illustrate the impact of internet finance on commercial banks, we take the third-party payment amount indicator, which changes the most in daily life, as an empirical study. This article focuses on the macroscopic effectiveness of internet finance services on the whole traditional banking industry, which includes asset business, intermediate business, and liability business. Among these aspects, the intermediate business of the traditional bank suffers the most. Therefore, we choose third-party payment amount as the independent variable and estimate the effect on the traditional banking industry.

###### 2. User statistics for the People’s Bank of China

This indicator measures the macroscopic amount of traditional banking service use, which represents the whole commercial banking accounting service. This service corresponds with the intermediate business of the traditional banking industry, which complies with our research goal.

###### 3. The origin and pre-processing of data

The variables selected for the empirical analysis of this paper include third-party payment amount and number of users of the People’s Bank of China. The time period is from the first quarter of 2013 to the third quarter of 2020. This time period is not very long, since China’s internet financial development has only gradually become explicit since 2010. The datasets are from Wind Information and the official website of the People’s Bank of China. To eliminate possible heteroskedasticity in the data, we take the natural logarithm of the above series, and the transformed variables become TP and PC accordingly. The data analysis and processing software used for the empirical analysis of this paper is R.

#### 4.3. Model building and testing

##### 4.3.1. Unit root test

For non-stationary time series, we can first test whether these two series exhibit a cointegration relationship before building a VAR model. Therefore, we first perform a unit root test on the difference between two time series to determine the order of single integers, and Figure 6. shows the test results.

```
Title:
Augmented Dickey-Fuller Test
```

```
Test Results:
PARAMETER:
Lag Order: 1
STATISTIC:
DF: -7.2658
P VALUE:
t: 4.481e-09
n: 0.04932
```

```
Title:
Augmented Dickey-Fuller Test
```

```
Test Results:
PARAMETER:
Lag Order: 1
STATISTIC:
DF: -2.8227
P VALUE:
t: 0.006361
n: 0.234
```

Figure 6: Augmented Dickey-Fuller Test

The number of users with banking accounts passed the unit root test after the first time difference. Third-party payment amount passed the unit root test without difference. Both series indicate that the original hypothesis is rejected at the 5%

significance level. Next, we determine whether the two have a cointegrated relationship.

We use the EG two-step method to first obtain the residuals of two time series regressions and then perform a unit root test on them to determine the relationship between them. The following tests are performed:

```
#####
# Augmented Dickey-Fuller Test Unit Root Test #
#####

Test regression none

Call:
lm(formula = z.diff ~ z.lag.1 - 1 + z.diff.lag)

Residuals:
    Min       1Q   Median       3Q      Max
-0.005945 -0.002393 -0.000297  0.001341  0.004829

Coefficients:
              Estimate Std. Error t value Pr(>|t|)
z.lag.1      -1.7331     0.2262  -7.661 3.07e-08 ***
z.diff.lag    0.2976     0.1427   2.085  0.0466 *
---
Signif. codes:  0 '***' 0.001 '**' 0.01 '*' 0.05 '.' 0.1 ' ' 1

Residual standard error: 0.002848 on 27 degrees of freedom
Multiple R-squared:  0.8082,    Adjusted R-squared:  0.794
F-statistic: 56.9 on 2 and 27 DF,  p-value: 2.077e-10

value of test-statistic is: -7.6607

Critical values for test statistics:
 1pct 5pct 10pct
tau1 -2.62 -1.95 -1.61
```

Figure 7: Augmented Dickey-Fuller Test with the EG two-step method

The results of the tests in Figure 7 indicate that at the 5% significance level, the original hypothesis is rejected, which means that the two variables are cointegrated. Therefore, there is a long-term stable equilibrium relationship, and we use these two series to build a VAR for the original time series model.

### 4.3.2 Building the VAR model

Before building the model, the lag order needs to be determined. To find a reasonable order, in this article we apply AIC, HQ, SC, and FPE criteria to ensure the best lag order of the VAR model, and then test results. The results are shown in Figure 8.

```
> VARselect(y, lag.max=9, type="const")
$selection
AIC(n)  HQ(n)  SC(n)  FPE(n)
   9     9     1     7
```

Figure 8: VAR model (Maximum lag order test statistic)

We find that for AIC and HQ the best value was 9, while for SC and FPE, the best values were 1 and 7.

Therefore, the next step is to find the best order among those three values. To compare which p value is the best, we depend on log likelihood and the t-value of the residuals of VAR.

First, looking at the log likelihood of these three models:

VAR(1)

VAR Estimation Results:

```
=====
Endogenous variables: Bank, Third_party
Deterministic variables: const
Sample size: 30
Log Likelihood: 165.983
Roots of the characteristic polynomial:
0.5899 0.06284
Call:
VAR(y = y, p = 1, type = "const")
```

VAR(9)

```
VAR Estimation Results:
=====
Endogenous variables: Bank, Third_party
Deterministic variables: const
Sample size: 22
Log Likelihood: 172.886
Roots of the characteristic polynomial:
1.192 1.192 1.031 1.031 0.9813 0.9813 0.9754
Call:
VAR(y = y, p = 9, type = "const")
```

VAR(7)

```
VAR Estimation Results:
=====
Endogenous variables: Bank, Third_party
Deterministic variables: const
Sample size: 24
Log Likelihood: 170.235
Roots of the characteristic polynomial:
1.008 1.008 0.9493 0.9493 0.9396 0.9396 0.921
Call:
VAR(y = y, p = 7, type = "const")
```

Depending on the log likelihood indicator, we find that VAR(9) fits the data best.

Then we look at the p-values of the residuals of models.

VAR(1)

```
Portmanteau Test (asymptotic)
data: Residuals of VAR object VAR1
Chi-squared = 52.857, df = 60, p-value = 0.7318
```

VAR(9)

```
Portmanteau Test (asymptotic)
data: Residuals of VAR object VAR2
Chi-squared = 55.836, df = 28, p-value = 0.001347
```

VAR(7)

```
Portmanteau Test (asymptotic)
data: Residuals of VAR object VAR3
Chi-squared = 38.685, df = 36, p-value = 0.3493
```

Depending on the residuals of the models, we find that VAR(9) brings uncorrelated residuals.

As a result, we use VAR(9) as the analyzing model.

Granger causality test

To determine if the correlation between two variables is meaningful, we also need to perform a Granger causality test. Depending on the result of the Granger causality test we decide the order of the variables when we conduct impulse response analysis.

First, to test whether traditional bank account amount Granger-cause Third party payment amount.

```
$Granger
      Granger causality H0: Bank do not Granger-cause Third_party
data:  VAR object VAR2
F-Test = 0.88679, df1 = 9, df2 = 6, p-value = 0.582
```

We find that the p-value for the test is 0.582, which means that we cannot reject H0 and that traditional bank account amount Granger-cause Third party payment amount.

Secondly, to test if third party payment amount Granger-cause traditional bank account, we perform the following:

```
$Granger
      Granger causality H0: Third_party do not Granger-cause Bank
data:  VAR object VAR2
F-Test = 1.1938, df1 = 9, df2 = 6, p-value = 0.4294
```

We find that the p-value for the test is 0.4294, which means that we cannot reject H0 and this indicates that third party payment amount Granger-cause traditional bank account amount.

Then, according to this result, the traditional bank account amount should be placed ahead of third party payment amount.

4.3.3 Impulse Response Analysis

By constructing the impulse response function, we see that a certain shock brings some dynamic impact to the system. Based on the VAR model, we obtain the traditional bank account amount and third party payment amount. The following is the impulse of the third-party payment to the traditional bank account:

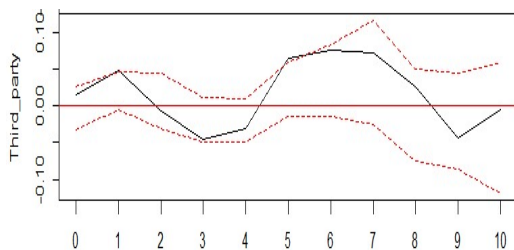


Figure 9: The impulse of the third-party payment to the traditional bank account

Figure 9 represents the bank response path caused by a positive shock to the third-party payment account. From this result, we found that third-party payment changes one unit in periods 1-4 has an increasing negative effect on the bank settlement account, and

then in periods 5-8, it maintains a comparatively stable positive effect. This shows that by giving a positive impact to third-party payments, traditional bank account amounts will be impacted in a floating manner, and also demonstrates that the development of the third-party payment market has caused a volatile boost to traditional bank account amounts.

This paper argues that this unstable effect is derived from a “backward mechanism” that arises from the impact of internet finance on commercial banks. For a very long period, commercial banks have acted as money intermediaries. This action artificially divides the market into savings and financing markets, and obtains spreads and commission during this process. However, the emergence of third party payments has changed this traditional function of banks, while it does not substitute for the whole function of traditional banks. Internet finance enables direct transactions between users and suppliers, which directly reduces exchange costs and thus breaks the monopoly of commercial banks. Commercial banks are forced to reduce the cost of capital financing, while improving capital utilization and thus developing higher competitiveness. The emergence of Internet finance has made the financial market more competitive, forcing commercial banks to actively reform and seize market share.



Figure 10: Third party payment response path

The influence of traditional bank accounts on third-party payment

Figure 10 is the third-party payment response path caused by a positive shock to traditional bank account users. Through this observation, we see that when there is one unit change in the traditional bank user account amount, the third-party payment user amount does not respond in periods 1-2, while during periods 3-10, it shows a small increase. However, in the very last period, the figure remains stable. This indicates that the traditional banking system causes a certain positive impact on third-party payment, but the impact is not obvious. This article suggests that internet finance has unique advantages, and it is not easy for traditional commercial banks to significantly influence Internet finance.

4.3.4 Variance Decomposition

We conduct variance decomposition to directly observe the impacts between two variables.

	Bank	Third_party
[1,]	1.0000000	0.0000000
[2,]	0.7866994	0.2133006
[3,]	0.5283925	0.4716075
[4,]	0.4890386	0.5109614
[5,]	0.4465499	0.5534501
[6,]	0.4355234	0.5644766
[7,]	0.2802778	0.7197222
[8,]	0.2527427	0.7472573
[9,]	0.5062509	0.4937491
[10,]	0.5284848	0.4715152
[11,]	0.3280038	0.6719962
[12,]	0.2340326	0.7659674
[13,]	0.3511434	0.6488566
[14,]	0.3785740	0.6214260
[15,]	0.2470474	0.7529526

We find that from the very beginning, third party payment does not influence traditional bank account users. Then, after some time passes, third party payment gradually gains great influence over traditional banks. Ultimately, third-party payment exerts 75% influence on traditional bank account users. Therefore, most of the influence on traditional bank account amounts is due to third-party payments.

#### 4.4. Predictions (future development forecasting)

In this part, this article will use results obtained from the VAR model to conduct forecasting analysis for both the traditional banking industry and third-party payment. Using about 30 seasons (3 months per season) of observations, we can predict development for two future seasons (3 months per season).

First, we can examine the forecasting result directly:

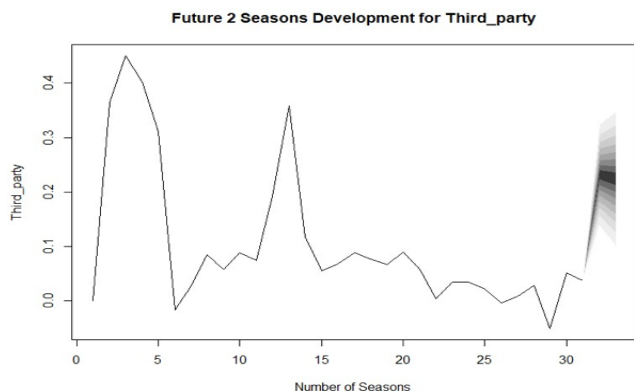


Figure 11: Traditional Bank Account Industry

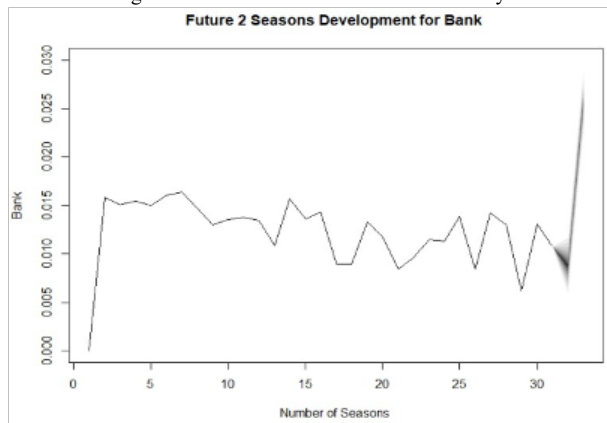


Figure 12: Third-Party Payment Industry

In our analysis, the time unit of the dataset is seasoned, which is shown on the x-axis. Seasonally changing rates are shown on the y-axis, which gives the changing percentage of the industry. (Data used are log-transformed.)

First, this study examines the traditional banking industry and finds that this industry is expected to decrease slightly and then increase very rapidly over about 5 months. Then, the third-party payment industry will first increase and then decrease slowly. The change in rate in the third-party payment industry is much higher than for traditional banking accounts. This indicates that the traditional banking industry is comparatively stable and mature, while the third-party payment industry is new and easily influenced by the outside environment.

### 5. Conclusion

Based on the results of impulse response analysis, the contribution of current traditional bank accounts to the scale of third-party payment becomes obvious only from periods 8-10. The influence of traditional bank accounts on the scale of the third-party payment industry is not significant. This suggests that traditional bank accounts have very little impact on the separate scale of third-party payments, which bring their own merits that cannot be ignored and have grown rapidly due to the development of internet platforms.

From the aspect of third-party payment, Internet finance has had a significant impact contribution on traditional bank accounts from very early periods that have grown rapidly from periods 5-10, finally reaching about 75%. This shows that third-party payment market size has a significant impact on traditional bank accounts. This phenomenon is inextricably linked to the rapid expansion of the third-party market after 2016.

All of these phenomena indicate that third-party payment has a growing positive impact on the traditional bank account business. This paper argues that the growing scale of the third-party payment market will make the related financial markets more competitive, thus forcing commercial banks to actively innovate and improve their market competitiveness, while the impact of bank settlement business on the third-party payment market remains insignificant. The impulse response plots of the VAR model confirm that there is a correlation between the number of bank settlement accounts and the amount of third-party online payment transactions, and it is not simply negative. In the long run, third-party payments may lead to unstable fluctuations in traditional bank account services.

This result highlights the fact that in the era of "Internet Plus," internet finance exerts an uncertain effect on the development of commercial banks, and also reveals that commercial banks should have prudent attitudes towards internet finance. Traditional banks should learn from the development of internet finance to enhance their own business in the future.

For future work, further studies are needed to delve deeper into the changing dynamics of the relationship between traditional banks and third-party payments. Specifically, how traditional banks can better adapt to the rising trends of internet finance and maintain stability amidst the rapid growth of third-party payment

systems. Furthermore, future perspectives should include an evaluation of policies and regulations that could facilitate a more harmonious development between internet finance and traditional banking.

## References

- [1] M. Shahrokhi, "E-finance: status, innovations, resources and future challenges," *Managerial Finance*, **34**(6), 2008, doi:[10.1108/03074350810872787](https://doi.org/10.1108/03074350810872787).
- [2] C. Bai, Hong Yan, Shanggang Yin, Chen Feng, Qian Wei, "Exploring the development trend of internet finance in China: Perspective from club convergence," *The North American Journal of Economics and Finance*, **58**, 2021, 1062-9408, doi:[10.1016/j.najef.2021.101505](https://doi.org/10.1016/j.najef.2021.101505).Yuk-shining
- [3] C. Onay, Ozsoz, E, "The Impact of Internet-Banking on Brick and Mortar Branches: The Case of Turkey," *J Financ Serv Res*, **44**, 2013, doi:[10.1007/s10693-011-0124-9](https://doi.org/10.1007/s10693-011-0124-9).
- [4] C Yuk-shing Cheng, "China's Reform of Rural Credit Cooperatives: Progress and Limitations," *The Chinese Economy*, **39**(4), 2006, doi:[10.2753/CES1097-1475390402](https://doi.org/10.2753/CES1097-1475390402).
- [5] B. Helms, "Access for All : Building Inclusive Financial Systems," World Bank Publications, 2006
- [6] L. Nicholas, "Indebted to Development: Microcredit as (De)marginalisation in Rural China," *Journal of Peasant Studies*, 2016, doi:[10.1080/03066150.2016.1236025](https://doi.org/10.1080/03066150.2016.1236025).
- [7] N. Loubere, N, Zhang, HX, "Co-operative financial institutions and local development in China," *Journal of Co-operative Organization and Management*, **3**(1), 2015, doi:[10.1016/j.jcom.2015.03.001](https://doi.org/10.1016/j.jcom.2015.03.001).
- [8] R. Chen, Huiwen Chen, Chenglu Jin, Bo Wei, Lean Yu, "Linkages and Spillovers between Internet Finance and Traditional Finance: Evidence from China," *Emerging Markets Finance and Trade*, **56**(6), 2020, doi:[10.1080/1540496X.2019.1658069](https://doi.org/10.1080/1540496X.2019.1658069).
- [9] Y. Xu, Y., "Design and research of bank Internet financial product pricing model," *Cluster Computing*, **22**(6), 2019, doi:[10.1007/s10586-018-2456-9](https://doi.org/10.1007/s10586-018-2456-9).
- [10] L. Chi-Chuan, Li, Xinrui, Yu, Chin-Hsien, Zhao, Jinsong, "Does fintech innovation improve bank efficiency? Evidence from China's banking industry," *International Review of Economics & Finance*, **74**(4), 2021, doi:[10.1016/j.iref.2021.03.009](https://doi.org/10.1016/j.iref.2021.03.009).
- [11] L. Chengming, He Si, Tian Yuan, Sun Shiqi, Ning Lu, "Does the bank's FinTech innovation reduce its risk-taking? Evidence from China's banking industry," *Journal of Innovation & Knowledge*, **7**, 2022, doi:[10.1016/j.jik.2022.100219](https://doi.org/10.1016/j.jik.2022.100219).
- [12] B. Chen, Xinyun Yang, Zhenzhong Ma, "Fintech and Financial Risks of Systemically Important Commercial Banks in China: An Inverted U-Shaped Relationship," *Sustainability*, **14**, 2022, doi:[10.3390/su14105912](https://doi.org/10.3390/su14105912).
- [13] N. Yitong, Linqian Jiao, Andrei Korneev, "Credit Development Strategy of China's Banking Industry to the Electric Power Industry," *Heritage and Sustainable Development*, **4**(1), 2022, doi:[10.37868/hsd.v4i1.81](https://doi.org/10.37868/hsd.v4i1.81).
- [14] K. Chan, Philip Gray, "Using extreme value theory to measure value-at-risk for daily electricity spot prices," *International Journal of Forecasting*, **22**, 2009, doi:[10.1016/j.ijforecast.2005.10.002](https://doi.org/10.1016/j.ijforecast.2005.10.002).
- [15] R. TREVOR, Thorp, Susan, "VAR Forecasting Models of the Australian Economy: A Preliminary Analysis," *Australian Economic Papers*, **27**, 2008, doi:[10.1111/j.1467-8454.1988.tb00697](https://doi.org/10.1111/j.1467-8454.1988.tb00697).
- [16] C. Brooks, C., Clare, A.D., Molle, J.W., Persand, G., "A comparison of extreme value theory approaches for determining value at risk," *Journal of Empirical Finance*, **12**, 2005, doi:[10.1016/j.jempfin.2004.01.004](https://doi.org/10.1016/j.jempfin.2004.01.004).
- [17] G. Persand, Chris Brooks, "Volatility Forecasting for Risk Management," *Journal of Forecasting*, **22**, 2003, doi:[10.1002/for.841](https://doi.org/10.1002/for.841).



Table 4. Previous work

id	Title <sup>1</sup>	Published in <sup>2</sup>	Theme <sup>3</sup>	Key points & special points <sup>4</sup>	Dataset <sup>5</sup>	Drawbacks <sup>6</sup>
1 <sup>1</sup>	The identification and governance of illegal fundraising crimes in Chinese internet finance <sup>1</sup>	CRIMINAL GEOGRAPHICAL JOURNAL (FEBRUARY 2020) <sup>2</sup>	Security risks in Chinese Finance <sup>3</sup> (Mainly focus on P2P) <sup>3</sup>	1. The crime of illegal fund-raising <sup>4</sup> 2. Information intermediaries, self-financing, Self-insurance, equity crowdfunding <sup>4</sup> 3. Private equity <sup>3</sup>	Chinese Judicial Document Network, Edited by Antal Forró <sup>5</sup>	1. Does not have specific mathematical models <sup>6</sup> 2. Only conducted a simple research on the theme <sup>6</sup>
2 <sup>1</sup>	Economic restructuring and sustainable development under the Internet finance mode <sup>1</sup>	E3S Web Conf. <sup>2</sup> Volume 235, 2021 (03 February 2021) <sup>2</sup>	The Internet finance mode leads to reforms on the traditional mode, and provides a fast and advanced platform for global trade. <sup>3</sup>	1. Traditional finance vs internet finance <sup>4</sup> 2. Changes for individuals and enterprises. <sup>4</sup> 3. Internet provide solutions to information sharing 'sharing economy' <sup>4,5</sup>	National Bureau of Statistics <sup>5</sup>	1. Does not conduct data analyzing using any code <sup>6</sup> 2. It described the problem in the internet finance industry but did not try to solve these problems. <sup>6</sup>
3 <sup>1</sup>	How Does Internet Finance Influence the Interest Rate? Evidence from Chinese Financial Markets <sup>1</sup>	Dutch Journal of Finance and Management 2018, 2(1), 01 <sup>2</sup>	four primary influencing paths to explain the Internet finance influence <sup>3</sup> two paths to study the influence of the Internet finance. <sup>3</sup>	1. Influence on the money market <sup>4</sup> 2. The influencing paths of the Internet finance <sup>4</sup> 3. 6 different paths <sup>4</sup> 4. P2P lending <sup>3</sup>	UCINET <sup>5</sup> WIND database. <sup>5</sup>	1. The article only chose one of the <sup>6</sup> 2. Paths to conduct specific research. <sup>6</sup> It does not compare different effects among different paths <sup>6</sup>
4 <sup>1</sup>	Internet finance development and banking market discipline: Evidence from China <sup>1</sup>	Journal of Financial Stability <sup>2</sup> Volume 22, February 2016, Pages 88-100 <sup>2</sup>	the depositor discipline of banking works under financial repression <sup>3</sup> implicit government guarantee <sup>3</sup> Internet finance development influences to banks <sup>3</sup>	1. bank risk are negatively associated with the deposit volumes <sup>4</sup> 2. Internet finance significant impacts on banks <sup>4</sup> 3. For large banks, market discipline works significantly. <sup>3</sup>	BankScope database <sup>5</sup> The Financial Yearbook of China-The statements of sample banks in their annual financial reports <sup>5</sup>	1. Used a very high dimension model <sup>6</sup> 2. It is too complex to get real effective result <sup>6</sup> 3. Variables are not independent <sup>6</sup>
5 <sup>1</sup>	Impact of digital finance on financial inclusion and stability <sup>1</sup>	Sciencedirect.com <sup>2</sup>	a discussion on digital finance <sup>3</sup> the impact of digital finance for financial inclusion. <sup>3</sup>	1. A digital transactional platform, retail agents <sup>4</sup> 2. accessibility and affordability of digital financial services <sup>4</sup> 3. Boost GDP of digitalized economies by providing convenient	WorldBank's Global Findex database. <sup>5</sup> Beck and Brown(2011) <sup>5</sup>	1. The graphs t in the article is very unclear <sup>6</sup> 2. a very simple dimension to conduct research <sup>6</sup> 3. exogenous variables the article did not consider. <sup>6</sup>
6 <sup>1</sup>	Urbanization and Economic Growth in China—An Empirical Research Based on VAR Model <sup>1</sup>	International Journal of Economics and Finance <sup>2</sup>	the dynamic relations between economic growth and the urbanization rate of resident population, the urbanization rate of land and the quality of urbanization. <sup>3</sup>	using the time series data <sup>4</sup> building VAR model. <sup>4</sup> Roots of the companion matrix, the Granger causality tests results, impulse response function of AGRGDP to GRP, <sup>4</sup> the graph of impulse response function of GRU to AGRGDP <sup>4</sup>	1982 to 2014 of the year-on-year growth rate regarding urbanization rate of population and of land in a figure <sup>5</sup>	1. The model structure, the principle and the assumption the article did not consider <sup>6</sup>
7 <sup>1</sup>	The impact of real exchange rate on international trade: Evidence from Panel Structural VAR model <sup>1</sup>	ResearchGate <sup>2</sup>	the importance of real exchange rates on export volumes by estimating a panel SVAR model using quarterly unbalanced panel data from 21 emerging markets over the 2005:Q1-2018:Q4 period. <sup>3</sup>	1. the heterogeneous Panel SVAR methodology that can be decomposed into both common and idiosyncratic parts <sup>4</sup> 2. Common Shocks, Idiosyncratic shocks, Variance decompositions from Panel SVAR model <sup>4</sup>	World Bank (2020) <sup>5</sup> OECD. (2020). Trade in Value Added (TIVA) Database <sup>5</sup>	1. The number of variables is too large <sup>6</sup> 2. It can lead to a overfitting problem <sup>6</sup> 3. The dataset the article used is not large enough
8 <sup>1</sup>	Econometric Analysis of Disequilibrium Relations Between Internet Finance and Real Economy in China <sup>1</sup>	International Journal of Computational Intelligence Systems <sup>2</sup>	evaluates the development level of internet finance by focusing on three major virtual economies. <sup>3</sup>	1. The mechanism of positive interaction between internet finance and real economy. <sup>4</sup> 2. Characteristic of Statistical Index Features Analysis of Characteristics of Statistical Indicators <sup>3</sup>	Tian Tian Fund <sup>5</sup> http://fund.eastmoney.com/ <sup>5</sup> WangLoanZhilia https://www.wdji.com/ <sup>5</sup>	1. The result analyzing part of this article is very simple <sup>6</sup> 2. It did not write any objective problem analyzing

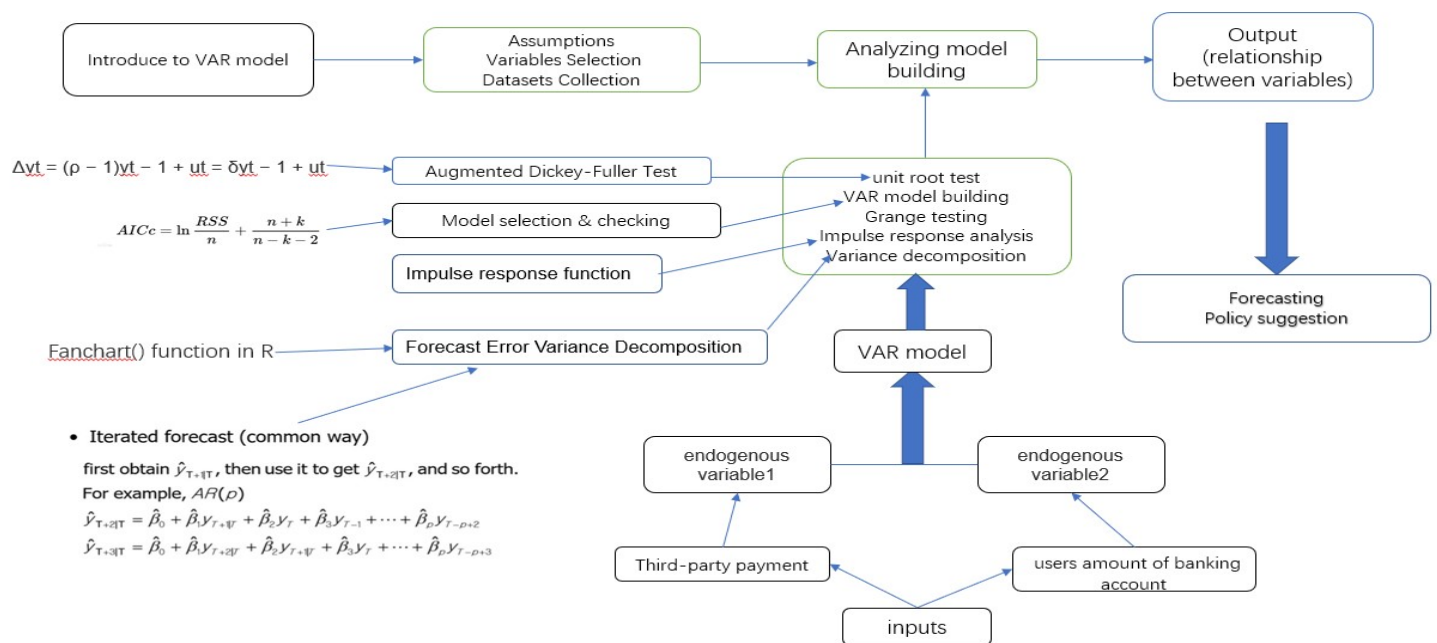


Figure 5: Modeling flow chart

## Improving License Plate Identification in Morocco: Intelligent Region Segmentation Approach, Multi-Font and Multi-Condition Training

El Mehdi Ben Laoula<sup>1,\*</sup>, Marouane Midaoui<sup>2</sup>, Mohamed Youssfi<sup>1</sup>, Omar Bouattane<sup>1</sup>

<sup>1</sup>2IACS Laboratory, ENSET Mohammedia, University Hassan II of Casablanca, 28830, Morocco

<sup>2</sup>M2S2I Laboratory, ENSET Mohammedia, University Hassan II of Casablanca, 28830, Morocco

### ARTICLE INFO

*Article history:*

*Received: 09 March, 2023*

*Accepted: 04 June, 2023*

*Online: 25 June, 2023*

*Keywords:*

*License plate recognition*

*YOLOv5*

*Detectron2*

*Intelligent region segmentation*

*Customized dataset*

*Moroccan license plate issues*

*Fonts-based data*

### ABSTRACT

*The exponential growth in the number of automobiles over the past few decades has created a pressing need for a robust license plate identification system that can perform effectively under various conditions. In Morocco, as in other regions, local authorities, public organizations, and private companies require a reliable License Plate Recognition (LPR) system that takes into account all plates specifications (HWP, VWP, DP, YP, and WWP) and multiple fonts used. This research paper introduces an intelligent LPR system implemented using the YOLOv5 and Detectron2 frameworks, which have been trained on a customized dataset comprising multiple fonts (such as CRE, HSRP, FE-S, etc.) and accounting for different circumstances such as illumination, climate, and lighting conditions. The proposed model incorporates an intelligent region segmentation approach that adapts to the plate's type, thereby enhancing recognition accuracy and overcoming conventional issues related to plate separators. With the use of image preprocessing and temporal redundancy optimization, the model achieves a precision of 97,181% when handling problematic plates, including those with specific illumination patterns, separators, degradations, and other challenges, with little advantage to YOLOv5 over Detectron2.*

## 1. Introduction

The global vehicle population has experienced substantial growth in recent decades fueled by a combination of factors, including demographic changes, lifestyle shifts, and advancements in the automotive industry. To accommodate this growth, numerous countries have developed their own vehicle registration systems, wherein each vehicle, including cars, trucks, and motorcycles, is assigned a unique license plate. These license plates typically consist of a combination of letters and numbers, serving as an alphanumeric identifier that may also be associated with the vehicle owner for easy identification.

To enable effective vehicle tracking and activity monitoring, the development of automatic number plate recognition (ANPR) systems took place. These systems employ optical character recognition (OCR) technology to analyze pre-captured images of license plates, which are captured by dedicated cameras. Through

this analysis, ANPR extracts the plate numbers and thereby identifies vehicles and their owners [1]. This advancement eliminates the need for manual identification of license plates, previously carried out by human agents and prone to errors. ANPR finds widespread use in law enforcement agencies for enforcement purposes and is also utilized by highway agencies to implement road pricing [2]. Furthermore, ANPR is employed in automated parking systems to facilitate charging processes [3].

Due to the progress in computer science and technology, alongside advancements in databases, Automatic Number Plate Recognition (ANPR) has emerged as a crucial component of traffic management systems within smart cities [4-6]. ANPR is recognized as a valuable tool for gathering traffic data and enhancing road efficiency and safety, aligning with the primary objectives of Intelligent Transportation Systems (ITS) [7]. The ANPR procedure encompasses a series of techniques and automated algorithms, typically comprising four steps: capturing an image of the vehicle, detecting the license plate, segmenting

\*Corresponding Author: El Mehdi Ben Laoula, [mehdi.benlaoula@gmail.com](mailto:mehdi.benlaoula@gmail.com)

[www.astesj.com](http://www.astesj.com)

<https://dx.doi.org/10.25046/aj080329>

the characters on the plate, and ultimately recognizing the characters.

## **2. Literature review**

### *2.1. License Plate Recognition System*

With the advent of artificial intelligence and especially deep learning, several license plate recognition system was built with interesting achievements. In fact, authors in [8] utilized a compact yet powerful network to classify characters on plates extracted by the Single Shot MultiBox Detector (SSD) [9]. Subsequently, various extensions of these neural networks have been proposed. In [10], a system for Automatic License Plate Recognition (ALPR) specific to Chinese license plates was introduced, utilizing two Convolutional Neural Networks (CNNs) based on the YOLO2 framework. The system was compared to other version of the framework and achieved a detection precision of 99.35% and a recognition precision exceeding 97.89% at a speed of 12.19ms. Another robust and efficient ALPR system based on Deep Neural Network was experienced in India [11]. It presents a License Plate Detection (LPD), followed by pre-processing of detected license plates and License Plate Recognition (LPR) using the LSTM Tesseract OCR Engine. Experimental results demonstrate high accuracy, with a 99% LPD accuracy and 95% LPR accuracy comparable to commercial ANPR systems such as Open-ALPR and Plate Recognizer.

In [12], a sliding window technique was proposed for identifying license plates in Taiwan. The system achieved a license plate detection accuracy of approximately 98.22% and a license plate recognition accuracy of 78%, with each image requiring 800ms for processing. Additionally, researchers introduced a novel ALPR system based on YOLOv2 in [13]. Their focus was on capturing license plates in uncontrolled scenarios with potential view distortions. The system employed a unique CNN capable of identifying and correcting multiple distorted license plates within a single image, using an Optical Character Recognition (OCR) approach. The final results were promising.

For recognizing Jordanian license plates, an ALPR system based on YOLOv3 was proposed [14]. This system underwent testing on genuine videos from YouTube, achieving an accuracy of 87% in recognition. Similarly, contributors of [15] implemented a YOLO framework to detect and recognize Iranian license plates. Their system demonstrated an accuracy of 95.05% after testing over 5000 images. Another Iranian study [16] has compiled a complete dataset comprising 19,937 car images and 27,745 license plate characters, annotated with the entire license plate information. This dataset was experienced in license plate detection using several optimization YOLOv5 and detectron2 frameworks.

### *2.2. Temporal redundancy*

The incorporation of a temporal redundancy stage within the proposed license plate recognition architecture has gained significant attention in the research community. Several studies have explored the importance of this stage in improving the accuracy and efficiency of license plate recognition systems. The benefits of temporal redundancy are widely recognized, the implementation and optimization of this stage can vary depending on the specific system requirements. Factors such as dataset size,

computational resources, and real-time constraints need to be carefully considered to ensure efficient and accurate license plate recognition.

One notable study [17] demonstrated the effectiveness of temporal redundancy in enhancing recognition accuracy. They presented a high-accuracy pole number recognition framework for high-speed rail catenary systems, overcoming challenges such as illumination changes, image blurs, and occlusions. Our approach combines a cascaded CNN-based Detection and Recognition model (DR-YOLO) with a temporal redundancy approach, achieving accurate results through global and local features and context-based combination of adjacent frames. Extensive experimental testing validates the effectiveness and efficiency of their approach in real-world working environments. In another related work [18], authors experienced the use of temporal redundancy in license plate detection. The results of their method reached an overall recognition rate of 86% and achieved an outstanding accuracy of 99% for four-letter plates. Furthermore, the incorporation of temporal redundancy significantly enhanced the recognition rate to 96%. Compared to Sighthound and OpenALPR, this method outperforms them by 9% and 4.9% respectively, showcasing its superiority. Also, authors of [19] explored temporal redundancy to stabilize OCR output in videos. They introduced an end-to-end Automatic License Plate Recognition (ALPR) method based on a hierarchical Convolutional Neural Network (CNN), leveraging synthetic and augmented data to enhance recognition rates yielding superior accuracy compared to academic methods and a commercial system on Brazilian and European license plate datasets.

### *2.3. License plate recognition in Morocco*

In [20], the authors introduced a Moroccan license plate recognition system consisting of two steps: hypothesis generation and verification. They utilized the Connected Component Analysis technique (CCAT) to detect rectangles considered as license plate candidates. Then, edge detection was applied within these candidates, followed by the close curves method to confirm their status as license plates and segment the characters. The experiment yielded promising results, with an accuracy of 96.37% when tested on three Moroccan road videos. In addition, authors of [21] proposed a three-phase method. Firstly, license plate localization under various environmental conditions was accomplished through a combination of edge extraction and morphological operations. Secondly, the segmentation process exploited the specific features of Moroccan license plates. Finally, optical character recognition relied on the Tesseract framework, known for its accuracy as an open-source OCR solution. The authors demonstrated the method's ability to recognize multiple license plates in real-time under different acquisition constraints, although no accuracy rate was provided.

Furthermore, [22] presented a robust method for detecting and localizing Moroccan license plates from images. This approach relied on edge features and characteristics of license plate characters. The model's robustness was verified using various images capturing Moroccan license plates from different distances and angles. The experimental results indicated a precision rate of nearly 95% with a recall rate of 81% and a standard quality measure of 87.44%. Moreover, authors of [23] contributed to the

field of Moroccan license plate recognition with their work. They developed a dataset specifically for Moroccan license plate OCR applications, consisting of 705 unique and labeled images collected manually. This dataset is freely available for use and compatible with CNN models like Yolov3.

Finally, a one-stage modified tiny-Yolov3 model was proposed for real-time Moroccan license plate recognition [24], enhanced with transfer learning techniques. This method achieved an excellent balance between speed and accuracy, executing the detection and recognition process in a single phase. It achieved an accuracy of 98.45% and a speed of 59.5 Frames Per Second (FPS).

#### 2.4. Plate detection issues

License plate detection systems face significant challenges in accurately identifying and recognizing license plates in Morocco. The country's license plate specifications, including multiple plate types, various fonts, separators, variable character spacing, partially written Arabic characters, and plate modifications, create complexities that hinder the recognition process. These unique specifications require advanced algorithms and techniques to overcome the challenges and ensure accurate license plate detection and recognition.

##### ➤ Plate formatting (PF)

- Multiple plate types in use :** In Morocco, there are multiple types of license plates used for different purposes. The most common type is the horizontal plate (HWP), which consists of three sections. The first section indicates the prefecture or province to which the vehicle is attached. The second section represents the registration series, which consists of Arabic letters in a specific order. The third section indicates the order of registration with digits. Some vehicles have a two-line plate (VWP), where the first line contains the first and second sections separated by a vertical line, and the second line displays the digits of the third section. Also, specific plates for local authorities (DP), which include an Arabic character indicating the concerned authority and a generic number specific to the vehicle. Diplomatic, consular agents, representatives, experts, and officials of international or regional organizations in Morocco have their own specific plates (YP) divided into two parts. Additionally, there are plates for vehicles related to international cooperation and temporary importation. In addition, new automobiles have special plates for provisional entry into service (WW) and vehicle purchased or sold by automobile dealers (W18). These plates are exclusively delivered by importers, manufacturers, or traders of new motor vehicles to buyers in Morocco. Figure 1 shows the multiple plates in use in the country.

- Multiple fonts in use :** Local lawmakers in Morocco have granted car owners the autonomy to choose the desired font for their license plates. The fonts listed in Table 3 are commonly utilized options. These fonts include Clarendon Regular Extra (CRE), High Security Registration Plate (HSRP), FE-Schrift (FE-S), Ingeborg Heavy Italic font (IHIF), Metalform Gothic JNL font (MGJF), Morton otf (400) (MOTF), and Moroccan Rekika Font (MRF).

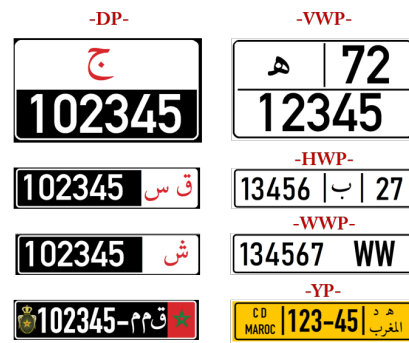


Figure 1: multiple plates in use in Morocco

- Separators:** Different separators are used by Moroccan plate makers. Even though the vertical line is the most typical separator, some constructors use hyphens, while others prefer slashes or don't use separators at all, as shown in figure 2. The configuration of plates is altered by the choice of separators or lack thereof, and this problem persists for plate identification systems.



Figure 2: multiple separators in use in Moroccan plates

- Distance between characters:** Morocco has a large number of plate constructors, thus their plates are not uniform, and the spacing between characters is not constant in all altered plates. The fact that the distance between characters differs from the plates poses a significant problem for LPR systems.
- Arabic letters specifications:** Moroccan license plates use Arabic characters that are partially written. For instance, "ب" has a dot protruding from its body. Additionally, small markings like a "ء" can be used to denote certain characters or they can stand alone (as in the case of the "ا" character). Because dots or short marks are left out, these types of characters cannot be accurately identified during the character segmentation phase [21].
- Plate modification and damage (PMD)**
  - Additions:** Even though local government agencies have waged a significant campaign against extra features on vehicle license plates, some owners still choose to add drawings, logos, stickers, or cameras to plates as presented in figure 3.



Figure 3: Plates with irregular additions

- **Degradation:** In the context of Morocco's developing status, vehicle owners often encounter difficulties in maintaining their license plates in pristine condition. This deterioration can manifest in different forms, such as scratches on metallic plates that resemble lines or additional features that may be mistaken for characters if they possess similar dimensions. Another common issue involves the degradation of character paint, resulting in misleading interpretations or even the omission of altered characters. These damages present a significant challenge for automated license plate recognition systems, as they can adversely affect the accuracy and reliability of the recognition process.

➤ **Visibility and image quality (VIQ)**

- **Illumination:** As the sample presented in figure 4, due to the light shift in the shadow zone, the presence of objects' shadows might present a number of difficulties that must be resolved in order to prevent any false positive detections. We use the median filtering technique to remove specific forms of noise in order to complete this objective.



Figure 4: multiple plates captured with shadow

- **Camera noise:** Issue caused by the sensor used can alter the taken image. Here, we discuss camera vibration, which can amplify blur, as well as weather-related noise. Vehicle position and speed can cause technical degradation by making it challenging to see images or video sequences.

- **Plate inclination and distortion:** Due to various factors such as improper mounting or external forces, license plates can become tilted or distorted, making it difficult for automated systems to accurately capture and interpret the characters. Plate inclination refers to the angle at which the plate is positioned, which can vary significantly from one vehicle to another. This variation in plate inclination introduces complexity in the recognition process, as the characters may appear skewed or slanted, leading to potential recognition errors. Plate distortion can occur due to factors such as physical damage, temperature changes, or poor plate material quality. Distortions may cause the characters to appear stretched, compressed, or warped [25, 26].

**3. Proposed solution**

**3.1. YOLOv5**

YOLO is a real-time object detection algorithm that directly predicts bounding box coordinates and class probabilities without the region of interest extraction, resulting in improved detection speed compared to faster R-CNN [27]. The latest version, YOLOv5, introduced by Ultralytics in 2020, outperforms previous versions in both speed and accuracy. Written in Python, YOLOv5 is easier to install and integrate with IoT devices, and it utilizes a new PyTorch framework for training and deployment, enhancing object detection results. During training, YOLOv5 incorporates online data augmentation techniques such as scaling, color space modifications, and mosaic augmentation. YOLOv5 offers four

models, including YOLOv5s, YOLOv5m, YOLOv5l, and YOLOv5x, by adjusting the width and depth of the backbone network [28]. The backbone, a convolutional neural network, collects and compresses visual features, leveraging the focus structure and stacking image edges to reduce calculations and speed up the process. The CSP1\_x and CSP2\_x modules split and combine feature mappings, increasing accuracy and reducing calculation time. The SPP network separates contextual features and expands the receptive field. YOLOv5 also includes a neck network that utilizes PANet and FPN structures to fuse and combine features from different layers, improving feature extraction and prediction [29-31]. Figure 5 displays the YOLOv5 network.

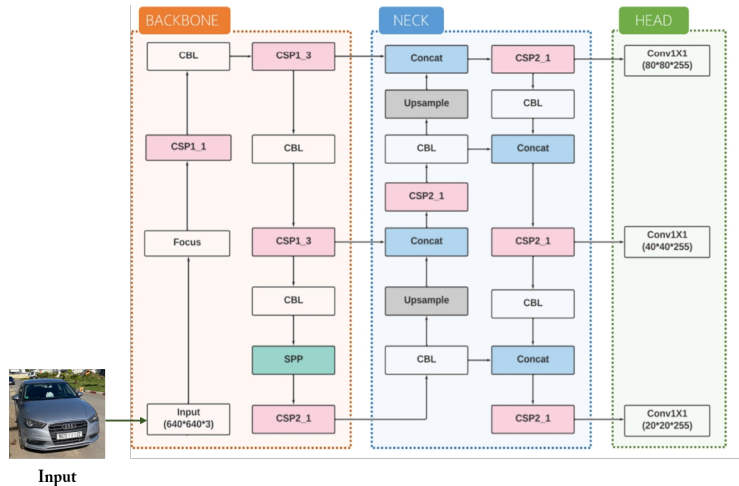


Figure 5: Network topology of YOLOv5s [27]

**3.2. Detectron2**

Detectron2 is a powerful open-source framework for object detection and instance segmentation [32]. It is built on top of PyTorch [33] and provides a modular and flexible platform for training and deploying state-of-the-art deep learning models. With a focus on research and production deployment, Detectron2 offers a wide range of functionalities and features that enable efficient and accurate object detection tasks. It includes a comprehensive set of pre-trained models and allows users to easily customize and extend the framework to suit their specific needs [32]. The architecture of Detectron2 is based on a modular design, with different components such as backbone networks, feature extractors, and prediction heads [34], allowing for easy experimentation and fine-tuning of models. It also supports distributed training and inference, enabling efficient utilization of resources and scalability [35]. Detectron2 has gained popularity in the computer vision community due to its performance, versatility, and user-friendly interface, making it a valuable tool for researchers and developers working on object detection and instance segmentation tasks. Figure 6 displays the network of Detectron2.

**3.3. Model**

In light of the aforementioned, the proposed Moroccan Automatic License Plate Recognition System (MALPR), shown in Figure 7, is intended to meet the requirements of the nation while minimizing as many difficulties as possible. It addresses the

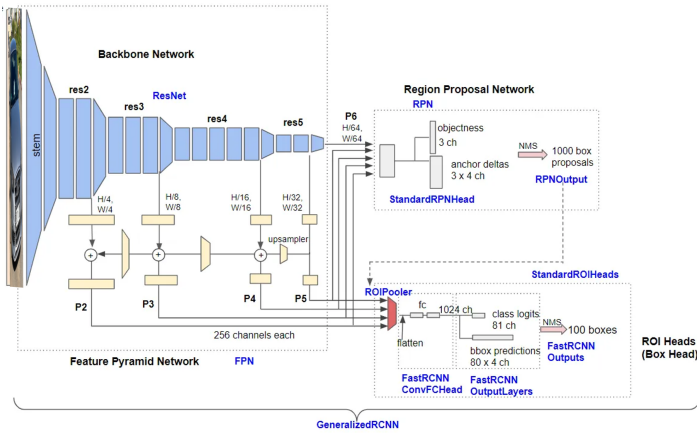


Figure 6: Network topology of Detectron2 [36]

recognition of all types of license plates used in Morocco, including both local and foreign vehicles. There are two main parts to the MALPR system [37]. An SDK-based system with embedded IoT devices like a camera, GPS, and GSM as well as a neural network framework for image analysis constitute the first part of the system. The second one is an API server-side system that carries out further processing, like character segmentation and digits recognition.

The proposed architecture involves capturing a real-time video from a camera and converting it into a specific number of frames per second, based on the deployment location of the device. For instance, if the system is used for detecting parking activity, a low frame rate of one or two frames per second would suffice. However, in areas with higher traffic density, such as highways, a higher frame rate would be necessary to enhance the accuracy of the detection.

Initially, as presented in figure 7, the device performs an analysis of the video and processes the frames to improve their quality and increase the accuracy of predictions through techniques such as compression, greyscale conversion, etc. [37, 38]. Subsequently, the captured vehicle is classified using the neural network framework [10-16] in object detection, vehicle classification, and plate localization within the frame. The better the vehicle classification, the more accurately the plate can be located within the image. Neural network can easily locate the plate with a simple configuration. Once the plate is detected, it is cropped and sent as a binary large object (BLOB). On the server side, the software development kit (SDK) completes the process by performing region segmentation, character detection, and gathering recognized characters to construct the final output. The current architecture extends beyond the steps outlined above.

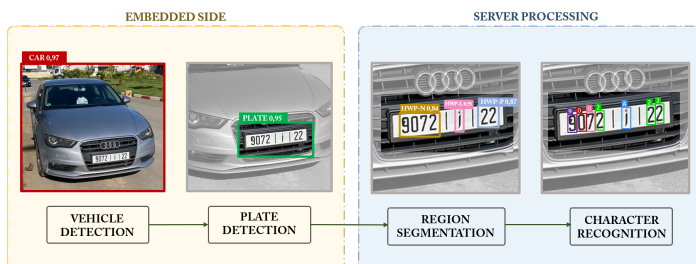


Figure 7: Moroccan License plate overview.

The Moroccan license plate detection system involves several key steps to accurately identify and process license plates in real-time. The system begins by capturing a video feed from a camera and converting it into frames per second based on the location of the device. The frames undergo analysis and processing to enhance their quality and accuracy using techniques like compression and grayscale conversion. The neural network (Yolo, detectron2, CRAFT, etc.) is then employed to classify the captured vehicles and locate the license plates within the frames. The output of this stage consists of the coordinates of the predicted plate as presented in equation (1). Once the plate is detected, it is cropped and sent for further processing.

$$y = (pc, bx, by, bh, bw, c) \tag{1}$$

With bw and bh are the width and height of the rectangle, c stands for the class found and bx and by are the coordinate of the center of the box. pc corresponds to the confidence of the prediction:

$$pc = Pr(\text{Object}) * IoU \tag{2}$$

With IoU corresponds to the area of overlap between the predicted BB and the ground-truth BB [39] which corresponds to the labeled BB from the testing set that specify where is the object.

The system incorporates region segmentation to categorize the license plate into major digit regions, allowing for individual analysis of each part. The plate undergoes color inversion if necessary, and character recognition techniques are applied to extract characters and numbers from separated regions. The recognized characters are assembled to form the final output.

Additionally, the system employs temporal redundancy, where the largest plate within the frame is selected as a basis for prediction. Comparative analysis is conducted with previously stored data to assess the similarity of predicted characters. Plates with higher dimensions and better prediction precision are prioritized, while redundant results are rejected to avoid duplication and optimize efficiency.

Overall, the Moroccan license plate detection system integrates video analysis, plate detection, cropping, region segmentation, character recognition, and temporal redundancy stages to achieve accurate and efficient recognition of license plates, enabling further processing and utilization of the obtained information.

### 3.4. Improvements

**Temporal redundancy.** The incorporation of a temporal redundancy stage within the proposed license plate recognition architecture plays a pivotal role in elevating the accuracy rates and optimizing the utilization of the entire frame. This stage serves as a crucial component that effectively verifies the output and facilitates a comparative analysis with previously obtained results, ultimately leading to the refinement and advancement of the model's overall performance.

To ensure a comprehensive evaluation, the model begins with meticulously selecting the output derived from the largest plate within the frame. The rationale behind this selection lies in the inherent understanding that plates with larger dimensions often provide a more accurate basis for prediction. Remarkably,

empirical evidence has demonstrated that this approach can lead to an impressive increase in the accuracy of the proposed model by up to 20% [19]. Such an improvement is substantial, indicating the crucial role played by this temporal redundancy stage in the enhancement of recognition capabilities.

In recognizing the vast number of vehicles traversing Moroccan roads, estimated to exceed an impressive count of 4 million, it becomes evident that the likelihood of detecting multiple plates simultaneously with similar digit patterns, occupying identical positions, and preserving the same order is exceedingly low. Therefore, it becomes viable to employ the system to compare the predicted characters from the cropped license plate to an existing collection of previously conserved data, in order to ascertain their level of similarity and make informed decisions based on such assessments.

The initial step involves verifying the presence of an existing output within the redundancy collection for comparative purposes. If an older output is identified, the model proceeds to scrutinize whether the predicted license plate corresponds to the same plate as the last output stored within the redundancy collection. This verification process is accomplished through the establishment of a similarity rate, serving as a threshold to determine the degree of resemblance between the predicted characters and the existing collection.

Subsequently, in instances where the similarity rate surpasses the pre-established threshold, confirming that the detected characters unequivocally belong to the same license plate, a thorough comparison ensues to ascertain the most relevant output. Notably, the determination of relevance primarily revolves around the consideration of plate dimensions and the level of prediction precision. As shown in figure 8, plates with larger dimensions are inherently attributed with a higher potential for providing more accurate predictions, thereby warranting their prioritization within the selection process.

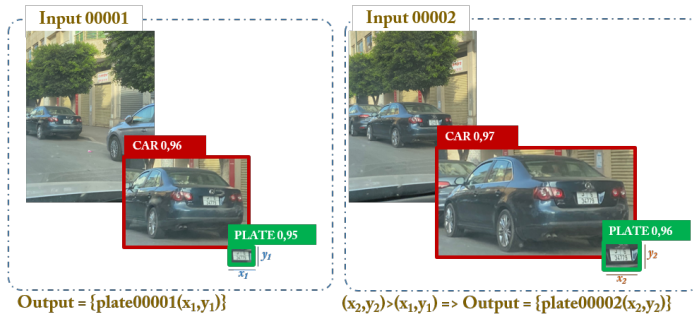


Figure 8: Temporal Redundancy optimization sample.

However, in scenarios where the output unequivocally replicates a redundant result with a similarity rate of 100%, it indicates that the information has already been transmitted to the embedded side. Consequently, to avoid redundancy and unwarranted repetition, such results are promptly rejected, effectively curtailing the transmission of duplicate outputs to the API side.

The temporal redundancy stage constitutes a critical juncture within the license plate recognition system, serving as a formidable mechanism for bolstering accuracy rates. By incorporating comparative analyses with previously obtained results, the system

can intelligently discern the most relevant output, leveraging the dimensions of the license plate and the level of prediction precision as key criteria. In doing so, the system avoids the needless transmission of duplicate information to the API side, thus optimizing the overall efficiency of the recognition process.

**Algorithm 1: Temporal redundancy**

```

Algorithm temporalRedundancyCheck(newOutput,
redundancyCollection)
    largestPlateOutput <- selectLargestPlateOutput(newOutput)
    if redundancyCollection.isEmpty() then
        redundancyCollection.add(largestPlateOutput)
        return largestPlateOutput
    end if
    existingOutput <- redundancyCollection.getLastOutput()
    similRate <- calculateSimilRate(largestPlateOutput, existingOutput)
    if similRate > threshold then
        if similRate = 100 then
            return "Redundant output"
        else
            if largestPlateOutput.dimensions > existingOutput.dimensions
then
                redundancyCollection.remove(existingOutput)
                redundancyCollection.add(largestPlateOutput)
                return largestPlateOutput
            else
                return existingOutput
            end if
        end if
    else
        redundancyCollection.add(largestPlateOutput)
        return largestPlateOutput
    end if
End Algorithm
    
```

**Region segmentation.** The proposed model makes a significant addition to the field of region segmentation. Before extracting each character, it divides the license plate into its major digit sections. This step is essential to ensuring that every component of the plate is examined separately and no area is missed. The regions are created to be as large as feasible during the training phase in order to support all potential typefaces during the test phase. In the second stage of isolating the digits for analysis, extreme care is used to prevent overlapping regions. This model does not take separators into account, such as the lengthy Arabic letter "أ" and does not divide the alphabet into discrete pieces, in contrast to other Moroccan license plate recognition systems. Figure 9 presented the region segmentation.

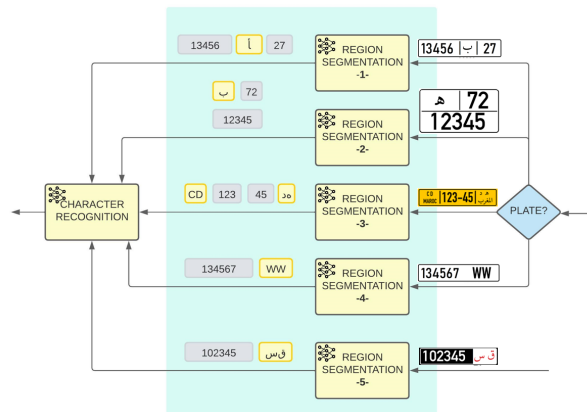


Figure 9: Region segmentation overview

**Image processing :** Stage at the beginning of the workflow where the video input is processed in order to remove small components and noises, to increase the quality necessary for further operations (binarization, contrast maximization, Gaussian blur filter and Adaptive threshold) [40] as well as to reduce the computation cost.

- **Image binarization** consist on converting the frame to black and white [40, 41]. And essential processing for the digits detection where the input is considered as a collection of subcomponents (text, background and picture). To each pixel, a local threshold is set in order to reduce noise, illumination issues and source type-related degradations.
- **Thresholding** is used in the aim of classifying dark pixels as black and others as white. The most important is to set the optimal threshold value for particular image, hence the use of adaptive thresholding. A threshold can be selected by user manually or it can be selected by an algorithm automatically which is known as automatic thresholding. Also called automatic tresholding, this mode is used to set automatically the threshold value by an algorithm when it becomes difficult or almost impossible to select optimal one [42].
- **Histogram Equalization (HE)** is the method that standardize the intensities of the input image by spreading out the most recurrent ones, which results in an improved contrast. Figure 10 shows the impact of applying the histogram equalization technique on a vehicle image. Accordingly, HE equalize the light intensity and improve dark and indistinguishable license [15].



Figure 10: Vehicle image before and after HE optimization.

## 4. Experiment and results

### 4.1. Dataset

Machine learning systems require a ivolume of high-quality data. Although efforts have been made to solve the issue of license plate detection, it is still difficult to identify license plates in uncontrolled and unconstrained contexts. In fact, whether attempting to detect license plates that are rotated, in uneven illumination, in snowy conditions, or in a dimly lit environment, the majority of offered algorithms have low accuracy. The vast majority of researchers have trained and tested their detectors on really short datasets, which only contain a small number of unique

photos or modest variations in angles, limiting their usefulness to particular scenarios.

In fact, a unique dataset is created based on the plate types (HWP, VWP, YP, WWP, and DP) and fonts used (CRE, HSRP, FE-S, IHIF, MGJF, MOTF, and MRF) to test the proposed method. This dataset, shown in figure 11, consists of 11617 photos of unique vehicles taken from Moroccan roads in a variety of settings (including location, time, rotation, background, lighting, and weather). These photos are organized based on the plate style and font used. After being cropped, each annotated plate is segmented (HWP-N, HWP-P, HWP-L, etc.). This serves as a segmentation data that may be trained on and annotated.

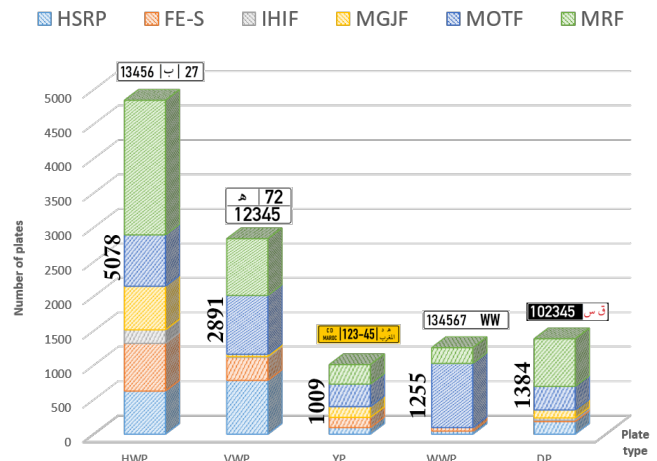


Figure 11: Dataset composition (fonts and plate types).

Also, specific folders are built to test the present model on problematic plates: Plates Formating (PF) having plates with difference distance between characters with almost all fonts in use and with several types of separators, Visibility and Image Quality (VIQ), having plates with illumination and shadowing issues, pictures with camera noise and plates under different inclinasion. Also a folder named (PMD) Plate Modification and Damage is built with plates with degradation and those having additions to test the robustness of the model to deal with these issues.

### 4.2. Training

The dataset is labeled using Labelling [43]. This desktop software analyzes the image annotation process for training Deep learning models in modern image recognition systems. This tool creates a classes.txt file and saved annotation with the following structure, with the first character corresponding to the order of the class in class.txt. The next four values are the coordinates of the BB annotated.

To perform the training we used NVIDIA GeForce RTX 3070 (total memory 16196 MB) build on AMD Ryzen 9 3900XT 12-Core Processor computer with 16384 MB RAM and Windows 10 Pro N 64-bit (10.0, Build 19045). The model was built with Python-3.9.13, torch-1.9.1+cu111 CUDA:0.

The usual approach of the presented model involves categorizing outcomes into four cases denoted by T and F, representing true or false predictions. The letters P and N indicate whether the instance is expected to be part of a positive or negative class. Evaluating the model's performance involves examining the



distribution of these prediction outcomes, which can be formed by various combinations of these categories. To gauge the model's precision, the following metrics are commonly employed.

$$Accuracy (A) = \frac{TP + TN}{TP + TN + FP + FN} \times 100\% \quad (3)$$

$$Precision (P) = \frac{TP}{TP + FP} \times 100\% \quad (4)$$

$$Recall (R) = \frac{TP}{TP + FN} \times 100\% \quad (5)$$

$$F_1 = 2 \times \frac{P \times R}{P + R} \quad (6)$$

$$mAP = \frac{1}{N(T)} \sum_{r \in T} AP_r \quad (7)$$

True positive (TP) refers to a test result that correctly detects the presence of a certain characteristic, while true negative (TN) indicates accurate identification of the absence of the region or character. False positive (FP) occurs when a result wrongly suggests the presence of a specific region or character, and false negative (FN) represents a test result that falsely indicates the absence of a particular condition or attribute. Figure 12 illustrates three types of losses: classification loss, objectness loss, and box loss. The box loss evaluates the algorithm's ability to accurately determine an object's center and how well the estimated bounding box encompasses the object. Objectness measures the probability of an object's existence within a suggested region of interest. A higher objectness indicates a higher likelihood of an object being present in the image window. Classification loss demonstrates how effectively the algorithm can assign the correct class to a given object. The model's precision, recall, and mean average precision show significant improvement initially, reaching stability around 50 epochs. The validation box, objectness, and classification losses also showed a noticeable decrease until approximately epoch 50. We employed early stopping to select the best weights for the model.

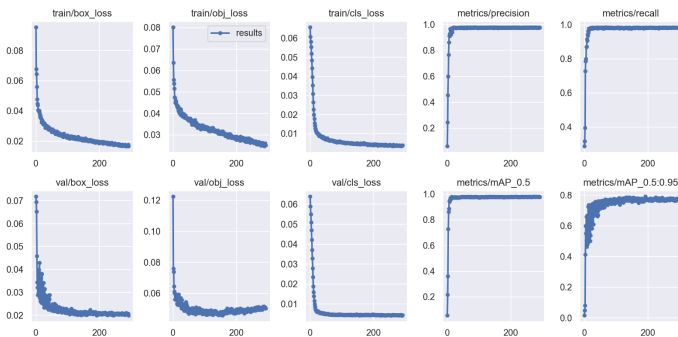


Figure 12: Plots of box loss, objectness loss, classification loss, precision, recall and mean average precision (mAP) over training and validation epochs.

### 4.3. Result and discussion

After performing precision of 95.492%, a recall of 98.259% and mAP 50% up to 97.768% in training, the model performed excellent rates on problematic dataset. In fact, as shown in figure

[www.astesj.com](http://www.astesj.com)

13, almost all PF images were detected and correctly predicted and the model showed very good results when tested on VIQ and PMD datasets with little advantage to Yolov5 over Deteron2. The average speed of all detection stages (vehicle detection, plate type, plate segmentation, and plate characters) is up to 135.3ms when run under experimentation configuration.

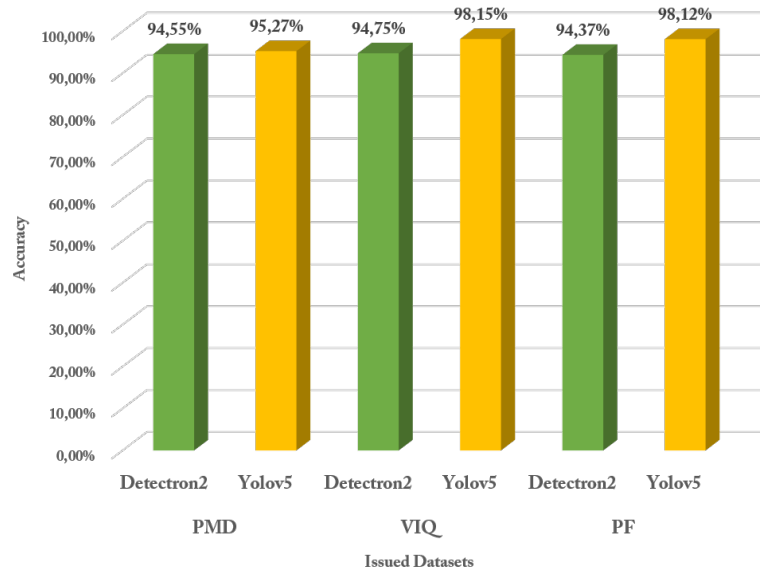


Figure 13: Model precision on issued datasets.

By implementing the described architecture, the model has effectively addressed the aforementioned issues. The current model guarantees the following outcomes:

- Accurate recognition of characters confined within regions, addressing the problem of separators.
- Elimination of false recognition of separators as characters, specifically the Arabic letter "ا".
- Proper identification of the desired result from region segmentation, ensuring that letters are not misidentified as numbers (such as "1" and Arabic letter "أ", "و" and the number 9, etc.).
- Enhanced recognition of Arabic characters "ب", "ت", "س", and "ش" that often have separated parts (dots), through optimized contour finding solutions.
- Improved handling of repeated inputs by considering the most precise result obtained from the most relevant frame.
- Optimization of the training dataset to include a wide range of fonts used on license plates, degraded digits, variations in shadows, and different lighting conditions.
- Capability to add new license plates (foreign plates) by incorporating new categories in plate detection (HWP, VWP, YP, WWP, DP, FRP, GERP, etc.).

### 5. Conclusion

Based on the aforementioned considerations, the increasing number of vehicles on the roads has led to a growing demand for a reliable and versatile license plate recognition system. This requirement is shared not only in Morocco but also in other regions, where local governments, government agencies, and private businesses seek a robust License Plate Recognition (LPR) system that can effectively handle the specific plate specifications (HWP,

VWP, DP, YP, and WWP) and typefaces used by plate manufacturers. To address this need, a CNN-based intelligent LPR system is introduced in this study. The system was trained on diverse datasets focusing on multiple fonts (CRE, HSRP, FE-S, etc.) and environmental factors such as illumination, climate, and lighting conditions and testes using both Yolov5 and Detectron2 frameworks. Notably, the model incorporates an intelligent region segmentation stage that adapts to the specific type of license plate. This segmentation process greatly enhances recognition precision and successfully resolves previous separator-related challenges. The results obtained from testing the trained model indicate its exceptional capability in accurately identifying automobiles, license plates of various types and fonts, as well as individual digits and plate components. Specifically, the model achieved an average precision rate of 97,18% when tested on issued plates.

### Data availability statement

The data used in this study was collected manually by the authors and sorted by type of plate: WWP, VWP, YP, and DP. After further analyzing the collected pictures, the data was sorted into four folders: PDEG, PDI, PSS, and PADD. A part of this datasets used in the analysis will be available upon request by contacting the corresponding author.

### Conflict of interest

The authors of this manuscript declare that they have no financial or personal relationships with other people or organizations that could inappropriately influence their work. The authors confirm that this article is original, has not already been published in any other journal, and is not currently under consideration by any other journal. The authors also confirm that all the data presented in this manuscript are original and authentic.

### References

- [1] C. Patel, D. Shah, A. Patel, "Automatic Number Plate Recognition System (ANPR): A Survey," *International Journal of Computer Applications*, **69**(9), 21–33, 2013, doi:10.5120/11871-7665.
- [2] S. Bouchelaghem, M. Omar, "Reliable and secure distributed smart road pricing system for smart cities," *IEEE Transactions on Intelligent Transportation Systems*, **20**(5), 1592–1603, 2019, doi:10.1109/TITS.2018.2842754.
- [3] S.S. Omran, J.A. Jarallah, "Iraqi car license plate recognition using OCR," in: Baghdad, I., ed., in 2017 Annual Conference on New Trends in Information and Communications Technology Applications, NTICT 2017, 298–303, 2017, doi:10.1109/NTICT.2017.7976127.
- [4] K. Yogheedha, A.S.A. Nasir, H. Jaafar, S.M. Mamduh, "Automatic Vehicle License Plate Recognition System Based on Image Processing and Template Matching Approach," 2018 International Conference on Computational Approach in Smart Systems Design and Applications, ICASSDA 2018, 1–8, 2018, doi:10.1109/ICASSDA.2018.8477639.
- [5] C. Bila, F. Sivrikaya, M.A. Khan, S. Albayrak, "Vehicles of the Future: A Survey of Research on Safety Issues," *IEEE Transactions on Intelligent Transportation Systems*, **18**(5), 1046–1065, 2017, doi:10.1109/TITS.2016.2600300.
- [6] S.K. Lakshmanaprabu, K. Shankar, S. Sheeba Rani, E. Abdulhay, N. Arunkumar, G. Ramirez, J. Uthayakumar, "An effect of big data technology with ant colony optimization based routing in vehicular ad hoc networks: Towards smart cities," *Journal of Cleaner Production*, **217**, 584–593, 2019, doi:10.1016/j.jclepro.2019.01.115.
- [7] M. Soyuturk, K.N. Muhammad, M.N. Avcil, B. Kantarci, J. Matthews, "From vehicular networks to vehicular clouds in smart cities," *Morgan Kaufmann*: 149–171, 2016, doi:10.1016/B978-0-12-803454-5.00008-0.
- [8] Q. Wang, "License plate recognition via convolutional neural networks," *Conf. Softw. Eng. Serv. Sci. ICSESS*, 2017–November, 2018, doi:10.1109/ICSESS.2017.8343061.
- [9] W. Liu, D. Anguelov, D. Erhan, C. Szegedy, S. Reed, C.Y. Fu, A.C. Berg, "SSD: Single shot multibox detector," *CVPR*. tesseract-ocr, 2016, doi:10.1007/978-3-319-46448-0\_2.
- [10] X. Hou, M. Fu, X. Wu, Z. Huang, S. Sun, "Vehicle license plate recognition system based on deep learning deployed to PYNQ," *ISCIT 2018 - 18th International Symposium on Communication and Information Technology*, 2018, 422–427, 2018, doi:10.1109/ISCIT.2018.8587934.
- [11] J. Singh, B. Bhushan, "Real Time Indian License Plate Detection using Deep Neural Networks and Optical Character Recognition using LSTM Tesseract," in *Proceedings - 2019 International Conference on Computing, Communication, and Intelligent Systems, ICCIS 2019, Communication, and Intelligent Systems (ICCIS)*, Greater Noida, India: 347–352, 2019, doi:10.1109/ICCIS48478.2019.8974469.
- [12] Hendry, R.C. Chen, "Automatic License Plate Recognition via sliding-window darknet-YOLO deep learning," *Image and Vision Computing*, **87**, 47–56, 2019, doi:10.1016/J.IMAVIS.2019.04.007.
- [13] S.M. Silva, C.R. Jung, "License plate detection and recognition in unconstrained scenarios," *Lecture Notes in Computer Science (Including Subseries Lecture Notes in Artificial Intelligence and Lecture Notes in Bioinformatics)*, 11216 LNCS, 593–609, 2018, doi:10.1007/978-3-030-01258-8\_36.
- [14] S. Alghyaline, "Real-time Jordanian license plate recognition using deep learning," *Journal of King Saud University - Computer and Information Sciences*, 2020, doi:10.1016/j.jksuci.2020.09.018.
- [15] A. Tourani, A. Shahbahrami, S. Soroori, S. Khazaei, C.Y. Suen, "A robust deep learning approach for automatic Iranian vehicle license plate detection and recognition for surveillance systems," *IEEE Access*, **8**, 201317–201330, 2020, doi:10.1109/ACCESS.2020.3035992.
- [16] M. Rahmani, M. Sabaghian, S.M. Moghadami, M.M. Talaie, M. Naghibi, M.A. Keyvanrad, "IR-LPR: A Large Scale Iranian License Plate Recognition Dataset," in 2022 12th International Conference on Computer and Knowledge Engineering, ICCKE 2022, Mashhad, Iran, 0: 53–58, 2022, doi:10.1109/ICCKE57176.2022.9960129.
- [17] Y. Yang, W. Zhang, Z. He, D. Li, "High-speed rail pole number recognition through deep representation and temporal redundancy," *Neurocomputing*, **415**(16), 201–214, 2020, doi:10.1016/j.neucom.2020.07.086.
- [18] W. Riaz, A. Azeem, G. Chenqiang, Z. Yuxi, Saifullah, W. Khalid, "YOLO Based Recognition Method for Automatic License Plate Recognition," in *Proceedings of 2020 IEEE International Conference on Advances in Electrical Engineering and Computer Applications, AEECA 2020, 1109/AEECA49918.2020.9213506: 87–90, 2020, doi:10.1109/AEECA49918.2020.9213506.*
- [19] S.M. Silva, C.R. Jung, "Real-time license plate detection and recognition using deep convolutional neural networks," *Journal of Visual Communication and Image Representation*, **71**, 10277, 2020, doi:10.1016/j.jvcir.2020.102773.
- [20] I. Slimani, A. Zaarane, A. Hamdoun, I. Atouf, "Vehicle license plate localization and recognition system for intelligent transportation applications," 2019 6th International Conference on Control, Decision and Information Technologies, CoDIT 2019, **2019**(6), 1592–1597, 2019, doi:10.1109/CoDIT.2019.8820446.
- [21] F. Zahra Taki, A. El Belrhiti El Alaoui, "Moroccan License Plate recognition using a hybrid method and license plate features," *ResearchGate*, (March), 2018.
- [22] H. Anoual, S. El Fkhi, A. Jilbab, D. Aboutajdine, "Vehicle license plate detection in images," *International Conference on Multimedia Computing and Systems -Proceedings*, 2011, doi:10.1109/ICMCS.2011.5945680.
- [23] A. Alahyane, M. El Fakir, S. Benjelloun, I. Chairi, "Open data for Moroccan license plates for OCR applications : data collection, labeling, and model construction," *Dec*, **19**(7), 146–158, 2021, doi:10.48550/arXiv.2104.08244.
- [24] A. Fadili, M. E. Aroussi, and Y. Fakhri, "A one-stage modified Tiny-YOLOv3 method for real-time Moroccan license plate recognition," *International Journal of Computer Science and Information Security (IJCSIS)*, **19**(7), 146–158, Jul. 2021. doi: 10.5281/zenodo.5164655.
- [25] C.H. Lin, C.H. Wu, "A Lightweight, High-Performance Multi-Angle License Plate Recognition Model," in *International Conference on Advanced Mechatronic Systems, ICAMechS, 09/ICAMechS.2019.8861688: 235–240, 2019, doi:10.1109/ICAMechS.2019.8861688.*
- [26] D. Xiao, L. Zhang, J. Li, J. Li, "Robust license plate detection and recognition with automatic rectification," *Journal of Electronic Imaging*, **30**(01), 1, 2021, doi:10.1117/1.jei.30.1.013002.
- [27] G. Jocher, A. Stoken, J. Borovec, NanoCode012, et al., "ultralytics/yolov5: v3.0," 2020, doi:10.5281/zenodo.3983579.

- [28] K. He, X. Zhang, S. Ren, J. Sun, "Spatial pyramid pooling in deep convolutional networks for visual recognition," arXiv, 2014, doi:10.1007/978-3-319-10578-9\_23.
- [29] W. Jia, S. Xu, Z. Liang, Y. Zhao, H. Min, S. Li, Y. Yu, "Real-time automatic helmet detection of motorcyclists in urban traffic using improved YOLOv5 detector," IET Image Processing, **15**(14), 3623–3637, 2021, doi:10.1049/ipr2.12295.
- [30] X. Xu, Y. Jiang, W. Chen, Y. Huang, Y. Zhang, X. Sun, "DAMO-YOLO : A Report on Real-Time Object Detection Design," 2022.
- [31] K. Wang, J.H. Liew, Y. Zou, D. Zhou, J. Feng, "PANet: Few-shot image semantic segmentation with prototype alignment," Proceedings of the IEEE International Conference on Computer Vision, 2019-October, 9196–9205, 2019, doi:10.1109/ICCV.2019.00929.
- [32] A. Venkata, S. Abhishek, S. Kotni, "Detectron2 Object Detection & Manipulating Images using Cartoonization," Article in International Journal of Engineering and Technical Research, 2022.
- [33] S. Imambi, K.B. Prakash, G.R. Kanagachidambaresan, "PyTorch," Springer International Publishing, Cham: 87–104, 2021, doi:10.1007/978-3-030-57077-4\_10.
- [34] V. Pham, C. Pham, T. Dang, "Road Damage Detection and Classification with Detectron2 and Faster R-CNN," Proceedings - 2020 IEEE International Conference on Big Data, Big Data 2020, 5592–5601, 2020, doi:10.1109/BIGDATA50022.2020.9378027.
- [35] Y. Wu, A. Kirillov, F. Massa, W.-Y. Lo, R. Girshick, "Detectron2: A PyTorch-based modular object detection library," in Meta AI, 1–10, 2019, doi:10.1007/978-3-030-58553-6\_49.
- [36] M. Ackermann, D. Iren, S. Wesselmecking, D. Shetty, U. Krupp, "Automated segmentation of martensite-austenite islands in bainitic steel," Materials Characterization, **191**, 2022, doi:10.1016/j.matchar.2022.112091.
- [37] S. Du, M. Ibrahim, M. Shehata, W. Badawy, "Automatic license plate recognition (ALPR): A state-of-the-art review," IEEE Transactions on Circuits and Systems for Video Technology, **23**(2), 311–325, 2013, doi:10.1109/TCSVT.2012.2203741.
- [38] H. Rezaatoughi, N. Tsoi, J. Gwak, A. Sadeghian, I. Reid, S. Savarese, "Generalized intersection over union: A metric and a loss for bounding box regression," Proceedings of the IEEE Computer Society Conference on Computer Vision and Pattern Recognition, 2019-June, 658–666, 2019, doi:10.1109/CVPR.2019.00075.
- [39] G.R. Gonçalves, D. Menotti, W.R. Schwartz, "License plate recognition based on temporal redundancy," IEEE Conference on Intelligent Transportation Systems, Proceedings, ITSC, 2577–2582, 2016, doi:10.1109/ITSC.2016.7795970.
- [40] H. Michalak, K. Okarma, "Improvement of image binarization methods using image preprocessing with local entropy filtering for alphanumerical character recognition purposes," Entropy, **21**(6), 1–18, 2019, doi:10.3390/e21060562.
- [41] M.R. Gupta, N.P. Jacobson, E.K. Garcia, "OCR binarization and image preprocessing for searching historical documents," Pattern Recognition, **40**(2), 389–397, 2007, doi:10.1016/j.patcog.2006.04.043.
- [42] P. Roy, S. Dutta, N. Dey, G. Dey, S. Chakraborty, R. Ray, "Adaptive thresholding: A comparative study," 2014 International Conference on Control, Instrumentation, Communication and Computational Technologies, ICCICCT 2014, 1182–1186, 2014, doi:10.1109/ICCICCT.2014.6993140.
- [43] L.Y. Chan, A. Zimmer, J.L. Da Silva, T. Brandmeier, "European Union Dataset and Annotation Tool for Real Time Automatic License Plate Detection and Blurring," 2020 IEEE 23rd International Conference on Intelligent Transportation Systems, ITSC 2020, 2020, doi:10.1109/ITSC45102.2020.9294240.

## The Design, Optimization, and Experimental Study of Hub and Axial Flux BLDC Motor Under Operating Conditions For Light Electric Vehicles

Ozturk Tosun<sup>\*1</sup>, Kenan Toker<sup>1</sup>, Ozturk Tosun<sup>2</sup>, Necibe Fusun Oyman Serteller<sup>1</sup>, Vedat Topuz<sup>3</sup>

<sup>1</sup>*Electrical-Electronics Engineering, Faculty of Technology, Marmara University, Istanbul, 34854, Turkey*

<sup>2</sup>*Electrical-Electronics Engineering, Institute of Pure and Applied Sciences, Marmara University, Istanbul, 34854, Turkey*

<sup>3</sup>*Computer Technology Programming, Vocational School of Technical Sciences, Marmara University, Istanbul, 34854, Turkey*

### ARTICLE INFO

*Article history:*

*Received: 02 March, 2023*

*Accepted: 30 May, 2023*

*Online: 25 June, 2023*

*Keywords:*

*Axial flux BLDC motor*

*Hub BLDC motor*

*Efficiency*

### ABSTRACT

*In this study, we conducted an experimental study and efficiency optimization of the outer rotor (hub) BLDC (brushless direct current) motor and axial BLDC motor for light electric vehicles. Both motors were investigated in the simulation environment and experimentally. The axial flux BLDC motor had a rated power of 10 KW, and a rated speed of 4550 rpm, while the outer rotor (hub) BLDC motor had a rated power of 1 KW and a rated speed of 300 rpm. The speed, efficiency, torque, and weight values of both motors were examined comparatively. The torque/volume values of the hub motor and axial flux motor were used as references for analysis. The hub motor and axial flux motors, with equal volume values, were simulated using ANSYS Electronics Desktop software. The simulation data were also compared with experimental studies. To optimize these motors using a genetic algorithm (GA), lower and upper limit values were determined for various parameters such as the outer and inner diameter of the stator, the outer diameter of the rotor, air gap length, slot height, axial length, air gap flux density, magnet thickness, and tooth width in the hub motor. Similarly, in the axial flux motor, parameters such as the outer and inner diameter of the stator, air gap length, slot height, air gap flux density, magnet thickness, tooth width, stator length, and rotor length were optimized using the GA method. The application of GA optimization has led to a 1.91% increase in the hub motor efficiency and a 3.45% increase in the axial motor efficiency.*

## 1. Introduction

Recently, BLDC motors are preferred mostly in automotive, home applications, and electric vehicles (EV) due to their high torque, wide speed region, high efficiency, and low maintenance requirement. Researchers are continuously studying ways to maximize the efficiency of electric motors in order to enable EVs to travel longer distances on a single charge, as the efficient use of battery energy is crucial [1]–[5]. Like other motors, BLDC motors consist of two main parts: a stator and a rotor. Generally, a stator, which is the fixed part, is located on the outside, while the rotor, the rotating part, is inside. However, due to the geometric shape of the rotor and the structure of the magnets, BLDC motors are manufactured in a way where the rotor is on the outer part and the stator is on the inner part, as it affects the torque and efficiency [6], [7]. In order to achieve high efficiency and

high torque improvements the geometric structure of the BLDC motor is studied increasingly. In addition, features such as the winding method, pole type, and magnet type are also examined during the design phase[8]. The rotor design and optimization of the 10 KW BLDC motor with the desired torque and speed have been carried out in [9], considering the effect of rotor design on BLDC motor performance is effective on torque, speed, and efficiency. To optimize the two-wheel electric motor in terms of required torque, speed, size, mass, and cost, the effect of the air gap length on the efficiency was investigated between the determined mere limited values. In addition, the effect of stator inner diameter change on efficiency and torque was analyzed [10], [11]. Due to the increasing demand for energy and concerns about environmental pollution, the popularity of EVs has been on the rise. Among equivalent motors, BLDC motors are preferred due to their robustness, high efficiency, high power density, and wide

<sup>\*</sup>Corresponding Author: Ozturk Tosun, [ozturktosun@marun.edu.tr](mailto:ozturktosun@marun.edu.tr)

constant power operation range. The use of NdFeB as a PM magnet in the rotor structure generally provides better performance compared to SmCo, AlNiCo, and Ceramic magnets[12]. Although induction motors are commonly used in electric vehicles today, their large size results in high magnetic losses and limited efficiency (around 85%). BLDC motors, on the other hand, are preferred for their high efficiency and environmentally friendly operating conditions[13]. Cogging torque is one of the major limitations of PM motors, and efforts during the design phase aim to reduce it[14], [15]. Different results in terms of efficiency, torque, torque density, and power density can be achieved between axial flux BLDC motors and radial flux BLDC motors using the same materials [16].

In this study, we compared the outer rotor and axial flux BLDC motors, taking the torque/volume ratio as a reference. These motors are illustrated in the 3D general schematics in Figure 1(b) and (c) respectively. The axial flux and hub BLDC motors were simulated using Ansys Electronics Desktop software. Additionally, current values, speed, and the torque of both motors were simultaneously investigated experimentally to validate the results obtained from the simulation environment. The study focused on examining efficiency speed, torque-time characteristics, air gap flux, and magnetic flux density distribution. By determining low and high limit values for the parameters that define the geometry of both motors, efficiency optimization was performed using the genetic algorithm method. Furthermore, adaptive multiple objectives were utilized for efficiency optimization in both motors.

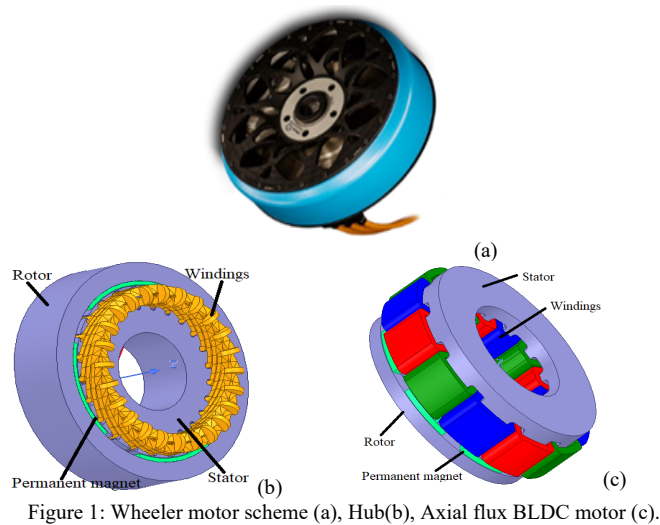


Figure 1: Wheeler motor scheme (a), Hub(b), Axial flux BLDC motor (c).

## 2. Design Analysis of Hub and Axial BLDC Motor

Geometric measurements of the Axial Flux and Hub BLDC motor were taken and the design was realized with the help of the Ansys/RMxpert package program. Efficiency, speed, torque, material consumption, and no-load flux density values were analyzed. Efficiency-speed curve, torque-time curve, and flux density distribution were observed with Ansys Maxwell 2D [17]. The specification of the axial flux and outer rotor BLDC motor are displayed in Table 1.

Table 1: Hub and axial flux BLDC motor specification.

Definition	Axial	Hub
Nominal Power	10 KW	1 KW
Nominal Voltage	72 V	50 V
Slot Numbers	12	18
Pole Numbers	8	24
Axial length	115.5 mm	33.7 mm
Thickness of Magnet	4 mm	4 mm
Length of the air gap	0.75 mm	0.75 mm
Nominal Speed	4550 rpm	300 rpm
Torque/volume	0.01 Nm/cm <sup>3</sup>	0.01 Nm/cm <sup>3</sup>

The hub BLDC motor has a unique design where the rotor is positioned outside and the stator is inside, which is the opposite of classical motors. The volume of the motor is determined by factors such as the inner and outer diameters of the stator, the length of the air gap, the thickness of the magnet, the inner and outer diameters of the rotor, and the axial length of the motor. On the other hand, the volume of the axial flux BLDC motor is determined by factors such as the length of the stator axial, length of the magnet axial, length of the rotor axial, and length of the air gap, in addition to the outer and inner diameters of the stator and the outer and inner diameters of the rotor. Based on these measurements and analytical calculations, simulations were conducted in the ANSYS/Maxwell software package for both motor designs[17]. The torque, speed, current, and efficiency values of the hub BLDC motor were investigated in both the simulation program and the experimental environment. The torque/volume (Nm/cm<sup>3</sup>) ratio of both motors was compared with the reference. In Figure 2(a), the motor identifications of the hub motor; Dro, Dri, Dso, Dsi, bts (thickness of tooth), and hs (height of slot) are shown. In Figure 2(b), the motor identifications of the axial flux motor, such as the length of the rotor (Lr), the length of the stator (Ls), the thickness of the magnet (lm), the length of the air gap (g), the height of the slot (hs), and the thickness of the tooth (bts), are indicated.

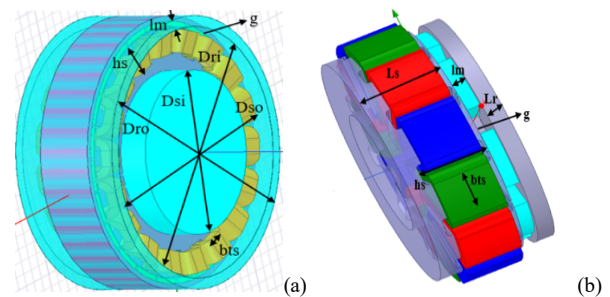


Figure 2: 3D view of hub motor and (a), 3D view of axial flux BLDC motor parameters (b).

Axial flux and hub BLDC motor having equal torque density have been compared. The advantages and disadvantages of these motors, which have different output powers and rated speeds, have been examined in terms of weight and volume. The outer diameter of the hub BLDC motor was calculated in Equation (1). The outer diameter (Dro) of the hub BLDC motor is affected by the stator outer diameter (Dso), magnet thickness (lm), air gap length (g), and rotor yoke height (hry), which is in the radial direction.

$$D_{ro} = D_{so} + 2g + 2l_m + 2h_{ry} \quad (1)$$

In Equation (2), the axial length of the axial flux BLDC motor was calculated. The axial length ( $L_{AF}$ ) of the axial flux BLDC motor affects the stator length ( $L_s$ ), rotor length ( $L_r$ ), magnet length ( $l_m$ ), and air gap length ( $g$ ), which is in the axial direction.

$$L_{AF} = L_r + 2L_s + 2g + 2l_m \quad (2)$$

The air gap length of the axial flux and hub BLDC motors were kept equal. The torque density was given in (3). Torque density for the axial flux and hub BLDC motor are  $0.01 \text{ Nm/cm}^3$ .

$$\text{Torque density} = T / (\pi(D_{ro} / 2)^2 L) \quad (3)$$

where  $T$  is the nominal torque.

The efficiency of the Axial flux and the hub BLDC motor was comparatively examined with respect to torque/volume. The parameters and calculation methods that influence the efficiency of both motors are the same. The input power applied to both motors is determined by the sum of the output power, friction and windage losses, copper losses, and core losses. Since the magnets on the rotor provide a constant flux source, there is no generation of a rotating magnetic field, and thus, core losses on the rotor are neglected. The losses are calculated in the iron core where the stator windings are located. In this case, the size of the stator volume and the characteristics of the ferromagnetic material affect the core losses. The same type of steel is used in both motors. Copper losses are dependent on the winding currents used in the stator slots and the electrical resistance of these windings. The phase resistance is determined by the cross-sectional area and length of the conductor. To determine the length of the conductor, parameters such as the stator's outer diameter, slot height, number of slots, and slot pitch need to be considered. Friction and windage losses are assumed to be 1% of the rated power of the motors [17]. Motor efficiency is calculated as the ratio of output power to input power. The output power is obtained by subtracting copper losses, core losses, friction losses, and windage losses from the input power. The axial flux motor consists of two stators and a single rotor with magnets on both sides. Each stator package has a length of 48 mm. The outer diameter of the stator and rotor core is 150 mm, and the inner diameter is 80 mm. The stator windings have 14 conductors per slot with a conductor diameter of 2.58 mm. It has a two-layer winding and a whole-coil winding type. There are 2 parallel branches. The number of slots is 12. The rotor package length is 10 mm. The magnet thickness is 4 mm, and the radial length of the magnet is 34 mm. The number of magnet poles is 8.

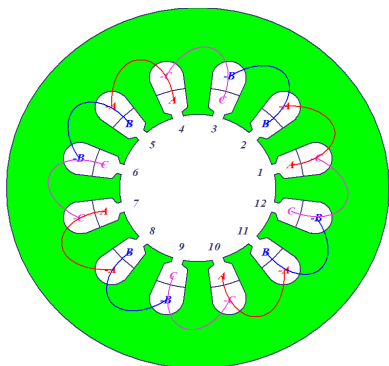


Figure 3: Axial flux BLDC motor winding type

Stator wire density, stator core steel density, rotor core steel density, and rotor magnet density are  $8900 \text{ kg/m}^3$ ,  $7820 \text{ kg/m}^3$ , and  $7500 \text{ kg/m}^3$ , respectively. The net steel weight in the axial motor stator core is 8.53 kg. Rotor net steel weight is 2.39 kg, magnet weight is 0.51 kg, and stator copper weight is 2.74 kg.

The hub motor is in a structure with the stator, which is the fixed part, in the inner part, and the rotor, which is the rotating part, in the outer part. The outer diameter of the stator core is 195 mm and the inner diameter is 128 mm. The number of conductors per slot in the stator windings is 42 and the conductor diameter is 2,304 mm. The two-layer winding and winding types are whole-coiled. The number of parallel branches is 1. The number of stator slots is 18. The rotor has an outer diameter of 213 mm and an inner diameter of 196.5 mm. The package length of the rotor is 33.7 mm. Magnet thickness is 4 mm.

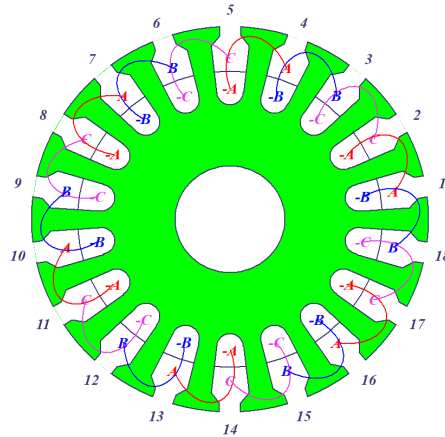


Figure 4: Hub BLDC motor winding type

Stator wire density, stator core steel density, rotor core steel density, and rotor magnet density are  $8900 \text{ kg/m}^3$ ,  $7820 \text{ kg/m}^3$ , and  $7500 \text{ kg/m}^3$ , respectively. The net steel weight in the axial motor stator core is 2.51 kg. Rotor net steel weight is 0.65 kg, magnet weight is 0.44 kg, and stator copper weight is 1.59 kg.

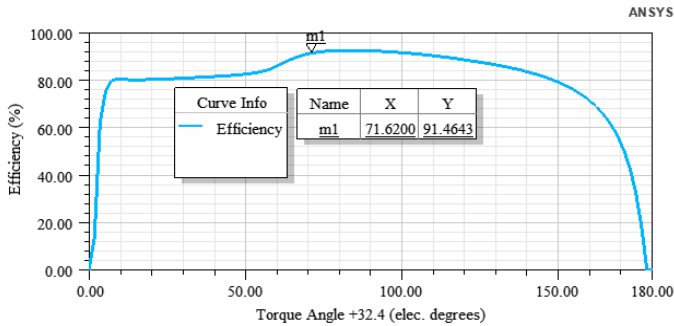
D23\_50 steel was preferred for the selection of ferromagnetic material in the stator and rotor core. It has been determined that there is an N42H magnet as the flux source in the rotor[18], [19]. The simulation outcomes for the hub BLDC motor are presented in Table 2.

Table 2: Axial and hub BLDC motor simulation results

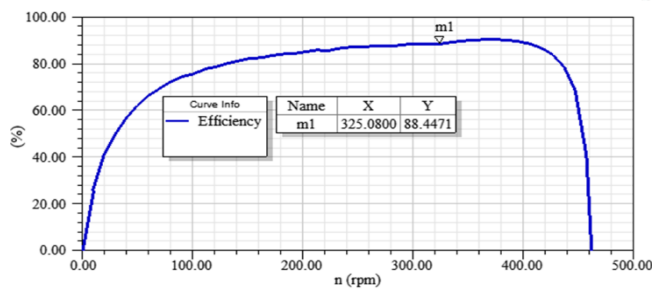
Definitions	Axial	Hub
Efficiency	91.461%	88.441%
Nominal torque	20.991 Nm	22.621 Nm
Nominal speed	4550 rpm	325 rpm
The flux density of stator yoke	1.431 T	1.061 T
The flux density of rotor yoke	1.351 T	2.171 T
The flux density of air gap	0.781 T	0.881 T
Total weight	22.50 Kg	5.21 Kg

Figure 5(a) presents the efficiency-speed curve of the hub BLDC motor, while Figure 5(b) displays the efficiency-torque angle of the axial flux BLDC motor.

Based on the simulation results obtained from the Ansys/RMxpert program, the hub BLDC motor exhibited an efficiency of 88.44% with a rated speed of 325 rpm. Similarly, the axial flux BLDC motor demonstrated an efficiency of 91.46% at the rated speed of 4550 rpm.



(a)



(b)

Figure 5: (a) Axial flux Efficiency Vs Torque (b) Hub BLDC motor Efficiency vs speed.

Figure 6 shows the axial flux BLDC motor flux density of the air gap curve. The air gap has an average flux density of 0.78 Tesla.

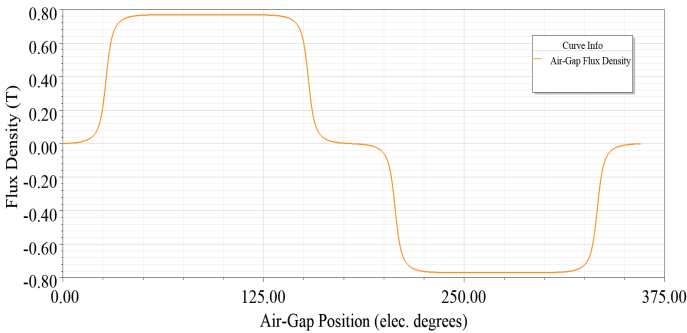


Figure 6: Axial flux BLDC motor air gap flux density

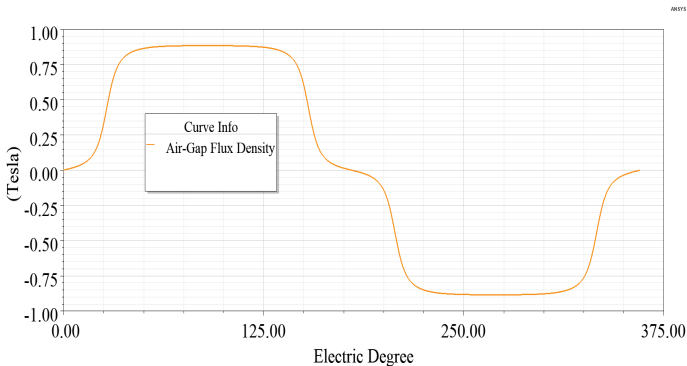


Figure 7: Hub BLDC motor air gap flux density.

Figure 7 shows the hub BLDC motor flux density of the air gap curve. The air gap has an average flux density of 0.88 Tesla. As seen in Figures 6 and 7, It has been aimed and composed that the flux density of the air gap was satisfactorily and uniformly distributed in both motors. Figure 8 shows the hub BLDC motor moving torque curve. The torque ripple value is 38 %.

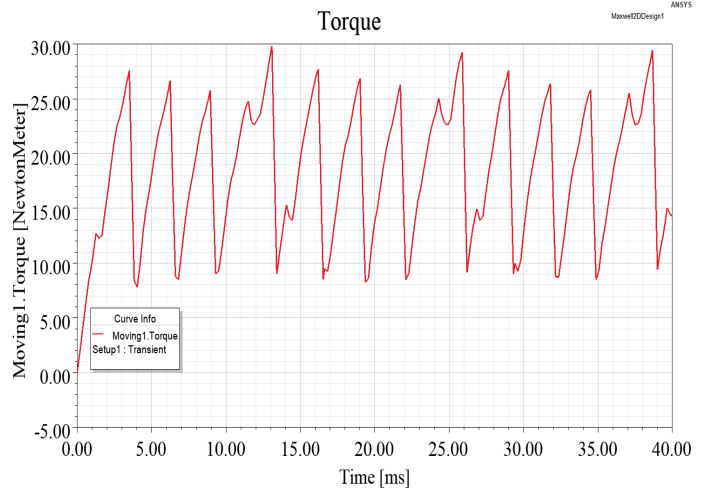


Figure 8: Hub BLDC motor moving torque

Figure 9 shows the axial flux BLDC motor moving torque curve. The torque ripple value is 28%.

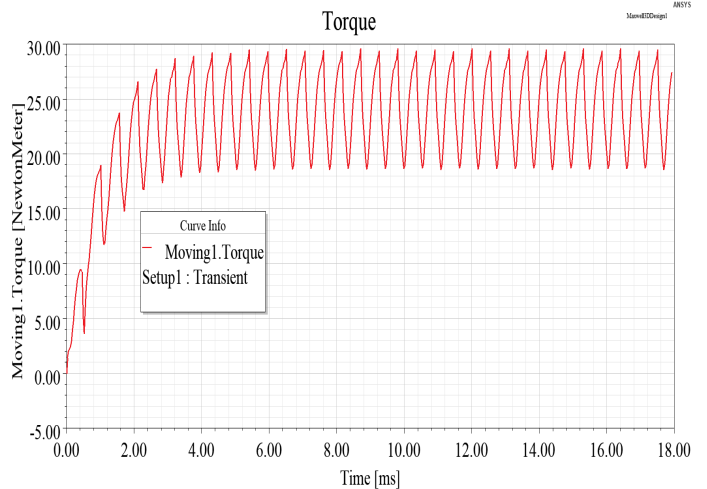


Figure 9: Axial flux BLDC motor moving torque

In Figure 10, the flux distribution of hub (a) and axial flux(b) BLDC motor has shown.

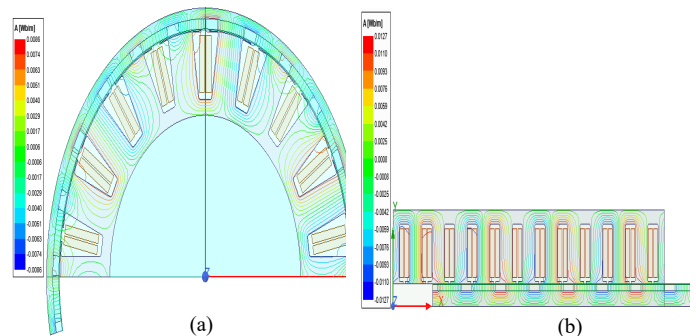


Figure 10: Flux distribution (a) Hub, (b) Axial flux BLDC motor

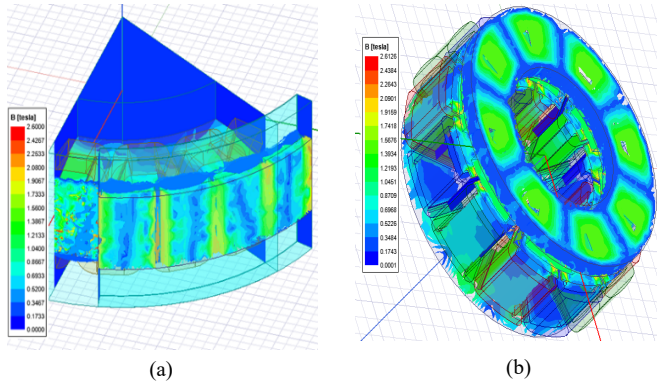


Figure 11: (a) Hub and (b) Axial flux BLDC motor flux density.

The flux distribution of the hub motor and the axial motor is shown in Figure 11. The dominant colors on the stator surface and stator inner were obtained as blue and green. This shows that the steel material used in the core doesn't reach the saturation point. Both motors operate in efficient conditions. In Figure 11(a), the hub motor flux density of stator teeth is 1.43 T, the flux density of the stator core is 0.72 T, the flux density of the rotor core is 2.16 T, the flux density of the air gap is 0.88 T, the magnet flux density is 0.91 T. In Figure 11(b), the axial flux BLDC motor flux density of stator teeth is 1.56 T, the flux density of stator core is 1.40 T, the flux density of rotor core is 1.33 T, the flux density of air gap is 0.77 T, and the magnet flux density is 0.82 T.

### 3. Axial Flux and Hub BLDC Motor Experimental Studies

The stator windings of the axial flux and hub BLDC motor are connected in a 3-phase-star configuration. These motors are powered by a DC voltage source using a PWM trapezoidal strategy and inverters. At any given time, current flows through only two of the stator phase windings. Figure 12 illustrates the experimental setup.

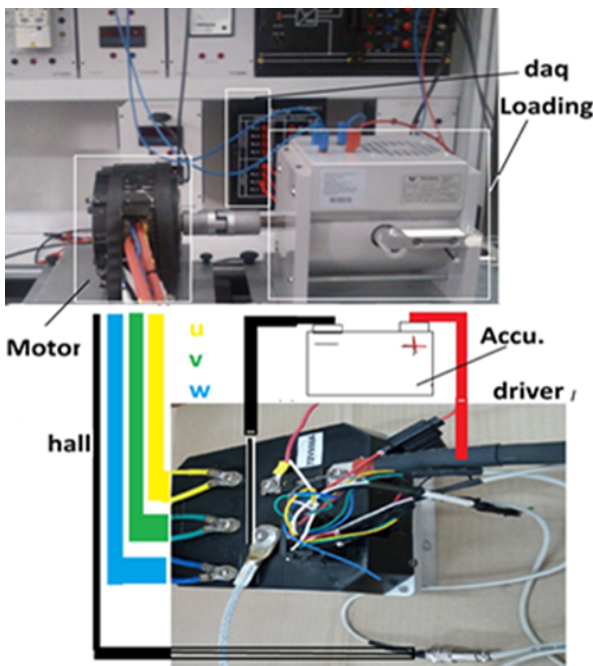


Figure 12: Axial Flux BLDC Motor Experimental Setup

The operating voltage of the axial flux BLDC motor is 72 volts. It has a 3-phase distributed winding structure. It is controlled by the chopped current control method. The maximum current level is 30 A, minimum current level is 10 A. It is fed with a direct current source. Voltage is applied to the stator windings through sensors that determine the rotor position. The direct current motor (25 Nm) has been coupled to the shaft of the axial motor as a load. As a result of the experiment, torque, current and speed values were measured. The efficiency value was determined according to these values. In Figure 13, the experiment results of the speed curve versus the efficiency of the axial flux motor are given.

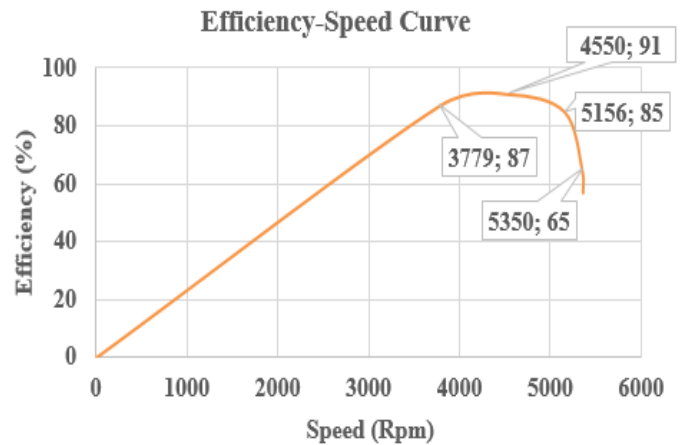


Figure 13: The efficiency-to-speed curve of the axial flux BLDC motor.

Table 3 presents the simulation and experimental results for the axial flux motor. The simulation results show a high level of agreement with the experimental results.

Table 3: Experimental and Simulation Results Of Axial Flux BLDC Motor.

Axial Flux Motor	Efficiency (%)	Current(A)	Torque (Nm)
Simulation results	91.46	149	20.99
Experiment results	91	140	19.36

In the experimental study for the hub motor, the control type is DC. Similar to an axial motor, voltage is applied sequentially to the stator windings. The operating voltage of the hub motor is set at 50 Volts.



Figure 14: Experimental Setup of Hub BLDC Motor.



In Figure 15, the experiment results of the efficiency-speed curve of the hub BLDC motor are given.

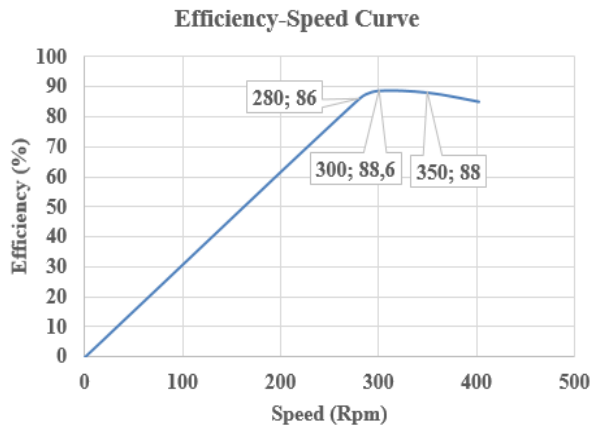


Figure 15: Hub BLDC Motor Experiment Efficiency-Speed Curve

The experimental and simulated outcomes for the hub motor are presented in Table 4. The experimental results indicate an efficiency value that is 0.25% higher, a current value of 2.32 A, and a torque value of 0.82 Nm greater than the simulation data.

Table 4: Experiment and Simulation Results of Hub BLDC Motor

Hub BLDC Motor	Current (A)	Torque (Nm)	Efficiency (%)
Simulation results	18.18	22.62	88.44
Experiment results	20.5	23.44	88.69

In Table 5, the main advantages and disadvantages of both the axial flux BLDC motor and the hub BLDC motor are highlighted.

Table 5: Comparison of Axial Flux and Hub BLDC Motor

Motor Type	Power density	Speed	Torque/Weight	Efficiency
Axial Flux	+++	+++	+	+++
Hub	+	+	+++	++

+: normal; ++: medium; +++: high

#### 4. Optimization of Efficiency to Axial Flux BLDC Motor and Hub BLDC Motor using Genetic Algorithm

Genetic Optimization (GA) is basically a five-step process. In the first step, the population of the problem to be solved is created. In the second step, the fitness value is calculated for each individual. In the third step, the selection is made using methods such as the roulette wheel and the tournament method. In this study, the roulette wheel selection method has been applied. Afterward, the crossover operation is performed on the chromosomes of the newly generated individuals. By applying the mutation operator to the resulting individual, an individual with better characteristics is obtained. The GA process continues until the best solution to the problem is found[20]. Table 6 shows the Axial Flux and Hub BLDC motor's constant parameters.

Table 6: Axial Flux BLDC Motor and Hub BLDC Motor Constants

Motor Type	B <sub>sy</sub> (T)	B <sub>ry</sub> (T)	B <sub>t</sub> (T)	E <sub>ph</sub> (V)	T(Nm)	N(rpm)
Axial Flux	1.6	1.4	1.6	36	20.99	4550
Hub	1.6	1.4	1.6	25	22.62	325

The variable parameters selected in the GA for the axial flux and hub BLDC motors are represented by equations (4) to (9). Equation (4) describes the electromechanical power of both motors. Equation (5) defines the back emf generated by the windings specifically for the hub BLDC motor. Equation (6) represents its electromechanical torque. In Equation (7), the flattop value of the back emf of phase is provided for the axial flux BLDC motor. Lastly, Equation (9) presents its electromechanical torque[21].

$$P_m = 2 \cdot E_{ph} \cdot I_p \quad (4)$$

Where  $P_m$  is induced output power,  $E_{ph}$  is the back emf by windings, and  $I_p$  is the current drawn from the DC power source.

$$E_{ph} = N_{ph} \cdot B_g \cdot D_{ri} \cdot \omega_m \quad (5)$$

Where,  $N_{ph}$  is the number of turns per phase,  $B_g$  the is magnetic flux density of the air gap,  $L$  is the axial length the of motor  $\omega_m$  is the angular speed, and  $D_{ri}$  is the diameter of inner of the hub motor.

$$T = 2 \cdot N_{ph} \cdot B_g \cdot D_{ri} \cdot L \cdot I_p \quad (6)$$

Where T is induced nominal torque.

In (7), (8), and (9) are about axial flux motor. Where  $R_o$ ,  $R_i$  are the inner and outer radius of the axial motor.

$$E_{ph} = N_{ph} \cdot B_g \cdot R_o^2 \cdot (1 - K_r^2) \cdot \omega_m \quad (7)$$

$$K_r = \frac{R_i}{R_o} \quad (8)$$

$$T = 2 \cdot N_{ph} \cdot B_g \cdot R_o^2 \cdot (1 - K_r^2) \cdot I_p \quad (9)$$

The GA was used to optimize the parameters affecting the efficiency of the hub BLDC motor and the axial flux BLDC motor. For the hub BLDC motor, variables such as the inner diameter of the stator, the outer diameter of the rotor, the length of the air gap, the height of the slot, the length of the motor axial, air gap flux density, magnet thickness, and tooth thickness were defined as optimization variables. The number of magnets, number of slots, conductors per slot, and conductor diameter were considered constant variables. Similarly, for the axial flux BLDC motor, variables such as the inner diameter of the stator, the outer diameter of the stator, the length of the air gap, the height of the slot, the axial length of the stator, the axial length of the rotor, air gap flux density, magnet thickness, and tooth thickness were defined as optimization variables, while the number of magnets, number of slots, conductors per slot, and conductor diameter were kept constant. The GA was implemented using codes created with the Delphi software package[22]. The optimization process involved defining the problem and evaluating the fitness value. A population of solutions was created, and the parameters affecting the efficiency of the motors were chosen as members of the population. The fitness value of each member in the population

was determined, and the selection process was carried out using the roulette wheel method. After selection, the crossover operator (with a probability of 0.90) was applied to generate new individuals, and mutation (with a probability of 0.01) was performed. The optimum efficiency value of the hub BLDC motor (90.35%) was achieved in the 30th iteration, while the optimum efficiency value of the axial flux BLDC motor (94.91%) was obtained in the 50th iteration. The new values resulting from the GA for the variable parameters of the hub BLDC motor are presented in the right column of Table 7. Similarly, the new values resulting from the genetic algorithm for the variable parameters of the axial flux BLDC motor are given in the right column of Table 8. The efficiency values obtained at the end of the GA process for both motors can be found in the last column of Table 7 and Table 8.

Table 7: Hub BLDC Motor Variables

Hub BLDC Motor	Low limits	Up limits	GA Results
The outer diameter of the stator	190 mm	196 mm	195 mm
The Inner diameter of the stator	122 mm	128 mm	125.27 mm
The outer diameter of the rotor	210 mm	215 mm	211.41 mm
Air gap length	0.5 mm	1.5 mm	1.449 mm
Height of slot	18 mm	25 mm	19.51 mm
Axial length	30 mm	35 mm	30.649 mm
The flux density of the air gap	0.201 T	1 T	0.8301 T
Thickness of magnet	3 mm	8 mm	4.919 mm
Thickness of tooth	3 mm	5 mm	4.7411 mm
Efficiency	88.441 %		90.351 %

Table 8: Axial Flux BLDC Motor Variables

Axial Flux BLDC Motor	Low limits	Up limits	GA Results
The outer diameter of the stator	145 mm	155 mm	145.28 mm
The inner diameter of the stator	76 mm	82 mm	81.81 mm
Air gap length	0.5 mm	1.5 mm	0.501 mm
Height of slot	32 mm	38 mm	35.33 mm
The flux density of the air gap	0.21 T	1 T	0.571 T
Thickness of magnet	3 mm	8 mm	3.359 mm
Thickness of tooth	3 mm	5 mm	3.149 mm
Length of stator	45 mm	55 mm	45.499 mm
Length of rotor	8 mm	13 mm	8 mm
Efficiency	91.461 %		94.911 %

### 5. The optimization of both the axial motor and hub motor using adaptive multiple objectives.

In the literature, there have been several studies focusing on the design optimization of BLDC motors using GA. These studies aim to achieve high efficiency and reduce torque ripple in classic BLDC motors[23]–[25]. In this particular section, the efficiency optimization is carried out using GA along with the adaptive multiple-objective method. For the axial flux BLDC motor, the variables considered are the stator outer diameter, stator inner diameter, stator axial length, rotor axial length, magnet thickness, and magnet radial length. The magnet pole number and stator slot number are kept constant throughout the optimization process.

Figure 16 illustrates the simulation values of efficiency plotted against the stator inner diameter (dsi) for the axial flux BLDC motor. At the highest efficiency point, the stator's inner diameter is determined to be 75.8627 mm, resulting in an efficiency value of 92.3493%.

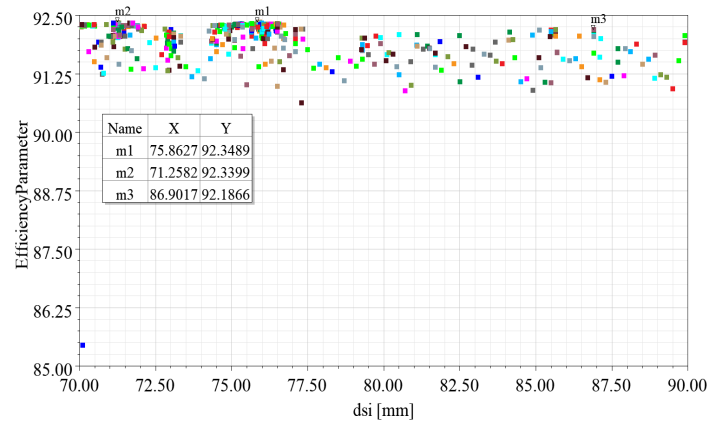


Figure 16. Axial flux BLDC motor efficiency-stator inner diameter)

The efficiency-stator outer diameter (dso) simulation values for the axial flux BLDC motor are given in Figure 17. At the highest efficiency (92.3493 %) point, the stator outer diameter is 156.3145 mm.

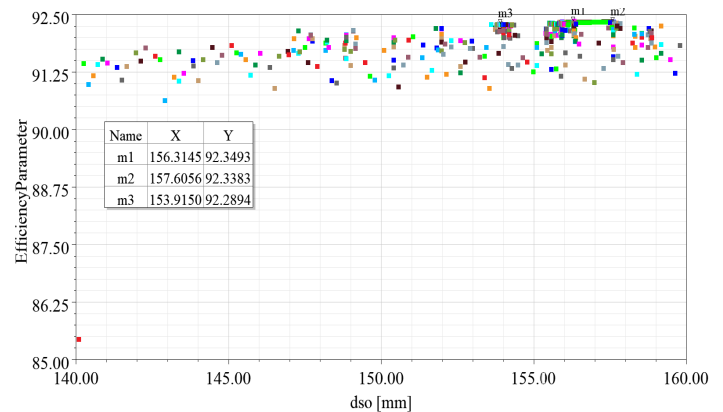


Figure 17. Axial flux BLDC motor efficiency-stator outer diameter

The efficiency-stator axial length (ls) simulation values for the axial flux BLDC motor are given in Figure 18. At the highest efficiency (92.3493 %) point, the stator axial length is 41.1670 mm.

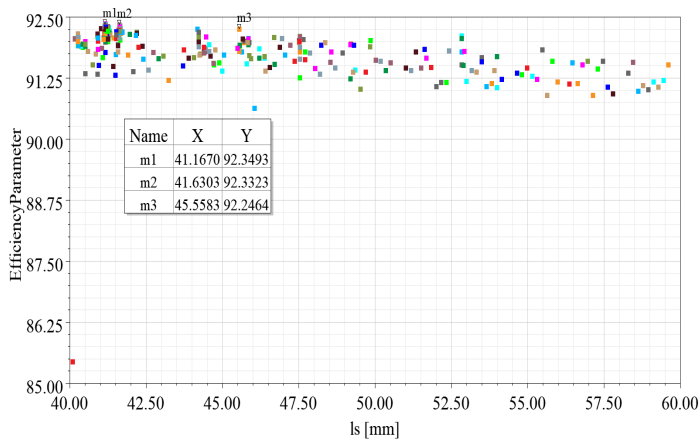


Figure 18. Axial flux BLDC motor efficiency-stator axial length

The efficiency-rotor axial length ( $l_r$ ) simulation values for the axial flux BLDC motor are given in Figure 19. At the highest efficiency (92.3493 %) point, the rotor axial length is 5.2167 mm.

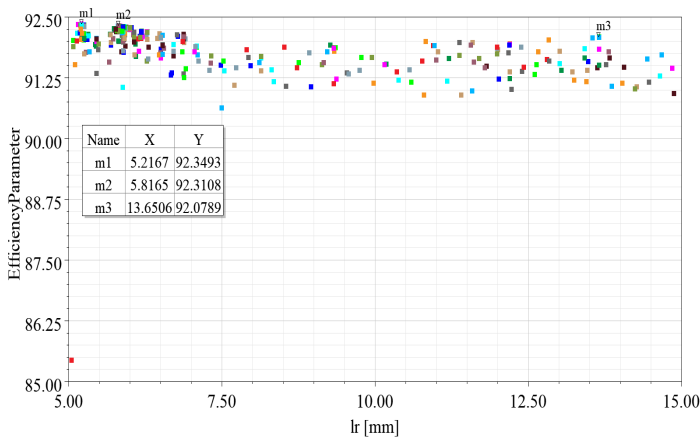


Figure 19. Axial flux BLDC motor efficiency-rotor axial length

The efficiency-magnet thickness ( $l_m$ ) simulation values for the axial flux BLDC motor are given in Figure 20. At the highest efficiency (92.3493 %) point, the magnet thickness is 4.5528 mm.

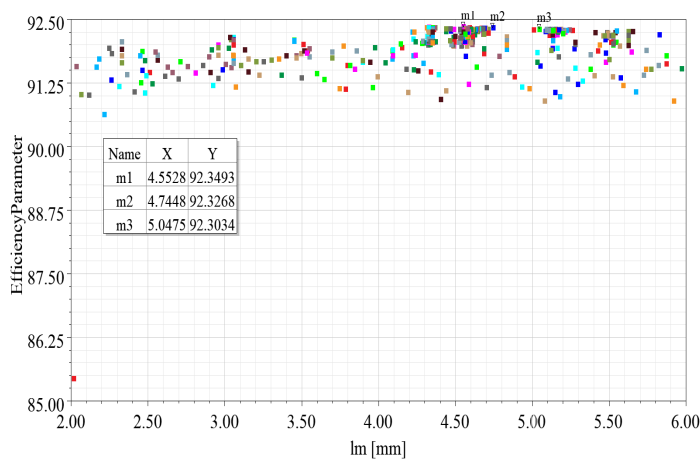


Figure 20. Axial flux BLDC motor efficiency-magnet thickness

The efficiency-magnet length ( $l_{mag}$ ) simulation values for the axial flux BLDC motor are given in Figure 21. At the highest efficiency (92.3493 %) point, the magnet length is 32.5770 mm.

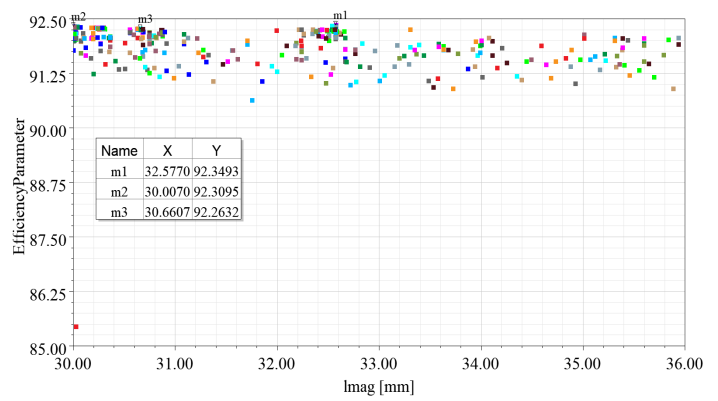


Figure 21. Axial flux BLDC motor efficiency- magnet length

In Figure 22, the highest efficiency value (92.3493 %) was obtained at the 982 th step according to the adaptive multiple objective optimizations.

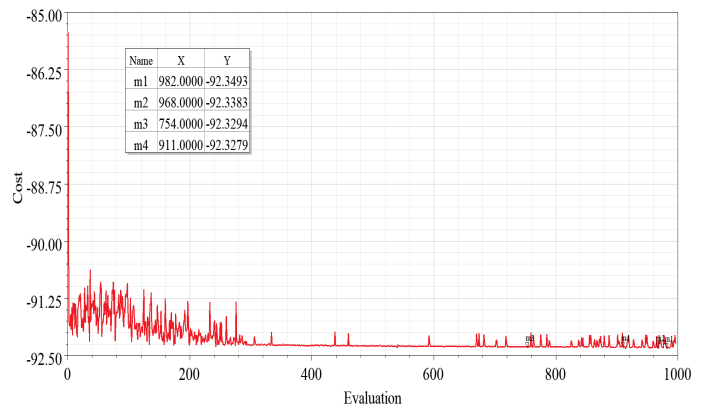


Figure 22. Axial flux BLDC motor adaptive multiple objective efficiency curve

The surface efficiency graph of the relationship between efficiency-output torque-stator outer diameter is given in Figure 23. Efficiency in the Z axis, output torque in the X axis, and stator outer diameter in the Y axis.

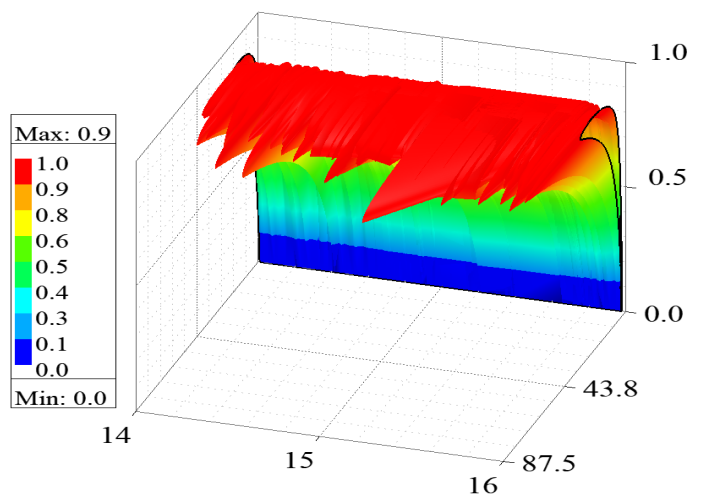


Figure 23. Axial flux BLDC motor efficiency-output torque-stator outer diameter

For the hub BLDC motor, outer diameter of stator, inner diameter of stator, axial length of stator, outer diameter of rotor, inner diameter of rotor, axial length of rotor, and thickness of

magnet are defined as variables. The number of magnet poles and the number of stator slots are fixed. The efficiency-stator outer diameter (dso) values obtained according to the simulation results for the hub motor are given in Figure 24. At the highest efficiency (89.1632 %) point, the stator outer diameter is 194.8250 mm.

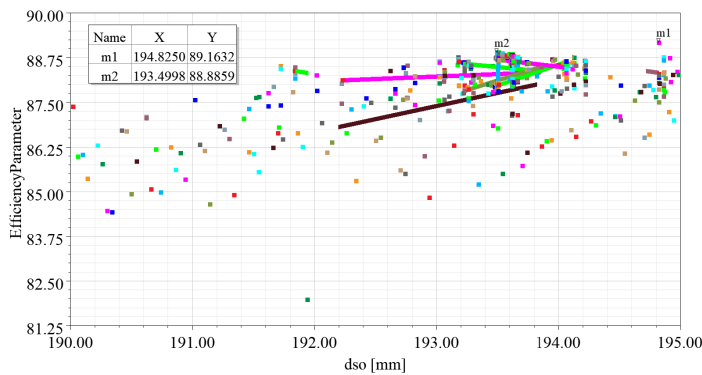


Figure 24. Hub BLDC motor efficiency-stator outer diameter

The efficiency-stator inner diameter (dsi) simulation values for the hub BLDC motor are given in Figure 25. At the highest efficiency (89.1632 %) point, the stator outer diameter is 126.0130 mm.

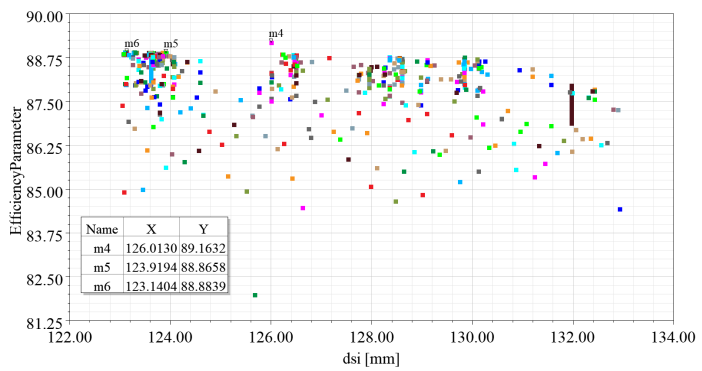


Figure 25. Hub BLDC motor efficiency-stator inner diameter

The efficiency-stator axial length (lsr) simulation values for the hub motor are given in Figure 26. At the highest efficiency (89.1632 %) point, the stator axial length is 32.0335 mm.

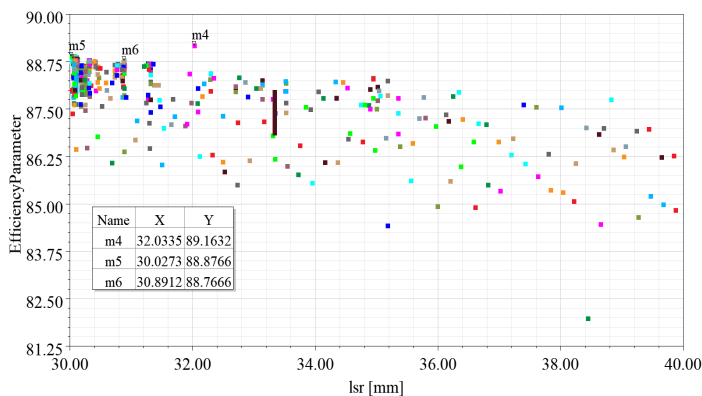


Figure 26. Hub BLDC motor efficiency-stator axial length

The efficiency-rotor outer diameter (dro) simulation values for the hub motor are given in Figure 27. At the highest efficiency (89.1632 %) point, the rotor outer diameter is 208.9875 mm.

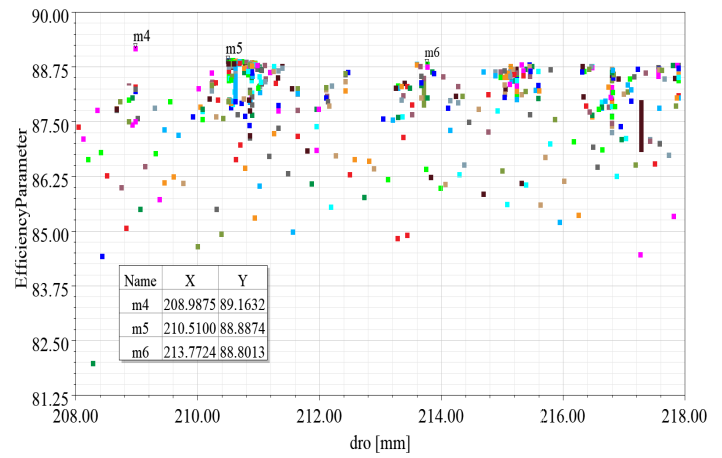


Figure 27. Hub BLDC motor efficiency-rotor outer diameter

The efficiency-magnet thickness (lm) simulation values for the hubBLDC motor are given in Figure 28. At the highest efficiency (89.1632 %) point, the magnet thickness is 3.9792 mm.

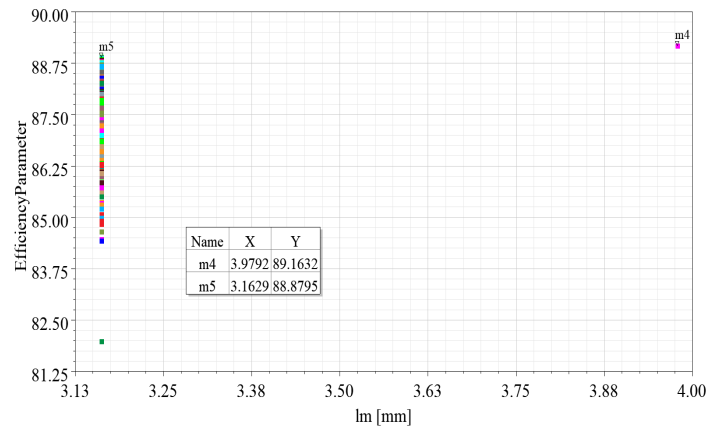


Figure 28. Hub BLDC motor efficiency-magnet thickness

The efficiency-rotor inner diameter (dri) simulation values for the hub motor are given in Figure 29. At the highest efficiency (89.1632 %) point, the magnet thickness is 197.7250 mm.

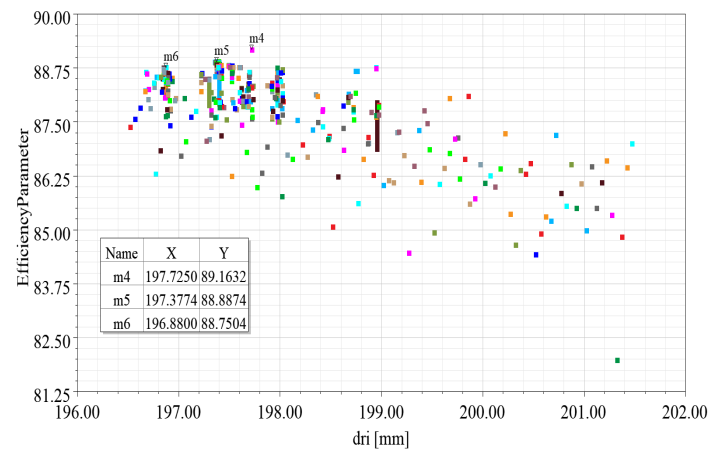


Figure 29. Hub BLDC motor efficiency-rotor inner diameter

In Figure 30, the highest efficiency value (89.1632 %) was obtained at the 878th step according to the adaptive multiple objective optimizations.

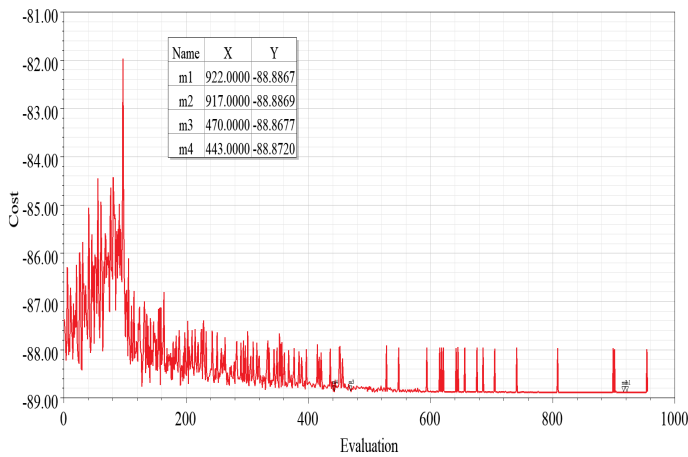


Figure 30: Hub BLDC motor adaptive multiple objective efficiency curve

## 6. Conclusions

In this study, the design and efficiency optimization of axial flux and hub BLDC motors were conducted through both theoretical (simulation) and experimental approaches. The main objective was to compare these two motor types and determine their suitability for light electric vehicles. The simulations were performed using the ANSYS/Maxwell package program, while the experimental data were collected to validate the simulation results. Parameters such as current, torque, speed, and efficiency were analyzed for both motor types. In the simulation environment, the axial flux BLDC motor achieved an efficiency of 91.46%, while the experimental results showed an efficiency of 91%. Similarly, the hub BLDC motor attained an efficiency of 88.44% in the simulation and 88.69% in the experimental setup. Furthermore, efficiency optimization was carried out using the GA method for both motor types, resulting in an efficiency of 94.91% for the axial flux BLDC motor and 90.35% for the hub BLDC motor. Additionally, adaptive multiple objective methods were employed to optimize the efficiency of both motor types, with the axial flux BLDC motor reaching the highest efficiency value of 92.3493% and the hub BLDC motor achieving 89.1632%. This comparative experimental study provides valuable insights for researchers working on light electric vehicle applications.

## Conflict of Interest

The authors declare no conflict of interest.

## Reference

- [1] K. T. Chau, C. C. Chan, C. Liu, "Overview of permanent-magnet brushless drives for electric and hybrid electric vehicles," *IEEE Transactions on Industrial Electronics*, **55**(6), 2246 - 2257, 2008, doi: 10.1109/TIE.2008.918403.
- [2] K. Toker, O. Tosun, N. F. O. Serteller, V. Topuz, "Design, Optimization and Experimental Study of Axial and Hub BLDC Motors in-Wheel Application for Light Electric Vehicles," in *MELECON 2022 - IEEE Mediterranean Electrotechnical Conference, Proceedings*, 2022, doi: 10.1109/MELECON53508.2022.9842975.
- [3] A. Eldho Aliasand, F. T. Josh, "Selection of Motor foran Electric Vehicle: A Review," in *Materials Today: Proceedings*, **24**(3), 1804-1815, 2020, doi: 10.1016/j.matpr.2020.03.605.
- [4] J. A. Sanguesa, V. Torres-Sanz, P. Garrido, F. J. Martinez, J. M. Marquez-Barja, "A review on electric vehicles: Technologies and challenges," *Smart Cities*, **4**(1), 372-404, 2021, doi: 10.3390/smartcities4010022.
- [5] D. Murgoci, M. Adam, "Research on the Influence of the Nominal Current on the Torque and Respectively on the Efficiency for the BLDC Motor with Variable Geometry," in *EPE 2022 - Proceedings of the 2022 12th International Conference and Exposition on Electrical and Power Engineering*, 610 - 616, 2022, doi: 10.1109/EPE56121.2022.9959742.
- [6] H. S. Shin, K. H. Shin, G. H. Jang, S. K. Cho, K. H. Jung, J. Y. Choi, "Experimental Verification and 2D Equivalent Analysis Techniques of BLDC Motor with Permanent Magnet Overhang and Housing-Integrated Rotor Core," *IEEE Transactions on Applied Superconductivity*, **30**(4), 1-5, 2020, doi: 10.1109/TASC.2020.2972233.
- [7] F. Messine, B. Nogarede, J. L. Lagouanelle, "Optimal design of electromechanical actuators: A new method based on global optimization," *IEEE Trans Magn*, **34**(1), 299 - 308, 1998, doi: 10.1109/20.650361.
- [8] M. Akar, M. Eker, F. Akın, "BLDC Motor Design and Application for Light Electric Vehicle," *Afyon Kocatepe University Journal of Sciences and Engineering*, **21**(2), 326-336, 2021, doi: 10.35414/akufemubid.889877.
- [9] O. Tosun, N. F. O. Serteller, "The Design of the Outer-Rotor Brushless DC Motor and an Investigation of Motor Axial-Length-to-Pole-Pitch Ratio," *Sustainability (Switzerland)*, **14**(19), 2022, doi:10.3390/su141912743.
- [10] A. Vadde, S. Sachin, "Influence of Rotor Design in BLDC Motor for Two-Wheeler Electric Vehicle," in *ICPEE 2021 - 2021 1st International Conference on Power Electronics and Energy*, 1-6, 2021, doi: 10.1109/ICPEE50452.2021.9358520.
- [11] S. Tripathi, M. Gumma, and S. R. Potarlanka, "Virtual design optimization of a BLDC motor for a two wheeler electric cargo vehicle," in *2022 2nd Asian Conference on Innovation in Technology*, 1-6, 2022, doi: 10.1109/ASIANCON55314.2022.9909490.
- [12] M. Toren, "Comparative analysis of the magnet effects on the permanent magnet BLDC motor performance used in electric vehicles," *Electrical Engineering*, **104**(5), 3411-3423, 2022, doi: 10.1007/s00202-022-01536-1.
- [13] P. Chandran, K. Mysamy, P. Umopathy, "Conceptual Design and Material Analysis of BLDC Motor Using FEA Tools for Electric Vehicle Applications," *Tehnicki Vjesnik*, **29**(3), 1010-1018, 2022, doi: 10.17559/TV-20210425201219.
- [14] A. N. Patel, B. N. Suthar, "Double layer magnet design technique for cogging torque reduction of dual rotor single stator axial flux brushless dc motor," *Iranian Journal of Electrical and Electronic Engineering*, **16**(1), 58-65, 2020, doi: 10.22068/IJEEE.16.1.58.
- [15] E. Yesilbag, Y. Ertugrul, L. Ergene, "Axial flux PM BLDC motor design methodology and comparison with a radial flux PM BLDC motor," *Turkish Journal of Electrical Engineering and Computer Sciences*, **25**(4), 3455-3467, 2017, doi: 10.3906/elk-1611-23.
- [16] K. D. Prasetyo, M. N. Yuniarto, "Design and Performance Test of Axial Halbach Brushless DC Motor with Power Density 1.5 Kw/Kg," *Jurnal Teknik ITS*, **5**(2), 664-667, 2017, doi: 10.12962/j23373539.v5i2.20658.
- [17] A. S. Cabuk, S. Saglam, Ö. Üstün, "Investigation on efficiency of in-wheel BLDC motors for different winding structures," *Journal of the Faculty of Engineering and Architecture of Gazi University*, **34**(4), 1975-1985, 2019, doi: 10.17341/gazimmfd.571649.
- [18] O. Tosun, N. F. O. Serteller, G. Yalcin, "Comprehensive Design and Optimization of Brushless Direct Current Motor for the Desired Operating Conditions," in *Proceedings of the 2021 25th International Conference Electronics, ELECTRONICS 2021*, 1-6, 2021, doi: 10.1109/IEEECONF52705.2021.9467459.
- [19] M. Çunkaş, R. Akkaya, "Design optimization of induction motor by genetic algorithm and comparison with existing motor," *Mathematical and Computational Applications*, **11**(3), 193-203, 2006, doi: 10.3390/mca11020193.
- [20] P. R. Upadhyay, K. R. Rajagopal, "Genetic algorithm based design optimization of a permanent magnet brushless dc motor," in *Journal of Applied Physics*, **97**(10), 10Q516, 2005, doi: 10.1063/1.1860891.
- [21] Y. Sun, M. Li, C. Liao, "Analysis of wheel hub motor drive application in electric vehicles," in *MATEC Web of Conferences*, **100**(4), 1-6, 2017, doi: 10.1051/mateconf/201710001004.

- [22] D. Bruellmann, S. Sander, I. Schmidtman, "The design of an fast Fourier filter for enhancing diagnostically relevant structures - endodontic files," *Comput Biol Med*, **72**, 212-217, 2016, doi: 10.1016/j.combiomed.2016.03.019.
- [23] M. Markovic, Y. Perriard, "Simplified design methodology for a slotless brushless DC motor," *IEEE Trans Magn*, **42**(12), 3842 - 3846, 2006, doi: 10.1109/TMAG.2006.884108.
- [24] M. Markovic, P. Ragot, Y. Perriard, "Design optimization of a BLDC motor: A comparative analysis," in *Proceedings of IEEE International Electric Machines and Drives Conference, IEMDC 2007*, **2**, 1520-1523, 2007, doi: 10.1109/IEMDC.2007.383653.
- [25] P. K. Shahri, V. Izadi, A. H. Ghasemi, "Design a High Efficiency and Low Ripple BLDC Motor Based on Multi-Objective Optimization Methods," in *Proceedings of the American Control Conference*, 156-161, 2020, doi: 10.23919/ACC45564.2020.9147907.